



Terms and Conditions of Use of Digitised Theses from Trinity College Library Dublin

Copyright statement

All material supplied by Trinity College Library is protected by copyright (under the Copyright and Related Rights Act, 2000 as amended) and other relevant Intellectual Property Rights. By accessing and using a Digitised Thesis from Trinity College Library you acknowledge that all Intellectual Property Rights in any Works supplied are the sole and exclusive property of the copyright and/or other IPR holder. Specific copyright holders may not be explicitly identified. Use of materials from other sources within a thesis should not be construed as a claim over them.

A non-exclusive, non-transferable licence is hereby granted to those using or reproducing, in whole or in part, the material for valid purposes, providing the copyright owners are acknowledged using the normal conventions. Where specific permission to use material is required, this is identified and such permission must be sought from the copyright holder or agency cited.

Liability statement

By using a Digitised Thesis, I accept that Trinity College Dublin bears no legal responsibility for the accuracy, legality or comprehensiveness of materials contained within the thesis, and that Trinity College Dublin accepts no liability for indirect, consequential, or incidental, damages or losses arising from use of the thesis for whatever reason. Information located in a thesis may be subject to specific use constraints, details of which may not be explicitly described. It is the responsibility of potential and actual users to be aware of such constraints and to abide by them. By making use of material from a digitised thesis, you accept these copyright and disclaimer provisions. Where it is brought to the attention of Trinity College Library that there may be a breach of copyright or other restraint, it is the policy to withdraw or take down access to a thesis while the issue is being resolved.

Access Agreement

By using a Digitised Thesis from Trinity College Library you are bound by the following Terms & Conditions. Please read them carefully.

I have read and I understand the following statement: All material supplied via a Digitised Thesis from Trinity College Library is protected by copyright and other intellectual property rights, and duplication or sale of all or part of any of a thesis is not permitted, except that material may be duplicated by you for your research use or for educational purposes in electronic or print form providing the copyright owners are acknowledged using the normal conventions. You must obtain permission for any other use. Electronic or print copies may not be offered, whether for sale or otherwise to anyone. This copy has been supplied on the understanding that it is copyright material and that no quotation from the thesis may be published without proper acknowledgement.

**DEVELOPMENT AND VERIFICATION OF YIELD
SURFACES FOR I-SECTIONS**

**By
Afaq Shoaib**

Thesis submitted to the University of Dublin, Trinity College,
for the Degree of Doctor of Philosophy

April 2009

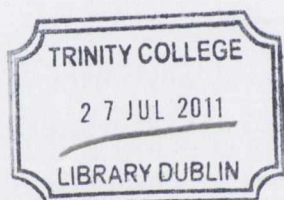


Department of Civil, Structural and Environmental Engineering
University of Dublin, Trinity College
Dublin, Ireland

DECLARATION

The author hereby declares that this thesis, in whole or in part, has not been submitted to any other university as an exercise for a degree. Except where reference has been given in the text, it is entirely the author's own work.

The author confirms that the Library may lend or copy the thesis upon request, for academic purposes.



THESIS
9263



ABSTRACT

In the design of many building structures for ultimate states the use of interaction equations is quite common. Despite this there is still a need for more advanced and flexible equations which consider all forces in space. Steel I-section members are often employed as beam and column elements for both structural and aesthetic reasons. The purpose of this thesis is to develop, in principle, the interaction equations for I-sections and verify it using experimental and finite element techniques. Two types of interaction equations are developed. One is the approximate approach in which single equation interaction equation is developed for biaxial bending moment and bimoment. The yield surface developed based on this approach fills the large gap in the previously developed yield surface. Second is the exact solution in which interaction equations for biaxial bending, biaxial shear, axial force, uniform torsion and bimoment are developed. This exact solution results in an improved, closed, continuous and convexed yield surface for an I-section. These two types of interaction equations are verified using a series of experiments and numerically using finite element analysis using software LUSAS.

The development of the interaction equation using approximate approach provided the opportunity for practical applicability of these equations using the available British steel sections. In the development the variation in the yield surface was explained by consideration of the governing equations and possible neutral-axis patterns. Later the developed approximate approach was compared with a limited previously published yield surface model and good correlation was found between them. The developed approximate approach was verified and extended using finite element analysis and simplified using a curve fitting technique.

The development of the interaction equation using exact solution was based on a lower bound theorem of limit analysis. They were developed for biaxial bending, biaxial shear, axial force, uniform torsion and warping torsion. In the development both the direct stresses and shear stresses acting on the sections were treated separately. A procedure is developed in which neutral-axis patterns were first obtained and later used in the development of interaction equation, its yield surface and a procedure to identify the formation of plastic hinge. The solution obtained by a lower bound approach was verified using an upper bound approach. Both solutions match each other which show that the equations satisfy the uniqueness theorem of plasticity thereby furnishing the correct yield surface within the limits of validity of the assumptions made.

The experimental program included in this research was designed to verify the yield surfaces and included both beam flexural tests and torsional test for single forces (which provided the necessary information on the capacities of sections). Two types of tests were carried out when more than one force are considered. In the first case biaxial bending and torsional loads are applied, whereas in the second case a unique experiment in which axial force, biaxial bending and torsion are applied. The test provided vital information on the response which helped to better understanding the phenomena of bending and torsion when applied simultaneously. A special test

rig was designed purposely to rotate beam sample up to a rotation of 180° to observe the effects of torsion and other forces at such a large rotation.

The finite element analyses of the experiments were performed under a non-linear monotonic loading condition. Following the pattern of the experiments, first forces and then multidimensional forces were analysed. A special analysis was also performed in which biaxial bending and torsion was applied by attaching a cable at the end of the beam sample. The purpose of the cable was to restrict the movement of the beam sample and observe the tension developed in the cable and the change in the behaviour of the beam sample due to the cable. Using the finite element analysis developed interaction equations and experimental results are verified.

*Hum Khud Tarashtain Hain Manaziil Ka Sang -e-
rah*

Hum Woh Nahin Jin Ko Zamana Bana gaya

TABLE OF CONTENTS

TITLE PAGE	i
DECLARATION	ii
ABSTRACT	iii
DEDICATION	v
TABLE OF CONTENTS	vi
LIST OF FIGURES	x
LIST OF TABLES	xix
CHAPTER-1: INTRODUCTION	1
CHAPTER-2: LITERATURE REVIEW	7
2.1 INTRODUCTION	7
2.2 THEORY OF THIN WALLED BARS	8
2.2.1 Kinematics of thin walled bars	10
2.3 THEORY OF PLASTICITY	13
2.3.1 Plastic Admissibility	13
2.3.2 Static Admissibility	14
2.3.3 Kinematic Admissibility.....	15
2.3.4 Postulate of Maximum Plastic Dissipation	16
2.3.5 Fundamental Theorem of Limit Analysis	17
2.4 FLEXURAL BEHAVIOUR OF A BEAM.....	18
2.4.1 Elastic behaviour.....	18
2.4.2 Inelastic behaviour	19
2.4.3 Impact of residual stresses on flexural behaviour	20
2.4.4 Lateral torsional buckling	22
2.5 THEORY OF TORSION	24
2.5.1 Elastic Analyses.....	24
2.5.2 Non-linear Analyses	31
2.6 INELASTIC MATERIAL BEHAVIOUR AND YIELD CRITERIA	39
2.6.1 Uniaxial Stress Strain Relationship	39
2.6.2 Multiaxial stress state.....	40
2.6.3 Yield criteria for different sections	48
2.6.4 Single Equation Yield Surfaces	70
2.7 EXPERIMENTAL AND NUMERICAL STUDIES FOR MULTI-DIMENSIONAL FORCES	72
2.8 CONCLUSION	75
CHAPTER3: DEVELOPMENT OF A SINGLE EQUATION YIELD SURFACE	77
3.1 INTRODUCTION	77
3.2 CODE IN MATLAB	78
3.2.1 Generation Of Yield Surfaces.....	78
3.2.2 Check for Yielding Of Section	79
3.3 SINGLE EQUATION YIELD SURFACE FOR BIAXIAL BENDING AND BIMOMENT.....	79

3.3.1 Yield Surface Variation.....	80
3.3.2 Curve Fitting Technique	82
3.3.3 The Developed Single Equation	87
3.3.4 Yield surface diagrams.....	89
3.4 YIELD SURFACE VERIFICATION	90
3.4.1 What is a Yield Surface Verification?	90
3.4.2 LUSAS and Finite Element Analysis	93
3.4.3 Finite Element Model Attributes.....	94
3.4.4 Single Stress Resultants	95
3.4.5 Verification of 2-D yield surface using LUSAS.....	98
3.4.6 Verification of 3-D yield surface.....	100
3.4.7 Verification of 4-Dimensional Yield Surface.....	101
3.4.8 Yield Surface verification procedure and the shell element	101
3.5 EXTENSION AND VERIFICATION OF THE DEVELOPED SINGLE EQUATION YIELD SURFACE	102
3.5.1 Limitations at low m_y values.....	102
3.5.2 Rise of curve if gap is filled.....	103
3.5.3 Procedure to extend the yield surface	105
3.5.4 Verification of the extended curves	106
3.5.5 Verification of the yield surface	108
3.6 CONCLUSION	109

CHAPTER-4:PLASTIC INTERACTION RELATIONSHIPS FOR GENERAL STRUCTURAL I-SECTIONS.....	110
4.1 INTRODUCTION	110
4.2 STATEMENT OF PROBLEM.....	111
4.3 SIGN CONVENTION AND COORDINATE SYSTEM.....	112
4.4 ASSUMPTIONS	114
4.4.1 Stress-Strain Relationship.....	114
4.4.2 Kinematics and neutral-axis patterns	114
4.4.3 Bimoment and cross section warping.....	115
4.4.4 Residual stress	116
4.4.5 Developed stresses.....	116
4.4.6 Yield criterion	117
4.4.7 Choice of yield criterion.....	118
4.5 EQUILIBRIUM CONDITION, YIELD CRITERION AND STRESS DISTRIBUTION.....	118
4.6 SHEAR STRESS AND THE INTERACTION EQUATION	123
4.6.1 Developed Interaction Equation	126
4.7 KINEMATICS AND PLASTIC NEUTRAL-AXIS PATTERNS.....	127
4.7.1 Development of Different Neutral-Axis patterns.....	129
4.7.2 The finalised patterns.....	143
4.7.3 Kinematic limit of field for patterns when the neutral-axis does not intersect the web.....	146
4.7.4 Different quadrants and finalised patterns	147
4.7.5 Sign of internal forces and finalised patterns.....	148
4.8 INTERACTION RELATIONSHIP FOR NORMAL STRESS (LOWER BOUND SOLUTION)	150

4.8.1 A possible Interaction relationship when the neutral-axis passes through web and both the flanges	151
4.8.2 Element Yield Surface and Equilibrium Condition	152
4.8.3 Yield surface development and identification of the plastic hinge	160
4.9 INTERACTION RELATIONSHIP (UPPER BOUND SOLUTION)	177
4.10 CONCLUSION.....	184

CHAPTER-5: PRELIMINARY TEST AND SINGLE STRESS RESULTANTS

EXPERIMENT	185
5.1 INTRODUCTION	185
5.2 COUPON TEST.....	186
5.2.1 Coupon test results	190
5.3 TESTING BEAM SECTIONS IN FLEXURE.....	191
5.3.1 Experimental set-up	191
5.3.2 Bending of beam about the major-axis.....	197
5.3.3 Cantilever beam bending about the minor axis.....	202
5.4 TESTING BEAM SECTION IN TORSION.....	204
5.4.1 Experimental Set-up.....	204
5.4.2 Torsion of the beam sample.....	214
5.5 CONCLUSION	227

CHAPTER-6: BEAM SAMPLE SUBJECTED TO MULTI-DIMENSIONAL FORCES

.....	229
6.1 INTRODUCTION	229
6.2 BIAXIAL BENDING AND TORSION EXPERIMENTS	229
6.2.1 Experimental Set-up.....	229
6.2.2 Experiments Performed	230
6.2.3 Strains at two different locations at different stages of loading	230
6.2.4 Torsion rotation relationship	237
6.2.5 Load-Deflection Relationship	241
6.2.6 Failure of the beam samples.....	243
6.2.7 Elastic limit load and yield surface.....	244
6.2.8 Practical hinge formation and yield surface	246
6.2.9 Measured strain	250
6.2.10 Displacement in two orthogonal directions	255
6.2.11 Displacement in Y-direction and measured rotation	259
6.2.12 Displacement in X-direction and measured rotation	260
6.3 AXIAL FORCE, BIAXIAL BENDING AND TORSION EXPERIMENT	261
6.3.1 Experimental Set-up.....	261
6.3.2 Load application by two different means	264
6.3.3 Strains at two different locations at different stages of loading for axial force, biaxial bending and torsion experiment.....	266
6.3.4 Torsion-Rotation Response.....	268
6.3.5 Lateral Load against Deflection.....	271
6.3.6 Elastic limit load and yield surface.....	272
6.3.7 Practical hinge and yield surface.....	274
6.3.8 Plot of strain against lateral load	275
6.3.9 Displacement in two orthogonal directions	279

6.3.10 Displacement in Y-direction against rotation.....	280
6.3.11 Displacement in X-direction against rotation.....	280
6.3.12 Failure of the beam sample.....	281
6.3.13 Buckling of samples.....	283
6.4 COMPARISON OF RESULTS OF ALL MULTI-DIMENSIONAL FORCE EXPERIMENTS	283
6.5 CONCLUSION	284

**CHAPTER-7 FINITE ELEMENT ANALYSIS OF A BEAM UNDER VARYING LOAD
CONDITIONS** 286

7.1 INTRODUCTION.....	286
7.2 SELECTION OF PROGRAM.....	286
7.3 AVAILABLE ELEMENTS.....	287
7.4 MATERIAL MODEL IDEALIZATION.....	288
7.5 MODELLING THE EXPERIMENTS.....	289
7.5.1 Finite Element Mesh refinement.....	289
7.5.2 Modelling torsion experiments.....	290
7.5.3 Axial pre-stressing load and sequence of load applications.....	293
7.6 FINITE ELEMENT RESULTS.....	294
7.6.1 Bending of the beam about the major-axis.....	295
7.6.2 Bending of beam about the minor-axis.....	297
7.6.3 Torsion applied to the section.....	300
7.6.4 Biaxial bending and torsion case, with dominant minor-axis bending.....	303
7.6.5 Biaxial bending and torsion case, with dominant major-axis bending.....	310
7.6.6 Analysis of beam with a passive pre-stressing cable attached.....	317
7.6.7 Axial force, biaxial bending and torsion experiment.....	320
7.7 CONCLUSION	326

CHAPTER-8 CONCLUSION..... 329

8.1 SUMMARY	329
8.2 CONCLUDING REMARKS.....	331
8.3 RECOMMENDATIONS FOR FUTURE WORKS.....	333

REFERENCES 335

APPENDIX A	341
APPENDIX B	348
APPENDIX C	389
APPENDIX D	396
APPENDIX E	402

LIST OF FIGURES

Figure 1.1(a) Local coordinates and elements of the Section.....	3
Figure 1.1(b) Direction of positive forces.....	3
Figure 2.1(a) General form of an open thin walled beam (Gjelsvik, 1981).....	9
Figure 2.1(b) Stress-strain relationship of elastic-perfectly plastic material.....	9
Figure 2.2 Plastic flow and stress and strain variation (Englekirk, 1994).....	20
Figure 2.3 Strain hardening phase when stress is more than the yield stress (Englekirk, 1994).....	21
Figure 2.4 Residual stresses for an I-beam section (Englekirk, 1994).....	22
Figure 2.5 Shaded region indicates those regions which have reached σ_y (Englekirk, 1994).....	22
Figure 2.6 Lateral torsional buckling of a cantilever beam (Dowling et al, 1988).....	23
Figure 2.7(a) Shear stress distribution due to uniform torsion (Yang and Fan 1988).....	26
Figure 2.7(b) Mitre model shear stress distribution due to uniform torsion (Billinghamurst etal. 1992).....	26
Figure 2.7(c) Local coordinates, elements of I-section, positive coordinate system with direction of positive forces.....	27
Figure 2.8 Torsional behaviour of beam when one end is restrained (Boresi and Schmidt, 2003).....	29
Figure 2.9(a) Beam subjected to torsional restraint at both ends (Boresi and Schmidt, 2003).....	30
Figure 2.9(b) Constant slope roof indicating full plastic yielding across each section in Sand Heap Analogy.....	31
Figure 2.10(a) Pure torsion can be obtained based on a value of $\frac{tF_p}{v\tau_y Sh}$ (Boulton, 1962).....	34
Figure 2.10(b) Torsion against rotation for the beam specimen tested by Dinno and Gill (1964).....	34
Figure 2.10(c) Torsion against rotation for the beam specimen tested by Farwell and Galambos (1969).....	34
Figure 2.10(d) Wagner strains (Pi and Trahair, 1995).....	35
Figure 2.11 Experimental and idealized stress strain curve for mild steel (Boresi and Schmidt, 2003).....	40
Figure 2.12 Experimental and idealized stress strain curve for steel alloys (Boresi and Schmidt, 2003).....	40
Figure 2.13 Idealized curve for small elastic strain (Rigid perfectly plastic curve) (Boresi and Schmidt, 2003).....	41
Figure 2.14 Yield surface of maximum principal stress yield criterion (Boresi and Schmidt, 2003).....	43
Figure 2.15 Yield surface of maximum principal strain yield criterion (Boresi and Schmidt, 2003).....	45
Figure 2.16 Yield surface of strain energy density yield criterion (Boresi and Schmidt, 2003).....	46
Figure 2.17 Yield surface in principal stress space for the Tresca and Von-Mises yield criteria (Boresi and Schmidt, 2003).....	46
Figure 2.18 Distribution of shear stresses and normal stresses considered by Heyman and Dutton (1954), Sobotka (1959) and Strelbitzkaya (1958) to develop the interaction equation considering bending moment and shear force.....	52

Figure 2.19 An I-section subjected to bending about the Y-axis shear force and axial force. Distribution of normal and shear stresses when neutral-axis passes through the web and flange.....	53
Figure 2.20 a) Neutral-Axis intersects the web, An I-section subjected to bending about the X-axis and to shear force and axial force. Distribution of normal and shear stresses when the neutral-axis passes through the web and flange	56
Figure 2.20 b) Neutral-Axis intersects the flange, An I-section subjected to bending about the X-axis and to shear force and axial force. Distribution of normal and shear stresses when the neutral-axis passes through the web and flange	56
Figure 2.21 Three neutral-axis patterns assumed for the solution of interaction equations of a rectangular section when biaxial bending is applied with axial force.....	58
Figure 2.22 Shear stress distribution and neutral-axis pattern based on the approach by Morris and Fenves (1969)	60
Figure 2.23 Two yield surfaces one before application of St Venant's torsion and the other after its application	61
Figure 2.24 Neutral-axis pattern for the stress distribution for the case when P , M_x , M_y and B act on the section (Mrazik et al, 1987)	62
Figure 2.25(a)Diagrams showing strain distributions due to different internal forces, Strain distribution and three neutral-axis patterns for the yield surface for interaction of biaxial bending, axial force, bimoment and St Venant's torsion	63
Figure 2.25(b)Three neutral-axis patterns, Strain distribution and three neutral-axis patterns for the yield surface for interaction of biaxial bending, axial force, bimoment and St Venant's torsion	64
Figure 2.26 Developed yield surface for a W12 x 31 I-section for the interaction of biaxial bending, axial force, bimoment and St Venant's torsion (=0).....	68
Figure 2.27 (a) Neutral-axis pattern for direct stress Neutral axis pattern for the case when direct stress and shear stress act on an I-section for interaction of bending moment, shear force, bimoment, pure torsion and warping torsion	69
Figure 2.27 (b) Neutral-axis pattern for shear stress Neutral axis pattern for the case when direct stress and shear stress act on an I-section for interaction of bending moment, shear force, bimoment, pure torsion and warping torsion	69
Figure 3.1 Comparison of yield surfaces of several I-sections under minor-axis and major-axis bending.....	81
Figure 3.2 Constant parameter, P_1 for $b=0.00$	86
Figure 3.3 UB 762 x 267 x 147, single equation yield surface based on Equation 3.6 and yield surface developed by Yang et. al (1989).....	90
Figure 3.4 Comparison of yield surfaces by Yang et al. (1989)] (shown in coloured) with Equation 3.6 (shown in black) From upper to lower curve different b values of 0.00,0.20,0.40,0.60,0.80 exist	92
Figure 3.5 Details of cross sections of (a)10UB29 section, (b) Sample section and (c) Experimental section.....	94
Figure 3.6 $p - m_{maj}$ yield surface of the I-section.....	99
Figure 3.7 Yield surface of a rectangular section for biaxial bending and axial force	103
Figure 3.8 Developed single equation yield surface (shown in black) after extension, compared with yield surfaces by Yang et al. 1989 (shown in colour). From the upper to lower curve the order of curve is for different b values of 0.0,0.2,0.4,0.6,0.8	106

Figure 4.1(Figure 2.7 reproduced here for discussion) Local coordinates, elements of the section, positive coordinate system with direction of positive forces.....	113
Figure 4.2 Stress-strain relationship of elastic-perfectly plastic material.....	114
Figure 4.3 Diagrams showing strain distributions due to different internal forces ...	115
Figure 4.4 Shear Stress distribution due to uniform torsion.....	123
Figure 4.5 Parabolic and assumed constant stress distribution when S_x is applied	124
Figure 4.6 P, M_x and S_x curve (Mrazik et al, 1987) for the solution given by Paltchevskiy (1948)-dotted curves, Sobotka (1975)-full curves and Smirak (1967)-dashed curves	125
Figure 4.7 Neutral-Axis pattern for the case when S_x, S_y and T_u act on the section	126
Figure 4.8 Five possibilities of different neutral-axis patterns for an I-section when strains due to P, M_x and M_y are considered	128
Figure 4.9 Warping strains as a result of bimoment applied in positive and negative directions based on the assumed coordinate system (see Figure 4.1)	129
Figure 4.10 Fifteen patterns describing the positions of the neutral-axis when P, M_x and M_y are applied (divided into three figures for illustration only).....	130
Figure 4.11 Two extreme positions of the neutral-axis of Figure 4.8(d)	130
Figure 4.12 Strain pattern, when P, M_x and M_y only are considered	131
Figure 4.13 Obtained patterns by adding Figure 4.9(a) and Figure 4.12	132
Figure 4.14 Patterns concluded based on the study in which Figures 4.8(b, d and e) are used with the warping strain (with bimoment applied in the negative direction)	133
Figure 4.15 Original and obtained neutral-axis pattern of special case (First case)	136
Figure 4.16 Original and obtained neutral-axis pattern of special case (Second case)	136
Figure 4.17 Patterns concluded based on the study in which Figures 4.8(b, d and e) are used with the warping strain of Figure 4.9(b) (bimoment applied in a positive direction).....	138
Figure 4.18 Patterns concluded based on the study in which Figures 4.8(a) and (c) are used with the warping strain (bimoment applied in the negative direction)	140
Figure 4.19 Patterns concluded based on the study in which Figures 4.8(a) and (c) are used with the warping strain of Figure 4.9(b) (bimoment applied in the positive direction).....	142
Figure 4.20 Finalised patterns when bimoment applied in the positive direction ...	144
Figure 4.21 Finalised pattern when warping is applied in the negative direction ...	145
Figure 4.22 Patterns which are not possible when Kinematic assumption of Section 4.4.2 are used to obtain the patterns.....	147
Figure 4.23 Nine possible neutral-axis patterns for the pattern given by Figure 4.20(a), three patterns are required for each rectangular plate (see Figure 2.21, Section 2.5 for patterns of rectangular section subjected to axial force and biaxial bending).....	152
Figure 4.24. Bottom flange shown with the global X and Y coordinates showing the position of the neutral-axis when two forces P_i and M_{xi} act on the flange.....	156
Figure 4.25 Three possible patterns when rectangular section is considered.....	157
Figure 4.26 Neutral-Axis parameters for the third pattern.....	158
Figure 4.27 Yield surface developed in this work and previous work by Yang et al. (1989) (shown as dashed red) for the case when $p = 0$ the curve at the top is $b=0.0$ the next curve is $b=0.2$ and the rest follow a series as $b=0.4, b=0.6$ and $b=0.8$. Ellipse in the above figure represent that yield surface for $b=0.0$ and $b=0.2$ are close to each other.....	167

Figure 4.28 Yield surface developed in this work and previous work by Yang et al (1989) (shown as dashed red) for the case when $p = 0.2$ the curve at the top is $b=0.0$ the next curve is $b=0.2$ and the rest follow a series as $b=0.4$, $b=0.6$ and $b=0.8$. . Ellipse in the above figure represents that yield surface for $b=0.0$, $b=0.2$ and $b=0.4$ are close and intersect each other	168
Figure 4.29 Yield surface developed in this work and previous work by Yang et al (1989) (shown as dashed red) for the case when $p = 0.4$ the curve at the top is $b=0.0$ the next curve is $b=0.2$ and the rest follow a series as $b=0.4$, $b=0.6$ and $b=0.8$. Ellipse in the above figure represents that yield surface for $b=0.0$, $b=0.2$, $b=0.4$ and $b=0.6$ are close and intersect each other.....	169
Figure 4.30 Yield surface developed in this work and previous work by Yang et al (1989) (shown as dashed red) for the case when $p = 0.6$ the curve at the top is $b=0.0$ the next curve is $b=0.2$ and the rest follow a series as $b=0.4$, $b=0.6$ and $b=0.8$. Ellipse in the above figure represents that yield surface for $b=0.0$, $b=0.2$, $b=0.4$ and $b=0.6$ are close and intersect each other.....	170
Figure 4.31 Yield surface developed in this work and previous work by Yang et al (1989) (shown as dashed red) for the case when $p = 0.8$ the curve at the top is $b=0.0$ the next curve is $b=0.2$ and the rest follow a series as $b=0.4$, $b=0.6$ and $b=0.8$. Ellipse in the above figure represents that yield surface for $b=0.4$, $b=0.6$ and $b=0.8$ are close and intersect each other.....	173
Figure 4.32 Detail of curvature of each plate, strain rate at the centroid of each plate and definition of areas on each plate.....	179
Figure 5.1 Different locations of an I-section from which coupon samples were taken .	186
Figure 5.2 Typical residual stress pattern of an I-section (Englekirk, 1994).....	187
Figure 5.3 Tensile test coupon (Goggins, 2004)	187
Figure 5.4 Typical load deflection graph for a coupon test (taken from one of the specimens)	189
Figure 5.5 Coupon test results of the first specimen up to a deflection of $1mm$	191
Figure 5.6 Average uni-axial stress-strain diagram	191
Figure 5.7(a) Experimental set-up for the cantilever beam, bending about the major-axis	190
Figure 5.7(b) Beam welded to the base and connected to the internal reaction frame by nut and bolt arrangement.....	192
Figure 5.7(c) Load cell and RDP actuator mounted horizontally to the frame.....	193
Figure 5.8 Location of strain gauges for cantilever beam, bending of beam about the major and minor-axes	194
Figure 5.9 System 5000 unit and Personal Computer	195
Figure 5.10 Actuator command console.....	196
Figure 5.11 Flow chart of data processing and storage for experiments	196
Figure 5.12 Load-deflection behaviour of beam of span $1.18m$	197
Figure 5.13 Graph showing relationship between flexural stress and flexural strain	198
Figure 5.14 Load-deflection curve of cantilever beam of span $1.24m$	199
Figure 5.15 Load-deflection graph of beam bending in minor direction	202
Figure 5.16 Initial set-up for the application of torsion load	205
Figure 5.17 Cable-wire set-up used for pure torsion experiment.....	205
Figure 5.18 Different radii and arc/cable lengths for similar rotations	206
Figure 5.19 Final Set-up of the Experiments (Not to Scale)	207
Figure 5.20 Lever arm action to provide additional movement at point A	207
Figure 5.21 The beam failed in torsion fixed to the internal reaction frame.....	208

Figure 5.22 Pure torsion experimental set-up	209
Figure 5.23 Position of the strain gauges for torsion experiments	210
Figure 5.24 Position of the camcorders.....	212
Figure 5.25 Position of Odometers and Grid papers used to measure deflection... ..	212
Figure 5.26 Torsion- rotation plots for the cantilever beams of span 1.24m	215
Figure 5.27 Strain at the fixed end at the tips of flanges for both the torsion experiments.	217
Figure 5.28 Strain at the mid span at the tips of flanges for torsion applied in the two experiments	219
Figure 5.29 Strains at the centre of web near the support and at mid span for both the torsion experiments.....	220
Figure 5.30 Strain at edges of the web for both the torsion experiments.....	221
Figure 5.31 Torsion-horizontal movement graph for the second experiment.....	224
Figure 6.1 Modified set-up for torsion-biaxial bending experiment.....	230
Figure 6.2 Position of I-section with respect to the direction of load application for both the torsion-biaxial bending experiments.....	231
Figure 6.3 Strain patterns for biaxial bending and torsion experiment (Experiment 1) at fixed end, where strain numbers are given in square boxes and strain readings in rectangular boxes.....	234
Figure 6.4 Strain patterns for biaxial bending and torsion experiment (Experiment 1) at mid span, where strain numbers are given in square boxes and strain readings in rectangular boxes.....	234
Figure 6.5 Strain patterns for biaxial bending and torsion experiment (Experiment 2) at fixed end, where strain numbers are given in square boxes and strain readings in rectangular boxes.....	236
Figure 6.6 Strain patterns for biaxial bending and torsion experiment (Experiment 2) at mid span, where strain numbers are given in the square boxes and strain readings in rectangular boxes.....	238
Figure 6.7 Torsion against rotation in the biaxial bending and torsion experiment when minor axis behaviour dominates (Experiment # 1).....	239
Figure 6.8 Torsion against rotation in the biaxial bending and torsion experiment when major axis behaviour dominates (Experiment # 2).....	239
Figure 6.9 Comparison of torsion and rotation for Experiments 1 and 2 of biaxial bending and torsion experiments.....	240
Figure 6.10 Load against deflection plot of the biaxial bending and torsion experiment when minor axis bending dominates (Experiment # 1).....	241
Figure 6.11 Residual lateral displacement and rotation of the beam under biaxial bending and torsion experiment when minor axis bending dominates (Experiment # 1).....	242
Figure 6.12 Load against deflection of biaxial bending and torsion experiment when major axis behaviour dominates (Experiment # 2).....	243
Figure 6.13 Residual lateral displacement and rotation of beam in the biaxial bending and torsion experiment when major axis bending dominates (Experiment # 2).....	248
Figure 6.14 Strain # 1,2,4 and 5, Load against strain of biaxial bending and torsion experiment when minor axis behaviour dominates (Experiment # 1) at the fixed end of the beam.....	250
Figure 6.15 Strain # 1,2,4 and 5, Load against strain of biaxial bending and torsion experiment when major axis bending dominates (Experiment# 2) at the fixed end of the beam.....	250

Figure 6.16 Strain # 3, 6 and 7, Load against strain of biaxial bending and torsion experiment when minor axis behaviour dominates (Experiment # 1) at the fixed end of the beam.....	252
Figure 6.17 Load against strain of biaxial bending and torsion experiment when minor axis behaviour dominates (Experiment # 1) at the mid section of the beam.....	253
Figure 6.18 Strain # 3, 6, and 7 Load against strain of biaxial bending and torsion experiment when major axis bending dominates (Experiment # 2) at the fixed end of the beam.....	255
Figure 6.19 Strain # 9,10,11,12 and 13. Load against strain of biaxial bending and torsion experiment when major axis bending dominate (Experiment # 2) at the mid span of the beam.....	256
Figure 6.20 Displacement in two perpendicular directions of biaxial bending and torsion experiment when minor axis bending dominates (Experiment # 1).....	258
Figure 6.21 Displacement in two perpendicular directions of biaxial bending and torsion experiment when major axis bending dominates (Experiment # 2).....	258
Figure 6.22 Displacement in Y-axis and rotation of biaxial bending and torsion experiment when minor axis bending dominates (Experiment # 1).....	259
Figure 6.23 Displacement in Y-axis and rotation of biaxial bending and torsion experiment when major axis bending dominates (Experiment # 2).....	260
Figure 6.24 Displacement in X-axis and rotation of biaxial bending and torsion experiment when minor axis bending dominates (Experiment # 1).....	261
Figure 6.25 Displacement in X-axis and rotation of biaxial bending and torsion experiment when major axis bending dominates (Experiment # 2).....	261
Figure 6.26 Arrangement of applied axial load (with load cell and cross beam).....	262
Figure 6.27 Position of hydraulic jack and load cell during load application.....	263
Figure 6.28 Location of strain gauges near the fixed end of the beam, where the strain gauges numbers are shown in square box and all dimensions are in <i>mm</i>	264
Figure 6.29 Variation of induced vertical tendon force with applied horizontal load for the case when axial load is applied in combination with biaxial bending and torsion.....	265
Figure 6.30 New position of the prestressing strand and the part beam after lateral load application giving rise to flexure.....	266
Figure 6.31 Strain patterns at the fixed end for axial force, biaxial bending and torsion experiment where strain numbers are given in a square box and strain readings in a rectangular box.....	270
Figure 6.32 Torsion against Rotation response for the case when axial load is applied in combination with biaxial bending and torsion.....	271
Figure 6.33 Comparison of Torsion against Rotation response for the case a) for pure torsion and b) torsion is applied in the presence of biaxial bending and axial load.....	272
Figure 6.34 Load against Deflection, for biaxial bending and torsion and for biaxial bending, torsion and axial load cases.....	273
Figure 6.35 Measured strains for the top flange near the fixed end of the beam for the case when axial load is applied in combination with biaxial bending and torsion.....	276
Figure 6.36 Measured strains for the web near the fixed end of the beam for the case when axial load is applied in combination with biaxial bending and torsion.....	277
Figure 6.37 Measured strains for the bottom flange near the fixed end of the beam for the case when axial load is applied in combination with biaxial bending and torsion.....	278

Figure 6.38 Displacement in two perpendicular directions for biaxial bending and torsion and for biaxial bending, torsion and axial load cases.....	280
Figure 6.39 Displacement in Y-direction against rotation of axial load, biaxial bending and torsion experiment.....	281
Figure 6.40 Displacement in X-direction against rotation of axial load, biaxial bending and torsion experiment.....	282
Figure 6.41 Failed beam experiment in which axial force is applied, residual rotation and deflection are visible in the beam.....	282
Figure 7.1 Model used for the pure bending analysis.....	291
Figure 7.2 End condition of beam sample.....	291
Figure 7.3 Model from Figure 7.1 developed with square end plate.....	292
Figure 7.4 Loads applied to the square end plate for the case when pure torsion is applied.....	292
Figure 7.5 Loads applied to the square end plate for the case when torsion was applied in combination with other forces.....	292
Figure 7.6 Cable attached to a pinned support and the beam end plate.....	293
Figure 7.7 Load deflection graph of bending of beam about the major-axis, Expreimental result produce here are also given in Figure 5.14.....	296
Figure 7.8 Longitudinal stress contour of beam bending about the major-axis.....	297
Figure 7.9 Load deflection graph of bending of beam about the minor-axis, Expreimental result produce here are also given in Figure 5.15.....	299
Figure 7.10 Longitudinal stress contour of beam bending about the minor-axis.....	299
Figure 7.11 Torsion vs rotation response of the beam sample, Expreimental result produce here are also given in Figure 5.26.....	301
Figure 7.12 Rotation of the rectangular plate viewed along the longitudinal axis at an angle of rotation of 32°.....	301
Figure 7.13 Deformation of the beam sample viewed from the lateral direction.....	302
Figure 7.14 Torsion vs maximum axial deflection of the beam sample.....	302
Figure 7.15 Stress contour of beam applied in pure torsion.....	303
Figure 7.16 Load deflection curve for biaxial bending and torsion case, with dominant minor-axis bending. Expreimental result produce here are also given in Figure 6.10.....	304
Figure 7.17 Measured deflections in two different directions for biaxial bending and torsion case, with dominant Minor-Axis bending. Expreimental result produce here are also given in Figure 6.20.....	305
Figure 7.18 Torsion rotation curve for biaxial bending and torsion case, with dominant minor-axis bending. Expreimental result produce here are also given in Figure 6.7.....	306
Figure 7.19 Measured deflection in X-direction and rotation of the beam sample for biaxial bending and torsion case, with dominant minor-axis bending. Expreimental result produce here are also given in Figure 6.24.....	307
Figure 7.20 Measured deflection in Y-direction and rotation of the beam sample for biaxial bending and torsion case, with dominant Minor-Axis bending. Expreimental result produce here are also given in Figure 6.22.....	308
Figure 7.21 Deformation of the beam viewed along the longitudinal axis for biaxial bending and torsion case, with dominant minor-axis bending.....	309

Figure 7.22 Deformation pattern of the beam for biaxial bending and torsion case, with dominant minor-axis bending.....	309
Figure 7.23 Stress contours of beam biaxial bending and torsion for biaxial bending and torsion case, with dominant minor-axis bending.....	310
Figure 7.24 Load deflection curve for biaxial bending and torsion case, with dominant major-axis bending. Expreimental result produce here are also given in Figure 6.12.....	312
Figure 7.25 Measured deflections in two different directions for biaxial bending and torsion case, with dominant Major-Axis bending. Expreimental result produce here are also given in Figure 6.21.....	312
Figure 7.26 Torsion Rotation curve for biaxial bending and torsion case, with dominant major-axis bending. Expreimental result produce here are also given in Figure 6.8.....	313
Figure 7.27 Measured deflection in Y-direction and rotation of the beam sample for biaxial bending and torsion case, with dominant major-axis bending. Expreimental result produce here are also given in Figure 6.23.....	314
Figure 7.28 Measured deflection in X-direction and rotation of the beam sample for biaxial bending and torsion case, with dominant major-axis bending. Expreimental result produce here are also given in Figure 6.25.....	314
Figure 7.29 Deformation of the beam viewed along the longitudinal axis for biaxial bending and torsion case, with dominant major-axis bending.....	316
Figure 7.30 Stress contours of beam biaxial bending and torsion, Second Experiment (Primarily about major axis).....	316
Figure 7.31 Deformation pattern of the beam for biaxial bending and torsion case, with dominant Major-Axis bending.....	317
Figure 7.32 Model from Figure 7.3 with cable attached at the end plate.....	318
Figure 7.33 Load-deflection curves for beam with passive cable attached.....	319
Figure 7.34 Axial load in the cable in comparison with the lateral load for beam with a passive cable attached.....	319
Figure 7.35 Load-deflection graph for the experiment where axial load applied using active tendon. Expreimental result produce here are also given in Figure 6.34.....	320
Figure 7.36 Measured deflections in two different directions where axial load applied using active tendon. Expreimental result produce here are also given in Figure 6.38.....	321
Figure 7.37 Torsion-rotation response of the experiment where axial load applied using active tendon. Expreimental result produce here are also given in Figure 6.32.....	321
Figure 7.38 Measured deflection in Y-direction and rotation of the beam sample where axial load applied using active tendon. Expreimental result produce here are also given in Figure 6.39.....	322
Figure 7.39 Measured deflection in the X-direction and rotation of the beam sample when axial load is applied using active tendon.....	323
Figure 7.40 Increase of axial load during lateral load application and lateral load of the beam sample when axial load is applied using active tendon. Upper line is finite element result and lower is the experimental result. Expreimental result produce here are also given in Figure 6.29.....	324
Figure 7.41 Deformation pattern of the beam when axial loads applied using active tendon.....	325

Figure 7.42 Finite element response of lateral load against deflection for the cases discussed in section 7.6.5-7.....326

Figure 7.43 Finite element responses of axial load developed in the cable for the passive case and axial load applied.....326

LIST OF TABLES

Table 2.1 Cantilever with mechanism formed due to uniform torsion (Pi and Trahair, 1995b).....	36
Table 2.2 Cantilever with mechanism formed due to warping torsion (Pi and Trahair, 1995b).....	37
Table 3.1(a) Format of different types of equations tried to best fit the yield surfaces.....	84
Table 3.1(b) Comparison of RMSE values for different equations	85
Table 3.2(a) Values of parameters p_{11} , p_{21} and q_{21}	88
Table 3.2(b) Values of parameters p_{12} , p_{22} and q_{22} in which $S_w = S_{web} / S_{xx}$	88
Table 3.3 Parameters of Equation 3.8.	89
Table 3.4 Comparison of theoretical plastic capacities with finite element analysis for axial force and biaxial bending.....	97
Table 3.5 Comparison of torsional analysis of LUSAS with previous work.....	98
Table 3.6 Yield surface verification results for 2-D stress resultants	100
Table 3.7 Comparison of yield surface by Morris and Fenves (1969) and LUSAS... ..	100
Table 3.8 Comparison of the yield surface by Yang et al. (1989) and LUSAS.	101
Table 3.9 Comparison of the yield surface by Yang et al. (1989) with finite element results.....	102
Table 3.10 Comparison of the yield surface of equation 3.6 and finite element analysis.	107
Table 3.11 Comparison of the single equation yield surface and the yield surface by Yang et al. 1989 with the finite element analysis.....	108
Table 5.1 Material properties obtained from coupon test results.....	188
Table 5.2 Stresses at different stages of the specimens obtained from Coupon test results.....	189
Table 5.3 Percentage difference between the compressive face and the tensile face of the beam at different locations.....	201
Table 5.4 Percentage variation of stress at the tensile face and at the compressive face of the beam.....	203
Table 6.1 Strains at different location along the beam for experiments 1 and 2 in biaxial bending and torsion	232
Table 6.2 Biaxial bending moment and bimoment for load and torsion applied in Experiment 1 and 2	247
Table 6.3 Measured strains at different loads near the fixed end.....	268
Table 6.4 Measured strains at different loads near the mid section	269
Table 6.5 Normalized biaxial bending moment, bimoment and axial load when biaxial bending, torsion and axial force are applied.....	274
Table 6.6 Factors for elastic limit load/yield surface load, practical hinge formation/yield surface load and peak load/yield surface load.	284
Table 7.1 Stress-strain results obtained from coupon tests used in the finite element material model.....	288
Table 7.2 Comparison of finite element results and the theoretical value for different numbers of elements	290
Table 7.3 Comparison of the loading actions and the capability of finite element in predicting primary and secondary effects. The terminologies in the table are	

Local buckling (LB), Lateral torsional buckling (LTB) and Axial shortening (AS).....	327
--	-----

CHAPTER-1

INTRODUCTION

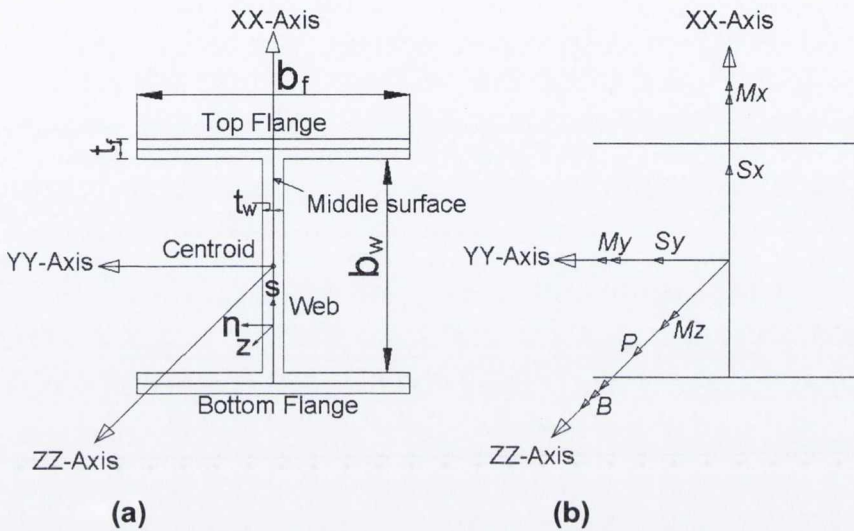
From the early days, structural engineers have been interested to determine the load beyond the elastic limits so that elements of a structure can be designed based on its ultimate capacity.

Structural elements can be subjected to various types of loading. The simplest case is when members of a structure are subjected to axial forces only and such types of structure are called plane or 3D trusses. There are cases when a structure can be subjected to forces or moments applied in three directions. Whatever type of loading acts on a member, a certain failure parameter is defined for the member based on the shape, boundary conditions and material from which the member is built. This failure parameter change may not govern the design, however the design may have to be based on a serviceability requirement for the structure. For example a design parameter can be set for members to remain elastic during its loading cycle or members can be allowed to undergo non-linear behaviour during the loading cycle. Non-linear behaviour can be determined by assuming the construction material as elastic perfectly plastic, or based on nonlinearity considering strain hardening or, in some cases, based on determining the ultimate load which a member can sustain. One such failure parameter is the yield criterion for yielding of material of members. This failure criterion relates the failure of a structure to yielding of material. Yielding for example, can be determined for a certain cross sectional element so that a kinematic mechanism forms in the structure or it can be due to the commencement of yielding at any location of the structure. There can be several approaches to set the yield criterion of the structure but two are most common, namely when it can be set for yielding of an infinitesimal element of a member or it can be set for yielding of the cross section of a member. Several criteria exist in both the cases. For example, for yielding of an infinitesimal element, different criteria exist for both ductile and brittle materials such as Von-Mises, Tresca, Mohr-Coulomb yield criterion and etc.

In the other cases a cross section which is yielded totally on the application of different combination of forces so that it cannot take further load is called a generalized plastic hinge. When yielding of a cross section is considered, the formation of a generalized plastic hinge is determined by developing what can be called an interaction equation, plastic limit envelope, yield locus, failure envelope, yield surface or interaction curve. Different criteria have been developed for yielding of a cross section based on load application, type of cross section and type of material. The simplest case when more than one force acts on the section is when a rectangular section is subjected to an axial force and bending moment simultaneously. Advancements in computer technology offer the opportunity to investigate the spatial nature of application of the yield criteria. This investigation is required because of the three dimensional analysis which reveal high forces acts on an element of structure in three dimensions. A structural element such as column can receive biaxial bending moments and axial force (due to gravity loads). In addition it can receive large torsional load and biaxial shear forces due to the lateral forces applied to the building which are seismic forces and wind forces. Also girders of bridges can receive biaxial bending moment biaxial shear forces and torsion under the combination of gravity and lateral loads, and receive large torsion especially when the centroid of the deck slab do not coincide with the centroid of the beam. Because of such nature of forces resisted by an element of structure, works on yield criteria is needed to develop interaction equations for the case when forces and moments are applied in three dimensions. One such effort will be performed in this research when yield criterion for forces and moments in three directions are developed. These forces are axial force, biaxial shear force, biaxial bending moment and torsion. Several yield criteria for different types of cross sections for different combination of three dimensional forces are already developed and are discussed in Chapter-2. However, the three forces and the three moments are not considered before for the development of yield criterion.

The problem this thesis will address is the development of interaction equations by having two forms of solutions, one is the approximate approach and the other is the exact approach. These will be for an I-section. A general form of an I-section with

local coordinates of the element, positive global coordinate system used, direction of positive forces used and details of the I-section is given in Figure 1.1.



(a) Local coordinates and elements of the section (b) Direction of positive forces

Figure 1.1 Local coordinates, elements of the section, positive coordinate system with direction of positive forces

In the approximate approach single unifying equation for biaxial bending and bimoment will be developed for available British steel sections (BS EN10056: 1999 sections). This single equation fills the gap which was present in the previously developed yield surface, hence removing the discontinuity in the previous yield surface. Apart from the approximate approach, a better exact approach will also be developed in this work for biaxial bending moment, biaxial shear force, axial force, uniform torsion and bimoment. Interaction equations, yield surfaces and a procedure for the identification of the formation of plastic hinge are obtained in the exact approach. This exact approach will be developed using the lower bound theorem of limit analysis and verified using the upper bound theorem of limit analysis, hence satisfying the uniqueness theorem of limit analysis. Presently the only solutions

which exist are those proposed by Yang and Fan (1988) who developed yield surfaces based on axial force, biaxial bending moment, bimoment and uniform torsion. However the solution was based on some approximations, due to which the yield surfaces developed were not closed. In the exact approach yield surfaces will be obtained by eliminating the approximations and obtaining a closed, continuous and convexed yield surfaces.

Experiments will be performed firstly for sections subjected to single forces and subsequently for sections subjected to multi-dimensional forces. These experiments will be performed to verify the interaction equations developed by both the approximate approach and exact approach, and to identify different behavior of an I-section beam when it is under the influence of one force and combination of more than one force. Especially for combination of more than one force when in one case biaxial bending moment and bimoment is applied and in the other case a unique approach in which axial force, biaxial bending moment and bimoment is applied to the beam specimen. The behavior which will be observed during the experiments are the load-deflection relationship, torsion rotation relationship, interaction between horizontal and vertical movement of the beam, interaction between horizontal movement and rotation, interaction between vertical movement and rotation and strain developed as the load progressed.

Those experimental responses will be verified by finite element analysis using London University Structural Analysis Software (LUSAS). Finite element analysis will be performed to compare all the experimental results and different behaviors (as discussed above) which will be observed during the experiment. In addition, an intermediate analysis is performed to between two cases of biaxial bending moment and torsion and axial force, biaxial bending moment and torsion. In the intermediate analysis a passive cable was attached to the beam sample. This cable was used only to restrict the movement of the beam without its use to apply the axial force. Obtained results will be discussed and future work based on the finding of the results will be recommended.

Initially in Chapter-2 a literature review of related works in the field will be presented. Basic theories of thin walled bars and plasticity are discussed. Classification of torsion problems applied to different cross section and different types of boundary conditions are discussed. Theories related to multiaxial stress state and yield criteria are discussed. Yield criteria for the different state of loadings are discussed for the cases when a cross section is subjected to one, two or many forces. Both numerical modeling and experimental work are discussed. The aim of this chapter is to provide the reader with background knowledge which would be required for an interpretation of the theory developed in later chapters for experimental results and their numerical verification.

Chapter 3 considers a single equation yield surface which is developed for biaxial bending moment and bi-moment. A yield surface varies for different sections and the variation depends on various section properties. Section properties of British steel sections were taken into account so that the developed equation can be shown to be valid for a wide range of available sections (BS EN10056: 1999 sections). The developed single equation was based on previous work by Yang et al. (1989) where currently limitations exist in the yield surface. This limitation was later removed using a finite element approach. Later using the finite element yield surfaces are verified numerically.

A yield criterion is developed in Chapter 4 in which axial force, biaxial bending, biaxial shear, uniform torsion and bi-moment are considered. An equation is first described to relate shear stress to the forces (biaxial shear and uniform torsion) which causes shear stresses while forces (axial force, biaxial bending and bi-moment) related to direct stress are considered and a unique closed yield surface is obtained. The procedure to obtain the yield surface is outlined. Later a procedure is developed for the identification of the formation of a plastic hinge based on the developed yield surface.

Experimental results are presented in Chapter 5, comprising those experiments when a beam sample is subjected to only one force. It is also required to determine the material properties of the steel of the beam sample. These results are compared

with the theoretical development and the differences between the results of the theoretical development and experiment are discussed

Chapter 6 presents the results of the second phase of the experiments in which multiple stress resultants are applied simultaneously. Results in the form of deflections, rotations and strain gauge readings are discussed. In addition experimental results are compared with the developed yield surface. The developed equations are verified in the linear and non linear phases of response with discussions about the plastic and strain hardening phases.

A numerical study of the experimental response is presented in Chapter 7. The study is performed by finite element analysis in LUSAS. Both of the sets of cases when beam samples are subjected to single forces and to multiple forces are analysed. Load-deflection and torsion-rotation responses are compared using the finite element response. From the results it is concluded that finite element successfully models the experimental behaviour of the samples and verifies the developed interaction equations.

The final conclusions and suggestions for further work will be presented in Chapter 8.

CHAPTER-2

LITERATURE REVIEW

2.1 INTRODUCTION

The theory of thin walled bars constitutes a major section in the field of structural mechanics especially when both static and dynamic analysis solutions are taken into consideration. The development of a yield criterion has led to the use of it in the theory of plasticity, the flexural behaviour of beam and the application to torsion problems.

One of the more obvious structural applications is the development of yield criteria under multidimensional forces for steel open sections. Studies have taken several approaches in this regard. Yield surfaces for stress at a point for both ductile and brittle materials have been developed. In another approach yield surfaces have been developed for different steel sections. Both the upper bound and lower bound theorems of plasticity are used to develop the yield surfaces. Sometimes it is required to obtain the behaviour of steel sections when only one force is considered, as for the case of pure flexural and pure torsional behaviour of a section.

Discussions about the different theories are presented here by nature of structure and load application. Sections 2.1 and 2.2 discuss briefly the theory of thin walled bars and the theory of plasticity. In the sub section of each section, different assumptions and different terminologies are used relating them to their application in structural engineering. Sections 2.3 and 2.4 discuss details about flexural behaviour and torsional behaviour. In their sub sections, the response under different loading conditions are discussed. The numerical and experimental approaches adopted to these problems are also discussed. In Section 2.5, the yield criteria related to stress at a point and for different steel sections are discussed. In addition, the use of the curve fitting technique is also identified for dealing with yield criteria. The last section discusses the study of different experimental and numerical approaches adopted when a structure is subjected to multi-dimensional forces.

2.2 THEORY OF THIN WALLED BARS

In structural engineering, the types of elements of structures can be divided into four classes according to the spatial characteristics of these elements (Vlasov, 1959). These are 1) massive bodies 2) plates and shells 3) solid beams and 4) thin walled beam. They are defined as follows:

Massive bodies: Massive bodies are those whose three dimensions are such that any one dimension is not small as compare to the remaining two. For example, a cube, a prism, an ellipsoid, a continuum filling all space or half space are all massive bodies.

Plates and Shells: For this class of element, one dimension is small as compared to the remaining two dimensions. Examples of such elements are slabs, shells and plates of various shapes.

Solid Beams: For this class of element, two dimensions of the beam are small as compared to the third dimensions and are called solid beams.

Thin walled beam: For this class of element, the shape is such that it has the form of long prismatic shells. All three dimensions of the elements are of a different order of magnitude. The thickness of the shell is small compared to the characteristic dimension of cross-section and the cross-sectional dimensions are small as compared to the length of the shell.

A thin walled open cross-section beam with a right hand coordinate system (x,y,z) is depicted in Figure 2.1(a). In the figure the surface lying midway through the plates of the beam is called the middle surface. Straight lines on the middle surface which are parallel to the longitudinal axis of the beam are called generators of the beam. If a section is cut through the middle surface such that it is perpendicular to the longitudinal axis then it is called a contour of the cross-section of the bar. Sharp corners and junctions in the contour are allowable and are called junctions. Part of the contour lying between junctions of a contour or between a junction and end of a

contour is called a branch of the contour and part of the bar related to the branch is called an element.

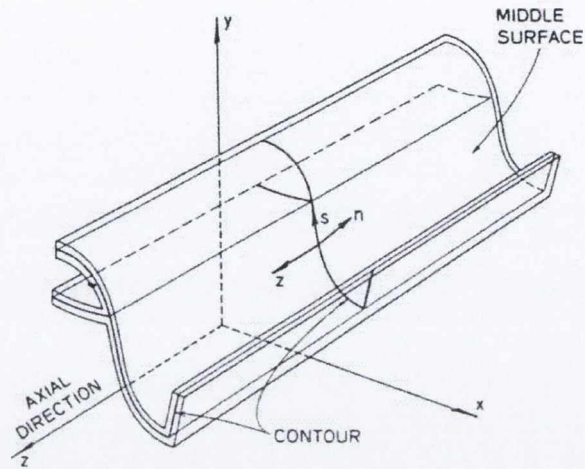


Figure 2.1(a) General form of an open thin walled beam (Gjelsvik, 1981).

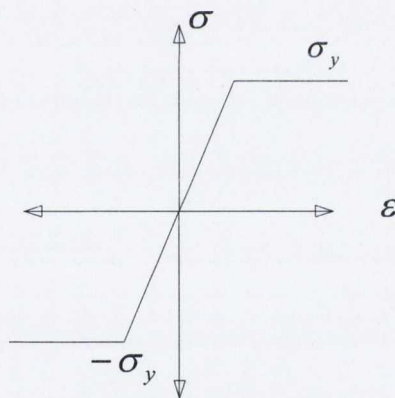


Figure 2.1(b) Stress-strain relationship of elastic-perfectly plastic material

Figure 2.1 General form of an open thin walled section and stress-strain relationship of elastic-plastic material

A right-handed coordinate system for the middle surface can be introduced as depicted in the figure such that the axis n is always normal to the tangent drawn at the point of the contour considered whereas s is perpendicular to n following the contour. The wall thickness is taken to be constant in the longitudinal axis of the bar

which implies that wall thickness can vary with the s axis and can be written mathematically as $\bar{t}(s)$.

A thin walled beam consists of plates where each plate in the cross section is between junctions or between junction and two ends of the contour. For example an I-section consists of three plates. When thin walled elements satisfy the relations $\bar{t}/b_c \leq 0.1$ and $b_c/l_c \leq 0.1$, they can be classified as thin walled beams. where b_c is any characteristic dimension of the cross section and l_c is the length of the beam

2.2.1 Kinematics of thin walled bars

There are three kinematic (i.e. strain, displacement etc) assumptions which are the basis of the theory of torsion and flexure of thin walled bars (Gjelsvik, 1981). These are

1. A contour can be considered as a rigid section i.e. no deformation takes place in the contour in its own plane
2. Shear deformation (i.e. change in the angle of the middle surface) is zero in each element.
3. Each element of the beam behaves as a thin shell, which means Kirchhoff's assumption of straight lines remaining normal to the middle surface during deformation is valid.

Displacement in the longitudinal direction

Considering the theory of a thin walled elastic beam, axial displacement w at any point on a cross-section parallel to the longitudinal axis of the bar is determined by an equation (Gjelsvik, 1981) given by

$$w(x, y, z) = W(z) - U'(z)x - V'(z)y - \Phi'(z)\omega(x, y) \quad 2.1$$

In the above equation $W(z)$ represents an average axial displacement of the bar, U' and V' are the slope component in the x and y direction respectively and Φ is the rotation about the positive z direction. The last term, $\omega(x, y)$ in the equation is the warping function obtained by Goodier (1941) and represents warping deformation of the cross-section. Warping deformation is related to two types of deformation, one is warping of the contour $\bar{\omega}$ and the other is warping of the wall relative to the contour $\bar{\omega}$. Mathematically it can be written as

$$\omega = \bar{\omega} + \bar{\omega} \quad 2.2$$

Many authors, such as Timoshenko and Gere (1961), refer to $\bar{\omega}$ as the warping function and neglect $\bar{\omega}$. For sections where $\bar{\omega}$ is much larger than $\bar{\omega}$ the approach by Timoshenko and Gere is very convenient, however, in general this approach could be misleading.

Strain in the longitudinal direction

Knowing the displacement at any point on a cross-section of the beam, longitudinal elastic strain can be determined by differentiating Equation 2.1 with respect to the z -axis (longitudinal axis) of the beam. Hence, a general equation (Gjelsvik, 1981) is obtained for the axial strain, ϵ_{zz} as

$$\epsilon_{zz} = \frac{\partial w}{\partial z} = W' - U''x - V''y - \Phi''(z)\omega(x, y) \quad 2.3$$

where W' is the first derivative of W with respect to Z and U'' , V'' and Φ'' are the second derivatives with respect to Z of U , V and Φ respectively. The above equation determines the axial strain field of the beam. The diagram of the strain field is obtained by superposing four diagrams, each of which is related to one term in the above equation. The first term W' determines a uniform axial strain. The second

and third terms U'' , V'' determine the strain due to flexural action about the two principal axes of the beam, which are perpendicular to each other. The fourth term Φ'' determines the strain due to warping of a section. Combining the four diagrams, the strain field for the entire thin walled elastic beam is obtained.

Thin walled beam and non-linear behaviour

The basic assumption made to develop plastic theory is that the kinematics of the elastic and plastic bar are the same. This means that equations which define the displacement field or strain field in an elastic case will still be valid for plastic behaviour. Therefore, Equation 2.3 for the direct strain will still be valid. This strain is related to the stress by the theory of plastic potential (Prager, 1959). According to this theory the increment of strain (or the strain rate vector) not the strain itself is related to stress and the sign of the strain rate vector is considered to determine the bar forces. Mathematically it can be related as

$$\sigma_{zz} = \sigma_y \text{Sgn} \left[\dot{\varepsilon}_{zz}^- \right] \quad 2.4$$

where $\dot{\varepsilon}_{zz}^-$ is the plastic strain rate vector in the z-direction. In the equation $\text{Sgn}[a]$ is the signum function (Gjelsvik, 1981) and is defined as

$$\text{Sgn}[a] = 1 \text{ when } a > 0 \quad 2.5(a)$$

$$\text{Sgn}[a] = -1 \text{ when } a < 0 \quad 2.5(b)$$

$$\text{Sgn}[a] = 0 \text{ when } a = 0 \quad 2.5(c)$$

Equation 2.5 can be well understood by having a elastic-perfectly plastic stress-strain diagram as depicted in Figure 2.1(b). a in the equation is the plastic strain rate. If the strain rate is more than and less than zero its results are 1 and -1, which represent here a condition in which stress reach the yield stress σ_y whereas if a is zero i.e. when there is no plastic strain rate means the case of stress when it is less

than σ_y . In that case it will be elastic and between the limit of -1 and +1. Therefore, for example, the plastic moment capacity, M_p , can be written as

$$M_p = \sigma_y \int_c \int_{-t/2}^{t/2} y \text{Sgn} \left[\dot{\varepsilon}_p \right] dnds \quad 2.6$$

In the above equation $\dot{\varepsilon}_p$ is the plastic strain rate vector, c represents the domain of a branch of the contour, t is the thickness which varies from $-t/2$ to $t/2$.

Yielding of a section in the axial direction can be written as (Gjelsvik, 1981)

$$P_p = \sigma_y \int_c \int_{-t/2}^{t/2} \text{Sgn} \left[\dot{\varepsilon}_p \right] dnds \quad 2.7$$

Here P_p is the plastic axial load in pure tension or compression. If deformation of the beam is considered as a vector in a four dimensional space, having components W' , U'' , V'' and Φ'' (Gjelsvik, 1981), the value of the plastic bar forces (for example given here by Equations 2.6 and 2.7) depends on the direction of this vector, not on its magnitude. Hence for example, it can result in a positive moment for a negative curvature.

2.3 THEORY OF PLASTICITY

2.3.1 Plastic Admissibility

If the state of stress at a point in a material does not exceed the yield limits, it is called a plastically admissible condition (Jirasek and Bazant, 2002). Considering the same magnitude of yield stress (σ_y) in compression and tension, the condition of plastic admissibility of stress σ for the uniaxial stress state can be defined as

$$-\sigma_y \leq \sigma \leq \sigma_y \quad 2.8$$

When the conditions are applied to multi-axial states then the yield limits are replaced by yield functions (as discussed in Section 2.5). When forces in members of a structure are considered then the condition of plastic admissibility can be written in matrix notation as

$$-s_o \leq s \leq s_o \quad 2.9$$

where s is the matrix of internal forces and s_o is the matrix of plastic capacities of the sections of members on which forces are applied.

For the plastically admissible condition if inequalities are satisfied such that they will always be less than or greater than internal forces then the state of internal forces are said to be inside the elastic domain. Mathematically it can be written as

$$-s_o < s < s_o \quad 2.10$$

2.3.2 Static Admissibility

When any state which is plastically admissible and is in equilibrium with a certain multiple of the reference loading (actual service load or design load) and satisfying the yield condition, then the state is called a statically admissible state (Jirasek and Bazant, 2002). If the load multiplier is defined as a factor which relates the reference load applied to the factor then, for a structure in a statically admissible state, the load multiplier μ_s is called a statically admissible load multiplier. A statically admissible state can be defined by a vector of internal forces, s , and by μ_s and satisfies the plastic admissibility and equilibrium condition, it can be written as

$$B^T s = \mu_s \bar{f} \quad 2.11$$

Here B^T is the static matrix which is the transpose of the kinematic matrix B (which can be extracted from kinematic equation which relate deformation of a member to

the displacement of the joint to which the member is connected), where B relates the strain in a structure to displacement using

$$e = Bd \tag{2.12}$$

where e and d are the strain and displacement vector matrices. \bar{f} is the reference load vector.

2.3.3 Kinematic Admissibility

Any structure can become a kinematic mechanism when yielding of bars or hinge formation of members exceeds the degree of static redundancy. There can be more than one possible failure mechanism depending upon the structure type and the number of degrees of freedom in the structure (Jirasek and Bazant, 2002).

When any potential failure mechanism for which external work done (which is the product of the reference loading \bar{f} and displacement rate \dot{d}) is positive then the state is expressed as a kinematically admissible state and the load multiplier μ_k is called a kinematic admissible load multiplier. μ_k can be determined from the power equality, where the power equality is when the external work done on the structure is dissipated internally by a plastic process during yielding. A kinematically admissible state can be described by vectors of both displacement rates, \dot{d} , and the vector of strain rates, \dot{e} , written mathematically as:

$$\dot{e} = B\dot{d} \tag{2.13}$$

for which

$$\bar{f}^T \dot{d} > 0 \tag{2.14}$$

where the left hand side of Equation 2.14 has the meaning of external work done obtained by the reference load \bar{f} . The external work done at the formation of any potential failure mechanism can be expressed as:

$$\dot{W}_{ext} = \mu_k \bar{f}^T \dot{d} \quad 2.15$$

At the formation of a mechanism the structure is in equilibrium and the external work done is dissipated by the plastic process in the yielding of a section of structure. Then the external work done is equal to the rate of dissipation during yielding in a plastic process and is written mathematically as

$$\dot{W}_{ext} = D_{int} \quad 2.16$$

where D_{int} is the dissipation rate and can be defined as the product of the plastic strain rate vector \dot{e} and plastic capacity vector s_o^T . Mathematically it can be written as

$$D_{int} = s_o^T \left| \dot{e} \right| \quad 2.17$$

Comparing Equation 2.15, 2.16 and 2.17, μ_k can be determined as

$$\mu_k = \frac{s_o^T \left| \dot{e} \right|}{\bar{f}^T \dot{d}} \quad 2.18$$

2.3.4 Postulate of Maximum Plastic Dissipation

If s_s is any plastically admissible vector of internal forces such that

$$-s_o < s_s < s_o \quad 2.19$$

and e is any vector of generalized plastic strain rates, then the product of the internal forces and the plastic strain rates must be less than or equal to the dissipation rate. Mathematically it can be written as

$$s_s^T \dot{e} \leq D_{\text{int}} \quad 2.20$$

Maximization of the product of the left hand side of Equation 2.20 can occur if

$$D_{\text{int}} = \max s_s^T \dot{e} \quad 2.21$$

Then maximization of the product of the right hand side of Equation 2.21 is when the internal force is a maximum (which is the yielding of the section). Therefore it can be written as

$$D_{\text{int}} = s_o^T \dot{e} \quad 2.22$$

and the above obtained equation, which maximize the dissipation rate, can be stated as

For given plastic strain rates, plastic dissipation rates are maximized by the actual internal forces for all the plastically admissible internal forces (Jirasek and Bazant, 2002).

2.3.5 Fundamental Theorem of Limit Analysis

No statically admissible multiplier is larger than any kinematically admissible multiplier, which can be written mathematically as (Jirasek and Bazant, 2002)

$$\mu_s \leq \mu_k \quad 2.23$$

As the plastic limit state is both statically and kinematically admissible, if μ_o is the safety factor related to the plastic limit state, therefore it can be written that

$$\mu_s \leq \mu_o \leq \mu_k \quad 2.24$$

Therefore two theorems can be written based on the above equation for a plastic limit state, as follows:-

Lower bound theorem

The statically admissible load multiplier is always less than or equal to the safety factor for the plastic limit state and the safety factor is the largest statically admissible load multiplier.

Upper bound theorem

The kinematically admissible load multiplier is always more than or equal to the safety factor for the plastic limit state and the safety factor is the smallest kinematically admissible load multiplier.

2.4 FLEXURAL BEHAVIOUR OF A BEAM

2.4.1 Elastic behaviour

Consider the behaviour of a generalized beam with a rectangular cross-section which is subjected to a bending moment. This bending moment will produce stress and strain variation which is assumed to be linear for the elastic phase. The section will behave elastically up to the point when the outer fibre reaches the yield stress σ_y (Englekirk, 1994). The bending moment M can be related to stress σ at the outer most fibre, by section modulus S by

$$M = \sigma S \quad 2.25$$

If σ reaches σ_y at the outer most fibre of the section, then the moment is called the yield moment M_y and the above equation becomes

$$M_y = \sigma_y S \quad 2.26$$

Similarly, curvature ϕ can also be related to moment as

$$\phi = \frac{M}{EI} \quad 2.27$$

and curvature at yield ϕ_y can be related to M_y as

$$\phi_y = \frac{M_y}{EI} \quad 2.28$$

Here E is Young's modulus of elasticity and I is second moment of area about the major axis of the section (Englekirk, 1994).

2.4.2 Inelastic behaviour

When the applied moment M for the cross-section exceeds M_y , a linear relationship between M and ϕ no longer exists and behaviour is commonly referred to as inelastic or nonlinear. In non linearity, the applied moment can be related to curvature if it is assumed that beyond yield strain ε_y there is plastic flow of the material, as depicted in Figure 2.2 for a rectangular section. For the region of plastic flow, stress will be a constant at σ_y and the additional moment is now taken by the inside region where strain is still less than ε_y . Now, in this case, the incremental change in curvature $\Delta\phi$ becomes

$$\Delta\phi = \frac{\Delta M}{EI_R} \quad 2.29$$

where I_R is the reduced second moment of area of the section where the strain is less than ε_y and ΔM is the change in moment beyond M_y . The resulting total

moment can be calculated using the stress distribution given by Figure 2.2. In the figure σ_{sh} is strain hardening stress and σ_{max} is the maximum stress considered. If strain hardening is considered beyond plastic flow, then there can also be a region where the stresses are more than σ_y . The distribution of stress for the strain hardening region is described in Figure 2.3. Using this distribution of stress, a moment and moment curvature relationship can be obtained.

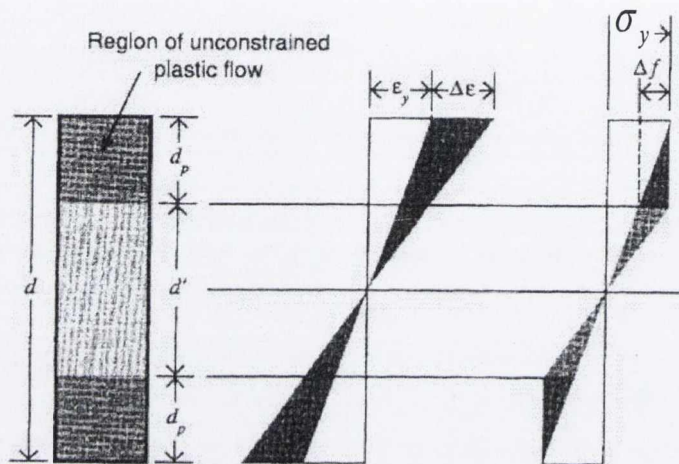


Figure 2.2 Plastic flow and stress and strain variation (Englekirk, 1994).

2.4.3 Impact of residual stresses on flexural behaviour

Non-linear behaviour in a beam is affected by the presence of residual stresses, which are locked into steel sections during the rolling process. Because of residual stresses non-linear behaviour starts considerably earlier than the theoretical yield moment M_y . During cooling of hot rolled sections, those portions of the beam which have most exposure to air cool and shorten first. In the case of an I-section, flange tips and the web cool first and compressive stresses develop in them, whereas mid flange cools later and tensile residual stresses develop in that section. Residual stress in a typical I-section is depicted in Figure 2.4. Residual stress affects the flexural behaviour as reflected in Figure 2.5. The shaded portion in the figure indicates that portion of the section which has reached σ_y . Therefore, due to the variation in the distribution of stress, the change in curvature is significantly affected

by residual stress. Though it affects the curvature, flexural strength of the section at yield will not be affected because at the outer fibre a uniform stress σ exists at some curvature. Though not entirely accurate, the residual stresses given by Figure 2.4 give a reasonable relationship between stress and moment at yield (Englekirk, 1994).

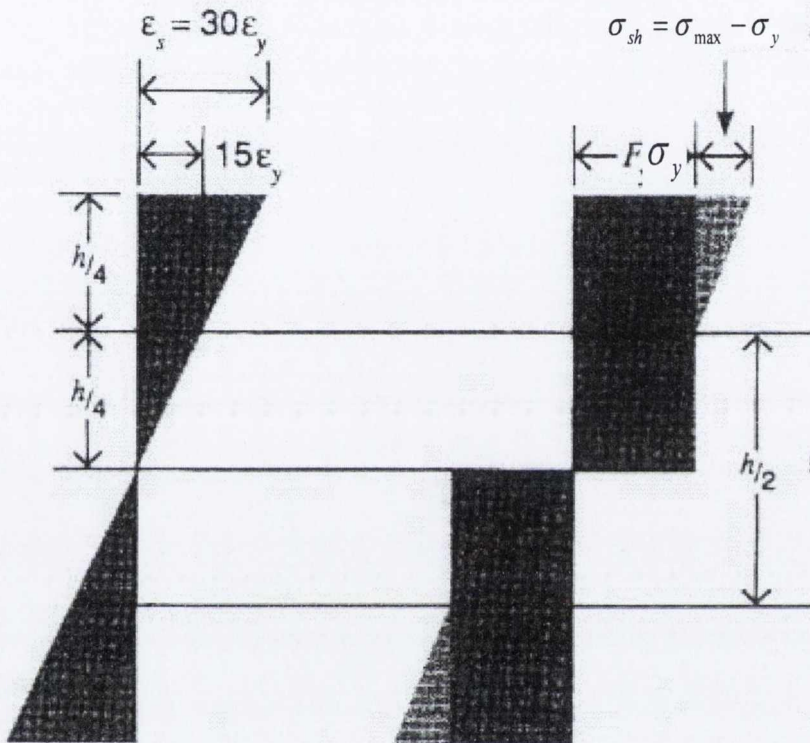


Figure 2.3 Strain hardening phase when stress is more than the yield stress (Englekirk, 1994)

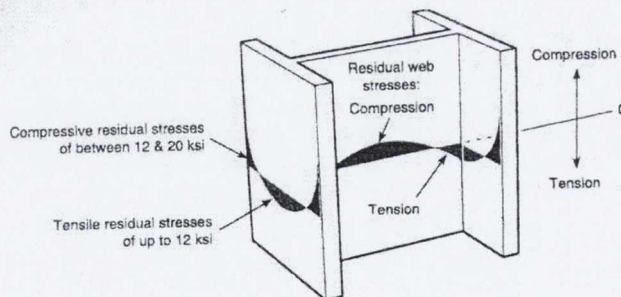


Figure 2.4 Residual stresses for an I-beam section ($1ksi = 0.006894kN/mm^2$) (Englekirk, 1994)

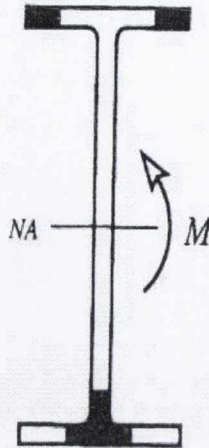


Figure 2.5 Shaded region indicates those regions which have reached σ_y (Englekirk, 1994).

2.4.4 Lateral torsional buckling (LTB)

Lateral torsional buckling is a phenomenon which occurs with beams and girders. Figure 2.6 shows a cantilever beam which buckles due to lateral torsional buckling (Dowling et al. 1988). It happens with beams which do not have sufficient lateral stiffness or lateral support and which experience local compression leading to lateral torsional buckling. In that case, the beam may buckle out of plane of loading as shown in the figure. Two mechanisms are possible; the first is when the beam buckles by deflecting laterally and the second is twisting of the beam. Buckling of the beam can be divided as elastic buckling and inelastic buckling. When the beam remains in the elastic phase when it buckles, this type of buckling normally occurs with long span beams. There are cases when a portion of the beam is inelastic when it buckles, where this type of buckling normally occurs in short span beams. The moment at which the beam buckles is called its critical moment M_{cr} . The buckling depends on the loading type, support conditions and any lateral restraint. Various solutions exist for different support type and boundary conditions (Trahair, 1993).

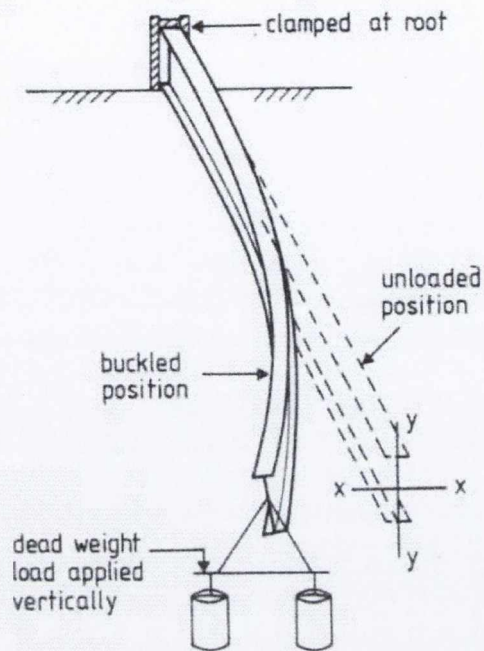


Figure 2.6 Lateral torsional buckling of a cantilever beam (Dowling et al. 1988)

Elastic beams

There are many cases solved to determine the critical moment for lateral torsional buckling. As an example the cantilever beam with load at the end is discussed here.

M_{cr} for a cantilever beam with a concentrated load applied at the end of the beam acting at a distance y_q below its centroid is given as (Trahair, 1993)

$$\frac{M_{cr}L}{\sqrt{(EI_y GJ)}} = 11 \left\{ 1 + \frac{1.2c}{\sqrt{(1+1.2^2 c^2)}} \right\} + 4(K-2) \left\{ 1 + \frac{1.2(c-1)}{\sqrt{(1+1.2^2 (c-0.1)^2)}} \right\} \quad 2.30$$

where

$$c = \frac{y_q}{L} \sqrt{\frac{EI_y}{GJ}}, \quad K = \sqrt{\pi^2 EI_w / GJL^2}$$

Here E is Young's modulus of elasticity, I_y is second moment of area about the Y-axis, G is the shear modulus, J is torsion section constant, I_w is warping section constant and L is the length of the bar.

Inelastic beams

In short span beams, yielding occurs before the beam reaches its ultimate moment capacity and it happens that some portion of the beam is inelastic when buckling commences. For these cases, the equations for the elastic beam are not valid. These cases are dealt in detail by Trahair and Bradford (1988), Nethercot and Trahair (1976) and Trahair (1983) and are not discussed here as they are not relevant to the current research.

Bracing effects on lateral torsional buckling

The purpose of providing bracing for the beam is to reduce the loss of strength through instability. Bracing sub divides the original unbraced span into shorter lengths restraining the compression flange against lateral torsional buckling. As the beam is practically neither straight nor free from lateral deformations or twist, some force will be induced in the bracing system. The force will normally be quite small but it considerably increases with the load carrying capacity of the beam section.

2.5 THEORY OF TORSION

2.5.1 Elastic Analyses

Uniform Torsion

Circular cross-section

The basic theory of the torsion of prismatic sections is restricted to elements with a circular cross-section (Johnson and Mellor, 1973). They referred to the theory which was first presented by Coulomb in 1784 and comprises the following equations

$$\frac{T}{J} = G\theta \quad 2.31(a)$$

$$\frac{\tau}{r} = G\theta \quad 2.31(b)$$

where T is the applied torque, J the polar moment of area, G the shear modulus, θ the angle of twist per unit length of the bar, τ the shear stress on a transverse section at a radius r from the longitudinal axis of the bar.

Rectangular cross-section members

In the case of uniform torsion of a rectangular member, the above equation is still valid. The only difference is the J value which is a torsional constant which can be evaluated using

$$J = \frac{h^3 b}{3} \left[1 - \frac{192}{\pi^5} \left(\frac{h}{b} \right) \sum_{n=1,3,5,\dots}^{\infty} \frac{1}{n^5} \tanh \frac{n\pi b}{2h} \right] \quad 2.32$$

In this equation, h and b are the cross-sectional dimensions of a rectangle and $h > b$.

I-Section members

An I section can be considered as composed of three rectangular plates. Therefore Equation 2.32 can be used to determine the torsional constant. In this case the torsional constant for both flanges and web are obtained separately using the equation by treating them as rectangular sections and the torsional constant of the three are summed to obtain the torsional constant of the entire section.

Similar exact solutions exist for elliptical and equilateral triangular cross-sections. For complex cross-sections, the exact solutions are difficult to obtain and Prandtl's membrane analogy can be used to obtain the approximate solutions (Boresi and Schmidt, 2003).

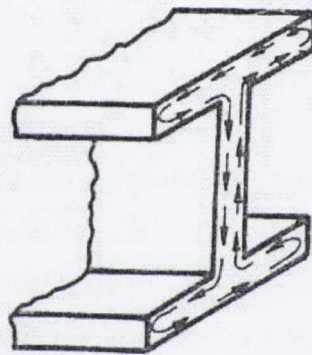
Prandtl's membrane analogy

This method is known to be effective for complex cross-sections. It is based on the similarity of the equilibrium equations related to membrane behaviour which is

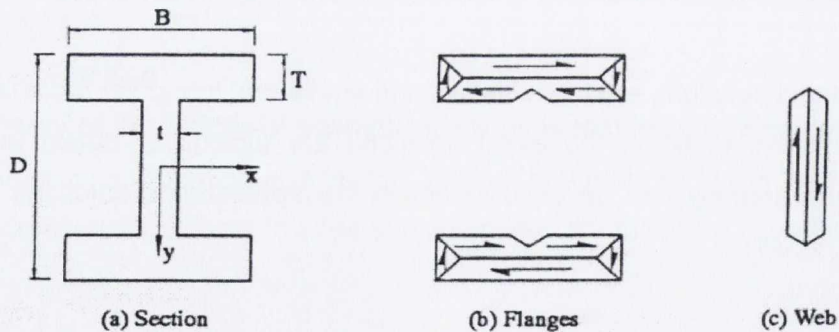
subjected to torsion and lateral pressure. This method is rarely used nowadays to obtain the solution of torsion problems of different cross-sections, although the details of the solution are given by Prandtl (1903).

St Venant's torsion

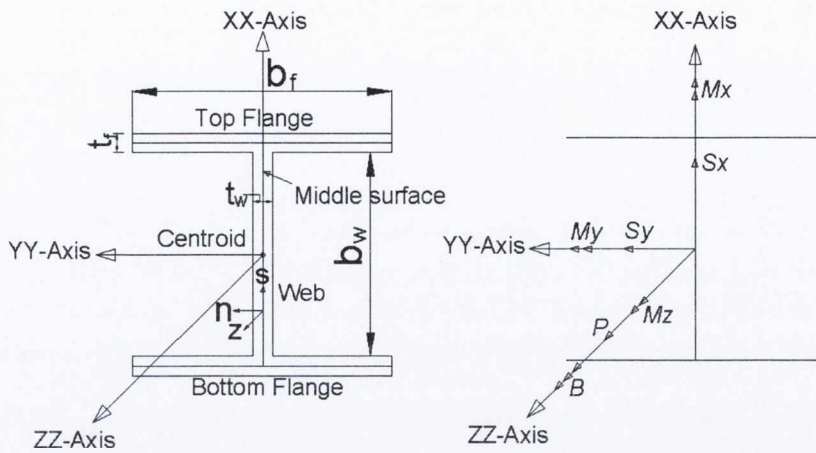
St Venant presented the theory of uniform torsion for which he gave the solution of the classical torsional problem and applied to different cross-sections (Boresi and Schmidt, 2003) to obtain the shear stress distribution. For circular cross-sections it results in Equation 2.31. For an I-section (details of the elements of I-section is given in Figure 2.7(c)), the stress distribution for St Venant's torsion is depicted in Figure 2.7(a).



a) St Venant's torsion shear stress distribution due to uniform torsion (Yang and Fan 1988)



b) Mitre model shear stress distribution due to uniform torsion (Billinghamurst et al. 1992)



(c) Local coordinates, elements of I-section, positive coordinate system with direction of positive forces

Figure 2.7 Shear stress distribution due to uniform torsion for an I-section

Mitre model

Another solution exists for the uniform torsion of steel members as given by the mitre model depicted in Figure 2.7(b). Both elastic and inelastic types of behaviour are considered. In the solution, the shear strain distribution in steel members under uniform torsion is considered by developing a mitre model for circular, rectangular and I-sections (Billinghurst et al. 1992). The elastic torque/twist relationship is predicted with high accuracy. The shear stress distribution for an I-section for the mitre model is given in Figure 2.7(b). Considering the solution for an I-section (details of the elements of I-section is given in Figure 2.7(c)) using the mitre model, the maximum elastic flange stress $\tau_{f\max}$ and web stress $\tau_{w\max}$ are given as:

$$\tau_{f\max} = Gt_f\theta\alpha_1 \text{ and } \tau_{w\max} = Gt_w\theta\alpha_1, \text{ where } \alpha_1 \text{ is defined below.}$$

The torque stress resultant T is given as (Billinghurst et al. 1992)

$$T = \tau_{f\max} \left[\frac{2b_f t_f^2}{3} + \frac{(D - 2t_f) t_w^3}{3t_f} + \frac{(D - 2t_f)(t_f - t_w) t_w^2}{4t_f} - \frac{(t_f^3 - t_w^3/2)}{6} \right] \quad 2.33$$

where

$$\alpha_1 = \frac{J}{\left[\frac{2b_f t_f^3}{3} + \frac{(D-2t_f)t_w^3}{3} + \frac{(D-2t_f)(t_f-t_w)t_w^2}{4} - \frac{(t_f^3-t_w^3/2)t_f}{6} \right]}$$

In the above, J is a torsional constant which is closely approximated by

$$J = \frac{2b_f t_f^3}{3} + \frac{(D-2t_f)t_w^3}{3} + 2\beta_1(t_f + t_w^2/4t_f)^4 - 0.42t_f^4$$

where

$$\beta_1 = -0.1\left(\frac{t_w}{t_f}\right)^2 + 0.03\left(\frac{t_w}{t_f}\right) \text{ for } 0 \leq t_w/t_f \leq 0.6$$

or

$$\beta_1 = -0.25\left(\frac{t_w}{t_f}\right)^2 + 0.53\left(\frac{t_w}{t_f}\right) - 0.175 \text{ for } 0.6 \leq t_w/t_f \leq 1.0$$

Non-Uniform Torsion

I-Section with one end restraint

An I-section tends to warp when subjected to a torque. When an I-section warps the flanges bend in two different directions. However, if the I-section is restrained at one end, torsional moment is resisted by the warping rigidity of the two flanges acting as beams parallel to the xy plane (Figure 2.8) and is also resisted by the torsional rigidity GJ of both web and flanges. At a small distance from the restrained end, partial warping takes place and the twisting moment may be considered to be made up of two parts (Boresi and Schmidt, 2003). One part is due to the twisting moment T_w which produces warping on the section in the absence of end restraint. The second part is a twisting moment T produced by lateral shear forces. Mathematically the total twisting moment T' can be written as the sum of both the moments as (Boresi and Schmidt, 2003):

$$T' = T_w + T \quad 2.34$$

where T_w and T can be obtained as (Boresi and Schmidt, 2003)

$$T_w = T' \left[1 - \frac{\cosh(L-x)/\alpha}{\cosh(L/\alpha)} \right] \quad 2.35(a)$$

$$\alpha = \frac{h}{2} \sqrt{\frac{EI_z}{JG}}$$

where E is the Young's modulus and I_z is the second moment of area about the Z-axis (as indicated in the figure).

$$T = JG\theta \quad 2.35(b)$$

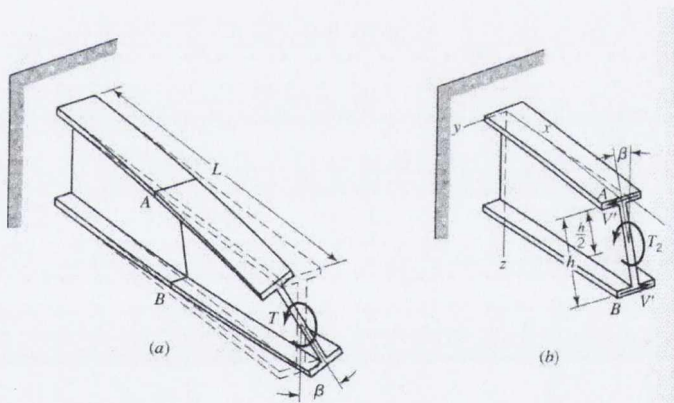


Figure 2.8 Torsional behaviour of beam when one end is restrained (Boresi and Schmidt, 2003)

When the flange is restricted against warping it will create a lateral bending moment in the flanges, where the moment is a maximum at the restrained end and can be obtained as (Boresi and Schmidt, 2003)

$$M_{z_{\max}} = \frac{T}{h} \alpha \tanh \frac{L}{\alpha} \quad 2.36(a)$$

The maximum rotation β occurs at the free end and is given as (Boresi and Schmidt, 2003):

$$\beta = \frac{T}{JG} \left(L - \alpha \tanh \frac{L}{\alpha} \right) \quad 2.36(b)$$

The maximum stress τ_{\max} is calculated as (Boresi and Schmidt, 2003)

$$\tau_{\max} = 2Tb / J \quad 2.36(c)$$

In the above equations L is the length of the beam, x is the distance from the restrained end of the beam

I-section with both end restraint

There are cases when an I-section is restrained at both the ends, as depicted in Figure 2.9(a). In that case, the maximum lateral bending moment and angle of twist at one end can be obtained as (Boresi and Schmidt, 2003)

$$M_{z_{\max}} = \frac{T}{h} \alpha \tanh \frac{L}{2\alpha}, \quad \beta = \frac{T}{JG} \left(L - 2\alpha \tanh \frac{L}{2\alpha} \right) \quad 2.37$$

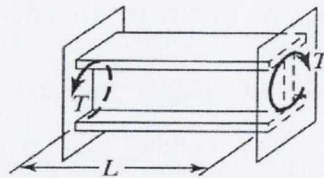


Figure 2.9(a) Beam subjected to torsional restraint at both ends (Boresi and Schmidt, 2003)

2.5.2 Non-linear Analyses

Uniform Torsion

The simplest solution in non-linear torsional analysis is given by Nadai (1950) called the Sand Heap Analogy. In this method a roof of constant slope is obtained by placing a heap of dry sand over the cross-section for which torsional capacity is required. The constant slope represents the total shearing stress at a point and is physically interpreted to be the maximum slope at a point in the membrane surface. The torque is thus obtained by the product of the volume of sand heap and the slope of sand heap which is the shear stress. Sand heaps are useful especially when section shapes are difficult to handle mathematically. For different sections, the plastic torque obtained using the sand heap analogy are

For a circular section, $T_p = \frac{2}{3} \pi a^3 \tau_y$, where a is the radius of circle.

For an equilateral triangle, $T_p = \frac{2}{3} a^3 \tau_y$, where $2a$ is the side of the triangle.

For a rectangular section, $T_p = a^2 \tau_y \frac{(3b-a)}{6}$, where a and b are the dimensions of a rectangle where $b > a$.

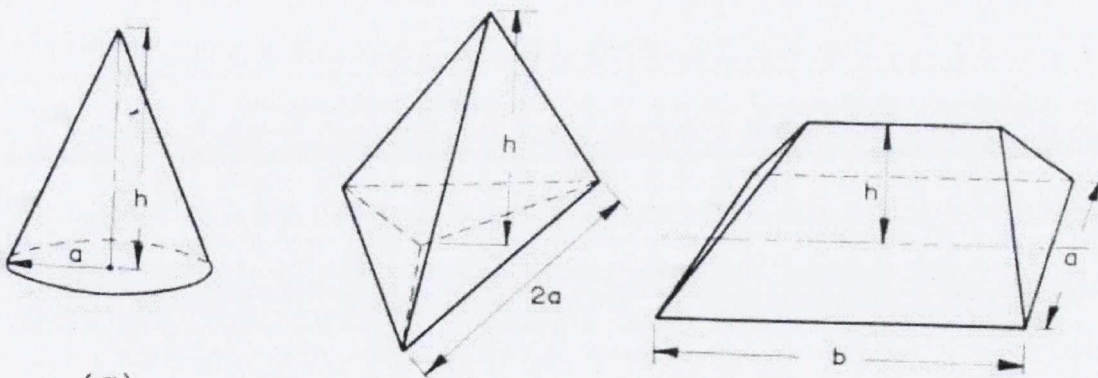


Figure 2.9(b) Constant slope roof indicating full plastic yielding across each section in Sand Heap Analogy

For an I-section, T_p can be obtained by considering it as composed of three rectangles and using the formula for a rectangular section three times, from which its T_p can be determined. Based on the mitre model, inelastic uniform torsion of an I-section can also be calculated as discussed in Billingham et al. 1992.

Non-Uniform Torsion

In both the approaches of the sand heap analogy and the mitre model it is assumed that the section is free to warp. This situation is not always practical because any element of a structure can be restrained at its end, especially I-sections where members subjected to torsion may well be prevented from warping. Several solutions exist for such problems where the end is restricted. The earliest such solution is an expression for the torque T_o to cause full yielding of the section under a warping restraint condition for a cantilever, given as

$$T_o = T_p + M_p h / L \quad 2.38$$

This expression was first proposed by Dinno and Merchant (1965) for cantilever beams subjected to applied torque at the free end, as an upper bound value to T_o . In this equation T_p is the sand heap torque for the entire section, M_p is the full plastic bending moment in one flange about the Z-axis, h is the distance between centroids of the I-section flanges and L is the length of the beam.

The above expression for the torque at the free end is assumed to be the sum of T_p and a torque which is due to a differential bending mechanism. The net force in each flange causes a plastic hinge at the restrained end of the beam. This equation approaches the T_p value as the length of the beam approaches infinity.

In the above approach to the torsion mechanism using the sand heap analogy, torque and moment hinge formation in the flanges are assumed. In another approach, it is considered that the web is only subjected to the sand heap torque

whereas the flange is composed of an interaction of the sand heap torque, transverse bending moment and shear force. This approach proposed by Augusti (1966) is based on assumptions regarding the relationship between the torque applied and the length and section dimensions. For this solution it is found that this approach always gives a torque less than that given by the previous approach.

In another approach (Boulton, 1962) a solution was obtained for I-section beams restrained at one or both the ends. In this approach, a system of stress distribution is assumed which has resultants in equilibrium with the applied torque and bending moment. The stress distribution was such that it does not violate the yield criterion at any point of the section. The solution was obtained for the case when torsion is applied in combination with bending about the major axis. A particular solution for the pure torsion case was obtained from the more general solution when major axis bending was assumed to be zero. The equation which leads to the solution in the pure torsion case is:

$$\frac{lT_p}{\nu\tau_y M_{xp} h} = \frac{2t_1}{\sqrt{t_1^2 - 1}} \tan^{-1} \frac{\sqrt{t_1^2 - 1} \tan \frac{1}{2} \beta_o}{t_1 - 1} - \beta_o \quad 2.39(a)$$

where

$$t_1 = \cos \beta_o \left(\frac{2A_v h \tau_y}{T_p} + 1 \right) \quad 2.39(b)$$

In the above equations, l is the length of the beam, $\nu = \sqrt{3}/2$ a factor derived for Von Mises yield criterion (as discussed in the reference), M_{xp} is the plastic moment capacity of the section about the X-axis, τ_y is the yield value of shear stress, $h = b_f + 0.5t_f$, $t = T_o/T_p$ and $\cos \beta_o = 0.15t$. Using both these equations, a theoretical curve is obtained as depicted in Figure 2.10 from which a value of t_1 can be calculated.

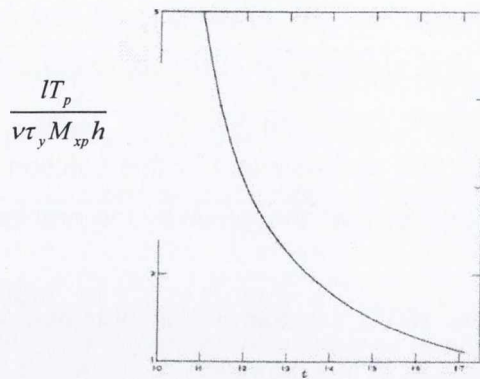


Figure 2.10(a) Pure torsion can be obtained based on a value of $\frac{IT_p}{v\tau_y M_{xp} h}$

(Boulton, 1962)

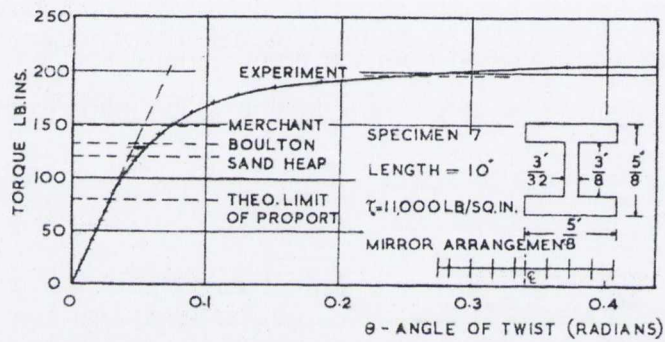


Figure 2.10(b) Torsion against rotation for the beam specimen tested by Dinno and Gill (1964)

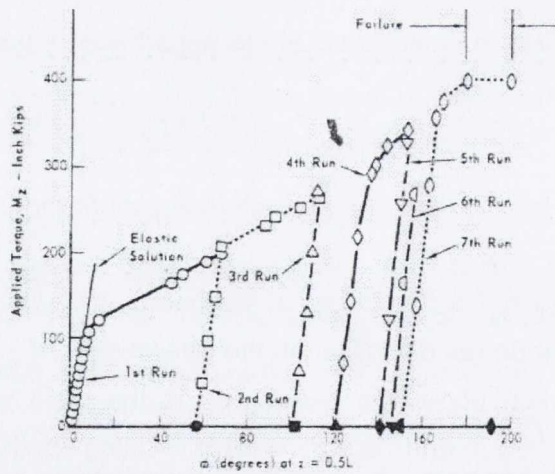


Figure 2.10(c) Torsion against rotation for the beam specimen tested by Farwell and Galambos (1969)

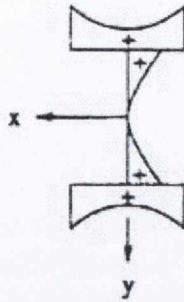


Figure 2.10(d) Wagner strains (Pi and Trahair, 1995)

Figure 2.10 Torsion experimental results, pure torsion graph by (Boulton, 1962) and Wagner strains

The cases which have been discussed up to this point are those in which the section is restrained at one or both the ends. There can be several other cases with different boundary conditions for which the torsional response of structure is required. A method has been developed (Pi and Trahair, 1995b) for plastic collapse analysis to predict plastic torsional collapse loads for different boundary conditions. In this method, a load factor at plastic collapse of a member in torsion is obtained. Independent analyses are undertaken, that no interaction at plastic collapse is assumed between uniform and warping torsion. In the analysis, the collapse load factor for the uniform torsion factor λ_{up} and warping torsion factor λ_{wp} are obtained separately and the actual plastic collapse load factor is approximated by the following equation

$$\lambda_p = \lambda_{up} + \lambda_{wp} \quad 2.40$$

These factors are obtained as follows:

Uniform torsion plastic collapse

A mechanism is assumed for different boundary conditions in which the collapse mechanism develops when a sufficient number of cross-sections of the member become fully plastic. The locations of the fully plastic sections are usually where the

reaction torque acts i.e. at the support. Load factors for different boundary conditions and loadings are given in Table 2.1. In the second column of the table, the diagrams shows the collapse mechanism i.e the dashed line is the new position of the remaining beam sample after hinge formation.

Warping torsion plastic collapse

When warping torsion is the only method of resisting the applied torque, it is assumed that a collapse mechanism develops in which a sufficient number of warping hinges form as a consequence of which the member turns into a mechanism. Load factors for different boundary conditions and loadings are given in Table 2.2.


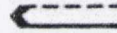
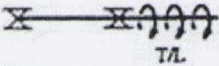

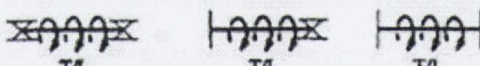

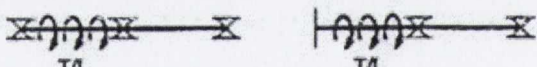

Members and Loadings	Collapse Mechanism	λ_{sp}
		$\frac{M_{sp}}{T}$
		$\frac{M_{sp}}{T}$
		$\frac{2M_{sp}}{T}$
		$\frac{2M_{sp}}{T}$

Table 2.1 Cantilever with mechanism formed due to uniform torsion (Pi and Trahair, 1995b)

In the table the load factor for warping torsion is related to M_{fp} , d , T and L where M_{fp} is the flange plastic moment given as $M_{fp} = \sigma_y b_f^2 t_f / 4$, $d = b_w + t_f$, T is the applied torque and L is the length of the member.

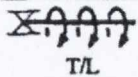

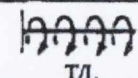

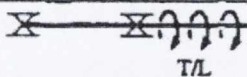

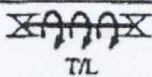

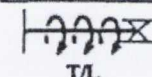

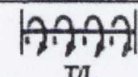

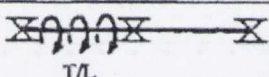
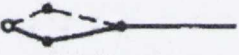
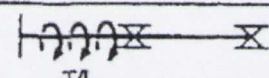

Members and Loadings	Collapse Mechanism	λ_{wp}
 T/L		0
 T/L		$\frac{2M_{fp} h}{TL}$
 T/L		$\frac{2M_{fp} h}{TL}$
 T/L		$\frac{8M_{fp} h}{TL}$
 T/L		$\frac{11.66M_{fp} h}{TL}$
 T/L		$\frac{16M_{fp} h}{TL}$
 T/L		$\frac{11.66M_{fp} h}{TL}$
 T/L		$\frac{16M_{fp} h}{TL}$

Table 2.2 Cantilever with mechanism formed due to warping torsion (Pi and Trahair, 1995b)

Numerical method for non-linear analysis of torsion

For an I-section, elastic-plastic torsional behaviour has been analysed numerically by developing a finite element model (Chen and Trahair, 1992). For uniform torsion, strain due to the mitre model was considered, whereas for non uniform torsion, the effects of warping and Wagner (Direct strains in the longitudinal direction perpendicular to the cross section, which appear at large rotations as depicted in Figure 2.10(d)) are considered. The finite element results obtained were compared with the result obtained by Merchant (as discussed above) for the cantilever case and a good correlation is made between both the results. The modelling was performed by Chen and Trahair (1992). However this model was improved later by Pi and Trahair (1995) which included an axial shortening (AS) effect for the analysis

keeping all the strains remain the same. The analysis shows good comparison with the experimental work performed by Farwell and Galambos (1969).

Experimental verification

To obtain the response of an I-section, two sets of experiments were performed independently by Dinno and Gill (1964) and Farwell and Galambos (1969). The difference between the experiments was the boundary conditions. The former researchers performed experiments on nineteen I-sections specimens in pure torsion to find the torsional carrying capacity. One of the results of the experimental result by Dinno and Gill (1964) is depicted in Figure 2.10(b). For all the experiments warping was restrained at both the ends. It was found that the actual torsion at yield was higher than the predicted sand heap value. In the second case Farwell and Galambos (1969) performed five experiments to obtain the torsional carrying capacity of beam samples which were subjected to simply supported conditions that is the beams were restrained against rotation but free to warp at the end. All the experiments were performed for large rotations and only in one case did failure occur at a total angle of twist of about 200° . The torsion against rotation response when Farwell and Galambos (1969) achieved 200° rotation is depicted in Figure 2.10(c). It was concluded from the experiments that I-sections can sustain very large rotations before failure occurs and the actual capacities of sections were more than the sand heap value.

Warping effects of Torsion

In an I-section beam, torsion cause distortion of the plane section and it is called warping of the section. The warping of the beam accompanied by longitudinal normal stresses appearing in each flange of the beam (Vlasov, 1959). This longitudinal normal stresses is a system of mutually balancing longitudinal tension. This generalized force is called bimoment of the beam. For an I-section it creates moment in the flanges in two different direction and bimoment is the product of moment and the centroidal distance between the flanges. As moment of the flanges is multiplied by the centroidal distance of the beam, hence, its units are unit of moment multiplied by the unit of length. Therefore in the current work its unit is $kN.m^2$

Secondary effects of Torsion

Two secondary effects which are the Wagner effects and axial shortening are discussed. The Wagner effect causes direct positive strains and occurs at large rotations. The distribution of Wagner strain for an I-section is depicted in Figure 2.10(d). Axial shortening causes shortening of a member in torsion and it develops negative strains in a member.

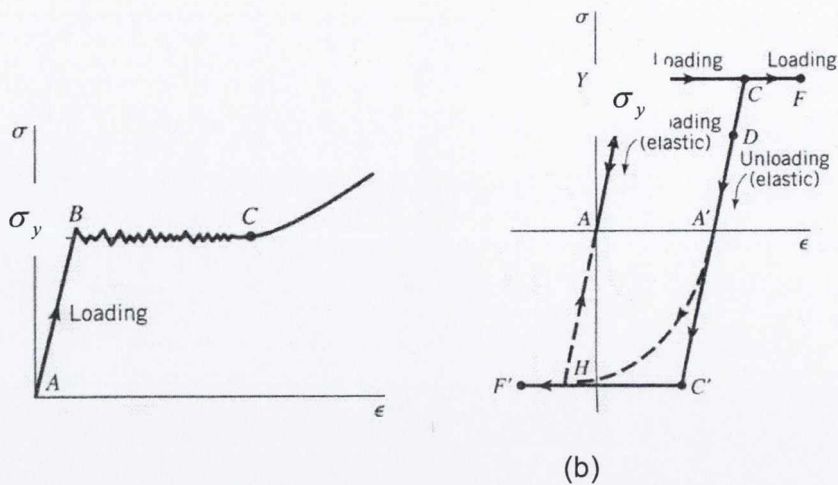
2.6 INELASTIC MATERIAL BEHAVIOUR AND YIELD CRITERIA

2.6.1 Uniaxial Stress Strain Relationship

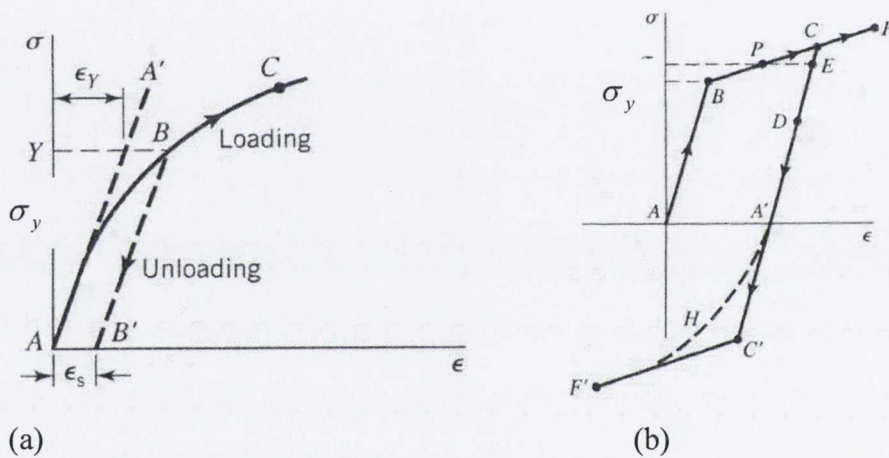
When a uniaxial tension test is performed, the change of response from linear elastic to inelastic can be abrupt or gradual (Boresi and Schmidt, 2003). Ductile materials like mild steel show an abrupt response when their elastic limit is reached. The stress level at this point is called the yield stress σ_y . The stress-strain diagram for such a response is shown in Figure 2.11(a). Such stress strain curves are difficult to use in the solution of complex problems, hence, an idealization of the response is made. The idealized curve is shown in Figure 2.11(b).

There are materials, such as steel alloys, for which the response is not abrupt but a relatively smooth decline of the slopes of the uniaxial stress strain diagram occurs as depicted in Figure 2.12(a). Yield stresses for those cases are arbitrarily defined as those stresses that correspond to a given permanent strain which remains upon unloading. The unloading is a path given by BB', parallel to AA' as depicted in the figure. Hence, such curves exhibit strain hardening in the initial plastic region. The stress strain curve for such a material might be idealized with a bilinear curve as shown in Figure 2.12(b).

There are cases when the deformation obtained for a material is so large that the elastic strain is very small compared to the total strain. For those cases, such a curve is modelled by a rigid perfectly plastic curve, as depicted in Figure 2.13(a). In the case of hardening, such curves are idealized as depicted in Figure 2.13(b).



(a) (b)
Figure 2.11 Experimental and idealized stress strain curve for mild steel (Boresi and Schmidt, 2003)



(a) (b)
Figure 2.12 Experimental and idealized stress strain curve for steel alloys(Boresi and Schmidt, 2003).

2.6.2 Multiaxial stress state

Inelasticity can occur when a member is subjected to a multiaxial stress state. Under a multiaxial stress state, yielding is initiated at values other than individual stress components. All components of stress are combined into an effective uniaxial stress. This effective stress is compared with a material property (assumed to be some function of uniaxial yield stress) by a yield criterion to identify the commencement of the inelastic response.

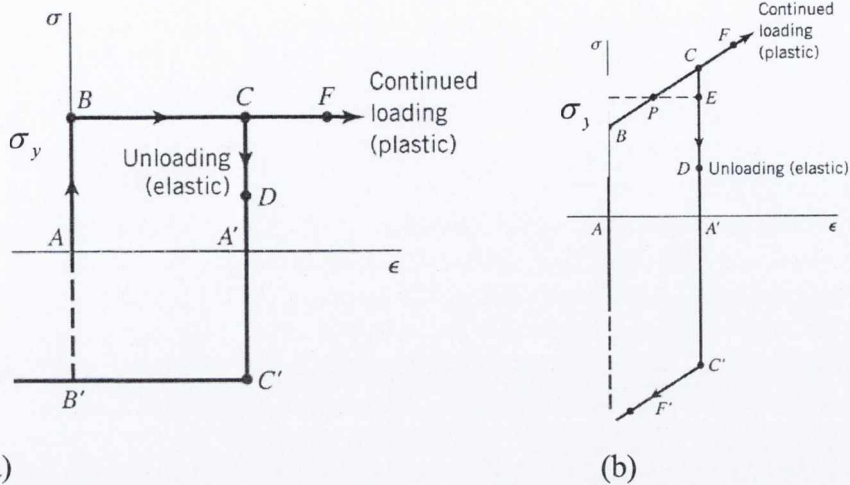


Figure 2.13 Idealized curve for small elastic strain (Rigid perfectly plastic curve) (Boresi and Schmidt, 2003).

Yield criterion

A yield criterion can be any statement (usually in mathematical form) that defines the conditions for yielding to occur. It can be expressed in terms of some specified terms. For example, it can be expressed as the stress state, the strain state, a strain energy quantity or other. In mathematical form, a yield criterion is usually expressed by means of a yield function f , where

$$f = f(\sigma_{i,j}, \sigma_y) \quad 2.41$$

where f is a general form of yield function which express yield criterion in mathematical form. $\sigma_{i,j}$ defines the actual state of stress and σ_y is the yield stress in uniaxial tension (or compression). For a yield function, three conditions can be defined; first is when the yield criterion is satisfied $f(\sigma_{i,j}, \sigma_y) = 0$, the second condition is when the stress state is elastic $f(\sigma_{i,j}, \sigma_y) < 0$ and the third condition is undefined $f(\sigma_{i,j}, \sigma_y) > 0$. Unfortunately, no single yield criterion has been developed that can predict yielding of brittle or ductile materials to such an accuracy that it can be universally used. Different parameters are used to define yield criterion of both ductile and brittle materials.

The simplest approach adopted for yield criteria considers the maximum principal stress criterion (Boresi and Schmidt, 2003). This criterion states that “yielding begins for a material at a point when the maximum principal stress reaches a value equal to the yield stress σ_y in tension (compression)”. When a uniaxial stress state is considered, yielding will occur when principal stress σ_1 reaches a value equal to σ_y . For biaxial stress states, it predicts yielding when $\sigma_1 = \sigma_y$ in spite of the fact that other principal stresses σ_2 also act at the point. This means that the criterion ignores the effect of principal stresses from other directions. Hence, it can be defined as

$$f = \max(|\sigma_1|, |\sigma_2|, |\sigma_3|) - \sigma_y \quad 2.42$$

The yield surface for the maximum principal yield criterion is defined by the locus of stress states, hence, satisfying the yield criterion; therefore the yield surface for the criterion is defined by relations

$$\sigma_1 = \pm\sigma_y, \sigma_2 = \pm\sigma_y, \sigma_3 = \pm\sigma_y \quad 2.43$$

The yield surface for this criterion consists of six planes which are perpendicular to the principal stress coordinate axes as depicted in Figure 2.14. This criterion was first given by Rankine, as referred in Boresi and Schmidt (2003) and is known as Rankine’s criterion. This criterion is applicable for brittle materials where materials fail by brittle fracture.

The previous criterion was based on principal stress and was simple to apply. There are certain criteria for brittle materials which depend on other different parameters, such as the one which depends on the maximum principal strain. According to this criterion, yielding begins when the maximum principal strain at a point reaches a value equal to the yield strain. In uniaxial strain it is stated that yielding begins when the maximum principal strain at a point reaches a value equal to $\varepsilon_1 = \varepsilon_y$.

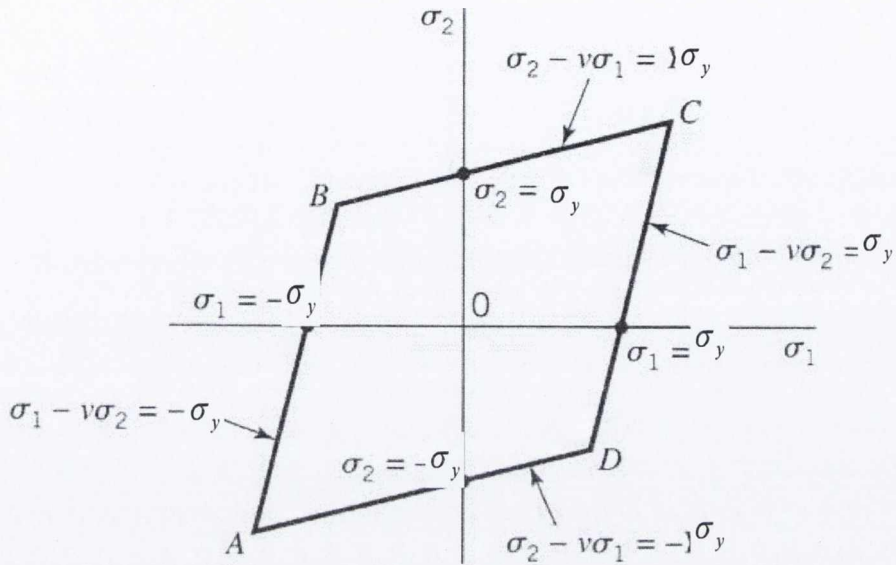


Figure 2.14 Yield surface of maximum principal stress yield criterion (Boresi and Schmidt, 2003)

Consider an isotropic material subjected to a biaxial stress condition; the maximum principal strain can be related to the principal stress as $\varepsilon_1 = (\sigma_1 / E) - \nu(\sigma_2 / E)$. Although this criterion predicts yielding in the form of magnitudes of strain, its yield function can be expressed in terms of stress. Assuming ε_1 as the principal strain, it can be related to principal stresses as (Boresi and Schmidt, 2003)

$$\varepsilon_1 = \frac{1}{E}(\sigma_1 - \nu\sigma_2 - \nu\sigma_3) \quad 2.44$$

Equating ε_1 to ε_y , the yield function can be obtained as:

$$f_1 = |\sigma_1 - \nu\sigma_2 - \nu\sigma_3| - \sigma_y = 0 \quad 2.45$$

If it is assumed that the principal strain ε_1 is not always the largest, then the other two principal strains ε_2 and ε_3 may have the largest magnitude and the additional possibilities can be written as;

$$f_2 = |\sigma_2 - \nu\sigma_1 - \nu\sigma_3| - \sigma_y = 0, f_3 = |\sigma_3 - \nu\sigma_1 - \nu\sigma_2| - \sigma_y = 0 \quad 2.46$$

This criterion as referred in Boresi and Schmidt (2003) is also called St Venant's criterion. The yield surface for the maximum principal strain criterion considering the biaxial stress state is shown in Figure 2.15.

Another yield criterion proposed by Beltrami as referred to in Boresi and Schmidt, (2003) states that yielding at a point commences when the strain energy density at the point equals the strain energy density when yielding occurs in uniaxial tension (or compression). In terms of principal stress, strain energy density can be defined as:

$$U_o = \frac{1}{2E} [\sigma_1^2 + \sigma_2^2 + \sigma_3^2 - 2\nu(\sigma_1\sigma_2 + \sigma_1\sigma_3 + \sigma_2\sigma_3)] > 0 \quad 2.47$$

If considering a uniaxial stress state, where $\sigma_1 = \sigma_y, \sigma_2 = \sigma_3 = 0$ the above equation reduces to

$$U_{oy} = \frac{\sigma_y^2}{2E} \quad 2.48$$

This criterion states that yielding is commenced when the strain energy density U_o for any stress state equals U_{oy} . Therefore Equations 2.47 and 2.48 can be related to derive the equation as

$$\sigma_1^2 + \sigma_2^2 + \sigma_3^2 - 2\nu(\sigma_1\sigma_2 + \sigma_1\sigma_3 + \sigma_2\sigma_3) - \sigma_y^2 = 0 \quad 2.49$$

From the above equation it is evident that the yield surface for this criterion depends on the Poisson's ratio and its shape varies with the Poisson's ratio. The yield surface for the biaxial stress state for this criterion is depicted in Figure 2.16.

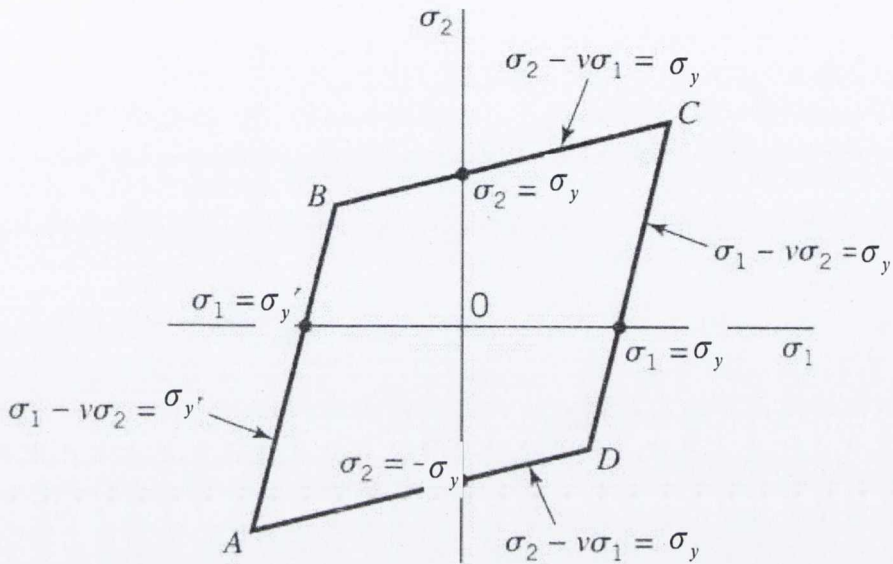


Figure 2.15 Yield surface of maximum principal strain yield criterion (Boresi and Schmidt, 2003).

There are certain materials where metal crystals have slip planes which offer low resistance to shear force. During to this, the yield criterion for such metals depends on certain limits of shear stress. Two such criteria are common (Boresi and Schmidt, 2003). One states that yielding begins when the maximum shear stress at a point reached a value equal to the maximum shear stress at yielding for a uniaxial tension (or compression). The other criterion states that yielding begins when distortional strain energy density at a point reached a value equal to the distortional strain energy density at yielding for a uniaxial tension (or compression). Considering the first criterion, also called the Tresca criterion for a multiaxial stress state, the maximum shear stress is $\tau_{\max} = (\sigma_{\max} - \sigma_{\min})/2$ where σ_{\max} and σ_{\min} are the maximum and minimum principal stress state respectively. The magnitude of

maximum shear stress will be the maximum absolute value obtained from the following three equations:

$$\tau_1 = |\sigma_2 - \sigma_3|/2, \tau_2 = |\sigma_3 - \sigma_1|/2 \text{ and } \tau_3 = |\sigma_1 - \sigma_2|/2 \quad 2.50$$

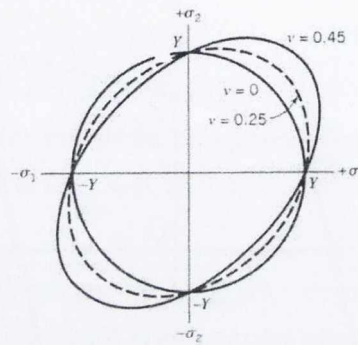


Figure 2.16 Yield surface of strain energy density yield criterion (Boresi and Schmidt, 2003)

Yielding for any of the following conditions under the multiaxial state can occur.

$$\sigma_2 - \sigma_3 = \pm\sigma_y, \sigma_3 - \sigma_1 = \pm\sigma_y \text{ and } \sigma_1 - \sigma_2 = \pm\sigma_y \quad 2.51$$

Using the above equations, the yield surface for this criterion can be drawn in principal stress space, as depicted by the hexagon in Figure 2.17.

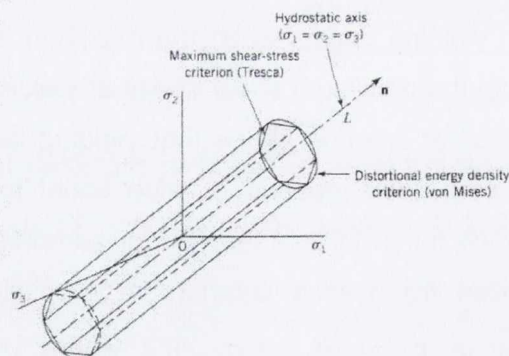


Figure 2.17 Yield surface in principal stress space for the Tresca and Von-Mises yield criteria (Boresi and Schmidt, 2003)

The other yield criterion attributes to Von Mises, often called the Von Mises yield criterion. This criterion is related to distortional strain energy density at a point. In terms of principal stress distortional strain energy density, it can be defined as:

$$U_D = \frac{(\sigma_1 - \sigma_2)^2 + (\sigma_2 - \sigma_3)^2 + (\sigma_3 - \sigma_1)^2}{12G} \quad 2.52$$

For a uniaxial stress state, $\sigma_1 = \sigma, \sigma_2 = \sigma_3 = 0$, if yielding takes place whence, distortional strain energy density at yielding for the uniaxial state is defined as:

$$U_D = \sigma_y^2 / 6G \quad 2.53$$

As the definition states, yielding occurs when distortional strain energy density at a point reached a value equal to distortional strain energy density at yielding for a uniaxial tension (or compression). Therefore Equations 2.52 and 2.53 can be equated to obtain the yield function for the distortional strain energy density criterion as:

$$f = |J_2| - \frac{1}{3}\sigma_y^2 \quad 2.54$$

where

$$J_2 = -\frac{1}{6}[(\sigma_1 - \sigma_2)^2 + (\sigma_2 - \sigma_3)^2 + (\sigma_3 - \sigma_1)^2]$$

Using the above equation, the yield surface for the distortional strain energy density criterion can be drawn which forms a cylinder that circumscribes the Tresca hexagon, as depicted in Figure 2.17.

In terms of the local coordinate system, J_2 can be defined as

$$J_2 = \frac{1}{6} \left[(\sigma_{zz} - \sigma_{ss})^2 + (\sigma_{ss} - \sigma_{nn})^2 + (\sigma_{nn} - \sigma_{zz})^2 \right] + (\sigma_{zs}^2 + \sigma_{sn}^2 + \sigma_{zn}^2)$$

Putting the value of J_2 in Equation 2.54 and, for plasticity with, $f = 0$, gives the equation as

$$f = \frac{1}{2} \left[(\sigma_{zz} - \sigma_{ss})^2 + (\sigma_{ss} - \sigma_{nn})^2 + (\sigma_{nn} - \sigma_{zz})^2 \right] + 3(\sigma_{zs}^2 + \sigma_{sn}^2 + \sigma_{zn}^2) - \sigma_y^2 = 0 \quad 2.55$$

When a section is subjected to direct stress in one direction and a shear stress, then $\sigma_{ss} \approx \sigma_{nn} \approx \sigma_{zn} \approx \sigma_{sn} \approx \sigma_{nz} \approx \sigma_{ns} \approx 0$, which reduces the above equation to

$$f = \sigma_{zz}^2 + 3\sigma_{zs}^2 - \sigma_y^2 = 0 \quad 2.56$$

Under condition of pure yielding in shear, σ_{zs} can be replaced by the yield shear stress τ_y which can be related to uniaxial yield stress σ_y and the above equation reduces to

$$3\tau_y^2 = \sigma_y^2 \quad 2.57$$

2.6.3 Yield criteria for different sections

When a material is assumed to behave in a elastic-perfectly plastic manner, a plastic hinge forms due to bending moment at the plastic moment capacity M_p of a section. When more than one force acts on a section, the resulting plasticized cross section is known as a generalized plastic hinge. For example, considering the simplest case when moment about one axis is acting on a section in combination with an axial force, then there can be different combinations of values of moment and axial force for which a hinge can form. The set of all such combinations of values can be represented graphically and is called a yield surface. A yield criterion for any section is first obtained normally, called the equation of the yield surface or

interaction equation or equations. Yield criteria when any section is subjected to two forces or more are discussed presently.

Interaction equations when sections are subjected to two forces

Interaction of bending moment, and axial force

The simplest of such equations is for a rectangular section subjected to a bending moment M applied about a centroidal axis and axial force P . Its equation is given as (Jirasek and Bazant, 2002):

$$\left(\frac{P}{P_p}\right)^2 + \frac{M}{M_p} = 1 \quad 2.58$$

Other axial force and bending moment solutions were also given by Kom and Galambos (1968), Harung and Millar (1973) and Mrazik et al. (1987).

Several interaction equations have also been developed when combinations of two other forces are considered for different sections. For example, the solution for an I-section when biaxial bending moments are considered was given by Strelbitzkaya (1958) who gives a solution, in which forces cause two different stresses namely shear stresses and direct stresses. One such combination is that of the bending moment causing direct stresses while the associated shear force causes shear stresses. This combination is studied by many authors and is discussed presently.

Interaction of shear force and bending moment

Two approaches are adopted for the solution of an interaction equation of an I-section when a shear force and bending moment act on a section. In the first approach, only plasticisation of the web is considered, whereas the state of stress in the flanges is not considered. In the second approach, plasticisation of the entire cross section is considered, with the shear stress is only in the web or in both the flanges and web.

One such solution, based on the first approach, is given by Broude (1953). In the solution, a rectangular section is considered for the web, while shear stress in the

flanges are ignored. An empirical equation of the solution for the interaction between applied bending moment M_p and applied shear force S_x is given as:

$$\left(\frac{M}{M_p}\right)^2 + \left(\frac{S_x}{S_{XP}}\right)^2 - \bar{\alpha} \left(\frac{M}{M_p}\right)^2 \left(\frac{S_x}{S_{XP}}\right)^2 = 1 \quad 2.59$$

In which $\bar{\alpha} \approx \frac{2.9 - 2.7 \bar{\beta}}{3 \left(1 - \frac{\bar{\beta}}{3}\right)^2}$

where $\bar{\beta}$ is the ratio of static moment of half the web area A_w on one side of the neutral-axis to the static moments of the entire cross sectional area A_g on the same side. S_{XP} is the plastic capacity in shear.

Another solution was obtained based on the first approach. Here it was assumed that at a proportional increase of both types of stresses in the cross section, its plasticisation spreads from the web edges inwards and also outwards from the mid point. The point when both the domains are fully plasticized represent the boundary of the stress distribution. This solution, given by Juhas (1975) is not related to the current research and is not discussed further here.

Several solutions exist when the second approach is taken. The simplest solution is when shear stresses are only considered in the web, where the distribution of shear stresses and normal stresses in the web are assumed constant and are depicted in Figure 2.18. This assumption was considered by Heyman and Dutton (1954), Sobotka (1959) and Strelbitzkaya (1958). This assumption results in an interaction equation given by:

$$\frac{M}{M_P} + \frac{1}{1 + 4 \frac{t_f b_f d}{t_w b_w b_w}} \left[1 - \sqrt{1 - \left(\frac{S_X}{S_{XP}} \right)^2} \right] = 1 \quad 2.60$$

Several solutions were developed for rectangular cross-sections as given by Broude (1953), Hodge (1959), Rzhanitzyn (1954), Snitko (1952) and by several other authors such as Sobotka, Strelbitzkaya, Juhas, Bezukhov, Zhudin and Neal as discussed in Mrazik et al (1987). Their solutions can be found in Mrazik et al (1987) but are not discussed here as the solutions were not directly relevant to the scope of the current research.

Interaction of bending moment and torsion

Bending and torsion actions on various sections has been studied by Gaydon and Nutall (1957) while for circular and tubular sections, Hill and Siebel (1951, 1953) presented solutions. Their solutions are not discussed further as they were not relevant to the scope of the current research.

Interaction equations when sections are subjected to three forces

Interaction of bending moment, axial force and shear force

This case is different from the previous case of bending moment and shear force in the sense that the neutral axis location now changes due to the addition of an axial force. However, the approach adopted will be the same as it also involves direct stress and shear stress.

In the case of an I-section both bending moment and shear force can be applied in two different ways. One is when the bending moment is applied about the major axis of the section and shear force is applied in the X direction: the second is when the bending moment is applied about the minor axis of the section and the shear force is applied in the Y direction. Both these cases will now be considered.

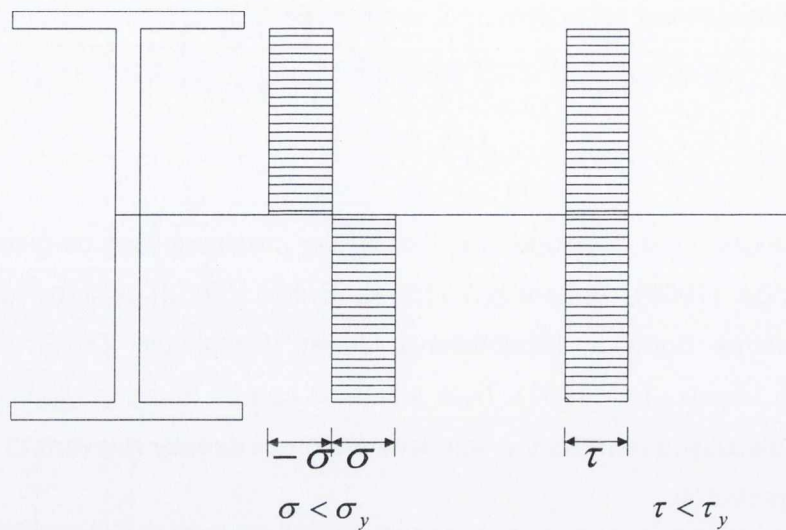


Figure 2.18 Distribution of shear stresses and normal stresses considered by Heyman and Dutton (1954), Sobotka (1959) and Strelbitzkaya (1958) to develop the interaction equation considering bending moment and shear force

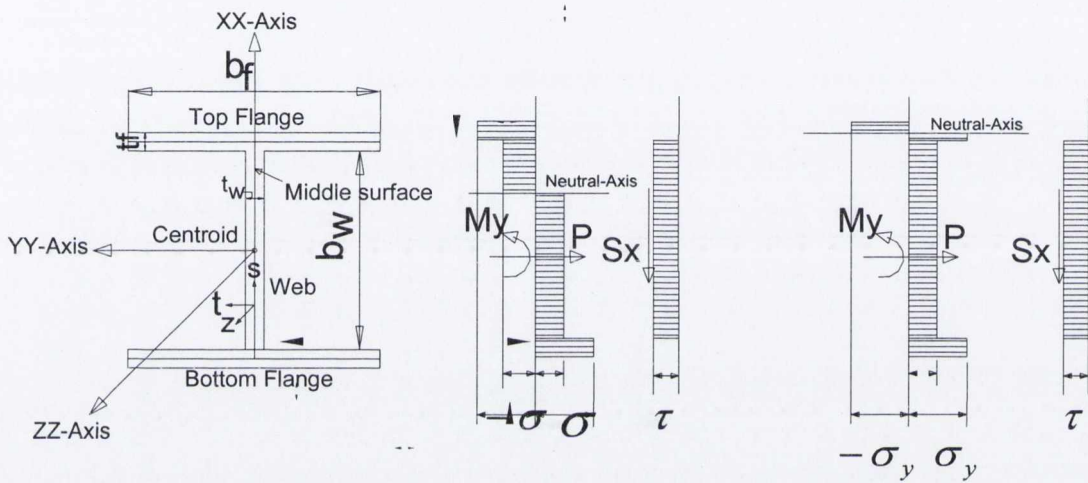
When the bending moment, M_y , is applied about the major axis of the section and the shear force in the X-direction, in addition to an axial force being applied, the solution depends on the assumption that the shear stress is confined to the web only. Two cases can be arise:

- a.) The neutral-axis passes through the web
- b.) The neutral-axis passes through the flange

The distribution of normal and shear stress through the depth when the neutral-axis passes through the web is depicted in Figure 2.19(a). The stress distribution in the web consists of a constant direct stress and shear stress distribution in the web. The distribution of stress in the flange is due to direct stress only. The direct stress and shear stress are related by a distortional strain energy density yield criterion given by Sobotka (1975), as follows:

$$\frac{M_y}{M_{yp}} + \frac{\left(1 + 2A_f / \left[A_w \sqrt{1 - (S_x / S_{XP})^2}\right]\right)^2}{1 + 4A_f / \left[A_w \sqrt{1 - (S_x / S_{XP})^2}\right]} \left(1 + \frac{t_f}{b_w}\right) \left(\frac{P}{P_p}\right)^2 = 1 \quad 2.61$$

Here M_y is the bending moment applied about the Y-axis of the section and M_{yp} is the plastic moment capacity of the section about the Y-axis.



a) Neutral-Axis intersects the web b) Neutral-Axis intersects the flange

Figure 2.19 An I-section subjected to bending about the Y-axis shear force and axial force. Distribution of normal and shear stresses when neutral-axis passes through the web and flange

The distribution of normal and shear stress through the flange when the neutral-axis passes through the flange is depicted in Figure 2.19(b). The same distribution of stress in both flanges and web will be valid except the neutral-axis is lying in the flange as depicted in the figure. A similar approach is adopted as in the previous case, to obtain the interaction equation, given as follows:

$$\frac{M_y}{M_{yp}} + \frac{\left(1 + 2\left[\frac{P}{P_p}(1 + 2S_{XA}) - 1\right] + \frac{t_f/b_w}{S_{XA}}\left[\frac{P}{P_p}(1 + 2S_{XA}) - 1\right]^2\right)}{1 + 4S_{XA}\left(1 + \frac{t_f}{b_w}\right)} = 1 \quad 2.62$$

where $S_{XA} = A_f / \left[A_w \sqrt{1 - (S_x / S_{xp})^2} \right]$

In the case when bending moment M_x is applied about the minor axis of the section and shear force in the Y-direction, in addition to an axial force, the solution depends on the assumption that the shear stress is confined to the flanges only. Again two cases can arise

- a). The neutral-axis passes through the web
- b). The neutral-axis passes through the flange

For the case when the neutral-axis passes through the web, the distribution of normal and shear stresses through the depth is depicted in Figure 2.20(a). A constant direct and shear stress distribution is assumed for the flange, whereas the distribution of stress in the web is only due to direct stress. A similar approach by Sobotka (1975) is adopted as in the previous case to obtain the interaction equation. The relationship is given by:

$$\frac{M_x}{M_{xp}} + \frac{\frac{\sigma_{sf}}{\sigma_y} \frac{t_f}{b_w} \left(1 + 2 \frac{P_{pf}}{P_{pw}}\right)^2}{\left(1 + 2 \frac{\sigma_{sf}}{\sigma_y} \frac{t_f}{b_w}\right) \left[\frac{\sigma_{sf}}{\sigma_y} \frac{t_f}{b_w} + 2 \left(\frac{P_{pf}}{P_{pw}}\right)^2\right]} \left(\frac{P}{P_p}\right)^2 = 1 \quad 2.63$$

In the above equation

$$\sigma_{sf} = \sigma_y \sqrt{1 - \left(\frac{S_x}{S_{XP}}\right)^2}, \quad P_{pf} = \sigma_y t_f b_f \sqrt{1 - \left(\frac{S_x}{S_{XP}}\right)^2} \quad \text{and} \quad P_{PW} = \sigma_y A_w$$

and here, M_x is the bending moment applied about the X-axis of the section and M_{xp} is the plastic moment capacity of the section about the X-axis.

For the case when the neutral-axis passes through the flange the distribution of normal and shear stress through the depth is depicted in Figure 2.19(b). Similar approach is adopted as adopted in the previous case to obtain the interaction equation. The relationship is given as follows

$$\frac{M_x}{M_{xp}} + \frac{1}{2} \frac{\left[\frac{P}{P_p} \left(1 + 2 \frac{P_{pf}}{P_{PW}} \right)^2 - 1 \right]^2}{\frac{\sigma_{sf} t_f}{\sigma_y b_w} + 2 \left(\frac{P_{pf}}{P_{PW}} \right)^2} = 1 - \frac{\frac{\sigma_{sf} t_f}{\sigma_y b_w}}{\frac{\sigma_{sf} t_f}{\sigma_y b_w} + 2 \left(\frac{P_{pf}}{P_{PW}} \right)^2} \quad 2.64$$

Several equivalent solutions exist for the case of a rectangular section. The earliest solution by Paltchevskiy (1948) is based on the stress distribution of normal and shear stress, with further solutions given by Sobotka (1975) and Smirak (1967), where they assume a different stress distribution as compared to Paltchevskiy. The solution of all the three cases are not relevant to the current research and are therefore not discussed further here.

In the case of an I-section both bending moment and shear force can be applied in two different ways. One is when the bending moment is applied about the major axis of the section and shear force is applied in the X direction: the second is when the bending moment is applied about the minor axis of the section and the shear force is applied in the Y direction. Both these cases will now be considered.

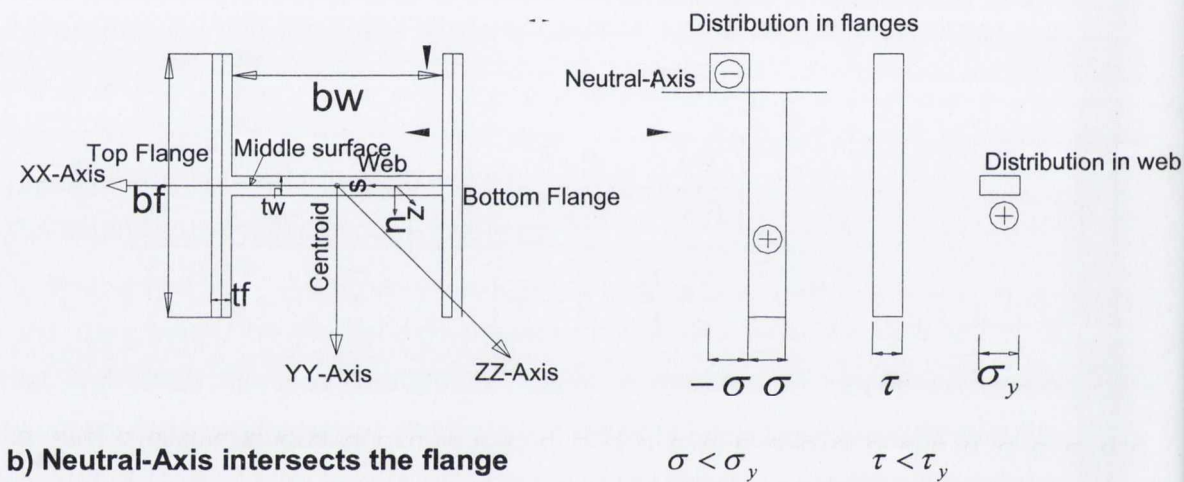
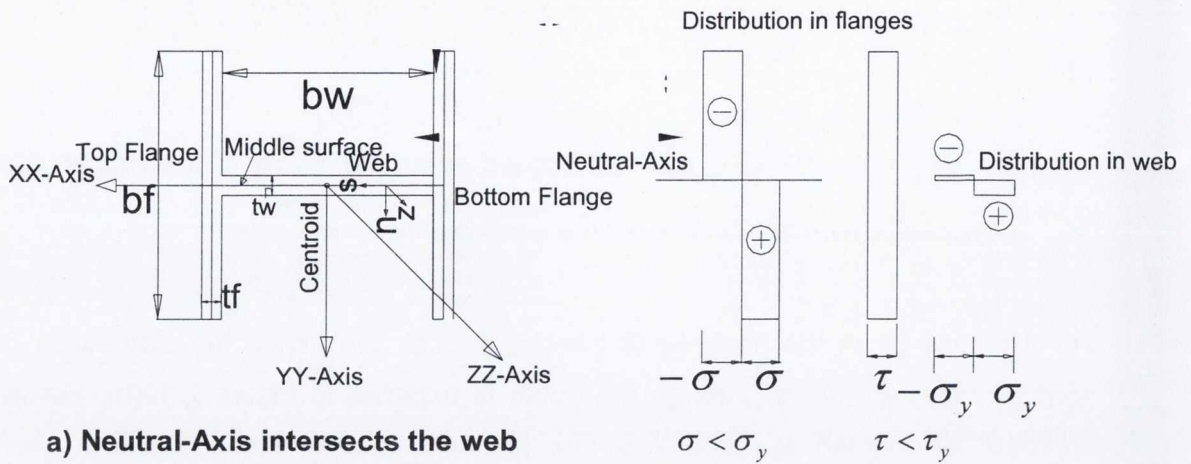


Figure 2.20 An I-section subjected to bending about the X-axis and to shear force and axial force. Distribution of normal and shear stresses when the neutral-axis passes through the web and flange

Interaction of biaxial bending and axial force

Three approaches were adopted to obtain the solution for a rectangular section, all of which give exact solutions. In two of the approaches by Morris and Fenves (1969) and by Santhadaporn and Chen (1970) three neutral-axis patterns are assumed, as depicted in Figure 2.21. Based on these patterns, three equations are obtained from which yield surfaces can be drawn. These equations are:

For the first pattern depicted in the figure the interaction equation is

$$p^2 + m_x + 0.75m_y^2 = 1 \quad 2.65(a)$$

valid for $m_x \geq (2/3)(1-p)$, $m_y \leq (2/3)(1-p)$

For the second pattern

$$p^2 + m_y + 0.75m_x^2 = 1 \quad 2.65(b)$$

valid for $m_x \leq (2/3)(1-p)$, $m_y \geq (2/3)(1-p)$

And for the third pattern

$$p + \frac{9}{4} \left[1 - \frac{m_x}{2(1-p)} \right] \left[1 - \frac{m_y}{2(1-p)} \right] = 1 \quad 2.65(c)$$

valid for $m_x \geq (2/3)(1-p)$, $m_y \geq (2/3)(1-p)$

In these equations

$$p = \frac{P}{P_p}, \quad m_x = \frac{M_x}{M_{xp}} \quad \text{and} \quad m_y = \frac{M_y}{M_{yp}}$$

In the other approach, the position of the neutral-axis is defined by an angle and a reference distance from the centroid of the section. For a series of these two parameters a set of forces are obtained from which yield surfaces are drawn. Details of the procedure are given by Chen and Atsuta (1977) and are not discussed here as it is not relevant to the current research.

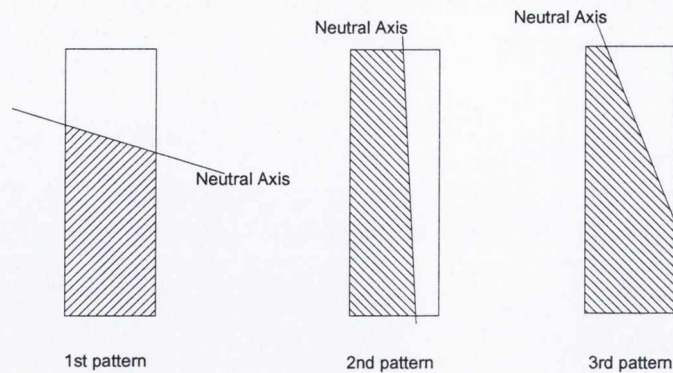


Figure 2.21 Three neutral-axis patterns assumed for the solution of interaction equations of a rectangular section when biaxial bending is applied with axial force

Several approaches were adopted when the interaction relationship of an I-section for biaxial bending in combination with an axial force was derived. Both approximate and exact solutions exist, as shall now be discussed.

Two approaches were adopted for the approximate solutions, both of which are based on a lower bound approach. A lesser number of neutral-axis patterns were assumed as compared to the number of neutral-axis patterns required for the exact solution. The solution given by Morris and Fenves (1969) has five neutral-axis patterns, whereas the solution given by Santhadaporn and Chen (1970) has six neutral-axis patterns. Based on these neutral-axis patterns, equations of yield surfaces are obtained. These equations are not relevant to the current research and are not discussed here.

To obtain the exact solution for an I-section, first the exact solution of a rectangular section is obtained. To obtain the I-section yield surface, it is assumed that the section is made up of three rectangular sections. The forces in each rectangle are then determined for a given neutral-axis pattern. Then the forces are again determined by varying the position of the neutral-axis. Using this procedure, a series of sets of forces are obtained and the yield surface can be drawn (Chen and Atsuta, 1977). Detail of the procedure is not relevant to the current research and is not discussed here.

Yield surfaces of other sections, such as RHS and CHS may also be obtained both approximate and exact (as given by Chen and Atsuta, (1977)).

Interaction equations when sections are subjected to four forces

Interaction of biaxial bending, axial force and St Venant's torsion

In this approach the distribution of shear stress due to St Venant's torsion is taken as constant over the entire cross section but the direction of stress in each plate is opposite for each side of the plate as depicted in Figure 2.22. The full torque based on the distribution of shear stress can be written as:

$$T = \frac{\sum_{i=1}^N b_i t_i^2 \tau}{2} \tag{2.66}$$

In the above equation summation is carried out for all rectangular plate elements of dimension $b_i \times t_i$. Therefore, the fully plastic torque can be obtained as

$$T_p = \frac{\sum_{i=1}^N b_i t_i^2 \tau_y}{2} \tag{2.67}$$

where τ_y is the shearing yield stress and the magnitude of torsional moment can be obtained by a term t such that $t = T/T_p = \tau/\tau_y$. It is assumed that the distortional strain energy density criterion relating direct stress (obtained due to biaxial bending and axial force) and shear stress (obtained by torsion) is valid. As the section is subjected to direct stress in one direction and a shear stress Equation 2.56 is still valid and using the relation given by Equation 2.57, ignoring the subscripts in Equation 2.56 and writing shear stress in the form of “ τ ” it can be written as

$$\sigma^2 + 3\tau^2 = \sigma_y^2 (= 3\tau_y^2) \tag{2.68}$$

Using the above relationships, the following can be obtained.

$$\frac{\sigma}{\sigma_y} = \sqrt{1-t^2} = \bar{t} \quad 2.69$$

To include the effect of St Venant's torsion on biaxial bending and axial force, Equation 2.69 is replaced in the interaction equation developed by Morris and Fenves (1969), thus:

$$p \text{ by } p\sqrt{1-t^2}, m_x \text{ by } m_x\sqrt{1-t^2} \text{ and } m_y \text{ by } m_y\sqrt{1-t^2}. \quad 2.70$$

The yield surface thus obtained on addition of St Venant's torsion is such that the domain of yield surface of biaxial bending and axial force is reduced by a factor $\sqrt{1-t^2}$ as depicted in Figure 2.23 This approach is applicable for an I-section, rectangular section, RHS and CHS.

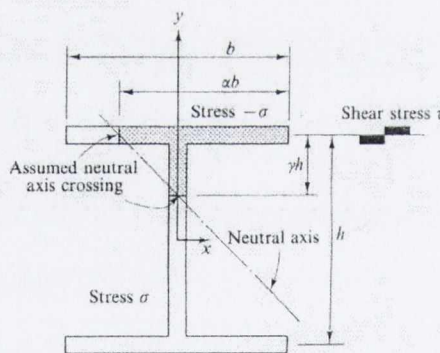


Figure 2.22 Shear stress distribution and neutral-axis pattern based on the approach by Morris and Fenves (1969)

Interaction of bending moment, axial force, bimoment and St Venant's torsion

The warping of the beam causes normal stresses to appear in the cross section in addition to tangential stresses. These normal stresses form a system of mutually balancing longitudinal tension and lead to a generalized force. This generalized force is called the bimoment of the beam. For an I-section the Bimoment consists of

bending moments for the flanges of the beam which for any I-section have the same magnitude for both the flanges but different directions.

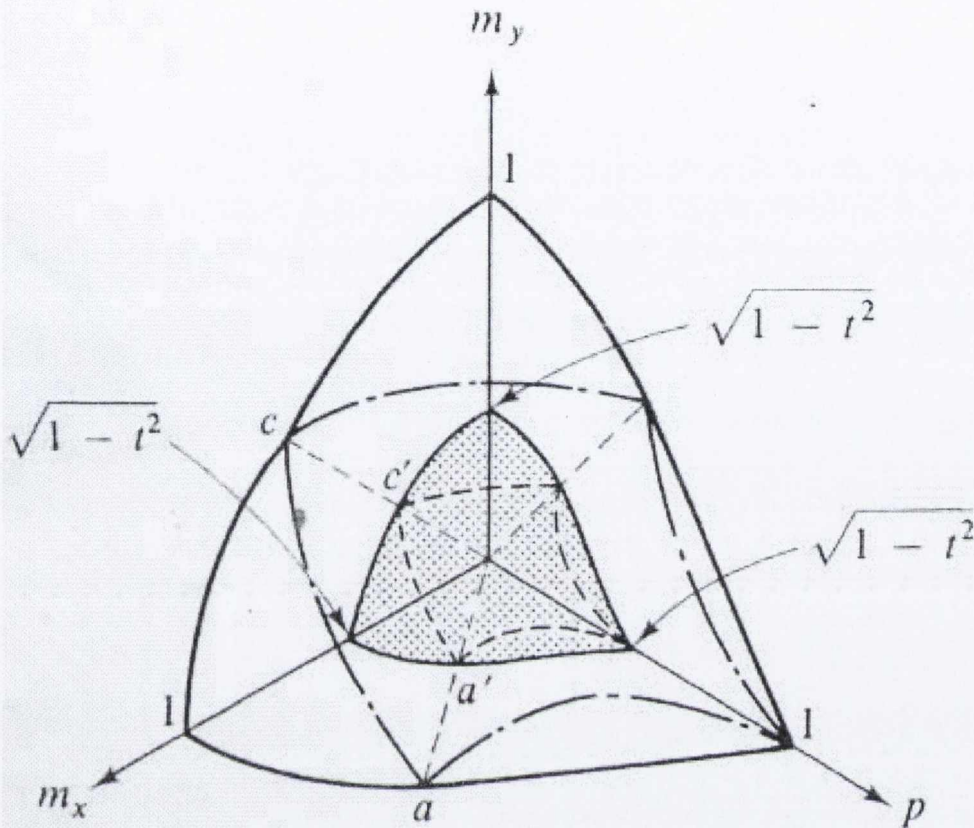


Figure 2.23 Two yield surfaces one before application of St Venant's torsion and the other after its application

An interaction equation was developed (Strelbitzkaya, 1964) for an I-section subject to an axial force, P , a bending moment about the Y-axis, M_y , a bimoment B and a pure torsion, T . Two neutral-axis patterns were assumed, one for direct stresses which is caused by P , M_x and B and the other for shear stress which is caused by T . Two equations were obtained for the neutral-axis patterns which are then combined into one interaction equation based on the distortional strain energy density yield criterion. Details of this interaction equation are not related to current research and are not discussed here.

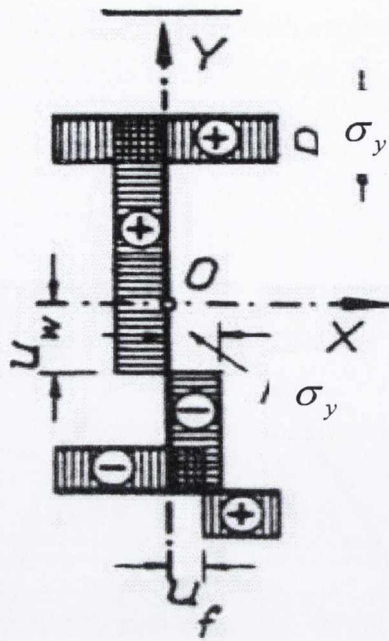


Figure 2.24 Neutral-axis pattern for the stress distribution for the case when P , M_x , M_y and B act on the section (Mrazik et al. 1987)

Interaction of biaxial bending, axial force, and bimoment

An interaction equation has been developed for an I-section for P , M_x , M_y and B by Strelbitzkaya (1964) based on the lower bound approach using the neutral-axis pattern depicted in Figure 2.24. The interaction equation is

$$\frac{M_x}{M_{xp}} - \frac{t_f}{2t_w M_{xp}} \left(M_y + \frac{2B_w}{d} + \frac{P^2}{2\sigma_y t_f} - \frac{P}{t_f} A' \right) + \frac{P - \sigma_y A'}{2M_{xp}} \left[d + \sqrt{d^2 - \frac{4}{\sigma_y t_w} \left(M_x - M_{xp} + \frac{Pd}{2} \right)} \right] = 1 \quad 2.71$$

where in the above equation $A' = t_f b_f + t_w d$ and $B_w = 0.5 \sigma_y t_f \left(\frac{b_f}{4} - u_f^2 \right) d$

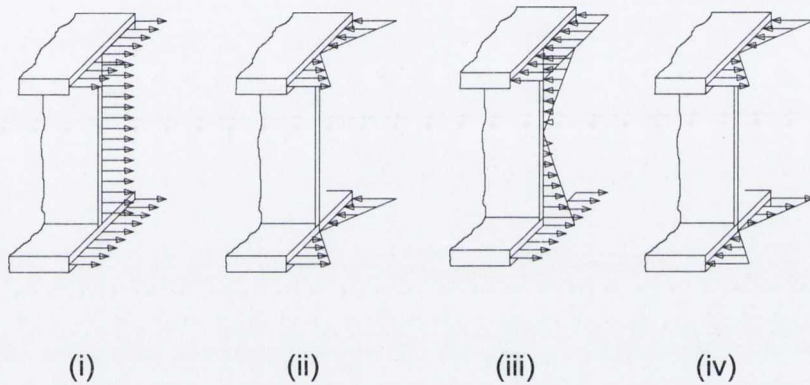
and U_w and U_f are the positions of the neutral axis with respect to centroidal X and Y axis.

Interaction equations were developed for a Z-Section by Daddazio et al (1983) when P , M_x, M_y and B are considered. Different neutral-axis patterns were assumed and interaction equations developed based on a lower bound approach.

Interaction equation when sections are subjected to five forces

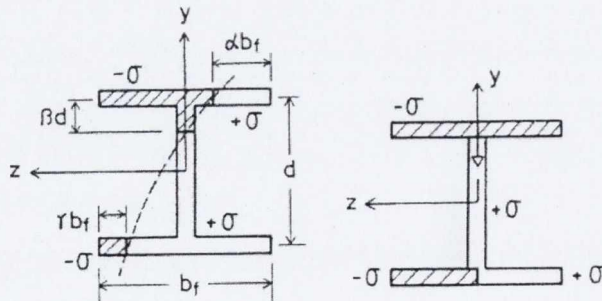
Interaction of biaxial bending, axial force, bimoment and St Venant's torsion

Yield surface equations are developed for biaxial bending, axial force, bimoment and St Venant's torsion for an I-section (Yang and Fan, 1988). Three neutral-axis patterns, as depicted in Figure 2.25 are assumed in order to develop the interaction equations. The salient features of each pattern are as follows:

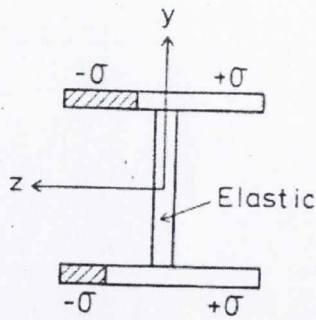


- (i) Axial strain
- (ii) Flexural strain (XX-Axis)
- (iii) Flexural strain (YY-axis)
- (iv) Warping strain

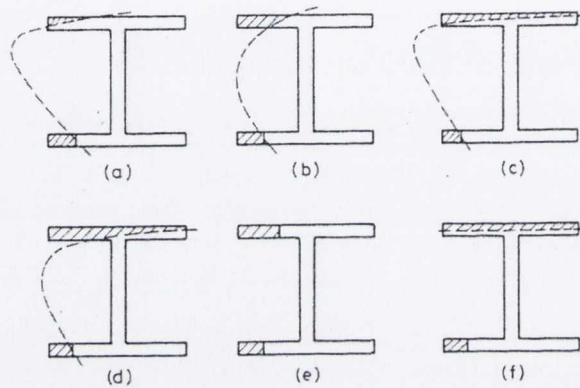
(a) Diagrams showing strain distributions due to different internal forces



Pattern-1



Pattern-2



Pattern-3

(b) Three neutral-axis patterns

Figure 2.25 Strain distribution and three neutral-axis patterns for the yield surface for interaction of biaxial bending, axial force, bimoment and St Venant's torsion

From Figure 2.25 it can be inferred that the neutral-axis is not a straight line. The reason is that in the presence of bimoment direct stresses developed in different direction in both the flanges which causes a change in the pattern of neutral-axis and result in a non-straight neutral-axis.

In the 1st pattern the neutral-axis is assumed to pass through both flanges and web, as depicted in the figure. An important feature of this pattern is continuity of stress at the junction of the plates. As the stress changes its sign within each plate, the axial force acting on the web will always be less than its full plastic value in normalized form p_{2max} . Mathematically it can be written as

$$|p_2| < p_{2\max} \quad 2.72(a)$$

where p_2 is the axial force in the normalized form in the web.

In the right hand diagram in Pattern-1 the extreme case representing the total axial force in its normalized form p can be obtained as

$$p = p_{2\max} - p_{1\max} \quad 2.72(b)$$

This equation gives the maximum axial force in normalized form for this pattern. When the axial force gets smaller, a region of compression will develop in the web (as indicated by the arrow), and p will be less than that given by Equation 2.72(b). Therefore, p will always be less than that obtained by the equation for this pattern and thus the following inequality represents a sufficient condition for pattern-1 yielding to occur

$$|p| < p_{2\max} - p_{1\max} \quad 2.72(c)$$

One additional feature for this type of pattern is that the signs of the axial force in both the flanges are different.

The 2nd pattern is a special case of yielding of the section where it is assumed that the web remains elastic while the flanges have become fully plastic. Although it violates the criterion of yielding because the web is elastic, it can be accepted as a valid yielding pattern because the web offers no resistance to bending moment about the minor-axis M_y and B (as assumed in the development of the yield surface equations). Hence, for this case, both flanges can plasticize while the web remains elastic.

In the 3rd pattern it is assumed that the web is fully plasticized under the action of the axial force P_2 and no moment acts on the web. The extreme case of pattern-1 can also be taken as an extreme case for this pattern. Comparing Figure 2.25(1st pattern) to that of Figure 2.25(3rd pattern) indicates that the axial force acting on each plate in Figure 2.25(3rd pattern) will always be greater than that of Figure 2.25(1st pattern). Therefore, the relationship which was valid for the 1st pattern will be the direct opposite limit for this pattern, that is, $|p| > p_{2\max} - p_{1\max}$ is the necessary condition for yielding to this pattern.

Yield Surface Equations

Interaction equations can be developed for each neutral axis pattern considered but such an attempt to develop interaction equations is avoided here. Instead, it is assumed that an I-section consists of 3 plates, where each flange and the web represent a plate. A stress resultant acting on each plate was considered as a combination of compression (or tension) and uniaxial bending moment; hence, two forces act on each plate. Therefore, yielding of each plate can be obtained by a two dimensional yield curve and such a yield curve is called a component yield surface. For the top flange, web and bottom flange interaction equations for the component yield surfaces respectively are (Yang et al. 1989)

$$Sgn(m_1)(2\bar{t} m_1) + p_1^2(2 + c')^2 + t^2 = 1 \quad 2.73(a)$$

$$Sgn(m_2)\left(\frac{4+c'}{c'}\right)\bar{t} m_2 + p_2^2\left(\frac{2+c'}{c'}\right)^2 + t^2 = 1 \quad 2.73(b)$$

$$Sgn(m_3)(2\bar{t} m_3) + p_3^2(2 + c')^2 + t^2 = 1 \quad 2.73(c)$$

where m_1, m_2 and m_3 are the moments in normalized form applied to the top flange, web and bottom flange respectively. In the same way p_1, p_2 and p_3 are the axial force in normalized form applied to the top flange, web and bottom flange

respectively, $Sgn(x) = \text{sign of } x$ as previously defined and $c' = \frac{A_w}{A_f}$. The above equation is valid for the first yield pattern.

The stress resultants for the entire cross section can be related to moments m_1, m_2 and m_3 and axial force p_1, p_2 and p_3 based on the equilibrium condition. Mathematically, they can be written as

$$p = p_1 + p_2 + p_3 \quad 2.74(a)$$

$$m_y = m_1 + m_3 \quad 2.74(b)$$

$$m_z = (p_3 - p_1) \left(\frac{4 + 2c'}{4 + c'} \right) + m_2 \quad 2.74(c)$$

$$b = m_3 - m_1 \quad 2.74(d)$$

In the above equation b is the bimoment in normalized form. p is the axial force in normalized form. m_1, m_2 and m_3 are the normalized major bending moment about the local axis and t is the torque in normalized form. The above equations can be used to develop yield surfaces and identify formation of plasticisation. A procedure to determine the formation of a hinge and the development of a yield surface is briefly discussed in the next section.

In the procedure, yielding is first checked for the 2nd type of neutral-axis pattern. The reason for first checking the 2nd type of procedure is that only two stress resultants m_y, b are required to check the procedure (as both the forces exist when yielding occurred for the second type) and this can be done by simply obtaining m_1 and m_3 values. If yielding is not found a check is made for the 1st type of pattern. If the 1st

type is not found then a check is made for the 3rd type of pattern. Details of the procedure are given in Yang et al. (1989).

For given values of p , m_y , t and b using the yield checking procedure, the allowable load m_z can be determined. In this way, a series of m_z values can be obtained for a series of values of p , m_y , t and b . And two dimensional yield surfaces can be drawn with m_y and m_z on the X and Y axes respectively, the remaining stress resultants p , t and b , are kept constant. The yield surface for a standard steel W12 x 31 I-section is shown in Figure 2.26 as an example.

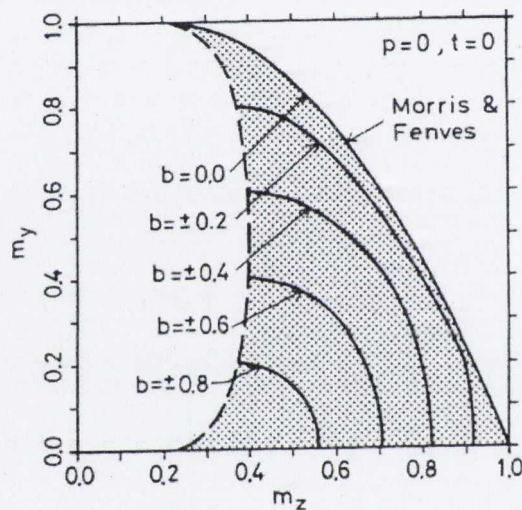
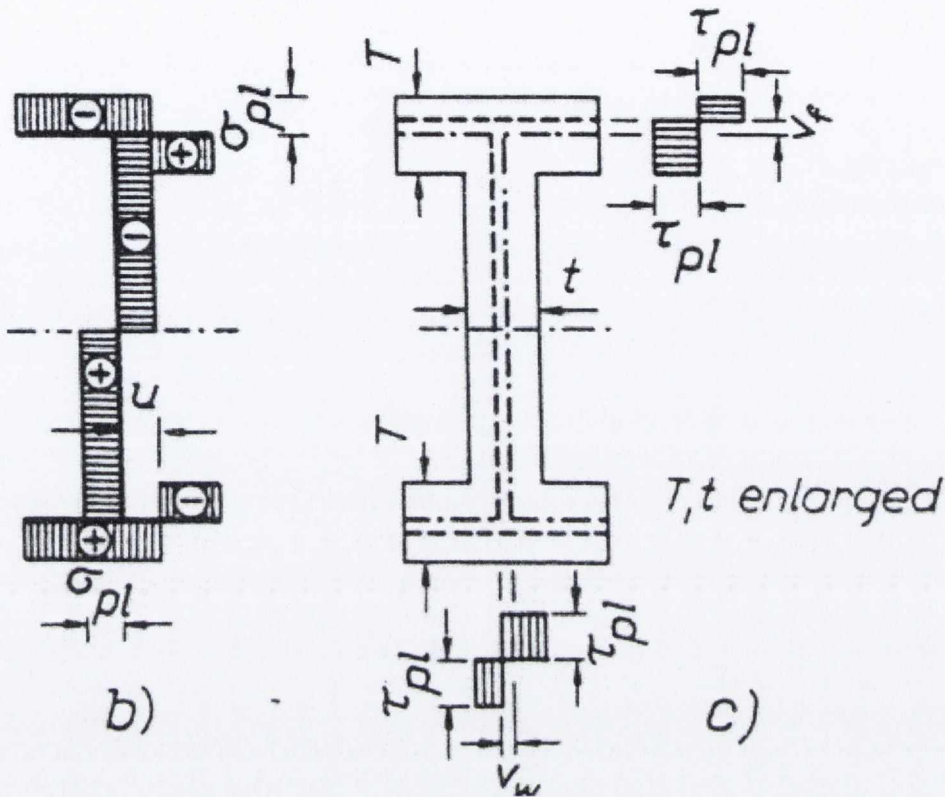


Figure 2.26 Developed yield surface for a W12 x 31 I-section for the interaction of biaxial bending, axial force, bimoment and St Venant's torsion (=0)

Interaction of bending moment, shear force, bimoment pure torsion and warping torsion

The interaction relationship for the I-section case when bending moment, M_y , shear force, S_x , bimoment, B , pure twisting moment, T , and warping torsion, T_w , is now explored (Mrazik et al 1987). M_y and B cause normal stresses whereas S_x , T and T_w cause shear stresses. The neutral-axis patterns assumed for normal stress

and shear stress are depicted in Figure 2.27. Two equations are obtained, one for direct stress and the other for shear stress.



a) Neutral-axis pattern for direct stress b) Neutral-axis pattern for shear stress

Figure 2.27 Neutral axis pattern for the case when direct stress and shear stress act on an I-section for interaction of bending moment, shear force, bimoment, pure torsion and warping torsion

For direct stress, a quadratic equation is obtained as follows:

$$\sigma^2 \frac{b_f^2 t_f d}{4} - \sigma \left(B - \frac{t_w d}{8 t_f} M_y \right) \frac{1}{K} - \frac{M_y^2}{4 t_f d K} = 0 \quad 2.75$$

where $K = 1 - \frac{t_w^2 d^2}{16 t_f^2 b_f^2}$. For shear stress, another quadratic equation is obtained as follows:

follows:

$$\tau^2 Z_t - \tau T - \frac{S_x^2}{2d} - \frac{T_w^2}{b_f d^2} = 0 \quad 2.76$$

where $Z_t = .65(2b_f t_f^2 + dt_w^2)$

Solving both the quadratic equations, normal stress and shear stress can be determined. These two stresses can then be related to each other by the maximum distortional energy density criterion for the case when one direct stress and other shear stress are considered as given by Equation 2.56.

Using a similar approach, equations for a channel section are obtained, as given in Mrazik et al. (1987). The equations are not relevant to the current research and are not discussed here.

Interaction equation when sections are subjected to six forces

Interaction relationship are obtained (Mohareb and Ozkan, 2004) for hollow structural square sections subjected to axial force, St Venant's torsion, biaxial bending moments and biaxial shearing forces using a lower bound approach.

Similarly, interaction relationships are obtained for pipe sections subjected to axial force, biaxial bending moments, biaxial shear forces, St Venant's torsion and internal or external pressure. Interaction equations are obtained based on a lower bound approach (Mohareb, 2002) and later confirmed by an upper bound approach (Mohareb, 2003).

2.6.4 Single Equation Yield Surfaces

A yield surface developed for any section can be based on many equations, where each equation represents a surface element of the yield surface. Based on the developed yield surfaces, mathematical equations can be obtained to fit the curves of yield surfaces (using a curve fitting technique). Curves thus obtained, have an equation and only one such equation which is used to fit the curve. The equation is called a single equation of the yield surface curves.

The first such work has been generally for simple surfaces, such as in four dimensional parabolic and elliptic functions used by Wen and Farhoomand (1970). Unfortunately, for practical steel sections, such as the wide flange sections, such simplicity is not realistic.

Single equation yield surfaces are also developed for different sections for axial force and biaxial bending moments. For wide flange sections, the yield surface by Chen and Atsuta (1977) is used as a reference to obtain a single equation for the developed yield surface. The equation thus obtained by Oribison et al. (1982) using the curve fitting technique, is

$$1.15p^2 + m_y^2 + m_x^4 + 3.67p^2m_y^2 + 3.0p^6m_x^2 + 4.65m_y^4m_x^2 = 1 \quad 2.77$$

It was found during the study by Duan and Chen (1990) that analytical yield surfaces developed by Chen and Atsuta (1977) for different doubly symmetrical sections vary due to section properties. This variation was taken into account when a single equation was proposed for different wide flanges, thin walled circular tubes, thin walled boxes, rectangular and solid circular sections. A general single equation was thus proposed, using a curve fitting technique, which is valid for all the doubly symmetrical sections, thus:

$$m_x^{\alpha_x} (1 - p^{\beta_y})^{\alpha_y} + m_y^{\alpha_y} (1 - p^{\beta_x})^{\alpha_x} - (1 - p^{\beta_x})^{\alpha_x} (1 - p^{\beta_y})^{\alpha_y} = 0 \quad 2.78$$

In the above equation, parameters α_x , α_y , β_x and β_y depend on sectional shapes and area distribution. For example an I-section yields $\alpha_x = 2$, $\alpha_y = 1.2 + 2p$, $\beta_x = 1.3$ and $\beta_y = 2 + 1.2(A_w / A_f)$. For other sections, values of these parameters are given by Duan and Chen (1990).

In an attempt to develop yield surfaces for asymmetrical sections, Al-Bermani and Kitipomchai (1990) develop yield surfaces for angular sections. In the same work,

single equation yield surfaces for circular hollow sections were also presented. Later Kitipornchai et al. (1991) developed single equation yield surfaces for monosymmetric and asymmetric sections.

2.7 EXPERIMENTAL AND NUMERICAL STUDIES FOR MULTI-DIMENSIONAL FORCES

Several experiments were performed to determine the behaviour of cantilever I-sections and were compared with theory developed in the same research by Kolbrunner et al. (1978). In the experiments, loads were applied which imposed torsion and bending about the major axis. Theories were developed for elasto-plastic and perfectly plastic cases and the results were compared with the experiments. In the theory, for the elasto-plastic case, two possible distributions of normal stresses were assumed. In one case it was assumed that stresses at both ends of both the flanges reached yield stress whereas, in the second case, it is assumed that only one end of both the flanges reached the yield stress. It was found that in the elastic region the experiment and theory were in good agreement. It was also found that the hypothesis of linear distribution of strains both in the elastic and plastic region is valid. An ultimate limit load was calculated and it was found that the actual limit load was attained at a value of plastic strain five times that reached at the yield value. At loads more than the limit load significant changes in the geometry of the structure were obtained. It was also found that at high loads large rotations took place.

In another attempt a similar type of experiment was performed, where the beams were fixed at both ends (Kolbrunner et al., 1979). In the work the ultimate load was also predicted by two theoretical procedures. In the first procedure, it was assumed that the ratio between bending about the major axis and bimoment remained the same until the ultimate load of the beam was reached. In the second procedure, a step-by-step method was adopted in which gradation of loads were made at the formation of each plastic hinge, up to the point when it turned into a kinematic mechanism. Both the procedures are not directly relevant to the current research and are not discussed further here.

Later the theoretical results were compared to the experimental results. It was found that in the elastic behaviour both theoretical and experimental responses matched each other very well. Ultimate loads obtained by the experiment showed good agreement with the step-by-step procedure. In this case, the distribution of strain was not linear in the elasto-plastic case. The beam showed a considerable amount of residual strain on unloading.

Six experiments on circular pipes were performed (Ozkan and Mohareb, 2003) to verify yield surfaces developed by Mohareb (2002). The load types applied in the experiments were shear force, bending and torsion. It was found from the experiments that the interaction equation developed by Mohareb (2002) gives a lower capacity than those obtained for the experiments. For diameter to thickness ratio less than 41 it was found that the interaction equations gave very good predictions. However, it is recommended in the conclusions that when the ratio is more than 41, more experimental work is required to be able to give conclusive design recommendations for use of the interaction equations for thinner pipes. Local buckling (LB) of the pipes was observed prior it reaching the peak load. It was found that local buckling is dependent on the ratios of bending, torsion and shear.

Elastic-plastic analysis of cantilever I-beams in bending and torsion were studied using finite element analysis by Bathe and Wiener (1983). Warping of the section was included in the analysis. Analyses were performed using the software ADINA. Different elements were used for the analysis and their capabilities to model accurately were compared. Elements used were rectangular cross section 2 noded Hermetian beam element, the 4 noded isoparametric beam element and the 9 noded isoparametric shell element. From the analysis it was concluded that 9 noded shell element yields more accurate stress distributions than the others. However, it was found that the isoparametric beam element can be used successfully to model an I-beam. Results were also compared for the torsion case with the Dinno and Merchant (1965) and the sand heap approach and good agreement was achieved between them and the analytical study.

In an attempt to perform finite element analysis of an I-section subjected to biaxial bending and torsion, a finite element model was developed by Pi and Trahair (1994a). To develop the model fully, buckling and post-buckling were considered. In addition, an elastic-plastic constitutive matrix was formulated using Von Mises yield criterion, the associated flow rule and the hardening rule. Both uniform and nonuniform torsion in the inelastic range was considered. Using the procedure of finite elements, different analyses were undertaken which included large-deflection, in-plane, elastic and inelastic behaviour of columns and beam-columns; torsional behaviour of beams and beam-columns; the different nature of loading applied to beams; the effects of initial imperfections and twist on the lateral buckling strength of beams; and the flexural-torsional behaviour at post-buckling of beams (Pi and Trahair, 1994b). It was found from the study that the model developed gives good results for nonlinear analysis including post-buckling analyses.

Interaction equations for bending and torsion for an I-section were proposed based on a study of finite element analysis by Pi and Trahair (1994c). The effects of secondary bending about the minor axis which was caused by rotation of the beam sample is also taken into account. To develop the interaction equation effects of large deformations, material inelasticity, residual stresses and geometric imperfections are considered. Interaction equations are developed for an I-section, firstly for bending and free torsion and secondly for combined effects of flexural torsional buckling and destabilizing torsion. It is found from the study that the interaction equation commonly called as circular (based on equation of a circle) for combined bending and torsion does not always give the lower bound solution when compared with current analysis.

A finite element model was developed by Hu et. al. (1996) for asymmetric cross-sections for coupled bending and torsion. The model developed can be used for both static and dynamic analysis.

Other studies have been performed in which both experiments are performed and are compared using finite element analysis. One such work was performed by Mohareb et al. (2001) for a pipe section. In this work seven experiments were

performed to find out the deformational behaviour of full scale pipes subjected to axial load, bending and internal pressure. A finite element study was performed using the software ABAQUS to predict the behaviour of the pipe sample and to incorporate the effect of local buckling which was observed during the experiment.

2.8 CONCLUSION

In this chapter, three different approaches are adopted to the problem of non-linear behaviour of structures subjected to multi-dimensional forces. Firstly a theoretical development in which theories of thin walled bars and plasticity is presented. Secondly, flexural and torsional behaviour is discussed. Thirdly, yield criteria for structures subjected to different combination of forces are given.

From the study of torsion it is found that it is a complicated phenomenon which varies with different boundary condition and types of sections. Much theoretical and numerical study have been performed in this regard and the need is for more experimental work in this area for different boundary conditions. It is found that different modes of behaviour in the case of a beam subjected to flexure are studied in detail and are accepted widely in their application.

From the study of yield criteria of stress at a point, it can be concluded that the subject has been dealt with in detail for both ductile and brittle materials. When yield criteria for different steel sections are studied, it is found that their development is a complicated phenomenon. Different approaches were adopted to deal with different section types. In addition, the complications are compounded when a section is subjected to multi-dimensional forces. Both the upper bound and lower bound theorems of plasticity were adopted. It has also been proposed by others that a yield surface can be represented by curve fitting technique. Useful and reasonably accurate equations can be developed based on this technique. It is concluded that this technique can also be used for other more complex yield surfaces to generate alternative single equations which can be a good representation of yield criteria.

Considering a structure subjected to multidimensional forces, it was found that cantilever I-sections and other types of section have been used as case studies in numerical and experimental studies. From this, it is found that experiments when torsion is considered in combination with biaxial bending and axial force have not been performed and wide scope is available for research work in this area.

From the study of previous work it is found that there is need for extension of the previous work. These are:

- a). To develop a single equation yield surface for multidimensional forces including torsion for an I-sections for a large variety of cases.

- b). To develop the yield surface of an I-section for biaxial bending, biaxial shear force, axial force, bimoment and pure torsion.

- c). To perform experiments for the case of biaxial bending and torsion in presence of axial force.

- d). To establish the capability of the finite element method in modelling the experiment under multidimensional forces.

DEVELOPMENT OF A SINGLE EQUATION YIELD SURFACE

3.1 INTRODUCTION

It has been shown in the previous chapter, that several yield surfaces have been developed by a lower bound approach and were verified by an upper bound solution. In this chapter, a single equation yield surface for biaxial bending and bimoment is developed using a curve fitting technique and is verified by a numerical method using finite element analysis. Different developed yield surfaces are also verified using the analysis. The verification process is also used to extend the single equation yield surface to fill the gaps which were present in the previously developed yield surface by Yang et al. (1989).

The development of the single equation is based on a curve fitting technique in which different types of mathematical equations are fitted to regressed yield surfaces developed by Yang et al. 1989. Firstly yield surfaces developed by Yang et al. are generated by writing a code in MATLAB. The group of sections considered for the development of the single equation are the Universal Beams listed in BS EN10056: 1999 sections. In the development of the single equation, the variations in the yield surfaces for the different I-sections are also considered.

A finite element study is performed using the popular software package LUSAS using four-noded isoparametric thick shell element (LUSAS Manual, 2001) for yield surface verification and extension. Single stress resultants are verified first followed by the verification of different combinations of stress resultants. The single stress resultants are verified to establish the capability of the finite element method in dealing with non-linear analysis, and to obtain a proper mesh size for the convergence criterion of the finite element model. In the case of yield surface verification, existing yield surface equations are verified for different combinations of stress resultants. Hence, an approach is developed to verify any yield surface using a numerical technique.

Later the approach is used to verify and extend the developed yield surface. The beam considered for the case study is a cantilever I-section beam with different dimensions and spans.

3.2 CODE IN MATLAB

MATLAB is both an environment and a programming language (Pratap, 2002) that allows development of programs and codes. MATLAB programs as either scripts or functions using data types, operators, expressions and statements, that is similar to programming languages such as C++. Object-orientated classes and objects can be created in MATLAB, or its built-in Java interface could be used to create and work with Java classes and objects.

Code in MATLAB is developed in order to generate yield surfaces and to check for yielding of cross sections.

3.2.1 Generation Of Yield Surfaces

Yield surface diagrams for different I-sections vary, and the variation is considered here in the development of a single equation. To investigate it, a series of yield surface diagrams are required, which is a difficult and time-consuming procedure. To generate a single point for a yield surface diagram, a detailed calculation is required, which includes use of different parameters and equations. Therefore, it was decided to use computational techniques for the development of the yield surfaces and a code in MATLAB is written to generate such yield surfaces. The code considers two types of yield surface equations: the equations by Yang et al. (1989) and the single equation developed in this work.

To develop the yield surface based on the procedure by Yang et al. (1989) a brief summary of the procedure on which code is written is given. In the code values of m_1 and m_3 were first calculated using Equations 2.74(b) and 2.74(d). Using Equations 2.73(a) and 2.73(b) p_1 and p_3 were calculated for obtained values of m_1 and m_3 . Plus and minus signs assigned to the values of p_1 and p_3 , and p_2 are calculated based on the equilibrium condition of the section using Equation 2.74(a). At this point the necessary condition for the first type of pattern is checked as discussed in the procedure by Yang et al. (1989). Based on the

check using Equation 2.74(c) m_y is calculated. It is further checked as a sufficient condition for the first pattern and a necessary condition for the third pattern, and the positions of neutral-axes were finalised for the flanges. Now the possibility of a third pattern is checked and m_y is calculated using Equation 2.74(c). This procedure used in the code given in detail by Yang et al. (1989) is used to calculate values of m_y for assumed values of b and m_x . Using this procedure a series of different values of m_y , b and m_x are generated to develop yield surfaces for different I-sections.

Later the developed single equation was added to the code to compare the yield surfaces generated by the developed single equation with the yield surfaces generated by the work by Yang et al. for different I-sections.

3.2.2 Check for Yielding Of Section

The previously developed equations by Yang et al. (1989) and the now developed single equation are used in the code to check yielding of a cross-section. A cross-section will yield when, for any combination of stress resultants, it reaches a yield surface. If it does not reach a yield surface then the cross-section can be considered as elastic. If the combination crosses the yield surface, then the section can be said to be overstressed which is not deemed possible. The code for yielding of a section is developed so that it can be compared with the solution obtained by finite element analysis (as discussed later in this chapter). In addition, the procedure to determine yielding of a section can also be used for elastic-plastic analysis.

3.3 SINGLE EQUATION YIELD SURFACE FOR BIAXIAL BENDING AND BIMOMENT

A single equation yield surface considering biaxial bending and bimoment for an I section is developed for the Universal Beams in BS EN10056: 1999. The single equation developed in this work is developed to provide a better choice for the designer to use in the design of structural elements. There are two main advantages which it has over analytical approach. First it consists of single equation and the analytical equation consists of several equations, hence the matrix which identifies the formation of hinge in elasto-plastic analysis will have

one column whereas the analytical approach has as many numbers of columns as the no of equations. This saves a lot of computational time. Secondly it can be useful because it provides tables for the design which can save time required to perform a rigorous calculation using analytical approach. In addition it can avoid chances of error in manual calculation which can occur during rigorous calculation.

The yield surface developed by Yang et al. (1989) is used for the development of the single equation. Using the computer code yield surfaces (developed by Yang et al. (1989)) were generated for several Universal Beam Sections. These yield surfaces were then curve fitted to obtain equations which represent the developed yield surfaces. Several types of equations were tried to best fit the yield surfaces and the equation which best fit the yield surfaces was taken to fit the curves of all the sections considered. The equation type which best fit the curves were used to curve fit all the sections to obtain one equation for each section. The obtain equations contained parameters each of which has a value for each section. All the values of each parameter were later linked by sectional properties and another equation is obtained to curve fit the parameters and link to the sectional properties. This procedure is repeated for yield surfaces for different values of bimoment. Another equation is curve fitted which links the parameters of previous curve fitted equations with the bimoment values. Yield surface graphs vary from section to section and this variation is considered here in the development of the single equation.

3.3.1 Yield Surface Variation

The variation of the yield surfaces of all the Universal Beams is studied. To illustrate the variation several yield surfaces are generated for minor moment m_x and major moment m_y , depicted in Figure 3.1. In the figure moments in normalized form are given which start with a zero value to a maximum of 1. Values in normalised form are obtained by dividing the moments by their plastic moment capacities. From the figure it can be observed that yield surfaces are different for five different sections and this is termed a variation of the yield surface.

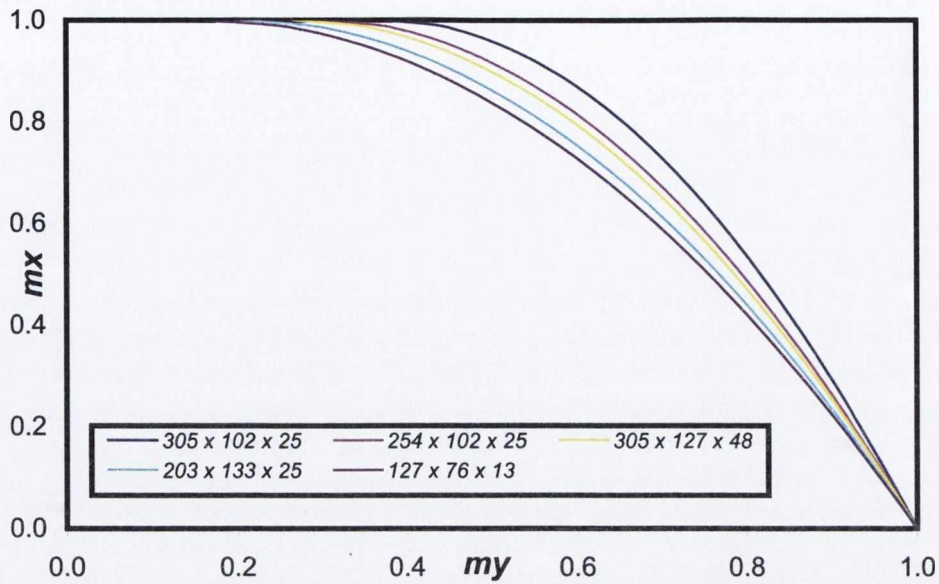


Figure 3.1 Comparison of yield surfaces of several I-sections under minor-axis and major-axis bending

Reasons for the Variation

It was observed previously (Duan and Chen, 1990) that the smaller the ratio of web area to flange area (A_w / A_f), the lower the yield surface. Hence, to determine the reasons for the variation, different section properties are considered, to relate the yield surface variation with the sectional properties. Five ratios of the different sectional properties are considered. These are the ratio of web area to flange area (A_w / A_f), the ratio of second moment of area about the major and minor axes (I_{xx} / I_{yy}), the ratio of polar moment of inertia to second moment of area about the major axis (I_{zz} / I_{xx}), the ratio of polar moment of inertia to second moment of area about the minor axis (I_{zz} / I_{yy}) and the ratio of first moment of area of the web about the major-axis to the first moment of area of the entire section about the major-axis (S_{web} / S_{xx}). It is found that the three ratios of (A_w / A_f), (I_{zz} / I_{xx}) and (S_{web} / S_{xx}) are closely related to the yield surface pattern, whereas, the other two ratios are not significant. The ratios related to the pattern, for all the Universal Beam sections, are given in Table A.1 in Appendix-A. In the table, sections are in sequential order of the pattern of yield surfaces, where the first section in the table has the upper yield surface, while the last section has the lowest yield surface. From the table, it is clear that the

variation of the pattern exactly relates to the ratio of (S_{web} / S_{xx}) , where a decrease in the ratio is always related to a fall in the yield surface pattern. For the other two ratios of (A_w / A_f) and (I_{zz} / I_{xx}) the pattern is not entirely related to the ratios, where on several occasions an increase in the ratio can be observed even for a fall in the pattern. The exact relation of the ratio (S_{web} / S_{xx}) with the yield surface pattern is because of the relationship of the moments with the first moment of area. To calculate the moments, for m_x and m_y the first moment of areas are calculated about the centroidal major and minor axes, and the resulting term is multiplied by a constant direct stress σ value to obtain the ultimate moments. For example to obtain the plastic capacities M_{xp} and M_{yp} Yang et al. (1989) use the following formulae:

$$M_{xp} = (0.5A_f b_f + 0.25A_w t_w) \sigma, \quad M_{yp} = (A_f d + 0.25A_w b_w) \sigma \quad 3.1$$

where d is the distance between the centroid of two flanges.

It can be observed in the formulae that the plastic capacities A_w and A_f are multiplied by a distance (lever arm) to give the first moment of area, which is multiplied by direct stress to obtain the plastic capacities. The same procedure is adopted to obtain m_x and m_y values. In addition, bimoment is predominantly the product of the first moment of area of the flange multiplied by the distance between the centre of the flanges and σ . Hence, for this reason, the dependency of a yield surface pattern is strongly related to the ratio of the first moment of area, thus the variation of the pattern of the yield surfaces is related to the ratio of (S_{web} / S_{xx}) .

3.3.2 Curve Fitting Technique

A curve fitting tool available in MATLAB is used to develop the single equation. MATLAB has different curve fitting techniques (Pratap, 2002), which includes linear polynomial, quadratic polynomial, exponential type, Gaussian type, Fourier type, power type, rational type, Sine function, Weibull type and an option for the user to define a customized equation. A main equation is first selected, followed

by the selection of different equations to combine the various parameters of the main equation obtained for each of the sections considered.

Selection of the main equation

Different equations were tried to best fit m_x, m_y yield surfaces for bimoment values of 0.0, 0.2, 0.4, 0.6 and 0.8. The forms of different equations, which are selected for curve fitting analysis, are shown in Table 3.1(a) and the outcome of Root mean square error (RMSE) values are given for different values of bimoment in Table 3.1(b).

MATLAB gives an indication of the degree of fit of the curve in terms of RMSE, where a lower value of RMSE indicates a good fit (Pratap, 2002). Eleven Universal Beam sections of different section properties are randomly selected to obtain the best-fit equation for the single equation of the values of bimoment. RMSE values of different equations for all the eleven sections are obtained, and an average RMSE value is thus calculated for all the equations for the values of the bimoments, as shown in the table. From the table, it can be observed, that cubic polynomial and rational quadratic type have the least RMSE values (shown bold in the table) for different values of bimoments. However the rational quadratic type equation has lower RMSE values as compared to the cubic type for bimoment values of 0.2, 0.4, 0.6 and 0.8. Therefore, this equation type is selected as the main equation for the single equation yield surface.

This equation is modified by the term of $(1 - b)$ to include the effects of bimoments. It is found that the addition of the term does not change the RMSE values.

The equation which is finalised for the single equation gives a very good fit for the curves considered and have very low values of RMSE. It can happen that for some curves it will not give a very good fit with high RMSE values but this format is also checked randomly after finalising the format and is reasonable and close enough for these curves also.

	Equation Type	Equation Format
1	Exponential	$f(x) = a \cdot \exp(bx)$
2	Exponential	$f(x) = a \cdot \exp(bx) + c \cdot \exp(dx)$
3	Fourier Type	$f(x) = a_0 - a_1 \cos(xw) - b_1 \sin(xw)$
4	Gaussian Type	$f(x) = a_1 \cdot \exp(-((x - b_1)/c_1)^2)$
5	Linear polynomial	$f(x) = p_1x + p_2$
6	Quadratic polynomial	$f(x) = p_1x^2 + p_2x + p$
7	Cubic polynomial	$f(x) = p_1x^3 + p_2x^2 + p_3x + p_4$
8	Power-1	$f(x) = ax^b$
9	Power-2	$f(x) = ax^b + c$
10	Rational-1	$f(x) = p/(x + q)$
11	Rational-2	$f(x) = p/(x^2 + q_1x + q_2)$
12	Rational-3	$f(x) = p/(x^2 + q_1x^2 + q_2x + q_3)$
13	Rational-4	$f(x) = (p_1x + p_2)/(x + q)$
14	Rational-5	$f(x) = (p_1x + p_2)/(x^2 + q_1x + q_2)$
15	Sum of Sin functions	$f(x) = a_1 \sin(b_1x + c_1)$
16	Weibull	$f(x) = abx^{(b-1)} \cdot \exp(-ax^b)$

Table 3.1(a) Format of different types of equations tried to best fit the yield surfaces

The form of the modified equation is

$$y = f(x) = ((p_1x + p_2)/(x^2 + q_1x + q_2))(1 - b) \quad 3.2$$

In the above equation, x represents the normalized moment of a section about the major axis, whereas y represents the normalized moment of a section about the minor-axis, and b is the bimoment of a section, while p_1, p_2, q_1 and q_2 are the parameters of the equation, which depend on the ratio of (S_{web} / S_{xx}) .

Equation Type	$b = 0.0$	$b = 0.2$	$b = 0.4$	$b = 0.6$	$b = 0.8$
Exponential	0.1298	0.107	0.1035	0.0696	0.0351
Exponential	0.0125	0.031	0.056	0.0184	0.0106
Fourier Type	0.0235	0.0464	0.0609	0.0429	0.0242
Gaussian Type	0.0517	0.056	0.0655	0.0414	0.0215
Linear polynomial	0.0631	0.0636	0.0765	0.0498	0.0251
Quadratic polynomial	0.0021	0.0332	0.0416	0.0244	0.0123
Cubic polynomial	0.0006	0.0306	0.0261	0.0157	0.0079
Power-1	0.1691	0.1244	0.1112	0.0739	0.0365
Power-2	0.1127	0.0853	0.089	0.0602	0.0316
Rational-1	0.1761	0.1405	0.1222	0.0835	0.0419
Rational-2	0.0915	0.0804	0.0828	0.0539	0.0271
Rational-3	0.058	0.0589	0.0646	0.0407	0.0205
Rational-4	0.0635	0.1163	0.0771	0.0501	0.0253
Rational-5	0.0025	0.0282	0.0131	0.0085	0.0043
Sum of Sin functions	0.0094	0.0667	0.0473	0.0259	0.0143
Weibull	0.1123	0.1033	0.0992	0.0675	0.0344

Table 3.1(b) Comparison of RMSE values for different equations

Parameters of the Yield surface for zero value of bimoment

Based on Equation 3.2, yield surfaces of moment about the major and minor axes for a zero value of bimoments are regressed for the sections given in Table A.1. For each of the resulting surfaces, different values of the parameters p_1, p_2, q_1 and q_2 in Equation 3.2 are obtained. A relationship is developed between the parameters and the ratio (S_{web} / S_{xx}) . One of the graphs, depicted in Figure 3.2, is drawn to show the relationship between the parameter p_1 and the ratio (S_{web} / S_{xx}) for $b=0.0$ for all Universal Beams listed in BS EN10056: 1999 sections. Values of the constant parameters obtained from the curve fitting for each section are shown as a cross in the figure. Graphs of similar patterns are obtained for the other parameters of p_2, q_1 and q_2 for bimoment values of 0.0, are shown in Figure A.1(a).

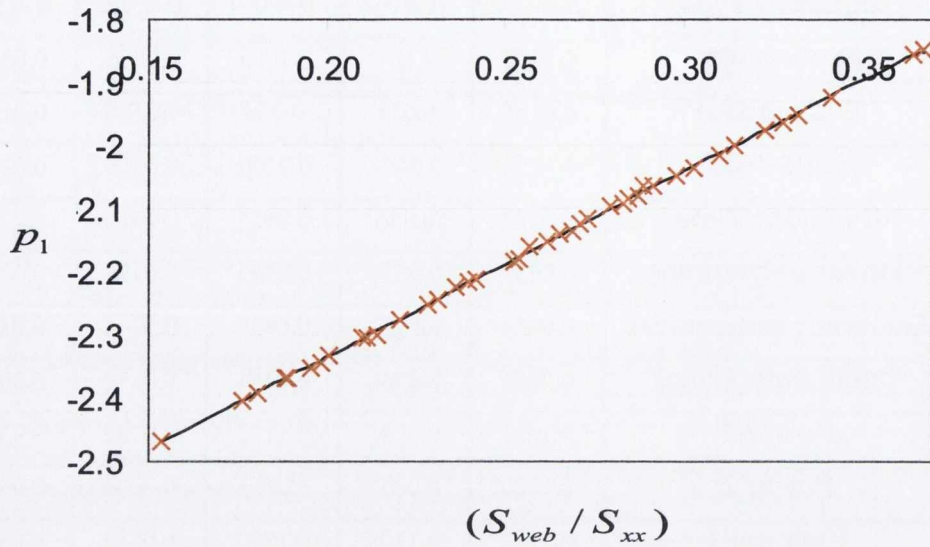


Figure 3.2 Constant parameter, P_1 for $b=0.00$

These values of the parameters obtained are very strongly related to the ratio (S_{web} / S_{xx}) , using curve fitting on the equation in 3.2. Values of the parameters p_1, p_2 and q_2 against (S_{web} / S_{xx}) are again regressed to obtain an equation of the form .

$$y = f(x) = a_i x^3 + a_i x^2 + a_i x + a_i \quad 3.3$$

In the above equation, x represents the ratio (S_{web} / S_{xx}) , y represents the regressed values of parameters p_1, p_2 and q_2 while a_i are parameters, where $i = (1-4)$ for p_1 , $i = (5-8)$ for p_2 and $i = (9-12)$ for q_2 . Therefore it results in five equations, one each for $b=0.0, 0.2, 0.4, 0.6$ and 0.8 for p_1, p_2 and q_2 .

Graphs showing the relationship between the parameters and the ratio (S_{web} / S_{xx}) for all the values of bimoment are shown in Figure A.1. For $b=0.2, 0.4, 0.6$ and 0.8 constant values of the parameter q_1 are obtained for all the regressed yield surfaces for the sections selected. Efforts were made to obtain constant values of q_1 for $b=0.0$ but this was not possible for the yield surfaces

regressed. Therefore, no graphs are required for the parameter q_1 for the bimoment values of 0.2, 0.4, 0.6 and 0.8 whereas q_1 for $b=0.0$ can be obtained by a linear equation given as

$$q_1 = 0.3432x - 2.344 \quad 3.4$$

The constant values of q_1 for values of $b=0.2, 0.4, 0.6$ and 0.8 are $-3, -16, -16$ and -20 respectively.

The parameters of Equation 3.3 are further related by another equation, for all the values of bimoments. The equation which is used is a fourth order polynomial equation of the form.

$$y = f(x) = t_{1i}x^4 + t_{2i}x^3 + t_{3i}x^2 + t_{4i}x + t_{5i} \quad 3.5$$

In the above equation, y represents the a_i terms in Equation 3.3 for different p_1, p_2 and q_2 values whereas x represents the bimoment value, and $t_{1i}, t_{2i}, t_{3i}, t_{4i}$ and t_{5i} are the constant parameters to be determined.

3.3.3 The Developed Single Equation

Repeatedly using the curve fitting technique discussed above, the developed single equation of the normalized bimoment b , and the normalized bending moments about the major and minor axes, m_y and m_x can be expressed as

$$\phi(b, m_x, m_y) = (p_1 m_y + p_2)(1 - b) - m_x(m_y^2 + q_1 m_y + q_2) = 0 \quad 3.6$$

For all the four parameters, Equation 3.3 can be written as

$$p_1 = (a_1(S_{web}/S_{xx})^3 + a_2(S_{web}/S_{xx})^2 + a_3(S_{web}/S_{xx}) + a_4)p_{11} - p_{12} \quad 3.7(a)$$

$$p_2 = (a_5(S_{web}/S_{xx})^3 + a_6(S_{web}/S_{xx})^2 + a_7(S_{web}/S_{xx}) + a_8)p_{21} - p_{22} \quad 3.7(b)$$

$$q_2 = (a_9(S_{web}/S_{xx})^3 + a_{10}(S_{web}/S_{xx})^2 + a_{11}(S_{web}/S_{xx}) + a_{12})q_{21} - q_{22} \quad 3.7(c)$$

Values of coefficients a_i can be represented by Equation 3.5 and parameters as given in the table below

$$a_i = t_{1i}b^4 + t_{2i}b^3 + t_{3i}b^2 + t_{4i}b + t_{5i} \quad 3.8$$

Values of p_{11}, p_{21} and q_{21} are given in Table 3.2(a) while values of p_{12}, p_{22} and q_{22} are given in Table 3.2(b) for bimoment values of $b=0.2, 0.4, 0.6$ and 0.8 , whereas for $b=0.0$ all the values of the parameters are one.

	b=0.0	b=0.2	b=0.4	b=0.6	b=0.8
p_{11}	1	1.005	1.003787879	1.003933309	1.002291673
p_{21}	1	0.994035785	0.990865756	0.990865756	0.987166831
q_{21}	1	1.006183686	1.009072105	1.009072105	1.025

Table 3.2(a) Values of parameters p_{11}, p_{21} and q_{21}

	b=0.2	b=0.4	b=0.6	b=0.8
p_{12}	0	0	$-\frac{(.07*(3669125 - S_w))}{0.2134811}$	$-\frac{(.17*(3669125 - S_w))}{0.2134811}$
p_{22}	0	0	$-\frac{(.05062*(S_w - .1534314))}{0.2134811}$	$-\frac{(.14697*(S_w - .1534314))}{0.2134811}$
q_{22}	$-\frac{(.011*(3669125 - (S_w)))}{0.2134811}$	$-\frac{(.05*(S_w - .261))}{0.1054591}$ for $S_w \geq 0.261$ for $S_w \leq 0.261 = 0$	$\frac{(.17*(S_w - .1534314))}{0.2134811}$	$-\frac{(355*(S_w - .1534314))}{0.2134811}$

Table 3.2(b) Values of parameters p_{12}, p_{22} and q_{22} in which $S_w = S_{web}/S_{xx}$

The constant parameters of Equation 3.8 are shown in Table 3.3.

a_i	t_{1i}	t_{2i}	t_{3i}	t_{4i}	t_{5i}
a_1	5754	-9586	4605	-547.1	-3.658
a_2	-7344	1.208e4	-5793	700.2	2.668
a_3	3542	-5781	2784	-350.4	2.292
a_4	-1652	2755	-1405	182.5	-2.87
a_5	-6481	1.04e4	-4974	599.3	3.393
a_6	7505	-1.204e4	5749	-699.9	-2.453
a_7	-3149	5071	-2413	304.8	-2.356
a_8	1400	-2345	1186	-154.2	2.88
a_9	-1.131e4	1.762e4	-8141	977.5	3.338
a_{10}	1.115e4	1.752e4	8170	-993.8	-.9956
a_{11}	-3635	5783	-2726	342.6	-2.767
a_{12}	1380	-2305	1161	-150.4	2.813

Table 3.3 Parameters of Equation 3.8

Example

Consider a UB 762 x 267 x 147 section, where if $b=0.0$ parameters then a_1 to a_{12} can be found using Table 3.2 and Equation 3.8. When these parameters are known p_1, p_2 and q_2 can be found using Equation 3.7, while q_1 can be obtained using Equation 3.4, based on the p_1, p_2, q_1 and q_2 values obtained, which are -1.96571, 1.968515, -2.23208 and 1.920563 respectively. yield surfaces can be drawn as depicted in Figure 3.3, compared to that of Yang et al (1989).

3.3.4 Yield surface diagrams

Using the single yield surfaces, prepared here for different I-sections, a comparison is made with the work of Yang et al. (1989). Yield surfaces of sections, which are considered, are shown in Figure 3.4. It can be observed in the figure, that yield surface diagrams obtained from Equation 3.6 are in good agreement with the previous solution (Yang et al. 1989).

Equation 3.6 is a quadratic equation, is continuous, can be implemented, and it fulfils the criterion of convexity (Jirasek, Bazant, 2001). The equation can be easily implemented in an elasto-plastic analysis.

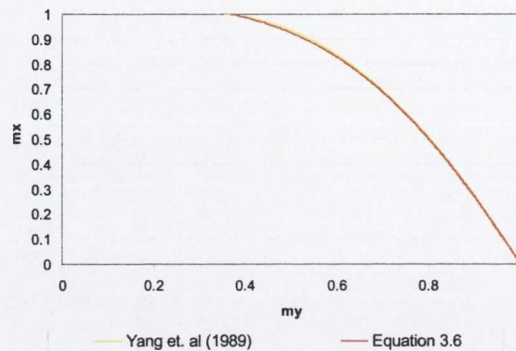


Figure 3.3 UB 762 x 267 x 147, single equation yield surface based on Equation 3.6 and yield surface developed by Yang et. al (1989)

3.4 YIELD SURFACE VERIFICATION

A procedure is developed to verify yield surfaces. Firstly single stress resultants are verified, then yield surfaces of biaxial bending and axial force, developed by Morris and Fenves (1969) and yield surfaces of biaxial bending, bimoment, axial force and uniform torsion by Yang et al. (1989) are verified. Later, using the verification procedure, the single equation developed in Section 3.3 is verified and extended to fill the gaps (for low m_y values, as identified in Figure 3.4) which were present in the yield surfaces by Yang et al. (1989).

3.4.1 What is a Yield Surface Verification?

The procedure to identify a generalized plastic hinge used in elasto-plastic analysis is based on a beam-column finite element approach. In the analysis, yielding is assumed to occur in the element based on yield surface equations. In an elasto-plastic analysis the force and deformation relationship is related as (McGuire et al. 2000)

$$\{dF\} = [[k_e] + [k_m]]\{d\Delta\} \tag{3.9}$$

where in the above equation, $[k_e]$ is the elastic stiffness matrix, $[k_m]$ is the plastic reduction matrix, and $[d\Delta] = [d\Delta_e] + [d\Delta_p]$ is a vector of incremental nodal point displacement, $[d\Delta_e]$ is the elastic contribution to the incremental displacement, whereas $[d\Delta_p]$ is the plastic contribution to the incremental displacement. Further, for one node of a beam-column element represented as 1

$$[d\Delta_{p1}] = \lambda_1 [G_1] \quad 3.10$$

where $[G_1]$ is the gradient to the yield surface at the point of yielding and λ_1 is the magnitude of plastic deformation. $[G_1]$ can further be defined as

$$[G_1] = \begin{Bmatrix} \frac{\partial \Phi}{\partial F_1} \\ \frac{\partial \Phi}{\partial M_1} \end{Bmatrix} \quad 3.11$$

where, in the above equation, Φ is a stress resultant yield surface equation, F_1 is the axial force at node 1 and M_1 is the moment at node 1.

In Equation 3.11, existing yield surface equations are used for elasto-plastic analysis, and are input in the equation to perform an elastic-plastic analysis for a beam-column element based on the input equations. Finite element analysis software, such as LUSAS or ANSYS, uses previously developed yield surface equations. For example, a cantilever beam made up of beam-column elements under the influence of stress resultants such as axial force and biaxial bending will form a hinge, based on the approach above, implemented by equations within the software.

If a yield surface equation is not described in the software then the beam analysis cannot use the equation for elasto-plastic analysis. Acknowledging this, a procedure is adopted in finite element analysis to verify yield surface equations whereby, for example, a cantilever beam is formed by the shell element. Forces are applied at the free end to produce different force actions at the fixed end. Hence, failure loads of the beam for different combination of forces can be determined. These forces or any combination of these forces at failure of a section are compared with the predictions

of the single yield surface equation that is being considered for verification. In the verification process, the forces obtained by finite element analysis are used in the single equation (omitting any one stress resultant) to allow calculation of the value of the omitted force. Hence, the value of this omitted force is compared with the value calculated by the finite element analysis to verify yielding of a point on a yield surface. Using this procedure, yield surface equations of any type of section, such as L, Z, I or etc can in principle be verified.

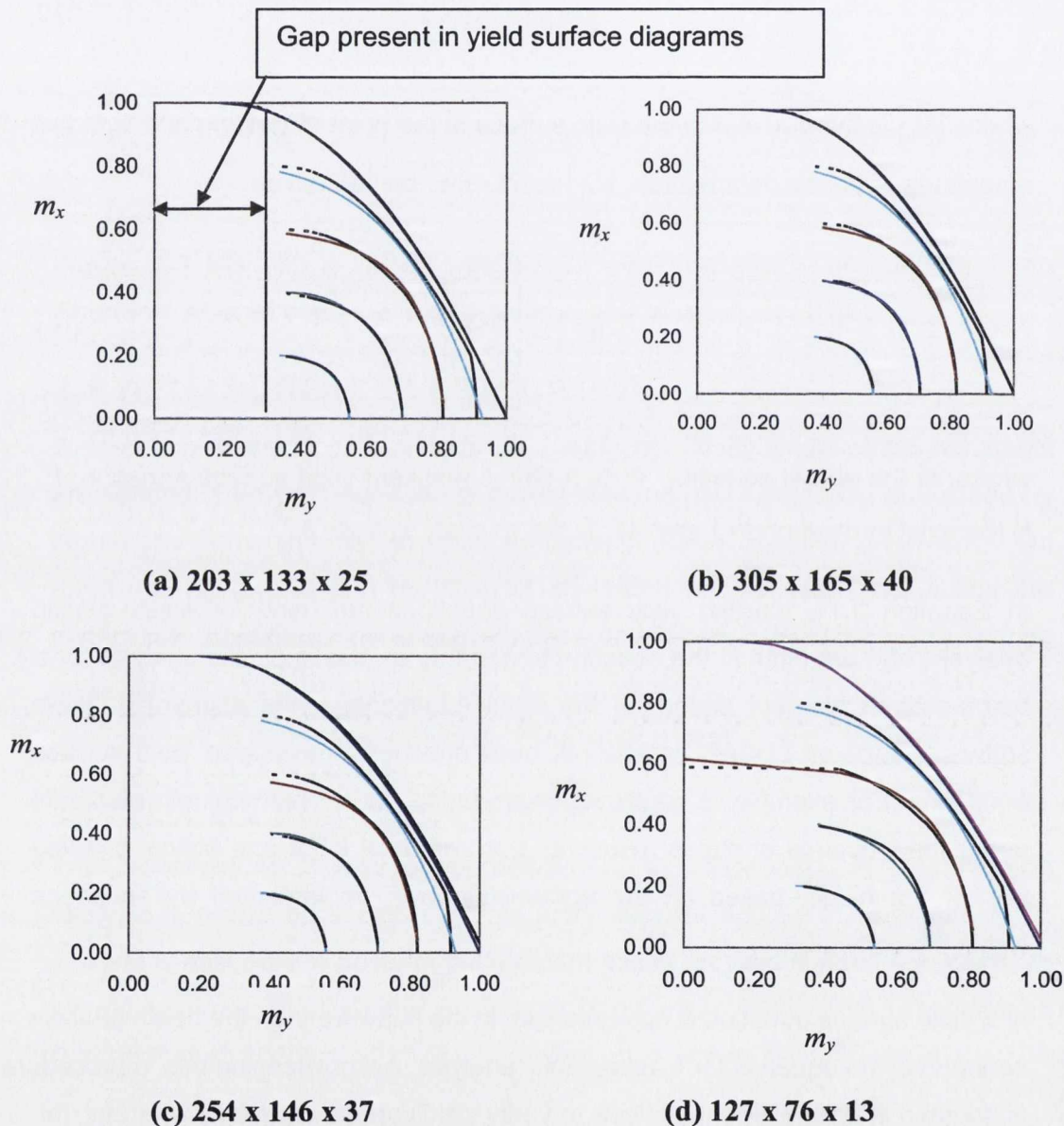


Figure 3.4 Comparison of yield surfaces by Yang et al. (1989)] (shown in coloured) with Equation 3.6 (shown in black) From upper to lower curve different b values of 0.00,0.20,0.40,0.60,0.80 exist

3.4.2 LUSAS and Finite Element Analysis

The finite element package employed for the verification is the London University Structural Analysis Software (LUSAS). This package, which is in worldwide use, is a large-scale multi-purpose finite element program for solving a variety of engineering problems. In LUSAS the model is a graphical representation, consisting of geometric features, which are points, lines, surfaces and volumes. The features in LUSAS form a hierarchy, where volumes are comprised of surfaces, which in turn are made up of lines, which are defined by points. Material properties, loading, support conditions and mesh size are assigned as attributes. Increasing the discretisation of the features usually results in an increase in accuracy of the solution, but with a corresponding increase in solution time and disk space required. All the analyses discussed in this chapter are performed in LUSAS. Advanced features of the LUSAS package are further discussed in Chapter-7, where experimental results are verified.

Different elements are available in LUSAS for modelling thin walled beams, but a 4-noded isoparametric thick shell element is considered for three reasons. Firstly, it has an option in the analysis to consider both material and geometric non-linearity. Secondly, this element adopts an assumed strain field for interpolation of the transverse shear strains, whose inclusion prevents the element from 'shear locking' when used as a thin shell element when the thickness of the element is considerably smaller than the other two dimensions. Thirdly, other elements in LUSAS require more nodes and degrees of freedom to achieve the two discussed objectives. For these reasons, this element is preferred to save time and cost of analysis.

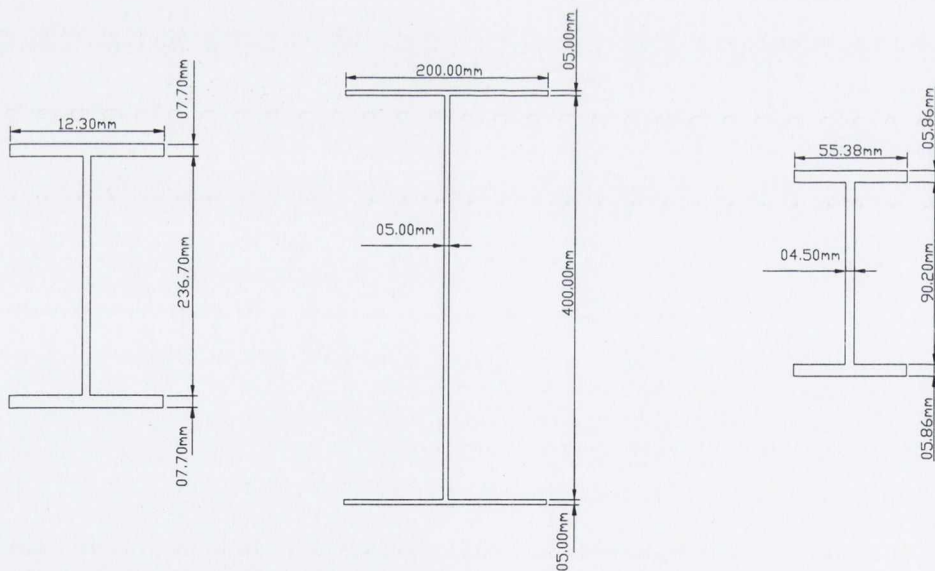
For the non-linear analysis, the incremental/iterative procedure adopted for the analyses is a constant load level incrementation. A Newton-Raphson iteration procedure is adopted to obtain convergence of the solution at each load level. If loading fails to converge then a step reduction is allowed with a smaller increment in loading. The increment in load is applied automatically although a user-defined criterion that can be used to define an increment in loading for each load step. Termination criterion used for the analysis is based on a user-defined displacement.

For the material non-linear analysis, the non-linear model used is a stress potential model applicable to a multi-dimensional axial stress state requiring the specification of yield stress in each direction of the stress state incorporating Von-Mises yield criteria (Reasons for the use of this criterion is given in Section 4.4.7).

3.4.3 Finite Element Model Attributes

Details of structures

Three cantilever I-section beams of spans $4.39m$, $5.00m$ and $1.24m$ are selected to verify yield surfaces for different combinations of active stress resultants. The section used for the $4.39m$ span is a 10UB29 beam, which was previously used by Pi and Trahair (1994) as shown in Figure 3.5(a), whereas for the $5.00m$ span, as shown in Figure 3.5(b), a sample section whose thickness is considerably less than the thickness of the 10UB29 beam is used. The third section used (which was tested in the experiments described in Chapters 5 and 6) is of lesser depth as compared to the other two, and is shown in Figure 3.5(c). Spans and dimensions of the beams are selected to fulfil the Vlasov's (Vlasov, 1959) criterion of thin walled beams.



(a) 10UB29 Section

(b) Sample section
section.

(c) Experimental

Figure 3.5 Details of cross sections of (a)10UB29 section, (b) Sample section and (c) Experimental section

Mesh size and load application

For the analysis, an appropriate mesh size is required to meet the convergence criterion of finite element analysis. Different mesh sizes were examined, and a mesh size at which finite element results closely matched the theoretical plastic capacities of a section is selected for the verification. After several analyses of different stress resultants, it was decided to use a size of $0.01256m \times 0.01463m$ for the 10UB29 section, $0.025m \times 0.025m$ for the section, and $0.011m \times 0.0069m$ for the experimental section.

It was observed during the analysis that a reasonable distribution of load was necessary to avoid local failure at the point of application of load due to concentration of stress at the point. This is true especially in the case of application of an axial stress resultant, where large direct stresses are more likely to lead to local failure. Therefore, loadings applied were distributed uniformly by a trial and error procedure in which loads were applied to obtain failure of a fixed ended section. If failure was initiated at the point of application of the load instead of a section at the fixed end, then loads were further distributed uniformly. This procedure continued up to the point not when failure was initiated due to a local concentration of stresses at the load point, but due to failure of a cross section. Von Mises yield criterion, with an elastic-perfectly plastic material was used for the analysis.

3.4.4 Single Stress Resultants

Single stress resultant analyses are performed for three reasons. Firstly, to establish the capability of 4-noded isoparametric thick shell elements to adequately model material non-linearity. Secondly, to obtain the plastic capacities of the section and to compare them with theoretical values and previously obtained results. Thirdly, to use the obtained plastic values in order to obtain the normalized stress resultants in the process of yield surface verification.

Analyses are performed for all the active stress resultants. Plastic capacities for each stress resultant are obtained, and compared with theoretical values and with several published works in the case of torsion (Bathe and Weiner, 1983 and Dinno and Merchant, 1965).

Results in the case of axial stress resultant vary by less than 2.0% , whereas variations for the cases of bending about the major and minor axes are between 2.0% and 3.0% . The results are shown in Table 3.4. Variations for the cases of bending moments about both the axes are because of the element considered for the analysis, which has six degrees of freedom with local in plane bending of each element, transverse shear stress variation and out of plane bending, whereas while the theoretical plastic capacities are calculated based on the hypotheses of Euler-Bernoulli (Vlasov 1959), which states that plane section remains plane after bending and no out of plane bending and shear deformation was considered. Therefore, it can be said that the LUSAS result is more accurate than the plastic capacities because plastic capacities do not take into account out of plane bending, transverse shear variation. However the difference between both the results is not substantial.

Elastic-plastic small rotational torsional stress resultant

Torsional stress resultants are discussed separately due to the amount of previous work (Bathe and Weiner, 1983 and Dinno and Merchant 1965) in this area.

Elasto-plastic analysis for torsional stress resultants is a complicated phenomenon. Different researchers have dealt with it previously, but no exact analytical solution exists. In this work, analyses are compared with previous work to verify the capability of the element in dealing with torsional problems.

Different analyses results are summarized in Table 3.5. In the table, previous work by Pi and Trahair, 1995b, Bathe and Weiner, 1983, and Dinno and Merchant 1965 are compared with the current analyses. It can be observed that results for all the cases for different boundary conditions and spans largely match one another. A small difference in percentage terms between the finite element study by Pi and Trahair 1995b and the current analysis is observed. The last result in the table is that which was first analysed by Bathe and Weiner in 1983, and is reanalyzed in this study: the result obtained is seen to be near the previous result. The reason for the difference is the same as discussed previously that thick shell element take into account secondary deformations and variations of stress and is much more accurate.

Stress resultants	Theoretical result	Finite element analysis	Percentage difference	Section type
Axial force	1661.16kN	1678.55kN	1	UB29
Bending about major-axis	171.09kN-m	175.89kN-m	2.8	UB29
Bending about minor-axis	43.12kN-m	44.44kN-m	3.05	UB29
Axial force	1200kN	1217kN	1.42	Sample
Bending about major-axis	181.5kN-m	187.13kN-m	3.1	Sample
Bending about minor-axis	30.75kN-m	31.64kN-m	2.9	Sample
Axial force	316.152kN	322.45kN	2	Experimental
Bending about major-axis	12.10kN-m	12.35kN-m	2	Experimental
Bending about minor-axis	2.83kN-m	2.92kN-m	3	Experimental

Table 3.4 Comparison of theoretical plastic capacities with finite element analysis for axial force and biaxial bending

The differences in the results are because of the methodologies that are adopted for finite element analysis which include the selection of element, and selection of different non-linear analysis and iteration techniques.

The variation in the results when compared to the approximate approaches by Dinno and Merchant 1965 and Pi and Trahair, 1995b is due to the fact that in these approaches, warping was taken by the flanges whereas warping of the web was not considered. Warping of the flanges causes the two flanges to bend in different directions, and it has been mentioned previously that bending action causes a variation between 2.0% and 3.0%.

The results of torsional analyses using the thick shell element in LUSAS when compared with the analyses previously performed do not vary substantially. Therefore, it can be concluded that small rotational torsional analysis using the thick shell element in LUSAS can perform satisfactorily.

S.No	Type of Structure	Finite element analysis	Previous work	%age difference
		<i>kN.m</i>	<i>kN.m</i>	
1	I-section, both ends fixed of span 4.39m torsion applied at the centre	16.8	16.1 (Pi and Trahair, 1995b)	4.35
2	I-section, cantilever beam of span 4.39m torsion applied at the free end.	4.85	5.2 (Dinno and Merchant, 1965)	7
3	I-section, torsionally simply supported of span 1.93m, Loads applied at the centre	14.9	15.07 (Pi and Trahair, 1995b)	1.15
4	I-section, cantilever beam of span 0.25m torsion applied at the free end	34.91	36 (Bathe and Weiner, 1983)	3.1

Table 3.5 Comparison of torsional analysis of LUSAS with previous work.

3.4.5 Verification of 2-D yield surface using LUSAS

Different combinations of 2-D stress resultants for plasticization of a section have been verified using finite element analysis. Stress resultants considered are axial stress resultants P , bending about the minor axis M_{\min} , bending about the major axis M_{\max} and bimoments B . For these four active stress resultants, there can be six combinations of graphs, which can be drawn for a 2-D yield surface.

One such combination is a $p - m_{max}$ yield surface, where, p and m_{max} are the stress resultants in normalized form. This combination of yield surface is developed using finite element analysis and is verified with the theoretical yield surface developed by Morris and Fenves (1969). The section used is shown in Figure 3.5(b). The yield surface obtained in this study is developed from 23 different combinations of P and M_{maj} stress resultants using material non-linear analysis. Both the theoretical yield surface and that from finite element analysis are shown in Figure 3.6. In the graph on the X-axis is the normalized major moment m_{maj} , whereas on the Y-axis is the normalized axial load p at plastification. From observing the graph, it can be concluded that the finite element analyses match the theoretical results very well.

Other stress resultant combinations are also verified. They are verified for the section that is used in the experiments as shown in Figure 3.5(c). Two different combinations of stress resultants are verified where two analyses for each of the different combinations of stress resultants are performed, namely for combinations of M_{maj} and M_{min} , and P and M_{min} .

Using one of the LUSAS analyses results, theoretical values are calculated for the other value using the equations. Those calculated theoretical values are compared with the results obtained from LUSAS. The results compared in normalized form are shown in Table 3.6. It can be observed in the table that for the cases of M_{maj} and M_{min} and P and M_{min} , results are very satisfactory.

Calculated theoretical values match well with the LUSAS results.

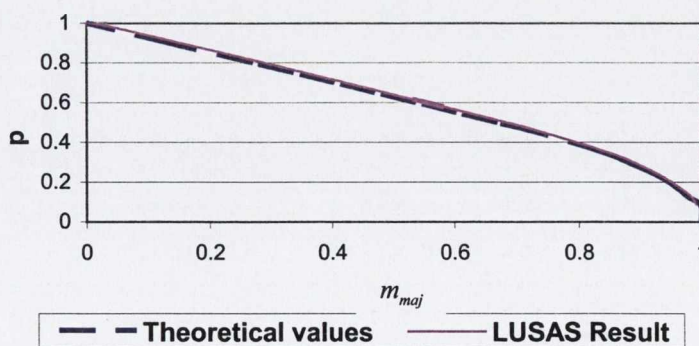


Figure 3.6 $p - m_{maj}$ yield surface of the I-section.

S.No	LUSAS			Theory	
	p	m_y	m_z	m_y	m_z
1	0.48	0.94		0.93	
2	0.18	0.98		0.98	
3		0.50	0.77		0.78
4		0.63	0.70		0.70

Table 3.6 Yield surface verification results for 2-D stress resultants

3.4.6 Verification of 3-D yield surface

The approach, which was adopted previously, is extended to the verification of different combinations of three stress resultants. Yield surface equations, for which verification is sought are those by Morris and Fenves (1969). Satisfactory results are obtained, when full plasticization of a section for different combinations of two dimensional stress resultants are verified.

Axial force and biaxial bending stress resultants

In the case of axial force and bi-axial bending stress resultants, the section used for the verification is an idealized section of span 5.00m, as shown in Figure 3.5(b). Results obtained are given in normalized stress resultant form in Table 3.7. Results of p and m_{\min} obtained from the finite element analyses are used to calculate the theoretical m_{maj} values using the equations and are compared with the m_{maj} values obtained from LUSAS. Comparison of results indicates good agreement of theoretical values with the LUSAS results.

p	m_{\min}	m_{maj}	m_{maj}
		LUSAS	Morris and Fenves (1969)
0.51	0.85	0.35	0.32
0.33	0.86	0.46	0.45
0.16	0.95	0.46	0.42
0.08	0.62	0.74	0.72

Table 3.7 Comparison of yield surface by Morris and Fenves (1969) and LUSAS.

Bimoment, axial force and major moment stress resultants

In the case of the combination of bimoment, axial force and moment about the major-axis, equations, which one seeks to verify, are from the approach by Yang et al. (1989). The experimental section in Figure 3.5(a) is used for the verification and details of the results are summarized in Table 3.8. It can be observed in the table that results obtained from LUSAS do vary somewhat. One reason for the variation was the assumption adopted by Yang in which bimoments are resisted only by the flanges, therefore the web doesn't take part in the yielding and hence more major moment is required for the yielding of the web in LUSAS. Also the reason for the difference is the same as discussed previously.

p	b	m_{maj}	m_{maj}
		LUSAS	Yang et al. 1989
0.53	0.47	0.61	0.55
0.44	0.46	0.71	0.65

Table 3.8 Comparison of the yield surface by Yang et al. (1989) and LUSAS.

3.4.7 Verification of 4-Dimensional Yield Surface

The yield surface of an I-section by Yang et al. (1989) for biaxial bending and torsional stress resultants are to be verified. A summary of the results is shown in Table 3.9 for a sample section (Figure 3.5(b)), where a comparison is made with LUSAS results.

Finite element analyses in LUSAS are performed. These results show good agreements with theoretical yield surface and are well matching with the theoretical results.

3.4.8 Yield Surface verification procedure and the shell element

The use of the thick shell element (QTS4) for non-linear analysis was first verified for the simple cases. This element was then used to verify 2-D, 3-D yield surfaces and good results were obtained. Using it further, the 4-D yield surface of an I-section was verified and it was found that the parametric approach by Yang et al. (1989) is a good approximation.

Different pre-existing theoretical yield surfaces are verified in LUSAS, and it appears that the FEA model reproduces with reasonable accuracy the theoretical predictions for a variety of sections and stress resultants types. It is concluded that 4-noded isoparametric elements can be used for material non-linear analysis and for verification of yield surface.

S.No	p	m_{\min}	b	m_{maj} LUSAS	m_{maj} Yang et al. 1989
1	-0.16	0.54	-0.29	-0.77	-0.76
2	-0.22	0.55	-0.34	-0.74	-0.73
3	-0.24	0.33	-0.30	-0.84	-0.83
4	-0.31	0.31	-0.26	-0.81	-0.80
5	-0.40	0.24	0.24	-0.77	-0.76
6	-0.43	0.46	0.41	-0.68	-0.67
7	-0.90	0.07	0.14	-0.14	-0.11

Table 3.9 Comparison of the yield surface by Yang et al. (1989) with finite element results

3.5 EXTENSION AND VERIFICATION OF THE DEVELOPED SINGLE EQUATION YIELD SURFACE

3.5.1 Limitations at low m_y values

The yield surfaces developed by Yang et al. (1989) do not approach zero values for the moment about the major-axis m_y . The graph of the yield surface terminates before touching the YY-axis for maximum values of m_x and a gap exists in the yield surfaces as indicated in Figure 3.4. This is due to the assumption, which was adopted by Yang et al. (1989) that the neutral-axis passes perpendicularly through the local longitudinal axis of both the flanges and web for the cases when neutral-axis passes through the web. When a perpendicular neutral-axis passes through any rectangular section (each flange itself is a rectangular plate) then the axial load contribution from the rectangular section remains the same for a fixed value of moment. This can be understood

from the equation when moment and axial force acts on a rectangular section, as given by Equation 2.58, reproduced again here as

$$\left(\frac{P}{P_p}\right)^2 + \frac{M}{M_p} = 1 \tag{3.12}$$

During to this, the contribution of the major moment from the flange remains constant (as it depends on the value of P which is constant). When an inclined neutral-axis is assumed for one flange, then the value of P varies for constant moment, as has been depicted in Figure 3.7 in which P varies for constant moment. Therefore, a series of P values can be obtained for constant moment and hence, this results in a series of different values of the component of major moment from the flange. This results in an ultimate value of major moment (when the contribution to the major moment from both flanges and web are added) such that it approaches a zero value for the major moment and results in a yield surface which does not have such gaps, as indicated by Figure 3.4. The P values of the flanges are summed to the P value of the web (which can be negative) and value of the other flange so that it results in a zero ultimate axial force.

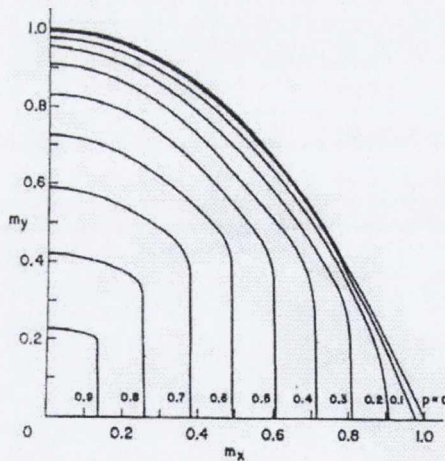


Figure 3.7 Yield surface of a rectangular section for biaxial bending and axial force

3.5.2 Rise of curve if gap is filled

It emerges that the curve, if extended to fill the gap, will not rise even if the contribution of minor moment from the web is taken into account. To understand

this consider the current approach by Yang et al. (1989) in which two equations, which are Equations 2.74(b) and 2.74(d), reproduce here, are used:

$$m_x = m_1 + m_3 \quad 3.13(a)$$

$$b = m_3 - m_1 \quad 3.13(b)$$

The graph of Figure 3.4 is for a fixed value of b . Based on the fixed value it can be said that Equation 3.13(a) can have several values while Equation 3.13(b) can have only one value. Therefore m_1 and m_3 can vary but always satisfy Equation 3.13(b). For example if $b = 0.2$ is taken then whatever value m_1 and m_3 will have their difference must be 0.2. Therefore, now it is required to establish what values m_1 and m_3 can have so that the maximum value of m_x can be obtained for the constant b value. The maximum contribution of m_1 and m_3 can be 0.5 (as both flanges take half of the moment) for the case when a section is plasticised in the presence of m_x only. However as $b = 0.2$ in that case the maximum m_3 can be 0.5 and maximum m_1 can be 0.3.

Two possibilities can exist; firstly, when the minor moment contribution from the web is not taken into account. In that case m_x is obtained by Equation 3.13(a) keeping Equation 3.13(b) valid. As m_x will be maximum as obtained by the equation and For example for constant $b = 0.2$ it will be 0.8 based on $m_1 = 0.5$ and $m_3 = 0.3$ so difference will give $b = 0.2$ So it means for the case when web does not take minor moment into account the value of m_x obtained by Equation 3.13(a) is the maximum m_x which can be achieved and gap is filled by a line of zero slope, if it is assumed that moment major moment will decrease.

A second possibility can arise when contribution of m_x from web is considered. In that case Equation 3.13(b) will still be valid (because bimoment contribution is only from both flanges), whereas one component of web contribution to minor moment will add on the right side of Equation 3.13(a). The contribution to minor moment m_x from the web is small (because of the small thickness of web) compared to the contribution from flanges to m_x . Therefore the increase of m_x

when the minor moment is considered for the web is small compared to the case when the minor moment contribution from web is not considered. Therefore the gap will be filled with a curve with a slight increase of global m_x value. This shows that when the gap is filled the increase of m_x value will not be substantial as compare to the case when the gap is not filled. This is further verified in finite element analysis as discussed in the next section.

3.5.3 Procedure to extend the yield surface

The purpose of the procedure will be to extend the graph given by Figure 3.4 to the edges (to fill the gap) based on the developed single equation and later verify the extended part of the graph using finite element analysis.

In the procedure, four Universal beam sections of BS EN10056: 1999 sections, which are 305 x 165 x 40, 254 x 146 x 37, 203 x 146 x 37 and 127 x 76 x 13, are selected randomly. The regions in the graphs of the yield surfaces for the sections where gaps exist is depicted in Figure 3.5. They can be extended using the values of m_y in the region for a particular value of bimoment b .

Using Equation 3.6 graphs are extended as depicted in Figure 3.8. In the equation values of p_1 , p_2 , q_1 and q_2 are calculated for constant values of b and all the obtained values are input in the equation. For low values of m_y as for example in Figure 3.4(d) when $m_y = 0.2$ the gap exists for all b values. Therefore, in the equation such low values of m_y are input to obtain m_x . In such a way graphs are extended. From the figure it can be observed that on the extension of graphs to the edges of the YY-axis, it maintained a small slope indicating a very low rise in the values of m_x for the gap region. (This property was also observed when the developed equation was investigated for all the sections checked from the list of sections of BS EN10056: 1999 sections present in the graph. As discussed previously, when the gap is filled m_x will not rise compared to the value when the gap is not filled and on that basis it can be said that the extension is reasonable, but this extension has to be verified. This extension is verified using finite element analysis and is discussed in the next section.

3.5.4 Verification of the extended curves

The verification technique already discussed in the previous section is used to verify the extended part (which is extended based on the single equation developed). Several finite element analyses are performed for the extension. Values of the loading for the analysis are based on such a combination of bimoment and biaxial bending that the analysis will the yield values, which will lie in the extended region, that is, for low values of m_y . If the results from the finite element analysis match the values of the extended part then the extension can be considered correct. The analysis is performed for all four sections.

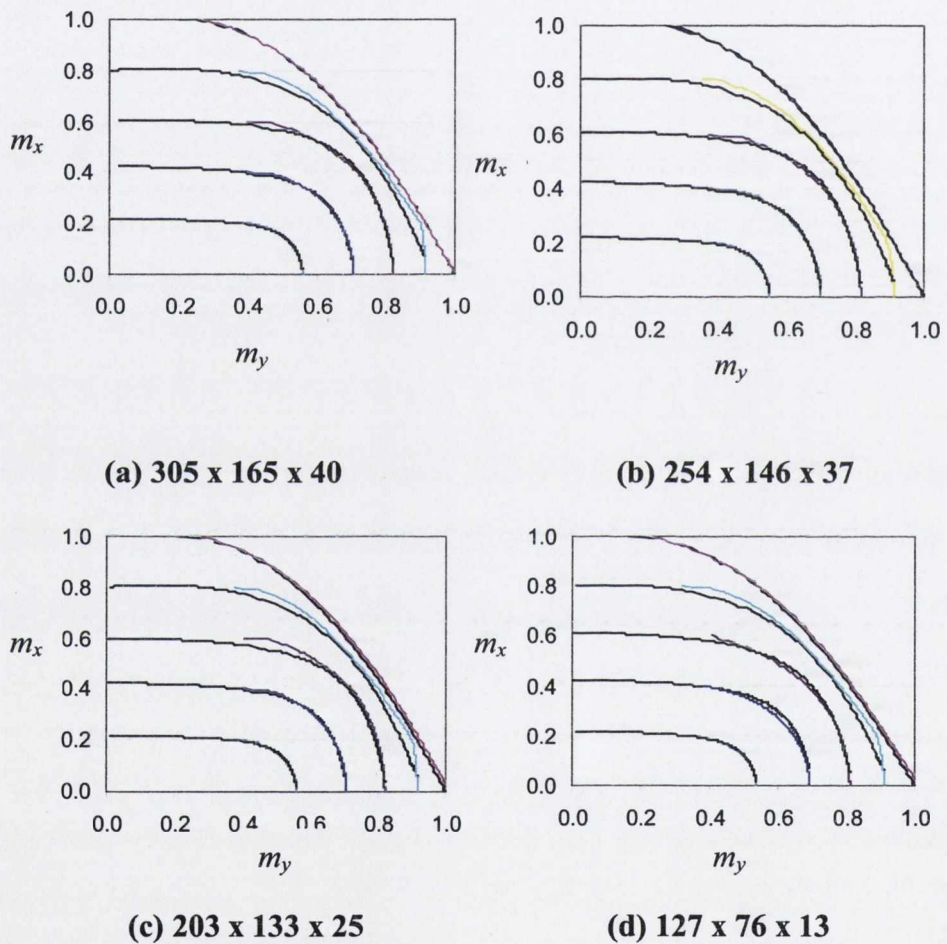


Figure 3.8 Developed single equation yield surface (shown in black) after extension, compared with yield surfaces by Yang et al. 1989 (shown in colour). From the upper to lower curve the order of curve is for different b values of 0.0,0.2,0.4,0.6,0.8.

Results obtained from the analysis for the extended region are given in Table 3.10. Values of m_y obtained from Equation 3.6 and the finite element analysis are given. It can be observed in the table that both the results match each other excellently. Such an analysis is also performed for other sections and satisfactory results are obtained. However, yield surfaces of these four sections only are drawn, therefore only their results are summarized in the table.

Hence, it can be inferred from the results that the extension adopted for the yield surface curve is correct. Therefore, the single equation can be used even for low values of the major moment m_y hence filling the gap which was present in the previous approach by Yang et al. (1989).

Section type	b	m_y	m_x (LUSAS)	m_x Developed equation	Percentage difference
305 x 165 x 40	0.013	0.146	0.99	0.99	0.0
305 x 165 x 40	0.087	0.137	0.903	0.89	1.5
305 x 165 x 40	0.212	0.119	0.777	0.78	0.4
305 x 165 x 40	0.261	0.097	0.728	0.745	2.3
305 x 165 x 40	0.018	0.187	0.973	0.99	2.6
254 x 146 x 37	0.01	0.092	0.976	0.99	1.4
254 x 146 x 37	0.182	0.23	0.808	0.81	0.2
254 x 146 x 37	0.074	0.208	0.916	0.93	1.5
254 x 146 x 37	0.011	0.137	0.975	0.99	1.5
254 x 146 x 37	0.028	0.164	0.968	0.98	1.2
254 x 146 x 37	0.097	0.17	0.893	0.91	1.9
203 x 133 x 25	0.024	0.29	0.99	0.97	2.1
203 x 133 x 25	0.023	0.17	0.99	0.99	0.0
203 x 133 x 25	0.339	0.186	0.7	0.68	2.9
203 x 133 x 25	0.02	0.17	0.99	0.99	0.0
203 x 133 x 25	0.248	0.13	0.8	0.76	5.2
127 x 76 x 13	0.03	0.297	0.943	0.943	0.0
127 x 76 x 13	0.046	0.254	0.938	0.94	0.2

Table 3.10 Comparison of the yield surface of equation 3.6 and finite element analysis.

Therefore, it can be concluded that the developed single equation and its extended portion can be considered as a single equation yield surface for bimoment and biaxial bending stress resultants. This equation, unlike the approach by Yang et al. (1989), is more complete and simple to adopt.

3.5.5 Verification of the yield surface

The developed yield surfaces and the yield surfaces by Yang et al. (1989) are verified using finite element analyses. The same sections are used for the verification as was used for the procedure to extend the yield surface. Details of the results are summarized in Table 3.11. It can be observed that the results obtained from LUSAS for all the analyses compare well with both the approaches.

Section type	b	m_y	m_x	m_x	m_x	Percentage
			(LUSAS)	Yang et al. (1989)	Developed equation	LUSAS and developed equation
305 x 165 x 40	0.022	0.63	0.68	0.68	0.675	0.7
305 x 165 x 40	0.672	0.287	0.535	0.53	0.52	2.9
305 x 165 x 40	0.026	0.541	0.741	0.74	0.74	0.1
305 x 165 x 40	0.397	0.359	0.756	0.743	0.725	4.3
305 x 165 x 40	0.499	0.331	0.696	0.68	0.669	4.0
254 x 146 x 37	0.018	0.933	0.359	0.39	0.38	5.8
254 x 146 x 37	0.099	0.838	0.47	0.48	0.46	2.1
254 x 146 x 37	0.021	0.803	0.537	0.54	0.53	1.3
254 x 146 x 37	0.039	0.685	0.635	0.64	0.629	1.0
203 x 133 x 25	0.031	0.47	0.802	0.78	0.784	2.2
203 x 133 x 25	0.036	0.37	0.85	0.83	0.836	1.7
203 x 133 x 25	0.04	0.588	0.74	0.72	0.713	3.8
203 x 133 x 25	0.535	0.45	0.57	0.51	0.55	3.6
127 x 76 x 13	0.041	0.433	0.794	0.792	0.79	0.5
127 x 76 x 13	0.036	0.33	0.846	0.847	0.844	0.2

Table 3.11 Comparison of the Single equation yield surface and the yield surface by Yang et al. 1989 with the finite element analysis.

This verification process concludes that the developed single equation yield surface is a good representation of the yield surface for bimoment and biaxial bending of a thin walled I-section. The developed yield surface also fills the gap that was present in the previously published yield surfaces and it can be used for elasto-plastic analysis of structures.

3.6 CONCLUSION

In this chapter a single equation yield surface for biaxial bending and bimoment stress resultants has been developed for thin walled I-section of Universal Beams to BS EN 10056 (BSI, 1999). The development of the yield surface equation is divided into two parts. The first part is based on a curve fitting analysis technique, whereas the second part fills the gap which was present in the yield surface developed by Yang et al. 1989 using a numerical approach.

For the development of the single equation yield surface, a computer code was written to develop yield surfaces based on the previous approach by Yang et al. 1989. Later the variation of the yield surface for different Universal Beams of BS EN 10056 (BSI, 1999) was investigated and a relationship was developed between the variation and the section property. The variation was considered in the development of the yield surface equation. The equation was developed using repeatedly a curve fitting technique with the parameters of the equations related to the variations.

In the second part of the chapter, a procedure is developed to verify the yield surface. Hence, authentication of the procedure and also the verification of the previously developed yield surface was accomplished. With the help of the verification procedure, the developed yield surface was extended to fill the gap which was present in the yield surface by Yang et al. (1989).

The developed yield surface is a single equation yield surface, therefore easy to apply without any discontinuity of slope for elasto-plastic analysis.

CHAPTER-4

PLASTIC INTERACTION RELATIONSHIPS FOR GENERAL STRUCTURAL I-SECTIONS

4.1 INTRODUCTION

In the previous chapter single equation yield surface for biaxial bending and bimoment were developed using curve fitting technique and verified using finite element analysis. This chapter shall develop plastic interaction relationships for I-sections subjected to general combinations of axial force, biaxial bending moments, biaxial shearing forces, uniform torsion and bimoment. Axial force, biaxial bending moments and bimoment cause direct stress, whereas biaxial shear forces and uniform torsion cause shear stress. The interaction equations of both direct and shear stresses shall be developed separately using the lower bound theorem of limit analysis (Hodge, 1959). Later it shall be demonstrated that for an equilibrium condition on an infinitesimal element both the stresses can be related to each other using the maximum distortional energy density yield criterion.

To obtain the relationships in the case of direct stresses a study shall be performed to obtain different neutral-axis patterns in the presence of warping strain. These obtained neutral-axis patterns are used to derive interaction equations and a procedure shall be developed to identify the formation of a generalized plastic hinge and development of the yield surface. Using this procedure, yield surfaces shall be developed for a W12 x 31 steel section and compared with previously developed work.

Using the upper bound theorem of limit analysis, a relationship for direct stress for a particular case shall be obtained and compared with the lower bound solution.

4.2 STATEMENT OF PROBLEM

Interaction relationships for structural I-sections subjected to the combined action of axial force, biaxial bending moments, biaxial shear forces, uniform torsion and bimoment are sought. To obtain the interaction equations it is assumed that fully plastic resistance of the cross section will be attained under the given forces. It should also be kept in mind that the equations are correct only for tension members without any secondary effects or for compression members with sufficient lateral bracing of members with negligible buckling effects. The formulation is based on the lower bound theorem of plasticity (Hodge, 1959).

An I-section, having geometry as depicted in Figure 4.1(a), is described by the following parameters: width of flanges b_f , thickness of flanges t_f , width of web b_w , and thickness of web t_w . The section, having a yield strength σ_y in uniaxial tension (or compression), is subjected to an axial force P , biaxial bending moments M_x and M_y , bimoment B , uniform torsion T_u and biaxial shear forces S_x and S_y applied along the principal centroidal axes XX and YY. The ZZ-axis is orientated along the centroidal axis of the member. It is required to determine whether or not the section can resist the applied combination of internal forces under the assumption that fully plastic resistance of the section is reached. Mathematically, this requirement means that a family of interaction relationships of the form

$$f_i'(P, M_x, M_y, B, T_u, S_x, S_y, b_f, t_f, b_w, t_w, \sigma_y) = 0 \quad 4.1$$

are required. It is convenient to formulate the relationships based on normalized force components, therefore, the arguments of functions f_i' in the normalized form is written as

$$f_i''(p, m_x, m_y, b, t_u, s_x, s_y, f(a)) = 0 \quad 4.2$$

in which the normalized terms $m_x = M_x / M_{xp}$ and $m_y = M_y / M_{yp}$ are the ratios of the applied bending moments about the XX and YY axes to the corresponding plastic moment capacities of the section; $s_x = S_x / S_{xp}$ and $s_y = S_y / S_{yp}$ are the ratios of the applied shear forces to the assumed plastic shear capacity; $p = P / P_p$ is that of the applied axial forces to the axial yield strength; $b = B / B_p$ is the ratio of the developed bimoment to its plastic bimoment capacity and $t_u = T_u / T_{up}$ is the ratio of the applied uniform torsion to its plastic torsional capacity. The plastic capacities for each applied internal force are those that fully plasticize the cross section in the absence of any other internal forces. The plastic capacities are (Mrazik et al. 1987)

$$P_p = (2A_f + A_w)\sigma_y, \quad T_{up} = \sigma_y / \sqrt{3}(A_f t_f + A_w t_w), \quad B_p = 0.25A_f b_f d \sigma_y,$$

$$S_{xp} = A_w \sigma_y / \sqrt{3}, \quad S_{yp} = 2A_f \sigma_y / \sqrt{3}, \quad M_{xp} = (0.5A_f b_f + 0.25A_w t_w)\sigma_y,$$

$$M_{yp} = (A_f d + 0.25A_w b_w)\sigma_y.$$

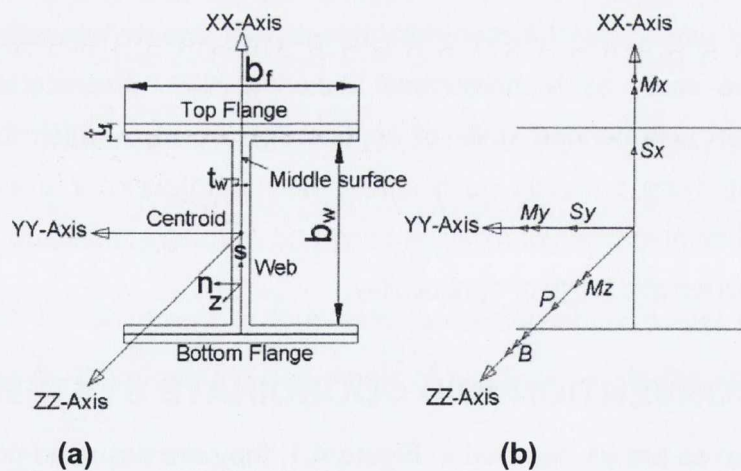
S_x and S_y are discussed in Section 4.6, whereas procedures and assumptions made to obtain the remaining plastic capacities are discussed in the references and it is not relevant to go into the detail of it in this research. The parameter $f(a)$ represents the function that is obtained due to the conversion of the section parameters by dividing it by other section parameters (which evolved when yield functions are developed) into its normalized form. It is found from the study by Mohareb and Ozkan (2004) that a yield function is applicable when well defined limits of applicability are met, which the author has obtained by studying probable positions of the neutral-axis for a warped section under different combinations of axial, bending and warping strains and are termed by the author as kinematic limits of applicability.

4.3 SIGN CONVENTION AND COORDINATE SYSTEM

If XX and YY axes are as depicted in Figure 4.1, they are assumed positive (having an origin of the coordinate system at the centroid of the section) using a right hand rule which can be applied to obtain the positive direction of the ZZ-axis, as depicted in the figure. The axial force P , is positive when it causes tension (acting along the positive Z-direction). Moments M_x , M_y and M_z (causing twisting of the member) are

positive when they induce moments about the positive XX, YY and ZZ axes following the right hand screw rule. Biaxial shear forces S_x , S_y are positive when acting along the positive directions of the XX and YY axes, respectively. Bimoment B is considered positive when it produces a twisting action in the positive Z direction. Positive directions of all the internal forces are depicted in the figure.

Considering axial force, biaxial bending moments and bimoment, each of which cause direct stress to the section, then there are sixteen quadrants for different combinations of positive and negative internal forces. The forces which cause shear stress are not considered when obtaining the number of quadrants. The reasons for not considering these forces are discussed in Section 4.6. Hence, a four dimensional yield surface is sought, where each dimension is related to one of the forces which causes direct stress. An internal force relationship is developed to represent all the quadrants based on the fundamental cases (discussed in Section 4.7.4). A local coordinate system (t , s and z) for the section is also shown in the figure. The direction along the contour is denoted by s , while the direction normal to the middle surface is n and along the generator of the plate is z .



(a) Local coordinates and elements of the section (b) Direction of positive forces
 Figure 4.1 (Figure 2.7 reproduced here for discussion) Local coordinates, elements of the section, positive coordinate system with direction of positive forces

4.4 ASSUMPTIONS

4.4.1 Stress-Strain Relationship

The stress-strain relationship is assumed to be bilinear elastic-perfectly plastic, where the maximum stress is given by the yield stress σ_y . The bilinear stress-strain diagram, depicted in Figure 4.2, has a uniform slope up to the yield stress beyond which it maintains a zero slope. The additional capacity of the material due to strain hardening is neglected; hence a conservative approach is adopted for the section's non-linear resistance. It is assumed that the yield stress has the same magnitude in compression and tension, where it cannot exceed the tensile and compressive bounds given by yield stress $+\sigma_y$ in tension and $-\sigma_y$ in compression. These stresses satisfy the condition of plastic admissibility, which is

$$-\sigma_y \leq \sigma \leq \sigma_y \quad 4.3$$

No distinction is made between true stress and engineering stress and formulation is restricted to small strain, as no distinction is made between logarithmic strain and engineering strain.

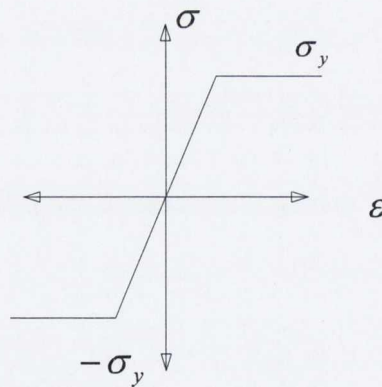


Figure 4.2 Stress-strain relationship of elastic-perfectly plastic material

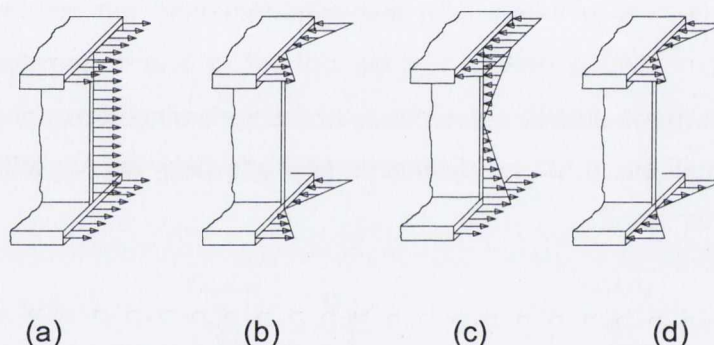
4.4.2 Kinematics and neutral-axis patterns

It is assumed that the kinematics (i.e. strain, displacement etc) for the elastic and plastic cases are the same. Considering the kinematics, axial strain at any point on a

cross section parallel to the longitudinal axis is given by Equation 2.3 (rewritten here) as (Gjelsvik, 1981)

$$\varepsilon_{zz} = \frac{\partial w}{\partial z} = W' - U''x - V''y - \Phi''(z)\omega(x,y) \quad 4.4$$

The above equation determines the strain field by superposing four diagrams, each of which is related to one term in the above equation, as depicted in Figure 4.3. Combining the four diagrams, the strain field for the entire section is obtained. Using Equation 4.4, different values of the four terms are derived to obtain different strain fields and a variety of possible neutral-axis patterns. Detailed procedures to obtain the patterns will be given in Section 4.7.



(a) Axial strain (b) Flexural strain (XX-Axis) (c) Flexural strain (YY-axis) (d) Warping strain

Figure 4.3 Diagrams showing strain distributions due to different internal forces

4.4.3 Bimoment and cross section warping

The warping of the cross section is composed of the warping of the contour (the I-shape) and warping of the wall thickness relative to the contour. The thickness contribution was investigated (Gjelsvik, 1981) and found to be about 3% of the warping of the contour for the heaviest available hot rolled steel section. In addition, several authors, such as Timoshenko and Gere (1961), ignore the thickness contribution (as discussed in Section 2.1). Therefore, following the approach by

Timoshenko and others, the warping of the wall thickness relative to the contour is not considered by the author. Hence, both flanges are assumed to behave as simple beams, where the flanges are bent in their own plane in two opposite directions, ignoring the web. For this case, the warping function, ω , is assumed to be equal to the contour warping function $\bar{\omega}$ and is written as

$$\omega = \bar{\omega} \quad 4.5$$

4.4.4 Residual stress

Standard manufactured I-sections are normally hot rolled sections. The effects of residual stress on the hot rolled sections are normally neglected (Mohareb and Ozkan, 2004). Therefore, in the development of the equations, sections are assumed to be free from any residual stress.

4.4.5 Developed stresses

Stresses of an infinitesimal element at a point in a solid body for a general three dimensional rectangular coordinate system x,y,z is defined by a stress tensor having nine components (Timoshenko and Goodier, 1987). Considering the local coordinate system of each plate of an I-section, as depicted in Figure 4.1(a), the tensor can be tabulated in array form as

$$T^\sigma = \begin{bmatrix} \sigma_{nn} & \sigma_{ns} & \sigma_{nz} \\ \sigma_{sn} & \sigma_{ss} & \sigma_{sz} \\ \sigma_{zn} & \sigma_{ns} & \sigma_{zz} \end{bmatrix} \quad 4.6$$

General I-sections normally used in Structural Engineering come under the class based on their spatial character, where all of its three dimensions are of different sizes as compared to each other (Vlasov, 1959). Therefore, most of the stresses out of the nine components have local effects and can be eliminated for forces applied.

Direct stress σ_{ss} in the direction of the middle surface is small as compared to the direct stress σ_{zz} and can be neglected (Gjelsvik, 1981). Considering Kirchoff's assumption for shell theory (see Section 2.1.1), σ_{nn} in the absence of any traction on any face of the flanges and web can also be neglected. Based on the same assumption τ_{sn} can also be neglected. Based on the first assumption (see Section 2.1.1) τ_{zn} can also be neglected. Therefore the only direct stress considered is σ_{zz} which acts in the local z-axis, perpendicular to the cross section. Based on the symmetry condition, it can be written that $\tau_{zn} = \tau_{nz} = \tau_{sn} = \tau_{ns} = 0$. Therefore, the remaining stresses are direct stress σ_{zz} and shear stress τ_{sz} for a plate in a local coordinate system-this is the normal structural engineering simplifying assumptions.

4.4.6 Yield criterion

The yield surface equations are applicable to ductile metals, where for the metals two yield criteria (the Tresca and Von Mises yield criteria) are commonly used (Boresi and Schmidt, 2003). The interaction relationships are developed based on Von Mises yield criterion, where the reasons for its preference are discussed in Section 4.4.7.

A general yield function for a plastic state is

$$f(\sigma_{ij}, \sigma_y) = 0 \quad 4.7$$

In terms of a Cartesian component of stress (which in this case for the local coordinate system, as discussed in Section 4.3), the yield function is written as (Boresi and Schmidt, 2003)

$$f = \frac{1}{2} [(\sigma_{zz} - \sigma_{ss})^2 + (\sigma_{ss} - \sigma_{nn})^2 + (\sigma_{nn} - \sigma_{zz})^2] + 3(\sigma_{zs}^2 + \sigma_{sn}^2 + \sigma_{zn}^2) - \sigma_y^2 = 0 \quad 4.8$$

It was concluded in the previous section that $\sigma_{ss} \approx \sigma_{tt} \approx \sigma_{zt} \approx \sigma_{st} \approx \sigma_{tz} \approx \sigma_{ts} \approx 0$. Based on this for a given section at a fixed distance Z_o in the direction of Z , the above equation reduces to

$$f = \sigma_{zz}(s, n)^2 + 3\sigma_{zs}(s, n)^2 - \sigma_y^2 = 0 \quad 4.9$$

4.4.7 Choice of yield criterion

A state of pure shear exists for a principal stress state. For this stress state yielding occurs when $\sigma_{zs} = \tau_{\max} = \tau_y$ and $\sigma_{zz} = 0$ which reduce the above equation to

$$3\tau_y^2 - \sigma_y^2 = 0 \quad 4.10$$

Therefore,

$$\tau_y = \frac{\sigma_y}{\sqrt{3}} = 0.577\sigma_y \quad 4.11$$

For the same stress state based on the Tresca criterion, τ_y is related to σ_y as

$$\tau_y = \frac{\sigma_y}{2} = 0.5\sigma_y \quad 4.12$$

Therefore, this difference of approximately 15% means that the Von-Mises criterion predicts a greater pure shear yield stress than the Tresca criterion, which indicates that the Tresca criterion is on the conservative side and hence is not preferred (Boresi and Schmidt, 2003). The other reason is that yield surfaces drawn based on Von-Mises yield criterion are continuous and also convex, whereas yield surfaces developed based on Tresca criterion are not continuous.

4.5 EQUILIBRIUM CONDITION, YIELD CRITERION AND STRESS DISTRIBUTION

A relationship between the equilibrium condition, yield criterion and stress distribution has been developed (Mohareb and Ozkan, 2004), in which it was

assumed that the variation of stresses across the thickness of the wall is constant. However, if the neutral-axis is inclined across the thickness (as will be obtained from the study in Section 4.7), then the thickness of wall must be considered in the theoretical development and a variation of stresses across the thickness cannot be avoided. Therefore, it is required to determine the nature of stress distribution of direct stress σ_{zz} and shear stress τ_{sz} which satisfies the equilibrium condition for the entire cross section, in which the variation of the stresses across the wall thickness is considered, in addition to their variation along the contour of the middle surface.

The 3-D equilibrium condition of an infinitesimal element in the absence of body forces (Boresi and Schmidt, 2003) are

$$\frac{\partial \sigma_{zz}}{\partial z} + \frac{\partial \tau_{sz}}{\partial s} + \frac{\partial \tau_{nz}}{\partial n} = 0 \quad 4.13(a)$$

$$\frac{\partial \sigma_{zs}}{\partial z} + \frac{\partial \tau_{ss}}{\partial s} + \frac{\partial \tau_{ns}}{\partial n} = 0 \quad 4.13(b)$$

$$\frac{\partial \sigma_{zn}}{\partial z} + \frac{\partial \tau_{sn}}{\partial s} + \frac{\partial \tau_{nn}}{\partial n} = 0 \quad 4.13(c)$$

From the previous discussion it is assumed that $\sigma_{ss} \approx \sigma_{nn} \approx \sigma_{zn} \approx \sigma_{sn} \approx \sigma_{nz} \approx \sigma_{ns} \approx 0$, which results in the reduction of the above equations to

$$\frac{\partial \tau_{zs}}{\partial z} = 0 \quad 4.14(a)$$

$$\frac{\partial \sigma_{zz}}{\partial z} + \frac{\partial \tau_{sz}}{\partial s} = 0 \quad 4.14(b)$$

The differential of Equation 4.14(a) leads to a zero value which shows that τ_{zs} does not vary with respect to z. Thus, a possibility exists that the integral of the equation

results in a shear stress distribution which can vary across the thickness and along the direction of the contour and can be written as

$$\tau_{zs} = \tau(s, n) \quad 4.15$$

From Equation 4.14(b) it can be deduced that the differential of σ_{zz} is not zero and a possibility exist that σ_{zz} can vary with respect to z . The integration of the equation with respect to z will therefore yield the direct stress which can also vary across the thickness and along the direction of the contour and can be written as

$$\sigma_{zz}(z, t, s) = -z\tau'(s, n) + f_1(s, n) + f_2(s) + f_3(n) \quad 4.16$$

Differentiating the yield criterion given by Equation 4.9 with respect to both s and n , to obtain the gradient in both directions, the following expressions are obtained

$$\sigma_{zz}\sigma'_{zz} + 3\tau_{zs}\tau'_{zs} = 0 \quad 4.17(a)$$

$$\sigma_{zz}\sigma^*_{zz} + 3\tau_{zs}\tau^*_{zs} = 0 \quad 4.17(b)$$

Here the prime denotes differentiation with respect to coordinate s while asterisk in the other equation denotes differentiation with respect to coordinate n . Putting the values of σ_{zz} and τ_{zs} in the above equations leads to an equation which fulfils both the equilibrium condition and yield criterion. Therefore substituting Equation 4.15 and 4.16 into Equation 4.17(a) leads to

$$\left(-z\tau'(s, n) + f_1(s, n) + f_2(s) + f_3(n)\right)\left(-z\tau''(s, n) + f_1'(s, n) + f_2'(s)\right) + 3\tau(s, n)\tau'(s, n) = 0$$

Dependency of the parameters shown in parenthesis are not shown in the next step to decrease the length of the equation. Multiplying this out yields

$$z^2 \tau' \tau'' - (\tau' f_1' + \tau' f_2' + \tau'' f_1 + f_2 \tau'' + f_3 \tau'')z + f_1 f_1' + f_1 f_2' + f_2 f_1' + f_2 f_2' + f_3 f_1' + f_3 f_2' + 3\tau \tau' = 0 \quad 4.18$$

Similarly substituting Equation 4.15 and 4.16 into Equation 4.17(b) leads to

$$\left(-z \tau'(s, n) + f_1(s, n) + f_2(s) + f_3(n)\right) \left(-z \tau^*(s, n) + f_1^*(s, n) + f_3^*(n)\right) + 3\tau(s, n) \tau^*(s, n) = 0$$

Multiplying this out yields

$$z^2 \tau' \tau'^* - (\tau' f_1^* + \tau' f_3^* + \tau'^* f_1 + f_2 \tau'^* + f_3 \tau'^*)z + f_1 f_1^* + f_1 f_3^* + f_2 f_1^* + f_2 f_3^* + f_3 f_1^* + f_3 f_3^* + 3\tau \tau^* = 0 \quad 4.19$$

In order to satisfy Equation 4.18 for an arbitrary value of z , the following conditions must be satisfied:

$$\tau' \tau'' = 0 \text{ and } \tau' f_1' + \tau' f_2' + \tau'' f_1 + f_2 \tau'' + f_3 \tau'' = 0$$

These two conditions are satisfied simultaneously when $\tau' = 0$ is met. Substituting this into Equation 4.17(a), the condition $\sigma_{zz} \sigma_{zz}' = 0$ is recovered which indicates that either $\sigma_{zz}' = 0$ or $\sigma_{zz} = 0$. However, when an axial force, bending moments and bimoment act on the section, $\sigma_{zz} = 0$ is not possible. Hence σ_{zz} is a constant piecewise function. Similarly, in the presence of biaxial shear forces and uniform torsion, τ cannot be equal to zero from which it follows that τ is a constant piecewise function. Therefore, it can be concluded that both τ_{zs} and σ_{zz} must be constant piecewise functions.

There is a possibility that $\tau'' = 0$. For that to occur, both $f_1'(s, t)$ and $f_2'(s) = 0$. Therefore, differentiating Equation 4.16 with respect to s gives

$$\sigma'_{zz}(z, n, s) = -z\tau''(s, n) + f'_1(s, n) + f'_2(s) = 0 \text{ as } \sigma'_{zz} = 0 \text{ from above.}$$

Therefore $\sigma'_{zz}(z, t, s) = 0$ indicates that σ_{zz} can be a function of z and n . By substituting the value of σ'_{zz} in Equation 4.17(a), $\tau_{zm}\tau'_{zm} = 0$ is obtained, which indicates that σ_{zz} and τ_{zm} are also constant piecewise functions.

In order to satisfy Equation 4.19 for an arbitrary value of z , the following conditions must be satisfied.

$$\tau'\tau'^* = 0 \text{ and } \tau'f_1^* + \tau'f_3^* + \tau'^*f_1 + f_2\tau'^* + f_3\tau'^* = 0$$

These two conditions are satisfied simultaneously when $\tau' = 0$ is met. Substituting the value in Equation 4.17(a) indicates that $\sigma_{zz}\sigma'_{zz} = 0$. As $\sigma_{zz} = 0$ is not possible (as discussed above), therefore, it can be concluded that both τ_{zs} and σ_{zz} are piecewise constant functions.

There is a possibility that $\tau'^* = 0$. For that to occur, both $f_1^*(s, n)$ and $f_3^*(n)$ must equal to zero, Therefore, differentiating Equation 4.16 with respect to n gives

$$\sigma^*_{zz}(z, t, s) = -z\tau'^*(s, t) + f_1^*(s, t) + f_3^*(t) = 0$$

Therefore $\sigma^*_{zz}(z, t, s) = 0$ indicates that σ_{zz} can be a function of z and s . By substituting the value of σ^*_{zz} in Equation 4.17(b), $\tau_{zm}\tau^*_{zm} = 0$ is obtained, which indicates that both σ_{zz} and τ_{zm} are constant piecewise function.

From discussions of both Equation 4.18 and 4.19, it is concluded that both direct stress and shear stress have to assume a constant piecewise form when s and n axes are considered.

Therefore, it can be concluded that when variation of stress across the thickness and along the direction of contour is considered, the relationship between the direct

stress and shear stress is such that both the stresses are assumed constant without variation of both the stresses in both the directions.

4.6 SHEAR STRESS AND THE INTERACTION EQUATION

Biaxial shear forces (S_x and S_y), uniform torsion T_u and warping torsion T_w cause shear stress in the cross section. An interaction equation is developed for the shear stress considering S_x , S_y and T_u , while T_w is not considered in the development. Numerical analysis has shown that the effect of T_w is small in the elastic domain and was ignored (Mrazik et al. 1987) in developing interaction equation for B and T_u . Therefore, following the previous approach T_w is not considered in the development.

The pattern of the stress on the cross section due to biaxial shear forces and uniform torsion are different. Biaxial shear forces cause constant stresses across the thickness of the plates of the section, whereas the distribution due to T_u varies across the thickness according to a skew-symmetrical (triangular or combination of rectangular and triangular) diagram, for example as depicted as triangular in Figure 4.4. As a consequence of the different patterns of stress due to the forces, different assumptions are made about the distribution of stress in the development of the interaction equation.

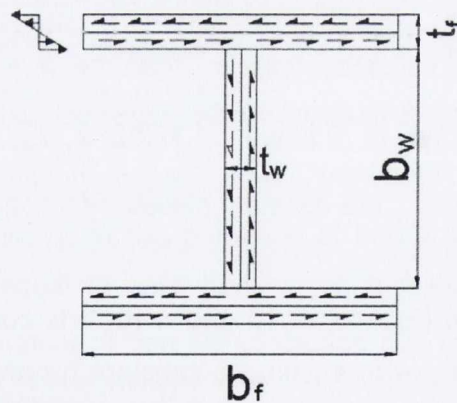


Figure 4.4 Shear Stress distribution due to uniform torsion

As discussed in Section 4.4.5, local stress τ_{nz} on each plate can be ignored. Therefore, shear force, S_x acting on the section is assumed to act on the web ignoring the flanges, and S_y is assumed to act on the flanges ignoring the web for the development. In addition, for the available steel structural I-sections (such as BS EN10056: 1999 sections) the shear stresses developed due to S_x in an elastic domain are extremely large in the web as compared to flanges. For example, a brief study is performed on many BS EN10056: 1999 sections (as given in Table B-1, Appendix-B) to determine the ratio of the stress developed between web and flanges. It is found that in almost every case, the stress in the web is more than ten times higher than the stress in the flanges. A same comparison is made between flange and web when S_y is applied to the section. It can be concluded that, again, most of the ratios are more than ten. It may be concluded that the application of both the shear forces can be assumed as acting on a rectangle, where it is applied to the web and flanges for S_x and S_y , respectively.

In the elastic case, the shear stress distribution has a parabolic distribution. When applied in the XX-direction, the approximate distribution is as depicted in Figure 4.5, which can be assumed as constant over the web because of the small variation as compared to its minimum value.

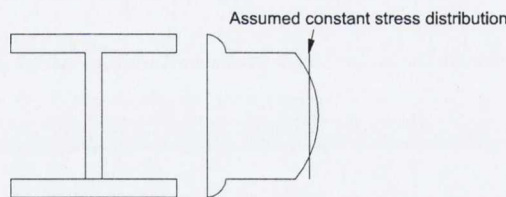


Figure 4.5 Parabolic and assumed constant stress distribution when S_x is applied

Similarly, the shear stress in the YY-direction has a parabolic distribution, where it is zero at the edges of the flanges and maximum at the centroid. Two approaches can be adopted to develop the interaction equation; either a parabolic distribution along the depth of the flange is assumed or a constant distribution along the depth is assumed. Previously both approaches have been adopted (as discussed in Section

2.5.3) to develop the interaction equation. For example, a constant stress distribution for P, M_x and S_x for a rectangular section is assumed by Paltchevskiy (1948) and Sobotka (1975). Comparing the interaction curve as depicted in Figure 4.6 (as discussed in Section 2.5.3) showed that the constant stress distribution curves lie below the complicated solution given by Smirak (1967), hence can be called a lower bound solution. In addition, the distribution of constant shear stress is in agreement with established design procedures (AISC 1999; CSA 2001). To circumvent the complications involved for an exact approach, following the references and the design procedure, a constant distribution of shear stress is assumed when shear forces S_x and S_y are applied.

Therefore S_x acts on the web only, and its plastic capacity in that direction will be $S_{xp} = A_w \tau_y$ and from Equation 4.10 it can be written as $S_{xp} = A_w \sigma_y / \sqrt{3}$. Similarly, S_y acts on the flanges, and its plastic capacity in that direction will be $S_{yp} = 2A_f \tau_y$ and from Equation 4.10 it can be written as $S_{yp} = 2A_f \sigma_y / \sqrt{3}$.

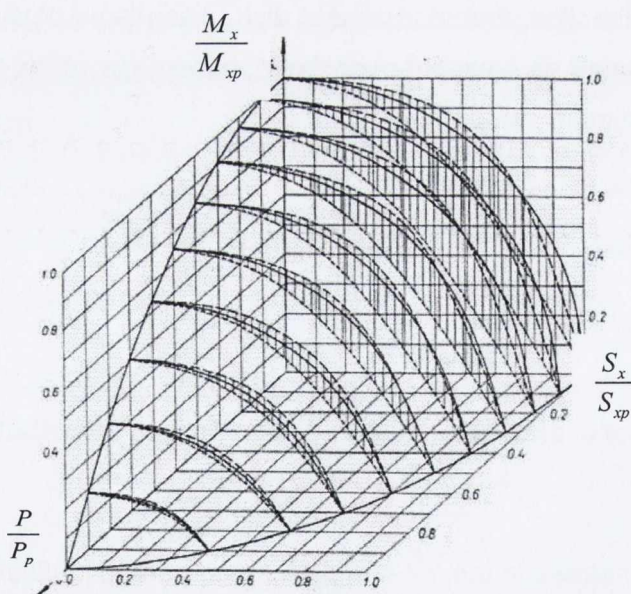


Figure 4.6 P, M_x and S_x curve (Mrazik et al. 1987) for the solution given by Paltchevskiy (1948)-dotted curves, Sobotka (1975)-full curves and Smirak (1967)-dashed curves

4.6.1 Developed Interaction Equation

The resulting neutral-axis patterns when constant shear stresses (as discussed above) due to S_x , S_y and variable shear stresses due to T_u (as depicted in Figure 4.4) are jointly considered are depicted in Figure 4.7. In the figure ζ_f is the distance from the contour line of both flanges to the neutral-axis, while ζ_w is the distance from the contour line of the web to the neutral-axis.

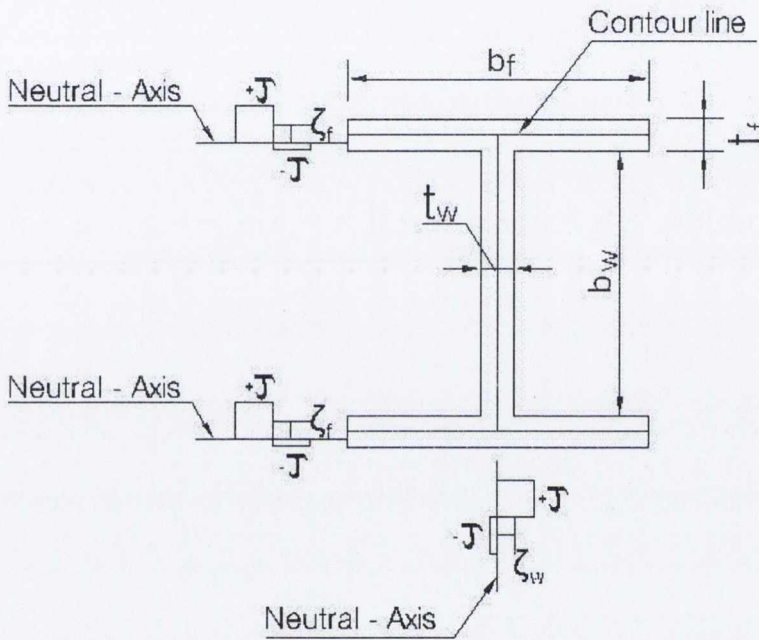


Figure 4.7 Neutral-Axis pattern for the case when S_x , S_y and T_u act on the section

Based on the neutral-axis pattern depicted in the figure both S_x , S_y are obtained as (details are given in Section B.2, Appendix-B).

$$S_x = 4\zeta_f t b_f \tag{4.20}$$

$$S_y = 2\zeta_w t b_w \tag{4.21}$$

Similarly, the distribution of uniform torsion for the section is obtained for the top flange, bottom flange and web as (details are given in Section B.2, Appendix-B).

$$T_u = T_{topflange} + T_{botflange} + T_{web} \quad 4.22(a)$$

$$T_{topflange} = (0.25A_f t_f + b_f b_w \zeta_f + A_f \zeta_f - \zeta_f^2 b_f) \tau \quad 4.22(b)$$

$$T_{botflange} = (0.25A_f t_f - b_f b_w \zeta_f - A_f \zeta_f - \zeta_f^2 b_f) \tau \quad 4.22(c)$$

$$T_{web} = (0.25A_w t_w - \zeta_w^2 b_w) \tau \quad 4.22(d)$$

Adding the terms result in the torsion for the entire section as

$$T_u = [(0.5A_f t_f - 2\zeta_f^2 b_f + 0.25A_w t_w - \zeta_w^2 b_w)] \tau \quad 4.23$$

Eliminating the parameters, ζ_w and ζ_f from Equation 4.20, 4.21 and 4.23, the expression for the relationship between shear stress and the three shear forces

$$(4A_f^2 b_w + 2A_w^2 b_f) \tau^2 - 8T_u b_f b_w \tau - b_w S_x^2 - 2b_f S_y^2 = 0 \quad 4.24$$

is obtained. The above equation is quadratic in nature, and shear stress can be obtained from it.

4.7 KINEMATICS AND PLASTIC NEUTRAL-AXIS PATTERNS

It has been discussed in Section 4.4.2 that a diagram can be obtained of the longitudinal strain on a cross section at a fixed distance along the beam-axis by combining all the four diagrams obtained by the four terms of Equation 4.4. The diagram thus obtained gives the strain field, having regions of positive and negative strains, separated by a neutral-axis.

A procedure is developed to add all the four diagrams, by assuming different values of the strains for the diagrams. For example for an I-section, if a strain field diagram is obtained by combining the first three diagrams (see Figure 4.3), ignoring warping of the section, and assuming the thicknesses of the plates as negligible as compared to their width, then there are five possibilities by which a neutral-axis may pass through the section, as depicted in Figure 4.8. The obtained diagram follows the Bernoulli-Navier hypothesis (Vlasov, 1959), having one radius of curvature for the entire section about the neutral-axis. These possibilities are

- Neutral-axis passes through one flange.
- Neutral-axis passes through one flange and web.
- Neutral-axis passes through both flanges.
- Neutral-axis passes through both flanges and web.
- Neutral-axis passes through web.

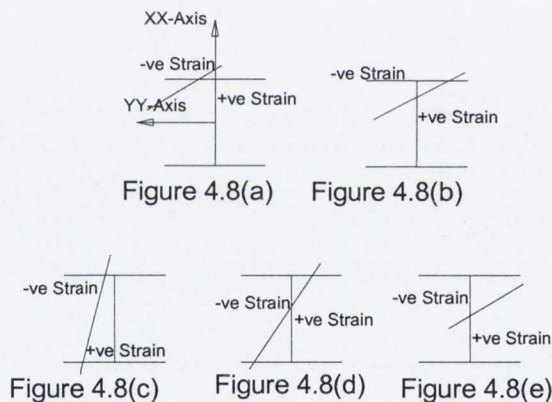


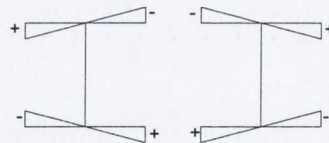
Figure 4.8 Five possibilities of different neutral-axis patterns for an I-section when strains due to P , M_x and M_y are considered

Following the coordinate system given by Figure 4.1, the sign convention of the strain field given by Figure 4.8 is such that P is positive. The Y component of radius of curvature is in the positive YY direction, therefore M_y is positive. The X component of radius of curvature is in the negative XX direction, therefore M_x is negative. If warping is considered for the section, having a pole at the centroid, the positive and negative warping strain diagrams are obtained as depicted in Figure 4.9.

To obtain different patterns which include strains due to P , M_x , M_y and the warping strains, the strain field of Figure 4.8 and Figure 4.9 are added to obtain different patterns (details are given in Appendix-B). Different values of the warping strain are assumed, based on a maximum unit value of the strain field diagram of Figure 4.8. Hence large and small values of the warping strain are assumed as compared to the maximum unit value.

Of the five patterns considered in Figure 4.8 three patterns intersect the web while the remaining two do not. Firstly those patterns in which the neutral-axis intersects the web are considered in conjunction with positive and negative warping strains.

A study is thus performed to determine different patterns based on various combinations of Figures 4.8 and Figure 4.9. In the study, fifteen neutral-axis patterns as depicted in Figure 4.10 of same type, as determined by Figure 4.8 are considered. The fifteen patterns are selected such that the neutral-axis passes through different possible positions of the section. For example it passes through the left edge of both flanges (Pattern 10-10), it passes near the centroid of web (Pattern 6-6), it passes through the bottom of top flange and top of web (Pattern 8-8), etc. A summary of the results of the study is given below while details are given in Appendix-B.



(a) Negative bimoment (b) Positive bimoment

Figure 4.9 Warping strains as a result of bimoment applied in positive and negative directions based on the assumed coordinate system (see Figure 4.1)

4.7.1 Development of Different Neutral-Axis patterns

Out of the fifteen patterns, a few extreme patterns are considered, while the remaining patterns are not discussed as they conclude same results to the others.

Cases when the neutral-axis intersects the web are discussed first followed by the cases when it does not intersecting the web.

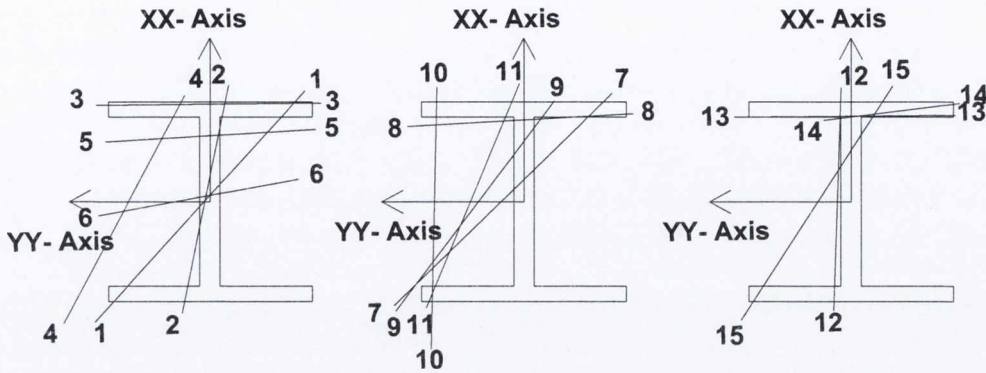


Figure 4.10 Fifteen patterns describing the positions of the neutral-axis when P , M_x , and M_y are applied (divided into three figures for illustration only)

Neutral-axis patterns intersecting the web

Warping strain applied in the negative sense

A procedure is adopted to obtain different patterns which include warping strain.

Two extreme cases in Figure 4.8(d) are possible, as depicted in Figure 4.11. Considering the cases, strains due to negative warping strain, given by Figure 4.9(a), are added to obtain the required patterns. Different values of maximum warping strains are assumed for the figure, keeping constant values of the strain field of Figure 4.11. For example if a maximum strain of one unit is assumed for a pattern (without any warping strain), as depicted for extreme case 1-1 (in Figure 4.11) in Figure 4.12, the values of strains at other points of the cross section can be obtained based on the position of the neutral-axis with reference to the coordinate system and trigonometric relationships (see Appendix-B for details).

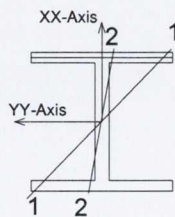


Figure 4.11 Two extreme positions of the neutral-axis of Figure 4.8(d)

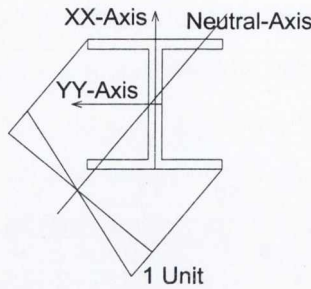
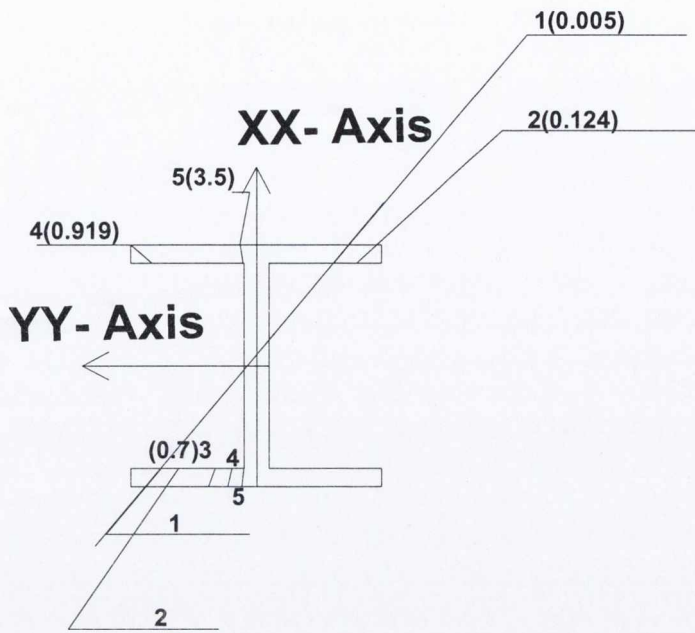


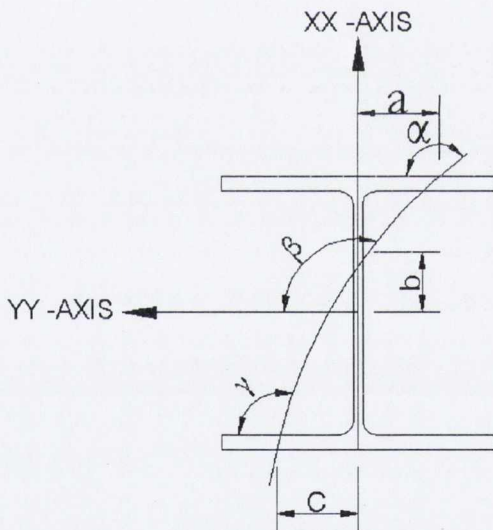
Figure 4.12 Strain pattern, when P , M_x , and M_y only are considered

The assumed values of the warping strain are now added to the strain pattern of Figure 4.12. Five different values (selected randomly in the range of 0.005 to 3.5) of the warping strains have been used to obtain the patterns. The obtained strain patterns are depicted in Figure 4.13(a), which are shown as numbers in the figure, where the values of the warping strain are given in parenthesis for each obtained pattern. Numbers are shown for both the top and bottom flanges, values for the web are as in Figure 4.11 and do not change. For example number 1 for the top and bottom flanges is the neutral-axis pattern obtained when Figure 4.12 is added to Figure 4.9(a) having a maximum warping strain of 0.005 (Details given in Appendix-B, Section B.3). Other cases given by Figure 4.8(b & e) are also studied and are discussed in the Appendix.

From the study of the extreme cases of Figure 4.8(b, d and e), it is found that the movement of the neutral-axis on addition of the warping strain for the bottom flange is always towards the right of the flange (1-5 in Figure 4.13(a)), while for the top flange the neutral-axis moves towards the right (1-2), then out of the flange and shifts to the left of the flange on further addition of the strain (4-5) (see Appendix-B, Section B.3). The position of angles α , β and γ with respect to YY-axis and a, b & c intercept are given in Figure 4.13(c). Based on the movement of the neutral-axis for the top flange, the author has suggested two different patterns, while the phase when it was out of the top flange is considered as a transition phase. The obtained patterns and the parameters defining the position of the neutral-axis are depicted in Figure 4.14.

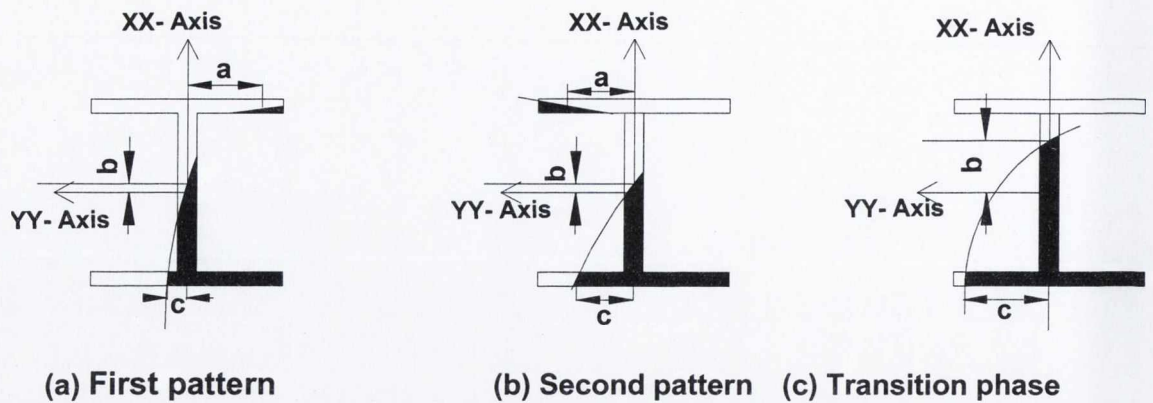


(a) Obtained patterns by adding Figure 4.9(a) and Figure 4.12



(b) Angles and intercept showing the position of neutral-axis

Figure 4.13 Obtained patterns by adding Figure 4.9(a) and Figure 4.12 and position of neutral-axis



(a) First pattern (b) Second pattern (c) Transition phase
Figure 4.14 Patterns concluded based on the study in which Figures 4.8(b, d and e) are used with the warping strain (with bimoment applied in the negative direction)

First pattern

The first pattern is that in which the neutral-axis is on the right of the top flange and on the left of the bottom flange, as depicted in Figure 4.14(a). In the figure the position of the neutral-axis is defined by six parameters, which are $\alpha, \beta, \gamma, a, b$ and c , where α, β, γ are the slopes measured with reference to the point of intersection of the contour line and neutral-axis in each plate and YY-axis. The relationships between the parameters are given in the form of equations. For example, if β is assumed to be the angle of the entire section before adding the warping strain, then after the addition, angle β for the top flange will rotate clockwise relative to the positive YY-axis, and the new angle is represented by α . For the bottom flange, it will rotate counter clockwise relative to the positive YY-axis and the new angle is represented by γ . a, b and c are the positions of the neutral-axis as defined in the figure. Relationships between the parameters are given in the form of equations (details are given in Appendix-B Section B.3).

It is found that there is a relationship between α and γ such that

$$\alpha + \gamma = 2\beta \tag{4.25(a)}$$

It is also found that the change in the absolute values of α and γ must be the same whereas the angle will be different for both the flanges (as discussed in Appendix-B). This will be valid throughout the study for all the obtained patterns. Therefore,

$$|\Delta\alpha| = |\Delta\gamma| \quad 4.25(b)$$

A relationship for γ is obtained as

$$90^\circ \leq \gamma \leq 180^\circ - \tan^{-1}\left(\frac{b_w}{b_f}\right) \quad 4.25(c)$$

and the relationship for α is obtained as

$$90^\circ \leq \tan^{-1}(\alpha) \leq 180^\circ \quad 4.25(d)$$

Second Pattern

The second pattern is that in which the neutral-axis for both the flanges are on the left hand side of the section, as depicted in Figure 4.14(b). The following relationships between the parameters for this pattern are (see Section B.3):

$$0^\circ \leq \tan^{-1}(\alpha) \leq 90^\circ \quad 4.26$$

In this case Equation 4.25(d) is not applicable, while Equations 4.25(a, b, and c) will be.

Transition phase

For the transition phase the neutral-axis is outside the top flange and on the left of the bottom flange as depicted in Figure 4.14(c). This phase is the intermediate phase from pattern-1 to pattern-2. Therefore, the pattern given by this phase is considered as a special case of both the first and second pattern with a value of greater than $0.5*b_f$ for a .

Special cases

It is concluded in the previous discussion that the neutral-axis for the top flange first moves towards the right of the positive XX-axis then shifts left of the axis. There are two cases when movement of the neutral-axis is different from the above discussed movement and these are now considered separately.

If the original position of the neutral-axis without the addition of warping strain is as depicted in Figure 4.15(a), where the position of the neutral-axis for the top flange is on the left of the XX-axis of the flange. Warping strain due to negative bimoment has strain distribution in the top flange in such a way that it has positive strain on the left of the top flange and negative strain at its right. Therefore the addition of warping strain due to negative bimoment always causes the neutral-axis for the top flange to shift towards the left of the axis and results in a pattern as depicted in Figure 4.15(b) (Details of the procedure of obtaining the patterns are given in Appendix-B). Further addition of the warping strain shifts the neutral-axis for the top flange to the right of the axis (and it continues to move towards the left on addition of the warping strain) which results in the pattern as depicted in Figure 4.15(c) with the transition phase between them (not shown in the figure) of the same type as obtained before. The procedure to obtain the pattern is the same as obtained in the previous cases. All relationships as given by Equation 4.25 remain valid for the patterns of Figure 4.15(b) whereas all relationships except Equation 4.25(d) remain valid for the pattern of Figure 4.15(c) where, instead of 4.25(d), Equation 4.26 is valid.

In case two, the initial position of the neutral-axis without the addition of warping strain is depicted in Figure 4.16(a), where the position of the neutral-axis for the top surface (for detail of lines see Figure B.1 Appendix-B) of the top flange is on the right of the positive XX-axis, while it is on the left of the axis for the bottom fibre of the top flange, as depicted in the figure. The addition of warping strain due to negative bimoment causes the point of the neutral-axis of the top line to move towards the right of the flange and the point of neutral-axis for the bottom line moves towards the left of the top flange, hence resulting in a pattern as given by Figure 4.16(b). Further addition of the strain shifts the neutral-axis point on the top line towards left while

shifting of the point on the bottom line is towards right of the XX-axis, as depicted in Figure 4.16(c). No transition phase is obtained in this case as the shifting of neutral-axis pattern is directly from the pattern given by Figure 4.16(b) to Figure 4.16(c). All relationships as given by Equation 4.25 remain valid for the pattern of Figure 4.16(b) whereas all relationships except Equation 4.25(d) remains valid for the pattern of Figure 4.16(c) where, instead of 4.25(d), Equation 4.26 is valid.

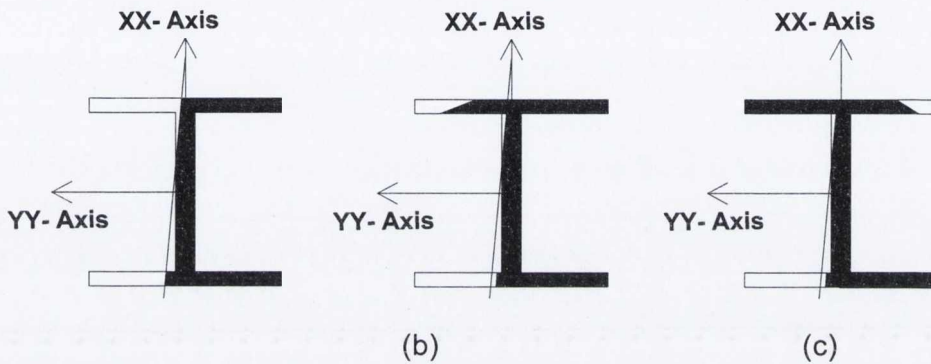


Figure 4.15 Original and obtained neutral-axis pattern of special case (First case)

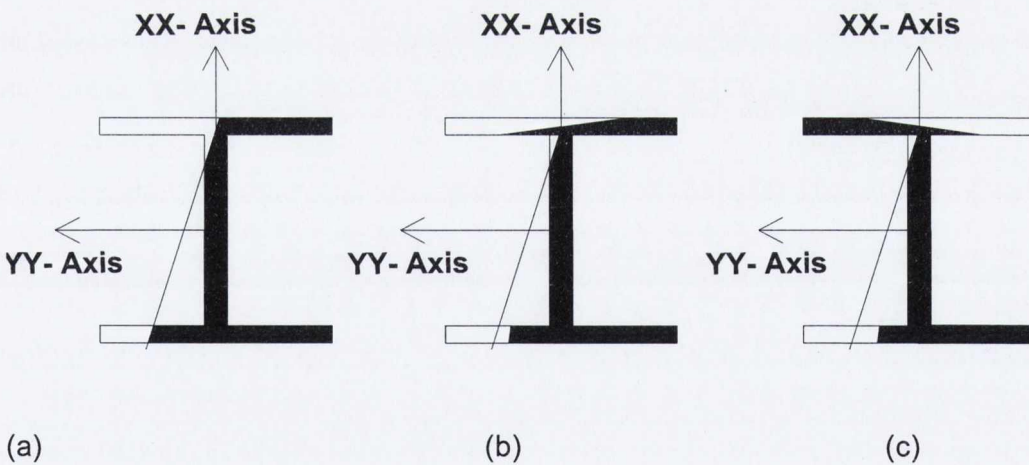


Figure 4.16 Original and obtained neutral-axis pattern of special case (Second case)

It can be concluded from the above study that the first pattern is as given by Figures 4.14a, 4.15b and 4.16b. The similarity between all the three figures is that the

direction of bending is the same in all three cases i.e. sagging moment cause positive strains below the neutral-axis in which Equation 4.25 is valid.

Figure 4.14b, 4.15c and 4.16c represent the second pattern. Similarities exist for the three figures for the top flange as discussed for the first pattern in which Equations 4.25(a, b and c) and 4.26 are still valid.

Warping strain when bimoment is applied in the positive direction

The movement of the neutral-axis is opposite to the previous case when warping strains due to positive bimoment is applied. The neutral-axis for the top flange is always to the right of the positive XX-axis, while for the bottom flange the neutral-axis shifts from the left of the XX-axis to the right of the axis, having a transition phase between them. Two neutral-axis patterns are suggested based on the movement of the neutral-axis of the bottom flange, as follows:

First Pattern

In this case, the neutral-axis is on the right of the top flange and the angle for the top flange decreases, whereas for the bottom flange the angle increases and it is on the left of the flange (see details in Section B.3). Only Figure 4.8(d) is involved in obtaining this pattern, whereas Figures 4.8(b and e) do not give this pattern on addition of the warping strain. The pattern is depicted in Figure 4.17(a) having the parameters $\alpha, \beta, \gamma, a, b$ and c which define the position of the neutral-axis. It is found from the study that angle α must fulfill the relationship

$$90^\circ \leq \tan^{-1}(\alpha) \leq 180^\circ - \tan^{-1}(b_w / b_f) \quad 4.27(a)$$

For the bottom flange angle, γ , the following relationship can be written

$$90^\circ \leq \tan^{-1}(\gamma) \leq 180^\circ - \tan^{-1}(b_w / b_f) \quad 4.27(b)$$

The relationships given by Equations 4.25(a) and (b) are still valid for this case.

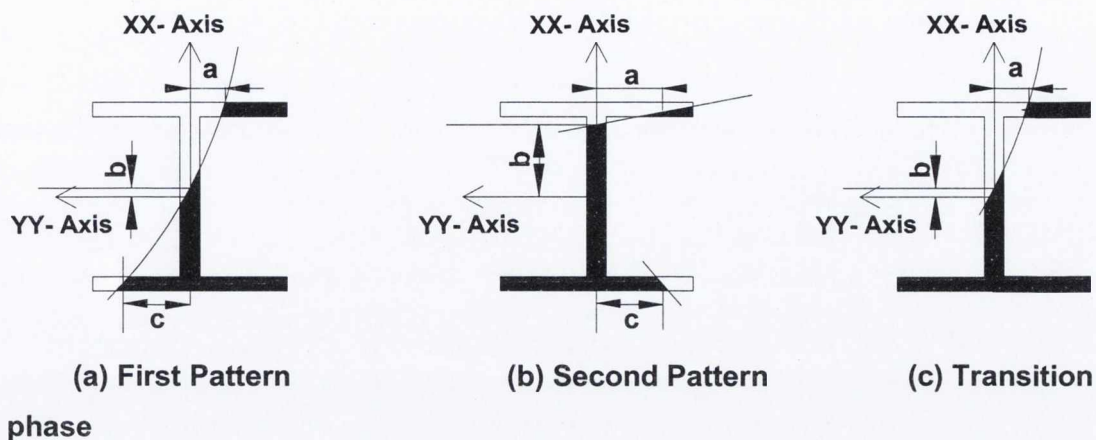


Figure 4.17 Patterns concluded based on the study in which Figures 4.8(b, d and e) are used with the warping strain of Figure 4.9(b) (bimoment applied in a positive direction)

Second Pattern

The second pattern is that in which the neutral-axis for both the flanges are on the right hand side of the section, as depicted in Figure 4.17(b) (see Section B.3). It is found from the study that angle α must fulfill the relationship

$$90^\circ \leq \tan^{-1}(\alpha) \leq 180^\circ \quad 4.28(a)$$

For the bottom flange angle γ , the following relationship can be written

$$\tan^{-1}(b_w / b_f) < \tan^{-1}(\gamma) < 90^\circ \quad 4.28(b)$$

The relationships given by Equations 4.25(a and b) are still valid for this case.

A same transition phase is also obtained for this case, where the neutral-axis is out of the bottom flange, as depicted in Figure 4.17(c). To obtain the pattern for this phase, a value greater than $0.5 \cdot b_f$ for c is assumed in the first and second pattern.

Special cases

Considering the special cases given by Figure 4.15(a) and Figure 4.16(a), as previously. when positive bimoment is applied, the shifting of the neutral-axis is on the bottom flange in this case Therefore the movement of the neutral-axis for the top flange will not shift side of the XX-axis.

In the first case, the movement is on the right side of the top flange on the addition of warping strain, while the nature of movement of the bottom flange remains the same as that which occurred in the first and second pattern as discussed in the above section. Hence, this resulted in same first and second pattern and a transition phase. Equations 4.27, 4.28, 4.25(a) and (b) are all valid.

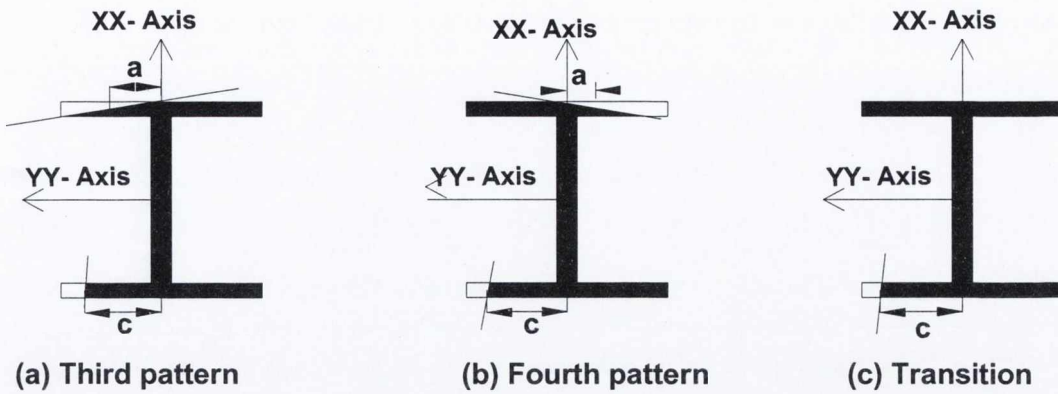
In the second case, the position of the neutral-axis for the top fibre of the top flange will move towards the left of its initial position whereas the bottom fibre of the top flange moves towards the right of its initial position on the addition of the warping strain. Hence the position of the neutral-axis remains the same for the top flange. However because of the same nature of movement for the bottom flange, this results in the first and second pattern and a transition phase same to that given by Figure 4.17. Equations 4.27, 4.28, 4.25(a) and (b) are all valid.

Neutral-axis patterns not intersecting the web

Warping strain when bimoment is applied in the negative direction

Following the same procedure adopted for the cases when the neutral-axis passes through the web, movements of the neutral-axis are obtained for the case when the neutral-axis does not pass through the web.

Neutral-axis patterns of the type given by Figures 4.8(a) and (c) are added to Figure 4.9(a) to obtain different patterns. In the case of the bottom flange, the neutral-axis will always be on the left of the flange on addition of the warping strain, whereas for the top flange the neutral axis shifts from one side of the flange to other (details are given in Appendix-B, Section B.3). Based on the movement of the top flange, two neutral-axis patterns and a transition phase are suggested. The obtained patterns are depicted in Figure 4.18 and are discussed as follows:



phase

Figure 4.18 Patterns concluded based on the study in which Figures 4.8(a) and (c) are used with the warping strain (bimoment applied in the negative direction)

Third pattern

In this pattern the positive strain is towards the right of the flange below the neutral-axis. The neutral-axis for the bottom flange is to the left of XX-axis as depicted in the figure. Equation 4.28(a) is still valid for this pattern whereas the relationship for γ valid for this pattern is:

$$90^\circ \leq \tan^{-1}(\gamma) \leq 180^\circ - \tan^{-1}\left(\frac{b_w}{0.5b_f}\right) \quad 4.29$$

Equations 4.25(a) and (b) are also valid for this pattern.

Fourth pattern

In this pattern, the positive strain is towards the left of the flange below the neutral-axis. The neutral-axis for the bottom flange is to the left of XX-axis as depicted in Figure 4.18(b). Equations 4.26, 4.29, 4.25(a) and (b) are valid for this pattern.

Transition phase

For this pattern the neutral-axis is on the left of the bottom flange and outside the top flange as depicted in Figure 4.18(c). By substituting a value greater than $0.5b_f$ for a for both the above patterns, this phase can be obtained as a special case.

Warping strain when bimoment is applied in the positive direction

Following the same procedure adopted in the previous cases, the movement of the neutral-axis is obtained for this case. Shifting of the neutral-axis is for the bottom flange as compared to the top flange in the previous case. Neutral-axis patterns of the type given by Figures 4.8(a) and (c) are added to Figure 4.9(b) to obtain different patterns.

In the case of the top flange, the neutral-axis will always be on the left of the positive XX axis, whereas in the case of the bottom flange, there is a shifting of the neutral axis from one side of the flange to the other (see Appendix-B, Section B.3). Based on the movement of the bottom flange, two neutral-axis patterns and a transition phase are suggested. The obtained patterns are depicted in Figure 4.19.

Third pattern

For this pattern, the neutral-axis is on the left of the top and bottom flanges, as depicted in Figure 4.19(a). This pattern is different from the third pattern in the previous case, when warping was applied in the negative direction. The reason is that the addition of any value of the positive warping strain to Figure 4.8(a) does not result in this pattern, whereas in the previous case both Figures 4.8(a) and (c) were involved in obtaining the pattern.

For the top flange, the angle will always decrease, whereas the angle for the bottom flange always increases if measured relative to the positive YY-direction. The relationships between the parameters for this pattern are

$$90^\circ \leq \tan^{-1}(\alpha, \gamma) \leq 180^\circ - \tan^{-1}\left(\frac{b_w}{0.5b_f}\right) \quad 4.30$$

Equations 4.25(a) and (b) are also valid for this pattern.

Fourth pattern

For this pattern the neutral-axis is on the right of the bottom flange and the neutral-axis for the top flange is such that it will create positive strain on the right below the

neutral-axis, as depicted in Figure 4.19(b). The relationships between the parameters for this pattern are

$$90^\circ \leq \tan^{-1}(\alpha) \leq 180^\circ, \quad \tan^{-1}\left(\frac{b_w}{0.5b_f}\right) \leq \tan^{-1}(\gamma) \leq 90^\circ \quad 4.31$$

Equations 4.25(a) and (b) are also valid for this pattern.

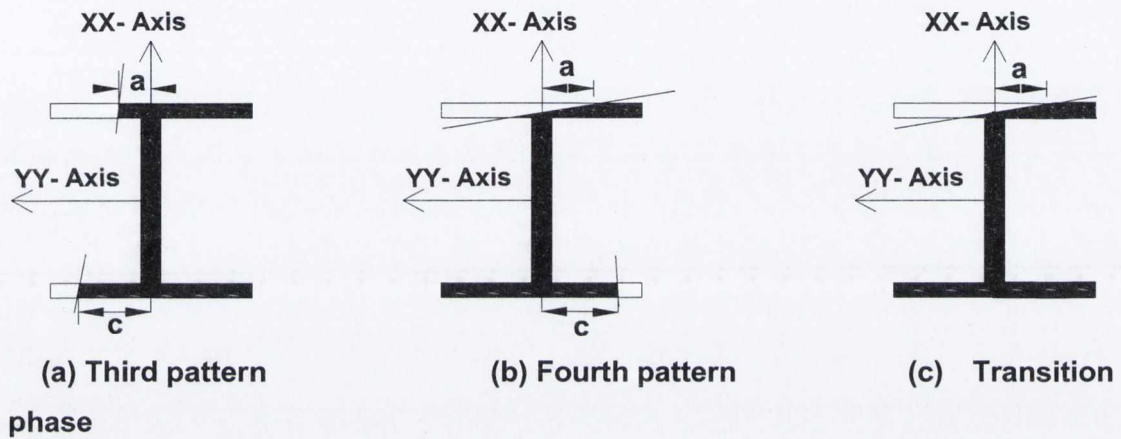


Figure 4.19 Patterns concluded based on the study in which Figures 4.8(a) and (c) are used with the warping strain of Figure 4.9(b) (bimoment applied in the positive direction)

Transition phase

For this phase the neutral-axis will be on the left of the top flange and outside the bottom flange as depicted in Figure 4.19(c). By substituting a value greater than $0.5 \cdot b_f$ for c for both the above patterns, this pattern can be obtained as a special case of the above patterns.

Based on the study of Figure 4.8, four neutral-axis patterns evolved for both the positive and negative warping strains as discussed above. Parameters defining the new position of the neutral-axis for the obtained strain field are obtained.

4.7.2 The finalised patterns

In the previous study it was found that the neutral-axes of the obtained patterns are not perpendicular to the longitudinal axis of each plate of the section. To develop interaction relationships for different patterns, it is extremely difficult to consider an inclined neutral-axis for all the plates. Therefore, it was not possible to consider the obtained patterns directly to develop the relationships. Hence, assumptions are made for the position of neutral-axis on each plate to develop yield surfaces and interaction equations.

Warping applied in the positive direction

First Pattern

Assumptions are made to the first pattern and its special cases obtained previously to finalise the neutral-axis pattern for this case. For the top flange and the bottom flange an inclined neutral-axis is replaced by a perpendicular axis.

The reason for adopting a perpendicular neutral-axis for the top flange is that the maximum angle for this pattern is given by Equation 4.27(a), which is a steep angle. In addition, there is a further decrease of angle on addition of the warping strain. Therefore, it will not significantly effect the result when the inclined neutral-axis is replaced by a perpendicular neutral-axis at the same location on the flange.

For the bottom flange, there is an increase in the angle, during the movement of the neutral-axis towards the left of the flange. However, it is found (Appendix-B, Section B.3) that the maximum angle up to the point when the axis is inside the flange (during its movement towards the left) is always less than the maximum angle given by Equation 4.27(b). Therefore the inclined neutral-axis can be replaced by a perpendicular neutral-axis for the same reason as discussed above. The finalised pattern is depicted in Figure 4.20(a).

Second Pattern

Assumptions are made regarding the second pattern and its special cases obtained previously to finalise the neutral-axis pattern for this case. In the case of bottom flange the neutral-axis is on the right of the flange. The limit on the angle for this

pattern is given by Equation 4.28(b) and will not change the result when an inclined neutral-axis is replaced by a perpendicular neutral-axis.

For the top flange an inclined neutral-axis is considered. because the maximum angle for this pattern is 180° as given by Equation 4.28(a), and cannot be reasonably replaced by a perpendicular neutral-axis.

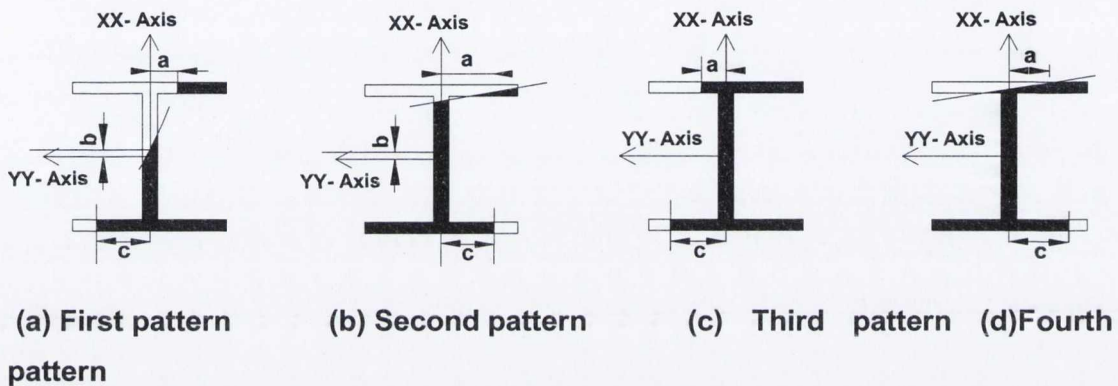


Figure 4.20 Finalised patterns when bimoment applied in the positive direction

Third pattern

Assumptions are made to the third pattern obtained previously to determine the position of the neutral-axis for this pattern. The maximum angle of both the flanges for this pattern is given by Equation 4.30 and can be replaced by a perpendicular neutral-axis because it will not make much difference to the results. The finalised pattern is depicted in figure 4.20(c).

Fourth pattern

Assumptions are made to the fourth pattern obtained previously to determine the position of the neutral-axis for this pattern. This pattern is obtained by combining Figures 4.8(a) and (c), where the slope of Figure 4.8(a) is such that it sometimes makes an angle approaching 180° . Therefore avoiding an angular neutral-axis pattern for the top flange can result in a gross error. For the bottom flange the angle given by Equation 4.31 can be replaced by a perpendicular neutral-axis because an inclined neutral-axis due to a small angle will not make much difference.

Warping applied in the negative direction

First pattern

The first pattern obtained previously and the first pattern obtained for both the special cases as depicted in Figures 4.15(b) and 4.16(b) have positive strains to the right and below the neutral-axis, therefore the first pattern and two special cases can be summarized as first pattern. Assumptions are made to the first pattern to finalise the position of the neutral-axis. Considering the neutral-axis for the bottom flange, the maximum angle obtained was always less than that given by Equation 4.25(c). Therefore, an inclined neutral-axis is replaced by a perpendicular neutral-axis for the same reason as discussed above.

For the top flange, an inclined neutral-axis is inevitable and Equation 4.25(d) remains valid. The inclined neutral-axis for this case cannot be replaced by a perpendicular neutral-axis, especially for wide flange sections and those sections which have relatively greater thickness of flange can lead to a gross error. The finalised pattern is depicted in Figure 4.21(a).

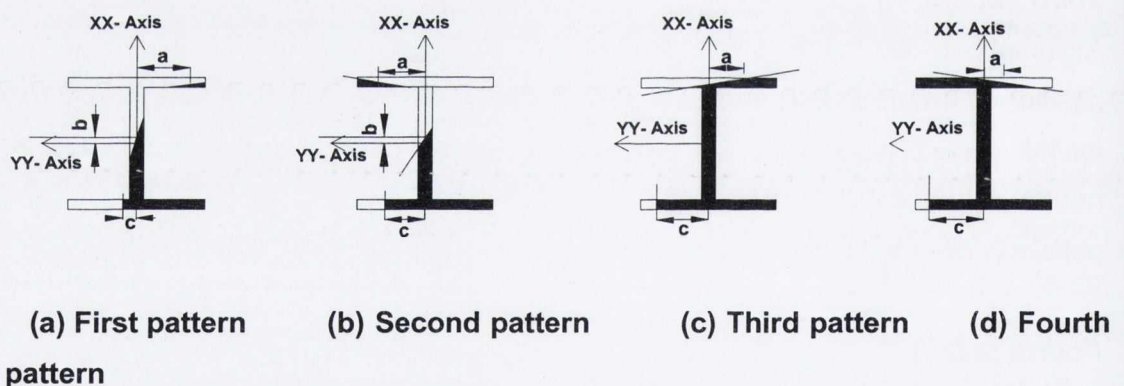


Figure 4.21 Finalised pattern when warping is applied in the negative direction

Second pattern

The second pattern obtained previously and the second pattern obtained for both the special cases as depicted in Figures 4.15(c) and 4.16(c) have positive strains to the left and below the neutral-axis, therefore all the three patterns can be summarized as

the second pattern. A perpendicular neutral-axis for the bottom flange and an inclined neutral-axis for the top flange are suggested for this pattern, for the same reasons as discussed above for the previous pattern. The pattern is depicted in Figure 4.21(b).

Third pattern

A perpendicular neutral-axis pattern for the bottom flange and an inclined neutral-axis for the top flange are assumed for the same reasons as was assumed for the previous two patterns. Equation 4.28(a) remains valid for this pattern. The finalised pattern is depicted in Figure 4.21(c).

Fourth pattern

An inclined neutral-axis for the top flange and perpendicular neutral-axis for the bottom flange are assumed for the same reasons discussed above. The finalised pattern is depicted in Figure 4.21(d).

4.7.3 Kinematic limit of field for patterns when the neutral-axis does not intersect the web

When the neutral-axis pattern does not intersect the web, a kinematic limit, which is not described by the equations previously is essential for these types of patterns. The reason they are called kinematic limits by the author is because these patterns are not possible on study (as performed in Section 4.7.1) based on the assumption of kinematics as given in Section 4.4.2. Considering Figure 4.22(a), the neutral-axis pass through the left of XX axis for the bottom fibre of top flange and is not valid because the neutral-axis must pass to the right of XX-axis when intersecting the bottom fibre of the top flange, therefore any pattern given by Figure 4.22(a) is not a valid pattern. Considering Figure 4.22(b), the neutral-axis passes through the right of XX axis for the bottom fibre of top flange and is not valid because the neutral-axis must pass to the left of XX-axis when intersecting the bottom fibre of the top flange, therefore any pattern given by Figure 4.22(b) is not a valid pattern. The feature with this pattern is that discontinuity of stress occurs at two points; firstly at the neutral-axis and secondly at the junction of top flange and web.

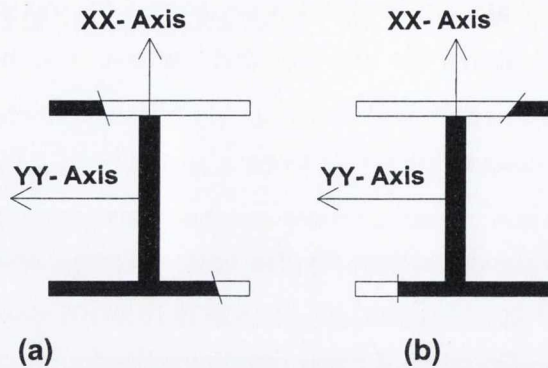


Figure 4.22 Patterns which are not possible when Kinematic assumption of Section 4.4.2 are used to obtain the patterns

4.7.4 Different quadrants and finalised patterns

In the previous sections, two types of patterns are finalised, one each for both the negative and positive bimoment. It is required to determine what other types of patterns can be obtained when other sign combinations of strain vector related to the remaining fourteen quadrants (sixteen quadrants in total relate to the four forces) are used, for example, when the sign of all the strain vectors considered are positive or all are negative. Other types of patterns can be obtained for other sign combinations using the same procedure as given in Section 4.7.1. However it is found in the current research that only two types of pattern as obtained previously are possible for any combination of sign of strains used and the two types are based on the product of signs of the strains. For example in the study in Section 4.7.1 the strain field related to P and M_y were positive, while the strain field due to M_x was negative. If the negative warping strains are considered, the product of the sign of all four strains is $+1$. From a study same to Section 4.7.1, it is found that, if the product of the signs of all four strains are considered positive then it will give the same type of pattern as obtained previously by addition of negative warping strain. Similarly another type of pattern is when the product of signs is -1 . It may be concluded that there are two types of pattern, irrespective of which quadrant is considered, one is when the product of the signs is $+1$ and the other when the product of signs is -1 .

As there are sixteen quadrants when four strain vectors are considered, therefore there are eight possibilities when the product of signs of all four strains are +1, and eight possibilities when the product of signs of all four strains are -1. Therefore, it can be said that one type of finalized pattern (Figure 4.21) can be obtained by using eight different combination of signs of four strains (having their products in all eight cases to +1). Similarly eight other sign combinations when the product of the four strains is -1 give only one type of finalised pattern (Figure 4.20).

4.7.5 Sign of internal forces and finalised patterns

Using the two types of finalised patterns (Figures 4.20 and 4.21), internal forces can be calculated. It is possible that any one or more signs of the internal forces calculated can be different from the signs of their strain vector. For example a constant tensile strain acting on the entire cross-section is added to the remaining three strain vector which are caused by bending in two different directions and warping of the section (using the procedure given in Section 4.7.1) to obtain a particular neutral-axis pattern. For that particular neutral-axis pattern it is possible that a compressive axial force is obtained when internal force P is calculated. This change of sign is also discussed in Section 2.2 as referred by Gjelsvik (1981). This change in signs of the forces compared to the strain vector was investigated to obtain any possible relationship between the finalised patterns and internal forces. For this a code in MATLAB was written which performed three functions; firstly it obtained different patterns (based on the procedure adopted in Section 4.7.1) for different values of warping strain; Secondly it calculated the forces based on the obtained patterns and thirdly it compared the sign of the forces with the sign of their strain vector. Patterns are obtained for both the positive and negative warping strain. As a case study, fifteen patterns same to those given by Figure 4.10 are investigated for which internal forces and their signs are calculated. Findings of the results obtained from the code are discussed below.

The above discussions lead to the conclusion that when the product of strain vectors is +1, a sign change can occur when internal forces are calculated, while when the product is -1, no change in sign occurs when internal forces are calculated.

Use of Findings

These findings are helpful in the development of yield surfaces and to determine yielding of the section. For example when the product of the sign of internal forces for which a yield surface is required or (yielding is checked) is +1, then those patterns which are obtained from the product of strain vector as +1 are used to obtain the yield surfaces. On the other hand when the product of strain vector is -1 then the internal forces calculated based on the strain pattern does not change sign, therefore will not result in such yield surfaces when the product of the forces of yield surface is +1. it means only one type of finalised strain pattern (see Figure 4.21) i.e. when the product of the signs of strain vector is +1 are required to develop yield surfaces, because other type of finalised pattern (Patterns when the product of their strain vectors are -1) does not change sign of calculated internal forces and never result in +1 for the product of signs of internal forces.

When the product of sign of internal forces for which yield surface is required (or yielding is checked) is -1, this means the finalized pattern (see Figure 4.20) when the product of signs of strain vector is -1 is used to calculate the internal forces (as no sign change of forces occur when it is calculated from the strain pattern). In addition the finalized pattern (Figure 4.21) when the product of signs of strain vector is +1 is also used because when internal forces are calculated it gives different sign at several occasions and result in the product of internal forces to -1.

Therefore, when the product of forces are +1 it implies only one type of finalised pattern can be used to obtain the yield surface and identify yielding of a section. When the product of forces is -1, it implies both types of finalised patterns can be used to obtain the yield surface and identify yielding. To determine which finalised pattern is required to develop the yield surface, a simple equation is proposed, thus :

$$TotalSign = Sign(M_x)Sign(M_y)Sign(B)Sign(P) \quad 4.32$$

If the product of the internal forces is +1, it means it will use the finalised pattern given by Figure 4.21 to generate the yield surface and identify yielding of the section. Alternatively if the product is -1 it means both types of finalised patterns (Figures 4.20 and 4.21) are used to generate the yield surface and identify yielding of the section.

4.8 INTERACTION RELATIONSHIP FOR NORMAL STRESS (LOWER BOUND SOLUTION)

General plastic interaction relationships for an I-section subjected to internal forces which cause normal stress to the section are developed. The forces are axial force, biaxial bending moments and bimoment. From the study in Section 4.7, it is found that an inclined neutral-axis is inevitable for one of the flanges for most of the cases, whereas an inclined neutral-axis is taken for the web and a perpendicular neutral-axis for the other flange. Four cases finalised before can be further generalised to two primary cases. The first is when neutral-axis does not pass through the web while the second is when it passes through the web. The number of parameters which define the position of the neutral-axis is different for both the cases. Therefore, different approaches are developed for both cases for yield surface development and identification of yielding (which is required before attempting an elasto-plastic analysis).

Following the lower bound approach, the four internal forces which are P , M_x , M_y and B are obtained by integrating the longitudinal stress, their respective moments and bimoment about the section centroid. In a normalised form they can be written as (Yang and Fan, 1988)

$$p = \frac{P}{P_p} = \frac{1}{P_p} \int_A \sigma_z dA \quad 4.33(a)$$

$$m_x = \frac{M_x}{M_{xp}} = \frac{1}{M_{xp}} \int_A \sigma_z y dA \quad 4.33(b)$$

$$m_y = \frac{M_y}{M_{yp}} = \frac{1}{M_{yp}} \int_A \sigma_z x dA \quad 4.33(c)$$

$$b = \frac{B}{B_p} = \frac{1}{B_p} \int_A \sigma_z \omega dA \quad 4.33(d)$$

4.8.1 A possible interaction relationship when the neutral-axis passes through web and both the flanges

Considering the first pattern given by Figure 4.21(a), the internal forces for the entire section can be obtained using Equation 4.33 as

$$P = -2\sigma_f t_f a + 2\sigma_w t_w b + 2\sigma_f t_f c \quad 4.34(a)$$

$$M_x = -\sigma_f [0.25A_f b_f - t_f^3 / 12\alpha^2 - a^2 t_f] - \sigma_w (t_w^3 \beta / 6) - \sigma_f [0.25A_f b_f - c^2 t_f] \quad 4.34(b)$$

$$M_y = \sigma_f (t_f^3 / 6\alpha) + \sigma_f P_1 \left(\frac{d}{2} \right) + \sigma_w [0.25A_w b_w - \beta^2 t_w^3 / 12 - b^2 t_w] + \sigma_f P_3 \left(\frac{d}{2} \right) \quad 4.34(c)$$

$$B = \left[-\sigma_f (0.25A_f b_f - c^2 t_f) + \sigma_f (0.25A_f b_f - \alpha^2 t_f^3 / 12 - a^2 t_f) \right] \frac{d}{2} \quad 4.34(d)$$

In Equation 4.34, there are five neutral-axis parameters and four equations. However, using the relationships (Equations 4.25(a, b, c and d)) and by developing the relationship between the five parameters (the relationships between the parameters are developed later to generate yield surfaces) a closed form interaction relationship can be developed. However in the current work such an approach is circumvented. The reason is that there are many possible neutral-axis patterns, and it is not viable to consider all of them to obtain the closed form relationships. For example, nine equations are required to cover all the nine possible neutral-axis patterns generated by Figure 4.21(a). The nine possible patterns are illustrated in

Figure 4.23. Similarly more equations will be required to develop the relationships for the finalised second, third and fourth patterns.

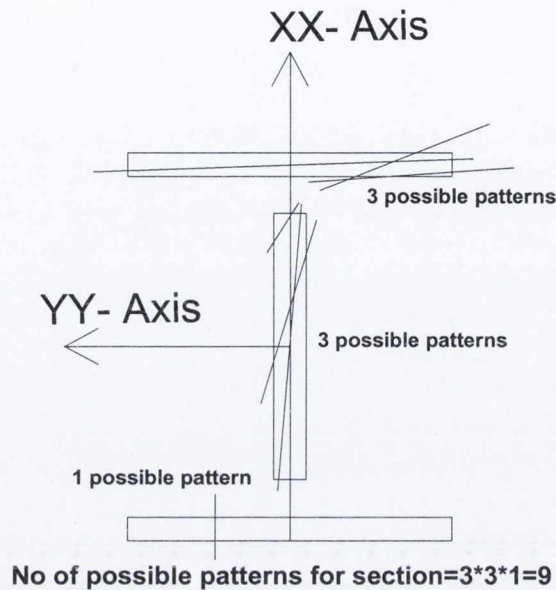


Figure 4.23 Nine possible neutral-axis patterns for the pattern given by Figure 4.20(a), three patterns are required for each rectangular plate (see Figure 2.21, Section 2.5 for patterns of rectangular section subjected to axial force and biaxial bending)

4.8.2 Element Yield Surface and Equilibrium Condition

Instead of going for a closed form solution, a parametric procedure is proposed herein for yield surface development and identification of yielding which can be used for both cases (i.e. when the neutral-axis intersects the web and when it does not). The procedure is based on a condition that equilibrium will be maintained throughout the elastic or plastic region. Terms in Equation 4.34 provide contributions to the internal forces from the top flange, web and bottom flange. They can be written individually as:

For the top flange

$$P_1 = -2\sigma_f t_f a \tag{4.35(a)}$$

$$M_{x1} = -\sigma_f \left[0.25A_f b_f - t_f^3 / 12\alpha^2 - a^2 t_f \right] \quad 4.35(b)$$

$$M'_{y1} = \sigma_f (t_f^3 / 6\alpha) \quad 4.35(c)$$

$$M''_{y1} = \sigma_f P_1 \left(\frac{d}{2} \right) \quad 4.35(d)$$

For the web

$$P_2 = 2\sigma_w t_w b \quad 4.35(e)$$

$$M_{x2} = -\sigma_w (t_w^3 \beta / 6) \quad 4.35(f)$$

$$M_{y2} = \sigma_w \left[0.25A_w b_w - \beta^2 t_w^3 / 12 - b^2 t_w \right] \quad 4.35(g)$$

For the bottom flange

$$P_3 = 2\sigma_f t_f c \quad 4.35(h)$$

$$M_{x3} = \sigma_f \left[0.25A_f b_f - c^2 t_f \right] \quad 4.35(i)$$

$$M_{y3} = \sigma_f P_3 \left(\frac{d}{2} \right) \quad 4.35(j)$$

The terms P_i , M_{xi} and M_{yi} (where $i=1, 2, 3$ are used for top flange, web and bottom flange respectively) are the contribution to P , M_x , M_y and B from the top flange, web and bottom flange. Therefore, based on the condition of equilibrium, this can be written as

$$P = P_1 + P_2 + P_3 \quad 4.36(a)$$

$$M_x = M_{x1} + M_{x2} + M_{x3} \quad 4.36(b)$$

$$M_y = M'_{y1} + M''_{y1} + M_{y2} + M''_{y3} \quad 4.36(c)$$

$$B = (M_{x3} - M_{x1}) \frac{d}{2} \quad 4.36(d)$$

It can be deduced that Equations 4.35(a), 4.35(b), 4.35(c) are the internal forces that are obtained by considering a rectangular section when axial force is applied in combination with biaxial bending having both the axes as the centroidal axes of the section (see Section 2.5 on Interaction equation of rectangular section subjected to axial force and biaxial bending). Similarly Equations 4.35(e), 4.35(f) and 4.35(g) are the internal forces that are obtained by considering a rectangular section when axial force is applied in combination with biaxial bending. Similarly from Equations 4.35(h) and 4.35(i), it can be deduced that they are related to a rectangular section having a neutral-axis assumed to pass perpendicularly through the longitudinal axis of the section (see Section 2.5 on the interaction equation of a rectangular section subjected to axial force and bending about the major axis). Therefore, it can be said that the contribution to the entire section is the same as obtained from three rectangular sections plus two terms as given by Equations 4.35(d) and 4.35(j). On this basis it is assumed in the procedure that both flanges and web are three elements of the section, fulfilling the equilibrium condition given by Equation 4.36. In the procedure, interaction relationships are developed for each element of the section, and the two terms are added to obtain the internal forces.

It has been finalised in Section 4.7, that for both the primary cases (as discussed in first Paragraph of Section 4.8), there are finalized patterns in which inclined neutral-axis pass through one flange. When inclined neutral-axis passes through any element (flange or web) for any primary case means contribution of three forces which are P_i , M_{xi} and M_{yi} to the section. For example inclined neutral-axis passes through the top flange of Figure 4.21(a) which resulted in three terms as given by Equations 4.35(a), 4.35(b) and 4.35(c) which are related to three forces which are P_i ,

M_{xi} and M_{yi} i.e. axial force and biaxial bending acting on the flange, while Equation 4.35(d) comes when equilibrium of the entire section is considered. Another example of inclined neutral-axis is that when it passes through the web and three Equations which are related to the three forces are Equations 4.35(e), 4.35(f) and 4.35(g). When three forces are considered a three dimensional yield surface is required and are called in this work a 3D element yield surface

When a perpendicular neutral-axis passes through any element. for example the bottom flange of Figure 4.21(a) this means two forces which are P_i , M_{xi} act on the element and the two forces are given by Equations 4.35(h) and 4.35(i), while Equation 4.35(j) applies when equilibrium of the entire section is considered. When two forces are considered a two dimensional yield surface is required and is called in this work a 2D element yield surface.

Both the 2D element yield surface and 3D element yield surface, are discussed in the next section

Element yield surfaces

Two types of element yield surfaces are obtained for the two and three forces and are discussed as follows:

2D Element yield surface

Considering the neutral-axis pattern given by Figure 4.24, the two internal forces P_i , and M_{xi} are obtained by integrating the longitudinal stress and the moment about the XX-axis of the section. In a normalized form these are obtained (Details given in Appendix-B, B.4) using Equation 4.33 as (Following the neutral-axis pattern of Figure 4.21(a), if it is assumed that forces are acting on the bottom flange then the subscript with the forces is 3) :

$$p_3 = \sigma_3 \frac{2t_f c}{A_s}, m_{x3} = \sigma_3 \frac{[0.5b_f^2 - 2c^2]}{(b_f^2 + 0.5c/t_w b_f)} \quad 4.37(a)$$

where $c' = A_w/A_f$, $A_s = (2A_f + A_w)$ and the parameter c gives the position of neutral-axis in the bottom flange

Eliminating the parameter c from the above equation to obtain a 2D element yield surface equation for the bottom flange:

$$\frac{p_3^2 A_s^2}{\sigma_3^2 A_f^2} + \frac{2m_{x3}(b_f^2 + 0.5c't_w b_f)}{b_f^2 \sigma_3} = 1 \quad 4.37(b)$$

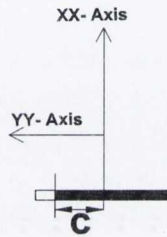


Figure 4.24. Bottom flange shown with the global X and Y coordinates showing the position of the neutral-axis when two forces P_i and M_{xi} act on the flange

3D Element yield surfaces

It has been discussed in section 4.7 that an inclined neutral-axis can pass through a flange and web. When inclined neutral-axis pass through any plate, then it represents the case when a plate is subjected to axial force and biaxial bending as discussed in the previous section. When an inclined neutral-axis passes through any plate (as each plate is rectangular in shape) then there are three possible locations for the inclined neutral-axis, as depicted in Figure 2.21 reproduced here as Figure 4.25.

In the following, two such 3D element yield surface equations are developed for the first and third pattern of the figure while equation of the second pattern will be the same as the first pattern with width replaced by the depth and vice-versa. Hence, it resulted in three equations related to the three patterns of the figure. If it is assumed that inclined neutral-axis passes through the top flange then the forces are considered to act on the top flange, therefore in the development of the equations,

depth is taken as b_f and width is taken as t_f , while the subscript use for the forces is 1.

Those 3D element yield surface equations for the three patterns obtained for the top flange are discussed as follows:

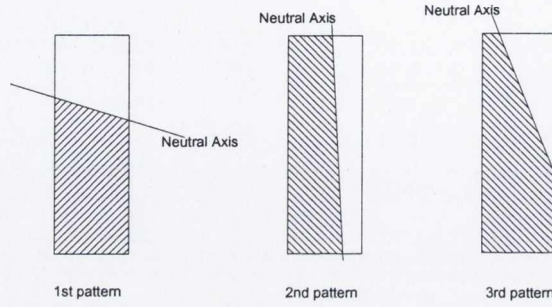


Figure 4.25 Three possible patterns when rectangular section is considered

3D element yield surface and 1st pattern

Considering the first pattern in Figure 4.25, the three internal forces P_i , M_{xi} and M_{yi} are obtained by integrating the longitudinal stress and the relative moments about the centroidal axes of the section. In a normalized form if they are considered for the top flange, and the two parameters of Figure 4.21(a) given as a and α then these are obtained (details are given in Appendix-B, B.4) using Equation 4.33 as

$$P_1 = \sigma_1 \frac{2t_f a}{A_s}, \quad m_{x1} = \frac{2\sigma_1 (0.25A_f b_f - 0.0833\alpha'^2 t_f^3 - a^2 t_f)}{c_1}, \quad m'_{y1} = \sigma_1 \frac{t_f^3 \alpha'}{6c_2} \quad 4.38(a)$$

where $\alpha' = 1/\alpha$, $c_1 = A_f (b_f + 0.5c' t_w)$ and $c_2 = A_f (d + 0.25b_w c')$

Eliminating the neutral-axis parameters, a and α' from the above equation results in an equation given as

$$P_1^2 \left(\frac{A_s^2}{A_f^2 \sigma_1^2} \right) + m_{x1} \left(\frac{2c_1 t_f}{A_f^2 \sigma_1} \right) + m_{y1}^{1/2} \frac{12c_2^2}{A_f^2 t_f^2 \sigma_1^2} = 1 \quad 4.38(b)$$

The above equation has limit (Santhadaporn and Chen, 1970) which for the top flange can be written as

$$\frac{M'_{y1}}{0.25A_f t_f} \leq \frac{2}{3} \left(1 - \frac{P_1}{A_f} \right) \leq \frac{M_{x1}}{0.25A_f b_f} \quad 4.38(c)$$

3D element yield surface and 2nd pattern

When the second pattern is considered, the same equation 4.38 will be used with t_f replaced by b_f and b_f replaced by t_f . m_{x1} replaced by m'_{y1} and m'_{y1} replaced by m_{x1} .

3D element yield surface and 3rd pattern

Similarly, considering the third pattern of Figure 4.25, redrawn in Figure 4.26 with suitable neutral-axis parameters, the three internal forces in a dimensionless form are obtained (details are given in Appendix-B, B.4) using Equation 4.33 as

$$p_1 = \sigma_1 \frac{(A_f - x_1 x_2)}{A_s}, m_{x1} = 2\sigma_1 \frac{x_1 x_2 (0.5b_f - 0.333x_1)}{c_1}, m'_{y1} = \sigma_1 \frac{(0.5x_1 x_2 t_f - 0.333x_1 x_2^2)}{c_2} \quad 4.39(a)$$

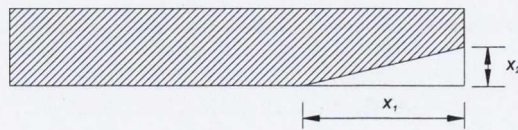


Figure 4.26 Neutral-Axis parameters for the third pattern

where the parameters x_1 and x_2 are defined in the figure. Eliminating the neutral-axis parameters from the above equation results in an equation given by:

$$(m'_{y1} c_2 \sigma_1 - 0.5 C_a t_f \sigma_1) (1.5 C_a b_f - 1.5 m_{x1} c_1) + 0.333 C_a^3 = 0 \quad 4.39(b)$$

where $C_a = (\sigma_1 A_f - p_1 A_s)$.

The above equation has limits (Santhadaporn and Chen, 1970) which for the top flange can be written as

$$\frac{M_{x1}}{0.25A_f b_f \sigma_f} \geq \frac{2}{3} \left(1 - \frac{P_1}{A_f \sigma_f} \right), \frac{M'_{y1}}{0.25A_f t_f \sigma_f} \geq \frac{2}{3} \left(1 - \frac{P_1}{A_f \sigma_f} \right) \quad 4.39(c)$$

Neutral-axis and web

Equations 4.38 and 4.39 obtained above are also valid for the three inclined neutral axis patterns of web as depicted in Figure 4.23. For both the equations t_f is replaced by t_w and b_f is replaced by b_w . In addition, m_{x1} is replaced by m_{y2} , m'_{y1} is replaced by m_{x2} and σ_1 by σ_2 .

In the above equations $\sigma_i = \sigma_a / \sigma_y$, $i=1,2,3$, σ_a is the normal stress, which causes all the three elements to yield in the presence of shear stress, while the subscript $a = f, w, f$ are used for top flange, web and bottom flange respectively. The subscripts 1, 2 and 3 in σ_i are used for top flange, web and bottom flange respectively.

For the web, $C_a = \sigma_2 A_w - A_s p_2$

Based on the contribution from the web and flanges a general equilibrium equation in normalized form can be written as

$$p = p_1 + p_2 + p_3 \quad 4.40(a)$$

$$m_x = m_{x1} + m_{x2} + m_{x3} \quad 4.40(b)$$

$$m_y = m'_{y1} + (p_3 - p_1) \frac{d(4 + 2c')}{(4d + c'b_w)} + m_{y2} \quad 4.40(c)$$

$$b = m_{x3} - m_{x1} \quad 4.40(d)$$

4.8.3 Yield surface development and identification of the plastic hinge

The purpose of a yielding criterion is to develop its graphical presentation (yield surface) and to use it in elasto-plastic analysis to identify the yielding of a section. In this section a procedure is developed to obtain the graphs and to identify the yielding. The procedure is based on the element yield surfaces (developed in Section 4.8.2) and the equilibrium equations which satisfy the forces acting on the entire section.

To identify the yielding for a given set of forces, it is assumed that all the forces are known except any one force. The value of the unknown force is obtained using the element yield surfaces, equilibrium equations and the remaining forces developed in Section 4.8.2. If the obtained value of the unknown force is less than the given value then the section is elastic; if it is equal to the given value then the section is plastic and it is overstressed if more than 1. The cases when the neutral-axis does and does not intersect the web are discussed separately due to the number of parameters involved in determining the position of the neutral-axis.

Procedure to develop yield surface when the neutral-axis does not intersect the web

Considering the seven forces which are P , M_x , M_y , B , S_x , S_y and T_u , it is assumed that M_y is the unknown force and its value is calculated based on the remaining six forces to identify yielding. To obtain the yield surface the same procedure is repeated by varying the known forces to obtain many values for the unknown force on the graph. The procedure is as follows:

1. Using Equations 4.9 and 4.24 obtain the normal stress for both flanges and web.
2. Considering the sign of those forces which cause normal stress to the section, obtain the product of the signs using Equation 4.32 to identify the type of pattern.

3. Check the given forces for the sufficient condition for the case when the neutral-axis is intersecting the web. The sufficient conditions are

$$A_w \sigma_2 - A_f \sigma_1 > |P|, |M_x| > \frac{b_f^2 t_f}{4} (\sigma_1 + \sigma_3) \text{ and } |M_y| > \frac{A_f d}{2} (\sigma_1 + \sigma_3) \quad 4.41$$

If any of the sufficient conditions is fulfilled, a pattern is considered in which the neutral-axis intersects the web, and yielding is determined in the next section. For the other case the procedure is continued in the next steps.

4. Obtain values of m_{x1} and m_{x3} called as m_{x1-1} and m_{x3-1} respectively using Equations 4.40(b) and 4.40(d) for given values of m_x and b . $m_{x2}=0$ as web is contributing to axial force only in this case.

5. Assuming a perpendicular neutral-axis for the bottom flange, p_3 is calculated using Equation 4.37(b).

6. Obtain the value of p_1 by assuming $p_2 = A_w \sigma_2 / P_y$ and using Equation 4.40(a).

7. For the obtained values of m_{x1-1} and p_1 , determine the type of element yield surface required to obtain m'_{y1} using Equation 4.38(c) or 4.39(c). If Equations 4.38(c) and 4.39(c) are not fulfilled m'_{y1} is obtained based on the 2nd pattern of 3D element yield surface.

8. Using Equation 4.40(c) obtain m_y by considering $m_{y2}=0$ as web is contributing to axial force only in this case and compare with the given m_y to determine the yielding separately when the product is +1 and -1.

When the product is +1 and section has yielded go to the next step. When the product is -1 and section has yielded go to the next step. If the section has not yielded or section is overstressed the section is checked for the case when a

perpendicular neutral-axis exists for the top flange, and the procedure from step-5 to step-8 is repeated. If found to have yielded the next step is continued. If the section has not yielded or overstressed the section is termed as elastic or overstressed respectively.

9. Obtain the parameters a or α or x_1 or x_2 using Equation 4.38(a) or 4.39(a) respectively or a or α is obtained based on the 2nd pattern of 3D element yield surface, which ever is valid for the three values of Equation 4.38(a) and 4.39(a) or the 2nd pattern, and check the kinematic limit as discussed in Section 4.7.3.

When the product is +1 if it fulfills the kinematic limit, the process of yielding of the section is complete, otherwise check the forces for the case when it is intersecting the web.

When the product is -1 if it fulfills the limit, the process of yielding of the section is complete, otherwise the section is checked (if not already checked) for the case when a perpendicular neutral-axis can exist for the top flange and procedure 5-9 is repeated. If after yielding it does not fulfill the kinematic limit, the section is checked for the case when it intersects the web. If the section has not yielded or is overstressed the section is termed as elastic or overstressed respectively.

Procedure to develop a yield surface when the neutral-axis intersects the web

1. Constant values of p and b are assumed for which the yield surface is required.
2. It was concluded in Section 4.7.2 that the neutral-axis can assume to pass perpendicularly through at least any one of the flanges. If that flange is the bottom flange then the component of moment m_x from the bottom flange is denoted as m_{x3} , a maximum and minimum value of m_{x3} can be obtained for the constant b based on Equation 4.40(d).

To determine the minimum value of m_{x3} , because the minimum value of m_x in the graph is zero, therefore using Equation 4.40(b) and assuming $m_{x2} = 0$ (a small value compared to flanges, hence ignored at this step), which shows that $m_{x1} = -m_{x3}$ (From Eq 4.40(b)). As m_x is zero then M_x is also zero, and from Equation 4.36(b) it can be concluded that $M_{x1} = -M_{x3}$. Therefore using the relation $B/B_p = b$ and Equation 4.36(d), $M_{x3-\min}$ is obtained as $M_{x3-\min} = b * \sigma_3 * b_f^2 t_f / 4$

In the case of establishing maximum contribution from m_{x3} , M_{x3} is required which means $M_{x3-\max}$ must reach the full plastic capacity of one flange, therefore, $M_{x3-\max} = \sigma_3 * b_f^2 t_f / 4$.

3. Generate a series of values of M_{x3} between $M_{x3-\min}$ and $M_{x3-\max}$ at any assumed interval and obtain P_3 and c for each M_{x3} using Equation 4.37(a) and relations $p_3 = P_3 / P_p$ and $m_{x3} = M_{x3} / M_{xp}$.

4. For each value of M_{x3} obtain M_{x1} using Eq. 4.36(d), and obtain m_{x1} using the relation $m_{x1} = M_{x1} / M_{xp}$.

5. If m_{x1} is assumed for the top flange, and it is discussed in Section 4.7.2 that a non-perpendicular neutral-axis can exist for the other flange then there can be three possible patterns for the top flange when the neutral-axis is inclined as depicted in Figure 4.25. Assuming m_{x1} , a range of p_1 can be obtained using Equations 4.38(c) and 4.39(c) for any possible neutral-axis pattern of this type. Therefore, values of p_1 are generated within the range by selecting a suitable interval. Hence, for one m_{x1} value, there is a series of p_1 values available from which one p_1 is to be obtained which is the correct p_1 .

6. For each p_1 and constant m_{x1} calculate a, α, x_1, x_2 using Equations 4.38 and 4.39, Analyses are performed in two stages: in one stage it is based on a, α and in other stage it is based on x_1, x_2 .

If the special case of Figure 4.16 is considered, then p_1 is obtained also for the the second pattern of Figure 4.25. In addition p_1 is also obtained based on Equations 4.38(c) and 4.39(c). Now in this case p_1 is obtained by three patterns and analyses are performed in three stages: in one stage it is based on a, α and in the second stage it is based on x_1, x_2 , whereas in the third stage it is based on the second pattern.

7. Obtain a series of p_2 values for a series of p_1 values and a selected p_3 using Equation 4.40(a). Now a series of p_1 and p_2 and one value of p_3 are known.

8. At this stage, assume that the neutral-axis passes through the web based on the first pattern, as depicted in Figure 4.25. Calculate b' for the web using first equation of Equation 4.38(a) by replacing a by b' and p_1 by p_2 . Calculate the angle β using the equation (derived in Appendix-B, Section B.5.1):

$$\tan(180^\circ - \tan^{-1}(\beta)) = \frac{cL_1 + aL_2}{2ac} \quad 4.42$$

where $L_1 = 0.5d - b'$ and $L_2 = 0.5d + b'$

9. It is assumed in step-8 that neutral-axis pass through the web based on the first pattern of Figure 4.25. Using the angle β (obtained in step-8) calculate a' where a' is defined in Figure B-13. If the value of $a' \geq 0.5t_w$ the assumption regarding the neutral-axis pattern is correct. If $a' < 0.5t_w$ the assumption regarding the neutral-axis pattern is not correct. If the assumption is correct step-10 is ignored and go to step-

11. If it is not correct angle β is recalculated by assuming different patterns as follows (derived in Appendix-B, Section B.5):

10. If the first pattern is not obtained, it means there are two possibilities; either the second or third patterns can be obtained. The procedure to obtain β for both the alternative patterns is discussed as follows:

Assuming the third pattern, a' is calculated thus (derived in Appendix-B, Section B.5.2):

$$0.5*t_f*ca'^2 - 0.5*t_f*aa'^2 + a'^2*da + 2A1a'c + 0.5a't_f*t_w*c - 2A1a'a - 0.5a't_f*t_w*a + a't_w*da + .125t_f*t_w^2*c - .125t_f*t_w^2*a + .25t_w^2*da = 4acA1 \quad 4.43$$

When a' is known L'_1 is calculated as

$$L'_1 = \frac{2a' A1}{(a' + a't_w + 0.25*t_w^2)} \quad 4.44$$

and β can be obtained using the relationship

$$\tan(180^\circ - \tan^{-1}(\beta)) = \frac{L'_1}{a'} \quad 4.45$$

Assuming the second pattern, β can be obtained using the relationship (derived in Appendix-B, Section B.5.3):

$$\tan(180^\circ - \tan^{-1}(\beta)) = \frac{b}{b_o} \text{ and } L_2 = \frac{cdb_o + acd}{(cb_o - ab_o + 2ac)} \quad 4.46$$

where $b' = L_2 - 0.5d$ and $b_o = P_{web} / 2b_w$

11. Based on the calculated β , a, b and c calculate the angle α_{new} for the top flange using (derived in Appendix-B, Section B.5.4):

$$\alpha_{new} = (lb1_{new} - lb_{new}) / t_f \quad 4.47$$

where $lb1_{new}$ and lb_{new} are as defined in Figure B-14 and the procedure to obtain $lb1_{new}$ and lb_{new} are given in the appendix.

12. Compare obtained α_{new} with the α obtained in step-6. If both α_{new} and α match each other to a certain tolerance, save the value and obtain m_y using 4.40(c), otherwise ignore the values.

13. Repeat the steps for other values of M_{x3} .

Developed yield surfaces

Yield surfaces are drawn based on the procedure discussed above. Surfaces are drawn for both the cases i.e. when the products of the signs of the forces as obtained by Equation 4.32 are +1 and -1. The curves are drawn for the W12 x 31 section, where p and b are constant, while m_y and m_x are x and y intercepts respectively. Forces t_u, s_x, s_y are assumed to be zero. Yield surfaces for both the product signs are discussed separately.

When the product of the signs of the forces is +1

Effect of axial force

The curves are shown in Figure 4.27-4.31. In all the figures, it can be observed that the presence of axial force shrinks the domain of the yield surfaces as the p value increases from $p = 0.0 - 0.8$. Up to $p = 0.4$ the magnitude of the maximum m_x value has not changed significantly for all the curves. For example for $b = 0.2$ it can be observed that the magnitudes for $p = 0.0, 0.2, 0.4$ are 0.82, 0.81 and 0.79 respectively. On further increase of the p value, the magnitude starts to decrease

rapidly, where the values for $p = 0.6$ and 0.8 are 0.64 and 0.32 respectively. This shows that small increases of axial force do not affect considerably the m_x capacity of the section. In the case of m_y , there is a gradual decrease with an increasing axial force. For example for $b = 0.2$ the magnitudes of m_y for $p = 0.0, 0.2, 0.4, 0.6$ and 0.8 are $0.92, 0.85, 0.73, 0.4$ and 0.17 respectively. With the increase in axial force, the capacity of the section to resist rotation decreases, For example for $p = 0.8$ a bimoment of $b = 0.6$ cannot be applied.

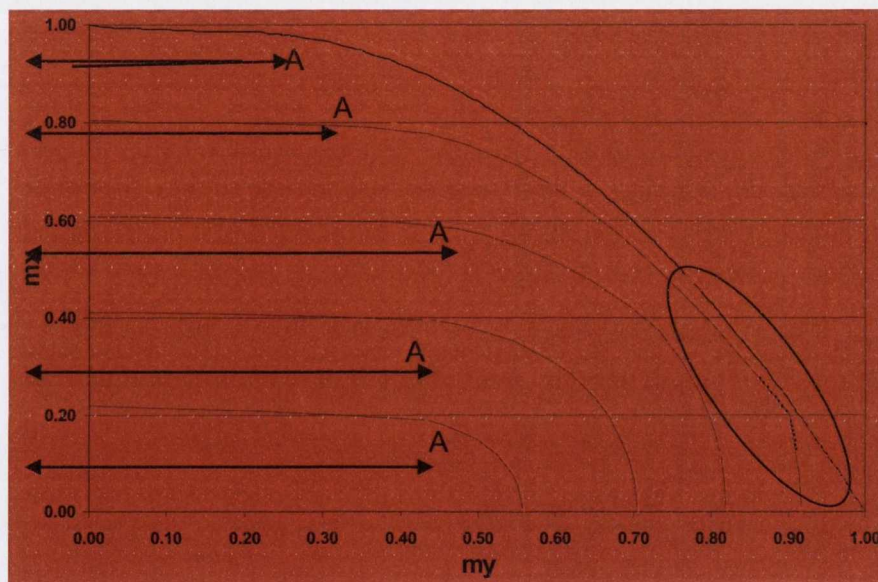


Figure 4.27 Yield surface developed in this work and previous work by Yang et al. (1989) (shown as dashed red) for the case when $p = 0$ the curve at the top is $b = 0.0$ the next curve is $b = 0.2$ and the rest follow a series as $b = 0.4, b = 0.6$ and $b = 0.8$. Ellipse in the above figure represent that yield surface for $b = 0.0$ and $b = 0.2$ are close to each other

Effect of bimoment

The increase of bimoment value shrinks the domain of all the surfaces, as can be deduced from the figures. A reduction of both m_x and m_y on the increase of b value can be observed. The decrease of m_x for an increase of say 0.2 in the value of

b is approximately 0.2 for all the surfaces, as can be observed in the figure. This is because the bimoment causes both flanges to bend in opposite directions. Therefore, an increase of bimoment nearly equally decreases the m_x value because of the major contribution of the flanges to m_x .

The decrease in the magnitude of m_y with b may also be observed from all the figures. For example, in the case when $p = 0.0$ for $b = 0.0$ and 0.2 (as noted as ellipse in Figure 4.27), there is a portion of the curve for which the shrinkage is small. This shows that a small increase of (low) bimoment values does not significantly affect curves for small values of m_x . This affect is not observed for larger values of p , as can be observed for $p = 0.2, 0.4, 0.6$ and 0.8 in Figures 4.28-31.

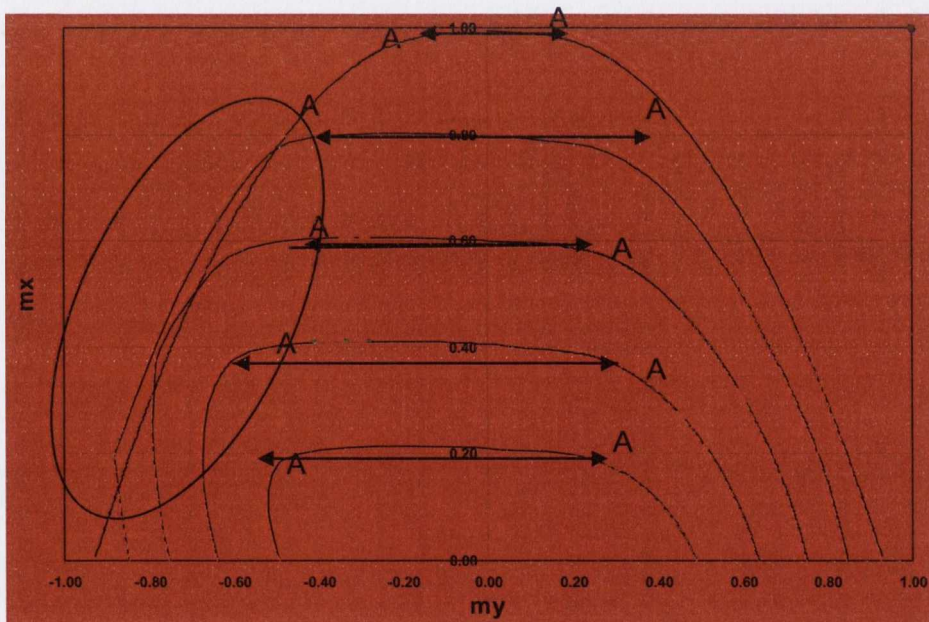


Figure 4.28 Yield surface developed in this work and previous work by Yang et al. (1989) (shown as dashed red) for the case when $p = 0.2$ the curve at the top is $b=0.0$ the next curve is $b=0.2$ and the rest follow a series as $b=0.4, b=0.6$ and $b=0.8$. . Ellipse in the above figure represents that yield surface for $b=0.0, b=0.2$ and $b=0.4$ are close and intersect each other

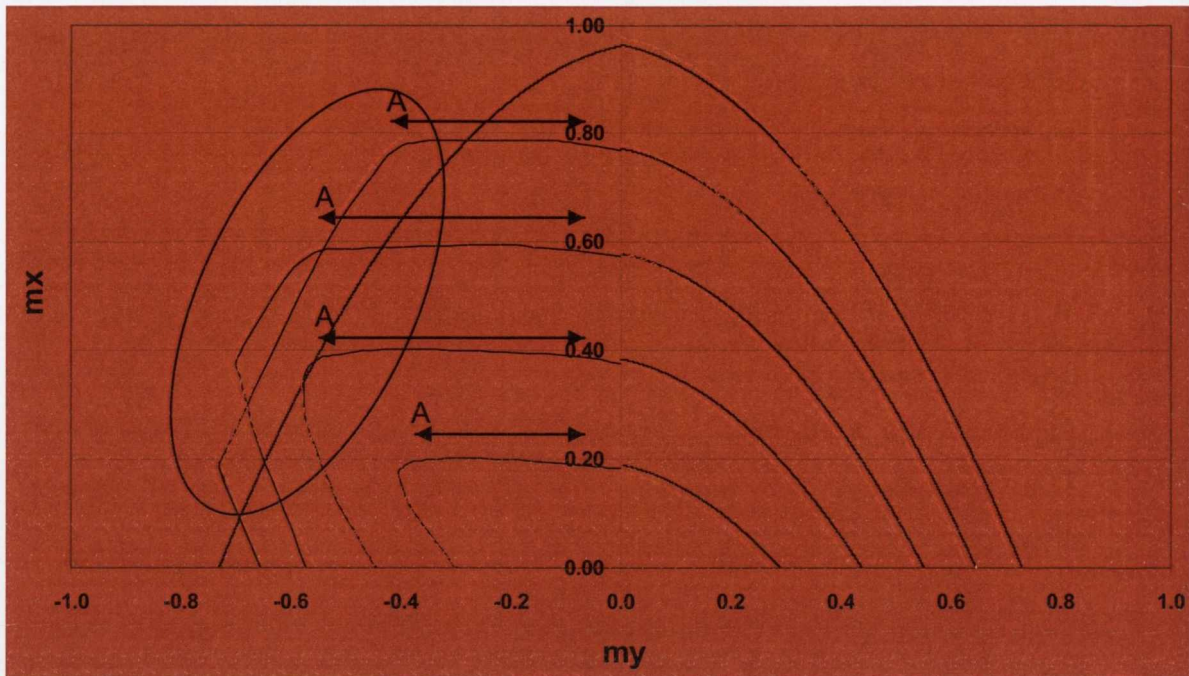


Figure 4.29 Yield surface developed in this work and previous work by Yang et al. (1989) (shown as dashed red) for the case when $p = 0.4$ the curve at the top is $b=0.0$ the next curve is $b=0.2$ and the rest follow a series as $b=0.4$, $b=0.6$ and $b=0.8$. Ellipse in the above figure represents that yield surface for $b=0.0$, $b=0.2$, $b=0.4$ and $b=0.6$ are close and intersect each other

Relationship between m_x and m_y for p and b values

The relationship between m_x and m_y depends on the neutral-axis passing through the web. When the neutral-axis passes through the web, a constant plateau can be observed for low m_y . For example the curves obtained for $p = 0.0$ and 0.2 are the cases when neutral-axis pass through the web. The reason is the low capacity of the web to resist m_x . Beyond the constant plateau, there is a gradual decrease of m_x on the increase of m_y up to the point when m_x reaches a zero value.

When the neutral-axis does not pass through the web, there will be no constant plateau, as can be deduced from Figures 4.29-31. The decrease will be gradual from the peak magnitude of m_x to a zero value at the maximum m_y value.

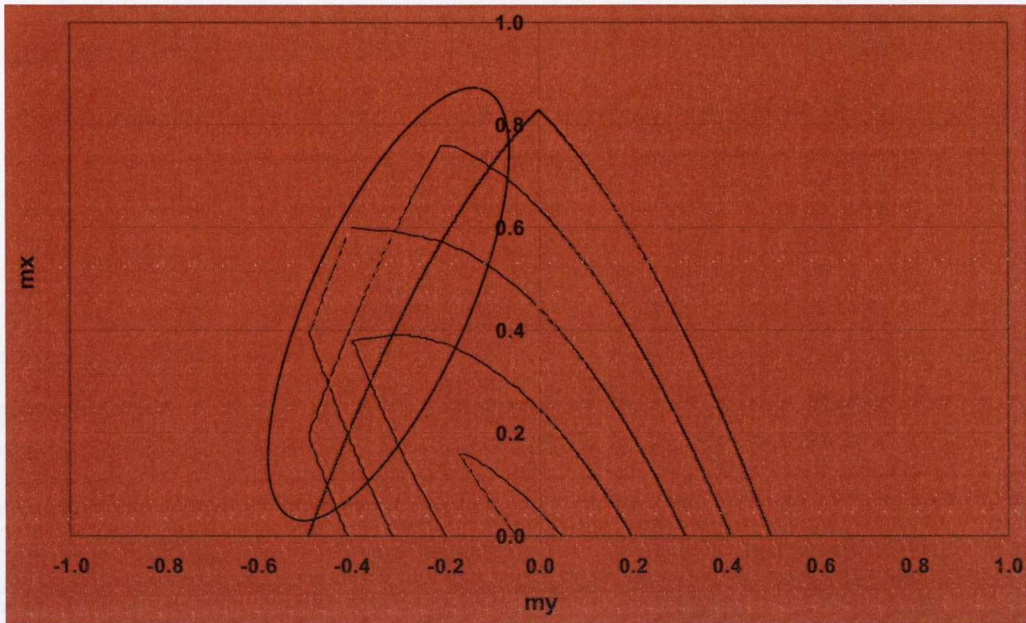


Figure 4.30 Yield surface developed in this work and previous work by Yang et al. (1989) (shown as dashed red) for the case when $p = 0.6$ the curve at the top is $b=0.0$ the next curve is $b=0.2$ and the rest follow a series as $b=0.4$, $b=0.6$ and $b=0.8$. Ellipse in the above figure represents that yield surface for $b=0.0$, $b=0.2$, $b=0.4$ and $b=0.6$ are close and intersect each other

Comparison with the previous work

The comparative curves from the previous work by Yang et al. (1989) in so far as they exist are shown dashed in Figures 4.27 to 4.31. For small values of p the exact solution obtained in this work gives curves slightly below the curves developed previously by Yang et al. as can be observed from the curves obtained for $p = 0.0$ and 0.2 in Figures 4.27 and 4.28. This difference is more pronounced for small values of b . The main reason for the difference is the assumption which was made in the previous work. In the previous work it was assumed that Neutral-axis pass perpendicular to the web and also perpendicular to the top flange. However, this assumption is not considered in the current research. To obtain an exact solution and fill the gap in the previous work, the original pattern of the neutral-axis in which neutral-axis pass inclined through both the top flange and web is considered. Two

main changes happen compared to the previous work. First that gap is filled, this is because of the inclined neutral-axis in the top flange. When inclined neutral axis is considered for the top flange, the contribution of major moment from the flange started to decrease and result in the reduction of major moment of the entire section and it reduce in such a way so that it nearly reach a zero value for major moment. During this process there is not much rise in the minor moment and result in nearly a constant plateau for the graph. Secondly, that neutral-axis pass inclined through web, it cause increase in the minor moment of the entire section and a reduction in the major moment component from the web. The decrease of the major moment component from the web was more than the increase of minor moment from the web, hence it shifts the curve towards the left and results in a curve below the Yang et al curve. Generally the web contribution to the major moment is large for an I section. Therefore, for sections where thickness of the web is larger or the depth of web is greater as compare to its flange dimensions, then the difference can become significant compared to the previous work of Yang et al. There are parts of the curve when the previous curve and current curve entirely match each other. This is due to the reason that in these cases neutral-axis passes perpendicularly to both flanges and web for the current research, as the assumption which was made previously. Therefore both the curves match at these points.

For the cases when p is larger i.e. when the neutral-axis does not pass through the web, the Yang et al curve is on the lower side for high values of minor moment, whereas for lower values of the minor moment, the current solution is on the upper side. The reason for this is the addition of component of major moment from the flange which is ignored in the previous case. This difference can become large if the flange considered has a large thickness.

Effect of shear and Torsion

T_u , S_v , and S_h cause shear stress on the section. Although shear stress is not considered in the development of the yield surface, their possible effects on the yield surface are discussed. Several possibilities exist when shear stress act on the section.

First is when all the three forces are present. In that case shear stress is related to direct stress by Equation 4.9, and the domain of the yield surfaces will shrink keeping its existing shape.

In the second case, one of the forces is zero. In that case, the reduced direct stresses on the web and flanges are different. If there is no change in the direct stress in the flange, there is a decrease in the stress of web. The magnitude of m_y will decrease, whereas the magnitude of m_x will nearly be the same because of the small contribution of the web to m_x .

There can also be a case when the direct stress in the flange is less than the direct stress in the web, whereupon the magnitude of m_x will decrease because of the flange contribution to m_x , whereas the magnitude of m_y will depend on the depth of the section. The m_y reduction will be more for higher values of depth of the section.

When the product of the signs of the forces are -1

Effect of Axial Force

The overall effect of an axial force is to reduce the domain of yield surface. Up to a value of $p = 0.4$ the maximum moment value of m_x has not changed. For example for $b = 0.2$, the magnitudes of m_x are 0.8 and 0.78 for $p = 0.2$ and 0.4 respectively. Beyond $p = 0.4$ there is a large reduction in the magnitude. The rotational capacity also decreases rapidly beyond this point. The magnitude of m_y decreases gradually with increasing p value. For $p = 0.2$ and 0.4 a decrease in the magnitude of m_y is observed for a nearly constant magnitude of m_x . It results in shifting of the yield surfaces to the right on increase of the p value.

Effect of Bimoment

For all the curves for different p values, shrinkage of curves can be observed on increase of the bimoment values except for portions of the curves highlighted with an

oval in each figure. The reason for the change of curve as highlighted in the figures is that the bimoment is a self balancing moment where both the flanges warped in two different directions, hence giving a summation of zero minor moment. Therefore it can give a high value of m_x for $b = 0.4$ as compared to the value for $b = 0.2$. This only happened to the curves when the product of forces is -1 . The reason is that when the product of the forces is $+1$, only those neutral-axis pattern are required to generate yield surfaces, whose product of the strain vectors is also $+1$, whereas when the product of forces is -1 , then those neutral-axis pattern are required whose product of their strain vector is both $+1$ and -1 . This can be observed for $p = 0.2, 0.4, 0.6$ and 0.8 . This also shows that warping can sometimes cause an increase in the plastic capacity of the section. This change of curve pattern as noted as ellipse in the figure for different b values or for two different values of m_x for the same curve is also due to the fact that in the theory of plasticity the solution is not unique (the Drucker postulate) (Drucker, 1956). Therefore there can be different failure points depending on the manner of loading of the entire member and the direction of the deformation vector for the yield surface.

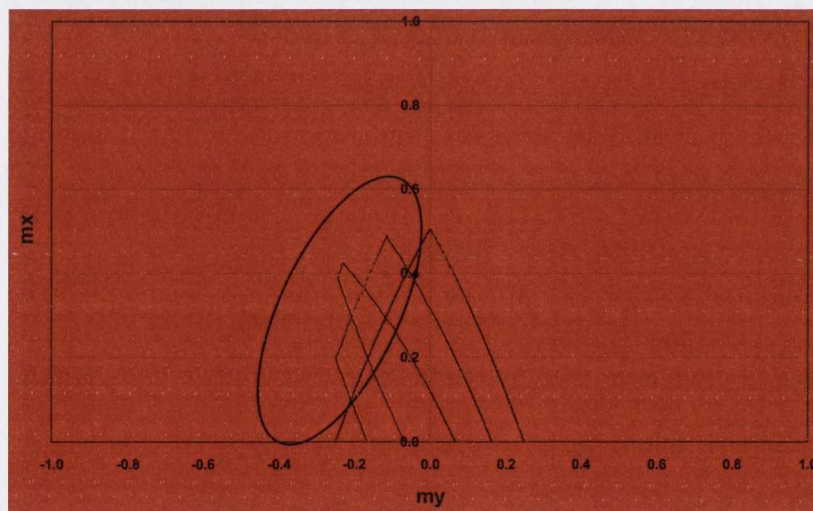


Figure 4.31 Yield surface developed in this work and previous work by Yang et al. (1989) (shown as dashed red) for the case when $p = 0.8$ the curve at the top is $b=0.0$ the next curve is $b=0.2$ and the rest follow a series as $b=0.4$, $b=0.6$ and $b=0.8$. Ellipse in the above figure represents that yield surface for $b=0.4$, $b=0.6$ and $b=0.8$ are close and intersect each other

Relationship between m_x and m_y for p and b values

When the neutral-axis passes through the web, a constant plateau can be observed. The curves obtained for $p = 0.2$ and 0.4 are the cases when neutral-axis passes through the web, as can be deduced from Figures 4.28 and 4.29. The reason is the low capacity of the web to resist m_x . For the cases when neutral-axis does not pass through the web, i.e. for $p = 0.6$ and 0.8 no constant plateau exist. For portion of all the curves, there is a gradual decrease of m_y on the decrease of m_x . This happened to the portion of the curves generated based on the neutral-axis pattern when the product of the sign of strain vector was $+1$. As the interaction curves are not unique (Drucker, 1956), it can happen that due to bimoment a decrease of m_x is obtained for a decrease of m_y .

Effect of shear and torsion

There will be the same effects due to the shear stress as discussed for the case when the product was $+1$.

Comparison with the previous work

When compared with previous curves (produced by Yang et al. (1989)) all the curves obtained by the current solution give curves marginally below the previous curves. The reason for the difference is the consideration of the minor moment in the web. In addition, two extensions to the existing curves can be observed. First, a constant plateau extension for $p = 0.2$ and 0.4 is now provided which is obtained by assuming an inclined neutral-axis for the web, which reduce the major moment of the section up to a zero value on a slight change of the minor moment. This slight change causes a decrease of the m_y value when contribution to m_x from the web is also considered. For $p = 0.6$ and 0.8 , it was assumed previously that an inclined neutral-axis can pass through one flange only. However, it is found in the current study in Section 4.7, that inclined neutral-axis can pass through both the flanges, which cause extension of the curves to the point when m_y reaches a zero value.

Kinematic Mechanism and Comparison between the two yield surfaces

Every point of the yield surface corresponds to a yield mechanism because, as shall be discussed in the next section the uniqueness theorem is satisfied. Observing all the graphs continuity between the cases when the product is +1 and -1 can be observed. This indicates that the yield surfaces are closed and continuous. Observing the domain of all the yield surface it can be deduced that all the curves are convex in nature. Hence it can be said that developed yield surface are closed and continuous (Morris and Fenves, 1970) and fulfill the criterion of convexity.

Yield surfaces, when $P=0$

From the study of neutral-axis patterns in section 4.7 a same pattern will be achieved for both positive and negative bimoment deformation. Therefore one obtains same curves for both positive and negative m_x values, which shows that there will be symmetry, unlike for the cases when $p>0$ (see Figure 4.27)

Procedure to identify yielding of the section when the neutral-axis intersects the web)

It is extremely difficult to identify yielding for the case when the neutral-axis passes through the web. The reason is that in the current work minor moment contribution to the web is considered, as compared to the previous case in which it is not considered. Because of this numbers of unknowns for the interaction equation exceeds number of equations. Therefore to identify yielding, the minor moment contribution to the web is not considered here.

From the developed yield surface, it is found that a portion of the yield surface when the neutral-axis passes through the web is almost a flat plateau, as identified by lines with arrows in Figures 4.27, 4.28 and 4.29 for the portion where there is a flat plateau. This is due to the fact that the minor moment contribution to web is very small (as discussed above). As the contribution of minor moment to web is small for available I-sections, a constant plateau can be assumed to identify yielding of a section.

For the constant plateau it can be observed that if point A is marked on each curve then to the left of it is constant plateau for product =+1. When considering the curves when the product of forces is -1, in that case another point A is given to the right of which is constant plateau. Therefore to identify yielding it is first required to determine point A of each curve at which flat plateau commence.

Obtaining point A

From the developed yield surface it is found that the summation of the absolute values of m_x and b reaches a value approximately equal to one for the region of the constant plateau. Therefore point A is the point where the summation equal to 1. Therefore three forces are known for point A, these being values of p , m_x and b . For example for $p = 0.2$ and $b = 0.2$, m_x used is 0.8. Therefore, only value of moment about major axis m_{yA} is required to obtain point A for each curve.

Using Equation 4.40(b and d) m_{x1}, m_{x3} are obtained by assuming $m_{x2} = 0$ (the contribution from the web to m_x is ignored). Therefore p_1, p_3 can be obtained by using Equation 4.37(b) by using appropriate parameters for a 2D element yield surface. Using Equation 4.40(a) p_2 is thus obtained and therefore, using Equation 4.37(b) for the web, m_{y2} can be obtained. Therefore, m_{yA} can be obtained using Equation 4.40(c) by assuming $m'_{y1} = 0$. The value obtained using Equation 4.40(c) is the required m_{yA} value.

In this procedure it is first required to determine the m_{yA} value, because For example considering the curves when the product of forces is +1, then if value of m_y is more than m_{yA} it means that at yield surface the summation of m_x and b is less than one, whereas if value of m_y is less than m_{yA} it means yield surface point lie on the flat plateau and the summation of m_x and b is nearly equal to one.

Therefore, considering the product=+1, if m_y is less than m_{yA} , then the summation of m_x and b are checked, if it is equal to 1, then the section is considered plastic, if it is less than 1 then it is elastic and it is over stressed if it is more than one.

If m_y is greater than m_{yA} , then the summation of m_x and b are checked: if it is equal to or more than one, then the section is considered over-stressed, while if it is less than 1 then the section is checked for plasticity as follows:

As above using Equation 4.40(b and d) m_{x1}, m_{x3} are obtained by assuming $m_{x2} = 0$ (that is, the contribution from web to m_x is ignored). Therefore p_1, p_3 can be obtained by using Equation 4.37(b). The sign of p_1, p_3 are determined as

$$p_1 = -\text{sgn}(m_y)p_1, \quad p_3 = \text{sgn}(m_y)p_3 \quad 4.48$$

Using Equation 4.40(a) p_2 is obtained. If the p_2 obtained is more than $p_{2\max}$ the section is considered to be over-stressed. If $p_2 \leq p_{2\max}$, m_y is calculated using Equation 4.40(c) by assuming $m'_{y1} = 0$.

If the obtained m_y is less than the given m_y section is considered elastic: if equal to the given m_y the section is considered plastic, and if more than the given m_y , the section is considered over stressed.

4.9 INTERACTION RELATIONSHIP (UPPER BOUND SOLUTION)

The above finalised patterns are based on several assumptions and it is required to verify the patterns in the theory of plasticity. For the verification, a solution is obtained by an upper bound approach and compared with the lower bound solution. If both the solutions give the same results, then the solutions satisfy the uniqueness

theorem of plasticity and equations obtained are termed as exact within the assumption made.

To obtain the upper bound solution, it is required that the deformation pattern (i.e. neutral-axis pattern) gives the minimum value of the forces. Considering the first pattern of Figure 4.21(a) the assumed strain rate field is specified by six variables with a plastic strain rate $\dot{\varepsilon}_i$ at the centroid of each of the three plates and a plastic curvature rate $\dot{\kappa}_i$ for the bending of the plates, where $i=1,\dots,3$. The subscripts 1, 2 and 3 are used for top flange, web and bottom flange respectively. Fulfilling the compatibility criterion, the strain rate in the flanges are related to web, and is written mathematically as

$$\dot{\varepsilon}_1 = \dot{\varepsilon}_2 - \frac{d}{2} \dot{\kappa}_{2y} \quad 4.49(a)$$

$$\dot{\varepsilon}_3 = \dot{\varepsilon}_2 + \frac{d}{2} \dot{\kappa}_{2y} \quad 4.49 (b)$$

where $\dot{\kappa}_{2y}$ is the Y-component of the plastic curvature rate in the web.

To satisfy the equilibrium condition during a kinematic collapse mechanism, the work done by the external forces \dot{W}_e must be equal to the internal work done (rate of dissipation of energy) during yielding \dot{W}_i and is written as

$$\dot{W}_i = \dot{W}_e \quad 4.50(a)$$

where the rate of dissipation across the section is

$$\dot{W}_i = \int_{A_i} \sigma_y \left| \dot{\varepsilon}_p \right| dA \quad 4.50(b)$$

and the external work done to the section is

$$\dot{W}_e = f \dot{e} \quad 4.50(c)$$

where, $\dot{\epsilon}_p$ is the plastic strain rate, f is the generalized force vector and \dot{e} is the generalized plastic strain rate vector. Considering the entire section, the internal rate of dissipation for the section is given as

$$\dot{W}_i = \left(\dot{W}_i \right)_1 + \left(\dot{W}_i \right)_2 + \left(\dot{W}_i \right)_3 \quad 4.50(d)$$

where the subscripts 1, 2 and 3 are used for top flange, web and bottom flange respectively.

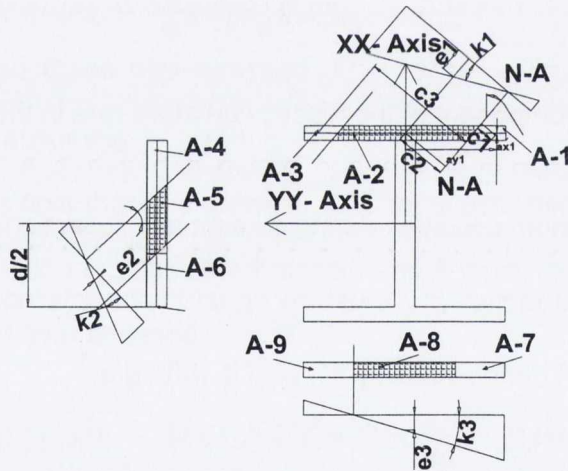


Figure 4.32 Detail of curvature of each plate, strain rate at the centroid of each plate and definition of areas on each plate

When the forces and moments in each plate are given by P_i, M_{xi} and M_{yi} , where i has the same meaning as before, the rate of work done by the external forces for the entire section can be written as

$$\dot{W}_e = P_1 \dot{\varepsilon}_1 + M_{x1} \dot{\kappa}_{x1} + M_{y1} \dot{\kappa}_{y1} + P_2 \dot{\varepsilon}_2 + M_{x2} \dot{\kappa}_{x2} + M_{y2} \dot{\kappa}_{y2} + P_3 \dot{\varepsilon}_{3o} + M_{x3} \dot{\kappa}_{x3} \quad 4.50(e)$$

where, $\dot{\kappa}_{xi}$ and $\dot{\kappa}_{yi}$ are the components of $\dot{\kappa}_i$ in the global X and Y direction of the section.

Considering the top flange, the rate of dissipation is given as

$$\left(\dot{W}_i \right)_1 = \sigma_y \dot{\kappa}_1 (2A_1 c_1 + 2A_1 c_2 + A_2 c_2) \quad 4.51(a)$$

where A_1 , A_2 and A_3 are the areas of different parts of the section, c_1 , c_2 and c_3 are the perpendicular distance from the neutral-axis to the centroid of each area, as depicted in Figure 4.32.

From the figure, it is evident that

$$A_1 = A_3, \quad c_3 = 2c_2 + c_1 \quad \text{and} \quad c_1 = a_{x1} \sin \alpha_l + a_{y1} \cos \alpha_l - a \cos \alpha_l, \quad c_2 = a \cos \alpha_l \quad 4.51(b)$$

where α_l is the angle, a_{x1} and a_{y1} are the centroidal distance of the area A_1 with respect to the global X and Y-axis respectively, as depicted in Figure 4.32 and a is the distance as given by Figure 4.21(a).

Substituting the values of Equation 4.51(b) into Equation 4.51(a) gives

$$\dot{W}_i = \sigma_y \dot{\kappa}_1 (2A_1 a_{x1} \sin \alpha + 2A_1 a_{y1} \cos \alpha + A_2 a \cos \alpha) \quad 4.51(c)$$

The curvature $\dot{\kappa}_1$ is resolved into two components along the XX and YY-axes, as $\dot{\kappa}_{x1}$ and $\dot{\kappa}_{y1}$ respectively such that

$$\kappa_{x1} = \kappa_1 \cos \alpha, \quad \kappa_{y1} = \kappa_1 \sin \alpha \quad 4.51(d)$$

Substituting the values of Equation 4.51(d) in Equation 4.51(c) gives

$$\left(\dot{W}_i \right)_1 = \sigma_y \left(2A_1 a_{x1} \dot{\kappa}_{y1} + 2A_1 a_{y1} \dot{\kappa}_{x1} + A_2 \varepsilon_1 \right) \quad 4.51(e)$$

Similarly the rate of dissipation of energy for the web can be written as

$$\left(\dot{W}_i \right)_2 = \sigma_y \left(2A_4 a_{y4} \dot{\kappa}_{x2} + 2A_4 a_{x4} \dot{\kappa}_{y2} + A_5 \varepsilon_2 \right) \quad 4.51(f)$$

Whereas for the bottom flange it can be written as

$$\left(\dot{W}_i \right)_3 = \sigma_y \left(2A_7 a_{y8} \dot{\kappa}_{x3} + A_8 \varepsilon_3 \right) \quad 4.51(g)$$

where β is the angle, A_4 and A_8 are the areas of web and the bottom flange respectively and a_{x4} , a_{y4} and a_{y8} are the centroidal distance of the area, with respect to the global X and Y-axis respectively.

In the absence of warping strain the curvature of top flange and web remains the same (as discussed in Section 4.7). Therefore when the curvature is resolved into X and Y components these will be the same for the top flange and the web are same. When the curvature of warping strain which is also in the X-direction is considered, it will add to the X component of the curvature (in the absence of warping strain) of the top flange, where as Y-component of the top flange will not change. As no addition of warping strain in the web so its Y-component of the curvature is also be the same as for top flange. Therefore Y-components of curvature of the top flange and web remains the same even after addition of warping strain, therefore, it can be written as

$$\kappa_{y1} = \kappa_{y2} = \kappa_y \quad 4.52$$

Putting the expressions from Equations 4.50(d and e) and 4.51(a, f, and g) and Equation 4.52 into Equation 4.50(a) gives

$$\begin{aligned} \dot{W}_e &= P_1 \left(\varepsilon_2 - \frac{d}{2} \kappa_y \right) + M_{x1} \dot{\kappa}_{x1} + M_{y1} \dot{\kappa}_y + P_2 \varepsilon_2 + M_{x2} \dot{\kappa}_{x2} + M_{y2} \dot{\kappa}_y + P_3 \left(\varepsilon_3 + \frac{d}{2} \kappa_y \right) \\ &+ M_{x3} \dot{\kappa}_{x3} = \dot{W}_i = \sigma_y \left(2A_1 a_{x1} \dot{\kappa}_y + 2A_1 a_{y1} \dot{\kappa}_y + A_2 \left(\varepsilon_2 - \frac{d}{2} \kappa_y \right) \right) + \\ &\sigma_y \left(2A_4 a_{y4} \dot{\kappa}_{x2} + 2A_4 a_{x4} \dot{\kappa}_y + A_5 \varepsilon_2 \right) + \sigma_y \left(2A_7 a_{y8} \dot{\kappa}_{x3} + A_8 \left(\varepsilon_2 + \frac{d}{2} \kappa_y \right) \right) \end{aligned} \quad 4.53(b)$$

writing the left term of the above equation after some rearrangement

$$\begin{aligned} \dot{W}_e &= P_1 \varepsilon_2 + P_1 \frac{d}{2} \kappa_y + M_{x1} \dot{\kappa}_{x1} + M_{y1} \dot{\kappa}_y + P_2 \varepsilon_2 + M_{x2} \dot{\kappa}_{x2} + M_{y2} \dot{\kappa}_y + P_3 \varepsilon_3 + P_3 \frac{d}{2} \kappa_y + \\ &M_{x3} \dot{\kappa}_{x3} \end{aligned}$$

$$\text{As } P = P_1 + P_2 + P_3$$

Therefore,

$$\begin{aligned} \dot{W}_e &= P \varepsilon_2 + P_1 \frac{d}{2} \kappa_y + M_{x1} \dot{\kappa}_{x1} + M_{y1} \dot{\kappa}_y + M_{x2} \dot{\kappa}_{x2} + M_{y2} \dot{\kappa}_y + P_3 \frac{d}{2} \kappa_y + M_{x3} \dot{\kappa}_{x3} = \\ \dot{W}_i &= \sigma_y \left(2A_1 a_{x1} \dot{\kappa}_y + 2A_1 a_{y1} \dot{\kappa}_y + A_2 \left(\varepsilon_2 - \frac{d}{2} \kappa_y \right) \right) + \sigma_y \left(2A_4 a_{y4} \dot{\kappa}_{x2} + 2A_4 a_{x4} \dot{\kappa}_y + A_5 \varepsilon_2 \right) \\ &+ \sigma_y \left(2A_7 a_{y8} \dot{\kappa}_{x3} + A_8 \left(\varepsilon_2 + \frac{d}{2} \kappa_y \right) \right) \end{aligned} \quad 4.54$$

Differentiating the above equation w.r.t. ε_2 gives

$$P = -\sigma_y A_2 + \sigma_y A_5 + \sigma_y A_8 \quad 4.55(a)$$

Again differentiating the above equation w.r.t. κ_y gives

$$P_1 \frac{d}{2} \kappa_y + M_{y1} + M_{y2} + P_3 \frac{d}{2} = 2\sigma_y A_1 a_{x1} + \sigma_y A_2 \frac{d}{2} + 2\sigma_y A_4 a_{x4} + \sigma_y A_8 \frac{d}{2} \quad 4.55(b)$$

But

$$M_y = P_1 \frac{d}{2} + M_{y1} + M_{y2} + P_3 \frac{d}{2} \quad 4.55(c)$$

Therefore,

$$M_y = 2\sigma_y A_1 a_{x1} + \sigma_y A_2 \frac{d}{2} + 2\sigma_y A_4 a_{x4} + \sigma_y A_8 \frac{d}{2} \quad 4.55(d)$$

Differentiating Equation 4.54 w.r.t. κ_{x1} , κ_{x2} and κ_{x3} gives, respectively

$$M_{x1} = 2\sigma_y A_1 a_{y1}, \quad M_{x2} = 2\sigma_y A_4 a_{y4} \quad \text{and} \quad M_{x3} = 2\sigma_y A_7 a_{y7} \quad 4.55(e)$$

Therefore,

$$M_x = M_{x1} + M_{x2} + M_{x3} = 2\sigma_y A_1 a_{y1} + 2\sigma_y A_4 a_{y4} + 2\sigma_y A_7 a_{y7} \quad 4.55(f)$$

Bimoment is obtained as

$$B = (-M_{x3} + M_{x1}) \frac{d}{2} \quad 4.55(g)$$

The above terms when compared with its lower bound solution (discussed in Appendix-B) gives same results, and the uniqueness theorem of plasticity is satisfied. Therefore, the solution is exact within the limits of the proposed theory and the assumption made. Similarly, using the upper bound solution of other patterns,

one may also show that the upper bound solution of other patterns matches the lower bound solution.

4.10 CONCLUSION

In this chapter a seven dimensional plastic interaction relationship is developed using the lower bound approach. The lower bound solution is divided into two parts. In the first part the interaction equations for shear stresses are developed. while the second part deals with the direct stresses.

The interaction equation for the first part is developed using a lower bound approach by assuming a neutral-axis pattern in the case of shear stresses. The equation developed is quadratic by nature. Different options are discussed when one or more of the three forces are not present for the interaction equations.

For the second part, first a study is performed to obtain possible neutral-axis patterns. Two basic types of patterns are obtained namely when the neutral-axis intersects the web and when it does not intersect the web. Lower bound solutions of the obtained neutral-axis patterns are obtained and a procedure is developed which identifies the formation of plastic hinges and the development of the yield surface.

Using the procedure developed, yield surfaces for a typical steel (W12 x 31) section are developed and compared with previous solutions. The inaccuracies and gaps in the previous work are identified. It is also found that the developed yield surface fulfills the theory of plasticity.

The solution of the second part is verified using an upper bound solution, and is found to be exact which verifies the uniqueness theorem of plasticity. The developed theory can be used for the development of yield surfaces and in elasto-plastic analysis.

PRELIMINARY TEST AND SINGLE STRESS RESULTANTS EXPERIMENT

5.1 INTRODUCTION

In the previous chapters, yield surfaces were developed. These developed yield surfaces and previously developed yield surfaces were verified by the numerical approach used in this research. To verify yield surfaces for different combinations of stress resultants experimentally, a testing program was been set up. Two combinations of stress resultants are investigated; firstly biaxial bending and torsional stress resultants and, secondly, axial force, biaxial bending and torsional stress resultants. The structure used throughout the programme for all the experiments is a cantilever thin-walled I-section beam. This chapter deals with the first part of the experimental program in which mechanical properties of the material and capacities of the section for single stress resultants are obtained. A numerical study was also performed to compare the experimental results with finite element simulations.

The mechanical properties of the material of the I-section, which is used in the experiments, were first obtained. Coupon samples were machined from a steel joist (as extracted from the I-section beam used for the main experiments) and tested in a uniaxial tension test at ambient temperature based on British standard BS EN 10002-1 (BSI, 2001).

Thin walled I-section beams were tested in bending separately about both principal axes to obtain the moment capacities and flexural behaviour of the beam. Cantilever beams were tested in bending about the major and minor axis. To obtain the torsional moment capacity and bimoment capacity of the section, two cantilever beams of equal dimensions were tested in torsion. A different test set-up was designed and used for the torsion experiments.

Results obtained from all the experiments of single stress resultants are compared with different theories and with experiments previously performed.

5.2 COUPON TEST

To obtain the mechanical properties of I-sections at ambient temperature, for theoretical verification of the experimental results using different theoretical and numerical approaches, standard coupon tests were performed. Longitudinal specimens were tested in accordance with the European standard BS EN 10002-1 (BSI, 2001) for mechanical properties of the specimens. Test pieces were obtained by machining samples from a 12m length of I-section used to obtain the specimens for several of the beam tests. Four samples were taken at different positions on the cross section, three from the web and one from the flange, as shown in Figure 5.1.

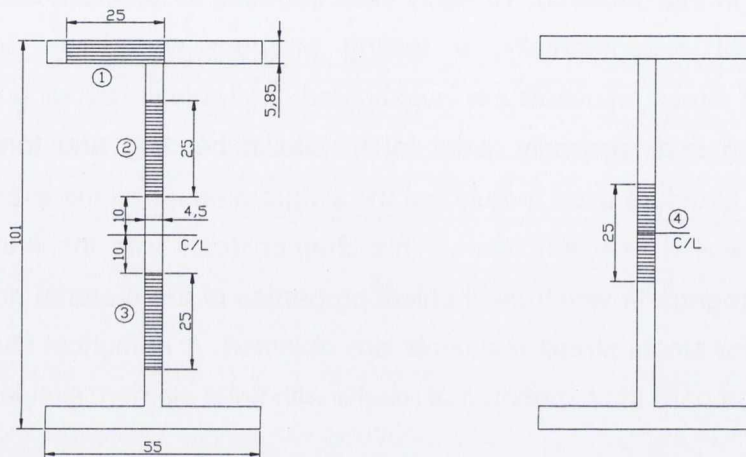


Figure 5.1 Different locations of an I-section from which coupon samples were taken

The locations of the samples were based on typical residual stress patterns (Erglekirk, 1994) for an I-section, as shown in Figure 5.2. Owing to an expected symmetrical residual stress pattern in the flanges, it was decided to machine one sample in such a way that the point of contra flexure lies at the centre of the sample, while the bottom flange and right edge of the top flange were ignored, as depicted in Figure 5.1. For the web, it was decided to take the samples equidistant from the centre of web. Therefore, two samples (numbered 2 and 3, as shown in Figure 5.1), where there is a change from tensile to compressive residual stress, were taken, while one sample (numbered 4, as shown in the figure) was taken from the centre of the web where there is maximum compressive residual stress.

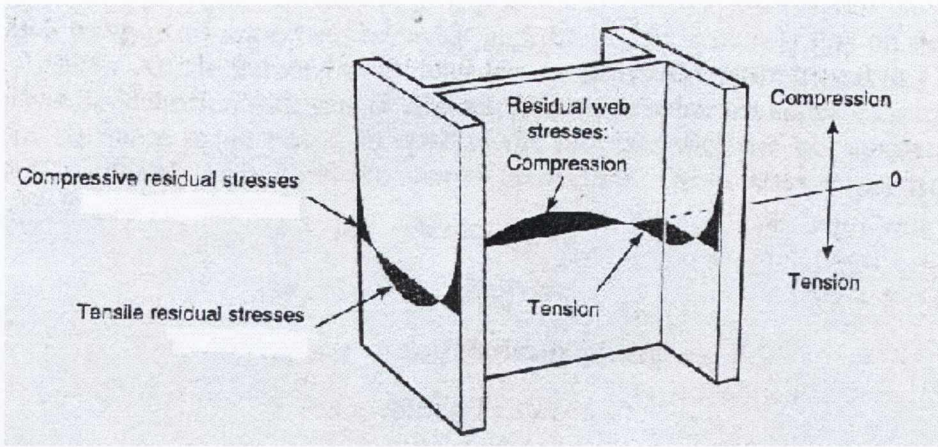


Figure 5.2 Typical residual stress pattern of an I-section (Englekirk, 1994)

Non-proportional samples were used according to the European standard. All coupons of thickness, 5.86mm (for flanges) and 4.5mm (for web) had a 75mm parallel length (L_c) of width 20mm (b), as depicted in Figure 5.3. The parallel length is connected to the grip ends by means of a transition curve with a radius of 20mm . The width of the ends (B) is 25mm . The original gauge length (L_o) of each sample was 50mm , which was marked by scribed lines. The values of these dimensions for the specimens are given in Table 5.1. In the table t is the thickness of the sample before the test, S_o is the cross sectional area of the sample before the test. t_u , b_u and S_u are the thickness, width and cross-sectional area of the sample after the test respectively.

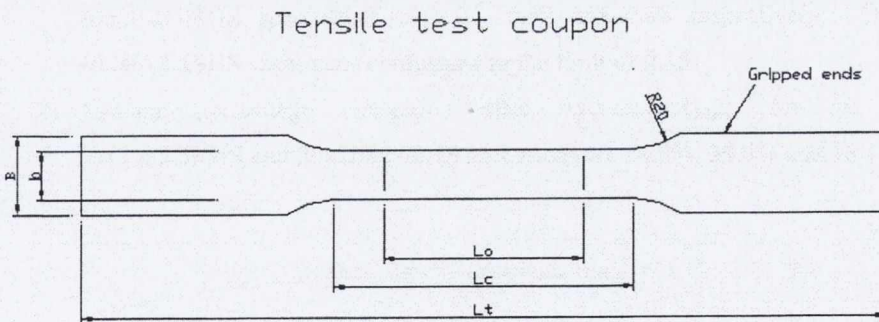


Figure 5.3 Tensile test coupon (Goggins, 2004)

The coupons were tested to failure in an INSTRON displacement controlled testing machine (with friction grips) at a displacement rate of 0.0833mm/sec . This is

S.No	b	t	So	Lo	Lc	Lt	Lu	B	Rm	bu	tu	Su	A50	Agt	Z	Fm	ReH	ReL	Rp,0.20	Rt,0.50	E
	(mm)	(mm)	(mm ²)	(mm)	(mm)	(mm)	(mm)	(mm)	(MPa)	(mm)	(mm)	(mm ²)	(%)	(%)	(%)	(kN)	(kN)	(kN)	(kN)	(kN)	(GPa)
1.00	20.00	4.80	96.00	50.00	75.00	300.00	78.11	25.00	0.44	14.81	3.65	54.06	36.57	28.38	43.69	42.08	32.34	30.01	30.20	29.41	189.08
2.00	20.00	4.10	82.00	50.00	75.00	300.00	69.08	25.00	0.47	15.12	3.51	53.07	38.17	29.97	35.28	38.38	29.98	27.39	27.21	27.46	204.10
3.00	20.00	4.10	82.00	50.00	75.00	300.00	68.72	25.00	0.41	14.70	3.23	47.48	37.45	28.04	42.09	39.73	32.10	29.38	29.64	29.55	208.76
4.00	20.00	4.08	81.60	50.00	75.00	300.00	69.32	25.00	0.47	14.54	2.95	42.89	38.64	29.59	47.43	38.30	29.51	26.92	27.70	27.41	204.40
Avg	20.00	4.27	85.40	50.00	75.00	300.00	71.31	25.00	0.45	14.79	3.34	49.38	37.71	28.99	42.12	39.62	30.98	28.43	28.69	28.46	201.58

Table 5.1 Material properties obtained from Coupon test results.

equivalent to a strain rate of $0.00166s^{-1}$ which is kept constant, as recommended by the standard. A calibrated extensometer of $50mm$ gauge length was used to measure the longitudinal strain. A data acquisition system was used to record the load and extension at regular intervals during the tests.

A typical load-extension graph for one of the specimen up to the point of failure is shown in Figure 5.4. A similar pattern was observed for the remainder of the three specimens, as shown in Figure C.1 in Appendix-C, Section C.1. In the figure, a large extension is observed indicating the ductility of the material. The material properties obtained from the coupon tests are summarized in Table 5.1 and 5.2.

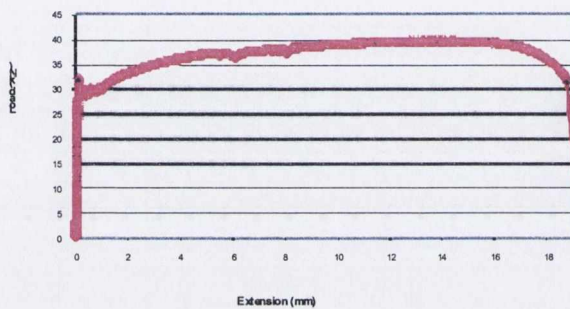


Figure 5.4 Typical load deflection graph for a coupon test (taken from one of the specimens)

S.No	Stress at peak σ_{peak}	Stress at 0.2% Yield $\sigma_{0.2\%}$	Stress at 0.5% Yield $\sigma_{0.5\%}$	Stress at lower yield stress σ_l
	(MPa)	(MPa)	(MPa)	(MPa)
1	438.33	314.58	306.35	312.65
2	468.10	331.80	334.88	334.06
3	484.48	361.17	360.37	358.26
4	467.10	337.80	335.91	329.90
Avg	464.50	336.34	334.38	333.72

Table 5.2 Stresses at different stages of the specimens obtained from Coupon test results.

The upper yield strength R_{eH} , lower yield strength R_{eL} , tensile strength, $R_{p0.2}$ 0.2% proof strength (non-proportional extension) and 0.5% proof strength $R_{p0.5}$ (total extension) were obtained as given in the table, details of which are discussed in BS EN 10002-1 (BSI, 2001). It can be observed that peak loads F_m for all the cases is nearly 30 % more than the load at 0.2 % yield strength ($R_{p0.2}$), as given in Table 5.2. The final gauge length after rupture, L_u , given in the table, was determined using the total extension recorded in the testing machine. It was then used to determine the percentage elongation of 50mm gauge length, A_{50mm} , after fracture. The percentage reduction in area, Z , was also determined and the percentage elongation at maximum force A_{gr} is given in the table.

5.2.1 Coupon test results

Yield stress determination of the constrained and unconstrained plastic flow, stresses at the strain hardening phase, peak stress and Young's Modulus were all required from the coupon test results to facilitate theoretical calculations and finite element analysis in the numerical verification of the experimental results. Yield stress is normally obtained based on a line which is 0.2% strain offset parallel to the slope of the stress-strain diagram (Englekirk, 1994), but this only holds for stress-strain relationships where there is no well-defined plastic plateau. In the case of a well-defined plastic plateau, the yield stress depends on the lower yield stress value R_{eL} .

In Figure 5.5, load against extension is shown for specimen 1 for a extension of 1mm which shows that the material has a well defined plastic plateau, and in these cases, the yield stress is defined using a lower yield stress, σ_l , of the section. In Figure C.2, Appendix-C, Section C.1, similar graphs are shown for the remainder of the specimens. Therefore, the average value of all the lower yield stresses, which is 333.7MPa, is taken as the yield stress of the section at a strain of 0.0017 ϵ , as shown in Table 5.2. A plastic plateau was observed up to a strain of approximately 0.02 in Figure 5.6, and the first strain-hardening slope was observed at a strain of 0.10 at a stress of 425.8MPa. The average peak stress is observed at a value of 464.50MPa and at a strain of 0.29. Young's modulus obtained from the samples ranges from 189.1GPa to 208.8GPa with an average value of 201.7GPa. A stress-strain diagram, based on the average values, is plotted in Figure 5.6.

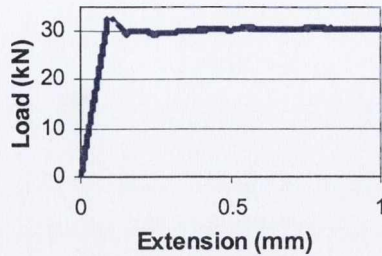


Figure 5.5 Coupon test results of the first specimen up to a deflection of 1mm

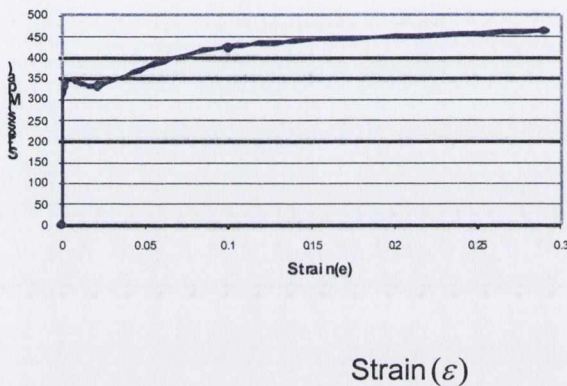


Figure 5.6 Average uni-axial stress-strain diagram

5.3 TESTING BEAM SECTIONS IN FLEXURE

5.3.1 Experimental set-up

Two types of experiments in bending were performed on an I-section, namely about the major and the minor axes using a cantilever arrangement (Figure 5.7(a)). Details of the section used for the experiments are given in Figure 3.5(c). Experiments were performed to establish the failure modes in flexure and the plastic moment capacity M_p of the section. These are compared with the theoretical flexural modes and the theoretical plastic moment capacity, which were calculated (given in Appendix-C, Section C.2) based on a uni-axial stress-strain relationship (Englekirk, 1994). The uni-axial stress-strain relationship was obtained from the coupon test results as discussed in the previous section. Ultimate moment capacities, M_u , for the section were also calculated using the uni-axial stress-strain relationship.

Beam specimen and internal reaction frame

Beams were orientated vertically and welded to a top base plate to create the fixity condition for a cantilever beam, depicted in Figure 5.7(a). There were two spans in

the tests, which were $1.18m$ and $1.24m$. They were used because for the first one, the top base plate was above three other base plates, as shown in Figure 5.7(b), which were used as packers because the tip of the beam as cut, depicted in Figure 5.7(a) was below the height of the tip of the shaft of the actuator of the loading arrangement. The packing was required so that the load can be applied horizontally. In the other experiment, packers were removed and a single base plate was used which increased the span to $1.24m$. All base plates were fixed to a 3000kN capacity internal reaction frame, part of which is shown in Figure 5.7(a).

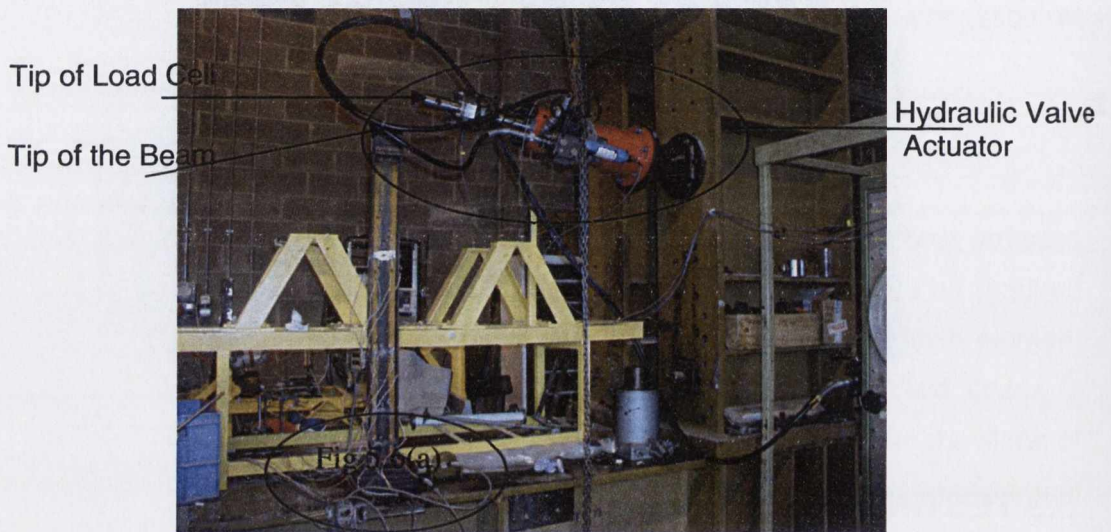


Figure 5.7(a) Experimental set-up for the cantilever beam, bending about the major-axis

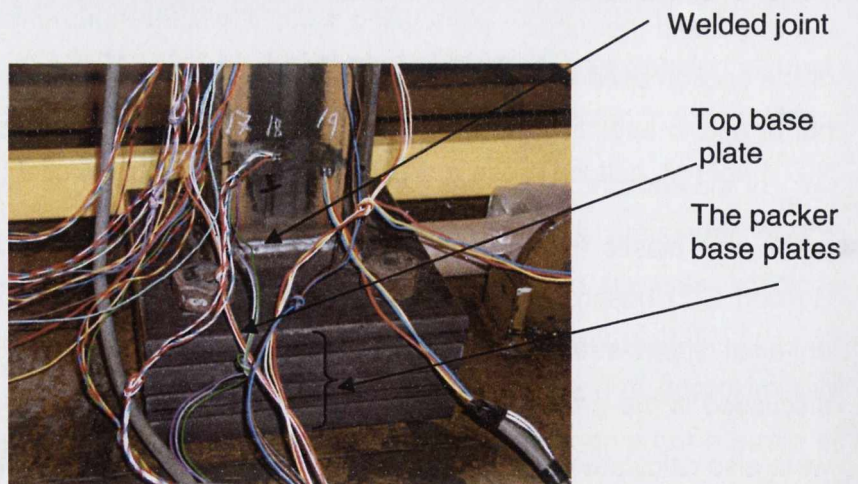


Figure 5.7(b) Beam welded to the base and connected to the internal reaction frame by nut and bolt arrangement.

Deflections, strain measurements and load control

The overall load-displacement responses, together with a measurement of strains at different locations were required in each test. Hence, a load cell, linear variable differential transformers (LVDT) and strain gauges were employed.

Deflections were measured at different locations: Deflection at the top was measured in each case by an internal LVDT contained in the hydraulic valve actuator, which is depicted in Figure 5.7(c). Deflections were measured at other locations using external LVDTs. The type of external LVDT used was an RDP electronic ACT200 LVDT with a linear range of $\pm 50mm$ and sensitivity of $28.44mV/V/mm$ with $5V(RMS)$ $5Hz$ energising supply.



Figure 5.7(c) Load cell and RDP actuator mounted horizontally to the frame.

For the initial test on a cantilever, with a span of $1.18m$, deflections were measured at distances of $0.195m$, $0.395m$ and $0.745m$, from the top base plate, whereas for a span of $1.24m$ (in the second cantilever test to be described presently), they were measured at distances of $0.33m$ and $0.60m$ from the base plate.

Strain gauges were installed at those locations where displacements were measured and also near the fixed end of the beam to measure the peak flexural strain and the axial strain. Axial strain measurement was required to observe any secondary axial effects that can arise in a cantilever type bending behaviour under large deflections. Flexural strains were measured at the outer edges of flanges for bending of the beam about the major-axis in order to measure both the peak tensile and compressive strains. Alternatively, strains were measured at the outer edges of both flanges at the left and right corner of the flanges for monitoring the bending of the beam about the minor-axis. The locations of the strain gauges are shown in Figure 5.8.

An RDP load cell of capacity $100kN$ was attached to the hydraulic valve actuator, which was mounted horizontally to the frame (as depicted in Figure 5.7(c)) and had a deflection range of up to $100mm$. The theoretical deflections obtained at the free end of the beam at plastic moment capacities about both the principal axes were less than this limitation of $100mm$ (Section C.2). Therefore, the restriction on the maximum deflection of the actuator was considered reasonable, as it should allow the beam to obtain its plastic moment capacities experimentally. The whole set-up for the bending of beams about the major and minor axes is shown in the foreground of Figure 5.7(a).

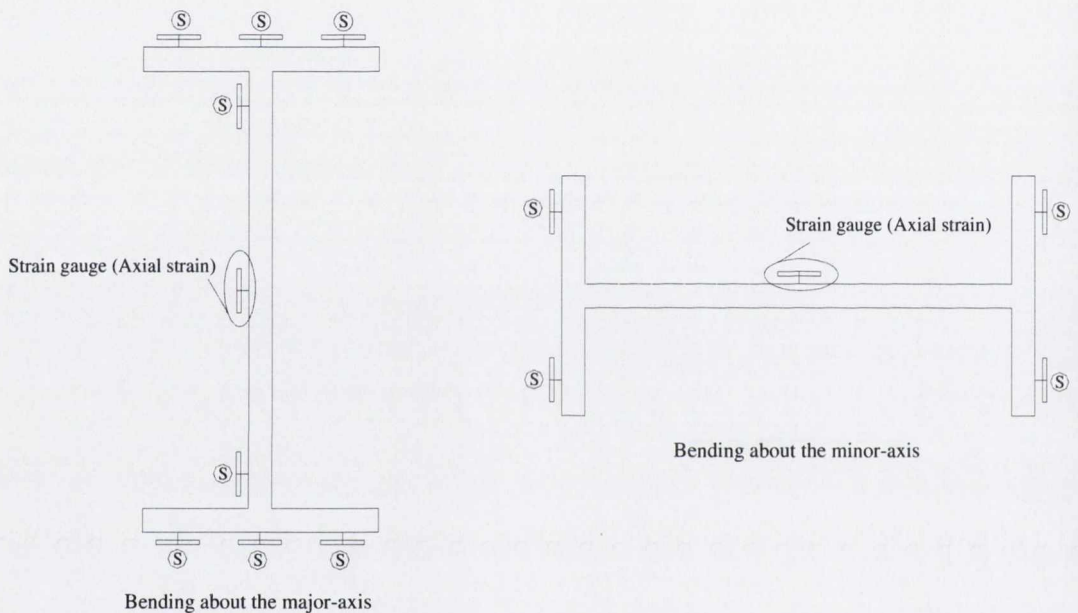


Figure 5.8 Location of strain gauges for cantilever beam, bending of beam about the major and minor-axes

Static monotonic loading was applied based on a deflection controlled loading method at a rate of no more than $0.02mm/sec$. The loading rate was selected to ensure that the beam has enough time to equilibrate, and was not influenced by any dynamic or impact effects (Goggins, 2004).

Data transfer and storage devices

The System 5000's instrumentation hardware depicted in Figure 5.9 is designed to incorporate all the features required for precision strain measurement under static loading conditions, while maintaining flexibility and ease of use. System 5000

components can easily be configured using Strain-Smart Software for each test requirement.

StrainSmart software, which works in the Windows environment, is used for acquiring, reducing, presenting and storing measurement data from strain gauges, strain-gauge-based transducers, thermocouples, temperature sensors, LVDTs, potentiometers, piezoelectric sensors, load cells and other commonly used transducers.

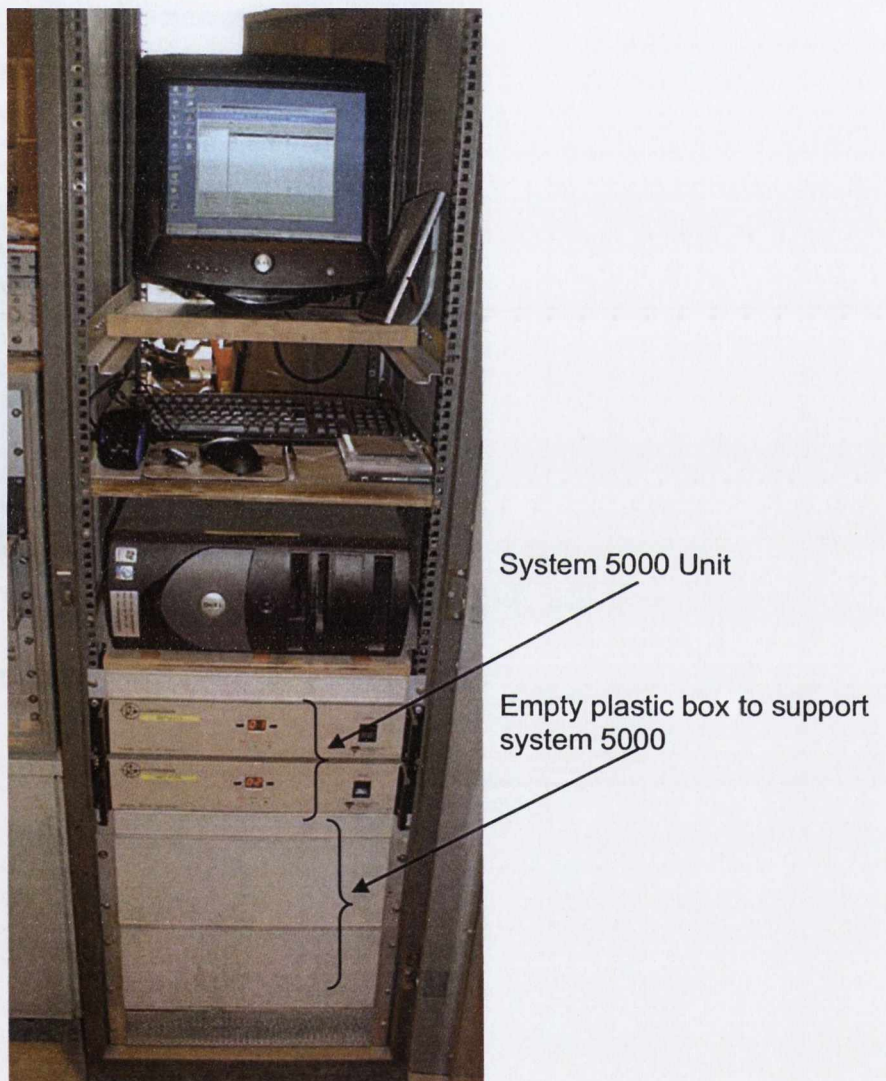


Figure 5.9 System 5000 unit and Personal Computer

Test Control

The actuator command console, shown in Figure 5.10, generates the signal and passes it to the servo-valve control. An Amsler hydraulic valve pump (power pack) is also attached to the servo-valve control (as shown in Figure 5.11). Based on the signal generated by the actuator, the pump pushes the actuator, which opens, or closes, to move the actuator to the required position. The load cell measured the load based on the resistance provided by the specimen, when it is displaced by the actuator. Both the load cell and the internal LVDT send a return voltage to the command console. The voltage, V_{ret} , from the displacement transducer is compared to the original voltage signal V_{out} . If the actuator has not reached the correct position, V_{out} is updated and sent to the servo-valve control. A flow chart of the process is shown in Figure 5.11.

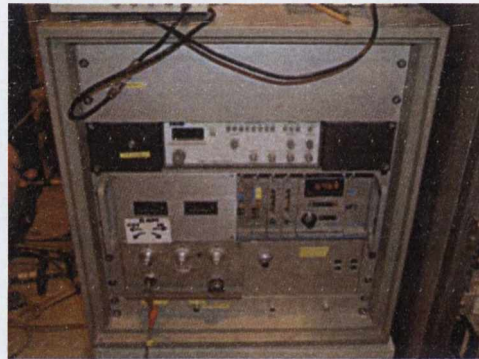


Figure 5.10 Actuator command console

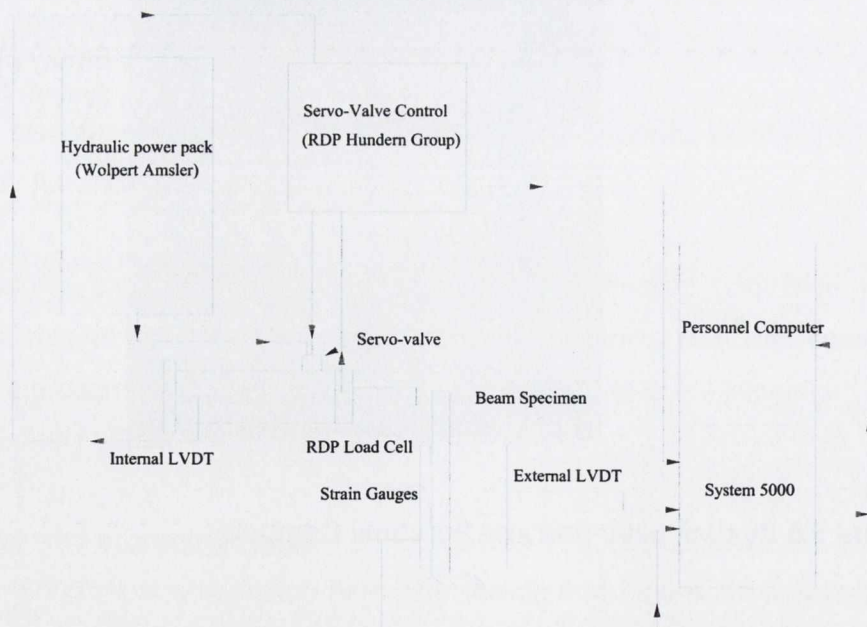


Figure 5.11 Flow chart of data processing and storage for experiments

This is a continuous process and may be assumed to happen virtually instantaneously. During the process, signals from the internal LVDT and the load cell are received by the actuator command control. At the same time, signals from the load cell, external LVDTs and strain gauges were received by the System 5000.

All the signals received by the System 5000 were transferred to a data storage card installed in the computer and is synchronized by the software StrainSmart. The StrainSmart stores the data in the computer hard disk in ASCII-Code where it can be read in Microsoft Excel to allow interpretation of the experimental results.

5.3.2 Bending of beam about the major-axis

Bending of the beam about the major axis was performed for a cantilever. Two experiments were performed in total in major axis bending. The spans selected were $1.18m$ and $1.24m$.

Cantilever beam bending about the major axis, $1.18m$ span

An experiment was performed for a span of $1.18m$ to obtain the flexural capacity and to observe the failure mode of the beam. The load-deflection graph is shown in Figure 5.12. The load was applied to a maximum value of $16.3kN$ yielding a tip deflection of $37.3mm$. In the load-deflection graph, non-linear behaviour was observed to commence at a load of approximately $7.0kN$, as shown in the figure. Fluctuations in loads can be observed around the peak-loading region between deflections of $20mm$ and $50mm$. Failure of the weld in the base plate was observed during the loading. This fluctuation of loads in the peak-loading region indicated that the welded connection started to crack at that time and was one of the reasons for beam failure.

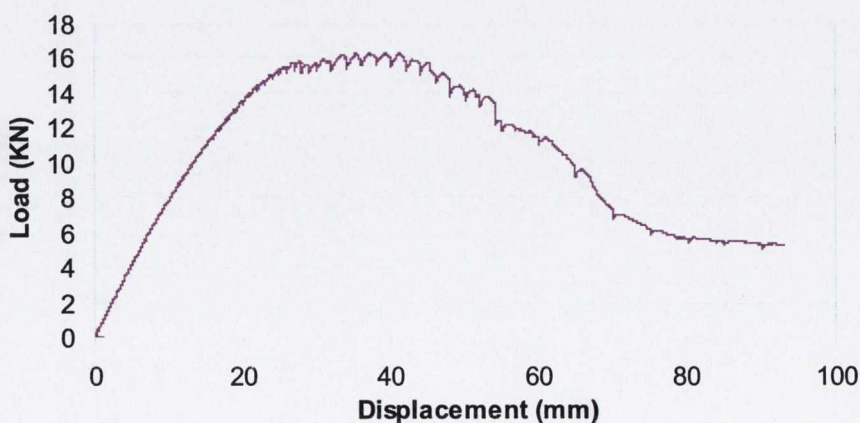


Figure 5.12 Load-deflection behaviour of beam of span $1.18m$

There can be two principal reasons for failure; firstly partly due to the development of a weld crack, and secondly due to yielding of the section. To investigate the cause of failure, the maximum flexural strain, near the fixed-end at the tensile face was observed. A graph is drawn for the flexural strain against the flexural stress, which is obtained based on elastic theory, as shown in Figure 5.13. Linear behaviour can be observed in the graph up to the peak stress of approximately 0.5GPa . Significant fluctuations in the flexural stress with an overall stress release were also observed in the graph, indicating the failure of the weld. A fall in the stress without a commensurate decrease in the strain was observed (also because of weld failure). This cause of failure due to weld failure is supported by the stress-strain graph. A destressing of the beam, as seen by a reduction in stress (with a linear pattern of similar slope to the original) and reduction in strain is followed by evidence of an amount of residual plastic strain in the beam indicating that the section had yielded.

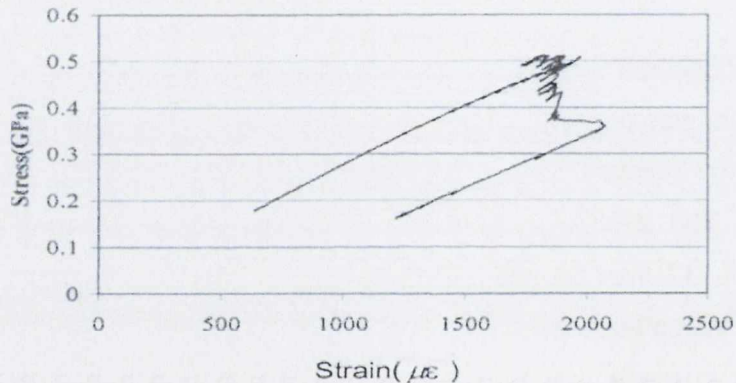


Figure 5.13 Graph showing relationship between flexural stress and flexural strain.

Hence, it can be concluded that failure of the beam was a combination of weld failure, and yielding of the section. Uplifting of the base plate was measured to determine its effects on the failure but was found to be negligible.

Cantilever beam bending about the major axis, 1.24m span

Owing to the failure of the 1.18m cantilever beam because of the weld cracking, another experiment of a cantilever beam in bending about the major axis was performed in pursuit of information on the approximate plastic moment capacity of the section about the major-axis.

The number of base plates in this experiment was reduced to one, as compared to four in the previous cantilever beam experiment. Therefore, a longer beam length

(1.24m) was required, due to the reduction in the number of base plates so that the tip of the beam, (depicted in Figure 5.7(a)) was able to coincide with the loading shaft of the actuator, which was kept horizontal during load application. To avoid welding failure, larger welding legs were provided. Deflections and strain gauges were measured at the locations discussed in Section 5.3.1.

The load-deflection graph is shown in Figure 5.14 in which a non-linear response is observed to commence at a load of approximately 7.0kN, which can be considered as the yield point. This decrease in slope of the load-deflection graph continues up to a load of approximately 11.3kN, producing a plastic moment capacity of 13.9kN.m. During this stage, the beam was in the elastic-plastic phase. Beyond this, it maintained an increase in load with a more or less constant slope. The constant slope was maintained up to a maximum actuator deflection of 100mm at which the maximum load of 13.4kN, produced a moment of 16.6kN.m. This stage of constant slope can be referred to as the strain-hardening phase. The graph shows a similar pattern to that observed for the bending of the beam in the previous experiment. Young's modulus obtained in this experiment is approximately 178GPa. This value differ from the Young's modulus obtained from the coupon's test result and the difference is discussed in the next section.

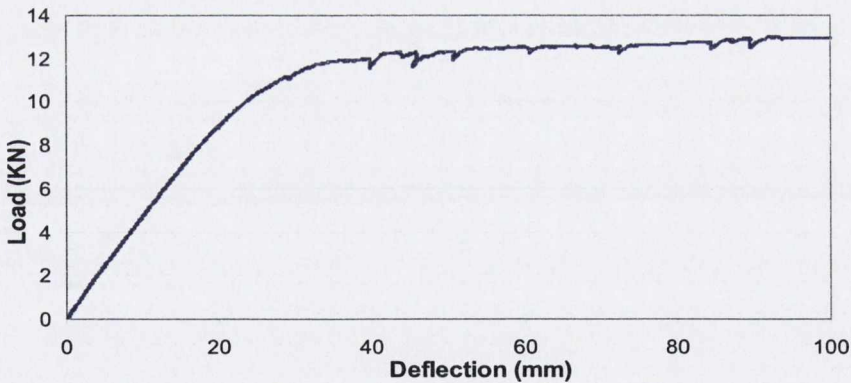


Figure 5.14 Load-deflection curve of cantilever beam of span 1.24m

The constant slope region has a low gradient, which can be considered as the plastic phase with strain hardening of the material. The moment at the start of the phase, which is 13.9kN.m (under a load of 11.3kN) can be considered as the plastic moment capacity of the section. The maximum moment of 16.6kN.m (under a load of 13.4kN) cannot be considered as the ultimate moment capacity because of the need to

terminate the experiment due to the limitation of the maximum deflection of the actuator, and it was not possible to achieve its ultimate load because of the limited maximum deflection. However, the ultimate load was predicted theoretically based on the results of coupon test (Appendix-C) to be $14.84kN$, yielding a moment of $18.4kN.m$.

A comparison is made in percentage terms between the differences of strain at the extreme faces of the section for both the tensile and compressive flanges (Table 5.3.) In the table, the second and third columns present the percentage differences of strain between both the faces of the section located at distances of $0.06m$ and $0.60m$ from the base under increasing load.

For the cross section nearer to the fixed end, the differences are satisfactory up to the limit of linear behaviour of approximately $6kN$. Beyond this limit, the difference in the strains of the two faces started to increase and is significant at a load of $10kN$. The difference in the strains is because the compressive strength of steel is practically higher than the tensile strength, in the strain hardening phase which resulted in further yielding at the tensile face without major increase of yielding at the compressive face. This is because that in tension the cross-sectional area decreases with increasing load, whereas in compression it increases with increasing load (Boresi and Schmidt, 2003). Hence, there was an increase in compressive stress, without an increase in stress at the tensile face. This was the major cause of differences in the strain results between the two faces in the non-linear region of behaviour. The other cause of the difference could have been axial strain due to secondary effects, but this was found to be insignificant.

For the cross section furthest from the fixed end results are stable, indicating no sign of local buckling.

Moment capacities and Young's modulus

The plastic moment capacity of the section when tested about its major-axis obtained by the experiment was $13.9kN.m$. In contrast, the plastic moment capacity based on the uni-axial yield stress predicted from the coupon test results was obtained as $13.47kN.m$. Therefore, the plastic moment capacity of the beam in flexure can be taken as an approximate average value obtained from both the experiments as $13.69kN.m$.

Load <i>kN</i>	% Variation at 0.06 <i>m</i> from the base	% Variation at 0.60 <i>m</i> from the base
2	2.30	2.00
3	2.30	1.81
4	2.70	2.12
5	3.10	2.17
6	3.86	1.96
8	6.80	1.87
10	14.71	1.70

Table 5.3 Percentage difference of strain between the compressive face and the tensile face of the beam at different locations

Owing to the restriction in the maximum deflection of the actuator, it was not possible to achieve the ultimate moment capacity. However, the maximum moment achieved was 16.6*kN.m*. Using the coupon test results, the ultimate moment capacity calculated (discussed in Appendix-C) based on the procedure discussed by Englekirk (1994) was 17.97*kN.m*.

Young's modulus was calculated based on the deflection obtained from both the cantilever experiments. The average value obtained was 178*GPa*. An average value obtained from the coupon tests result is 201.6*GPa*. There is a significant variation in the Young's modulus between the two results and there are several possible reasons for this. Firstly, in a hot rolled section, curvature and, hence, deflection is significantly affected by residual stresses (Englekirk, 1994) which result in a higher deflection as compared to deflection based on elastic theory. Secondly, shear deformation can influence the bending deformation of the beam (Trahair and Bradford, 1988). Thirdly, modes of application of loads were different in all the three cases. In the case of the coupon test results, samples were machined and tested for the uni-axial stress state in tension, where a Young's modulus is based on $k = AE/L$, which assumes a uniform distribution of stress on the cross section. Alternatively for the beam, when tested in flexural mode, Young's modulus was calculated based on tip deflection of cantilever of $\Delta = PL^3 / 3EI$, where these formulas are principally based on the Euler-Bernoulli hypothesis. This shows that machining the sample changes its mechanical properties. As discussed in Chapter 3, plastic moment capacities based on this assumption vary by 2-3%.

5.3.3 Cantilever beam bending about the minor axis

In the case of minor axis bending, the same experimental set-up was used (with a $1.24m$ span) as was used for the bending of the beam about the major-axis in the previous experiment. LVDT and strain gauges were used to monitor deflections and strains in the beam. Details about the locations of LVDT and strain gauges were given in Section 5.3.1.

The load-deflection graph is shown in Figure 5.15. In the figure, non-linearity, which can be considered as the first point of yielding, commenced at a load of approximately $1.7kN$ (This load is obtained based on 0.0017ε i.e. this strain is the yield limit for strain and this load produce a moment of $1.49kN.m$), beyond which the beam showed a sharp decrease in slope of the load-deflection graph, up to a load of nearly $2.40kN$, (which produced a moment of $2.98kN.m$) during which, the beam was in the elastic-plastic phase. Beyond this load, it maintained an increase in load with more or less constant slope, which could be identified as the plastic phase with the influence of the material property of strain hardening. The constant slope was maintained up to a maximum load of $2.70kN$, (which produced a moment of $3.35kN.m$) at the maximum actuator deflection of $100mm$.

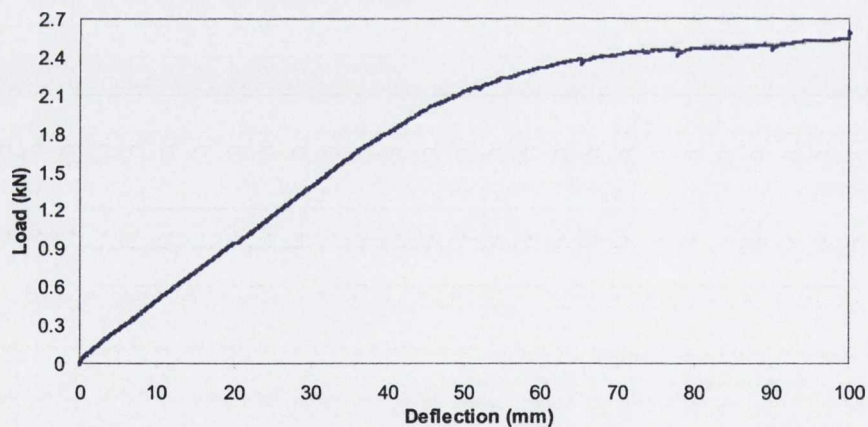


Figure 5.15 Load-deflection graph of beam bending in minor direction

A similar comparison to the previous experiment, was made between the differences of the flexural strain at both the faces (Table 5.4). Strain gauges were installed at distances of $0.06m$ and $0.6m$ from the base of the beam. It can be observed that the variation of strain for the left flange is 13.84% at a distance of $0.06m$ from the base. At higher loads in the same column there is a decrease of percentage differences. The reason for higher values of difference is due to local buckling or due to bedding down of the specimen during the start of the experiment. The percentage differences

at the other three sides were not more than 5.7%, which indicate that the beam behaviour was a typical flexural behaviour.

Load <i>kN</i>	% Variation at 60mm from the base		% Variation at 600mm from the base	
	Left flange	Right flange	Left flange	Right flange
0.4	13.84	2.94	2.22	1.93
0.8	12.17	3.38	2.40	1.52
1.2	11.05	1.16	1.53	4.65
1.6	9.45	2.20	3.08	3.71
2	11.53	1.80	1.01	3.84
2.5	6.80	not possible	0.80	5.66

Table 5.4 Percentage variation of stress at the tensile face and at the compressive face of the beam

Moment capacities and Young’s modulus

Young’s modulus obtained from the load deflection relationship of the beam is approximately 184GPa. The modulus was calculated by drawing a straight line on the linear part of the load-deflection graph. The value differs from the Young’s modulus obtained from the coupon tests result and the values of the modulus obtained in the previous experiment. The difference between the coupon’s test result and the experiment has been discussed previously.

The variation of difference between the experimental results for the two bending axis cases is 3.4% which is not substantial. Young’s moduli between both modes of the flexural bending of the experiments is slightly different for the section in the two different axes. It has been discussed that residual stresses change the curvature and ultimately the deflection of a beam, (Englekirk, 1994). Thus the residual stress pattern, depicted in Figure 5.2, can affect the deflection of the beam and, hence, the modulus. When the beam bends about the major axis, both web and flanges act in resisting the load and residual stress of the entire section affects the deflection. In contrast, bending about the minor axis is mainly resisted by flanges, hence the effect of residual stresses in the web is ignored. Hence residual stresses influence differently the deflection for both the cases and thus on the moduli which are measured.

The moment at the start of the plastic phase, which is $2.98kN.m$ can be considered as the plastic moment capacity of the section whereas, a maximum moment of $3.35kN.m$ occurred under a maximum deflection of $100mm$. The theoretical plastic moment capacity, M_p , and the theoretical ultimate moment capacity of the section based on the coupon's test results are $3.14kN.m$ and $3.91kN.m$ respectively. Both the theoretical and experimental plastic moment capacities compare well to each other with a difference of only 5.7%.

5.4 TESTING BEAM SECTION IN TORSION

5.4.1 Experimental Set-up

Design of Test Rig

Owing to lack of availability of an experimental set-up in the Structural Laboratory for the application of a torsional load at the free end of a cantilever beam, a rig was designed ab initio for this load application. The rig was designed not only for torsional loading, but it also had to have the provision to perform other experiments (as discussed in chapter-6), in which torsion in combination with the other active stress resultants are applied to the section.

Procedure to design Rig

To apply pure torsion without any flexure, it was decided to use a cable wire system in which the free end of the beam is welded to a base plate, which was welded to a circular drum around which the cables were wrapped, as depicted in Figure 5.16 and 5.17. Both the cables were parallel to each other throughout the load application, hence forming a pure couple or torsion to rotate the beam. Tension in the cable causes the drum and thus the beam to rotate. When other loadings were applied in combination with torsion, one of the two cables was removed to allow evaluation of the combined effects of bending and torsion (as discussed in Chapter-6). The position of the beam relative to the cable wire location is discussed later.

It was known that the force in the two cables had to be equal, if only pure torsion was to be applied. Therefore, an arrangement was finalized in which the cable was wrapped around the drum, guided by two pulleys, which were linked to the tip of the shaft of the actuator by another pulley, as depicted in Figure 5.16. Movement of the actuator shaft pulls the pulley, which causes the cables to move in the directions

depicted in the figure, which cause the drum and ultimately the beam to rotate in pure torsion.

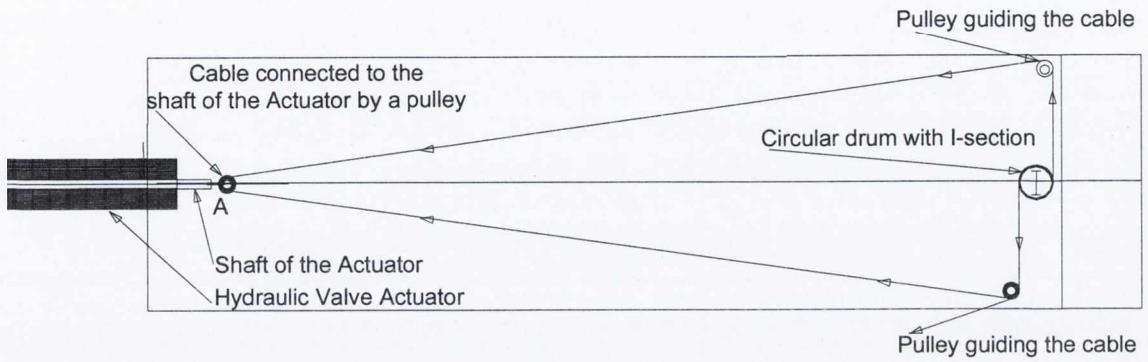


Figure 5.16 Initial set-up for the application of torsion load

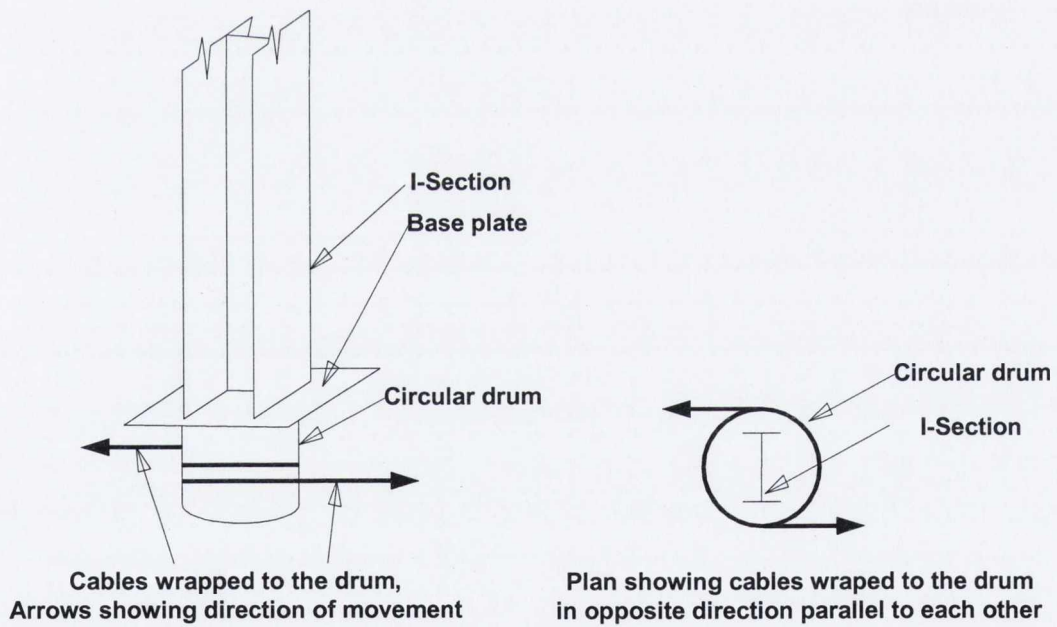


Figure 5.17 Cable-wire set-up used for pure torsion experiment

The movement of the shaft of the actuator is reflected in the movement of the cable, which causes rotation at the free end of the beam. Allowance must also be made for the extension of the cable as the tension develops with shaft movement.

Further the extent of the beam rotation depends on the diameter of the drum used. The greater the diameter of the drum the greater will be its circumference, and the greater the cable movement which is required to obtain a given rotation. This is illustrated in Figure 5.18, where different radii $R1$ and $R2$ are required to deliver the same degree of rotation θ . Therefore, two different arc lengths $A1$ and $A2$ of the cable (for the two different radii) are required for this rotation. Hence, a smaller diameter of the drum will require less length of movement to give a rotation θ , as compared to a larger diameter of the drum for the same rotation. Therefore, it was decided to keep the diameter of the drum to its minimum.

However, a problem could arise with a smaller diameter in those experiments (discussed in Chapter-6) when only one side of the cable is used. If one side of the cable is used only then the smaller diameter could restrict the amount of bending component when other loads were applied in combination with torsion. Therefore, it was decided to use a diameter that can attain a reasonable component of bending and torsion for the other experiments. A minimum diameter of $0.174m$ was thus selected.

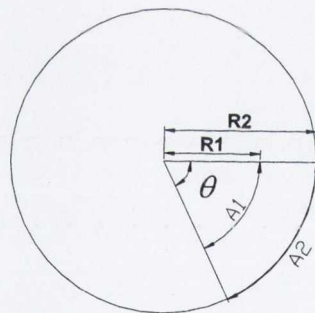


Figure 5.18 Different radii and arc/cable lengths for similar rotations

Given the selection of the diameter, it was required to calculate the corresponding amount of movement of the actuator shaft to induce pure torsional failure. The amount of movement in the shaft to achieve 180° rotation was deemed to be approximately $220mm$ (including cable extension), far beyond the actuator limit of $100mm$. Hence a new system of load application had to be devised, as shown in Figure 5.19. A fulcrum beam is used to amplify the actuator shaft movement (beam ABC in the figure). The shaft at C moves the pulley at point A rotating about the fulcrum in the figure. Movement of point A causes the cable to move to achieve the required rotation for the given diameter of the drum. In modifying the test rig set up

(in detail in Figure 5.20) by the use of a lever arm arrangement, movement of the shaft at C will cause a greater movement at point A based on the ratios of distances (D_1 , D_2) and (L_1 , L_2), as depicted in Figure 5.20. With a maximum $D_1=100\text{mm}$ and a required D_2 of a minimum of 220mm , the lever proportions were chosen as $L_1=1.36\text{m}$ and $L_2=3\text{m}$.

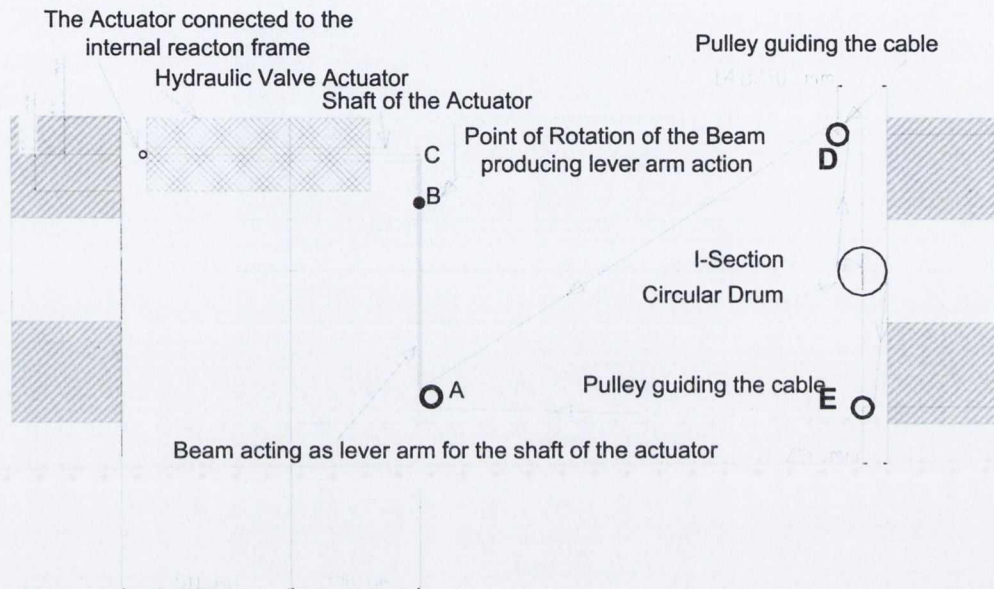


Figure 5.19 Final Set-up of the Experiments (Not to Scale)

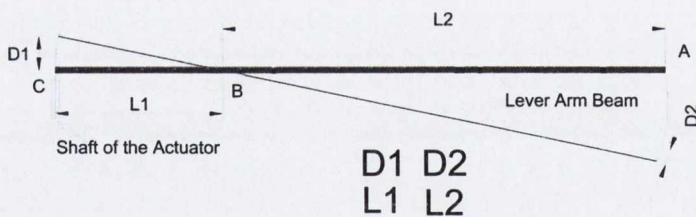


Figure 5.20 Lever arm action to provide additional movement at point A

The cross section of the lever arm beam was selected to minimize the local elastic deflection Δ , which would arrive during load transfer from the shaft to point A. To this end a $200\text{mm} \times 100\text{mm} \times 10\text{mm}$ hollow section was used.

The test cantilever I-beam was fixed vertically and welded to a base plate, which was connected to a larger base plate by a nut and bolt arrangement. The larger base

plate was rigidly fixed to the internal reaction frame, depicted in Figure 5.21. At the free end of the beam, the details as discussed above can be seen in the figure.

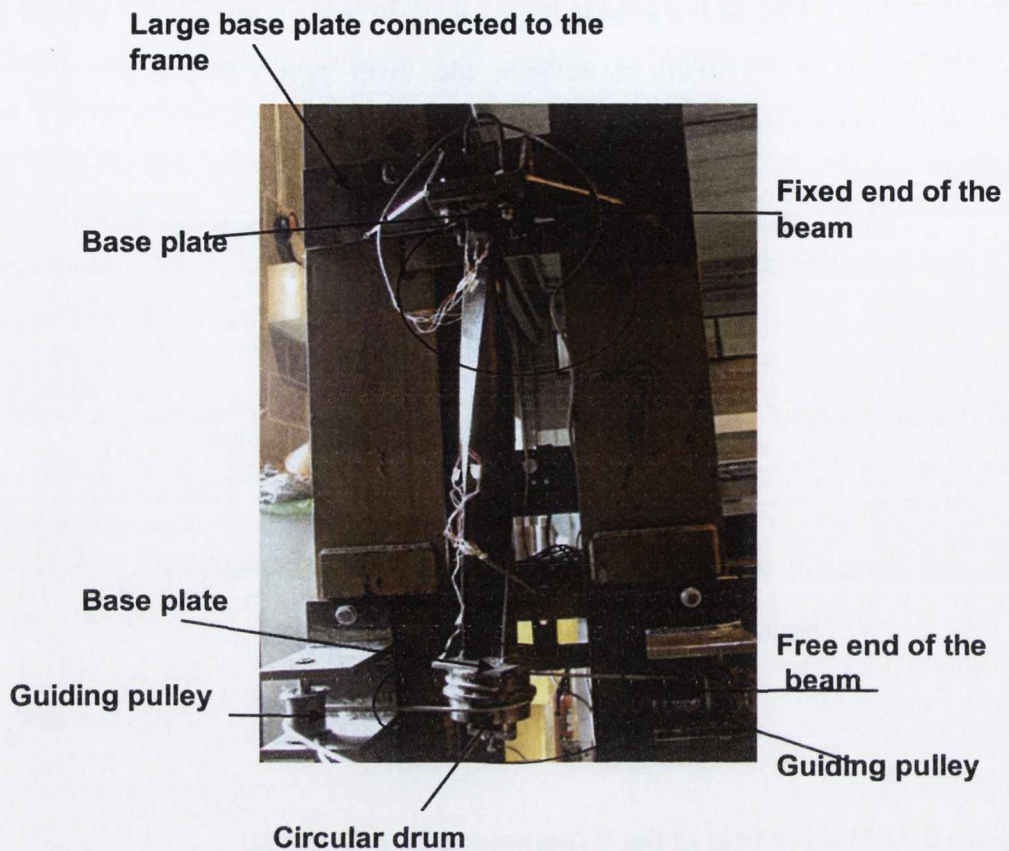


Figure 5.21 The beam failed in torsion fixed to the internal reaction frame

Mechanism of load application for torsional rotation of the beam

The movement of the shaft causes movement at point C, as indicated in Figure 5.19. The movement of this point will cause point A to move pivoting about B, which would tension the continuous cable using the 'frictionless' pulley at point A. Hence the movement of the pulley at A, through tensioning around pulleys D and E, will cause the rotation of the beam through equal and opposite tensions in the parallel cables attached to the drum, as depicted in Figure 5.17. Other effects which will occur will be because of stretching of the cable during transfer of load. The stretching will be elastic (by specific design of the cable diameter) and will thus demand more movement of the pivot A to achieve a required rotation. Therefore, an adjustment factor is required when a relationship is determined between cable load, cable extension, torque and I-beam rotation. It was decided to use a cable diameter which minimizes the stretching under tension. Based on the amount of load calculated, as discussed in Appendix-C, it was decided to use a diameter of 8mm for the cable,

which can have a maximum extension of less than $7mm$ under the anticipated cable maximum load.

Load control, rotation and strain measurements

Two experiments were performed for torsion. In the first experiment a lateral movement was noticed. However, the movement was not recorded. Therefore another torsion experiment was performed with the same setup but with the addition of a device for measuring horizontal movement. The overall torsion-rotation responses, together with a measurement of deflections (about major and minor axis) at the beam specimen end and strains at different locations along its length were required in each test. Rotation at the free end was measured using a $4.7kV$ potentiometer.

Loading was applied based on a deflection controlled loading method at a rate of $0.02mm/sec$. The same load cell that was used in the previous experiments was attached to the hydraulic valve actuator (Figure 5.7(c)), which was mounted horizontally to the frame. The whole set-up is depicted in Figure 5.22.

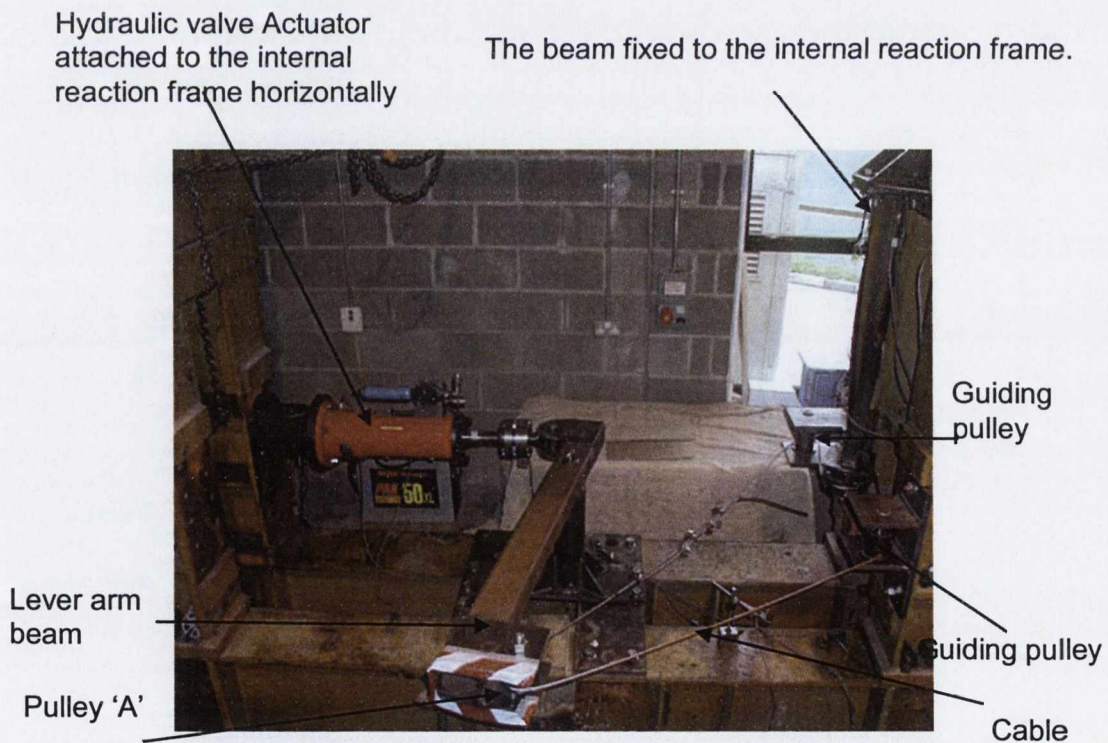


Figure 5.22 Pure torsion experimental set-up

Strain gauges were installed at two different locations. These are installed at distances of $75mm$ from the fixed end of the beam and at the mid span of the beam.

Different positions of the strain gauges were selected for the two experiments to establish the torsional response. Details of the position of the strain gauges are depicted in Figure 5.23. All the strain gauges 1-13 were installed to measure the direct strain, except number 8, which was used to measure the shear strain. Strain gauge numbers 14, 15, 16, and 17 in the second experiment were installed to measure the rotational strain. Strain gauges used to measure rotational and shear strain were installed at an angle of 45 degrees. Locations of strain gauges were finalized based on the behaviour of the beam in torsion, where warping and rotation distortion were considered during the selection.

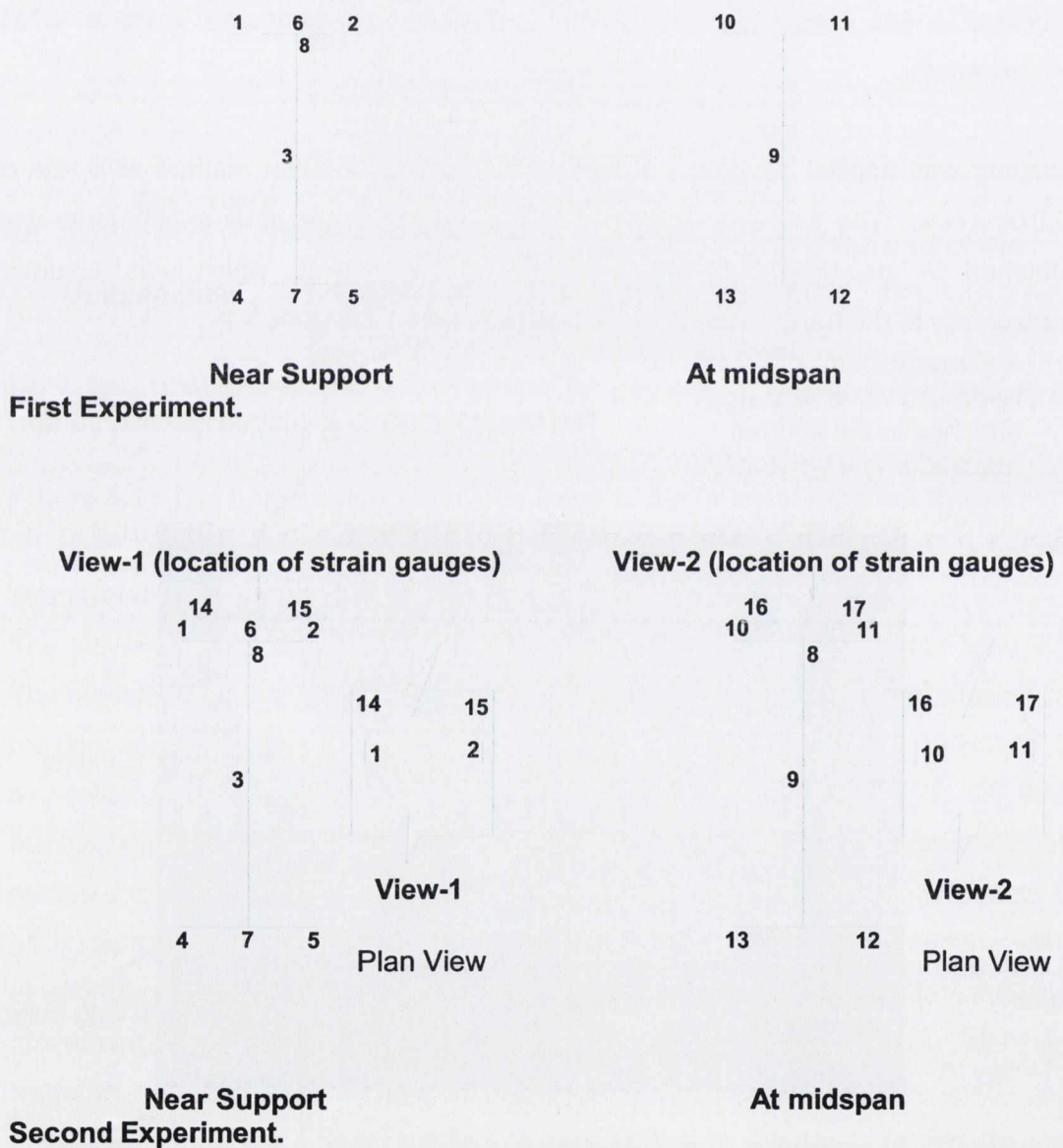


Figure 5.23 Position of the strain gauges for torsion experiments

Measuring Deflection

Deflection at the tip of the actuator was measured in each case by an internal LVDT contained in the actuator. In the first experiment, only rotations and strains at different locations are measured, and no arrangements were made to measure the deflection at the free end of the beam. However, a significant horizontal flexural deflection was observed to occur in the latter stages of the first torsion experiment and a permanent deflection (arising from plastic behaviour) can be observed after the torsion test in the unloaded beam, depicted in Figure 5.21. Hence, it was decided to measure the deflection at the end of the beam in the second experiment.

Owing to the rotation of the beam, it was not convenient to measure directly the deflection of the beam using LVDTs. Therefore, an indirect method was adopted, in which high resolution video images were recorded in two perpendicular directions using camcorders to measure the deflection by recording high resolution videos of the movement of the beam and measuring the deflection using advance editing software (called Measure) normally used for picture and film editing. The locations of the camcorders are identified in Figure 5.24. One of the camcorders is visible in the figure. The other camcorder, which was between the twin vertical columns of the internal reaction rig (where it was not possible to photograph its location), is not shown in the figure. The directions of images recorded by the camcorders are also shown, where they were positioned to record the movement of the beam with reference to two orthogonal grid boards (orientated with the flange/web axes), which were set-up so as to be visible in either one of the video images. A close view of the boards is depicted in Figure 5.25. Movement of the beam can be monitored in the video, where the amount of movement about either axis of the beam can be tracked after using the image processing software and the boards to measure lateral movement. To relate the deflection of the beam to the applied loads and applied deflection of the actuator, two odometers were installed (as seen in Figure 5.25), one of which shows the variation of load in terms of voltage on its screen and the other shows the deflection of the actuator in terms of voltage. Both were installed in the line of sight of the videos. The odometers were linked to the actuator command console box (depicted in Figure 5.10) where a change in the load and the deflection are related in terms of change in the voltage visible in the screen. Hence, changes of voltages were correlated to the loads and to the corresponding deflections of the tip of the beam in the horizontal plane.

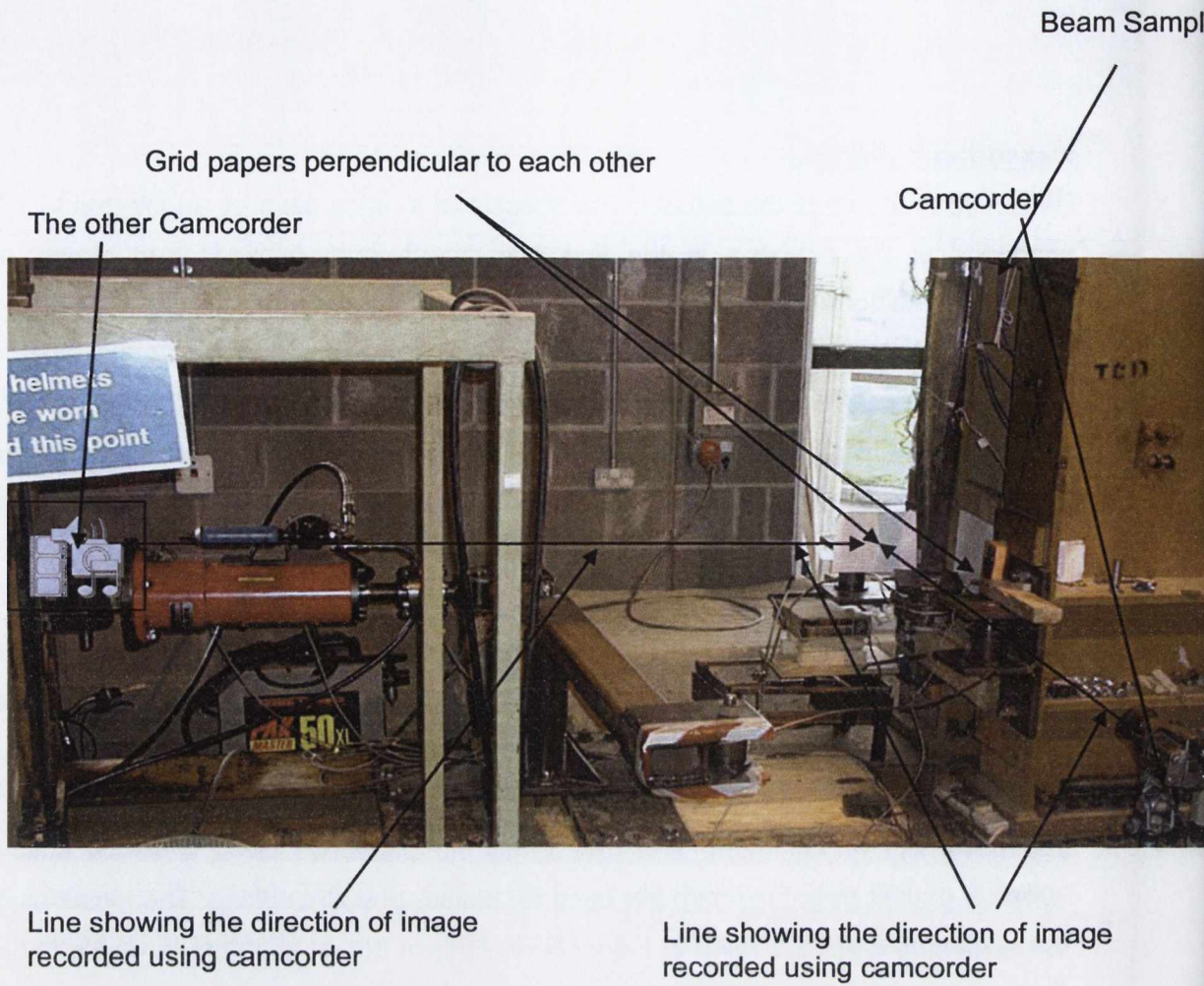


Figure 5.24 Position of the camcorders

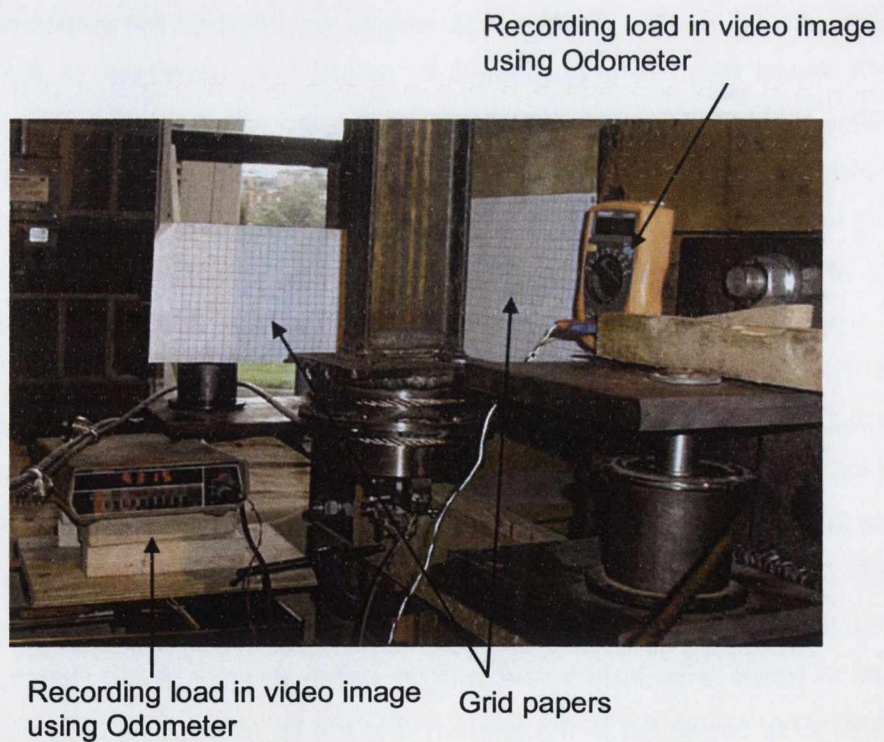


Figure 5.25 Position of Odometers and Grid papers used to measure deflection
Video processing and measuring images

Microsoft Windows Media Player 11 (Windows Media player, 2004) is a programme commonly used to play and organize digital media files on computer and on the Internet. In addition, the Player could be used to play, rip, and burn CDs, play DVDs and VCDs and synchronize music and videos.

Meazure is a program for measuring and capturing portions of the screen (Meazure Version: 2.0, 2004). It can perform measurements the size of a window on a computer screen, capturing an image of a video, determining the color of a pixel on the screen, and determining the screen size. Meazure provides different types of tools for measuring and capturing the screen such as cursor, point, line, angle and window tools. Line tool is used to measure a distance in an image. The line measurement tool allows one to position two crosshairs anywhere on the screen and measure the positions, distance, and other information for the line connecting them. In this way, the image of the beam movement relative to the background grid board can be translated into appropriate external deflections of the beam tip in that direction.

Using the Media Player and Meazure, deflections of the beam were related to the loads in the experiments. Every ten seconds, the video image in the player may be stopped and deflections are ascertained by measuring the movement of the edge of the beam with reference to any point on the grid paper. Images were first zoomed in on for accuracy. A calibration factor was calculated for the software to obtain the exact distances. Two grids on the board, whose grid spacing distance was known, were used to determine the value of distance obtained in Meazure and to calibrate its scale based on the known distance. When the scale of the software is calibrated, exact distances from the edge of the beam to one of the reference grid can be determined using the still images. Loads were related to the distance measured by noting the meter reading of the Odometers for every still image. Using this procedure, a series of tip deflections and their related loads were determined to monitor the (two) horizontal and the vertical deflections of the beam.

Data transfer, storage and test control

The procedure and equipment used for data transfer and storage are the same as was used in the pure flexure experiments. The same test control was adopted as in the experiments discussed in section 5.3.

5.4.2 Torsion of the beam sample

Two tests of the cantilever I-section beam samples of span $1.24m$ were performed for torsional loading to obtain the plastic torsional capacity of the beam restraint to warping and to observe the failure mode at large rotations. Previously torsion experiments were performed as discussed in Section 2.5 but as torsion response changes with boundary conditions and length. Therefore it was necessary to perform a torsion experiment for the current sample so that it can help to compare the results when multi-dimensional forces are applied. Both the beams used were from the same steel joist as for the previous flexural tests to maintain consistency of the material properties. It was noticed by Dinno and Gill (1964) that creep can be present during torsional tests, especially after the limit of proportionality has been reached. Therefore rotational measurements were taken on a time basis.

Before the final test to failure, each beam was tested in a regime of elastic cyclic loading (a practice adopted before by Kolbrunner et al (1978)) to verify the correct functioning of the instruments, especially the strain gauges which could break during their installation or could have a problem of terminal disconnection. Four to five cycles of loading were performed in the elastic range having strains not exceeding the elastic limit. After the verification tests, beams were loaded to failure in torsion.

Torsion results discussion

Torsion-rotation response

The torsion-rotation graphs of the beam for both the samples are given in Figure 5.26. It can be inferred from the graphs that a similar type of response was obtained from both the tests especially in the linear region where responses almost match each other identically up to a torque of $0.6kN.m$. Beyond this point, non-linearity was observed for the second test, whereas the response for the first test remained linear up to a torque of $0.7kN.m$. Rotations up to the maximum linear response in both the cases were approximately 16-18 degrees. A distinct change in both the graphs was observed between a torque of approximately $0.7kN.m$ and $0.8kN.m$ for the first experiment and between $0.6kN.m$ and $0.8kN.m$ for the second experiment, after which they maintained a roughly constant (and substantially reduced) slope with decrease stiffness up to the end of the experiment. The region of the change in the slope of the graphs was observed to be between an angle of 20 degrees to 45 degrees. At unloading, the slope of the graph (in the second experiment) follows the linear pattern much similar to the elastic linear pattern of the first phase, which resulted in a residual rotation in both the experiments.

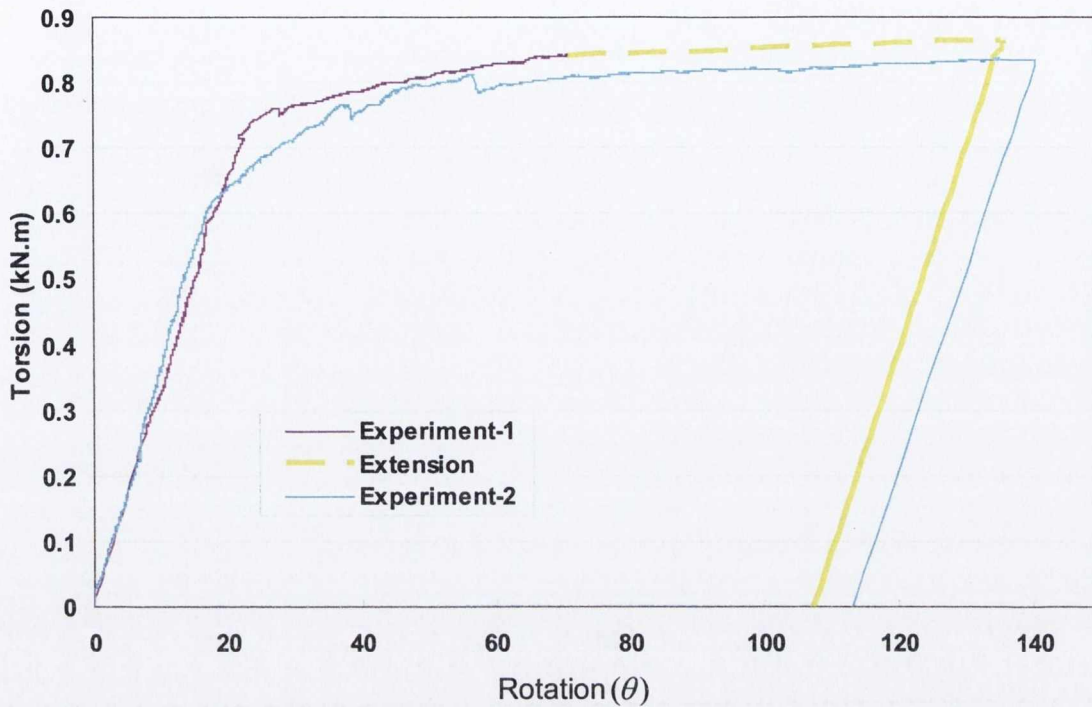


Figure 5.26 Torsion- rotation plots for the cantilever beams of span 1.24m .

The peak torque in the region of constant slope in the plastic phase (with a strain hardening property of the material) is $0.86kN.m$ for the first test and $0.84kN.m$ for the second test. The maximum rotation at the peak torque for the first test was unable to be determined because of the breaking of the support of the potentiometer. However, a maximum rotation of 140 degrees was recorded for the second test, beyond which it was not possible to further rotate the specimen due to lateral movement which brought the beam close to pivot E. At unloading, a residual rotation of 107 degrees and 113 degrees were measured for the first and the second tests respectively.

From the second experiment's graph, it can be inferred that the slope of the non-linear region after a transition phase (the phase in which the response changes from elastic to non-linear between angles of 20° and 45°) is nearly constant up to the peak load. Upon unloading all the other graphs follow a slope more or less the same as the slope in the linear elastic region of the graphs. Based on the similarity in the response in the second experiment, a tentative extension of the graph of the first experiment was made to observe the similarity in the response in both the experiment and is depicted in the figure.

Measured Strains

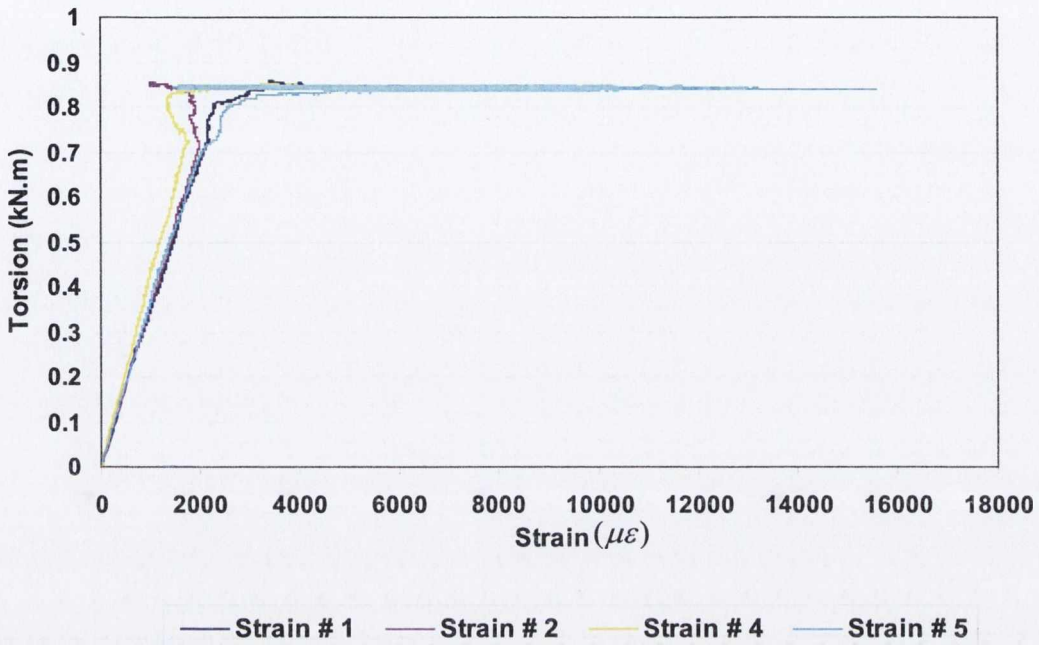
Strain at tip of flanges

Longitudinal strains were recorded at the tips of the flanges at a distance of 75mm from the end of the beam and at the mid span of the beam. Strain gauges installed to measure the strains were numbered 1, 2, 4 and 5 at the cross section near the fixed end and numbered 10, 11, 12 and 13 at the mid span. Precise details about the locations of the strain gauges are depicted in Figure 5.23. The applied torsion versus strain relationships at the tips of flanges for both the experiments are depicted in Figure 5.27 and Figure 5.28.

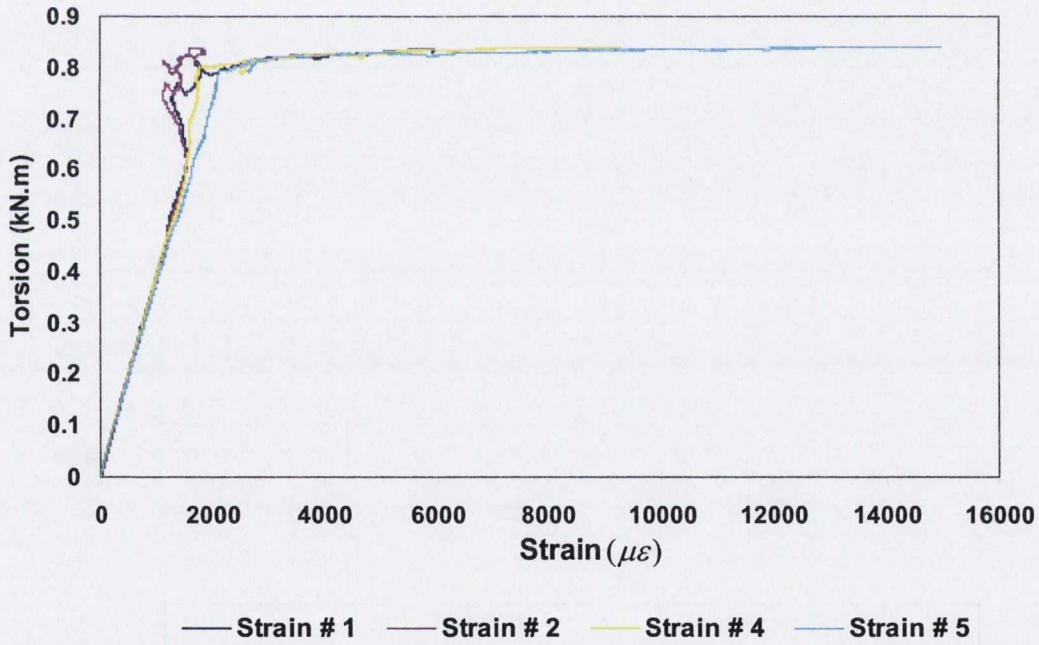
At the fixed end (Figure 5.27), strain numbers 1 and 5 were in tension, whereas 2 and 4 were in compression. However, strains which were in compression, having negative values, have their sign changed in the figures for comparison. Considering the figures, it can be inferred that up to a torque of 0.7kN.m for the first experiment, and 0.6kN.m for the second experiment, a highly linear pattern can be observed, where at the verge of linearity, strain ranges between $1700\mu\epsilon$ - $2000\mu\epsilon$. At the same torque values, the torque-rotation diagram depicted in Figure 5.26 also showed a linear response, which confirms that the torque-rotation and torque-strain diagrams have similar linear behaviour up to the torques at the verge of linearity. The similarity in the values of all the four strain gauges in both the experiments, up to a linear response, shows that the strain up to this point was mainly due to warping, where strains are equal in magnitude but opposite in directions at the flange tips, as expected. The other direct strains, which are due to axial shortening and Wagner effects (Section 2.4.2, Figure 2.10(d)) which appear significantly at larger rotations, were not significant at this stage.

At the end of the linear phase, three types of strains started to increase rapidly. Those were the Wagner and axial shortening strains, and the direct strain due to bending of the beam about the minor-axis. For strain gauge #-1, warping and Wagner effects cause direct tensile strains and axial shortening and the bending effect causes a compressive strain in both the experiments, the resultant of which was a tensile strain of nearly $4000\mu\epsilon$ at maximum torque. The same nature of warping strains, which were present in strain gauge # 1, was also present in strain gauge #-5 but the bending of the beam caused a tensile strain for strain #-5, which resulted in an increase in the tensile strain and a strain of more than $14000\mu\epsilon$, at maximum torque, in both the experiments. Although the same torsional strains must be present in both the strain gauges, due to the bending effect, the total strains as

depicted in the figure have a considerably lower value for the first strain gauge as compared to the fifth strain gauge.



(a) Experiment # 1



(b) Experiment # 2

Figure 5.27 Strain at the fixed end at the tips of flanges for both the torsion experiments.

The same nature of torsional strains must be present in strain #2 and #4, but due to the bending of the beam, which causes an increase in tensile strain at strain #2, a decrease in strain #4 occurs due to a compressive strain. Hence this resulted in a different strain pattern in both the strain gauges as depicted in the figures, where the strains in both the experiments are $2000\mu\epsilon$ and $4000\mu\epsilon$ in strain #2 and #4 respectively.

It is concluded that due to the secondary effects of minor-axis bending in the beam and Wagner strain (Section 2.4.2, Figure 2.10(d)) and axial shortening strains, which develop considerably more at large rotations, the patterns strains in the non-linear phase were quite different to the elastic phase and this is the reason for the complex patterns in both the graphs of the strain gauge readings.

At the mid span, where the effect of warping strains reduces substantially, the only strains effective are the Wagner and axial shortening effects, where all the strains are tensile, indicating domination of Wagner strains, as depicted in Figure 5.28. The effects of the bending strains were negligible at mid span, therefore a similar pattern can be observed in the figures for all the strain gauges.

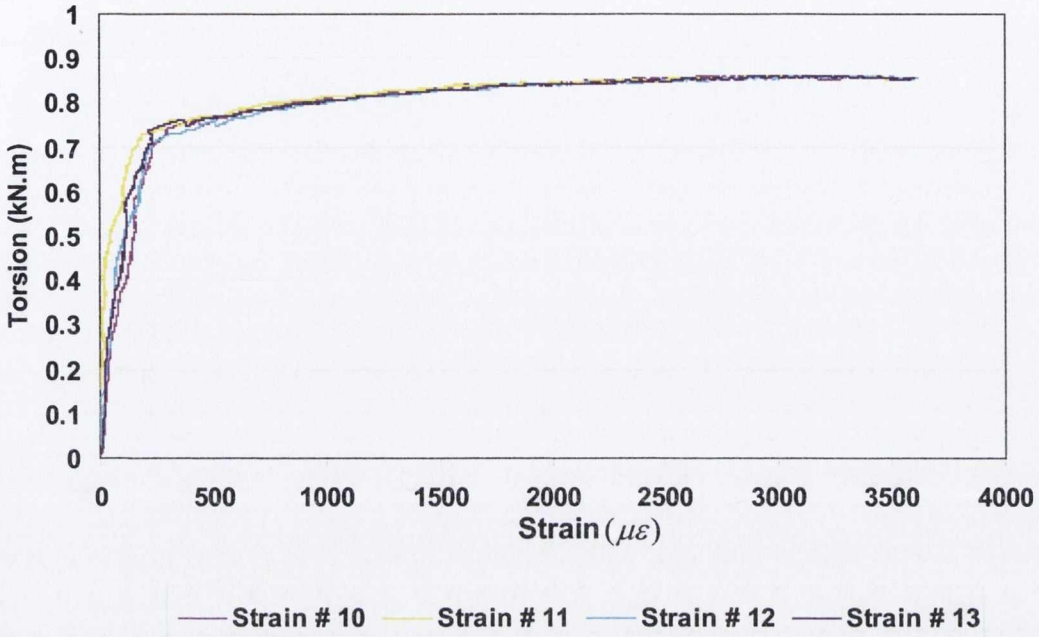
Strain at centre of the web

Two strains, which are numbered 3 and 9, were installed at the centroid of the section to measure the axial shortening effects at the fixed end and mid span respectively. Graphs plotted for both the tests are given in Figures 5.29. It can be inferred that up to the linear response the amount of strain in both the strain gauges was not increasing rapidly, whereas the rate of increase becomes very high in the non-linear stage. This is because of the axial shortening strain that is substantial in the large rotational range. Strain #9 yields high strain compared to strain #3 because strain #9 was at a greater distance from the restrained end. The pattern in both the experiments gives similar results, indicating the repeatability of the experiments.

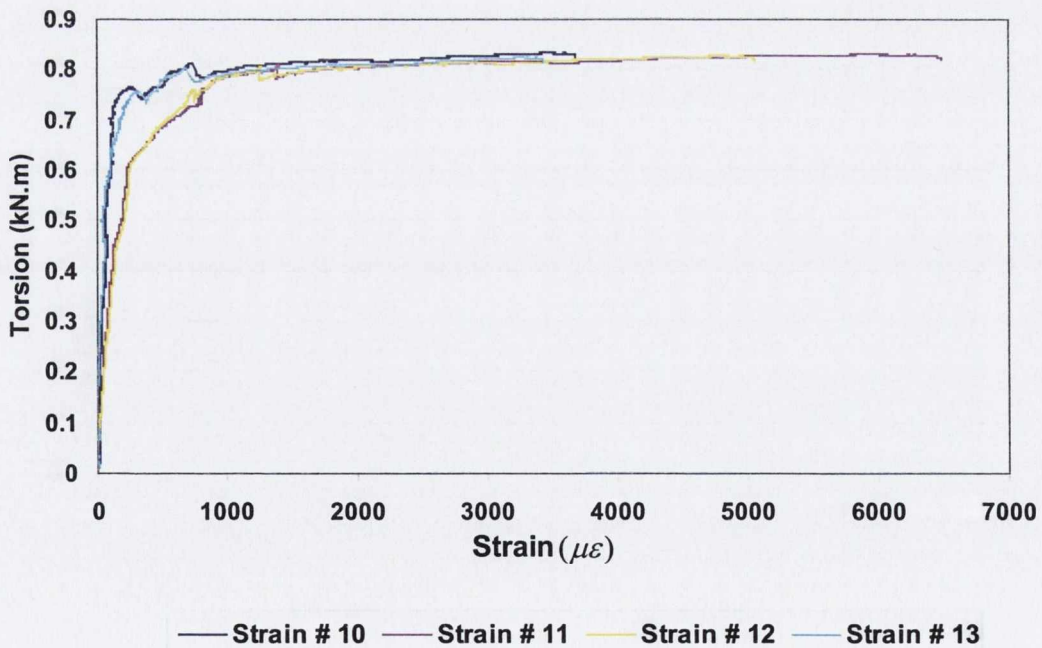
Strain at the edges of the web

Direct strains which occurred on the cross section are due to warping strain, axial shortening, Wagner strain (Section 2.4.2, Figure 2.10(d)) and strain due to minor axis bending, which occurred in the last stage of the experiment. Warping and minor axis bending strains do not occur at the edges of web. Only Wagner strain and axial shortening strain occur at that point (Figure 5.30), and these increase considerably at

large rotation. Therefore, in the linear phase, the strains are considerably smaller than in the non-linear phase, where the strains increase considerably.



(a) Experiment # 1

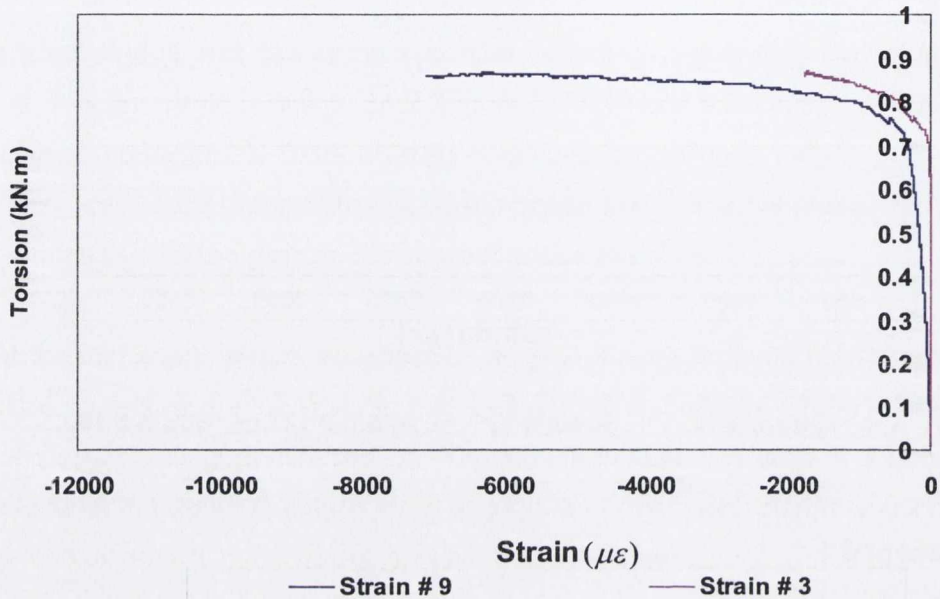


(b) Experiment # 2

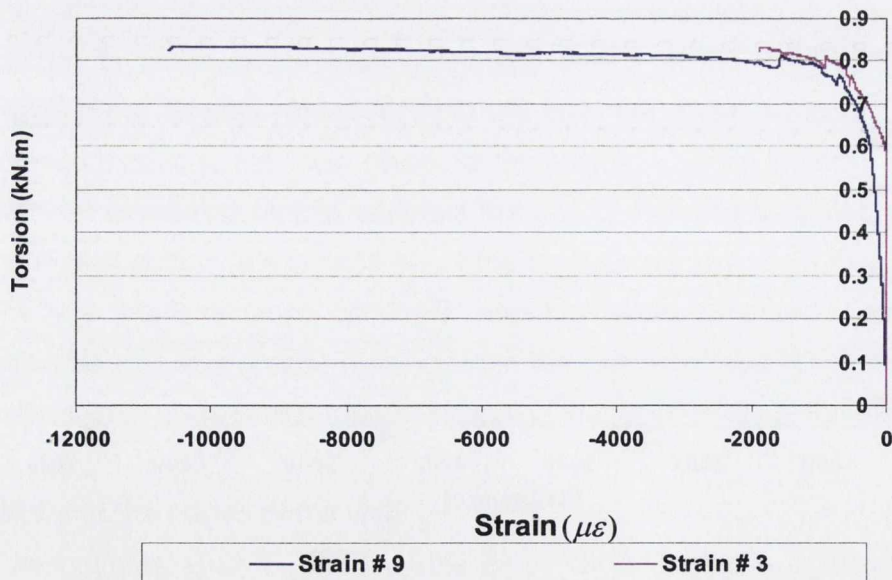
Figure 5.28 Strain at the mid span at the tips of flanges for torsion applied in the two experiments

Strain to monitor rotation

In the strain gauge # 14, 15, 16 and 17 were installed to monitor the rotation. These were installed at an angle of 45 degrees. They were installed in two different directions depicted in Figure 5.23. However, similarities were not observed in the results of strains # 14 and 15 and between strains # 16 and 17. and they do not give any satisfactory results, therefore the results are not given here.

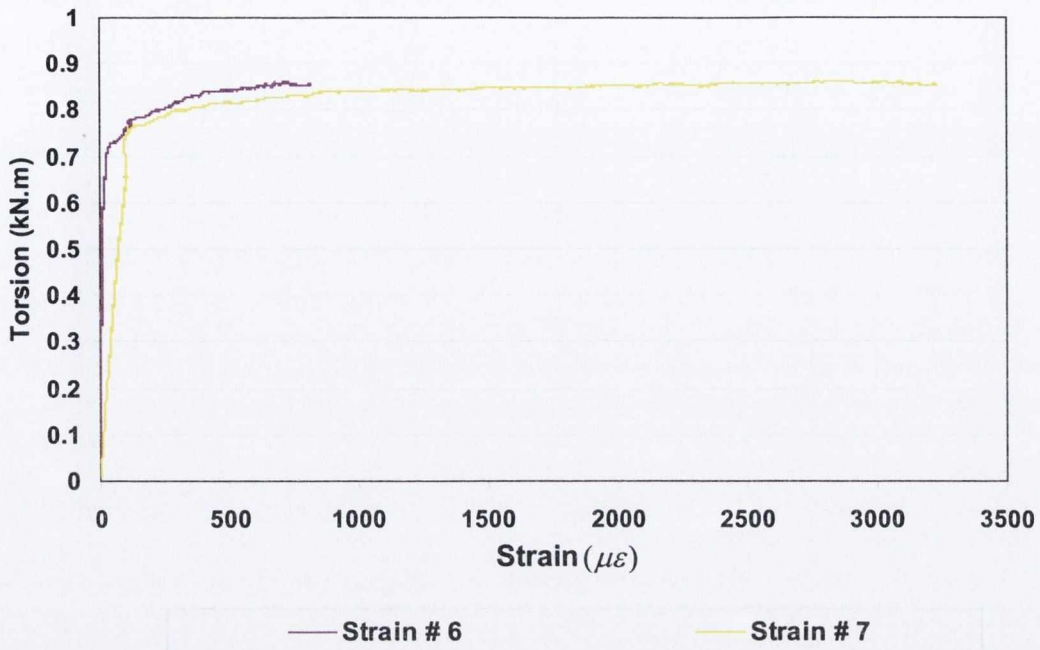


(a) Experiment # 1

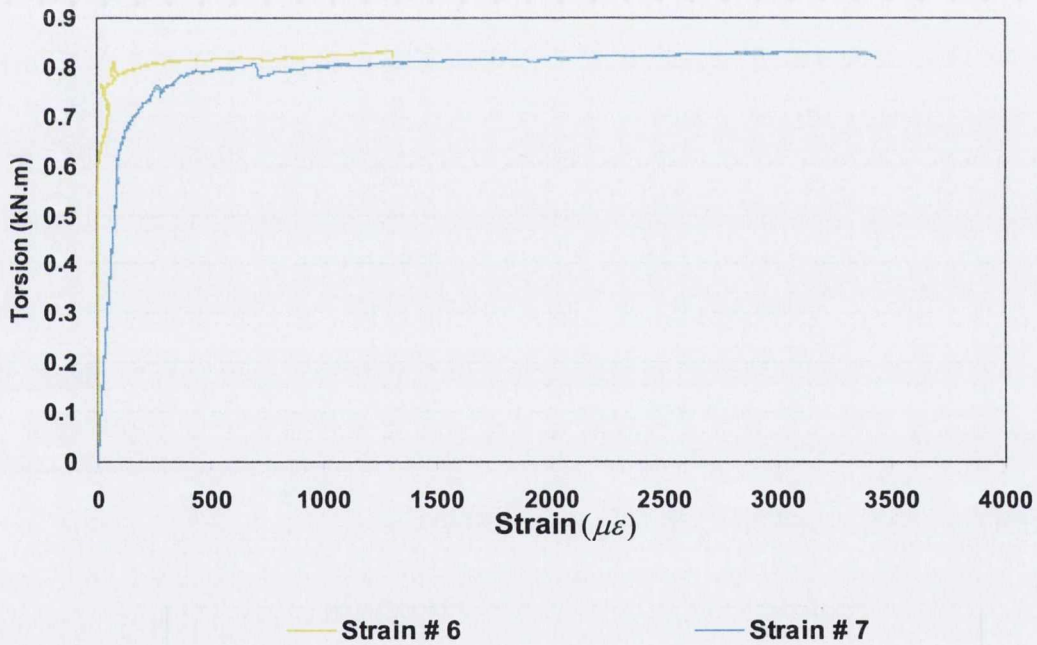


(b) Experiment # 2

Figure 5.29 Strains at the centre of web near the support and at mid span for both the torsion experiments



(a) Experiment # 1



(b) Experiment # 2

Figure 5.30 Strain at edges of the web for both the torsion experiments

Failure of the beam samples in torsion

If failure in a test can be defined as a point where a significant decrease in the torque is noticed, then it can be inferred that the beams in experiment # 1 and # 2 did not fail even at a rotation of nearly 145 degrees. Considering the torsion-rotation diagram

(Figure 5.26), it can be said that there continues to be a small increase of torsion without a drop of load near the end of the experiment. This shows that material has enough remaining strength which normally comes under strain hardening of the material. This is also confirmed when the strain diagrams at the support at the tips of the flanges (Figure 5.27) and in the web (Figures 5.29 and 5.30) are considered, where there is an increase of strain noticed without further loss of torsion at high strains, a pattern similar to that achieved when strains develop in the plastic phase with strain hardening of the material. Therefore it can be said that the beam specimen was in the plastic phase but did not fail during the experiments.

Although it can be argued that the rotation of 145 degrees is far beyond any rotation, which a member can expect to withstand practically in a structure, failure was not initiated due to the reasons discussed above. Globally the capacity of the beam to resist torque at such a large rotation is mainly due to two effects. Firstly, the helix effect (Dinno and Gill, 1964) in torsion that causes the beam to shorten axially and an additional stiffness (in addition to the torsional stiffness) exists for a beam to resist the torque. Secondly, the strain hardening property of the material has an effect of increasing the carrying capacity of the beam beyond its plastic capacity. As discussed in Section 5.2.1, based on coupon test, an average strain of $21800 \mu\epsilon$, is required for the commencement of strain in the strain hardening phase for the steel joist, whereas measured strains in both the experiments were not more than the value of $15610 \mu\epsilon$. This shows that strain hardening property of the material was not utilized. It can be concluded that failure if termed, as ultimate capacity of the section in torsion was not reached but the section was able to achieve torsional plasticity.

Collapse mechanism and plastic hinge formation

The cantilever samples tested in torsion were restrained at the fixed end, where warping stresses are at a maximum. A plastic hinge will develop due to warping in the flanges at the fixed end. To identify the formation of the hinge, strains were monitored throughout near the fixed end.

At the commencement of non-linearity, at an approximate angle of 20° (Figure 5.26), the strains at all the tips of the flanges near the support were found to be between $1519 \mu\epsilon$ and $1939 \mu\epsilon$, as depicted in Figure 5.27. As discussed in Section 5.2.1 based on coupon test at an average strain of $1700 \mu\epsilon$, the plastic phase commenced in the material of the beam. This gives evidence of the start of the formation of plastic

hinges in both the flanges in both the experiments. Meanwhile the centroid of the web was still elastic, which means that although the web was elastic, hinges were about to form in the flanges.

Between an angle of 20° and 45° , similar patterns can be observed in the figures with a substantial increase of strain in the web (Figures 5.29 and 5.30) and decrease of strain at one of the tips of the section (Gauge #2, in Figure 5.27) in both the experiments. This is because of the secondary effects which are Wagner strain (Section 2.4.2, Figure 2.10(d)), and axial shortening effects, which cause a strain in the opposite direction at the tip, whereas the strain for the remaining tips follow the same strain directions.

Observing the strains near the support at the peak load, and comparing the strains with the average strain obtained from the coupon tests, indicates that strains are in the plastic phase at locations 1, 3, 4, 5 and 7 for the first experiment and location no 1, 3, 4, 5, 6 and 7 for the second experiment. Hence, plasticity had definitely formed in the bottom flange in both the experiments, where high values of strain could be observed (Figure 5.27). For the top flange (in the first Experiment) at one edge (Strain #1 in Figure 5.27(a)) where there is a tensile strain the material has yielded. Whereas, at the other edge (Strain #2 in Figure 5.27(a)), due to the strain caused by the bending action and Wagner effects, the strain do not increase much and has an elastic strain at the end of experiment. Observing the overall torsion-rotation graph (Figure 5.26) in the third phase, there is no sign of change in the response, which means that the strain #2 which is elastic at the end of experiment has only local effects, while not disturbing the overall behaviour of the beam. At the centroid of the web in both the experiments, the strain value is more than the average plastic strain indicating that the centroid of the web can be considered in the plastic phase.

Therefore, it can be concluded that yielding has occurred near the fixed end in both the experiments and the strain which is elastic at the end of experiment (Strain#2, Figure 5.27) in one of the experiments has local effects only. This point can be assured by the fact that in both the experiments, the torsion-rotation graph, the maximum torque achieved and residual rotation obtained have values and graphs matching each other. Hence, it can be concluded that the section in both the experiments have yielded and were in the plastic phase.

Bending of the beam about the minor-axis

In both the experiments, bending of the beam about the minor-axis was also observed. The plot of horizontal movement versus applied torque for the second experiment is depicted in Figure 5.31, (horizontal movement was not recorded for the first experiment). Up to a torque of 0.2kN.m there is no graph, this is because the horizontal movement was measured using video images and no movement was observed by the image, theoretically there may be fraction of movement but it was not possible to physically measure it. From the torque of 0.2kN.m up to a torque of 0.4kN.m small movement was observed. However, the movement was recorded using a video image which can result in a difference of 1mm - 2mm and result in such type of graph. However in the initial stage up to a torque of 0.4kN.m the behaviour was mainly elastic and the beam behaves in pure torsional mode without any secondary effects. Therefore, results in insignificant horizontal movement of the beam. From the torque of 0.4kN.m up to a torque of 0.6kN.m the movement started to increase indicating the influence of horizontal movement on torque in the non-linear phase. It can be observed in the figure that the horizontal movement started to increase rapidly at a torque of 0.6kN.m . Referring back to Figure 5.26, it can be inferred that the point at which this torque value occurred is the point of commencement of the non-linear phase, at an angle of nearly 20° . This shows that the horizontal movement started to increase rapidly at the commencement of non-linear torsional phase.

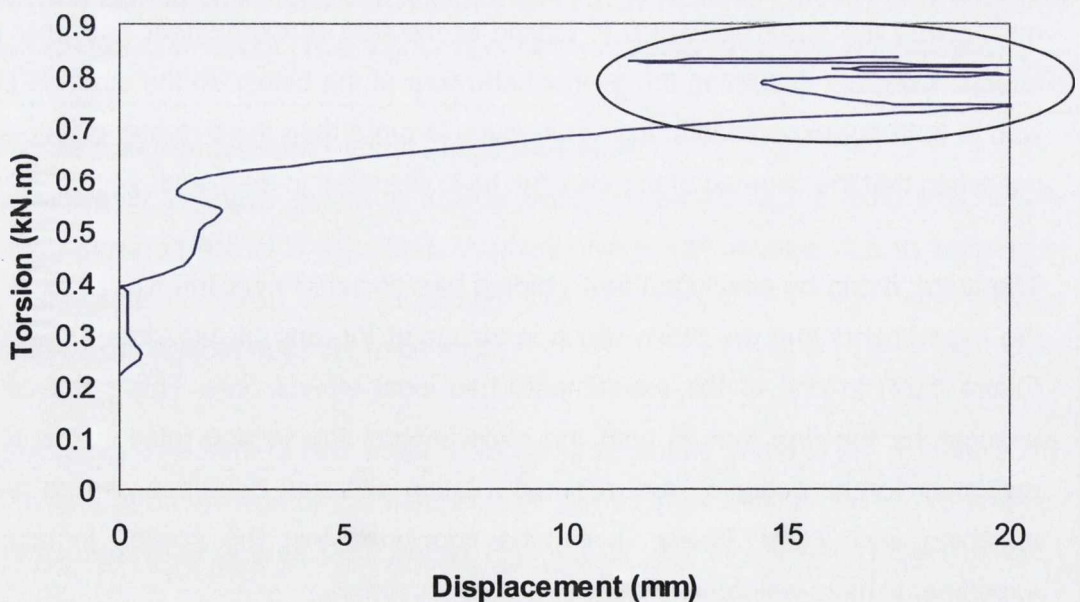


Figure 5.31 Torsion-horizontal movement graph for the second experiment

At this point of loading, there were two secondary effects which were active in the beam. One is a relatively small uniform bending moment on the entire beam because of bending due to a vertical distance d^p of $0.1m$ between the cables, as depicted in Figure 5.17. At the commencement of the non-linear phase, the section, which has the least flexural stiffness in the entire beam length, is at the fixed end, where the bending of the beam about the minor-axis will be resisted practically by flanges, whereas the web will not resist the bending. Therefore, this uniform secondary moment will cause a deflection about the minor-axis in the beam.

The other secondary effect is the axial shortening effects, which also started to increase significantly at the commencement of non-linear phase, as can be observed in Figure 5.29. Axial shortening will cause the same effect, which is caused by a compressive load on a cantilever beam to produce deflection on one side which causes the beam to deflect about its weaker axis, and in this case it will cause the beam to deflect about the minor-axis.

During these two effects, which were not possible to avoid, a deflection about the minor-axis was observed in both the experiments.

The portion of the graph in Figure 5.31 circled i.e. where there is a seemingly random increase and decrease of deflection is due to the fact that cable wedge which clamped the two ends of the cable slipped at higher load and caused this response.

Comparison of torsion results

Experimental comparison

Torsion results obtained here are compared with the previous experimental results of Dinno and Gill (1964), in which torsional behaviour of I-sections restrained at their ends were investigated, and Farwell and Galambos (1969), in which torsion behaviour was investigated in which the sections were free to warp. The graphs of these results are given in Chapter-2 (Section 2.4). Comparing these two results with the results obtained in this work, the same general failure characteristics of the beam in torsional seen to exist. The overall response of torsion and rotation gives a similar trend in which a gradual change of phase was noticed after a smooth linear phase. Beyond the gradual change in the slope, a constant slope of lesser value indicates a reduction in the torsional stiffness with a clear contribution from strain hardening of the material. Comparing the paths of unloading in this work with the work by Farwell

and Galambos (1969) also indicates a similar pattern, with the same slope as in the linear elastic phase, is observed.

Two conclusions can be drawn from all the experimental results; firstly, torsional behaviour of an I-section follows a typical response for a torsion-rotation graph; Secondly, the section has a high rotational capacity and failure is achieved at a very large rotation beyond any practical value which a structure needs to achieve.

Nadai's Sand Heap Analogy

The value obtained for pure torsion of the section based on Nadai's Sand Heap analogy (Johnson and Mellor, 1973) is $0.53kN.m$. This value is 56% less than the maximum value of $0.86kN.m$. Such a large difference is primarily due to three reasons:

The strain hardening property of the material has the effect of increasing the torsional capacity of the beam in the experiments, whereas it was assumed in the sand analogy that the material is elastic-perfectly plastic.

Two mechanisms are active in resisting torsion for sections subjected to warping restraints. One is a pure torsion mechanism which leads to St Venant's torsion for the elastic case and the sand heap analogy for the plastic case. The second mechanism is the warping mechanism, which causes flanges to bend in two different directions and results in shear forces in the flanges causing torsion.

Thirdly, it does not take account of the secondary effects of Wagner strain (Section 2.4.2, Figure 2.10(d)) and helix effects, which cause axial shortening of a specimen.

The sand analogy does not take account of these three factors when calculating the plastic torsional capacity. Therefore, it resulted in a low value as compared to the experimental values.

Dinno and Merchant

The value obtained based on the formula given by Dinno and Merchant (1964) is $0.65kN.m$, which is 32% less than the peak experimental torque. There are two possible reasons for a lower value. Firstly, they do not take account of the strain

hardening property of the material. Secondly, they do not take account of the secondary effects, which are the Wagner and the axial shortening effects.

Plastic torsion capacity and bimoment value

It has been assumed that the strain in structural steel sections during plastic flow can be from five to ten times that of ε_y (Kollbrunner et al. 1978), denoted as ε_u , then the relationship can be defined as $\varepsilon_u = n\varepsilon_y$, where $n = 5$ to 10 . The load at which strain reaches a value of ε_u anywhere in the section (where all other strains on the section as less than or equal to ε_u) can be defined as the plastic limit load. The yield strain obtained in the coupon test (Section 5.2.1) is $\varepsilon_y = 1700\mu\varepsilon$. Considering $n=5$, gives $\varepsilon_u = 8500\mu\varepsilon$, at which the torsion is $0.84kN.m$ at an angle of 61° for the first experiment and $0.82kN.m$ at an angle of 115° for the second experiment. This torsion could therefore be proposed as the plastic torsion capacity although this clearly conflicts with the plasticity predicted by the strain readings.

In conclusion plastic torsional capacity obtained by the theories based on the yield stress obtained from the coupon tests results vary between a range of $0.6kN.m$ to a range of $0.65kN.m$. This shows that experimental values are consistently higher than the predictions. Further, predicted values using the theoretical approaches described here range from 0.53 to $0.65kN.m$. Despite this, the practical work suggest plasticity is achieved between 0.7 and $0.8 kN.m$, based on the graphs discussed here.

5.5 CONCLUSION

In this chapter, experimental results for the first phase of the experimental program are presented and compared with previous theories and finite element models. The work was divided into two parts; the first part deals with establishing the material properties of an I-section beam, which was found by machining samples from the beam and testing them under uniaxial tension at ambient temperature, based on British standard BS EN 10002-1 (BSI, 2001) test. The second part of the work deals with obtaining the plastic capacities and failure modes for single stress resultants.

Standard coupon tests were extracted at different locations, based on the residual stress distribution in a hot rolled I-section. The mechanical properties obtained for different samples were as expected for steel with a well defined plastic plateau, but

have slight variations in the values because of residual stresses and because of the use of machined samples. The average values of the results were used in the theoretical study and finite element analysis.

The plastic flexural capacities of the section about both the principal axes were determined from experiments and found to be satisfactory when compared with theoretical values obtained using coupon test results. It was found that large deflections at the tip of the cantilever are required to achieve the ultimate moment capacity, which was not possible in the current set-up. It is also found that the method of loading could change mechanical properties to a small extent.

Torsional capacities of the sections were also obtained for the beam samples and yielding of the sections was identified. Results were compared with the previous theories and experimental results. It was found that the torsional capacities of the section were higher than the results predicted by different theories. Possible reasons for higher results were discussed. During the experiments, the beam experienced bending about the minor-axis the effects of which on the torsional results were discussed.

BEAM SAMPLE SUBJECTED TO MULTI-DIMENSIONAL FORCES

6.1 INTRODUCTION

In the previous chapter results of the single stress resultant experiments were discussed. The purpose of the experiments describe in this chapter is to investigate the behaviour of the beam sample subjected to multi-dimensional forces and to compare the capacities of the beam sample to resist different combinations of forces with the yield criterion developed in Chapter 4. Two such combinations of forces are investigated. For the first combination, the forces applied at the end of the beam sample were biaxial bending moments and torsion, while axial force, biaxial bending moments and torsion were applied for the second combination of forces. The specimen details and experimental set-up for these tests were outlined in the previous chapter; only minor changes to the previous set-up were made in these experiments and these are described here.

Section 6.2 and 6.3 discuss details about the set-up, results and observations from the experiments of the first and second combination of forces respectively. In the sub-sections of each section, changes in the experimental set-up, load-deflection response, torsion-rotation response, interaction of displacement and rotation, strain measured and comparison of the results with the developed theory of Chapter 4 are made. Section 6.4 presents a comparison of results of all the experiments and observations from which conclusions are drawn.

6.2 BIAXIAL BENDING AND TORSION EXPERIMENTS

6.2.1 Experimental Set-up

The same test arrangement is used with only a slight modification from the experiments used previously for the torsion experiment. In the new set-up, one guiding pulley and cable is removed compared to the previous case, as was depicted in Figure 5.19. This removal causes both bending and twisting of the beam sample simultaneously as the load is applied through the single remaining

cable. The new position of the cable and the guiding pulley is depicted in Figure 6.1. Strain gauges are installed at the same locations as in the second experiment on torsion, as depicted in Figure 5.23. All other devices which were used in the previous experiment are re-employed here to collect and store data related to applied load, displacement, rotation and strain measurement.

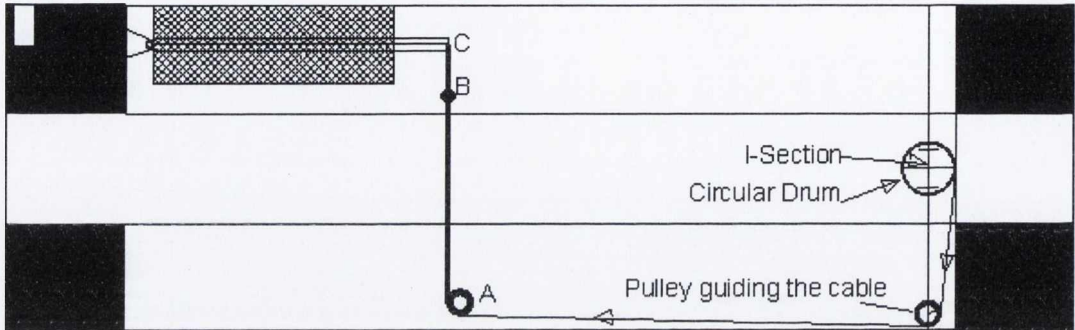


Figure 6.1 Modified set-up for torsion-biaxial bending experiment

6.2.2 Experiments Performed

Two experiments are performed, the difference between them being the direction of load application with respect to the orientation of the cross-section of the sample. The direction of loading was at an angle of 8° from the principal axis of the beam. In the first case, the minor axis of the section was almost perpendicular (at an angle of 82°) to the direction of load application whereas in the second case, the major axis of the section was almost perpendicular to the direction of load application. The positions in both the cases are depicted in Figure 6.2. The principal reason for undertaking tests with two different starting arrangements was to alter the balance of stress contributions from torsion, major and minor axis bending, thereby examining different yield criteria. In all the experiments, application of torsion rotates the beam, where the rotation will be at a maximum at the free end. Owing to this, flexural stiffness of the beam varies as the beam rotates. This causes deflection of the beam different from that of a beam bending about the major axis or minor axis, hence a variation in the contributions from major axis bending and minor axis bending is generated.

6.2.3 Strains at two different locations at different stages of loading

The strains at two different locations along the beam at the fixed end and at the mid span are given in Table 6.1 for both beams. To identify the start of yielding,

strains at several strain gauges are observed. If ε_y is defined as the strain at the start of yielding anywhere on the cross section (for the current experiments, based on the coupon tests, this value is taken as $1700 \mu\varepsilon_y$) and strains at all other location as less than ε_y then the load at which this occurs is defined as the elastic limit load. For both the experiments, ε_y is reached at strain gauge # 2 and the strains at all other locations are less than ε_y .

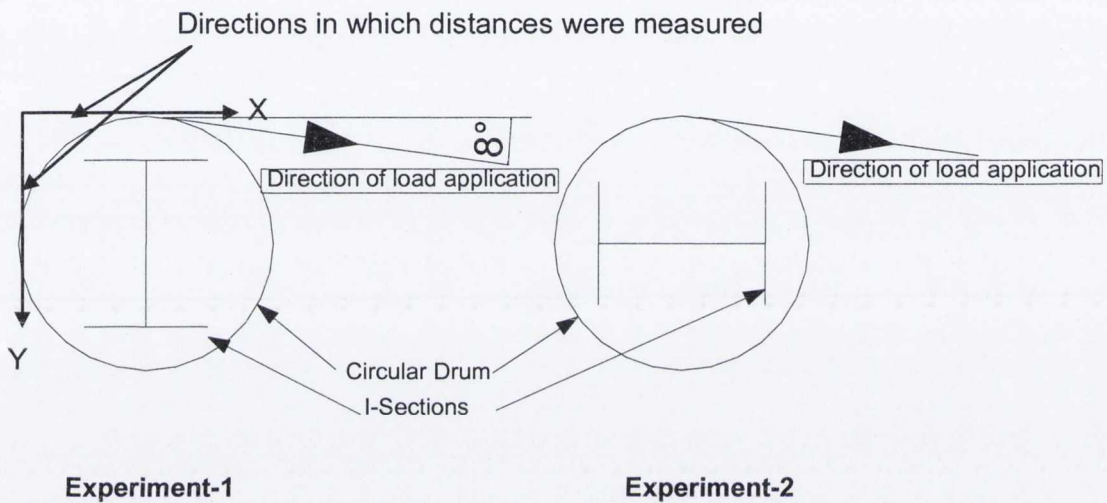


Figure 6.2 Position of I-section with respect to the direction of load application for both the torsion-biaxial bending experiments.

The strain when it reaches a value of ε_u anywhere in the section (where all other strains on the section as less than or equal to ε_u) can be defined as the plastic limit load (Section 5.4.2). The strain at which this maximum occurs is defined by the author as practical hinge formation. The load at which a practical hinge is deemed to have formed is given in the table for both Experiments 1 and 2. For Experiment-2 the practical hinge forms after the peak load, therefore the strain at the peak load is also given. Note that the result of strain #8 is not given in the table, where strain # 8 was used to obtain the shear strain but did not give any satisfactory results.

The values of strains as given in Table 6.1 are plotted on an I-section to observe the neutral-axis pattern at each relevant stage for the fixed end and the mid

section (in Figures 6.3 and 6.4 for experiment 1 and 2 respectively). Strains are not drawn to one scale for reasons of clarity, therefore strains have different sizes for each case.

Load kN	Torsion kN-m	Remarks	Strain at fixed end					
			1	2	4	5	3	6
Experiment-1								
1.78	0.155	Strain at start of yielding	1609	-1700	780	-780	74	-36
3.24	0.28	Strain at practical hinge formation	17000	-14562	15418	-11781	633	-32
Experiment-2								
4.26	0.37	Strain at start of yielding	534	-1701	-126	1222	5.7	-595
8.72	0.76	Strain at Peak load	1342	-3266	196	6859	-465	2184
7.44	0.65	Strain at practical hinge formation	5983	-17000	972	8198	-839	4025

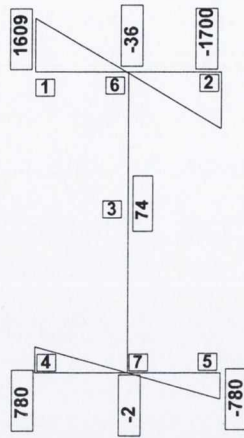
			Strain at Mid span				
			9	10	11	12	13
Experiment-1							
1.78	0.16	Strain at start of yielding	46	720	-724	-714	736
3.24	0.28	Strain at practical hinge formation	50	1115	1074	-1445	1573
Experiment-2							
4.26	0.37	Strain at start of yielding	-64	-282	-312	323	325
8.72	0.76	Peak load	-985	1924	1323	2225	496
7.44	0.65	Strain at practical hinge formation	-5557	4073	5878	12735	-1966

Table 6.1 Strains at different location along the beam for experiments 1 and 2 in biaxial bending and torsion

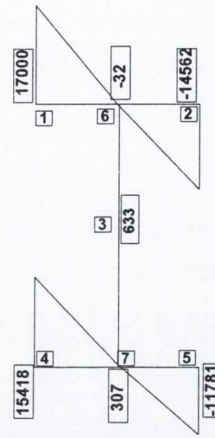
Considering Experiment-1 strain results at the fixed end, the strain pattern at the start of yielding shows positive strain on the left of both flanges, negative strains at the right of both the flanges, with small strains at the middle of both the flanges. Figure 6.3a indicates that bending in both the flanges has the same curvature as when it occurs in bending of a beam about its minor axis. This shows that deformation at the start of yielding was mainly flexural with a domination of minor axis bending. However, warping due to rotation and a minor component of major axis bending were also present, deduced because the four values at the extreme edges of the flanges do not match. The beam rotation at this point was still zero at the support due to the beam's fixity. Hence also no significant major-axis bending exists.

The strain pattern at the formation of a practical hinge is also given in the figure. It shows a similar pattern as that which was obtained for the strain distribution at the start of yielding. It is similar though the left and right flange values are no longer equal nor is the strain at the centroid nearly equal to zero. This means that the primary effects of warping and the contribution from major axis bending and the secondary effects of Wagner (Section 2.4.2, Figure 2.10(d)) and axial shortening were developed at large rotation and large deflection. However, minor axis behaviour continued to dominate the behaviour as the strains are positive and negative at left and right of the beam section. Considering Experiment 1 at the mid span at the start of yielding (Figure 6.4(a)), the strain at two edges of both the flanges have nearly opposite values as normally appeared when beams bend about minor axis bending. This shows the domination of minor axis bending at the start of yielding.

Considering Experiment 1 at the mid span at the formation of practical hinge (Figure 6.4(b)), the strain at the two edges of both the flanges have nearly equal but opposite values. However, a significant difference exists between values at the top and the bottom flanges where the values of the top flange are lower. This happens because the mid section rotates and causes additional warping strains which results in a decrease of strains for top flange and an increase of strain for bottom flange. Hence it can be said that at mid span both rotation and minor axis bending was present due to which change in the strain patterns were observed.

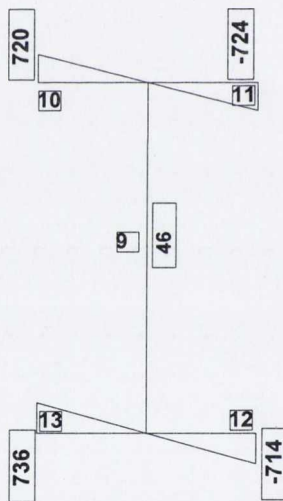


a) Strain at start of yielding

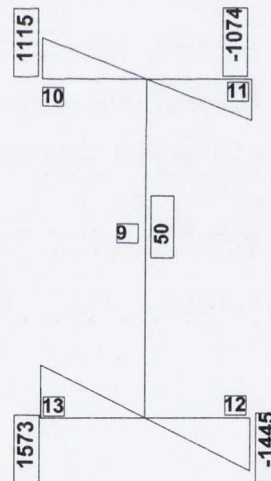


b) Strain at practical hinge formation

Figure 6.3 Strain patterns for biaxial bending and torsion experiment (Experiment 1) at fixed end, where strain numbers are given in square boxes and strain readings in rectangular boxes.



a) Strain at start of yielding



b) Strain at practical hinge formation

Figure 6.4 Strain patterns for biaxial bending and torsion experiment (Experiment 1) at mid span, where strain numbers are given in square boxes and strain readings in rectangular boxes.

Considering the strains in Experiment 2 at the fixed end as depicted in Figure 6.5(a), strains on the left and right of the flanges have different signs at the start

of yielding, whereas nearly equal strains exist at the middle of both the flanges with a very small value at the centre of the web. This suggests that the strain pattern was a combination of major axis bending (due to which two opposite strains of nearly equal magnitude were present at the web/flange junction) and rotation (due to the different signs for the flanges, which indicate warping of the section). Strains due to major axis bending also exist in the flanges and therefore the neutral-axes have different positions in the two flanges. In addition a small component of strain due to minor axis bending, Wagner strain (Section 2.4.2, Figure 2.10(d)) and axial shortening must be present (because the load is applied at 8° and the beam has not rotated at the support) but the strain distribution shows that the predominant effect was mainly due to a combination of major axis bending and rotation. These combined effects cause such a pattern that a non-straight line for the neutral-axis results.

Considering the strains at the peak load (Figure 6.5(b)), the distribution largely matches the strain at the start of yielding i.e. in both cases the top and bottom flanges have the same direction of bending about the longitudinal axis, with the same sense of bending in the web about its longitudinal axis. The same type of pattern is obtained as in the previous case which is an indication of the domination of major axis bending and rotation (Wagner + warping strains). However, now at the centre of the web there are significant strains which show that some axial shortening was present. Significant axial shortening was not evident in Experiment 1 because rotations were much smaller at the tip due to the domination of minor axis bending in the failure mode. A similar pattern of strain is obtained for the strains at the formation of a practical hinge, which shows that the beam responded in the same way from the elastic limit load to the formation of practical hinge at the cantilever support.

In Figure 6.6 strain at mid span is given. At the start of yielding the strains at the two edges of both flanges are nearly equal, which shows again the dominance of major axis bending which causes a stress distribution similar to the case obtained in major axis bending in Chapter 5. As the load increases, the section at mid span rotates which causes a mixed behaviour and strain at the peak load is a combination due to strain caused by bending about both the axes and rotation (Wagner and warping strain) and large strains at the centre of web is an

indication of axial shortening. Beyond this load at the formation of a practical hinge at the support, the mid span section rotates further which causes the load to act in such a way that the strain obtained is more likely to be dominated by minor axis bending, but different strains at the bottom flange indicate effects of warping strain, Wagner strain (Section 2.4.2, Figure 2.10(d)) and flexure strain due to major axis bending and rotation. High values of strain in the centre of the web is due to axial shortening which occur at large rotation.

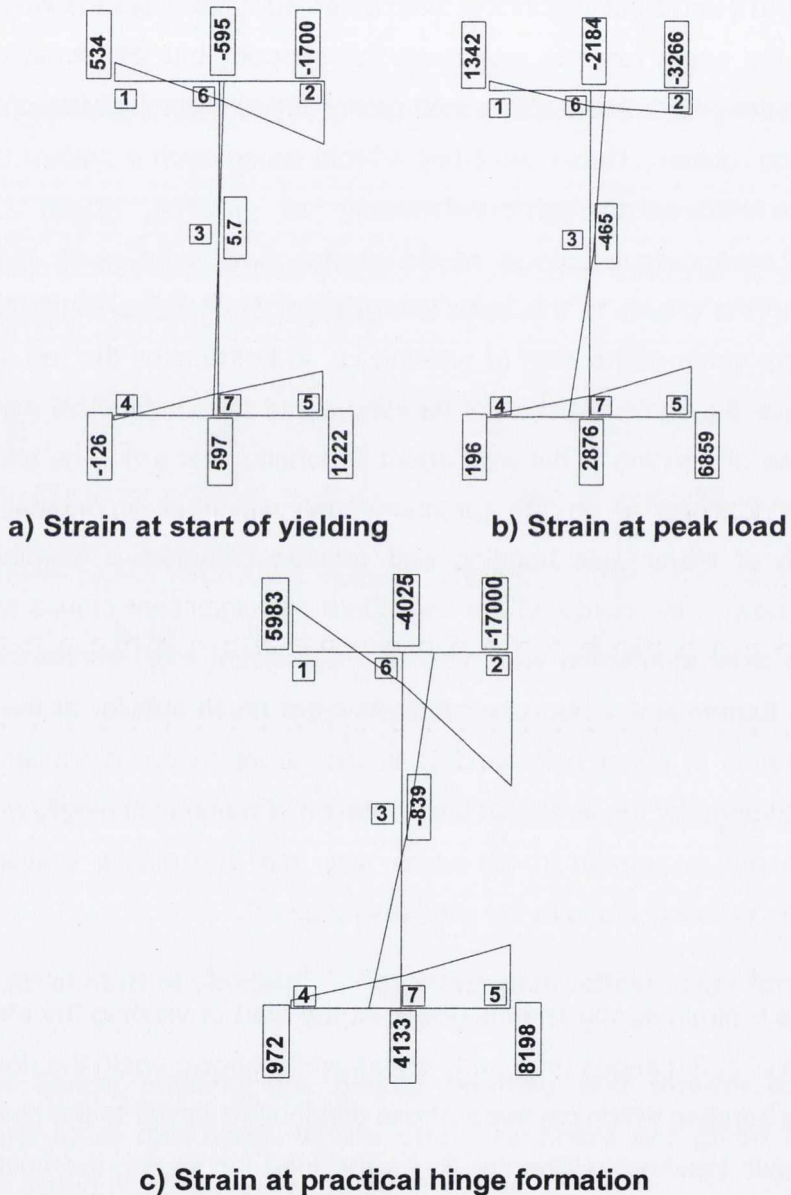


Figure 6.5 Strain patterns for biaxial bending and torsion experiment (Experiment 2) at fixed end, where strain numbers are given in square boxes and strain readings in rectangular boxes.

Comparing Figure 6.5(c) and 6.6(c) the different strain pattern is obvious in both the cases. The reason is that the section rotates at the mid span and is fixed at the support. Therefore both the sections are under different types of bending strain. However this was not the case when, in the first experiment, Figures 6.3(b) and 6.4(b) are considered. In Experiment 1 both strain distribution at the mid section and at the support have a similar pattern. Rotation has a large influence in the second Experiment because the section was weaker in rotation as compared to bending and resulted in more rotation, hence resulting in different strain patterns for the second experiment. In the case of Experiment 1 the section was weaker in bending compared to rotation hence not much rotation took place and the behaviour was mainly dominated by bending, hence a similarity in the strain pattern can be observed.

6.2.4 Torsion rotation relationship

The relationships between torsion and rotation for Experiments 1 and 2 are depicted in Figures 6.7 and 6.8 respectively. Considering Experiment-1, the torsion at which yielding starts is 0.155 kN.m as given in Table 6.1 and this occurs at a rotation of 4.6° . The torsion at which yielding starts can be defined as the elastic limit torsion. Up to the elastic limit torsion, the theoretical value (calculated in Appendix-D) coincides reasonably well with the experimental response, as can be deduced from the dashed line in the figure. However differences exist between both the experimental and theoretical response in the elastic range. There are potentially two main reasons for the difference; the first is the bedding down of the sample which takes place during load application. The second reason for the difference is that the theoretical value is based on a shear modulus which is obtained based on the Young's modulus obtained from Coupon tests while a different shear modulus can exist for this more complex experiment as both the experiment and Coupon tests are based on different loading set-ups. Different values for both the experiment and Coupon tests were also obtained by Goggins (2004) in his research program.

Considering Table 6.1, and assuming $n=10$, the torsion at the formation of the practical hinge is 0.28 kN.m at a rotation of 12.1° . Beyond this, the zone of strain hardening is assumed to start where, in this case, there was no rotation recorded because the potentiometer support broke during this experiment (the torsional

moment at this point was 0.31 kN.m). When the load was subsequently removed a residual rotation was recorded of approximately 11° . When this graph is compared with the graph of the pure torsion experiment, as depicted in Figure 5.26, it can be inferred that in the previous case linearity existed up to an angle of approximately 18° , whereas in this case it was at an angle of 3.7° . The low rotation in the linear phase in this case is an indication of the interaction of bending with torsion.

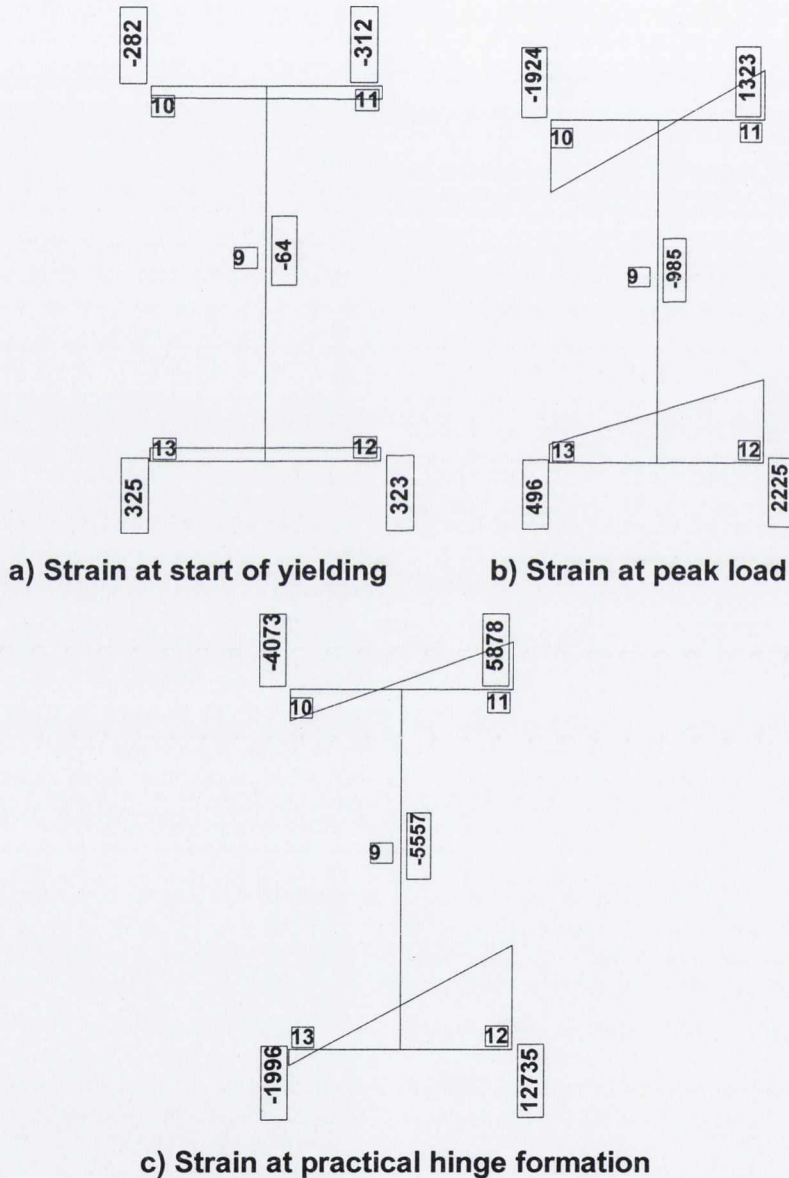


Figure 6.6 Strain patterns for biaxial bending and torsion experiment (Experiment 2) at mid span, where strain numbers are given in the square boxes and strain readings in rectangular boxes.

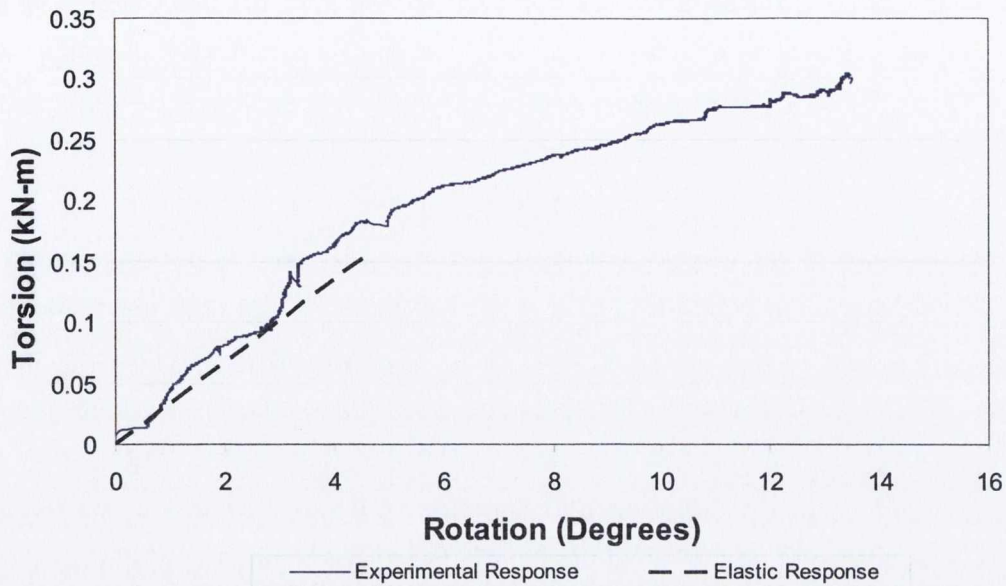


Figure 6.7 Torsion against rotation in the biaxial bending and torsion experiment when minor axis behaviour dominates (Experiment # 1)

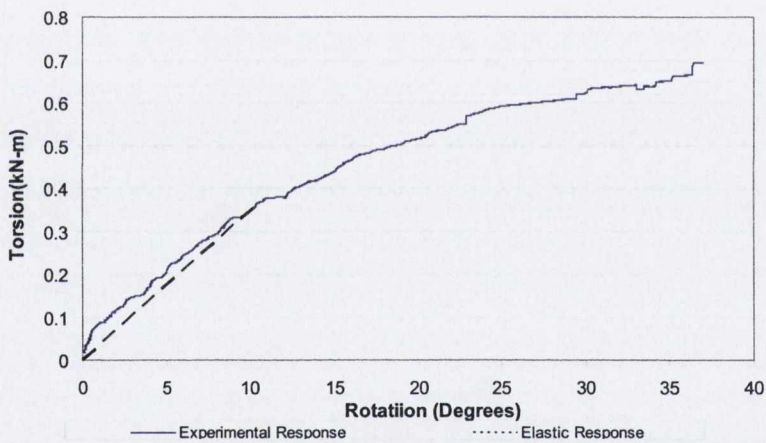


Figure 6.8 Torsion against rotation in the biaxial bending and torsion experiment when major axis behaviour dominates (Experiment # 2)

Considering the results of Experiment-2, as depicted in Figure 6.8, with key data in Table 6.1, it can be deduced that the value of torsion at the elastic limit is 0.37 kN.m at a rotation of 10.8° . Up to this point, the theoretical elastic torsion exhibits the same trend as does the experimental response as can be deduced from the figure. The rotation at the maximum torsion was not recorded due to the breaking of the support of the potentiometer as discussed previously. The peak value of torsion was 0.76 kN.m which was obtained based on the peak load

recorded. However practical hinge formation occurs after the peak load at which the limiting torsion was 0.65 kN.m . The residual rotation on unloading was recorded and was approximately 48° considerably higher than for Experiment 1 (11°)

A comparison of the torsion against rotation response of both experiments is given in Figure 6.9. From the figure it can be deduced that both the responses follow a similar trend up to a rotation of approximately 5° . However minor differences exist between the two up to this angle due partially to the difference in bedding down of the beam samples. Rotation at the elastic limit torsion for Experiment 1 was 3.7° whereas for Experiment 2 it was 7.5° , due to the flexural stiffness difference as explained previously. Beyond this angle of 5° the response of experiment 1 does not match the response of Experiment 2 due to the interaction of torsion with the flexural action. Therefore, it can be concluded that torsion is largely unaffected by flexure in the linear phase of the experiments whereas flexure does affect the torsional response in the non-linear phase of the experiments. Comparing the residual rotations for both the experiments (11° against 48°) the higher residual rotation obtained in the second experiment can be explained by the fact that in the first experiment the section was weak in minor axis bending compared to rotation, hence not much rotation takes place as failure is dominated by minor axis bending and this results in a lesser residual rotation. For the second experiment, the beam was stiffer against bending and relatively weaker in torsional stiffness compared to the bending. Owing to this more rotation takes place as the load to reach yielding is higher and this results in more residual rotation of the beam on unloading.

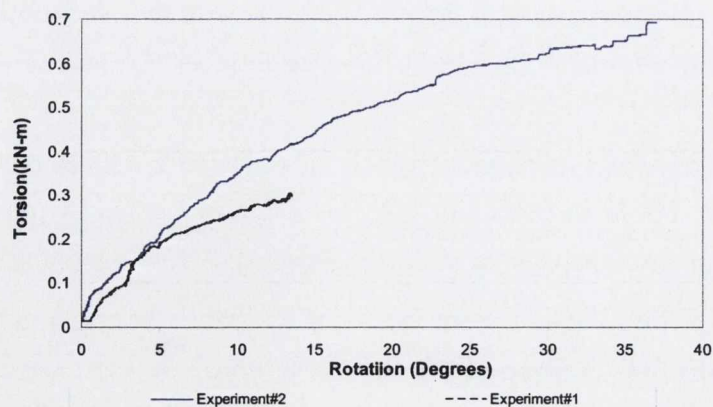


Figure 6.9 Comparison of torsion and rotation for Experiments 1 and 2 of biaxial bending and torsion experiments

6.2.5 Load-Deflection Relationship

The load against deflection relationship for Experiments 1 and 2 are depicted in Figures 6.10 and 6.12 respectively where "load" is the applied load at the free end of the sample and the deflection is the vector magnitude resultant of deflections which were measured in two orthogonal directions (as depicted in Figure 6.2) at the free end of the beam.

Considering Experiment-1 (and Figure 6.10), the graph can be divided into three phases. The first phase is the elastic phase, whose elastic limit load (as given in Table 6.1) is 1.78 kN (as indicated as point A in the figure), where the elastic limit load is the load at which ε_y is achieved anywhere on the beam sample by definition. Beyond this point, some strains remain less than the value at the start of yielding, i.e. they are elastic strains, whilst others are more than the strain at the start of yielding. This phase (A to B) is termed as the elastic - plastic phase, which extends up to a load where the first practical hinge formed at 3.24 kN (as indicated as point B in the figure) as recorded in the table. Beyond this point can be termed as the plastic phase with a strain hardening property of the material in which a slight increase of load can be observed in the figure.

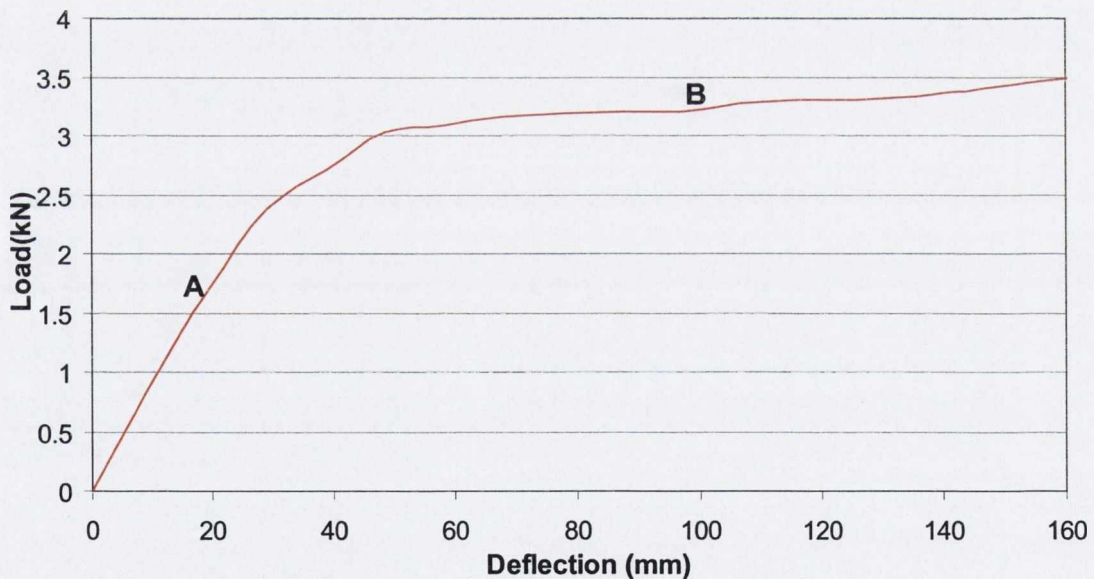


Figure 6.10 Load against deflection plot of the biaxial bending and torsion experiment when minor axis bending dominates (Experiment # 1)

A large residual lateral deflection (92mm in X-direction and 6mm in Y-direction) can be observed on unloading of the beam (Figure 6.11). The large lateral deflection of the beam in the elasto-plastic and strain hardening phases is an indication of the strong influence of bending deformation in the “failure” mode, although a significant residual rotation is also evident (approximately 11°) on unloading.

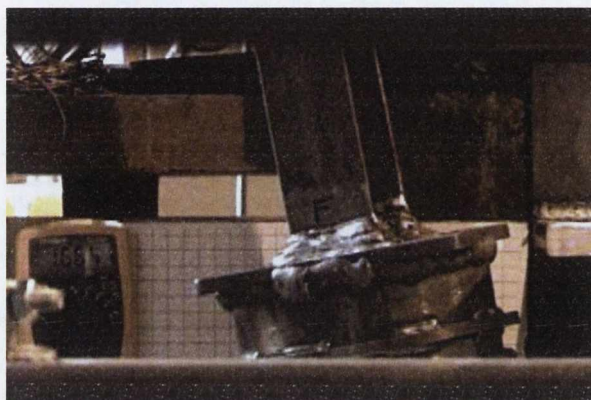


Figure 6.11 Residual lateral displacement and rotation of the beam under biaxial bending and torsion experiment when minor axis bending dominates (Experiment # 1)

Considering Experiment-2, from the strain results given in Table 6.1, it can be inferred that the sample reached its elastic limit load at 4.26 kN (point A in Figure 6.12). Beyond this point it reaches a peak load of 8.72 kN (as denoted as point B in the figure). At the peak load, strains have not reached the strain of 17000 $\mu\epsilon$ (which is the assumed limit of plastic flow) as can be observed from the table, where some strains are more than the elastic limit value but less than the ultimate strain at plastic flow. Figure 6.12 shows that the beam experienced a decrease in load capacity before the formation of the practical hinge. If one considers the strains at mid span at the peak load, they are less than ϵ_y , which shows that yielding started near the fixed end of the beam, not surprisingly. From the strain values given in the table, it can be inferred that the beam experienced a loss of stiffness in the elastic-plastic phase. The point when the beam reached the ϵ_u value is after reaching the peak load, at a load of 7.4 kN. This fall off in load is further discussed in Section 6.2.6. From an examination of the beam on

unloading, as depicted in Figure 6.13 a large residual rotation of approximately 48° can be observed to accompany the large lateral deflection (71mm in X-direction and 5mm in Y-direction). The large residual lateral deflection and rotation are an indication of the interaction of bending and torsional deformation in the plastic phase. Details about the failure of the beam are discussed in the next section.

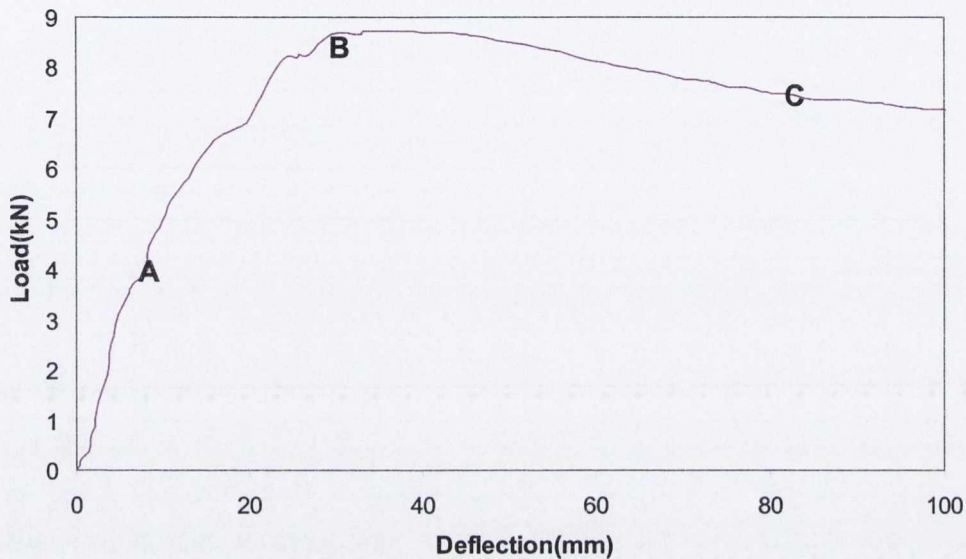


Figure 6.12 Load against deflection of biaxial bending and torsion experiment when major axis behaviour dominates (Experiment # 2)

6.2.6 Failure of the beam samples

From the strains given in Table 6.1 it can be inferred that “failure” was initiated in the first experiment due to yielding on the formation of a practical hinge due principally to minor axis bending. The hinge formed in the sample but the capacity of the beam to take further load on hardening was not exhausted. This can be said because no buckling or tearing of flanges or web was observed during the experiment and also there was a constant but slow increase of response with time, which showed that the beam had not reached its ultimate capacity. The experiment was terminated when the actuator reached its maximum deflection of 100mm . Under this condition, the maximum load applied was considerably more than the load at which a practical hinge was deemed to have formed, which confirms that the beam was in the strain hardening phase beyond the formation of a practical hinge.

Considering Experiment-2, failure occurred due to a different behaviour mode of the beam sample. When the load was applied it was almost perpendicular to the major-axis of the section (see Figure 6.2). During the load application, significant rotation of the beam sample occurs which causes a change in the flexural stiffness of the beam resisting the load. Also, throughout the length of the beam, the bending moment varies, with a maximum at the fixed end and zero at the point of load application. Therefore two key parameters vary along the length of the sample, namely, the cross-section orientation (due to large rotations at the tip in torsion uniformly distributed over the length) and the moment applied. As the orientation of cross section changes, the overall stiffness of the beam decreases and results in the drop of the load capacity. Despite some torsional rotation along the beam, the second moment of area for the fixed end will remain the same, whereas for the mid section, the second moment of area changes about the axis of the applied load. Therefore, two mechanisms interacted at that time after the drop in load; firstly as the beam rotates, a combination of moment and such a value of second moment of area are reached where the beam can have a smaller radius of curvature at the mid span instead of rotating primarily in flexure at the fixed end which results in more bending distribution about the mid span, as is evident from Figure 6.13. Also high values of strains at the mid span confirms yielding of the mid section. However, during this process, torsional rotation continues (see Figure 6.8) which causes an increase of strain at the fixed end. Hence, at the end of the experiment, yielding has occurred both at the fixed end and at the mid span. This is evident from the strain readings both at the fixed end and at the mid span at the formation of practical hinge, where strains are in the state of plastic flow for most of the strain gauges. However practical hinge formation is taken at the fixed end because the strain value of $17000 \mu\epsilon$ is reached at the fixed end and this strain is the basis of defining the point as a practical hinge.

6.2.7 Elastic limit load and yield surface

Considering Experiment-1, the elastic limit load and elastic limit torsion, as identified in the previous discussion, are $1.78kN$ and $0.155kN\cdot m$ respectively. These limit loads are based on the measured strain ϵ_y , where ϵ_y is the direct strain measured in the longitudinal direction. In addition, the beam considered has dimensions such that it comes under the class of a thin walled beam

(Vlasov's 1959), where for thin walled beams shear deformation can be ignored. Therefore only three forces are considered to compare the given loads at failure with the yield surface developed in Chapter-4, while shear forces are ignored. Two of these forces are biaxial bending moments, which occurred at the fixed end due to the limit load and the third is the warping moment which occurred due to the limit torsion. For a cable induced load of 1.78 kN , its component (if resolved in two orthogonal components based on a load direction of 8° with reference to the lateral directions (see Figure 6.2), are 1.76 kN and 0.25 kN in the X and Y directions respectively. This gives moments M_y of 1.82 kN.m and M_x of 0.26 kN.m respectively. The bimoment (defined in Section 2.4.2) obtained for the limit torsion condition is 0.046 kN.m^2 (Appendix-D). The plastic capacities obtained in Chapter 5 are summarized in Table 6.2. Using the plastic capacities, the three obtained forces are converted into their normalized form and are given in the table. For the same values of m_x , b and m_y , m_{xA} is calculated (Appendix-D) which is 0.45. As $m_x < m_{xA}$ and the summation of m_y and b are less than one this suggests that the section has not yet reached the yield surface. Hence the section remains elastic at the elastic limit load, not surprisingly, as the elasto-plastic phase has yet to be crossed.

Similarly considering the elastic limit load and torsion in the case of Experiment-2, the two components of limit load of 4.26 kN are 0.59 kN and 4.21 kN in the X and Y directions respectively. This gives moments M_y of 0.61 kN.m and M_x of 4.35 kN.m respectively. The bimoment obtained for the elastic limit torsion is 0.10 kN.m^2 (Appendix-D). Their capacities in normalized form are summarized in the table. Using the procedure given in Chapter 4, these can be compared with the developed yield surface. For the same values of m_x , b and m_y , m_{xA} is calculated (Appendix-D) as 0.45. As $m_x < m_{xA}$ and the summation of m_y and b are less than one again this implies that the section has not reached the yield surface. Hence, it can be concluded that the said applied load and torsion has not caused the yield point to be reached when compared with the theoretical yield surface.

6.2.8 Practical hinge formation and yield surface

In Experiment-1 a practical hinge is assumed to form at a load of 3.24 kN for which strains are given in Table 6.1. The torsion at which this occurs is 0.28 kN.m . This load creates moments of 0.46 kN.m and 3.3 kN.m in the X and Y directions respectively. No procedure exists to obtain the exact equivalent bimoment (defined in Section 2.4.2) in the inelastic range when biaxial bending moments are applied to the section in combination with torsion. To obtain the bimoment value in the presence of biaxial bending moments in the inelastic range, a factor by which torsion has increased on the formation of a practical hinge compared with the elastic limit torsion is calculated. The bimoment value obtained at the elastic limit torsion is then multiplied by this factor to obtain an estimate of the bimoment at the formation of a practical hinge. The increase in the torsion from the elastic limit value to a value at the formation of a practical hinge is by a factor of 1.81. Therefore, multiplying the bimoment of the elastic case by 1.81 yields a bimoment of 0.089 kN.m^2 . This gives an approximate value for comparison with the yield surface. All the forces at the formation of a practical hinge are shown in normalized form in Table 6.2. It can be observed in the table that m_y (at a load of 3.24 kN) is 1.13, which is more than its plastic capacity, which shows that the load point at the formation of a practical hinge is actually outside the yield surface. As it is known that the load at practical hinge formation was subjectively selected based on $n=10$ (see Equation 6.1), then as the m_y value has already exceeded its plastic capacity at this load, it demonstrates that the load point at which it will reach the yield surface must have a smaller value of n (but more than $n=1$ as the yield surface was not reached for the elastic limit load). As the summation of the normalized m_y and b for the elastic limit load is 0.94, therefore both these values are increased in the same proportion such that the summation of m_y and b equals to 1 and that load is used to compare with the yield surface. This load is calculated as 1.9 kN , which is 1.06 times more than the elastic limit load. Based on this load, the moments which it produces are 0.27 kN.m and 1.94 kN.m in the X and Y direction respectively, whereas torsion at this load is 0.165 kN.m , which gives a bimoment of 0.049 kN.m^2 . These forces are less than its load at practical hinge formation and are also shown in normalized form in the table. For the same values of m_x , b and m_y , m_{xA} is calculated (Appendix-D) which is 0.455. As $m_x < m_{xA}$ and the summation of m_y

and b is equal to one this suggests that the section has reached the yield surface. Hence it can be concluded that the applied load has caused the yield point to be reached as determined by the theoretical yield surface. However the value of 1.9 kN cannot be said to be the true yield value because it is not based on any experimental evidence.

	M_x	M_y	B
Plastic capacities	15.15 kN.m	2.93 kN.m	$.144\text{ kN-m}^2$
Experiment-1			
Load= 1.78 kN	0.26	1.82	0.046
Load= 1.78 kN (Normalized)	0.018	0.62	0.32
Load= 3.24 kN	0.46	3.3	0.089
Load= 3.24 kN (Normalized)	0.03	1.13	0.62
Load= 1.90 kN	0.27	1.94	0.049
Load= 1.90 kN (Normalized)	0.018	0.66	0.34
Experiment-2			
Load= 4.26 kN	4.35	0.61	0.1
Load= 4.26 kN (Normalized)	0.29	0.21	0.69
Load= 8.72 kN	9.5	1.33	0.2
Load= 8.72 kN (Normalized)	0.69	0.46	1.42
Load= 4.73 kN	4.82	0.68	0.11
Load= 4.73 kN (Normalized)	0.32	0.24	0.76

Table 6.2 Biaxial bending moment and bimoment for load and torsion applied in Experiment 1 and 2

Considering Table 6.1, the strain gauges which are in the plastic flow state are strain # 1, 2, 4 and 5. Considering the graph as depicted in Figure 6.14 it can be observed that plastic flow started in those four strain gauges at a value of approximately 3.1 kN . This shows that this load can be taken as a point of hinge formation (an increase of strain beyond this point is observed without much increase of load). Comparing with the load of 1.9 kN , it shows that the experimental load at which hinge forms is 1.63 times more than the theoretical load.

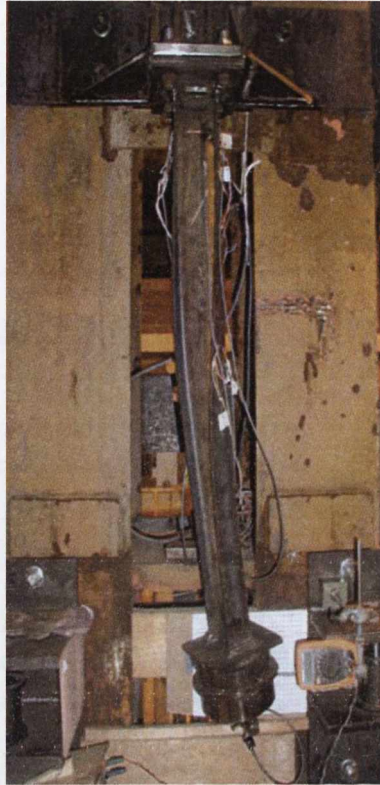


Figure 6.13 Residual lateral displacement and rotation of beam in the biaxial bending and torsion experiment when major axis bending dominates (Experiment # 2)

As discussed previously, the peak load is achieved before the formation of the practical hinge in Experiment 2. This load is 2.04 times more than the elastic limit load. The moments which it produces are 9.50 kN.m and 1.33 kN.m in the X and Y directions respectively, whereas torsion at the peak load is 0.76 kN.m . Following the same basis as previously, the bimoment value, in the presence of biaxial bending moments in the inelastic range, is obtained by multiplying the bimoment value obtained for the elastic limit load by a factor of 2.04 which gives bimoment as 0.20 kN.m^2 . The obtained forces in normalized form are summarized in Table 6.2. It can be observed that the bimoment obtained (1.42) is more than the plastic bimoment capacity. Considering the maximum recorded strain at this load, which is $6859 \mu\epsilon$ (Table 6.1) at strain gauge # 5 and, based on Equation 6.1, n obtained for this strain is 4.03, which is less than the earlier assumption of $n=5-10$ for practical hinge formation. Therefore, as the bimoment capacity has already exceeded its plastic capacity at the peak load, it implies that

the load point at which it will reach the yield surface must have a smaller value of n . Based on the procedure discussed in the previous section, the load is calculated as 4.73 kN which is 1.11 times more than the elastic limit load. Based on this load, the moments which it produces are 4.82 kN.m and 0.68 kN.m in the X and Y directions respectively, while the torsion at this load is 0.41 kN.m from which the bimoment obtained is 0.11 kN.m^2 . For the same values of m_x , b and m_y , m_{xA} is calculated as 0.45 (Appendix-D). As $m_x < m_{xA}$ and the summation of m_y and b is equal to one it means the section has reached the yield surface. Comparing this with the hinge formation based on experimental evidence, it can be observed from Figure 6.15 that plastic flow occurs in strains # 1, 2, 4 and 5 at a load of nearly 8.7 kN and this load can be taken as the point of hinge formation (an increase of strain beyond this point is observed without much increase of load). Comparing with the load at formation of the theoretical hinge this is 1.84 times greater.

For both the experiments, the yield surface given by Chapter 4 predicted a much lower capacity than those obtained in the experiments. There are two main reasons for the large difference between theoretical yield surface and experimental evidence of hinge formation. First in the development of yield surface, an elastic perfectly plastic material is assumed, and the stress strain diagram has a maximum yield stress, and that yield stress is 1.39 times (based on average Coupon result of Section 5.2.1) more than the ultimate yield stress, whereas experiments are based on ultimate stress. The theoretical yield surface is based on the maximum yield stress and does not consider the additional strength of material. Second is that the torsional capacity of a section is high when Wagner strain (Section 2.4.2, Figure 2.10(d)) and axial shortening are considered. Owing to this more resistance is provided from the beam to the load and results in high loads, whereas in the theoretical yield surface it is based on only three strains (four in reality including strain due to axial force), whereas experiments are based on biaxial bending strain, warping strain, Wagner strain, axial shortening strains. Hence due to secondary torsional strain more resistance is provided by the beam and this is the second reason for such a high load.

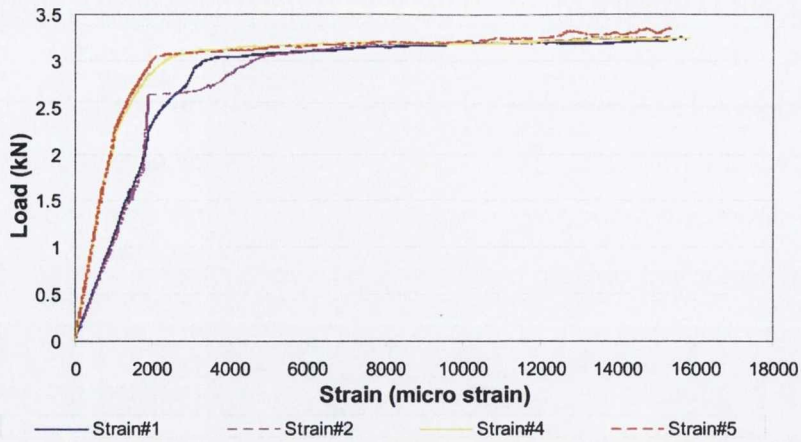


Figure 6.14 Strain # 1,2,4 and 5, Load against strain of biaxial bending and torsion experiment when minor axis behaviour dominates (Experiment # 1) at the fixed end of the beam

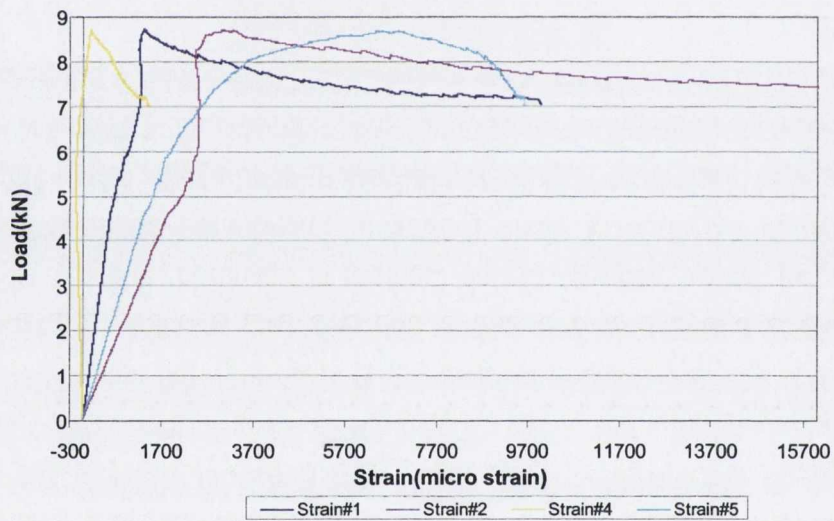


Figure 6.15 Strain # 1,2,4 and 5, Load against strain of biaxial bending and torsion experiment when major axis bending dominates (Experiment# 2) at the fixed end of the beam

6.2.9 Measured strain

Experiment - 1

The load against strain graphs may be plotted for strains at the fixed end and at the mid section of the beam. The location of these strain gauges is given in Figure 5.23. Consider the strains at the edges of the flanges near the fixed end,

where their load against strain graphs is given in Figure 6.14. Strain #2 and strain #5 are in compression as indicated by their negative direct strains but for comparison they are shown positive in the figure.

Up to the elastic limit load, the response is largely linear. Strains 1 and 2 and strains 4 and 5 clearly match each other and comparison with Figure 6.3 shows the domination of minor-axis bending in the linear phase. Beyond this point, strain increases are non-linear but, again, match each other for most of the phase. All the strains almost reached the assumed limit of plastic flow ($17000 \mu\epsilon$). Similar values of strains 1 and 2 and strains 4 and 5 indicate that minor-axis bending also dominates the non-linear phase of loading. This confirms that failure occurred mainly due to bending of the beam about the minor axis, with a influence from torsional rotation which causes warping of the section and Wagner and axial shortening at large rotation.

A load against strain plot for the web section near the fixed end is shown in Figure 6.16. Comparing Figure 6.14 and 6.16, it can be inferred that the strains in the web for all strain locations are less than the ϵ_y value and are all an order of magnitude less than the strains at the edges of flanges. This shows that the web was under a small amount of strain and that bending about the major-axis was not dominating (where strains would develop in the web considerably). However, the failure was not solely a failure of bending of the beam in the minor direction. This is because in the case of pure minor axis bending failure, the amount of strain developed in strain #3, 6 and 7 would be significantly less than the values observed here. Rotation/torsion warping can cause the neutral-axis not to be a straight line (see Section 4.7) and some major axis bending for the section and axial shortening takes place in such a way that they create greater strain for strain #3 as compared to strains #6 and 7. In addition, the beam's principal axes were not entirely perpendicular/parallel to the direction of load application at the support: hence, a small contribution of strain from the major axis bending component will have occurred.

It can thus be concluded that both the warping strain, and the strain from major-axis bending cause a non-straight neutral axis and results in more strain (also including axial shortening) for strain# 3 as compared to strains # 6 and 7. The

irregular pattern in the sign of the strain in the figure is due to the fact that the interaction between rotation and bending changes throughout the experiment while warping strain dominates at the start of the experiment the strains are later dominated by the major axis bending component, axial shortening and Wagner strain (Section 2.4.2, Figure 2.10(d)), hence this results in sign change of some of the web strain gauges.

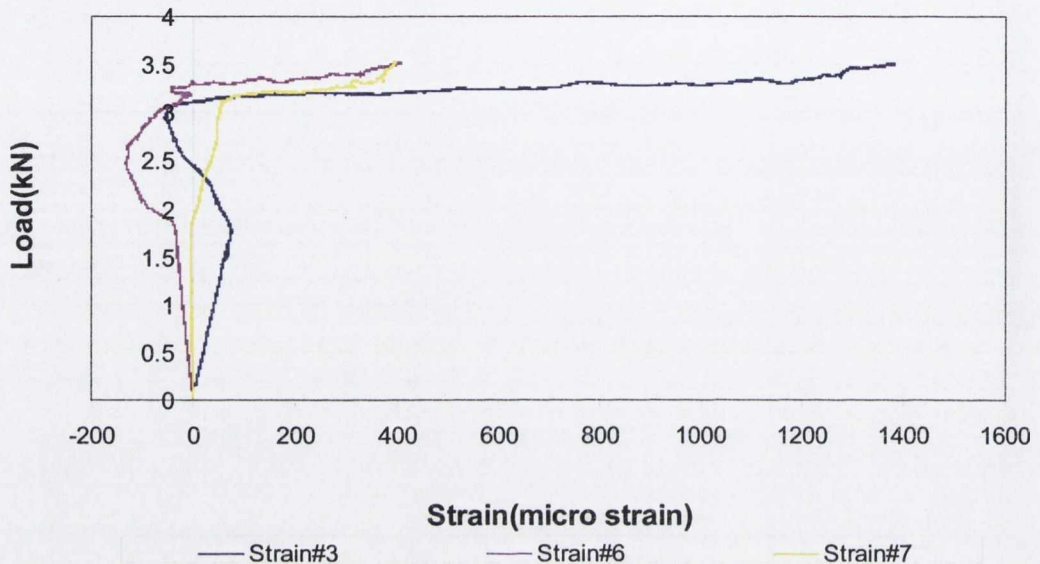


Figure 6.16 Strain # 3, 6 and 7, Load against strain of biaxial bending and torsion experiment when minor axis behaviour dominates (Experiment # 1) at the fixed end of the beam

Strains for the mid-section are shown in Figure 6.17. Strain # 11 and 12 are in compression and have a negative direct strain but for comparison they are shown positive. It can be deduced that all the strains are less than the elastic limit load strain ($1700 \mu\epsilon$) which shows that the beam responded linearly at mid-section up to the end of the experiment. A difference exists between strains #10, 11, 12 and 13 after a load of approximately $1.5kN$. This difference is due to the warping effects, Wagner effects and the strain component of major axis bending developing (as discussed before). However, the difference is not in the early stages of the loading which suggests that the interaction of bending and rotation changes as the load progresses, where almost identical values of strain for the four strain gauges at the start of loading is an indication that minor axis bending

was dominating strongly. Small values of strain for strain #9 was mainly due to axial shortening.

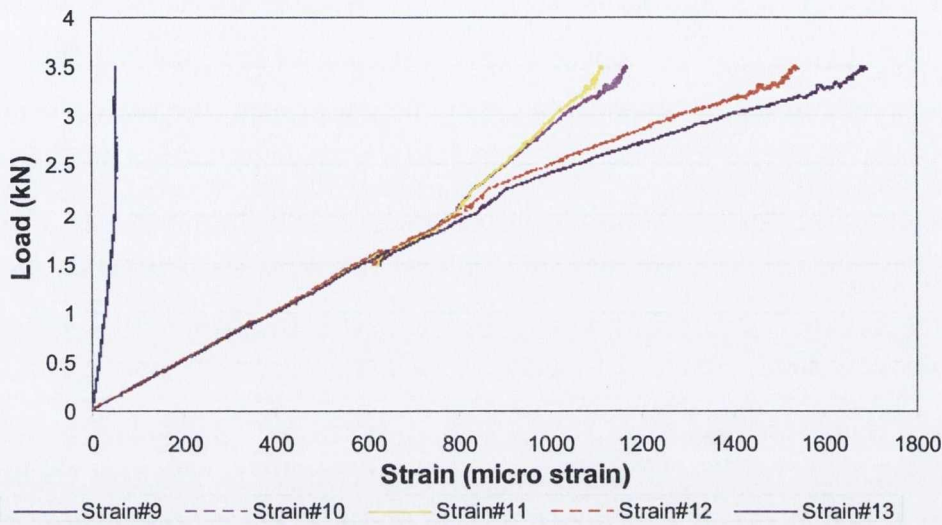


Figure 6.17 Load against strain of biaxial bending and torsion experiment when minor axis behaviour dominates (Experiment # 1) at the mid section of the beam

Experiment - 2

The load against strain relationship will be investigated at the fixed end and at the mid-section of the beam. The location of these strain gauges is given in Figures 5.23, 6.4 and 6.5.

Consider the strains at the edges of the flange near the fixed end, as depicted in Figure 6.15. Strain #2 is in compression and has a negative direct strain but for comparison it is shown positive in the figure, whereas the remaining strains are positive. Almost up to the assumed elastic limit load of 4.26 kN , the load-strain response is linear; beyond the elastic limit load, the response is non-linear up to the peak load. The responses of all the strain gauges show that it is not solely a major axis bending response (because in pure major axis bending response, strains #1 and 2 and strains # 4 and 5 would have similar signs because each flange will be either in compression or tension), whereas in the current distribution signs are different. Up to a load of approximately 7 kN strains #2 and 4 are negative whereas strains # 1 and 5 are positive. This shows that the strain

pattern was affected by warping strains which occurs due to rotation and causes an irregular pattern and a non-straight line for the neutral-axis (as it can occur in the presence of warping strain, see Figure 6.4). In addition there will be minor components of strain from minor axis bending, Wagner strain (Section 2.4.2, Figure 2.10(d)) and axial shortening. If strains are plotted at a load of $4.26kN$, as depicted in Figure 6.4, a non-straight neutral axis is evident. Between a load of $7kN$ and the peak load only the sign of strain #2 is negative, demonstrating that the interaction of rotation and bending changes the behaviour and causes the strain to change at a different rate. This happens because the rotation causes a decrease in the flexural stiffness of the beam and so results in a different behavioural mode.

The strains in the middle of the flanges and the centre of the web near the fixed end are shown in Figure 6.18. Strain #3 and strain #6 are in compression and have negative direct strains but for comparison they are shown positive. Up to the elastic limit load ($4.26kN$) the response is linear; beyond it the response became non-linear. Strain #6 and 7 have almost equal magnitude but opposite signs. This is because of the domination of major axis bending which causes two equal strains but of opposite signs for the middle of both the flanges, whereas at these locations warping strain has no effect. Strain #3 increases in the later stage of loading due to axial shortening effects caused by rotation, hence resulting in a considerable increase of strain after the peak load.

Strains for the mid section are shown in Figure 6.19. Strains # 9, 10 and 13 are in compression and have a negative direct strain but are shown as positive for comparison. Up to the peak load, all strains are within the elastic limit strain while beyond peak load, plastic flow occurs where the strains are considerably more than the elastic strain. Up to the elastic limit load strains #10 and 12 and strains #11 and 13 have similar magnitudes but different senses. This shows that the response is a combination of the domination of warping of the section due to rotation at the early stages and combined bending strain. Beyond this load up to the peak load the flexural stiffness starts to decrease, and the minor axis bending warping effect, Wagner effect (Section 2.4.2, Figure 2.10(d)) and axial shortening becomes more dominant. In this phase strains # 11 and 13 do not match each other while strains #10 and 12 indicate the strains were affected by the described

effects. This shows the change of interaction from one dominated by rotation towards a more even combination of bending and rotation effects. Beyond the peak load a change in the sign of strain #13 takes place because of the decrease of stiffness and the strain distribution is more like the strain distribution one gets for the minor axis bending case, as can be observed from Table 6.1 and Figure 6.6 for a load of $7.44kN$. This happens due to the change of stiffness because of the large rotations which occur beyond the peak load. The increase in strain # 9 beyond the peak load is an indication of axial shortening effects which increase at large rotations.

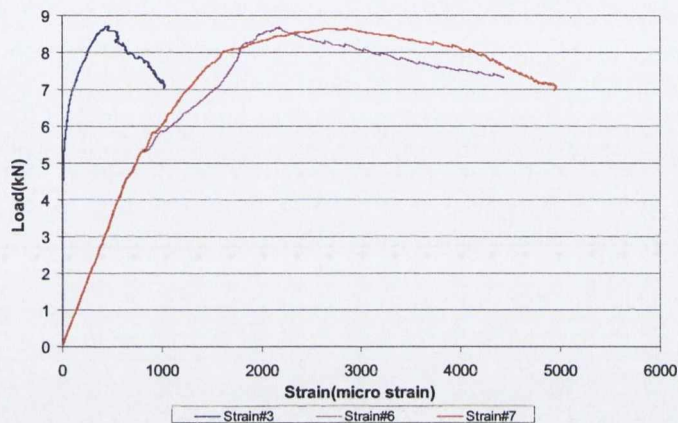


Figure 6.18 Strain # 3, 6, and 7 Load against strain of biaxial bending and torsion experiment when major axis bending dominates (Experiment # 2) at the fixed end of the beam

6.2.10 Displacement in two orthogonal directions

Figure 6.20 presents the cantilever tip displacement in two different directions for Experiment 1 where the directions are perpendicular to each other. The directions in which the displacements were measured are given in Figure 6.2 and the load-deflection plot is given in Figure 6.10. The displacement in the X-direction is large as compared to the displacement in the Y-direction, the reason being that the direction of load application was nearly parallel to the X-direction. The graph can be divided into three phases based on the variation of displacement in the Y-direction with respect to the X-direction. The phase distribution of this graph is different from the phase distribution of Figure 6.10. The first phase is from the origin to point A during which a gradual increase of displacement in the Y-direction can be observed. Comparing this with Figure

6.10, it can be said that this phase is when the response seems to be approximately linear at a load of $3kN$. In this phase, the increase of deflection in both the directions is such that it indicates a relation of uniform interaction between them. Although as the beam rotates slightly, this is a shift towards more Y-axis (major-axis movement). The second phase is from point A to point B where a large increase in the X-direction occurs for a relatively small increase in the Y-direction. Comparing this phase with Figure 6.10, it can be observed that the response was in the elasto-plastic phase where yielding takes place for a small increase of load. The large increase of displacement in the X-direction is an indication that yielding takes place mainly due to minor axis bending. Beyond point B up to the end of the experiment is the third phase of the graph in which a gradual increase of displacement in the Y-direction is an indication that deflection takes place for both the major and minor axis bending. This happens because of rotation of the beam with increasing torsion which causes a change in the flexural stiffness over the beam length and results in a greater interaction of bending about both the axes.

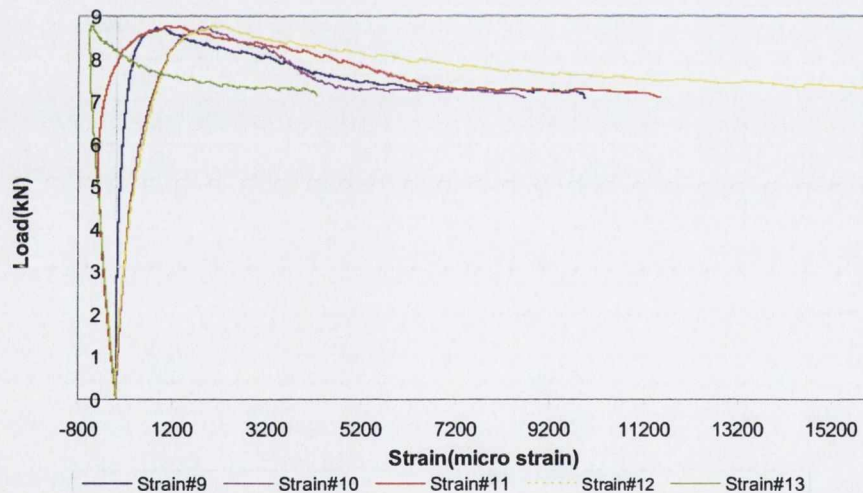


Figure 6.19 Strain # 9,10,11,12 and 13. Load against strain of biaxial bending and torsion experiment when major axis bending dominate (Experiment # 2) at the mid span of the beam

Figure 6.21 presents the displacements in the two different directions for Experiment 2. The reason for the different value of X-displacement compared to the Y-displacement is as discussed in the previous section where now the load

direction causes most of the bending to occur about the major-axis, although the small load component still causes significant deflection about the weaker axis. The graph can be divided into three phases (The phase distribution of this graph is different from the phase distribution of Figure 6.12). The first phase which is between the origin and point A, the response was broadly linear. From the load-deflection response given in Figure 6.12 it can be observed that this happens at a deflection of approximately 26mm (value calculated based on the X and Y values in Figure 6.21) at a load of 8.22kN beyond the elastic phase and before the peak load. Increase of displacement in both the directions indicates the trade off of load and stiffness in the interaction of bending in the X and Y directions. In the second phase which is between point A and B, as the deflection increases in the Y-direction a drop in the displacement in the X-direction can be observed. Point B of the figure when compared to Figure 6.12 lies at a displacement of 80mm as indicated as point C in the figure. It shows that there is a change in the interaction of both the displacements between point A and B of Figure 6.21 as compared to the first phase. Point A of the figure relates to loading near the peak load (near to Point B in Figure 6.12) and point B relate to the load at formation of practical hinge (near to point C in Figure 6.12). As the drop off of load is related to the decrease of stiffness of the section as a whole, a drop in the displacement of X direction will occur. This shows loss of stiffness in the X-direction takes place because of rotation of the beam and it continues up to the formation of practical hinge.

Beyond the practical hinge formation (beyond point B in Figure 6.21) a decrease in the deflection in X-direction compared to its initial position is observed. It can be argued that it is not possible that a value of X lesser than its initial value of zero can occur. However, the way beam failed it is possible. At the stage of Point C of Figure 6.12 the beam was not straight and bends more about the middle as can be observed from Figure 6.13. On further rotation, the beam deflects in such a way as to have a negative deflection in the X-direction. As now the beam was not rotating as a straight beam but as a highly distorted beam, this causes a negative deflection in X-direction.

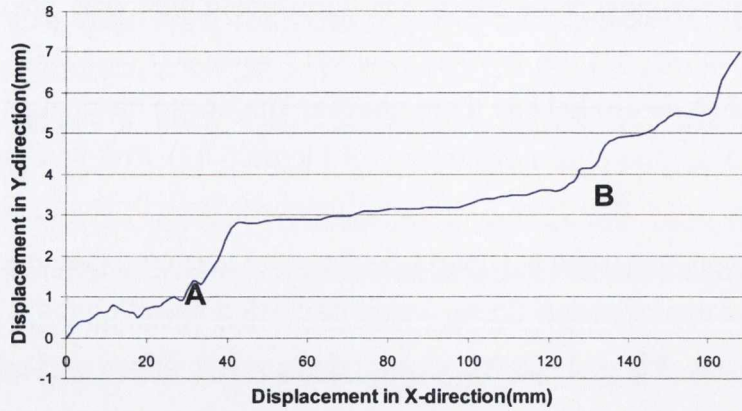


Figure 6.20 Displacement in two perpendicular directions of biaxial bending and torsion experiment when minor axis bending dominates (Experiment # 1)

Owing to the bending flexibility of the beam in Experiment 1, not a large amount of rotation occurred before it reached a plastic flow in flexure; hence, deflections relative to rotation are high. However, in Experiment 2, the beam was flexurally much stiffer when bending about its major axis. Therefore, the rotations were much higher for a given total deflection until the beam had rotated sufficiently to develop plastic flow in torsion and minor axis bending.

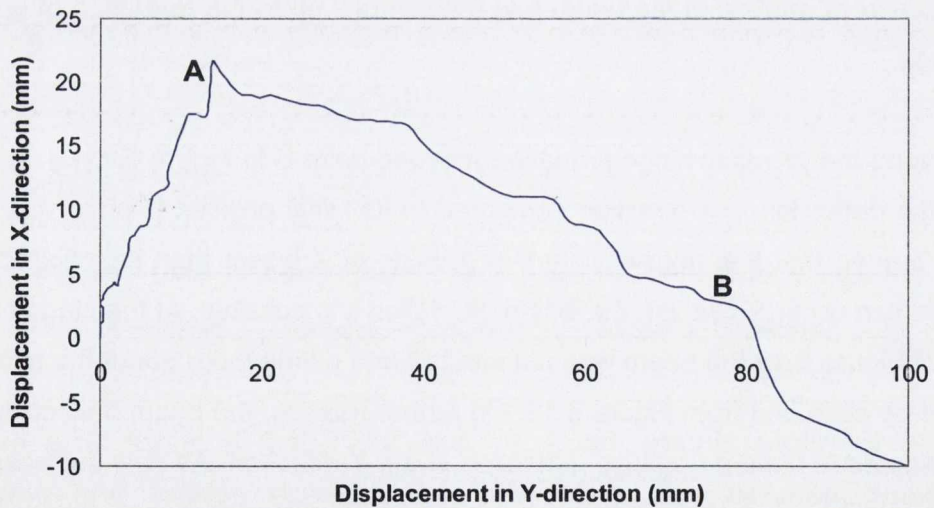


Figure 6.21 Displacement in two perpendicular directions of biaxial bending and torsion experiment when major axis bending dominates (Experiment # 2)

6.2.11 Displacement in Y-direction and measured rotation

Figure 6.22 presents the displacement in the Y-direction and rotation of the beam for Experiment 1. A reasonably uniform response can be observed in the graph initially i.e. there is a slow but constant rise of displacement on the increase of rotation (both of which are caused by the same cable load). However, a sharp rise of displacement is observed for a small amount of rotation after an angle of 12° . This shows that the interaction between displacement and rotation changes in the latter stages where the rise of displacement at the end of the stage is an indication of the decrease of flexural stiffness of the beam. At 12° rotation the Y – axis deflection is approximately 3mm which corresponds (in Figure 6.20) to an X – axis deflection of approximately 70mm. When this deflection is compared with Figure 6.10, it shows that the beam at this rotation was in the elasto-plastic phase. Therefore, at this stage, flexural plasticity took place giving rise to a sharp rise in the displacement without considerable increase of rotation.

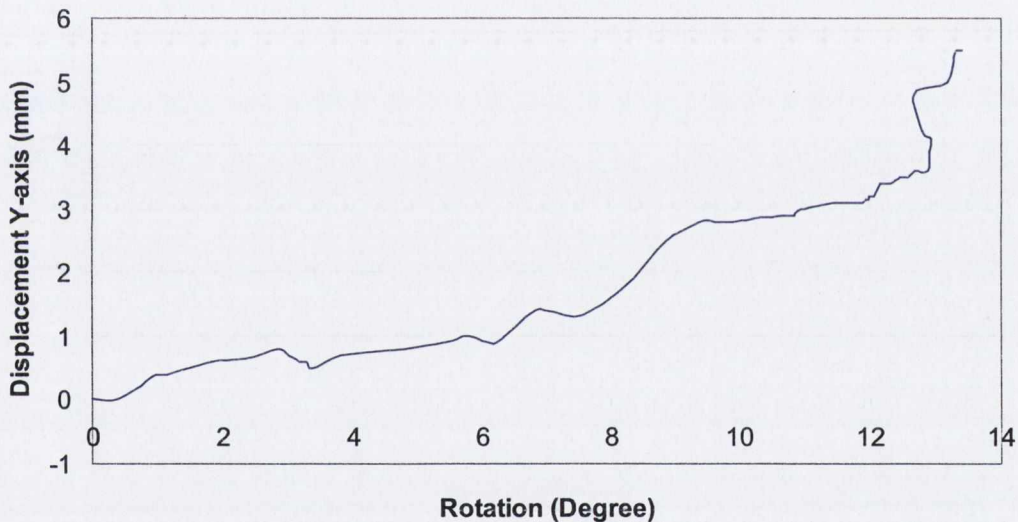


Figure 6.22 Displacement in Y-axis and rotation of biaxial bending and torsion experiment when minor axis bending dominates (Experiment # 1)

Figure 6.23 presents the displacement in the Y-direction and rotation of the beam sample for Experiment 2. Very little Y-axis movement is observed until about 8° . Beyond this point it can be observed that there is no change of response rate as the response is linear. This means that there is no change in the interaction of the response up to the point when rotation ceased to be measured. However, not

much information can be derived from this graph due to not recording rotation beyond 35° due to faulty equipment.

6.2.12 Displacement in X-direction and measured rotation

Figure 6.24 presents the displacement in the X-direction against rotation for Experiment 1. The relationship is broadly linear up to a rotation of approximately 11° after which a rapid development of X-displacement occurred. A different nature of interaction between rotation and deflection was present at large deflections. Comparing the deflection of approximately 50mm, which occurred at 11°, with the deflection in Figures 6.10 and 6.20 it can be inferred that this is the elasto-plastic phase for which increase of deflection takes place on flexural yielding. This is confirmed in Figure 6.24.

Figure 6.25 presents displacement in the X-direction against rotation for Experiment 2. Unlike the previous case (Figure 6.24), there was a linear response throughout. It shows that up to the point where the rotation ceased to be measured, the beam was in the elastic phase, where the relationship between the deflection and rotation was unchanged and nothing of significance can be gleaned.

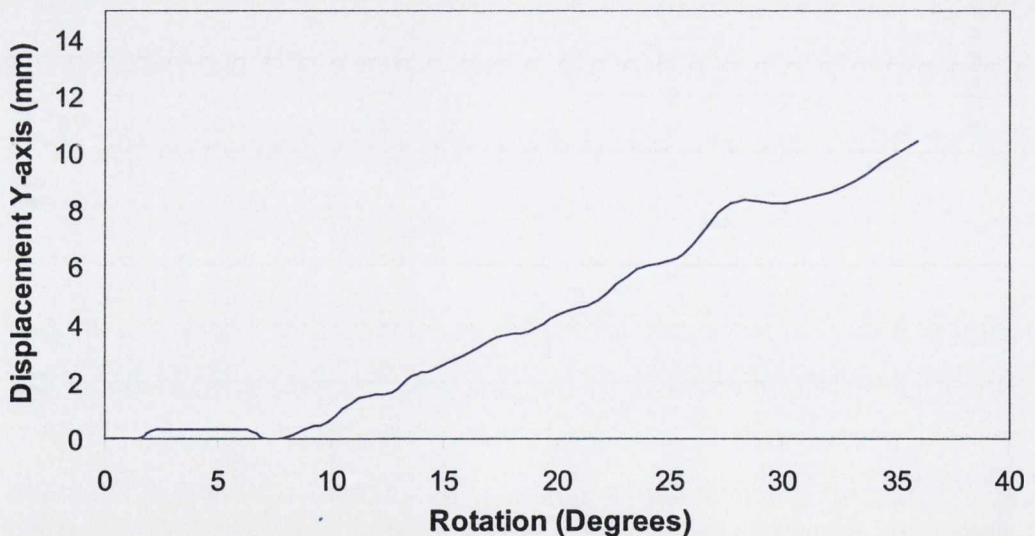


Figure 6.23 Displacement in Y-axis and rotation of biaxial bending and torsion experiment when major axis bending dominates (Experiment # 2)

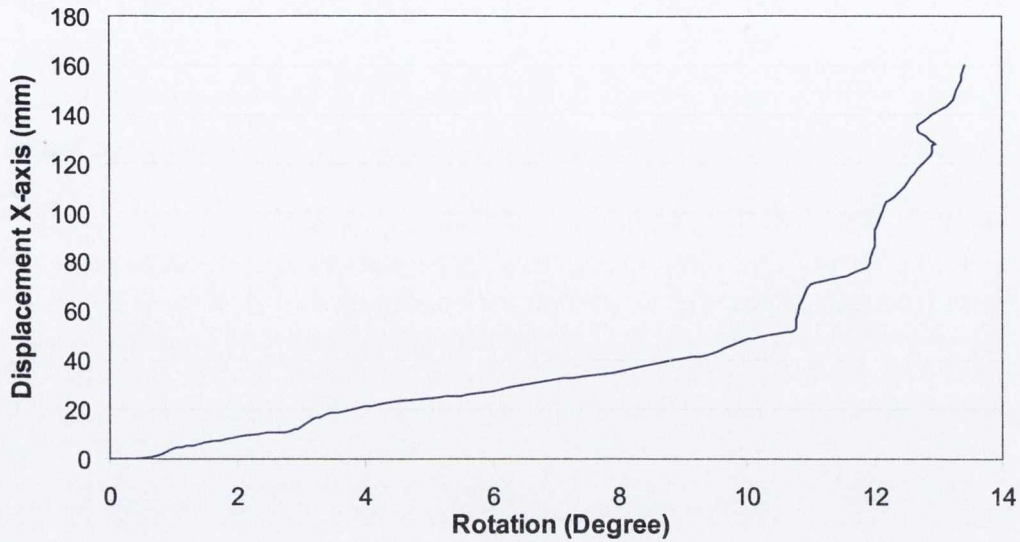


Figure 6.24 Displacement in X-axis and rotation of biaxial bending and torsion experiment when minor axis bending dominates (Experiment # 1)

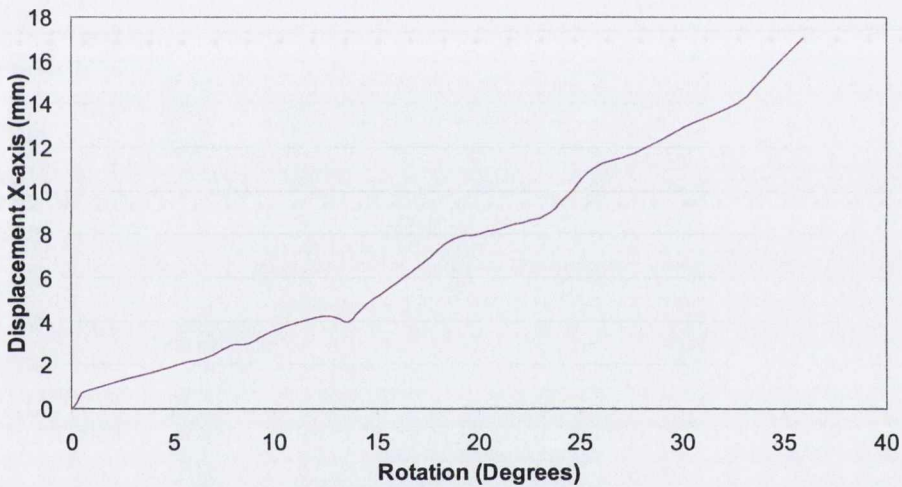


Figure 6.25 Displacement in X-axis and rotation of biaxial bending and torsion experiment when major axis bending dominates (Experiment # 2)

6.3 AXIAL FORCE, BIAxIAL BENDING AND TORSION EXPERIMENT

6.3.1 Experimental Set-up

To apply an axial load to the sample beam, an addition is made to the set-up of Experiments 1 and 2 (shown in Figure 6.1). The location of the prestressing tendon which delivers the axial load is on the longitudinal axis of the I-section, connected to the cantilever tip. In this direction a 30 tonne mechanical hydraulic

jack was fixed with a calibrated RDP load cell (also of capacity 30 tonnes) attached which measures the force applied by the jack in tensioning to the beam sample. There is also a cross-beam connected to the internal reaction frame which resists the thrust from the hydraulic jack in applying the axial load. The whole assembly is depicted in Figure 6.26.

Axial load application

A 25mm prestressing strand was connected to the beam sample using a typical wedge block. This strand passed through a hole in the cross beam and the other end of the strand was anchored to the end of the hydraulic jack as indicated in Figure 6.26. The position shown in the figure is during assembly prior to the load being applied by hydraulic jack. When the load was applied, the upper end of the hydraulic jack, which was placed outside of the load cell, reacted against the soffit of the cross-beam, to provide resistance as depicted in Figure 6.27. The direction of load application and resistance also is depicted in the figure.

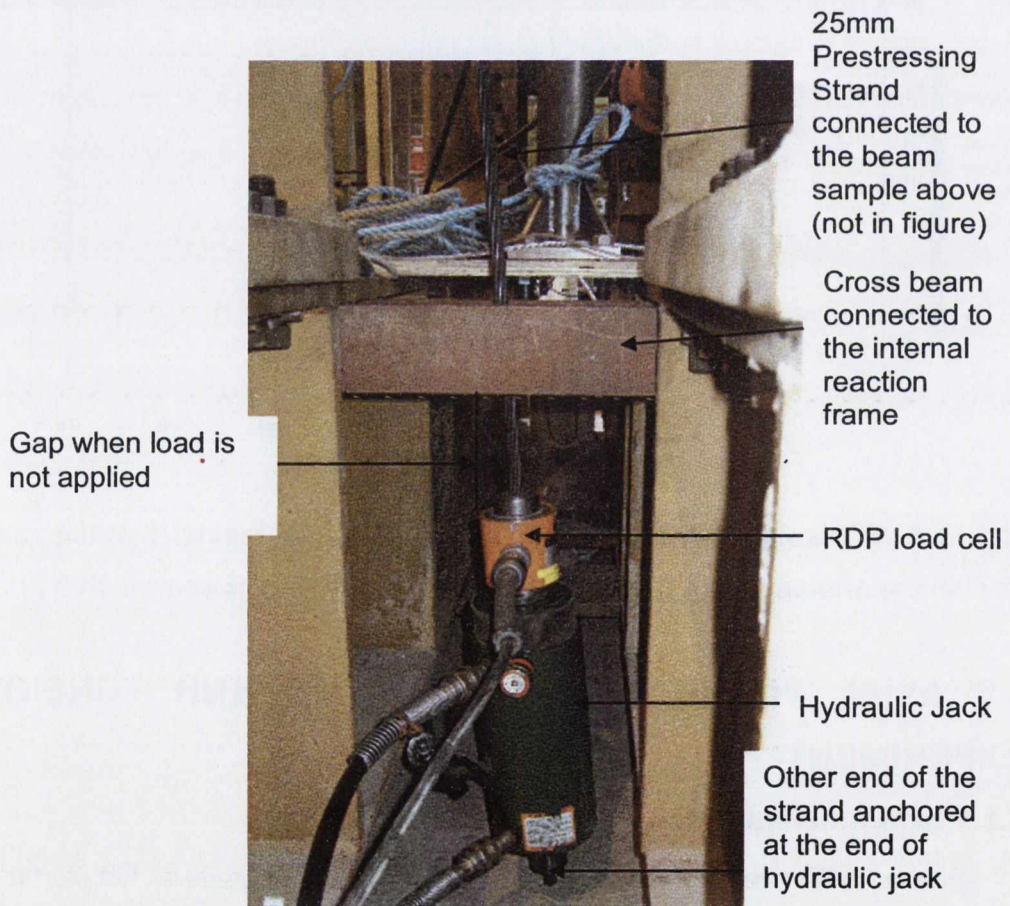


Figure 6.26 Arrangement of applied axial load (with load cell and cross beam)

Load measurement and data storage

Axial loading was applied by the hydraulic jack, where a load cell was attached to measure the actual loading. This load cell measured the load based on the resistance provided by the strand when it is extended during the pulling of the strand by the hydraulic jack. The load cell records the measured force in the cable including when further load is induced in the cell through subsequent displacement of the cantilever beam when subjected to biaxial bending and torsion loading. As previously, all the signals received by the System 5000 (data acquisition system) were transferred to a data storage card installed in a computer and is synchronized by the software "StrainSmart". The StrainSmart stores the data on the computer hard disk in ASCII-Code where it can be read in software Microsoft Excel to allow interpretation of the experimental results.

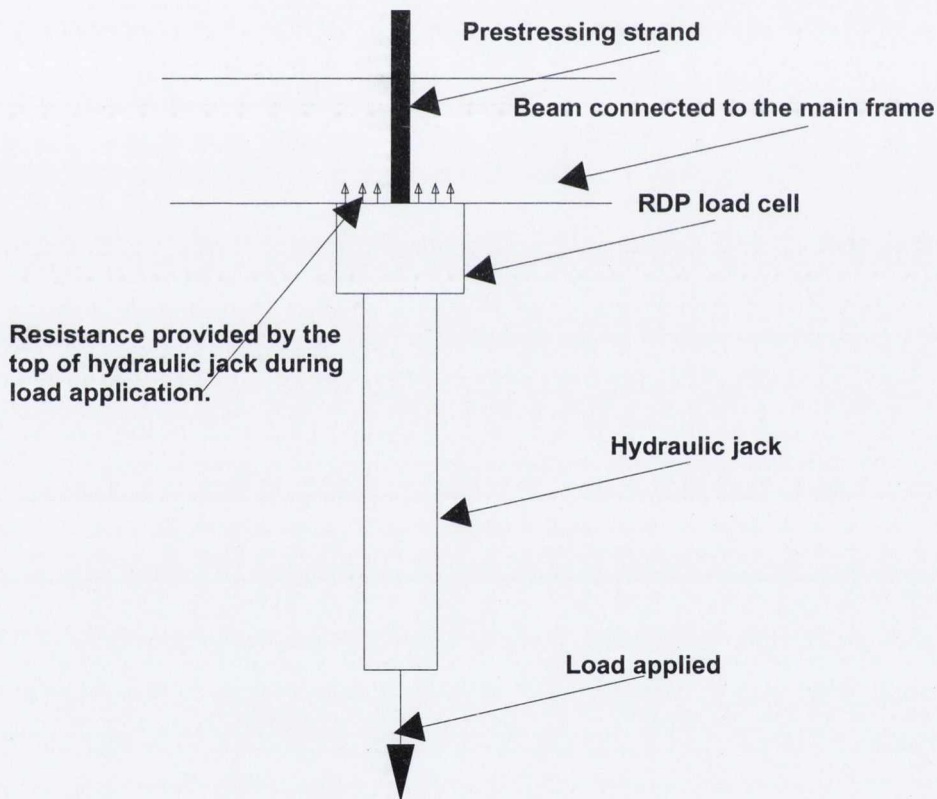


Figure 6.27 Position of hydraulic jack and load cell during load application

Strains are measured at two different locations as previously, one at the fixed end of the beam and the other near the mid span of the beam. 15 strain gauges were installed at the fixed end and 15 at the mid span location. The location of

strain gauges at the fixed end is shown in Figure 6.28. The same locations and numbering of strain gauges were used for the mid span of the beam.

6.3.2 Load application by two different means

Loads are applied to the sample in two directions. The axial force is applied vertically as depicted in Figure 6.26, while the lateral force is applied by a single cable in the same direction as was applied in the previous two experiments, as depicted in Figure 6.1.

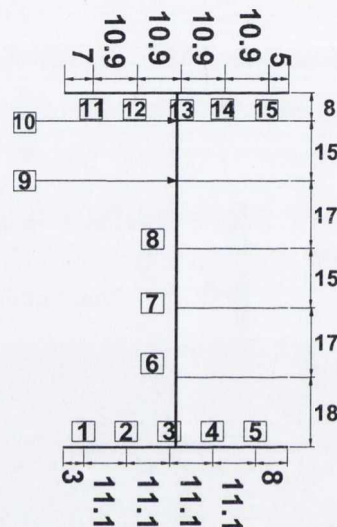


Figure 6.28 Location of strain gauges near the fixed end of the beam, where the strain gauges numbers are shown in square box and all dimensions are in *mm*

Orientation of sample and horizontal load applied from the sample

There is an infinite variety of possible initial orientations of the welded section with respect to the direction of the applied lateral load, only two of which are depicted in Figure 6.2. The sample in this experiment is held in position as shown for Experiment 2 in Figure 6.2. The principal reason for this choice is to have the direction of load applied almost perpendicular to the major-axis of the section. This orientation is selected so that more resistance can be provided during bending (because of higher flexural stiffness in that direction). Owing to this, it allows the section to rotate considerably more for the same amount of lateral deflection because of the lower torsional stiffness of section compared to its flexural stiffness.

Stages in which loads are applied

In the first stage of loading, an axial load of 35kN is applied (which is 10% of the axial yield strength of the I-section) using the prestressing tendon. Subsequently, in the second stage, the lateral load from the cable system developed previously is applied. Thus the beam rotates and moves laterally in the X and Y directions, as previously.

It emerged that with an increase of lateral load, an increase in the vertical tendon load arose. The development of the additional axial load in the tendon is depicted in Figure 6.29 in which it can be observed that there is no major increase of vertical load up to a horizontal load of approximately 5kN. Beyond this stage the tendon axial load started to increase gradually up to a load of 9kN, where upon it increased more rapidly as the experiment proceeded.

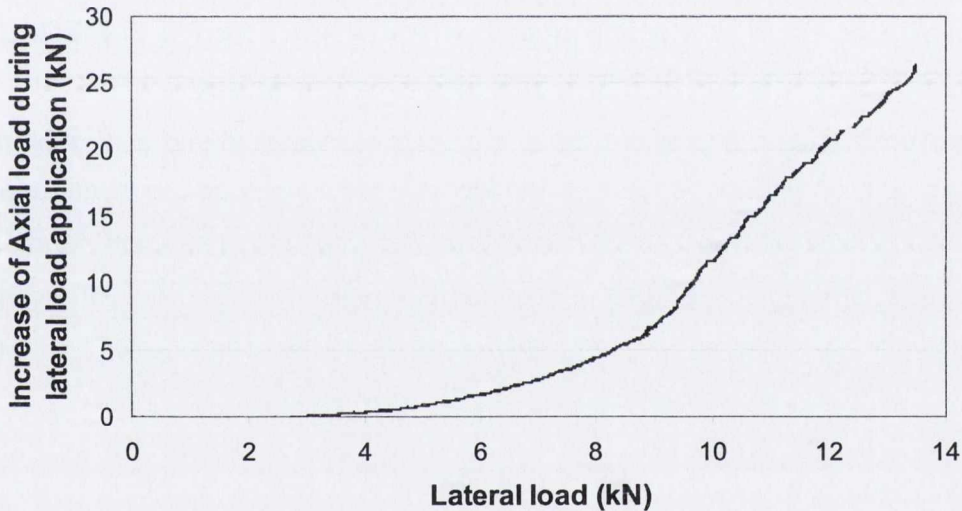


Figure 6.29 Variation of induced vertical tendon force with applied horizontal load for the case when axial load is applied in combination with biaxial bending and torsion.

Up to a lateral load of 5kN (corresponding to a torsion of 0.435kN.m), the deflections and rotations were small and in the elastic range, as can be deduced from Figures 6.31 and 6.33 to follow. Beyond the load of 5kN both the lateral displacement and rotation of the beam started to increase considerably causing two phenomena to take place; a) axial shortening due to torsion and b) geometrical non-linear effects due to tip lateral displacements under flexure, as depicted in Figure 6.30. Both of these caused vertical (i.e. axial) strain in the

beam during lateral load application. This movement caused the strand to exert extra force on the load cell (and hence the beam) as the tendon provides restraint to this movement.

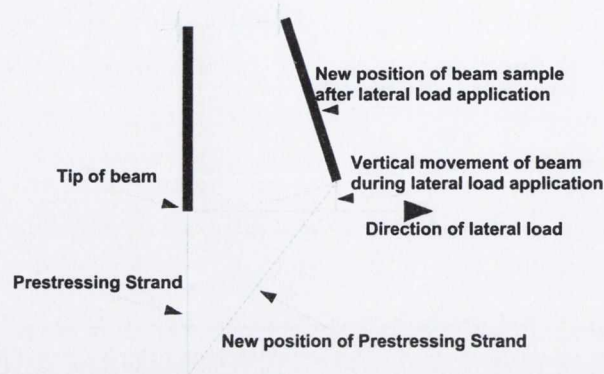


Figure 6.30 New position of the prestressing strand and the part beam after lateral load application giving rise to flexure.

6.3.3 Strains at two different locations at different stages of loading for axial force, biaxial bending and torsion experiment

Strains at two different locations along the beam (at the fixed end and at the mid span) are given in Tables 6.3 and 6.4. Strains at two loadings are given, one at the assumed elastic limit load (at $4.55kN$) and the other at the assumed formation of a practical hinge (at $8.9kN$). From the strain results it can be deduced that failure was due to a plastic hinge developing at the fixed end because, for the mid section, at a load of $8.9kN$, the strains are still less than ϵ_y .

The values of strain at the fixed end given in Table 6.3 are plotted on an I-section in Figure 6.31(a) to observe the neutral-axis pattern at both the indicated loads. The strains at the mid section are not plotted as failure occurred at the fixed end and results at this location only are of interest in the discussion of the failure.

Considering the strain pattern at the elastic limit load, as depicted in the figure, strains on the left of the top and bottom flanges have different signs which shows the significant influence of warping strain on the response (where in warping strain both flanges bend in different directions). The strain pattern in the web occurs when there is major axis bending acting on it, i.e. different signs at the top and bottom of the web with a neutral-axis in between them. In addition there must be a small component of minor axis bending strain and axial strain (as discussed

later) included in it which also influences this strain pattern. The neutral-axis was approximately a straight line in this case, as can be deduced from the figure.

When strains at practical hinge formation are plotted (Figure 6.31(b)), a similar type of strain pattern is obtained. It clearly shows that both major axis bending and rotation of the beam sample dominated the behaviour, both at elastic limit load and at formation of a practical hinge. The neutral-axes in both the cases also match i.e. in both the cases, the neutral-axis intersects the web and bottom flange.

Also in Table 6.3, axial strains are given when a prestressing force of $35kN$ acts on the section. From the table it can be inferred that the pre-load axial strains developed at each location are different. This is due to the fact that load applied were not exactly at the centroid, and some eccentricity can cause variation of load. For example an eccentricity of $10mm$, creates a moment of $0.35kN-m$ when this moment bends the beam about its minor axis which will cause a strain of $200 \mu\epsilon$ at the flange tips. In addition residual stresses are locked in the section which can influence the strain. However, the average of all strain is calculated to be $152 \mu\epsilon$. Based on a load of $35kN$ Young's Modulus is calculated for this value as $208GPa$, which is not much different from the value of Young's modulus of $201.7GPa$ obtained from coupon tests. This shows that the average strain applied corresponds closely with the load applied but strains were not distributed uniformly.

When the load at practical hinge formation for the biaxial bending and torsion only experiment (Experiment 2 in Section 6.2 when major axis bending dominates) is compared with the practical hinge formation in this experiment, higher values of load are obtained in this case. Although an additional axial tensile load is applied in this case, the strain developed due to axial load is small compared to the strain of $17000 \mu\epsilon$ for practical hinge formation. Hence the axial load has a small influence on the overall change in strain. However due to the presence of the prestressing strand, the beam's tendency to bend decreases and results in more load at practical hinge formation.

Comparing the neutral-axis pattern both at the start of yielding and at practical hinge formation it is found that the neutral-axis corresponds to the case in Chapter 4 with the second pattern, when the neutral axis intersects the web and bimoment dominates the behaviour.

LOAD	Torsion	FIXED END				
(kN)	kN.m					
		TOP FLANGE				
	STRAIN No	11	12	13	14	15
4.55	0.4	1407	1041	593	218	121
8.9	0.77	3061	2957	2139	884	75
Axial strain before the application of lateral load		-21	12	50	99	144
		WEB				
	STRAIN No	6	7	8	9	10
4.55	0.4	-160	-44	70	257	450
8.9	0.77	-2629	-1864	-952	113	1031
Axial strain before the application of lateral load		194	140	106	80	72
		BOTTOM FLANGE				
	STRAIN No	1	2	3	4	5
4.55	0.4	-1700	-916	-432	447	1068
8.9	0.77	-17000	-6725	-3627	2011	7525
Axial strain before the application of lateral load		54	185	260	401	493

Table 6.3 Measured strains at different loads near the fixed end

6.3.4 Torsion-Rotation Response

The torsion-rotation graph of the beam is given in Figure 6.32. The graph can be divided into three phases. The first phase is the elastic phase (as determined by $\epsilon_{\max} = \epsilon_y = 1700 \mu\epsilon$) which extends up to a torsion of 0.4 kN.m (as indicated as point A in the figure) where a rotation of about 11.8° was measured. During the elastic phase, theoretical predictions show a somewhat stiffer response as compared to the experimental response. The reasons for the difference of response are the same as discussed for Experiment 2 in Section 6.2.

Beyond point A is the second phase which can be termed as the elasto-plastic phase a gradual change of the slope of the graph was observed. At a torsion of 0.77 kN.m (as indicated as point B in the figure) a practical hinge forms (as can be seen in Table 6.3) where a maximum strain at this torsion reaches a value of $17000 \mu\epsilon$.

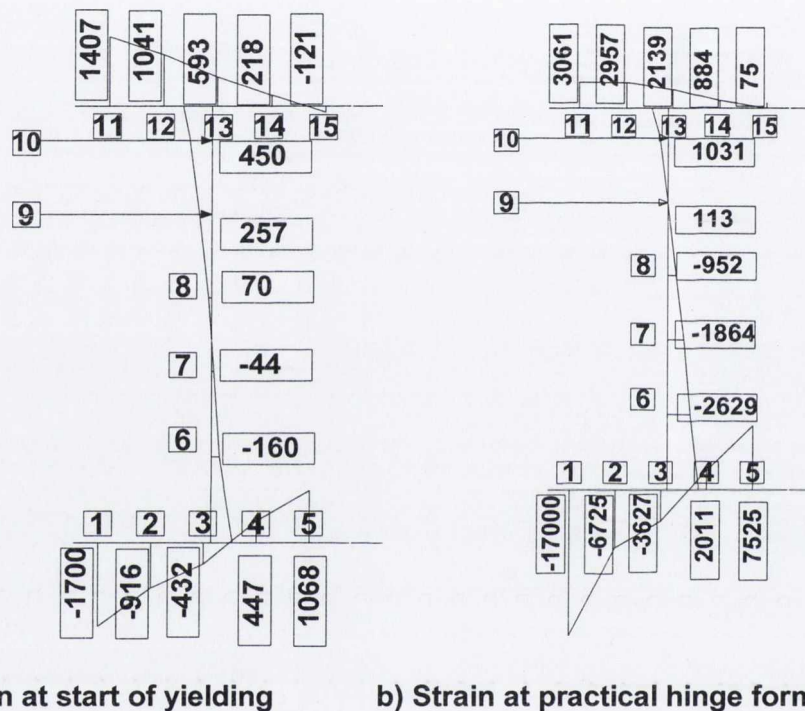
The third phase is beyond the formation of the practical hinge, up to the end of the experiment. However although this phase is categorized as the third phase, there is no substantial change in slope observed when compared to the second phase.

LOAD	Torsion	MID SECTION					
(kN)	kN.m						
		TOP FLANGE					
		STRAIN No	26	27	28	29	30
4.55	0.4		78	120	181	181	279
8.9	0.77		319	327	438	346	548
		WEB					
		STRAIN No	21	22	23	24	25
4.55	0.4		16	14	78	137	152
8.9	0.77		-254	-398	-288	-124	222
		BOTTOM FLANGE					
		STRAIN No	16	17	18	19	20
4.55	0.4		-120	-43	-36	6	96
8.9	0.77		488	334	-64	-331	-331

Table 6.4 Measured strains at different loads near the mid section

This graph when compared with the graphs of the pure torsion experiments as depicted in Figure 5.26 and the biaxial bending/torsion experiments (Figure 6.8) as superimposed here in Figure 6.33, indicates that both graphs approximately coincide up to a torsion of 0.3 kN.m . Beyond this torque, a difference between the graphs can be observed indicating a difference in behaviour in the non-linear phase of this experiment. Higher torsion values can be observed in this experiment as compared to the case of pure torsion though at lower stiffness

than the elastic region. The difference in torsional response between both the experiments is reflected in the different strains developed in both the cases. In the case of pure torsion strains develop in such a way as to reflect plastic torsional deformation and yielding. In the present experiment, both bending and axial stiffness have an influence on the strains developed. Therefore, as the torsion progresses the strains in the fibre of the section have a different pattern and do not show yielding of the section until much later and result in higher torsional loads as compared to the pure torsion case.



a) Strain at start of yielding

b) Strain at practical hinge formation

Figure 6.31 Strain patterns at the fixed end for axial force, biaxial bending and torsion experiment where strain numbers are given in a square box and strain readings in a rectangular box.

When the torsion in the cases when biaxial bending and torsion with and without axial force are compared, a similar type of response is obtained, as can be deduced from the figure. This shows that the axial force has less influence on the torsional response in the elastic and elasto-plastic phase, while near the end of the experiment the measured rotations show a slight difference in the response. This difference is due to the influence of the bending behaviour which changes in this case due to the presence of an axial force.

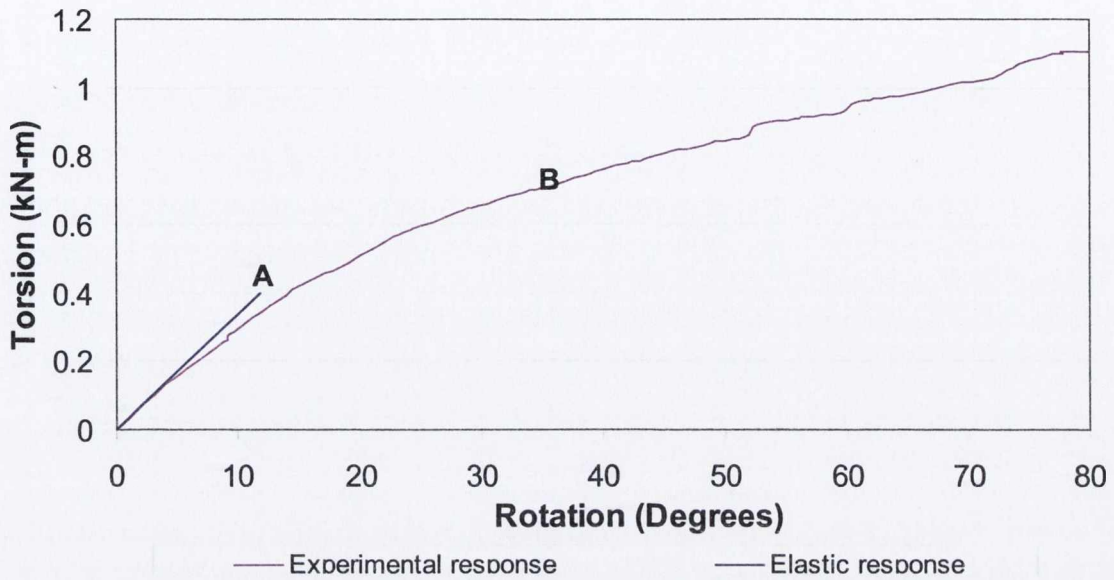


Figure 6.32 Torsion against Rotation response for the case when axial load is applied in combination with biaxial bending and torsion.

When compared with the load-deflection graph of the corresponding Experiment-2 in Section 6.2 (without an axial load as also depicted in the figure) notable differences exist between the graphs. The graph for the case when axial load is induced shows an overall stiffer response as might have been expected. The reason is that due to the axial force and stiffness provided by the tendon more resistance is provided to the beam against the lateral load and results in a stiffer flexural response. A fall in the load carrying capacity was observed in the previous case (see Figure 6.34) which is not observed in this case. The reason is that even though the torsion causes similar rotations, the reduced lateral bending deflections arise due to the tendon lateral restraint in the non-linear phase despite the reduced flexural stiffness on rotation as the minor axis bending becomes more predominant.

6.3.5 Lateral Load against Deflection

The load-deflection graph of the sample is depicted in Figure 6.34. The graph can be divided into three phases. The first phase (as determined by $\epsilon_{\max} = \epsilon_y = 1700\mu\epsilon$) is the elastic phase for which the response is linear up to

the elastic limit load of 4.55 kN for a deflection of 5.92 mm (as indicated by point A in the figure). A slight decrease of slope can be observed beyond the elastic limit load. The second phase is the elastic-plastic phase which goes up to the limit load of 8.90 kN where a practical hinge is deemed to have formed at a deflection of nearly 18.5 mm (as indicated by point B in the figure). Beyond this phase there is a gradual decrease of slope which is the strain hardening phase of the sample. The decrease of slope is an indication of a reduction in stiffness of the beam sample. No peak or fall in the graph is observed during this phase and the continuing increase in load capacity as deflections become very large is an indication that the beam has not reached its ultimate load carrying capacity.

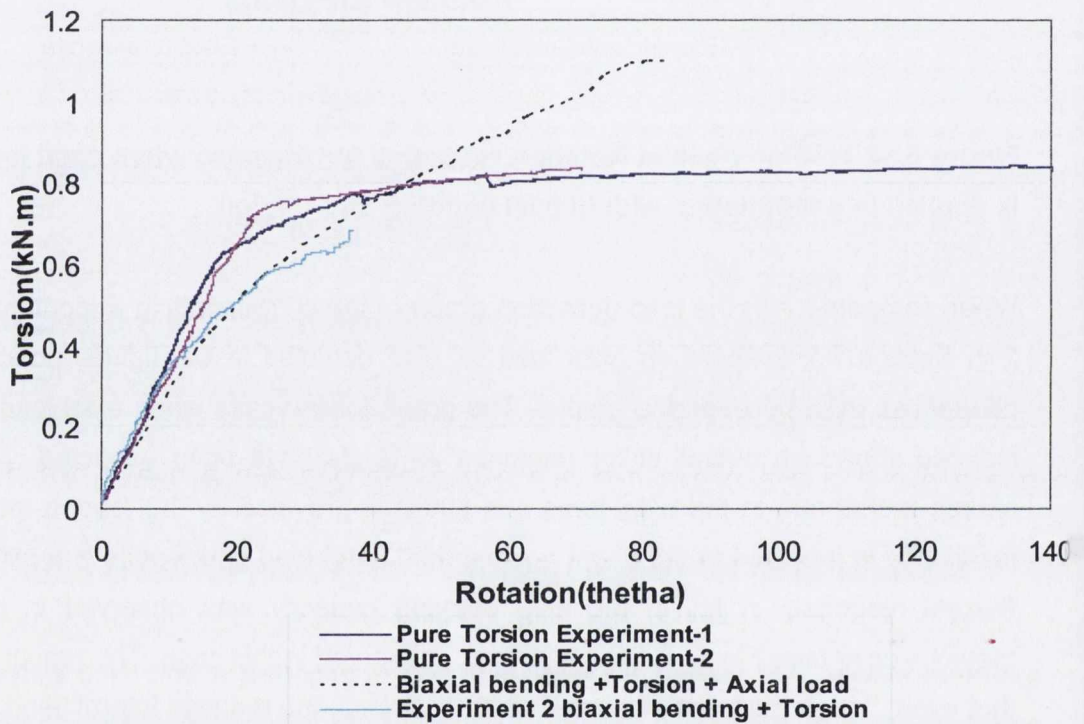


Figure 6.33 Comparison of Torsion against Rotation response for the case a) for pure torsion and b) torsion is applied in the presence of biaxial bending and axial load.

6.3.6 Elastic limit load and yield surface

The elastic limit load and elastic limit torsion, as identified in the previous discussion, are 4.55 kN and 0.40 kN.m respectively, while the elastic limit axial

load is 35.83 kN . Based on the assumption of thin walled beams (as discussed in Section 6.2.7) shear forces are ignored. Therefore, only four forces need to be considered to compare the given loads with the developed yield surface in Chapter 4, namely axial force, biaxial bending moments and bimoment (defined in Section 2.4.2). Resolving the elastic limit load of 4.55 kN into two components at the fixed end support gives loads 0.63 kN and 4.51 kN in the X and Y direction respectively which gives moments M_x of 4.65 kN.m and M_y of 0.65 kN.m respectively. The bimoment obtained for the elastic limit torsion is $.11\text{ kN.m}^2$ (details of this calculation are given in Appendix-D). Using the plastic capacities obtained in Chapter 5, these forces are converted into normalized form and are given in Table 6.5. Using the procedure given in Chapter 4, these are compared with the developed yield surface. For the same values of p , m_x , b and m_y , m_{xA} is calculated as 0.49 (Appendix-D). As $m_x < m_{xA}$ and the summation of m_y and b is not equal to one it means the section has not yet reached the yield surface. Hence, it can be concluded that for the applied load, the section is still elastic.

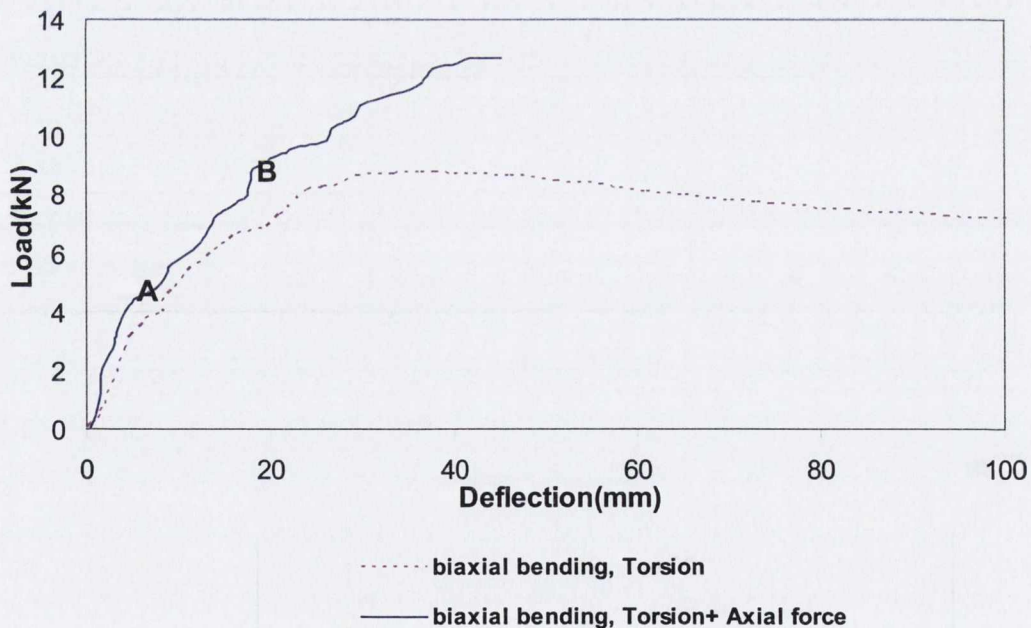


Figure 6.34 Load against Deflection, for biaxial bending and torsion and for biaxial bending, torsion and axial load cases

	M_x	M_y	P	B
Plastic capacities	15.15kN.m	2.93 kN.m	352 kN	.144 kN.m ²
Load=4.55kN	4.65	0.65	35.83	0.11
Load=4.55kN (Normalized)	0.31	0.22	0.1	0.76
Load=4.64kN	4.82	0.67	37.11	0.113
Load=4.64kN (Normalized)	0.32	0.23	0.1	0.78
Load=8.90kN	9.07	1.28	40.01	0.21
Load=8.90kN (Normalized)	0.6	0.44	0.11	1.46

Table 6.5 Normalized biaxial bending moment, bimoment and axial load when biaxial bending, torsion and axial force are applied

6.3.7 Practical hinge and yield surface

In the experiment, it appears that a practical hinge forms at a load of 8.90 kN for which strains for the fixed end are given in Table 6.3. The torsion at which it occurs is 0.77 kN.m and moments of 9.07 kN.m and 1.28 kN.m in the X and Y direction respectively. At this point the axial load has increased to 40.01kN. On the same basis (as discussed in Section 6.2.7) a bimoment (defined in Section 2.4.2) value obtained for the elastic limit torsion is multiplied by a factor by which torsion has increased (from the elastic limit torsion to the formation of the practical hinge) giving a bimoment of 0.21 kN.m². These forces are shown in normalized form in Table 6.5. It can be seen in the table that the bimoment obtained (1.46) is more than the plastic moment capacity, which suggests that the load point at which it will reach the yield surface must have a smaller value of n. Using the same basis (as discussed in Section 6.2.7), such a load is calculated as 4.64 kN which is 1.03 times more than the elastic limit load. Based on this load the moments which it produces are 4.82 kN.m and 0.67 kN.m in the X and Y direction, while torsion at this load is 0.41 kN.m and the bimoment obtained is calculated as 0.113 kN.m². For the same values of m_x , b and m_y , m_{x_A} is calculated as 0.49 (Appendix-D). As $m_x < m_{x_A}$ and the summation of m_y and b is equal to one it means the section has reached the yield surface.

However, the value of 4.64 kN for the applied load is not based on experimental evidence. Considering the strain at the fixed end, two types of strain response are evident from Figures 6.35-37, one is when strain at some point in the section is elastic up to the end of the experiment and the other when strains are more than ε_y . Only those strains which are more than ε_y are considered while the strains which are elastic are not. To determine yielding of the entire section, each flange and web element is considered separately. Loads at which both flanges and web show plastic behaviour are considered to be the load at yielding (an assumption which was considered by Yang et. al. (1989) for development of his yield surfaces). Considering the top flange, all the strains show plastic flow. However at a load of 6 kN all the strains have not reached ε_y , whereas at a load of 8 kN strain #4 has just reached the ε_y value. However, at a load of 9 kN all the strains are in a state of plastic flow. Therefore 9 kN can be considered as the load at which top flange showed complete yielding. Similarly consider those strains having values more than ε_y for the web. Using a similar basis as that used for the top flange the load when all the non-elastic strains reached plastic flow is 9.75 kN , while for the bottom flange it comes out to be approximately 8.5 kN . Hence complete yielding of the section can only be taken at 9.75 kN where the strains in both the flanges and web were in a plastic flow state. When compared with the theoretical prediction it is 2.1 times more than the theoretical load at hinge formation. The reasons for low value of the load obtained by the theoretical yield surface is the same as discussed previously. In addition due to axial load more resistance is provided to the beam against the lateral load and this is the third reason in this case for low values of theoretical yield surface load.

6.3.8 Plot of strain against lateral load

The strains measured on the top flange are depicted in Figure 6.35. Strains #1, #2 and #3 are in compression and have negative direct strain but are shown as positive for comparison. All the strains do not start from zero strain because of the pre-applied axial force. However, when the axial force was applied, all the strains do not show similar readings as given in Table 6.3.

All the strains are linear up to the elastic limit load of 4.55 kN . Beyond this load some strains show non-linearity while the remaining show non-linearity at relatively higher loads. Negative strains exist for gauges 1, 2 and 3 and positive strains for 4 and 5, indicating that the neutral-axis was at the centre mid of the flange as can be observed in Figure 6.31 at the two loading levels. The fact that gauges #3 and 4 always have opposite signs, indicates that throughout the loading the neutral-axis always passes through the flange between these two points.

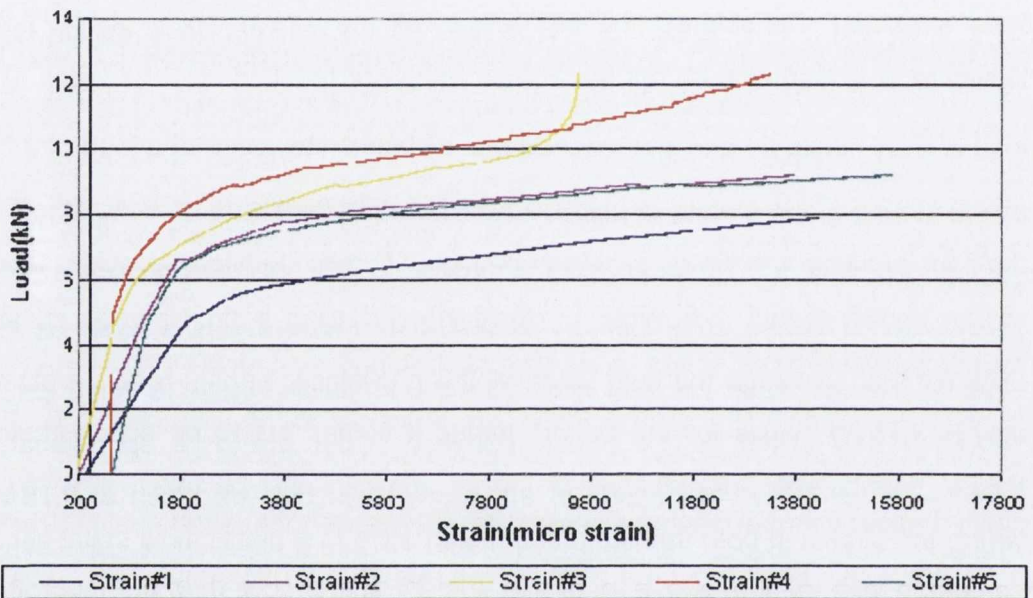


Figure 6.35 Measured strains for the top flange near the fixed end of the beam for the case when axial load is applied in combination with biaxial bending and torsion

The strain measured in the web is depicted in Figure 6.36. Strains #6, #7 and #8 are in compression and have negative direct strain but are shown as positive for comparison. All the strains do not start from zero for the reason discussed above. All the strains are linear up to the elastic limit load. Negative strains for gauges #6, 7 and 8 and positive strain for gauges #9 and 10 indicate bending of the web exists as can also be deduced from Figure 6.31 at the two loading levels. Observing the location of strain gauges in Figure 6.28 and the signs of the strains, it can be inferred that this patterns of strains occurs when the beam is subjected to major axis bending (which causes the web to bend in such a way

that positive and negative strains develop at the two ends of the web). This indicates that major axis bending was one of the dominating effects in the behaviour of the beam. No change in the signs of all the five strain gauges during loading shows that the bending behaviour was the same up to the end of the experiment. However, all the five strains show slightly different trends as can be observed in the figure. This is due to the fact that the interaction of bending and torsion was not uniform (as discussed later) which causes a change in the pattern as appropriate.

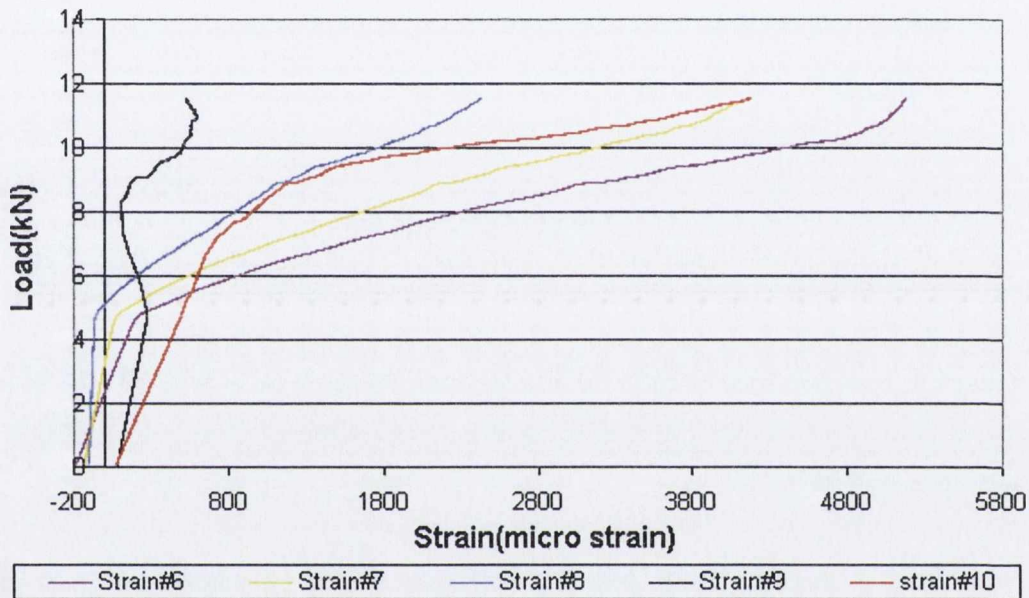


Figure 6.36 Measured strains for the web near the fixed end of the beam for the case when axial load is applied in combination with biaxial bending and torsion.

The strain measured in the bottom flange is depicted in Figure 6.37. Strain #15 is in compression and has a negative direct strain, but is shown as positive for comparison. All the strains do not start from zero for the reason discussed above. All the strains are linear up to the elastic limit load. A negative strain for strain #15 and positive strain for all the other strains indicates additional minor axis bending of the flange. Most of the portion of strain #15 has negative strain which shows there must be a non straight line neutral-axis present because neutral-axes exist for both the web and bottom flange and axial strain are different in direction for the top flange (as compare to the bottom flange). From Figure 6.31 it

can be inferred that bending of both the flanges are in different directions which shows the strong influence of warping strain in the response at both the loads.

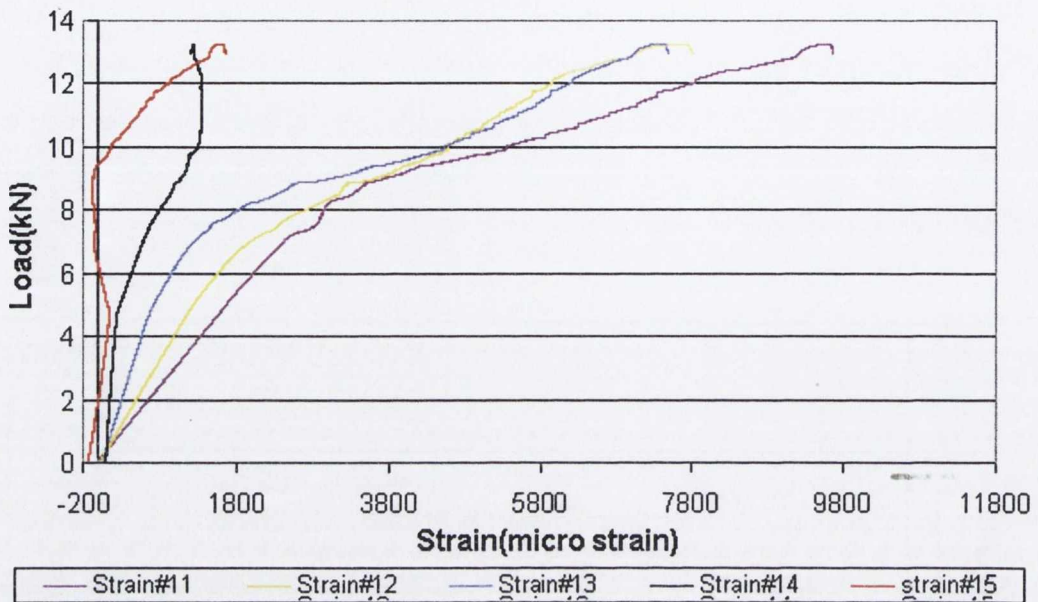


Figure 6.37 Measured strains for the bottom flange near the fixed end of the beam for the case when axial load is applied in combination with biaxial bending and torsion

The strain in the top flange has reached high values i.e. strains of more than $10,000 \mu\epsilon$. The reason is that warping due to torsion causes a positive curvature on the bottom flange while bending about the minor axis also causes a positive curvature, where both the curvatures accumulate. In addition, the major axis bending and Wagner strains (Section 2.4.2, Figure 2.10(d)) cause a positive strain on the top flange. All the actions add up and cause the maximum strains on the top flange. For the bottom flange, warping causes negative curvature whereas minor axis bending causes positive curvature, and Wagner causes positive strains, which reduces the strain and hence there are lower values of strains here compared to the top flange. The web is under the influence of curvature due to bending about the major axis, Wagner strain and axial shortening, whereas it is not influenced by warping action or bending about minor axis bending; hence it too has low values as compared to the top flange.

Axial strains that develop due to the prestressing axial force have relatively small effect on the overall strain distribution because low values of strains are developed due to the magnitude of the axial force (as calculated an average axial strain is $152 \mu\epsilon$ for a $35kN$ axial load). However, due to the axial stiffness provided by the tendon bending behaviour of beam changes which results in different strain distributions.

From Tables 6.3 and 6.4 it can be seen that strains for the fixed end reached the assumed limit of plastic strain whereas the mid section has not reached the plastic strain.

6.3.9 Displacement in two orthogonal directions

Figure 6.38 presents the cantilever tip displacement in the two perpendicular directions for the experiment. The graph can be divided into three phases. The first phase is from the origin to point A in which the response was broadly linear. The increase of displacement in both the directions indicates a consistent interaction of bending in both the directions. Beyond this is the second phase (which is between point A and B) where a decrease of displacement in the X-direction can be observed. A decrease of displacement in the X-direction occurs due to the rotation of the beam sample which causes a decrease of stiffness (as discussed in Section 6.2.9 for Experiment 2). Beyond this is the third phase (between point B and the end of the experiment) where broadly no further decrease of X-displacement occurred. An increase in displacement in the Y-direction without increase of displacement in the X-direction indicates a failure in bending mainly occurred in one direction.

When both the graphs of multi-dimensional force experiments are compared in the figure, a different response is evident in both the cases. This shows that the axial force has a significant influence on the interaction of displacement in both the orthogonal directions, where due to axial force the decrease of displacement in the X-direction is small. In the latter stage in the previous experiment the beam was not straight and bends more about the middle and was the reason for the decrease of displacement in the X-direction, whereas no bending of the beam about the middle was observed for the beam when axial force is applied, hence not much decrease in the X-displacement is observed.

6.3.10 Displacement in Y-direction against rotation

Figure 6.39 presents the displacement in Y-direction against rotation. A reasonably uniform response can be observed when a rise of displacement on increase of rotation takes place. The response is broadly linear which shows that the interaction of bending and rotation were uniform and it continues up to the end of the experiment. This shows that the interaction of the displacement and rotation does not change up to the end of the experiment.

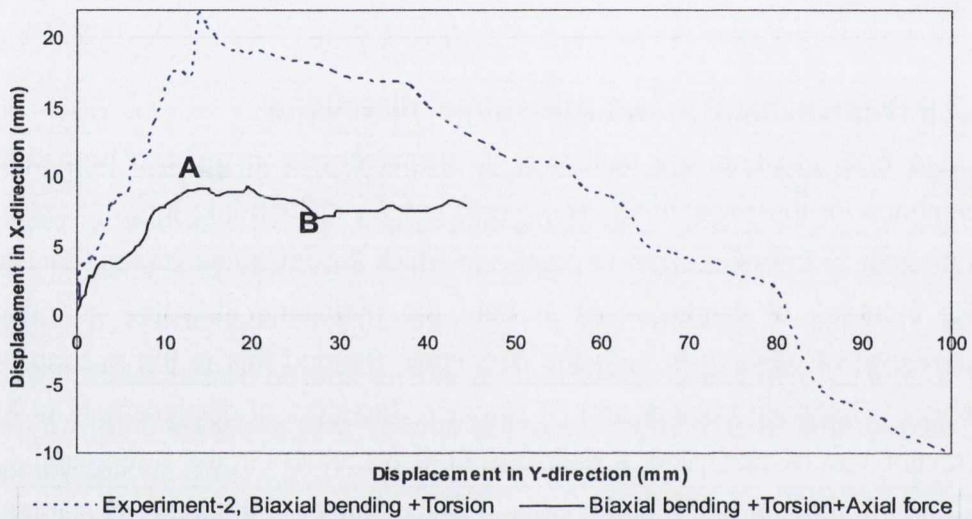


Figure 6.38 Displacement in two perpendicular directions for biaxial bending and torsion and for biaxial bending, torsion and axial load cases

6.3.11 Displacement in X-direction against rotation

Figure 6.40 presents displacement in the X-direction against rotation of the beam sample. The graph can be divided into three phases. The first phase is from the origin to point A in which the response was broadly linear. The gradual increase of displacement and rotation is an indication of the interaction of deflection and rotation. Beyond this is the second phase (which is between point A and B) where a decrease of displacement in the X-direction is due to the rotation of the beam sample. Rotation causes a change of stiffness of the beam (as discussed in Section 6.2.9 for Experiment 2) and results in decrease in the displacement in the X-direction. Beyond this is the third phase (between point B and the end of the experiment) where broadly no further decrease of X-displacement occurred on increase of rotation. This shows that the beam was weaker in rotation and

was able to rotate whereas it get stiffer (due to rotation) in bending in the X-direction and not much displacement occurs in the X-direction.

Comparing the results of both the experiments in Figure 6.40, it can be seen that patterns match up to an X-displacement of 8mm, beyond which the graphs bifurcate. The reason is that the beam bends more about the middle in the case of biaxial bending and torsion which results in a different response than the case of biaxial bending, torsion and axial force.

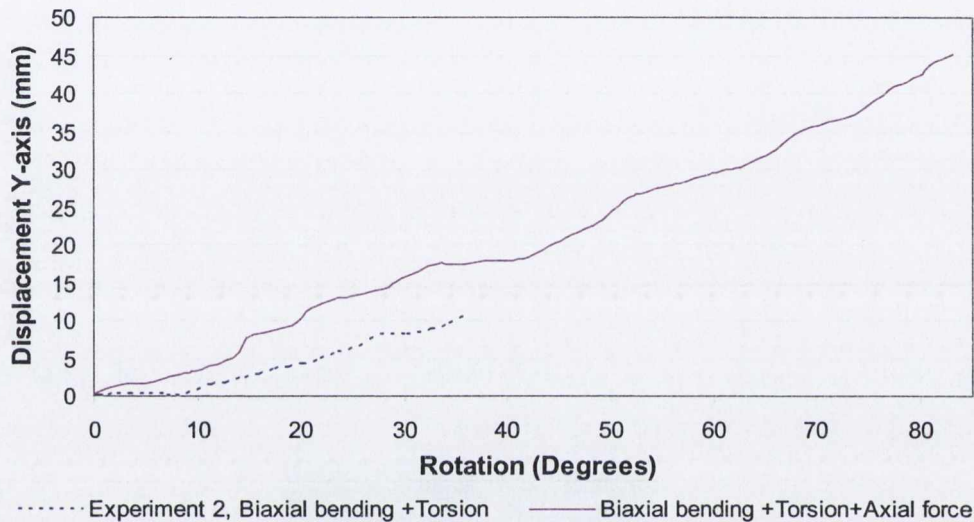


Figure 6.39 Displacement in Y-direction against rotation of axial load, biaxial bending and torsion experiment

6.3.12 Failure of the beam sample

The beam sample was under the influence of 4 possible types of loading actions. First an axial load was applied, then a lateral load was applied to the beam to produce biaxial bending and torsion actions. From the failed beam, as depicted in Figure 6.41, large residual rotation and a residual deflection of the section can be observed. A large residual rotation indicates that the beam was under plastic rotation when the peak load was applied to the beam sample, and the residual lateral deflection indicates that the beam was under plastic flexural deflection at the peak load. However the beam was also under the influence of an axial load (16 % of the plastic axial load) which had a significant effect on the response and

this is evident when Figure 6.41 is compared with Figure 6.13 (biaxial bending and torsion experiment).

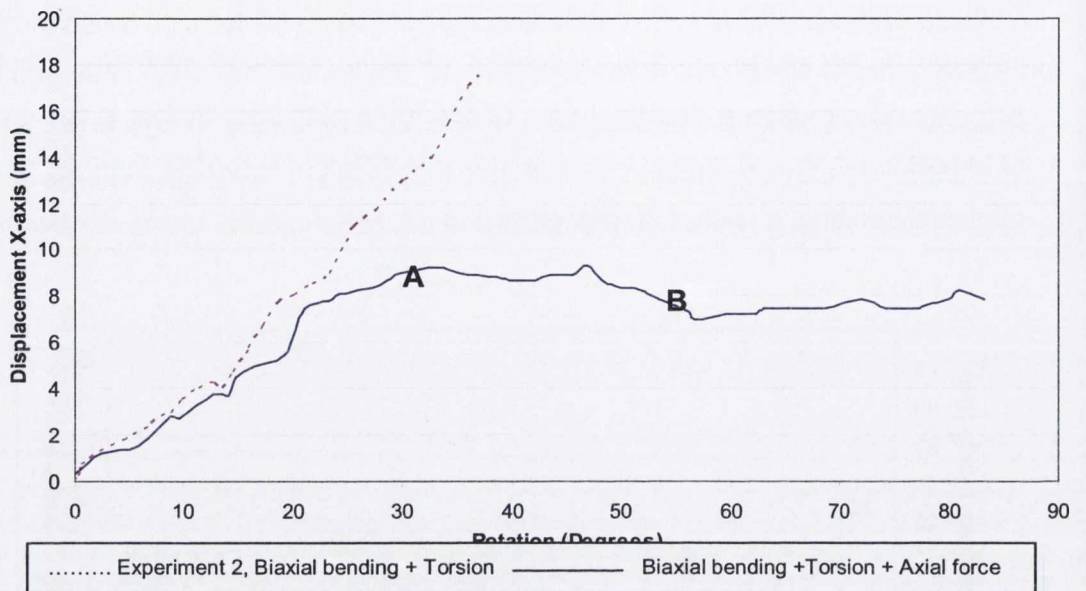


Figure 6.40 Displacement in X-direction against rotation of axial load, biaxial bending and torsion experiment

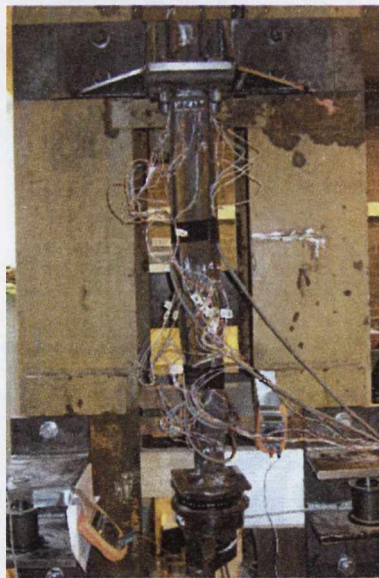


Figure 6.41 Failed beam experiment in which axial force is applied, residual rotation and deflection are visible in the beam

6.3.13 Buckling of samples

In no case is there any visible sign of local or lateral torsional buckling during the testing. On the strain gauge readings, it can be deduced that no abrupt change in the strain was observed in any case indicating that no local buckling was present where the gauges were placed. Also no sign of local buckling of the flanges or web was observed during any of the experiments.

6.4 COMPARISON OF RESULTS OF ALL MULTI-DIMENSIONAL FORCE EXPERIMENTS

It is found that the torsion against rotation response for all the three experiments do not match each other in the non-linear phase. This shows that the torsion behaviour is different depending to the interaction of bending (with axial load if any). Considering the response of Experiments 1 and 2 they do not match in the non-linearity stage which indicates that the orientation of the samples (which were different in both the experiments) was the cause for the change in response. When the response for Experiment 2 and Experiment 3 are compared, differences exist between them which show the significant effect of axial stiffness and axial load application. It is concluded that the torsion rotation response is influenced by both the orientation of the sample with respect to load application and due to the addition of other forces (such as an axial force in Experiment 3).

The load deflection responses in all the three cases were also quite different. Comparing the load deflection response of Experiments 1 and 2, a different trend is obtained in both the cases. In one case rotation causes a drop in the response in Experiment 2 whereas in the other case minor axis bending causes the failure at an early stage with low relative rotations. Comparing Experiment 2 and 3 the effect of the axial load is to have a significant reduction in the flexural response, and so despite small increase in axial load due to the tendon, less flexural stress is present due to lateral restraint, and torsional plasticity plays an increasing part.

At the elastic limit load the load point in all the three experiments has not reached the yield surface not surprisingly. However the load point reaches the yield surface at values slightly more than the elastic limit load. It is also found that load at "practical hinge formation" in all the three cases is considerably more than that

required to reach the yield surface. This shows that the assumption of $n=10$ on which basis practical hinge is chosen is an unreasonably high value. Factors are given which compare the load at practical hinge formation (or peak load for Experiment 2) to the load at reaching the yield surface as given in Table 6.6. From the table it is evident that the factors are quite high as compared to the load at which it reaches the yield surface.

	Elastic limit load	Practical hinge formation	Peak load
	/Load at yield surface	/Load at yield surface	/Load at yield surface
Experiment-1	0.94	1.71	-
Experiment-2	0.90	-	1.84
Experiment-3	0.98	1.92	-

Table 6.6 Factors for elastic limit load/yield surface load, practical hinge formation/yield surface load and peak load/yield surface load.

6.5 CONCLUSION

In this chapter the results of the experiments, when the beam is subjected to multi-dimensional forces are discussed. The topic has been split into several distinct sections. The first section comprises when a beam is subjected to biaxial bending and torsion. The second section consists of a case of biaxial bending, torsion and axial force. It is found that different responses of the beam samples were obtained in all the three cases. The torsional response is affected by the interaction of other forces. Load against deflection response also shows that the response was affected by interaction with stiffness about both bending axes especially when non-linear rotation changes the stiffness of the beam sample which results in a significant change in the response. It is also found that the load-deflection response is significantly influenced by the axial stiffness and lower deflection and high load capacities were obtained in this case. Displacement and rotation do not have uniform relationships where it continuously changes at different loading stages i.e. it depends on the change of cross section due to rotation which causes a different relationship between the displacements in both directions and between displacement and rotation.

It can be concluded that behaviour depends on the combination of forces and direction of load application. For the cases when axial force was not applied, the behaviour was different from the case when axial force was applied. load-deflection response, torsion-rotation response, interaction of displacement and rotation were all different between both the cases. Direction of load application also has an effect on the response. Considering Experiment-1 and 2 all the responses for both the cases were different.

The main purpose of performing the experiments was to compare the experimental results with the developed yield surface. It is found that the elastic limit loads in all the cases are always less than the value at which the section yielded by the criterion developed in Chapter 4. However the load point reaches the yield surface at slightly higher loads than the elastic limit load and the yield surface are verified. However in all the three cases it is found that the maximum load is considerably more than the yield surface value as discussed in the previous section.

CHAPTER-7

FINITE ELEMENT ANALYSIS OF A BEAM UNDER VARYING LOAD CONDITIONS

7.1 INTRODUCTION

The behaviour of the beam sample subjected to different loading conditions under monotonic loading is further examined through numerical analysis. A criterion is first set for the selection of a suitable software package and assumptions are made for modelling the experiments. Numerical analyses shall be initially performed on those cases when the beam is subjected to a load applied in one sense only. Later, other cases in which biaxial bending is applied in combination with torsion shall be modelled. The last case which shall be modelled is one in which the beam is subjected to axial loading, biaxial bending moments and torsion. Results, such as deformation and stress changes shall be studied for each case and compared with the experimental results obtained previously. In particular, the ability of finite element software to model primary and secondary effects will be investigated with a view to establishing the appropriateness of using finite element analysis in lieu of experimental work for these types of problems.

7.2 SELECTION OF PROGRAM

A finite element numerical model is developed using the LUSAS program in order to numerically determine the nonlinear response of the beam under different loading conditions. This program is selected because it possesses the following features;

- An elasto-plastic isotropic hardening material model based on Von-Mises Yield criterion (the reason for the selection of the Von-Mises Yield criterion is discussed in Section 4.4.8).

- An option is available for applying a prestressed axial force which later experienced second order effects in subsequent loading steps in the non-linear analysis.
- Elements are available which can adequately model large rotation and large deflection analysis.
- Accurate modelling of the relevant boundary conditions.
- Post processing capabilities which allow the user to view the deformed configuration and contour lines for the various stresses developed.

7.3 AVAILABLE ELEMENTS

Two types of elements are supported by LUSAS to model the geometry of the beam sample, namely the two dimensional triangular/quadrilateral shell elements and the three dimensional brick element. In the case of two dimensional elements, there are elements which provide membrane action only or out-of-plane action only, or there are shell elements which provide both of these actions. Owing to the nature of the response anticipated (that is including through thickness shear stress distribution in the case of uniform torsion, through thickness direct stress distribution in the case of biaxial bending), thick shell elements were selected because they can model through thickness shear and direct stresses. Therefore, in reality, only two types of elements were available; thick shell elements or brick elements, from which one type is selected for the analysis. The thick shell element provides in-plane and out-of-plane bending, shear and axial force, and through thickness shear and direct stress distributions and can consider bending and shear across the thickness of the element. It can provide, therefore, all the deformation modes which can occur when 3-D brick elements are used. Therefore, a thick shell element was selected for the analyses and brick elements are avoided firstly because the time which is required to analyse a brick element model is considerably more than the amount of time required to analyse the shell element and secondly there is easier interpretation of data in the case of shell elements as compared to the brick element.

To model the prestressing tendon used in the last experiment, bar elements are used. The bar elements which are available are BAR2, BAR3, BRS2 and BRS3. BAR2 and BAR3 are used for two dimensional cases, BRS3 is used for curved geometries; As the cables were straight in the experiment, the BRS2 element was selected to model the cable. It has a capability to be prestressed prior to and independent of incremental monotonic loading.

7.4 MATERIAL MODEL IDEALIZATION

The measured average stress-strain characteristics derived from coupon tests performed in tension are given in Table 7.1. This is derived from Figure 5.6 which is used to model the constitutive behaviour of the beam sample. From that figure it can be seen that initial elastic behaviour is followed by a flat plateau which defines the plastic flow of the material. A hardening is observed later after the flat plateau, where there is a change in the slope of hardening which extends up to the peak load. The tensile coupons were extracted from the I-section in the longitudinal direction (as discussed in Section 5.2). It is assumed in the finite element analysis that tensile stress-strain behaviour is identical in all directions. No attempts are made in the current model to establish different stress-strain relationships in different directions. Therefore, for this work, the material was assumed to be isotropic and follows the longitudinal tensile stress-strain curve given by the said figure. The material model was assumed to obey Von-Mises as discussed in Sections 2.5 and 4.4.

Stress (MPa)	Strain	Remarks
333.7	0.001654	Yield stress
333.7	0.02	plastic plateau
425.8	0.1	strain hardening
464.5	0.29	strain hardening up to the peak load

Table 7.1 Stress-strain results obtained from coupon tests used in the finite element material model

7.5 MODELLING THE EXPERIMENTS

In the experiments different loading set-ups were used which involved bending and torsion cases. The length of the beam for the bending cases was $1.24m$, while the length was $1.03m$ for the cases which involve torsion. The thickness of the web (t_w) and flanges (t_f) were $4.4mm$ and $5.68mm$ respectively, whereas the length of the web (b_w) and width of the flanges (b_f) were $90mm$ and $55mm$ respectively. Both of the setups are discussed in detail in Chapters 5 and 6.

To model numerically the pure bending case, a cantilever is assumed with a load applied laterally at the tip to each node on the end section. The model used for the analysis is depicted in Figure 7.1. The model is fixed in the three translational and rotational directions at the support. The fixed end is depicted on the left side of the figure. In the model two types of nodes are defined; one is the primary node and a further division between the primary nodes are secondary nodes. The cross sectional lines of the top and bottom flanges are divided into 4 parts and the cross sectional line of the web is divided into 7 parts based on primary nodes, as depicted in the figure. Meshing is further performed between primary nodes where each element formed by primary nodes is meshed into sixteen elements, as shown in the figure. Varying this sub grid, the total number of elements after meshing is 20640.

7.5.1 Finite Element Mesh refinement

It was shown after several analyses, that the results when using a coarse mesh are less accurate when compared to the finer mesh. The analyses are performed for different numbers of elements and the plastic moment capacity obtained in each case is compared with the theoretical value. The differences in the plastic moment capacities in percentage terms are given in Table 7.2. From the table it can be concluded that the model consisting of 20640 elements results in a variation of less than 1% between the numerical and exact plastic moment capacities. From the table it can also be seen that further mesh refinement did not yield any significantly different results from the mesh selected.

7.5.2 Modelling torsion experiments

For the load cases which involve torsion, the end condition where the cable was wrapped around the circular drum is modelled differently, as follows:

In the experiments, a square plate was welded to the end of the beam sample to which was welded the circular drum. Two cables were wrapped around the circular drum in opposite and parallel directions for the pure torsion case. The axial cable loads were transferred from the cable to the circular drum to the square plate and thus to the entire beam sample. The whole assembly of the end-condition is depicted in Figure 7.2.

No of elements	M_p (FEA)	M_p (Theoretical)	% change
	<i>kN-m</i>	<i>kN-m</i>	
5160	13.846	13.456	2.91
11610	13.711	13.456	1.90
20640	13.531	13.456	0.55
25800	13.510	13.456	0.41

Table 7.2 Comparison of finite element results and the theoretical value for different numbers of elements

For the torsion experiments, loads were applied to the square plate in two opposite and parallel directions, where they were at an equal distance from the centroid of the section, as depicted in Figure 7.4. For the cases (in the experiments) when torsion was applied in combination with the other forces, the single cable used to apply the force was positioned to one side only, making an angle of 8° with reference to the principal axis of the plate, where the position of the cable in Figure 6.2 is the direction in which load was applied. To allow for the inclined position of the cable (as depicted in the figure) in the analysis, two components of force are applied at the plate edge in the finite element analysis, as depicted in Figure 7.5. The relation between the two components of force and its resultant inclined force is also depicted in the figure. The components give a resultant force which represents the inclined direction of the cable force, and this direction of force is maintained throughout the analysis, as was the case in the experiment.

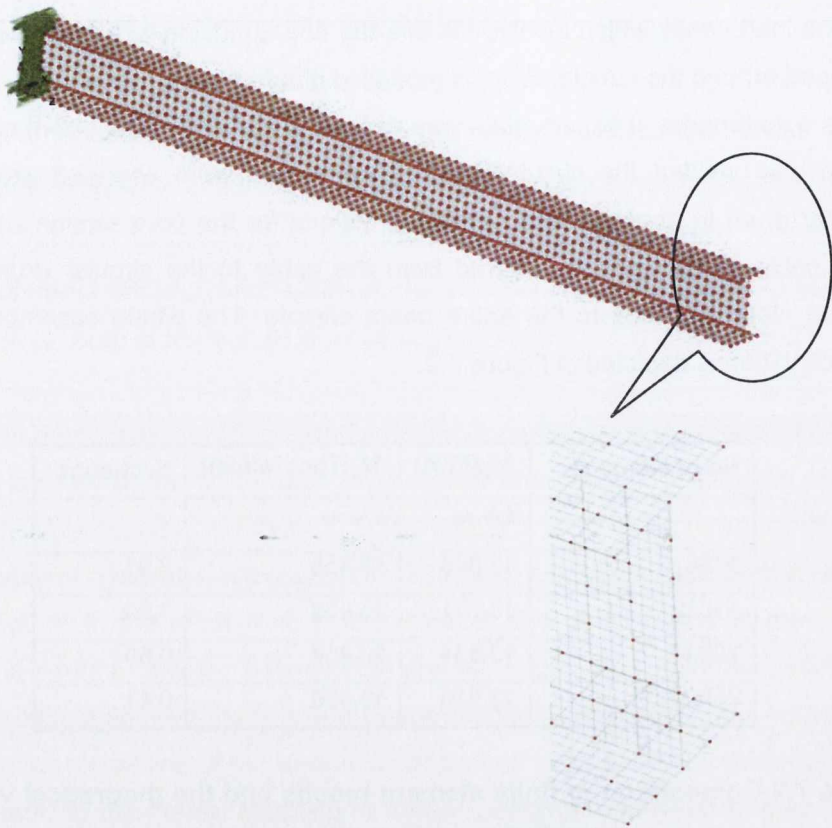


Figure 7.1 Model used for the pure bending analysis



Figure 7.2 End condition of beam sample

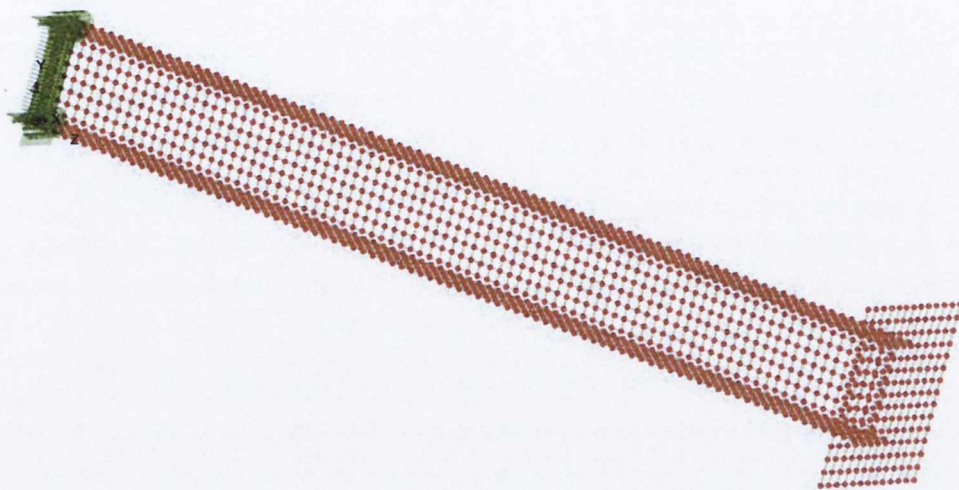


Figure 7.3 Model from Figure 7.1 developed with square end plate.

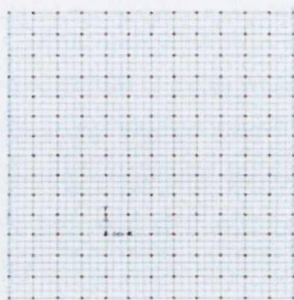
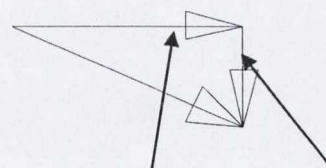
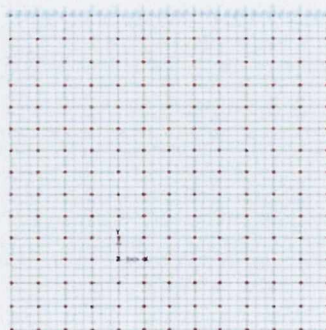


Figure 7.4 Loads applied to the square end plate for the case when pure torsion is applied



Two components of forces applied (as depicted for all the nodes at the edge on the plate on the left in FE model) and its inclined resultant

Figure 7.5 Loads applied to the square end plate for the case when torsion was applied in combination with other forces

7.5.3 Axial pre-stressing load and sequence of load applications

In the final experiment described in Chapter 6 an axial load of 35kN was first applied to the beam sample using a prestressing tendon and was locked off. Subsequently, an additional axial load developed in the sample during the non-linear response to the lateral load application. Therefore, two types of axial load are required to be modelled in the beam sample, one before the application of the lateral load and another represents the increase of axial force during the application of the lateral load. Therefore a cable is attached to the tip of the cantilever along its centroidal axis to model the pre-stressing tendon. In the model, one end of the cable is connected to the end plate while the other end of the cable is supported by a new support which is pinned in all the three directions. The cable with its two ends attached to the beam and to the support is depicted in Figure 7.6.

The two types of axial force are modelled differently by the program. To model the effect of an axial (pre-stressing) load which is applied before the application of the lateral load, LUSAS provides a facility to impose an initial strain which can be applied to the cable. These strains are subsequently included into (but not changed by) the incremental solution scheme for the analysis of non-linear problems upon load application. The imposed strain value equivalent to the pre-stressing load of 35kN was calculated based on the Young's Modulus obtained from the coupon tests and as applied to the material properties of the elements of the cable. Owing to the strain in the cable, the beam sample also stretches and develops the appropriate pre-lateral load tensile axial force in the cable/beam assembly.

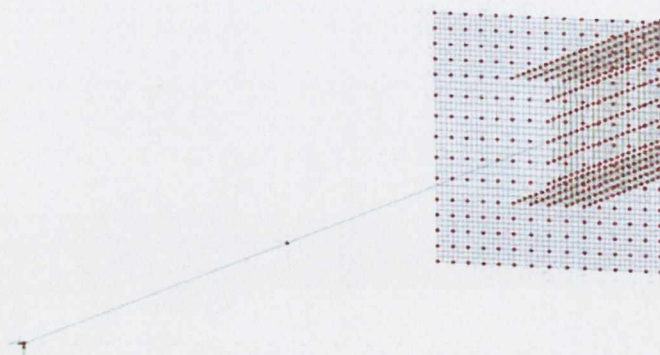


Figure 7.6 Cable attached to a pinned support and the beam end plate

The second part of the axial load in the cable arose due to the stretching of the cable during lateral load application. This load is not applied in LUSAS but it arose in the cable due to non-linear second order geometrical changes in the beam due to the lateral and torsional loads. The development of this latter axial load in the cable was first investigated for the case when no initial strain is applied to the cable (i.e. a passive cable is attached to the beam). Subsequently in a second analysis, the development of the axial load was obtained for the case when an initial axial prestressing force (due to an initial strain) was applied to the cable.

7.6 FINITE ELEMENT RESULTS

In the current research, failure is not related to the collapse of the beam sample (where collapse is defined as the complete failure of the beam sample by, for example, fracture of the flanges or web or by buckling of the beam so that the beam cannot maintain any significant load). Failure here is the state where, in the analysis, the beam cross section anywhere over the entire length of the statically determinate beam reaches plastic yielding (where, in the current analysis, plastic yielding is defined as the point where deformation occurs without further substantial increase in load capacity). As in the experiments, the results of the analyses are focussed on reaching a point where it is certain that plastic yielding has occurred. With the current beam geometry, where the experiments are based on loading until the failure of a determinate structure, the state of plastic yielding for an I-section in flexure is normally considered to exist at the fixed end of the beam (where there is a maximum moment). To obtain the yield value (on the load deflection plot) two tangents are drawn, one from the initial linear response and the other from the linear portion of the plastic plateau. The point at which they intersect can be taken as the appropriate load at which yielding of the section is deemed to have taken place, as will be the case for every result of analyses here. Therefore, analyses are limited to the case, when plastic yielding is assumed deemed to have occurred and all primary modes of deformations (i.e. due to bending, twisting or axial force) are obtained during the analyses. The termination criterion in all the finite element analyses is set to the maximum deflection measured in the experiment, and the analyses are terminated at reaching the maximum deflection.

7.6.1 Bending of the beam about the major-axis

Figure 7.7 shows a comparison between the finite element and experimental load-deflection relationship for the bending of the beam about its major axis. The analytical load-deflection graph exhibits the same trend as does the experimental response and reasonable agreement between analysis and experiments is obtained in this case. However, a difference exists in the linear phase between the two results, the reason being the different Young's moduli for the two graphs. The numerical study is based on the Young's modulus derived from the coupon tests ($201.7GPa$) whereas, as discussed in Chapter 5, a different Young's modulus was obtained for the bending case ($178.0GPa$) as compared to the coupon tests. Different Young's moduli for coupon tests and experimental results were also obtained by Goggins (2004) in his research program.

Another finite element analysis was performed with the modified Young's modulus while the other properties of the material were kept constant. The result is also shown in the figure, from which it can be inferred that the difference between the responses in the linear phase has considerably decreased.

Comparing the responses now, a difference between the finite element and experimental responses can be observed during the transition from the linear to the non-linear phase. The difference is partly due to the residual stresses present in the steel section during the experiment. Residual stresses cause a change in the curvature (Englekirk, 1994), whereas residual stress is not considered by the finite element analysis. This is one of the major causes of the difference in the responses, the other being the formation of the plastic hinge in the elasto-plastic region. Therefore, due to these effects, yielding is reached in the analyses by a sharp change in the load-deflection curve whereas yielding is reached more gradually in the experiment. When the beam is in the non-linear phase, a similar type of response is observed for both cases, where the slope of the response of both the analysis and the experiment are very similar and almost constant. The higher values of load capacity in the experiment in the later stages are due to the fact that the finite element analysis is based on simple coupon tests results whereas the experiments are based on the actual loading set-up. Goggins (2004) also observed these differences between the coupon's tests and experimental results.

Drawing tangents from the linear phase and yield plateau, as depicted in the figure, the yield load in the analysis is found to be approximately 11.5kN , which equates to a bending moment at yield of 14.26kN.m , which compares acceptably with the experimental value of 15.15kN.m . The corresponding axial plastic capacity is 13.46kN.m based on the coupon's test results.

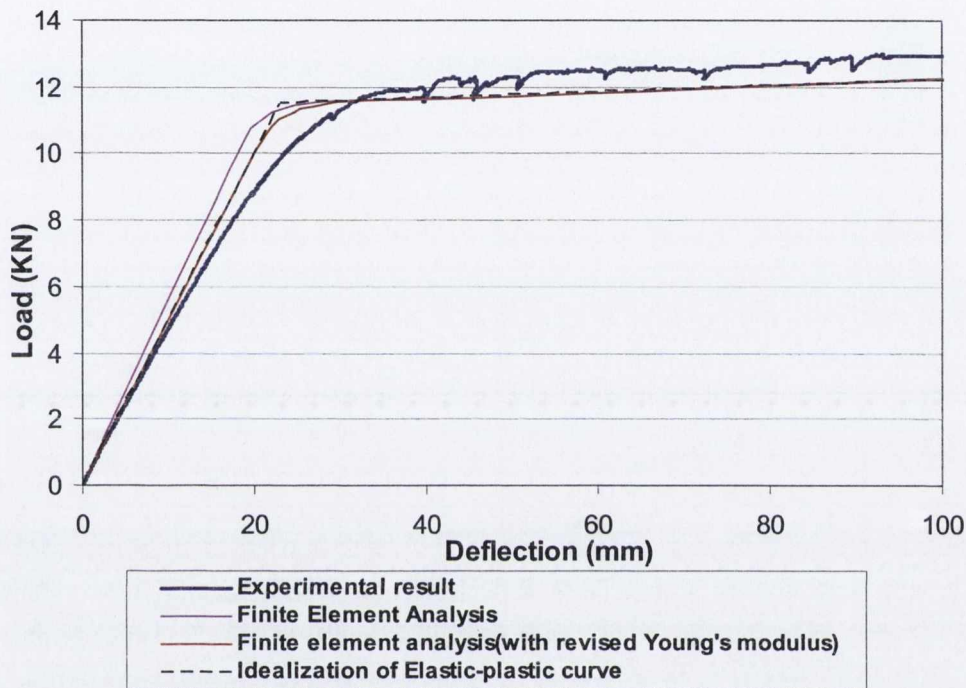


Figure 7.7 Load deflection graph of bending of beam about the major-axis. Experimental result produce here are also given in Figure 5.14

Figure 7.8 presents the contours of longitudinal stress extracted as a typical output from the incremental non-linear analysis. The analysis is at the stage when the beam was in the non-linear phase. The stress in the "SZ" direction represents the stresses in the middle of the shell element in the longitudinal Z-axis direction of the beam. It can be observed from the figure that the maximum stress is not surprisingly at the support (which is at the right hand side of the figure) and is more than the yield stress and its value is 378.5MPa , which indicates that stress at the support was near the strain hardening phase (see Table 7.1). The minimum stress is at the centroid of the section along the length of the beam. The same amount of stress on the tensile and compressive faces is an

indication that the stress distribution is a pure bending stress distribution without any secondary axial effects.

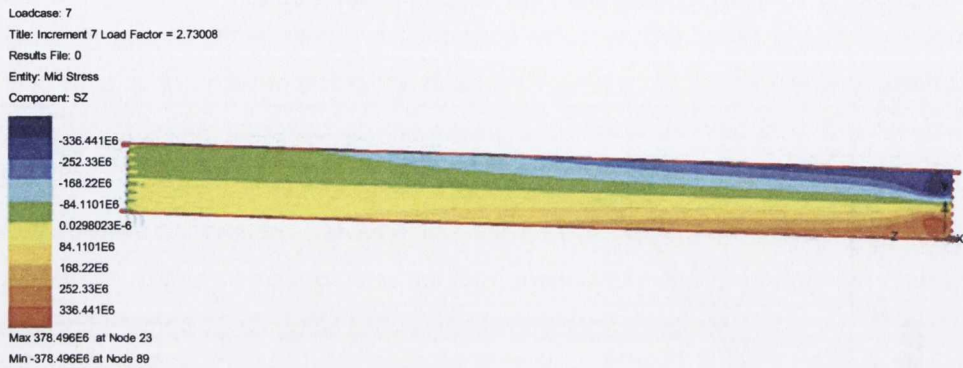


Figure 7.8 Longitudinal stress contour of beam bending about the major-axis

It is clear, therefore, that the primary effect of flexural plastic behaviour observed in the experiments is predicted reasonably accurately by the finite element approach. During the equivalent experiment discussed in Chapter 5, no secondary effects, such as lateral torsional buckling (LTB), were observed, nor were they predicted by the finite element analysis. As shall be observed presently, this is always the case.

7.6.2 Bending of beam about the minor-axis

Figure 7.9 shows a comparison between the finite element and experimental load-deflection relationship for the pure bending of the beam about its minor axis. The analytical load-deflection graph exhibits the same trends as does the experimental response and, again, reasonable agreement between analysis and tests is obtained in this case. However, as in the previous case, a difference exists in the linear phase between the two results and again the principal reason is the different Young's moduli for both the graphs as discussed previously. The Young's modulus obtained from the bending experiment was 184.0GPa whereas the Young's modulus obtained from the coupon tests estimated as 201.7GPa , as

given in the previous section. To study the difference which the Young's modulus can have on the results, another finite element analysis is performed in which Young's modulus is taken as that obtained in the experiment, while the other properties of the material are kept as given by Table 7.1. It can be observed in the figure that the analysis with this revised Young's modulus yields very similar results, which shows the significant effect of the modulus choice on the linear analyses. In the non-linear phase, the response of both the finite element analyses and experiment are also very similar. The increase in load capacity as deflections become very large is an indication that the beam in both the finite element analysis and experiment, although in the non-linear phase, has not reached its ultimate load carrying capacity.

It should be noted by comparing Figures 7.7 and 7.9 that the development of a plastic hinge in the case of minor-axis bending is more gradual than in the former case, as might have been expected from the experimental work. This happens because in the minor case the two flanges were mainly resisting the moment and each flange itself is a rectangular section whose shape factor is 1.5, hence a gradual change occurs in reaching plasticity. For the major axis bending, resistance is provided by an I-section whose shape factor is 1.1-1.2 (Mrazik et. al. 1987) and, due to this, relatively abrupt change to plasticity at the elastic limit occurs.

Drawing two tangents, one from the linear phase and the other from the plastic plateau in Figure 7.9, the yield load obtained is approximately $2.45kN$, which gives a moment at yield equal to approximately $3.05kN.m$ which compares extremely well with the experimental value of $3.0kN.m$ and the plastic capacity of $3.15kN.m$ based on the coupon tests results.

Figure 7.10 presents the contour profile of the longitudinal stress extracted as a typical output in the middle of the thick shell elements in the longitudinal (SZ) direction of the beam from incremental non-linear analysis. The stress near the support (right hand side in the figure) is more than the yield stress having a value of $377.7MPa$. A high value of stress indicates that the beam was in the strain hardening phase (see Table 7.1) with the same values of maximum stress in both the compression and tensile faces, which indicates that the behaviour of the

beam, as analysed by finite elements, shows it to be pure bending without any secondary effects. The minimum stress is at the centre of the cross section as indicated by the contour profile, as anticipated from the stress results in the experiment.

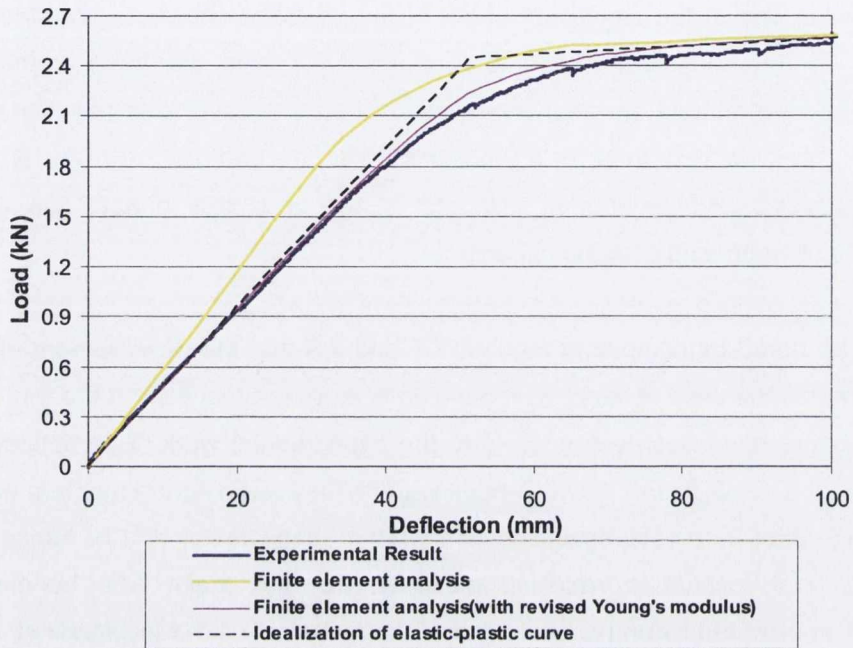


Figure 7.9 Load deflection graph of bending of beam about the minor-axis. Experimental result produce here are also given in Figure 5.15

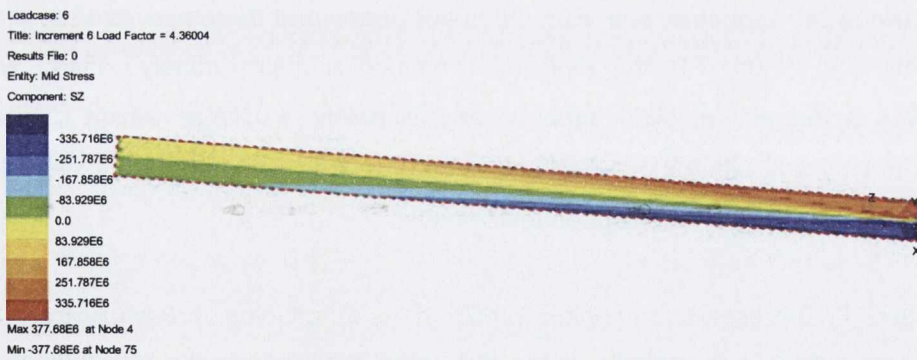


Figure 7.10 Longitudinal stress contour of beam bending about the minor-axis

As in the previous case, other modes of failure may be possible, depending on the geometry. However, in this case the plastic flexural hinge formation dominates and neither the experiment nor the finite element analysis predicts other modes, such as local buckling (LB) of the flange in compression at the support.

7.6.3 Torsion applied to the section

Two identical torsion experiments were conducted simply to reproduce the observed phenomena. Figure 7.11 shows a comparison between these torsion experiments and the finite element result for the torsion against rotation relationship. The analytical relationship exhibits the same trend as the experimental responses and has reasonable agreement between them. This shows that the finite element model managed to model accurately the primary torsional response even at very high rotations.

Two figures demonstrating the rotation of the beam sample are shown. Figure 7.12 views the beam sample along the longitudinal axis and shows the rotation of the rectangular plate. From this figure, a pure twisting of the plate can be observed indicating a solely torsional mode of deformation. Figure 7.13 views the beam sample in side elevation (in which it is confirmed that there is no lateral movement). The same amount of deformation above and below the undeformed model indicates that the predicted deformation was purely torsional without any secondary lateral (bending or second order) effects.

However, in the experiment, lateral movement was observed at an angle of nearly 140° , near the end of the experiment but this lateral movement was not replicated in the finite element analysis. This shows that finite element analysis was able to model accurately the torsional behaviour so far as the rotation in the experiment was considered but was unable to model the lateral movement which occurred near the end of the experiment arising from secondary effects. Lateral movement occurred in the experiment due to secondary moment which arose because both the cables were not in one plane, whereas in the finite element analysis the couple of forces were applied on the same end plate, that is at the same distance from the fixed end support.

To determine the appropriate yield value, two lines are drawn, one from the slope of the linear phase, the other from the plastic plateau (as depicted in Figure 7.11) from which the value of torsion is estimated to be 0.82kN.m which compares very well with the value of 0.80kN.m in the experiment.

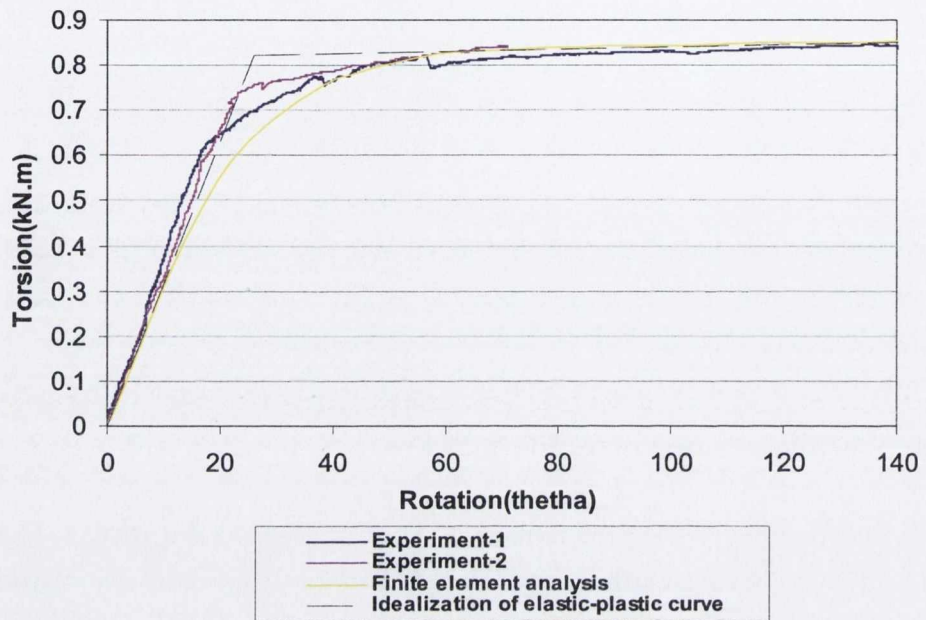


Figure 7.11 Torsion vs rotation response of the beam sample. Experimental result produce here are also given in Figure 5.26

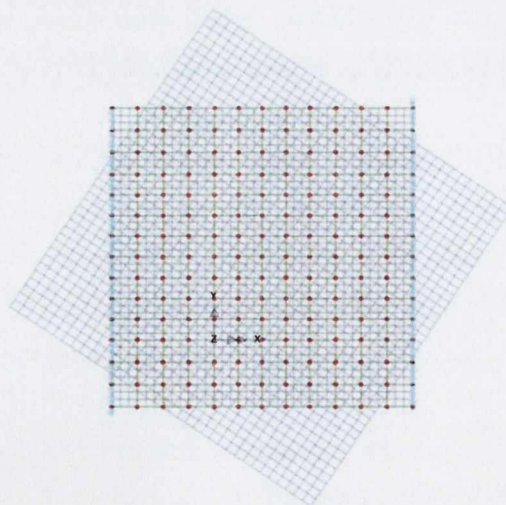


Figure 7.12 Rotation of the rectangular plate viewed along the longitudinal axis at an angle of rotation of 32°

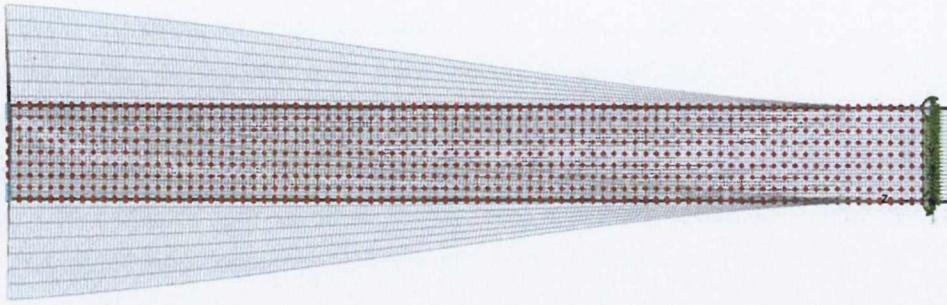


Figure 7.13 Deformation of the beam sample viewed from the lateral direction

Figure 7.14 depicts a plot of the maximum axial deflection against the applied torsion measured at the free end of the beam at the centre of the section. It can be seen from the figure that axial shortening (AS) increases significantly in the non-linear phase whereas only a small amount of axial shortening was observed in the linear phase. This shows that the finite element analysis managed to identify the secondary effects of axial shortening which arise substantially in the later stage of the analysis under large torsional rotations.

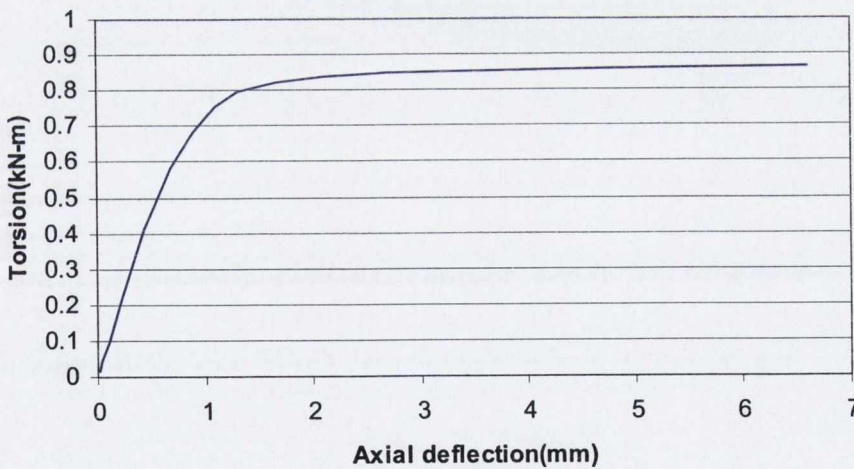


Figure 7.14 Torsion vs maximum axial deflection of the beam sample

Figure 7.15 presents the contours of the stresses developed in the longitudinal (SZ) direction of the thick shell elements for a typical incremental analysis where the stress near the support was more than the yield stress, having a value of

384.9MPa. It can be observed in the figure that the top flange at the support (on the right in the figure) has positive and negative stresses, whereas the direction of stress for the bottom flange is the opposite. The different directions of the stresses confirms the presence of warping stresses near the support, which are in different directions for both the top and bottom flanges, as would be expected. Higher values of stress than the yield stress indicate that stresses in some regions near the support were in the strain hardening phase (see Table 7.1). It can be seen that the stresses at both ends of the beam in the top flange have different signs and those stresses decrease as it reaches the mid span. At the mid-span, longitudinal stresses are at a minimum as depicted in the figure. Therefore a change of sign of stresses occur at the middle span, as indicated by the discrete change in the contours on the right and left of the mid-span part of the top flange (as depicted in the figure).

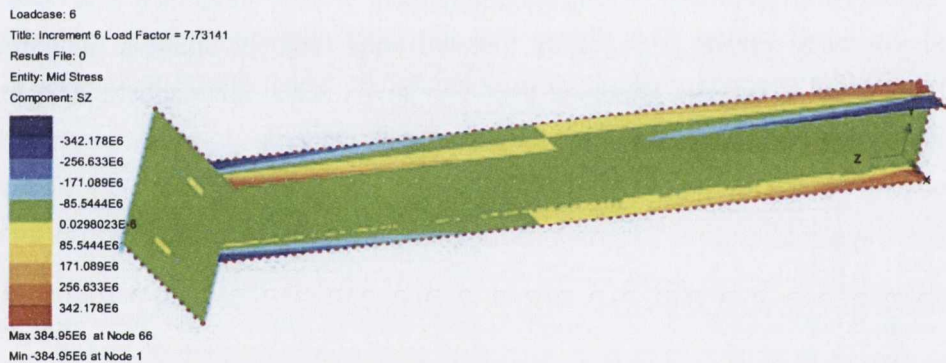


Figure 7.15 Stress contour of beam applied in pure torsion

7.6.4 Biaxial bending and torsion case, with dominant minor-axis bending

The first experiment in which a number of different forces were applied is under torsion and biaxial bending, with bending initially primarily acting in the minor axis direction (see Figure 6.2). Figure 7.16 shows the load-deflection response in this case. The load referred to is the measured load in the direction of the cable (as depicted in Figure 6.2). The deflection given in Figure 7.16 is the resultant of deflections which were measured in two different directions perpendicular to each other (as depicted in Figure 6.2). The idealized elastic-plastic curve as shown in

the figure is developed by drawing first line through the origin tangent to the linear portion of the experimental response. The second line is drawn by a tangent from the end of the curve up to the point when it intersects the first line. The finite element load-deflection curve exhibits the same trend as the experimental response although the results obtained from the finite element analysis are higher than the experimental results and there are several possible reasons for this. In the linear portion of the curves, a different modulus (as discussed in Section 7.6.1) is the main reason for the variation in the elastic response. In addition, finite element analysis does not take account of residual stresses which can increase the curvature and results in larger deflection.

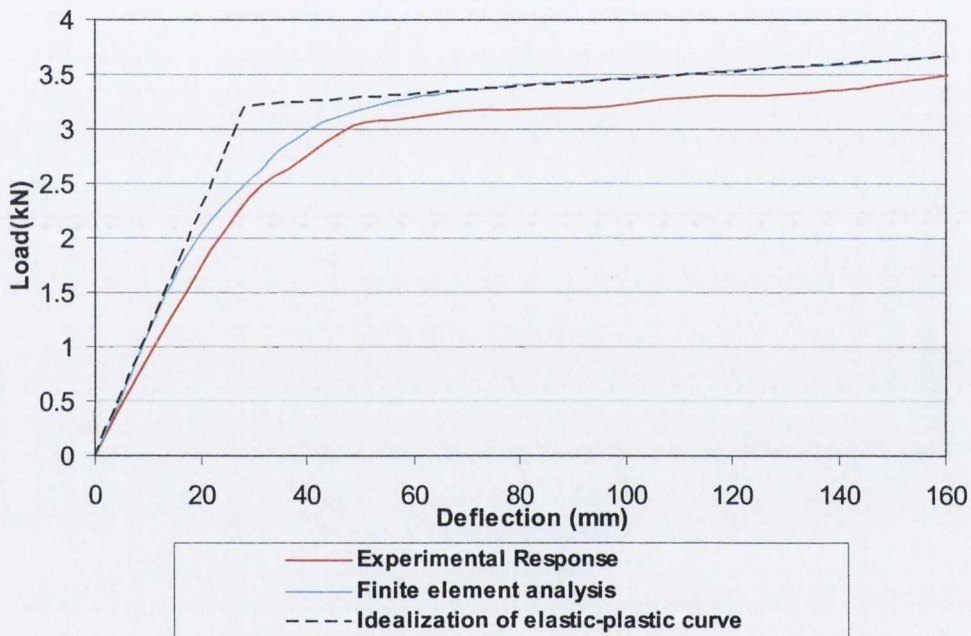


Figure 7.16 Load deflection curve for biaxial bending and torsion case, with dominant minor-axis bending. Experimental results are also given in Figure 6.10

The two orthogonal deflections are plotted against each other in Figure 7.17. The experimental response and finite element analysis shows that deflections in both the directions were not linear. Some variation from linearity in the predicted X-Y deflection is evident, reflecting the change in directional stiffness as the beam rotates under a torsional load. Considering the figure, it can be said that the finite element analysis and experimental results do not match each other

particularly well. However, at the end of the experiment, the deflections predicted by finite element analysis are reasonably close to the deflection in the experiment. There are two possible reasons for the non-matching of these results. One reason is that the displacement in the Y-direction is small as compared to the displacement in the X-direction, therefore small differences are on a larger scale on one axis. The second reason is that displacements are not measured by any LVDT or electronic displacement measuring device but through video images with reference to grid paper measured manually (as discussed in Chapter 6) where there can be an error of 1 to 2 mm in the readings. There are clearly random variations in the experimental readings. It can be concluded that both the response do not match in the non-linear phase.

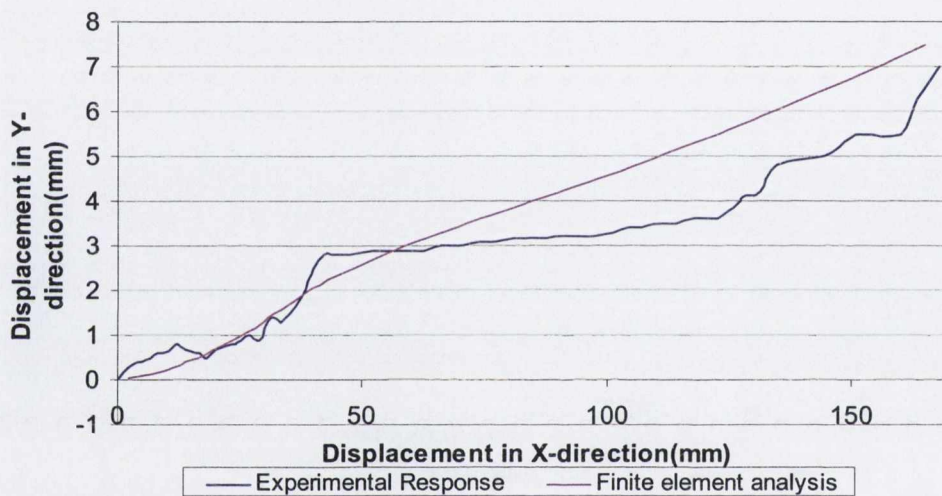


Figure 7.17 Measured deflections in two different directions for biaxial bending and torsion case, with dominant Minor-Axis bending. Experimental result produce here are also given in Figure 6.20

Figure 7.18 shows the torsion-rotation response of the beam sample. As discussed in Chapter 6, it was not possible to measure the rotation right to the end of the experiment. However rotation close to the end of the experiment is predicted reasonably accurately by the finite element analysis and exhibits the same broad trend as in the experimental response both showing some softening of the response. However, only a small difference exists between the curves, where the curve in the experiment is on the upper side. There can be several

reasons for this. Firstly, is the shear modulus (which is related to Young's modulus by Poisson's ratio) for the experiment and finite element analysis which are slightly different (as discussed in Section 7.6.1). Secondly geometric imperfections can occur during welding of the beam sample which can affect the straightness of the sample compared to the direction of the applied load and can make the system torsionally stiffer than that predicted by finite element analysis, in which a perfectly straight beam is modelled.

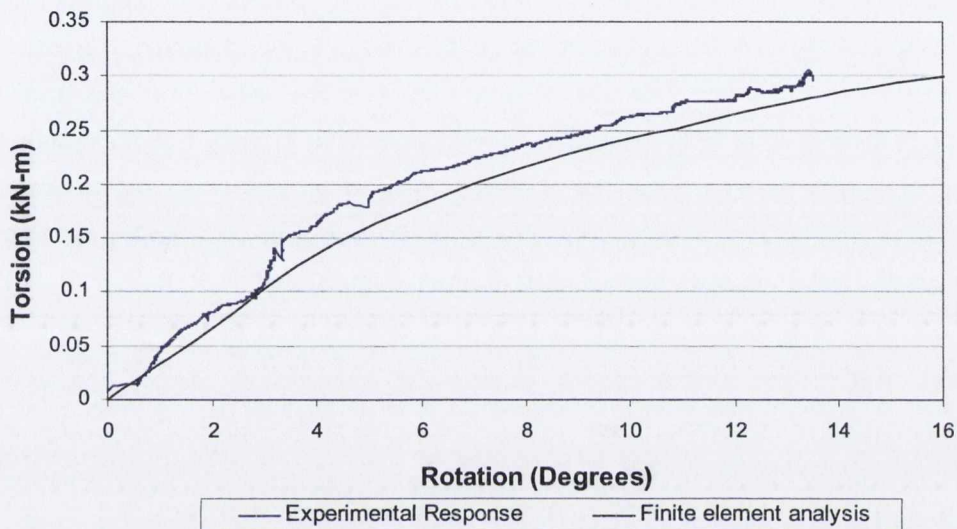


Figure 7.18 Torsion rotation curve for biaxial bending and torsion case, with dominant minor-axis bending. Experimental results are also given in Figure 6.7

To observe the interaction of rotation and the deflection, comparisons are made in Figures 7.19 and 7.20. Considering the displacement in the X-direction, a similar trend is observed for both the finite element results and experimental response where, up to nearly 11 degrees, the responses match each other to a good degree. Beyond this a considerably lesser rotation was observed for a given deflection increment for both the responses. This shows that there is a change of interaction between the bending and torsional mechanisms as noted in Chapter 6 and this change is confirmed by the finite element analysis in the graphs. The reason for the sudden change in the graph is that "failure" was essentially due to flexural plasticity where, in the figure, it can be observed that the change in the

interaction occurs at a displacement of nearly 50mm in the X-direction deflection. This significant change in the response was also observed in Figure 7.16 where the response showed plastic behaviour after the said deflection. This implies that failure in both the cases is mainly due to flexure with a small interaction with rotation. This is practically evident in the finite element graph where the line becomes nearly vertical at the end, which also shows that the failure was in flexure, where displacement occurs without a significant change in the rotation. Considering the displacement in the Y-direction (Figure 7.20), a similar trend is obtained for both the experimental and finite element results. The different nature of interaction for both small and large rotations can be observed for both the results and the reason for the different nature is the same as in the previous case. It shows that finite element analysis was unable to predict as accurately the rotation-deflection response as obtained in the experiment, but did predict the behavioural change of response. The similarity between both the figures is that both the response does not match in the non-linear phase.

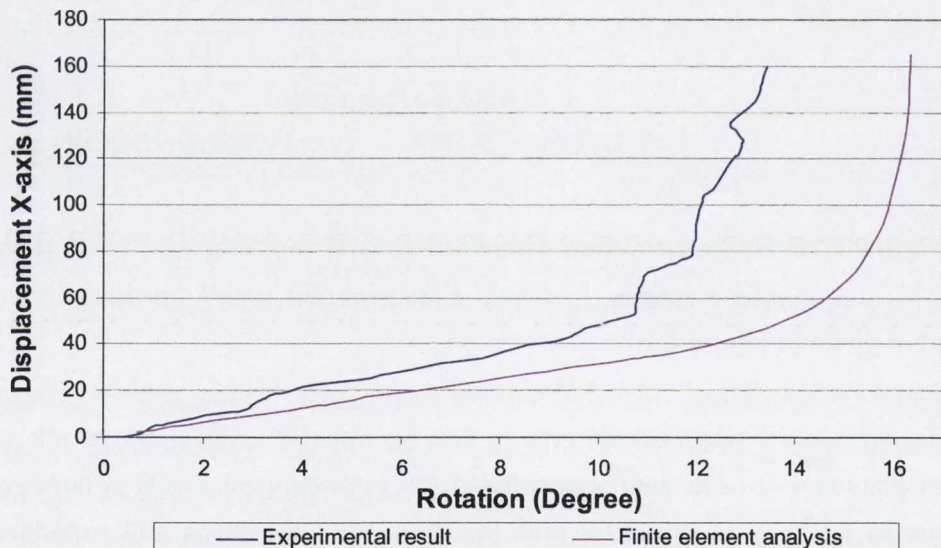


Figure 7.19 Measured deflection in X-direction and rotation of the beam sample for biaxial bending and torsion case, with dominant minor-axis bending. Experimental result produce here are also given in Figure 6.24

The yield value is determined by drawing the slopes of the two lines, one line from the linear phase and the second line from the plastic plateau. The lines intersect (Figure 7.16) at a value of nearly $3.15kN$ which can be taken as the

value at which the cross section yields under bending in two directions and torsion. Based on this value, stress resultants are calculated using the reaction obtained for each node at the support in the finite element analysis. The values obtained, given in their normalized form, are $m_y=1.1$, $m_z=0.04$ and $b=0.073$. A value of more than one for m_y (and also the accompanying values of m_z and b) shows that the section has yielded plastically as discussed in Chapter 4 which suggests that the yield surface developed in the chapter is a lower bound when compared with the numerical analysis.

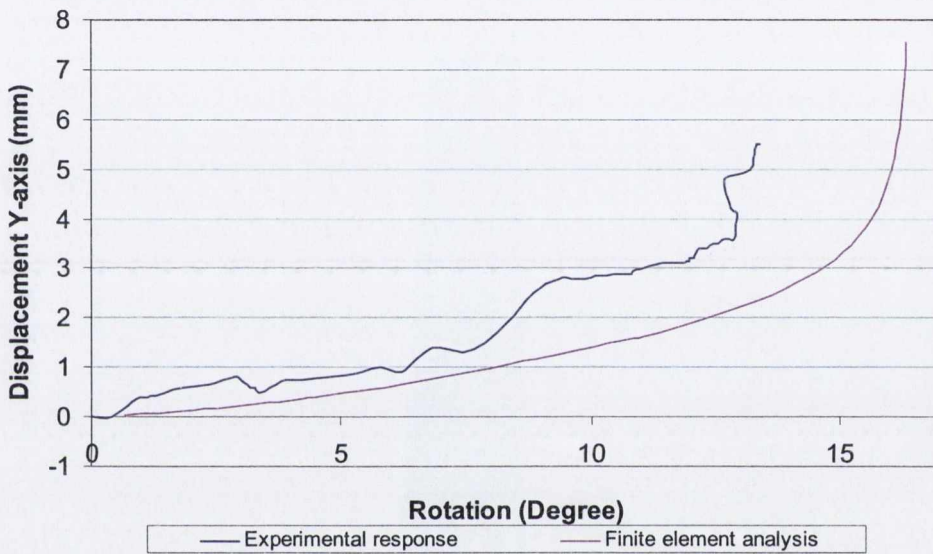


Figure 7.20 Measured deflection in Y-direction and rotation of the beam sample for biaxial bending and torsion case, with dominant Minor-Axis bending. Experimental results produced here are also given in Figure 6.22

Figure 7.21 shows the deflected square end plate viewed along the longitudinal axis of the beam. It can be observed that there are two modes of deformation of the plate, one is the rotational mode and the other is the lateral displacement mode. Considering Figure 7.22, a combined rotation and deformation pattern can be observed. This shows that the finite element model was capable of analysing the primary deformation patterns of the beam sample.

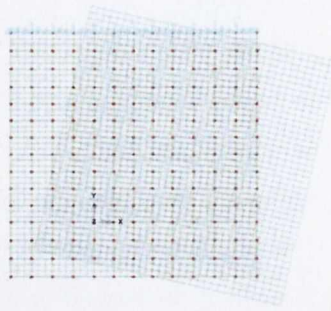


Figure 7.21 Deformation of the beam viewed along the longitudinal axis for biaxial bending and torsion case, with dominant minor-axis bending

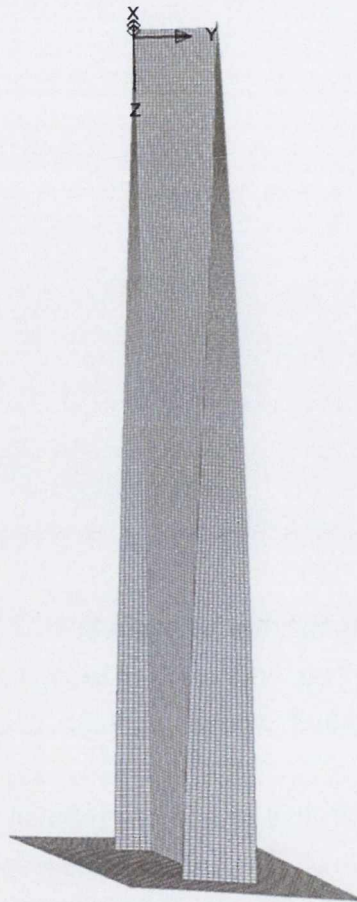


Figure 7.22 Deformation pattern of the beam for biaxial bending and torsion case, with dominant minor-axis bending

Figure 7.23 presents the contour of longitudinal stress extracted as a typical output from the middle of the thick shell from the incremental non-linear analysis

for the case when the stress at the support is more than the yield stress having a value of of 382.6MPa . It can be observed in the figure that there is a relatively small amount of stress in the web, whereas at the support both the flanges reached values above the yield stress. This is due to the fact that, in this experiment, rotation and minor axis bending were the main deformation patterns, where, in both deformation patterns, the least stress is taken by the web.

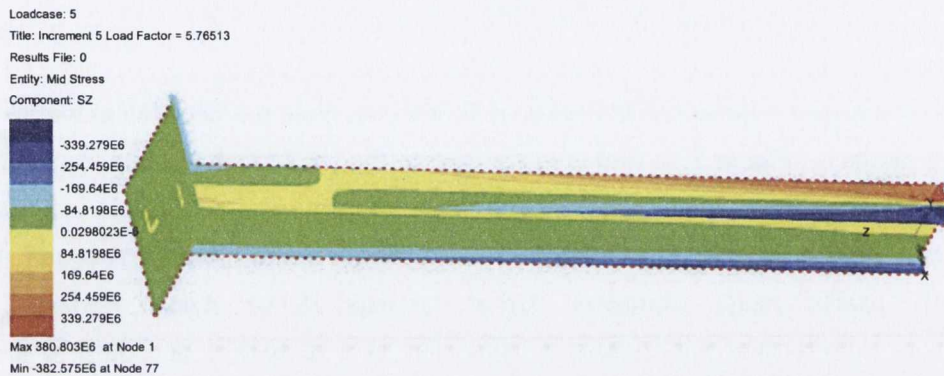


Figure 7.23 Stress contours of beam biaxial bending and torsion for biaxial bending and torsion case, with dominant minor-axis bending

7.6.5 Biaxial bending and torsion case, with dominant major-axis bending

The first experiment in which torsion and biaxial bending occurred was with bending initially primarily acting about the minor axis direction (see Figure 6.2). Figure 7.24 shows the load-deflection response of the beam sample, when biaxial bending is applied in combination with torsion with bending primarily about the major axis (see Figure 6.2). The finite element load-deflection curve matches the experimental curve up to a load of nearly 8.6kN , well above the elastic limit load of 4.19kN . The reason for the difference beyond this point is thought to be due to the mode by which failure occurred in the beam. Owing to rotation of the beam, the orientation of the cross-section with respect to the applied load varies over the entire length of the beam sample, which causes the stiffness of the beam to vary as the beam rotates progressively on application of the load. Owing

to the decrease of stiffness (at some cross section throughout the length), the load which the beam can resist will decrease. This phenomenon is also modelled in the finite element analysis but the decrease of load is not as sharp as the decrease of load in the experiment. One possible reason is that the exact interaction between deflection and rotation was not modelled by finite element analysis such that the decrease of stiffness, which resists the load, is different when small variations in rotation take place, hence resulting in the differences in the curves. Secondly, the geometric imperfections (as discussed in the previous section) can also cause the variations in the result.

The measured deflection in the two different directions (as depicted in Figure 6.2) is plotted in Figure 7.25 and is in contrast to Figure 7.17. A broadly similar trend is observed for both the experimental result and finite element values i.e. there is a rise of displacement in X-direction initially and a subsequent decrease of value on plastic hinge formation. Good correspondence exists between the experimental and finite element values up to a deflection of 20mm in the Y-direction. At this point the resultant deflection as given by Figure 7.24 was 26mm. At this point the two graphs in Figure 7.24 diverge and the reasons for the difference between the variations in graphs of Figure 7.25 are similar to that explained above. This shows that the finite element analysis was unable to consider the secondary effects leading to the interaction of both the deflections beyond that deflection of 20mm for the reasons as discussed above. The drop in the displacement in the X direction as Y deflection increases substantially is due to the reduction in bending resistance as the beam rotates and results in a decrease of deflection in the X-direction, as supported by the finite element results.

Figure 7.26 shows the torsion-rotation behaviour of the beam sample. Rotation up to the end of the experiment was not possible (as explained previously), however, rotation up to the end of the experiment is predicted by the finite element analysis. The maximum rotation in the finite element analysis given in the figure is the rotation obtained at maximum deflection obtained in the experiment. Up to the point where rotation was measured, the finite element exhibits very similar trends as the experimental response. Differences which exist between both the results are minor, principally due to bedding down of the beam

in the experiment at low force. At an angle of nearly 55° torsion drops, this happens due to the fact that the beam was in the elasto-plastic phase because of which rotation rates did not change during the decrease of load and results in a drop of torsion value.

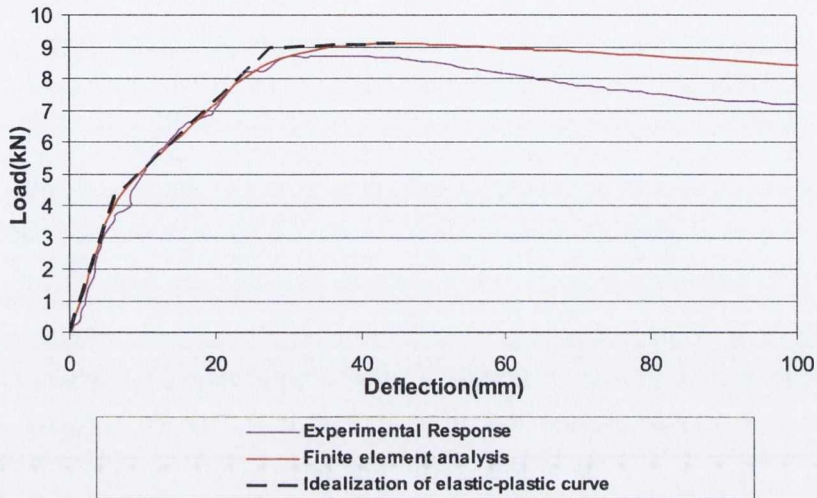


Figure 7.24 Load deflection curve for biaxial bending and torsion case, with dominant major-axis bending. Experimental results produced here are also given in Figure 6.12

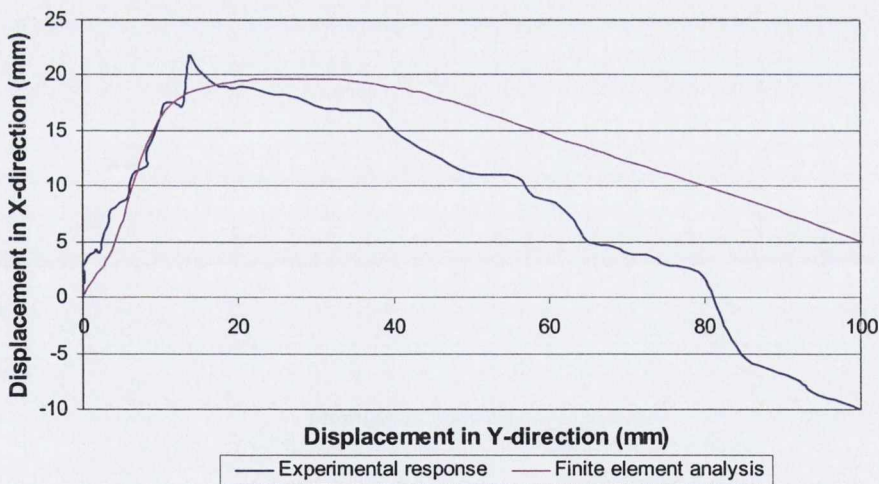


Figure 7.25 Measured deflections in two different directions for biaxial bending and torsion case, with dominant Major-Axis bending. Experimental results produced here are also given in Figure 6.21

Figure 7.27 presents the curve of deflection in the Y-direction against rotation. Consideration of the graph shows a similar response can be observed for both the experimental results and finite element values up to the point when rotation ceased to be measured in the experiment. Beyond this point significant increase of deflection can be observed compared to rotation. A similar response is observed in the previous case in which at large deflections the beam sample failed more because of flexure with only a small interaction due to torsional rotation.

Figure 7.28 presents the curve of deflection in the X-direction against rotation. Above approximately 10° rotation a poor relation exists between the experimental and finite element response. Two possible reasons for the difference is the procedure adopted to measure the deflection and the small scale on the Y-axis as discussed in the previous section. Lastly differences in the interaction between finite element and experimental response can occur for the reasons discussed above. The rise and fall in the X-axis response is an indication of change of flexural stiffness as compared to torsional stiffness of the beam sample. This happens because of the decrease of stiffness of the beam sample due to rotation as a consequence of which displacement in the X-direction started to reduce.

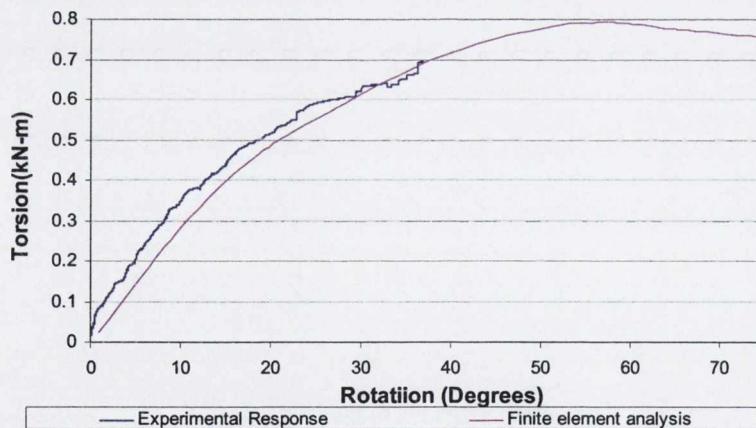


Figure 7.26 Torsion Rotation curve for biaxial bending and torsion case, with dominant major-axis bending. Experimental results are also given in Figure 6.8

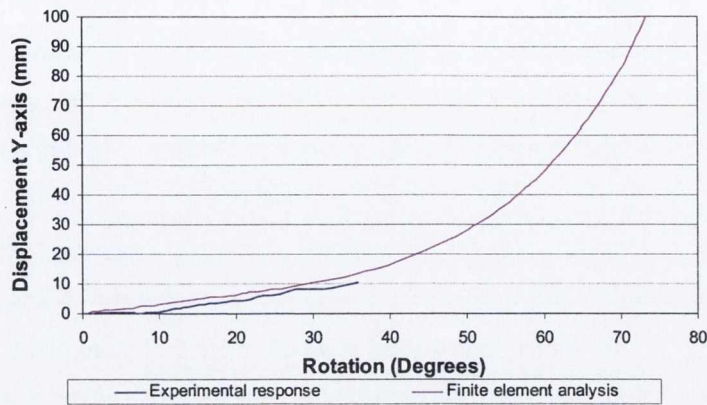


Figure 7.27 Measured deflection in Y-direction and rotation of the beam sample for biaxial bending and torsion case, with dominant major-axis bending. Experimental results produced here are also given in Figure 6.23

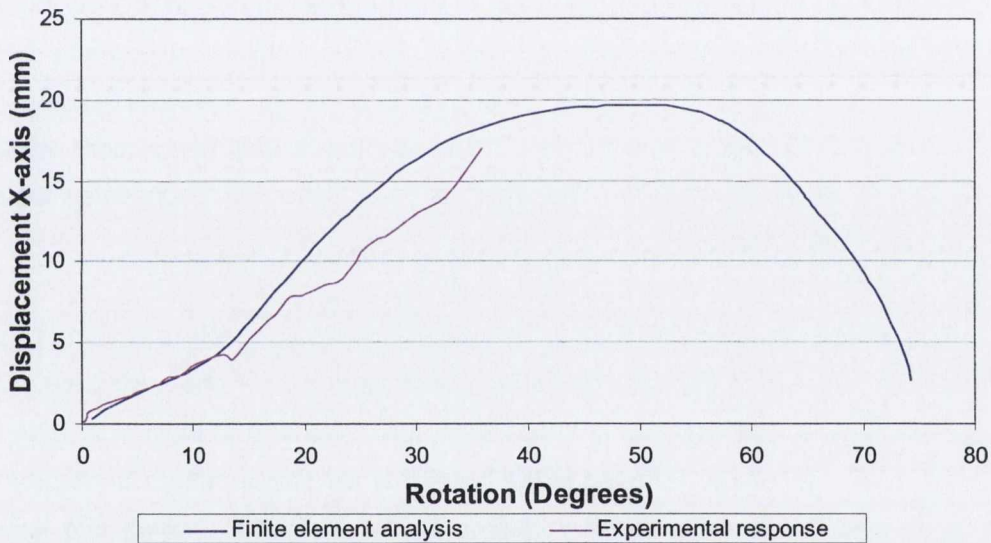


Figure 7.28 Measured deflection in X-direction and rotation of the beam sample for biaxial bending and torsion case, with dominant major-axis bending. Experimental results produced here are also given in Figure 6.25

Three lines are drawn to determine the approximate yield value as depicted in Figure 7.24. The last line is taken horizontally from the peak load as a decrease in load was then observed in the analysis. Two points are identified by the three lines. The point which forms on intersection of the first line (which starts at the origin) and the second line is a point, beyond which the beam sample is quasi elastic and cannot be considered as the point of section yielding. The second

point can be taken as the point for the yield value because at this point the section is assumed to be fully plasticized. Therefore, the value at which the second point is obtained (nearly $9kN$) can be taken as the value of section yielding under both the bending and torsion mechanism. For this assumed value, stress resultants in normalized form are obtained as $m_y=0.44$, $m_z=0.60$ and $b=0.27$ (Appendix-E). Keeping the values of m_y and b constant, the m_z value is calculated based on the developed theory given in Chapter 4 which shows that values obtained are more than values at which a section yield plastically. Hence it can be concluded that yield surface developed in the chapter are lower bound values when compared with the numerical approach.

Figure 7.29 shows the deflected rectangular end plate viewed from the longitudinal axis of the beam. It can be observed from the figure that there are two modes of deformation of the plate; one is the rotational mode and the other is the lateral displacement mode. This shows that the analysis managed to model both of the primary modes of deformation i.e. bending and rotational deformation. Comparing this figure with Figure 7.21 shows that in this figure more rotation takes place for the square plate whereas more deflection is observed for the square plate in Figure 7.21.

Figure 7.30 presents the contour of longitudinal stress which is extracted as a typical output from the incremental non-linear analysis for one such case when the stress at the support is more than the yield stress having a value of $389.7MPa$. It can be observed in the figure that the stress pattern is irregular as compared to the more regular patterns for the individual bending and torsion cases, as depicted in Figures 7.8, 7.10 and 7.15. This shows that stresses developed due to the combined action of bending and torsion results in non-uniform stress pattern.

Figure 7.31(b) shows the deformed wire mesh of the beam sample, in which, a rotation and deformation pattern can be observed. When compared with the deformed beam of the experiment in Figure 7.31(a) (after removal of load), the figures demonstrate a similar type of rotational and bending response. However differences exist between both of them, where the finite element analysis is the result of load application whereas the experimental result is for residual rotation

and deflection on unloading. Both the rotational mode and deflection modes of the displacements indicate that the finite element model was capable of predicting the correct primary deformation pattern of the beam sample. During the experiment, no secondary effects such as local buckling of the flanges or web or any other local failure were observed in the experiment nor were they predicted by the finite element analysis.

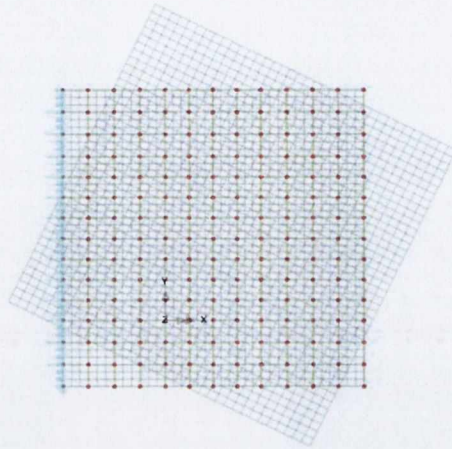


Figure 7.29 Deformation of the beam viewed along the longitudinal axis for biaxial bending and torsion case, with dominant major-axis bending

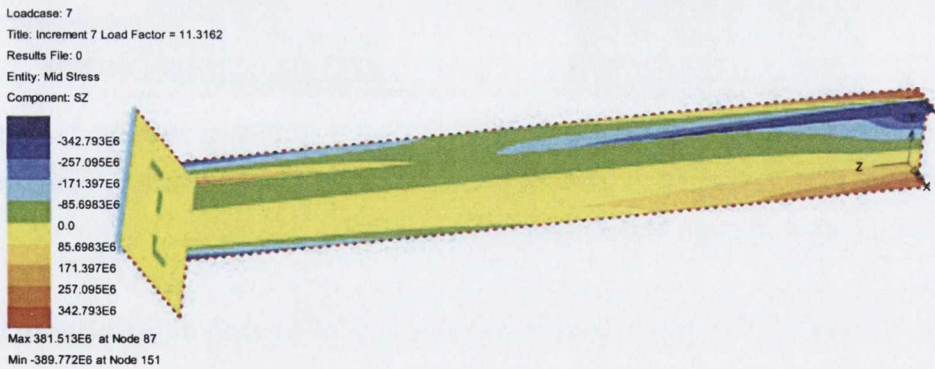
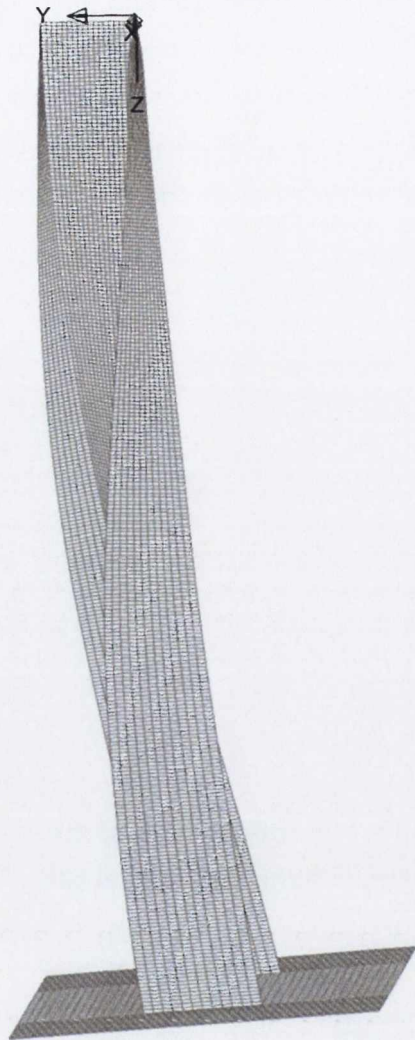


Figure 7.30 Stress contours of beam biaxial bending and torsion, Second Experiment (Primarily about major axis)



(a) Experiment



(b) Finite element Analysis

Figure 7.31 Deformation pattern of the beam for biaxial bending and torsion case, with dominant Major-Axis bending

7.6.6 Analysis of beam with a passive pre-stressing cable attached

In the previous analysis, an I-beam was modelled with a plate at its end, whereas in the next analysis, a steel cable is attached to the end plate and pretensioned to apply a pre loading axial force to the tip of the I-beam. In the current analysis however, a passive steel cable is attached, not to apply a limited axial force but to restrain the lateral movement of the beam geometrically. No experiment was performed for this analysis but it will enable an understanding to be developed of

the effects of the non-linear geometrical stiffness contribution of the cable. The whole model with cable attached is depicted in Figure 7.32.

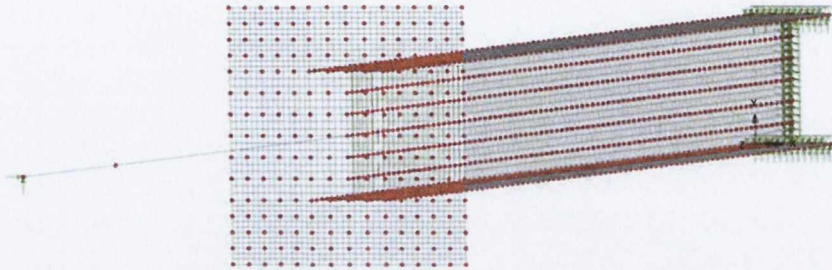


Figure 7.32 Model from Figure 7.3 with cable attached at the end plate

Figure 7.33 shows the load-deflection graph for this analysis, compared with the previous analysis. From the two graphs the strong effect of the cable is evident. In the presence of the cable, the response is much stiffer at higher loads, than the case when the cable was not present. The response during the elastic phase is nearly the same for both cases. During the nonlinear analysis, torsion causes large axial shortening (as seen in Figure 7.14) which will now be resisted by the cable. Further, the lateral load causes the beam to displace more from its original position (as compared to the position of the beam in linear phase) leading to non-linear geometry. These two phenomena give rise to the development of an axial force in the cable, which is caused by lateral resistance to lateral movement of the beam. This result in a lesser amount of deflection for the same amount of load compared to the previous case in which no cable is attached. The presence of a cable increases the resistance of the beam to the lateral loading and results in a relatively higher value of load when compared with the previous case for the same amount of deflection.

During the process of lateral load application, an axial load developed in the cable, as shown in Figure 7.34. As the applied lateral load increases, axial shortening due to torsion and lateral displacement increase, hence it exerts more force to the cable in the latter stages of the analysis due to non-linearity. In the early stages of lateral load, only minor axial shortening occurs (see Figure 7.14)

but non-linear shortening and geometry cause the rapid growth of axial load seen in Figure 7.34 as lateral load increases

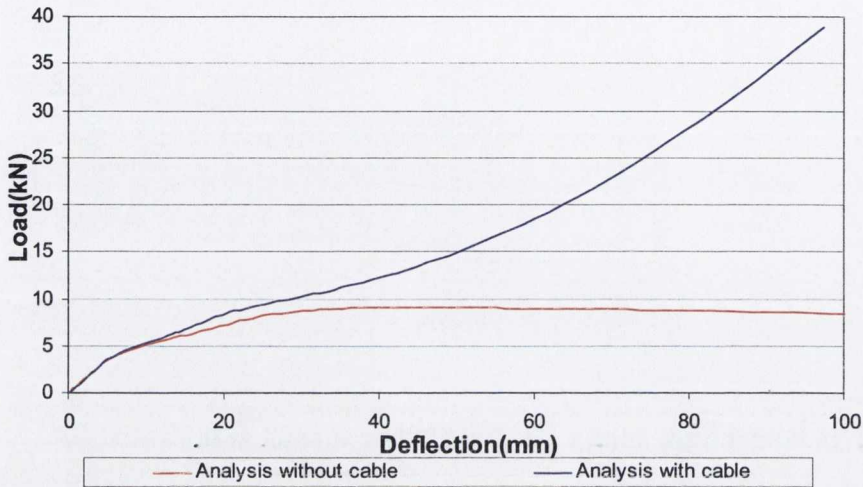


Figure 7.33 Load-deflection curves for beam with passive cable attached

The development of an axial load, which arose substantially due to secondary effects of axial shortening and large lateral displacements, shows that finite element analysis manages to pick up those secondary effects. Finite element analysis also manages to model the primary effects of bending and rotation which shows that the finite element method was able to model both the primary and secondary effects for this case.

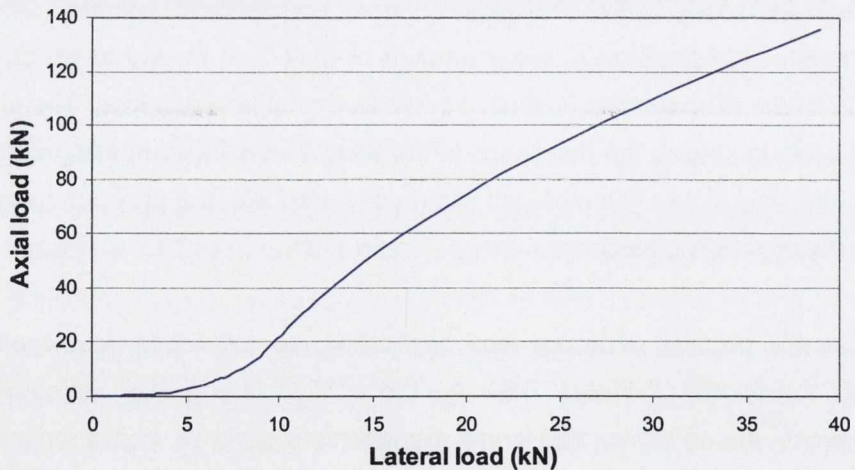


Figure 7.34 Axial load in the cable in comparison with the lateral load for beam with a passive cable attached

7.6.7 Axial force, biaxial bending and torsion experiment

Figure 7.35 shows a comparison between the load-deflection relationship for the experimental result and finite element analysis when all four forces are applied. An axial force of 35kN is first applied using an active tendon (as discussed in Section 7.5). Both the curves exhibit the same trends and very reasonable agreement between the experiment and analysis is obtained. However the finite element response is larger than the original response in the latter stage of the curves. One possible reason for this is the presence of residual stresses which can change the curvature for the same load applied as discussed in Section 7.6.1.

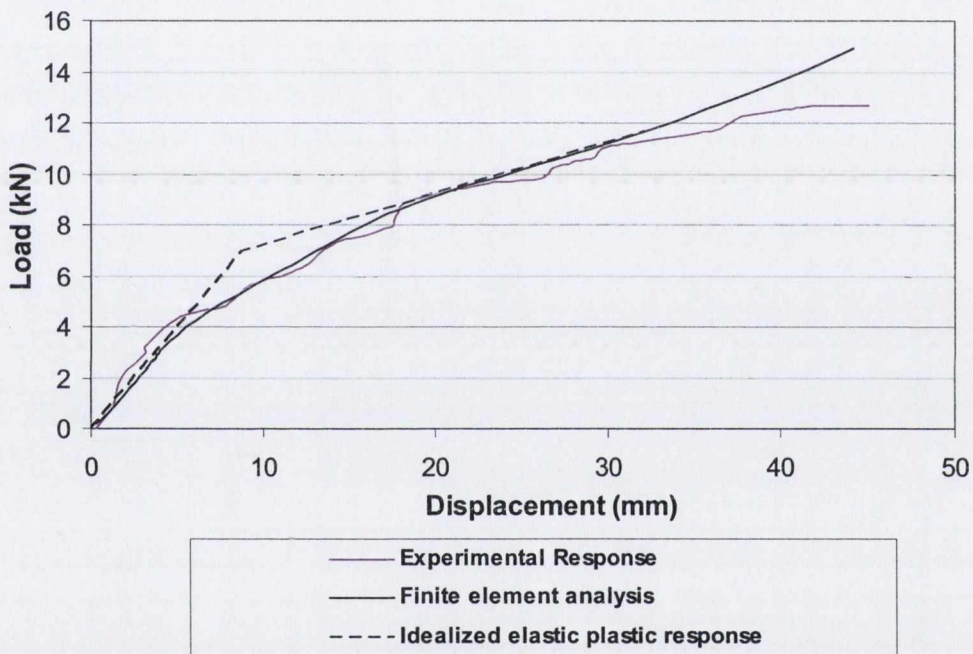


Figure 7.35 Load-deflection graph for the experiment where axial load applied using active tendon. Experimental result produce here are also given in Figure 6.34

Figure 7.36 presents the relationship between the deflections in the two perpendicular directions. Although the curves are approximately equal at low and high displacement, the curves do not match each other in the middle of the graphs. However, the differences which exist between both the results are relatively minor; and the main experimental trends are reproduced by the model.

One reason for the disparity is that displacements are measured manually (as discussed before) where errors of 1 to 2 mm are possible. This reason is valid because there is a maximum difference of 3.5mm between them at some places. A second possible reason is the interaction of secondary effects such as axial shortening and large lateral movement which can cause different interactions between the displacement in the experiment and finite element analysis.

Figure 7.37 shows the torsion against rotation response of the beam sample. The finite element response shows a very similar trend as the experimental response until a rotation of 50°. Finite element analysis shows a stiffer response after this angle. One reason for more torsion in the model is the presence of residual stresses. When rotation is applied warping action takes place, which is basically bending of both flanges in two different directions. As residual stresses cause increase of curvature (as discussed in Section 7.6.1) therefore a larger amount of warping can take place in the presence of residual stresses, (Vlasov, 1959) and results in higher rotations compared to the finite element analysis.

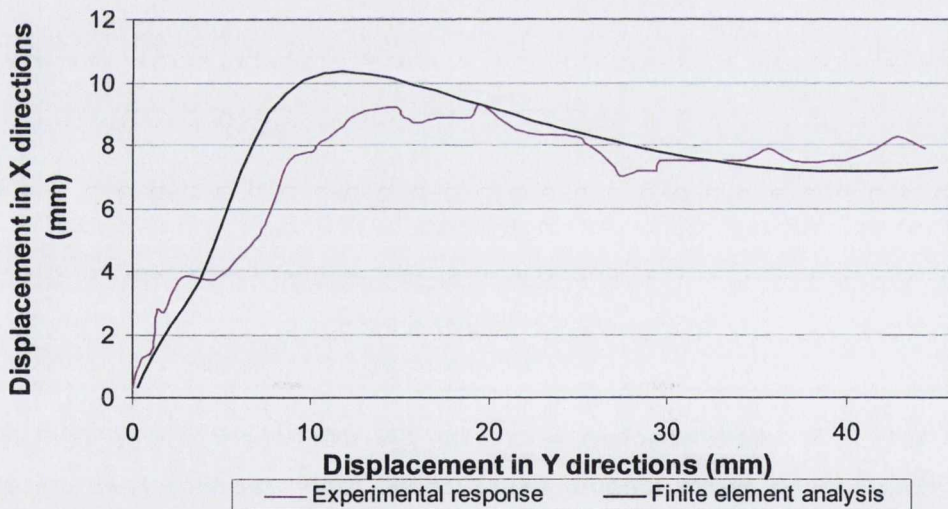


Figure 7.36 Measured deflections in two different directions where axial load applied using active tendon. Experimental result produce here are also given in Figure 6.38

Figure 7.38 presents graphs for the displacement in the Y-axis direction and rotation of the beam sample. However some differences exist between both the responses. The experimental response is largely linear whereas the finite

element analysis is non-linear. Finite element shows that failure will be due to flexural plasticity in the later stages therefore resulting in an increase of displacement compared to rotation, whereas the experiment shows that failure is a combination of both flexural plasticity and torsional plasticity. It shows that finite element analysis does not fully consider the interaction between rotation and displacement as observed in the experiment.

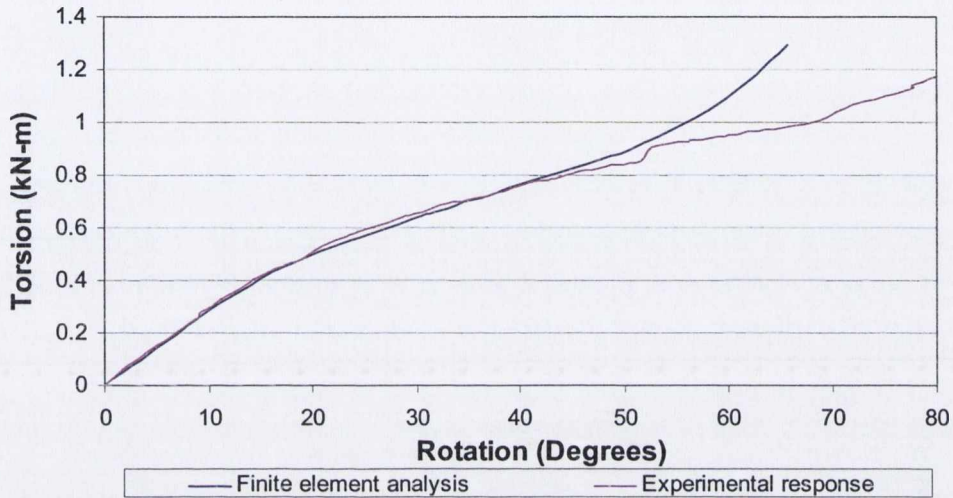


Figure 7.37 Torsion-rotation response of the experiment where axial load applied using active tendon. Experimental result produce here are also given in Figure 6.32

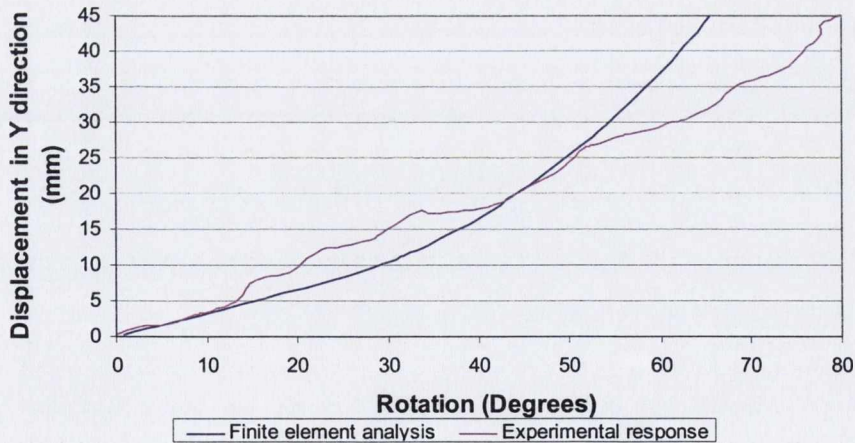


Figure 7.38 Measured deflection in Y-direction and rotation of the beam sample where axial load applied using active tendon. Experimental result produce here are also given in Figure 6.39

Figure 7.39 presents graphs for the displacement in the X-axis direction and the rotation of the beam sample. Both the graphs exhibit the same broad trends, however, differences exist between the graphs. Comparing the figure with Figure 7.36 shows a similar trend. A possible reason for the difference is as discussed for the difference of the graphs in Figure 7.36.

Figure 7.40 shows the increase of axial load during lateral load application. Both the experimental result and finite element analysis show a very similar trend and match each other very well. It shows that the finite element analysis manages to model the primary effects of torsion and rotation and the secondary effects of axial shortening and large displacement at large loads as it did in the previous case with a passive pre-stressing cable. Hence, due to the correct modelling of these effects, finite element analysis manages to replicate the force developed in the cable as obtained in the experiment and so predicts accurately the lateral deflections and hence beam stresses.

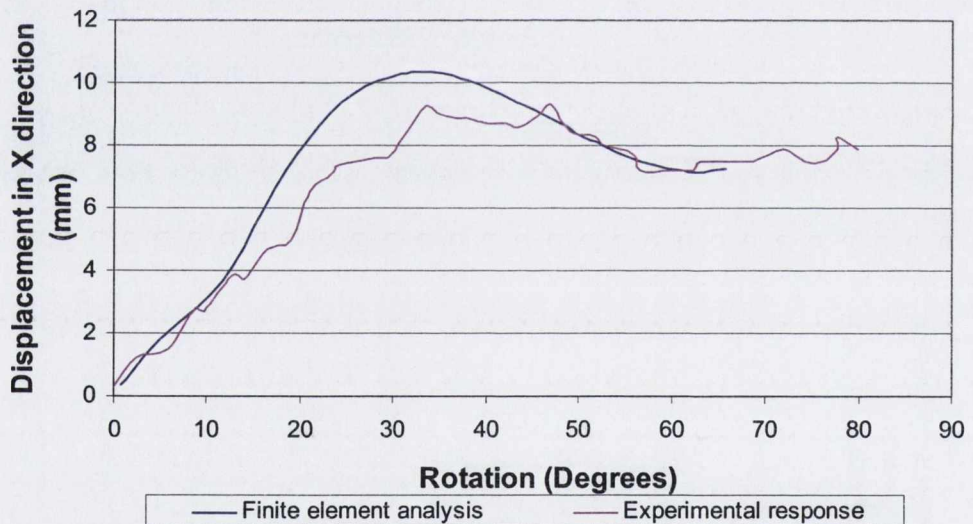


Figure 7.39 Measured deflection in the X-direction and rotation of the beam sample when axial load is applied using active tendon

Figure 7.41 presents the deformed configurations for the beam sample. The figure consists of two parts. The first part is a photograph of the tested specimen in the permanently deformed configuration. The second part consists of a wire mesh view of the beam sample in the deformed configuration during loading as

predicted by finite element analysis. Both the figures show a similar trend of rotation and bending.

To approximate the yield point, two lines are drawn as depicted in Figure 7.35, to determine the assumed value at which the section yields. The lines intersect at value of 7kN which can be considered as the yield value when biaxial bending and torsion are applied in combination with an axial force. For the given values, stress resultants in normalized form are obtained namely $p=0.1$, $m_y=0.44$, $m_z=0.60$ and $b=0.27$. Keeping p , m_y and b at those values m_z is calculated based on the developed theory given in Chapter 4 the value obtained is 0.45 which shows that values obtained are greater than that at which a section yields plastically, which shows that the yield surface developed in the Chapter 4 is a lower bound compared to the numerical analysis.

In Figure 7.42 the deflections obtained under different lateral loads, for the three cases discussed in Section 7.6.5-7 are given. It can be observed that the addition of the cable increases the lateral load required on the beam for a given deflection, whereas the application of an axial force to the sample through the cable decreased the deflection under a given lateral load. This shows that resistance to lateral displacement provided by a cable increases the lateral load for a given deflection and that the provision of a pre-loading axial load further increases that lateral load.

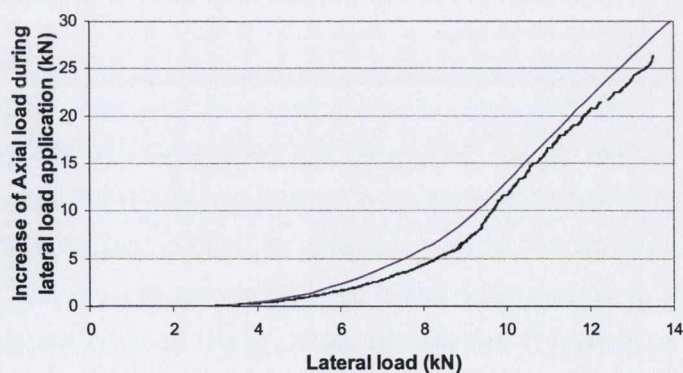


Figure 7.40 Increase of axial load during lateral load application and lateral load of the beam sample when axial load is applied using active tendon. Upper line is finite element result and lower is the experimental result. Experimental result produce here are also given in Figure 6.29



(a) Experiment



(b) Finite element Analysis

Figure 7.41 Deformation pattern of the beam when axial loads applied using active tendon

Figure 7.43 gives the graph of the increase of axial load during lateral load application against applied lateral load. For the passive case the rise in the graph is more than for the case when axial force is applied to the beam sample. This shows that the secondary effects of axial shortening and large displacement in the absence of an axial load has a significant influence on the development of axial force in the cable and the rise in the graph become steeper as both the secondary effects increase. Pre-loading the cable is therefore, significantly advantageous.

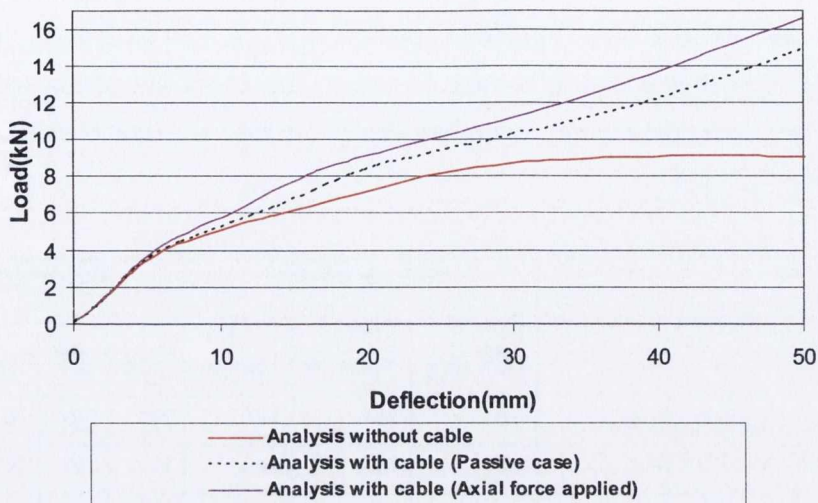


Figure 7.42 Finite element response of lateral load against deflection for the cases discussed in section 7.6.5-7.

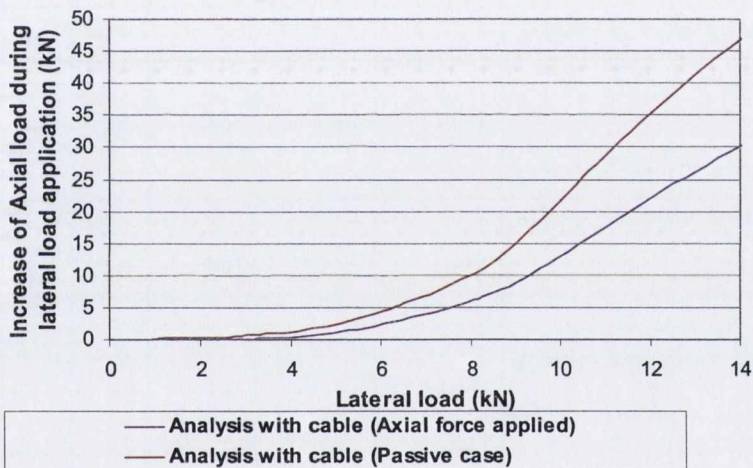


Figure 7.43 Finite element responses of axial load developed in the cable for the passive case and axial load applied.

7.7 CONCLUSION

The finite element analyses investigated the behaviour of the beam samples tested in the experimental program when subjected to different types of monotonically applied loading. Both the case types, that is when a single load or when more than one loading action was applied to the beam sample, were investigated for both primary and secondary effects, as observed in reality in experiments. It is found that finite element analysis can successfully analyse the primary mode of analysis, while secondary modes of analysis were also picked

for the cases when it was identified in the experiments. Certain phenomena which are related to certain modes of deformation (such as LTB) were not picked up nor were they found in the experiments. The capability of the software in modelling such primary and secondary effects for each analysis is summarized in the following table:

Loading Action	Primary effects			Secondary effects			
	Plastic Bending	Plastic Torsion	Axial effects	LTB	LB	AS	Lateral movement
Major-axis bending	Yes	N/A	N/A	No	No	N/A	N/A
Minor-axis bending	Yes	N/A	N/A	No	No	N/A	N/A
Torsion	N/A	Yes	N/A	N/A	N/A	Yes	Yes
Combined loading action							
Biaxial bending+Torsion (Primarily about minor axis)	Yes	Yes	N/A	No	No	Yes	N/A
Biaxial bending+Torsion (Primarily about major axis)	Yes	Yes	N/A	No	No	Yes	N/A
Biaxial bending+Torsion (Primarily about major axis with passive cable)	Yes	Yes	Yes	No	No	Yes	N/A
Axial force+ Biaxial bending+ Torsion (Primarily about major-axis with axial load)	Yes	Yes	Yes	No	No	Yes	N/A

Table 7.3 Comparison of the loading actions and the capability of finite element in predicting primary and secondary effects. The terminologies in the table are Local buckling (LB), Lateral torsional buckling (LTB) and Axial shortening (AS)

From the table it can be deduced that finite element analysis can model all the primary modes of deformation, while other secondary modes of deformation, which may be possible in general, were not always observed in the experiment nor were they predicted by the finite element analysis. Comparing the interaction of one mode of deformation to the other mode, finite element analysis manages to analyse successfully the interaction of different modes of deformation. In addition, it also gives good correlation when compared with the developed yield surface for interaction of different combination of forces. Different responses such as load against deflection, torsion against rotation, deformed geometry and contours of stress developed were also modelled successfully by finite element analysis. However, differences were found between the experimental result and finite element in the later stages of the response. The reason is that the finite element was unable to model the behaviour at the end of experiment because it was unable to model the rotation as it occurred in the experiment. It can thus be concluded that for the current nature of experimental program, the finite element method can be a reasonable substitute for experimentation, despite the complications of the interactions which inevitably occur at large deflection and rotations.

CHAPTER-8

CONCLUSION

8.1 SUMMARY

The overall objective of the research described in this thesis was to develop approximate and exact yield surfaces for an I-section and to verify the yield surface using experimental and numerical methods. To achieve this, yield surfaces were developed based on an approximate approach using a curve fitting technique, while a lower bound and an upper bound approaches are used to obtain the exact solution under the given assumptions. Experiments were performed for single forces and combination of forces. Owing to the lack of a facility in the laboratory to twist a specimen at high rotations, a test rig was designed specifically for that purpose. Using a numerical method, previously developed yield surfaces and approximate yield surfaces developed in this research were verified.

In the development of an approximate simplified yield surface equation, a curve fitting technique was used where surfaces for Universal Beams listed in BS EN10056: 1999 were curve fitted for biaxial bending and bimoment. It was found that a yield surface changed predictably with cross sectional properties and this was considered in the development of the equation. In the same work different yield surfaces were verified using a numerical technique. This verification was later used to extend the developed yield surface curve to fill the gaps which were present in the previously published yield surfaces.

In the case of the development of an exact solution for the case when biaxial bending, biaxial shear, axial force, bimoment and uniform torsion are considered, the development was divided into two parts. In the first part those forces which produced shear stress on the section were considered and, based on a lower bound approach, an interaction equation is obtained for these cases. For the second part those forces which produce direct stresses to the section were considered to develop interaction relationships. When direct stresses were considered first neutral-axis patterns were

obtained to derive the possible deformation patterns for the yield surface. Based on the neutral-axis patterns a parametric approach was developed to generate yield surfaces and identify yielding of the section. Two distinct cases were identified when neutral-axis patterns were obtained, namely when the neutral-axis passes through the web and when it does not pass through the web. Different approaches were taken for each case to develop yield surfaces and identify yielding of the section. The developed yield surfaces are compared with previously developed yield surfaces. The lower bound approach adopted to develop yield surfaces was also verified for one case using an upper bound solution.

Experiments were conducted in two sets to examine the behaviour of an I-section under realistic monotonic loadings. In the first set of experiments test specimens were manufactured from I-sections and tensile coupon tests were carried out to determine actual material properties. Great care was taken in manufacturing the specimens. Next three types of experiment were performed to obtain the plastic capacities of the section under the action of one force type. Experiments were performed for bending of a cantilever beam about the major and minor axes and were tested to failure of the beam in pure torsion. In the case of pure torsion a test rig was designed which has the property of being capable of rotating the sample to large rotations and this can be adopted when torsion needs to be applied with biaxial bending.

In the second set of experiments beam specimens were tested under biaxial bending and torsion in one case and biaxial bending, torsion and an axial force in other case. The same setup which was used for torsion was used here to apply bending in combination with torsion, and the response of the beam under the given forces was studied. In the axial force case, the axial force is pre-applied using a prestressing tendon and jack. Rotations, deflection and strains were monitored at critical locations and compared with the developed theory. Yield surfaces were also verified for the given set of loading combinations, to a reasonable level of confidence.

Numerical analyses were performed under monotonic loading for different loading conditions to verify the experimental results and the ability of the software to carry out such complex non-linear analysis in which different combination of loads can be applied. Following the same trend as was followed in the experiment, first analyses were

performed for single stress resultants. Material properties used for the analysis were those obtained in the coupon's test results. The results of the analysis under single stress resultants were then compared with experimental results. Later numerical analyses were performed for multidimensional stress resultants and results of the analysis are compared with experimental results. Results are also compared with the developed yield surfaces developed in previous and the current work.

8.2 CONCLUDING REMARKS

The experimental and theoretical work undertaken within the scope of this research leads to the following conclusions.

An approximate yield surface equation based on a suitable regression technique is a good alternative to the exact solution yield surface.

Yield surfaces of different Universal Beam sections were generated and it was found that approximate solutions compare well with the previously developed yield surfaces.

The approach which was adopted to verify yield surfaces using finite element analysis gives reasonably accurate results.

Using the approach previously developed, the approximate yield surfaces were verified. Using this verification technique, yield surfaces were extended to fill the gap which was present in the previously developed yield surfaces. From the verification of the extended part it is found that the extension of the curves to matched with the finite element analysis, hence showing the extensions were valid.

Exact yield surfaces are obtained for seven stress resultants. Probable deformation patterns are obtained and on this basis yield surfaces are obtained. Those yield surfaces are closed, convex and exact and compare well to the previous case when yield surfaces were not exact and not closed. In addition these yield surfaces are successfully developed for seven forces as compared to the previous approach in which five forces are considered.

These yield surfaces are also verified by an upper bound approach for one type of neutral-axis pattern and it compares exactly with its lower bound approach which shows that under the assumption made these yield surfaces are exact.

A procedure has been developed for the checking of hinge formation for this yield surface and two different approaches were adopted for the case when the neutral-axis intersects the web and when it does not intersect the web.

Experimental results of the coupon test show a typical result for mild steel where the stress-strain curve shows a well defined yield plateau. The Young's modulus obtained from Coupon testing was 201GPa . When Young's moduli are obtained for bending of a beam about both its axes, then the result shows lower values of Young's Modulus. The plastic capacities obtained in flexure, when compared with the plastic capacities obtained for the coupon test, show a close similarity in the results. When plastic torsion arises, it matches well with the theoretical results based on the coupon test results.

The experimental responses for the cases when a beam is subjected to more than one force are discussed. Three experiments were performed, the results of which for torsion against rotation compared well in the elastic range.

When torsion against rotation in the inelastic range is examined for the two experiments (one when minor-axis bending dominates and the second when major-axis bending dominates) the differences show the impact of the interaction of the forces. It is found that the value at which it is supposed previously that a hinge will form is too high and from the strain results it is evident that plastic behaviour occurs at a lesser load. This is also confirmed when based on the results at which a practical hinge is actually formed as compared with the developed yield surface of Chapter 4. It is found that the load at which it reaches the developed yield surface is far less than the load at which the practical hinge forms. It is also found that when in the third experiment axial load is applied in tension then the torsion-rotation diagram and load deflection diagram demonstrate a significant increase in the stiffness in the response. The strain diagrams also show that in the axial case the axial force started to increase the resistance to bending of the sections and the axial forces developed were high compared to the axial force applied initially by the prestressing tendons.

Using a numerical method of analysis the behaviour of the beam samples tested under different loading conditions were analysed and compared with experimental and finite element analysis. It showed that the finite element software managed to identify the primary modes of deformation which are bending and torsion and secondary modes which were also present in some cases. Some of the secondary modes like LTB were not identified nor they were present in the experiments. Yield surfaces were also verified using the finite element results.

The purpose of this thesis is to establish both an exact and approximate form of yield surface equations and these were later verified using finite element analysis and other numerical techniques.

8.3 RECOMMENDATIONS FOR FUTURE WORKS

This research mainly focussed on yield surfaces, then the development and verification using an experimental and numerical method. Although an attempt has been made within the scope of the current research to shed more light on the yield surface there remains scope for further research. In particular it would be desirable to examine the following areas in more detail:

- 1) Approximate single equation yield surfaces can be extended for all types of BS EN10056: 1999 sections and for other available steel sections such as the American sections.
- 2) Axial force and uniform torsion can also be included with biaxial bending moment and bimoment to obtain a single equation when five forces are considered.
- 3) An I-section interaction equation can be developed for a channel section when biaxial bending, axial force, warping torsion and biaxial shear force are considered.
- 4) The equations developed were for I-section with equal flange width and thickness, work can be extended to cases when both flange widths can vary.

- 5) A general procedure can be developed to generate yield surface for other open sections such as C sections and Z-sections.
- 6) The possibility of developing interaction equations for an L or T section when warping is considered. Equations exist for them but they do not take account of warping of the section.
- 7) An experimental development is required for the case when torsion is applied to the section. There needs to be more experimental research on torsion by varying three variables which are changing the boundary conditions, the size of cross section and by varying the length of the member.
- 8) Experiments should be performed for biaxial bending and torsion cases for different I-sections by varying the three parameters as discussed in the previous paragraph.
- 9) Experiments are performed when axial force, biaxial bending and torsion are applied. More axial force can be applied to obtain the behaviour of a beam under primarily axial force, hence obtaining different neutral-axis patterns. In addition they can be checked by varying the three parameters discussed above and also when axial force is applied in compression.
- 10) Using numerical techniques different cases can be studied by varying the parameters to arrive at a conclusion which can help to reduce the number of experiments.
- 11) Based on the experimental and numerical results interaction equations can be modified to take into account the practical differences which occur in the experimental and numerical results.

REFERENCES

- American Institute of Steel Construction (AISC). (1999). "Load and resistance factor design specification for structural steel buildings." Chicago.
- Augusti, G. (1966). "Full plastic torque of I-Beams." *Int. J. Mech. Sci.*, 8, 641-649.
- Al-Bermani, F. G. A., and Kitipornchai, S. (1990). "Elasto-plastic large deformation analysis of thin-walled structures" *Eng. Struct.*, 12(1), 28-36.
- Bathe, K. J., and Weiner, P. M. (1983). "On elastic-plastic analysis of I-beams in bending and torsion." *Comp. and Struct.*, 17(6), 711-718.
- Billinghurst, A., Williams, J. R. L., Chen, G., and Trahair, N. S. (1992). "Inelastic uniform torsion of steel members." *Comp. and Struct.*, 42(6), 887-894.
- Boulton, N. S. (1962). "Plastic twisting and bending of an I-beam in which the warp is restricted." *Int. J. Mech. Sci.*, 4, 491-502.
- Boresi, A. P., and Schmidt, R. J. (2003). *Advanced Mechanics of Materials*, 6th Ed., John Wiley and Sons, Inc., New York.
- British Standard Institution (2001): BS EN 10002-1:2001: 'Metallic materials-Tensile testing -Part 1: Method of test at ambient temperature', BSI, London, 2001.
- British Standard Institute (1999), BS EN 10056-1:1999: "Specification for structural steel equal and unequal angles, Dimensions.", BSI, London, 1999.
- Broude, B. M. (1953). *Predelnye sostoyania stalnykh balok*. (The limit states of steel girders.) Gosstroyizdat, Moscow/Leningrad.
- Canadian Standards Association (CSA). (2001). "Limit states design of steel structures." *CAN/CSA-S16.1*, Rexdale, Ont., Canada.
- Chen, W. F., and Atsuta, T. (1977). *Theory of beam-columns, vol, 2, space behavior and design*. McGraw-Hill Book Co., New York, N.Y., 195-269.
- Chen, G., and Trahair, N.S. (1992). "Inelastic Nonuniform Torsion of Steel I-Beams." *J. Constr. Steel Res.*, 23, 189-207.
- Daddazio, R. P., Bieniek, M. P., and DiMaggio, F. L. (1983). "Yield Surface for thin bars with warping restraint." *J. Engrg. Mech.*, ASCE, 109(2), 450-465.
- Dinno, K.S., and Merchant, W. (1965). "A procedure for calculating the plastic collapse of I-sections under bending and torsion." *The Struct. Engr.*, 43(7), 219-221.

- Dinno, K. S., and Gill, S. S. (1964). "The plastic torsion of I-sections with warping restraint." *Int. J. Mech. Sci.*, 6, 27-43.
- Dowling, P.J., Knowles, P., and Owens, G.W. (1988). *Structural Steel Design*, The Steel Construction Institute, Butterworths, London.
- Drucker, D. C. (1956). "The effect of shear on the plastic bending of Beams.", *J. Appl. Mech.*, ASME, 78(23).
- Duan, L., and Chen, W. F. (1990). "A yield surface equation for doubly symmetrical sections" *Eng Struct.* 12, April, 114-119.
- Englekirk, R. (1994). *Steel Structures, controlling behavior through design*, John Wiley & Sons, Inc., New York.
- Farwell, C. R., and Galambos, T. V. (1969). "Nonuniform torsion of steel beams in inelastic range." *J. Struct. Div.*, ASCE, 95(12), 2813-2829.
- Gaydon, F., and Nuttall, H. (1957). "On the combined bending and twisting of beams of various sections." *J. Mech. Phys. Solids*, 6, 17-21.
- Gjelsvik, A. (1981). *The theory of thin walled bars*. John Wiley & Sons, Inc., New York, N.Y.
- Goggins, J. (2004). *Earthquake resistant hollow and filled steel braces*, P.hD Thesis, Dept. of Civil, Structural and Environmental Engineering, Trinity College, Dublin.
- Goodier, N. J. (1941). "The buckling of compressed bars by torsion and flexure." *Bulletin No 27*, Cornell University Engineering Experiment Station.
- Harung, H.S., and Millar, M.A. (1973). "General failure analysis of skeletal plane frames." *J of Struct Div.*, ASCE, 99(6), 1051-1076.
- Heyman, J., and Dutton, V.L. (1954). Plastic design of plate girders with unstiffed Webs. *Weld and Metal Fabric* 22. p265.
- Hill, R., and Siebel, M.P.L. (1951). "On combined bending and twisting of thin tubes in the plastic range." *Philosophical Magazine*, LXXIII(42), 722-733.
- Hill, R., and Siebel, M.P.L. (1953). "On the plastic distortion of solid bars by combined bending and twisting." *J. Mech. and Physics Solids*, 1, 207-214.
- Hodge, P. G. (1959). *Plastic Analysis of Structures*. McGraw-Hill Book Comp., NewYork.

Hu, Y., Jin, X., and Chen, B. (1996). "A finite element model for static and dynamic analysis of thin-walled beams with asymmetric cross-sections." *Comp. and Struc.*, 61(5), 897-908.

Jirasek, M., and Bazant, Z. P. (2002). *Inelastic analysis of structures*, John Wiley & Sons, LTD., West Sussex, England.

Johnson, W., and Mellor, P. B. (1973). *Engineering Plasticity* Van Nostrand Reinhold Company, London.

Juhas, P. (1975) *Plasticka unosnost ocelovych nosnikov namahanychohybom a smykom.* (Plastic Load bearing capacity of Steel Beams subjected to bending and shear) *Staveb. Cas.* 23, 10, 761-781.

Kitipornchai, S., Zhu, K., Xiang, Y., and Al-Bermani, F. G. A. (1991). "Single-equation yield surfaces for monosymmetric and asymmetric sections" *Eng Struct.*, 13, Dec, 366-370.

Kolbrunner, C. F., Hajdin, N., and Coric, B. (1978). "Elastic-plastic thin walled I-section beam subjected to bending and warping torsion, Comparison between theoretical and experimental results." *Report of Institute for Engineering Research*, 43, 12.

Kolbrunner, C. F., Hajdin, N., and Obradovic, P. (1979). "Elastic-plastic beam of I-section subjected to bending and warping torsion, Comparison between theoretical and experimental results." *Report of Institute for Engineering Research*, 46, 5.

Korn, A., and Galambos, T.V. (1968). "Behavior of elastic-plastic frames." *J of Struct Div.*, ASCE, 94(5), 1119-1142.

LUSAS Manual, 2001, LUSAS Cooperation.

Meazure help menu, About Meazure, C Thing Software, 2001-2004.

McGuire, W., Gallagher, R.H., and Ziemian, R. D. (2000). *Matrix structural analysis*, 2nd Ed., John Wiley and Sons, Inc., New York.

Mohareb, M., Kulak, G. L., Elwi, A., and Murray, D. W. (2001). "Testing and analysis of steel pipe segments." *J. Transp. Eng.*, 127(5), 408-417.

Mohareb, M. (2002). "Plastic interaction relations for pipe sections.", *J. Engrg. Mech.*, ASCE, 128(1), 112-120.

Mohareb, M. (2003). "Plastic resistance of pipe sections: Upper bound solution.", *J. Struct. Eng.*, 129(1), 41-48.

- Mohareb, M., and Ozkan, I. F. (2004). "Plastic interaction relationships for Square Hollow Structural sections: Lower bound solution.", *J. Struct. Eng.*, ASCE, 130(9), 1381-1391.
- Morris, G. A., and Fenves, S. J. (1969). "Approximate yield surface equations." *J. Engrg. Mech. Div.*, ASCE, 95(4), 937-954.
- Mrazik, A., Skaloud, M., and Tochacek, M. (1987). *Plastic Design of Steel Structures*. Ellis Horwood Limited., West Sussex, PO191EB, England., 90-195.
- Nadai, A. (1950). *Theory of flow and fracture of solids*, Vol.1. McGraw-Hill, New York.
- Nethercot, D. A., and Trahair, N. S. (1976). "Inelastic lateral buckling of determinate beams." *J. Struct. Div.*, ASCE, 102(4), 701-717.
- Orbison, J. G., William, M., and Abel, J. F. (1982). "Yield surface applications in nonlinear steel frame analysis", *Comp Meth in Appl Mech and Eng.*, 33(1982) 557-573.
- Ozkan, I. F., and Mohareb, M. (2003). "Testing of steel pipes under bending, twist and shear." *J. Struct. Eng.*, 129(10), 1350-1357.
- Paltchevskiy, S. A. (1948)., "Opredelenye nesushchey sposobnosti stalnykh sterzhnei dlya nekotorykh sluchaev slozhnogo napryazhenogo sostoyaniya. (Determination of Load Carrying capacity of Steel Bars for some cases of complex state of stress.) In: *Kievskii inzhenerno-stroitelnyi institute, Sbornik trudov VIII. Gos. Izd. Techn. Lit. Ukrainy, Kiev-Lvov*, pp. 225-244.
- Pi, L. P., and Trahair, N. S. (1994a). "Nonlinear inelastic analysis of steel beam-columns, 1: Theory." *J. Struct. Eng.*, 120(7), 2041-2061.
- Pi, L. P., and Trahair, N. S. (1994b). "Nonlinear inelastic analysis of steel beam-columns, 11: Applications." *J. Struct. Eng.*, 120(7), 2062-2085.
- Pi, L. P., and Trahair, N. S. (1994c). "Inelastic bending and torsion of steel I-beams." *J. Struct. Eng.*, 120(12), 3397-3417.
- Pi, L. P., and Trahair, N. S. (1995a). "Inelastic torsion of steel I-beams." *J. Struct. Eng.*, 121(4), 609-620.
- Pi, L. P., and Trahair, N. S. (1995b). "Plastic-collapse analysis of torsion." *J. Struct. Eng.*, 121(10), 1389-1395.
- Prager, W. (1959). *An introduction to Plasticity*, Addison-Wesley, Reading, Mass.
- Prandtl, L. (1903). "Zur Torsion von prismaatischen Staben." *Physik Ziet.*, 4: 758-770.

R. Pratap, "Getting Started With MATLAB, A quick introduction for Scientists and Engineers", Version-6, Oxford University Press, 2002.

Rzhanitzyn, A. R. (1954). Raschet sooruzhenii s utchetom plasticheskikh svoystv materialov. (Analysis of Structures with consideration of the plastic properties of the Materials) Gos. Izd. Lit. po stroit. I arch., Moscow.

Santhadaporn, S., and Chen, W.F. (1970). "Interaction Curves for Sections under Combined Biaxial Bending and Axial Force." *Bulletin No 148*, Welding Research Council.

Smirak, S. (1967). Kotazce mezni plasticke unosnosti prurezu v ohybu prisoucasnem pusobeni smyku a tahu ci tlaku. (Limit Plastic Load-Bearing Capacity of a cross section Subjected to Bending with the simultaneous effect of Shear and Tension or Compression) In: *Sbornik VUT*, Brno, No. 3-4, 463-475.

Snitko, N. K. (1952). *Ustoychivost sterzhnevyykh system*. (Stability of Frame works) Gosstroyizdat, Moscow.

Sobotka, Z. (1959). Ramove konstrukce za plastickeho stavu. In: *Nove prispievky k teorii stavebných konstrukcií* (Frame Structure in the Elastoplastic state.), SAV, Bratislava, pp. 109-143.

Sobotka, Z. (1975). Plasticity of steel beams under combined bending shear and normal load. *Staveb. Cas.* 23, , No 9, 678-690.

Strelbitzkaya, A. I. (1958). Issledovanie prochnosti tenkostennykh sterzhney za predelom uprugosti. (Investigation of the strength of thin-Walled bars beyond the limit of Elasticity) Izd AN. USSR, Kiev.

Strelbitzkaya, A. I. (1964). Predelnoe sostoyanye ram iz tenkostennykh sterzhney pri izghibe s krucheniem. (Limit State of Frames with thin-Walled bars subjected to bending and Torsion.) Naukova Dumka. Kiev.

Timoshenko, S.P, and Gere, J.M. (1961). *Theory of elastic stability*, 2nd Ed., McGraw-Hill, NewYork.

Timoshenko, S., and Goodier, J. (1987). *Theory of elasticity*, 3rd Ed., McGraw-Hill, New York.

Trahair, N. S. (1983). "Inelastic lateral buckling of beams." Chapter 2 in *Beams and Beam-Columns. Stability and Strength*, (ed. R. Narayanan), Applied Science Publishers, London, 35-39.

Trahair, N. S. (1993). *Flexural-Torsional Buckling of Structures*. 1st Ed., E & FN Spon, Chapman & Hall, London.

Trahair, N. S., and Bradford, M. A. (1988). *The behaviour and design of steel structures*, Revised 2nd Ed., Chapman & Hall, London.

Vlasov, V. Z. (1959). *Thin walled elastic beams*, 2nd Ed., Moscow, USSR, Israel Program for Sci. Translation, Jerusalem, Israel, 1961.

Windows Media player help menu, About Windows Media player, Microsoft Corporation, 1994-2004.

Wen, R.K., and Farhoomand, F. (1970). "Dynamic analysis of inelastic frame works", *J. Engrg. Mech. Div.*, ASCE, 96(5), 667-686.

Yang, Y. B., and Fan, H. T. (1988). "Yield Surface Modelling of I-sections with nonuniform torsion.", *J. Engrg. Mech.*, ASCE, 114(6), 953-972.

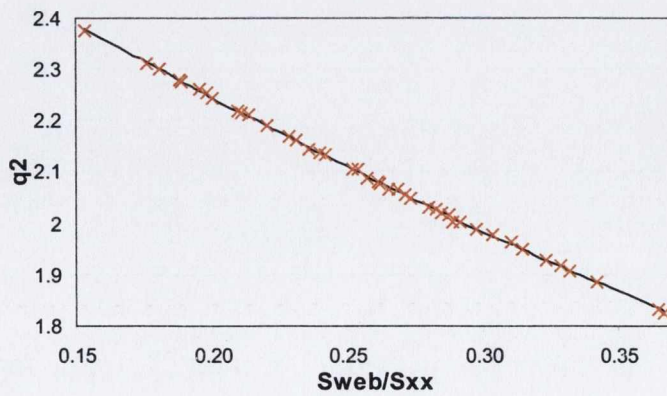
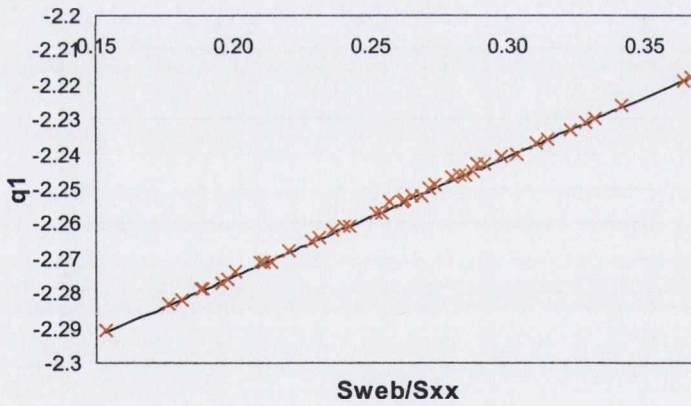
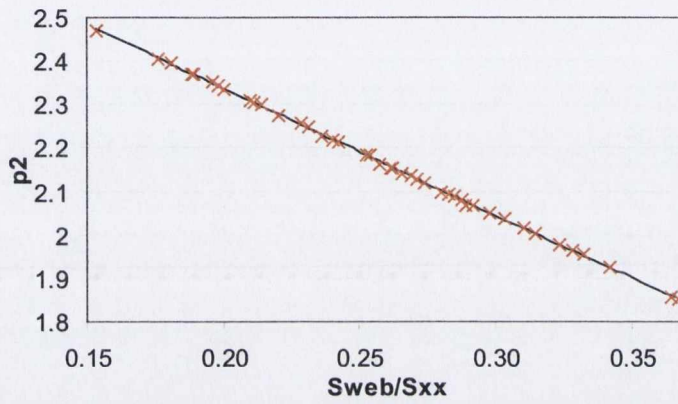
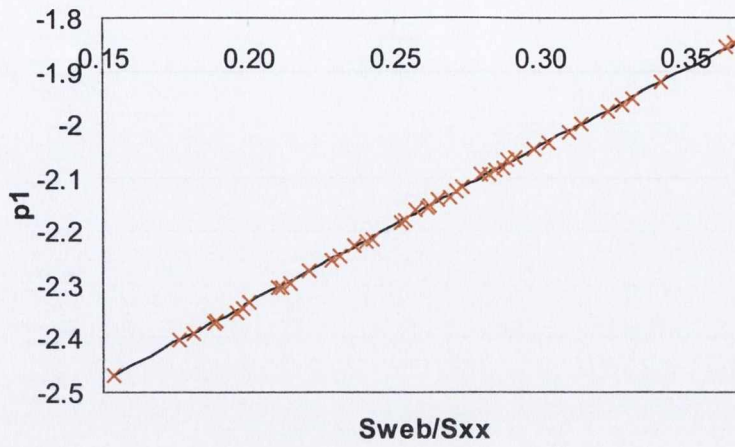
Yang, Y.B., Chern, S.M., Fan, H.T. (1989)., "Yield Surfaces for I-sections with Bi-moments", *J. Struct. Eng.*, 115(12), 3041-3058.

APPENDIX-A

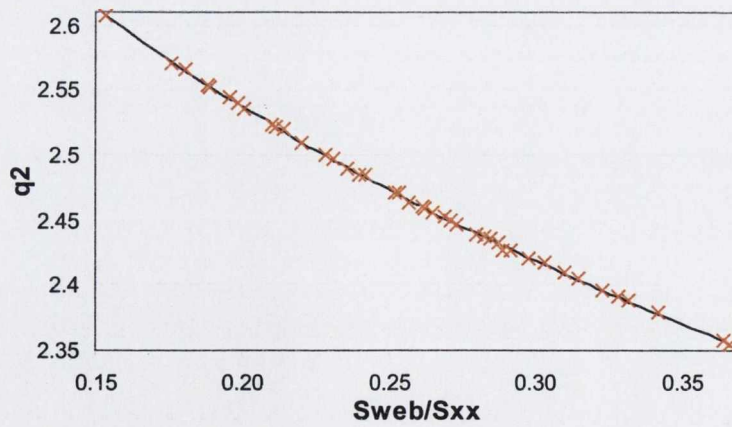
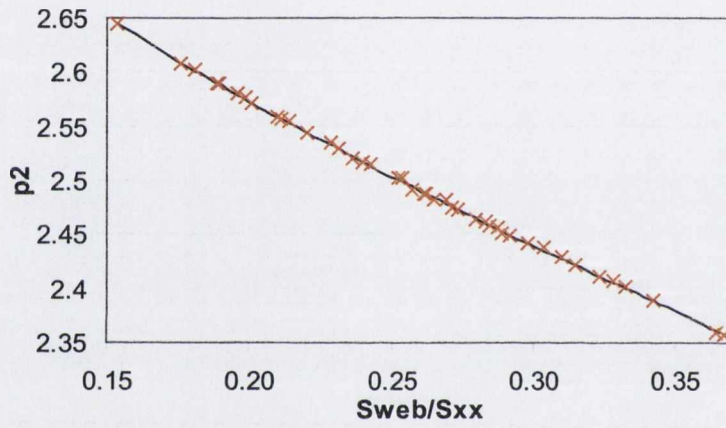
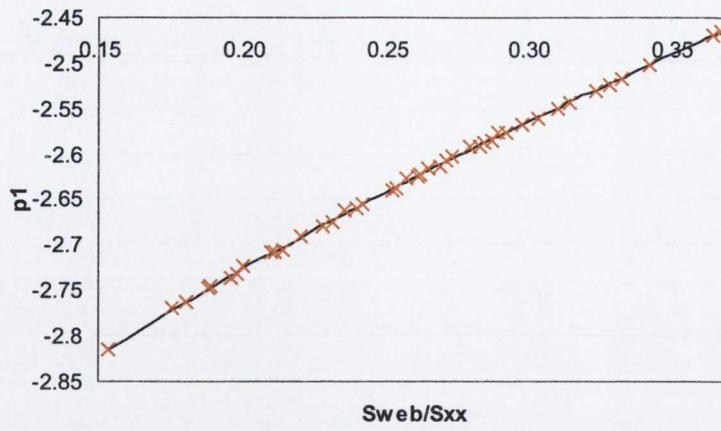
S.No	Universal Beam	S_{web} / S_{xx}	A_w / A_f	I_{zz} / I_{xx}
1	305 x 102 x 25	0.3669	2.3936	35.5750
2	1016 x 305 x 222	0.3644	2.3717	41.2637
3	914 x 305 x 201	0.3418	2.1511	34.0183
4	762 x 267 x 134	0.3400	2.1258	30.9394
5	838 x 292 x 176	0.3321	2.0599	31.0894
6	406 x 140 x 39	0.3282	2.0216	29.8335
7	762 x 267 x 147	0.3261	2.0089	30.4300
8	254 x 102 x 22	0.3253	2.0015	23.3161
9	1016 x 305 x 249	0.3232	2.0037	39.7556
10	457 x 152 x 52	0.3231	1.9883	32.6090
11	305 x 102 x 28	0.3212	1.9872	34.0149
12	914 x 305 x 224	0.3146	1.9221	33.0925
13	356 x 127 x 33	0.3130	1.8970	28.6731
14	838 x 292 x 194	0.3101	1.8796	30.4085
15	686 x 254 x 125	0.3101	1.8684	26.5228
16	610 x 229 x 101	0.3033	1.8129	25.6741
17	762 x 267 x 173	0.3023	1.8210	29.6260
18	533 x 210 x 82	0.2987	1.7732	23.3120
19	914 x 305 x 253	0.2977	1.7938	32.4774
20	305 x 102 x 33	0.2952	1.7874	33.1072
21	457 x 152 x 60	0.2925	1.7462	31.6770
22	914 x 305 x 289	0.2917	1.7578	32.0821
23	254 x 102 x 25	0.2893	1.7188	22.5806
24	1016 x 305 x 393	0.2890	1.7742	38.8886
25	457 x 152 x 67	0.2874	1.7165	31.3642
26	686 x 254 x 140	0.2874	1.6945	25.9616
27	1016 x 305 x 272	0.2849	1.6981	38.5529
28	762 x 267 x 197	0.2846	1.6926	29.0842
29	1016 x 305 x 314	0.2838	1.7057	38.8763
30	1016 x 305 x 437	0.2837	1.7474	38.4207
31	406 x 140 x 46	0.2831	1.6635	28.6339
32	838 x 292 x 226	0.2828	1.6740	29.6149
33	1016 x 305 x 487	0.2826	1.7545	37.9725
34	356 x 127 x 39	0.2825	1.6654	27.8418
35	610 x 229 x 113	0.2811	1.6459	25.1587
36	1016 x 305 x 349	0.2798	1.6871	38.5009
37	686 x 254 x 152	0.2785	1.6328	25.7101
38	533 x 210 x 92	0.2735	1.5866	22.8096
39	457 x 152 x 74	0.2735	1.6195	30.9463
40	686 x 254 x 170	0.2713	1.5879	25.4562
41	406 x 178 x 54	0.2690	1.5393	18.0561
42	610 x 229 x 125	0.2686	1.5600	24.8528
43	457 x 152 x 82	0.2682	1.5912	30.6721
44	305 x 127 x 37	0.2682	1.5605	21.0035
45	457 x 191 x 67	0.2681	1.5381	19.9926
46	305 x 127 x 42	0.2652	1.5489	20.8199
47	533 x 210 x 101	0.2639	1.5225	22.5887

48	254 x 102 x 28	0.2624	1.5275	22.1183
49	610 x 229 x 140	0.2621	1.5218	24.6290
50	533 x 210 x 109	0.2615	1.5112	22.4763
51	305 x 127 x 48	0.2570	1.5032	20.5709
52	356 x 171 x 45	0.2538	1.4231	14.6043
53	533 x 210 x 122	0.2530	1.4606	22.2607
54	457 x 191 x 74	0.2523	1.4311	19.7346
55	457 x 191 x 82	0.2502	1.4238	19.6323
56	406 x 178 x 60	0.2422	1.3551	17.7169
57	457 x 191 x 89	0.2411	1.3676	19.4821
58	406 x 178 x 67	0.2400	1.3485	17.6275
59	457 x 191 x 98	0.2359	1.3407	19.3610
60	406 x 178 x 74	0.2321	1.3026	17.5025
61	356 x 171 x 51	0.2314	1.2765	14.3736
62	914 x 419 x 343	0.2283	1.2647	15.7846
63	356 x 171 x 57	0.2242	1.2367	14.2802
64	914 x 419 x 388	0.2203	1.2211	15.6740
65	610 x 305 x 149	0.2139	1.1571	13.3378
66	2x4 x 146 x 31	0.2124	1.1432	9.7259
67	610 x 305 x 179	0.2111	1.1517	13.2685
68	356 x 171 x 67	0.2096	1.1552	14.1396
69	610 x 305 x 238	0.2035	1.1272	13.1370
70	203 x 102 x 23	0.2004	1.0974	12.6233
71	203 x 133 x 25	0.1981	1.0523	7.4802
72	305 x 165 x 40	0.1958	1.0389	10.9607
73	305 x 165 x 54	0.1891	1.0178	10.8931
74	305 x 165 x 46	0.1888	1.0047	10.9152
75	178 x 102 x 19	0.1882	1.0099	9.7079
76	203 x 133 x 30	0.1818	0.9659	7.4288
77	254 x 146 x 37	0.1809	0.9609	9.5973
78	254 x 146 x 43	0.1761	0.9437	9.5754
79	152 x 89 x 16	0.1760	0.9448	9.0680
80	127 x 76 x 13	0.1534	0.8241	8.2523

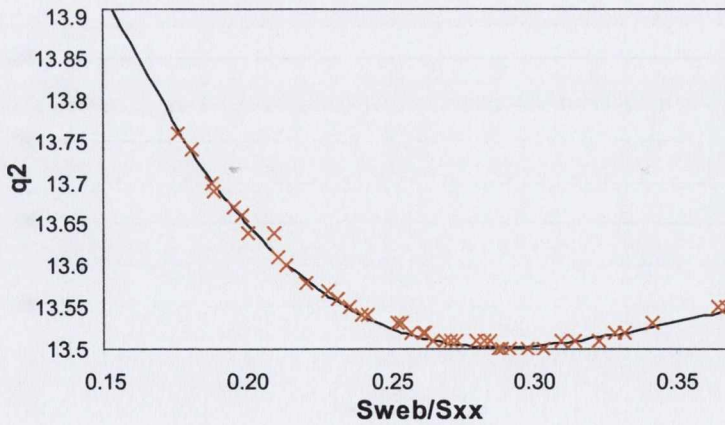
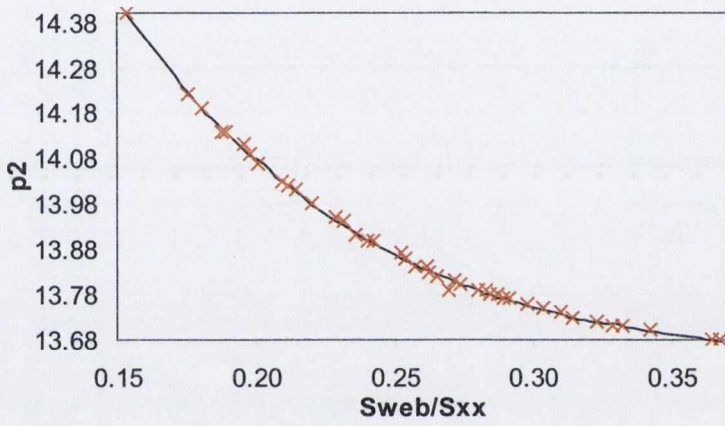
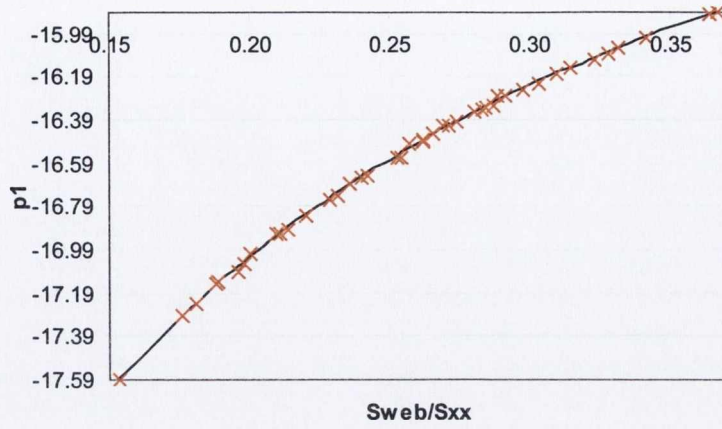
Table A.1 Ratios of different section properties of Universal Beam sections.



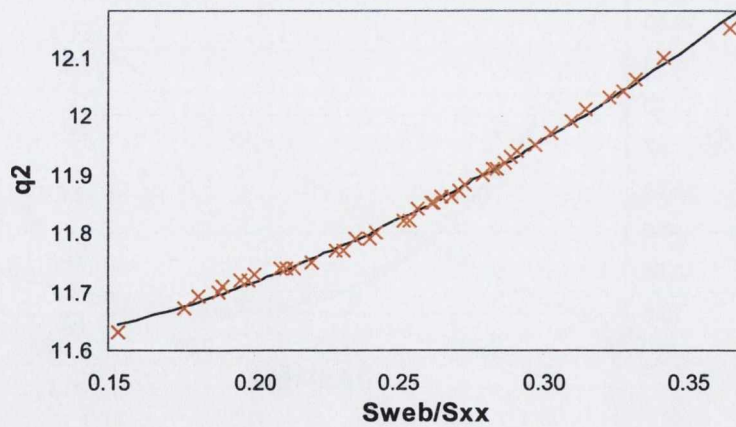
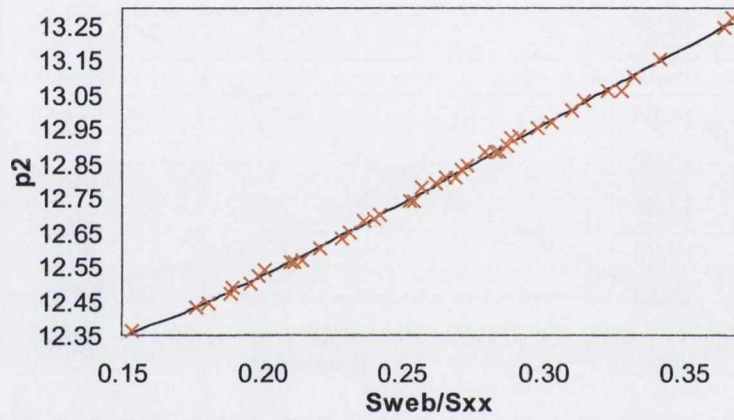
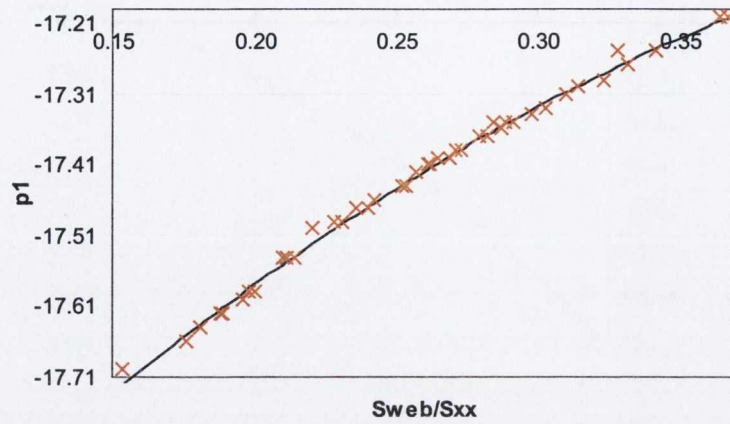
A.1 (a) Graph of Parameters p_1, p_2, q_1 and q_2 vs ratio (S_{web}/S_{xx}) for $b=0.0$



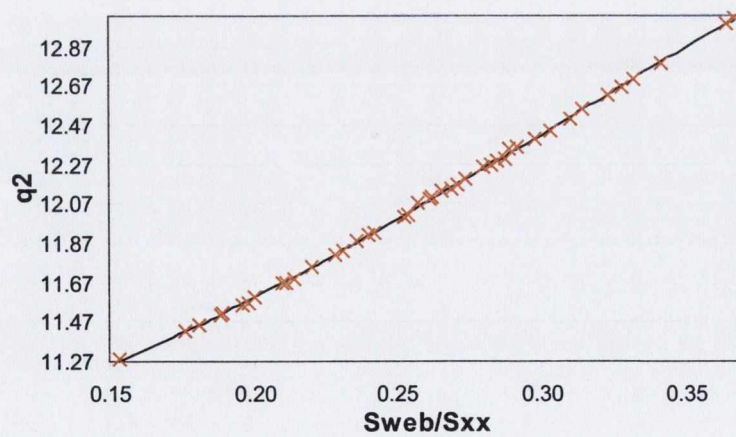
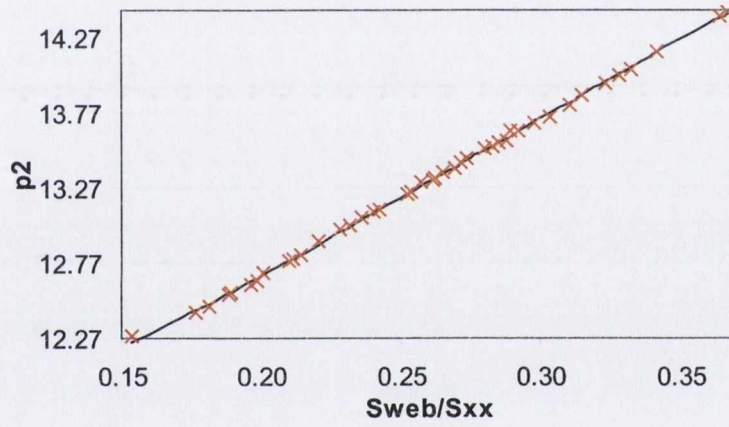
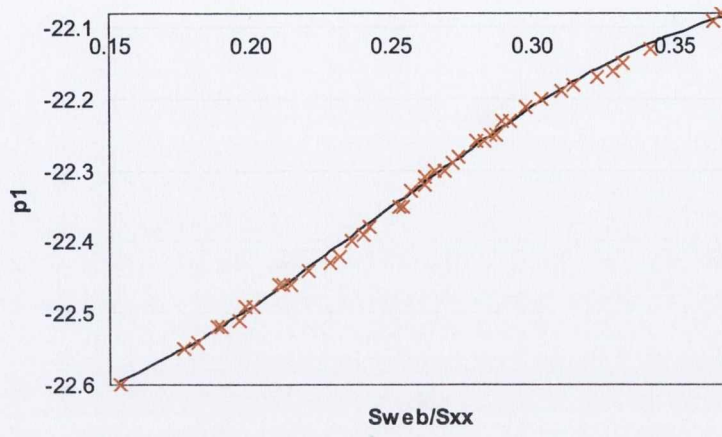
A.1(b) Graph of Parameters p_1, p_2 and q_2 vs ratio (S_{web}/S_{xx}) for $b=0.2$



A.1(c) Graph of Parameters p_1, p_2 and q_2 vs ratio (S_{web}/S_{xx}) for $b=0.4$



A.1(d) Graph of Parameters p_1, p_2 and q_2 vs ratio (S_{web}/S_{xx}) for $b=0.6$



A.1(e) Graph of Parameters p_1, p_2 and q_2 vs ratio (S_{web}/S_{xx}) for $b=0.8$

Figure A-1 Graphs of parameters p_1, p_2, q_1 and q_2 vs ratio (S_{web}/S_{xx}) for bimoment values of 0.0, 0.2, 0.4, 0.6 and 0.8

APPENDIX-B

B.1 TABLE SHOWING THE RATIO OF SHEAR STRESSES FOR THE WEB AND FLANGES

Universal Beam	Shear Applied in X-direction, S _x	Shear Applied in Y-direction, S _y
	S _x	S _y
	ratio between stress in web to flange	ratio between stress in flange to web
1016 x 305 x 487	10.28	5.70
1016 x 305 x 437	11.35	6.23
1016 x 305 x 393	12.42	6.90
1016 x 305 x 349	14.31	7.55
1016 x 305 x 314	15.71	8.36
1016 x 305 x 272	18.18	9.68
1016 x 305 x 249	18.18	11.54
1016 x 305 x 222	18.75	14.22
914 x 419 x 388	19.65	11.49
914 x 419 x 343	21.57	13.08
914 x 305 x 289	15.78	9.62
914 x 305 x 253	17.66	10.95
914 x 305 x 224	19.13	12.72
914 x 305 x 201	20.09	15.01
838 x 292 x 226	18.25	10.96
838 x 292 x 194	19.89	13.47
838 x 292 x 176	20.84	15.52
762 x 267 x 197	17.18	10.55
762 x 267 x 173	18.65	12.35
762 x 267 x 147	20.72	15.15
762 x 267 x 134	22.03	17.06
686 x 254 x 170	17.64	10.79
686 x 254 x 152	19.28	12.12
686 x 254 x 140	20.46	13.35
686 x 254 x 125	21.62	15.62
610 x 305 x 238	16.92	9.92
610 x 305 x 179	21.78	13.01
610 x 305 x 149	25.83	15.47
610 x 229 x 140	17.57	10.42
610 x 229 x 125	19.24	11.68
610 x 229 x 113	20.56	13.19
610 x 229 x 101	21.68	15.38

533 x 210 x 122	16.69	9.95
533 x 210 x 109	18.17	11.21
533 x 210 x 101	19.44	12.07
533 x 210 x 92	20.72	13.42
533 x 210 x 82	21.75	15.82
457 x 191 x 98	16.91	9.84
457 x 191 x 89	18.28	10.84
457 x 191 x 82	19.32	11.96
457 x 191 x 74	21.16	13.13
457 x 191 x 67	22.34	14.95
457 x 152 x 82	14.79	8.22
457 x 152 x 74	16.08	9.08
457 x 152 x 67	17.09	10.25
457 x 152 x 60	18.88	11.50
457 x 152 x 52	20.05	13.98
406 x 178 x 74	18.89	11.22
406 x 178 x 67	20.32	12.50
406 x 178 x 60	22.52	13.90
406 x 178 x 54	23.08	16.30
406 x 140 x 46	20.91	12.70
406 x 140 x 39	22.16	16.49
356 x 171 x 67	19.03	11.03
356 x 171 x 57	21.26	13.25
356 x 171 x 51	23.18	14.91
356 x 171 x 45	24.44	17.64
356 x 127 x 39	19.09	11.78
356 x 127 x 33	20.90	14.75
305 x 165 x 54	21.13	12.18
305 x 165 x 46	24.73	14.04
305 x 165 x 40	27.50	16.18
305 x 127 x 48	13.92	8.95
305 x 127 x 42	15.54	10.27
305 x 127 x 37	17.38	11.53
305 x 102 x 33	15.52	9.48
305 x 102 x 28	16.97	11.57
305 x 102 x 25	17.52	14.51
254 x 146 x 43	20.46	11.60
254 x 146 x 37	23.24	13.43
254 x 146 x 31	24.35	16.99
254 x 102 x 28	16.22	10.22
254 x 102 x 25	16.98	12.13
254 x 102 x 22	17.82	14.94
203 x 133 x 30	20.92	13.95
203 x 133 x 25	23.37	17.08
203 x 102 x 23	18.85	10.95
178 x 102 x 19	21.08	12.81

152 x 89 x 16	19.71	11.52
127 x 76 x 13	19.00	10.00
Universal Column		
356 x 406 x 634	8.91	5.51
356 x 406 x 551	9.94	6.20
356 x 406 x 467	11.51	7.11
356 x 406 x 393	13.30	8.27
356 x 406 x 340	15.15	9.39
356 x 406 x 287	17.65	10.93
356 x 406 x 235	21.46	13.07
356 x 368 x 202	22.71	13.88
356 x 368 x 177	25.88	15.66
356 x 368 x 153	30.12	17.90
356 x 368 x 129	35.44	21.06
305 x 305 x 283	12.02	7.31
305 x 305 x 240	13.84	8.45
305 x 305 x 198	16.47	10.02
305 x 305 x 158	19.70	12.45
305 x 305 x 137	22.41	14.25
305 x 305 x 118	25.62	16.44
305 x 305 x 97	30.84	19.82
254 x 254 x 167	13.81	8.37
254 x 254 x 132	17.08	10.33
254 x 254 x 107	20.22	12.62
254 x 254 x 89	24.88	14.82
254 x 254 x 73	29.60	17.93
203 x 203 x 86	16.46	10.20
203 x 203 x 71	20.64	11.93
203 x 203 x 60	21.89	14.49
203 x 203 x 52	25.86	16.34
203 x 203 x 46	28.28	18.51
152 x 152 x 37	19.30	13.43
152 x 152 x 30	23.52	16.27
152 x 152 x 23	26.24	22.38
Universal Piles		
356 x 368 x 174	18.65	18.55
356 x 368 x 152	21.12	21.01
356 x 368 x 133	23.96	23.81
356 x 368 x 109	28.98	28.76
305 x 305 x 223	10.75	10.71
305 x 305 x 186	12.58	12.54
305 x 305 x 149	15.34	15.27
305 x 305 x 126	17.88	17.78
305 x 305 x 110	20.31	20.18
305 x 305 x 95	23.21	23.21
305 x 305 x 88	24.82	25.02

305 x 305 x 79	27.85	27.60
254 x 254 x 85	18.08	18.21
254 x 254 x 71	21.50	21.50
254 x 254 x 63	24.21	23.98
203 x 203 x 54	18.38	18.22
203 x 203 x 45	21.67	21.67

Table B.1 Ratio of shear stresses for the web and flanges when shear forces S_x and S_y are applied

B.2 DISTRIBUTION OF SHEAR STRESSES DUE TO S_x , S_y AND

T_U

Biaxial shear stress distribution on the cross section due to the neutral-axis pattern given by Figure 4.7 is obtained as

Considering the stress distribution in one flange as S_x acts in the flange only it can be written as

$$S_x = \left(\frac{t_f}{2} + \zeta_f \right) \tau b_f - \left(\frac{t_f}{2} - \zeta_f \right) \tau b_f$$

Therefore results in

$$S_x = 2\zeta_f \tau b_f$$

Therefore as the pattern is same for both the flanges therefore the following equation is obtained

$$S_x = 4\zeta_f \tau b_f \quad \text{B-1}$$

Considering the stress distribution in web as S_y acts in the web only

$$S_y = \left(\frac{t_w}{2} + \zeta_w \right) \tau b_w - \left(\frac{t_w}{2} - \zeta_w \right) \tau b_w$$

$$S_y = 2\zeta_w \tau b_w \quad \text{B-2}$$

Calculation to obtain uniform torsion on the cross section (Figure 4.7)

Distribution of uniform torsion on the section can be obtained for the top flange, bottom flange and web separately as

For the top flange

$$\begin{aligned}
 T_{topflange} &= \left[(0.5A_f + b_f \zeta_f) (0.5b_w + 0.75t_f - 0.5\zeta_f) \right] \tau - \left[(0.5A_f - b_f \zeta_f) (0.5b_w + \right. \\
 & \left. 0.25t_f - 0.5\zeta_f - 0.5\zeta_f) \right] \tau \\
 &= \left[(0.25A_f b_w + 0.375A_f t_f - 0.25A_f \zeta_f + 0.5b_f b_w \zeta_f + 0.75A_f \zeta_f - 0.5\zeta_f^2 b_f) \right] \tau \\
 & - \left[(0.25A_f b_w + 0.125A_f t_f - 0.25A_f \zeta_f - 0.5b_f b_w \zeta_f - 0.25A_f \zeta_f + 0.5\zeta_f^2 b_f) \right] \tau \\
 T_{topflange} &= (0.25A_f t_f + b_f b_w \zeta_f + A_f \zeta_f - \zeta_f^2 b_f) \tau \quad \text{B-3(a)}
 \end{aligned}$$

For the bottom flange

$$\begin{aligned}
 T_{botflange} &= - \left[(0.5A_f + b_f \zeta_f) (0.5b_w + 0.25t_f + 0.5\zeta_f) \right] \tau + \left[(0.5A_f - b_f \zeta_f) (0.5b_w + \right. \\
 & \left. 0.75t_f + 0.5\zeta_f) \right] \tau \\
 &= - \left[(0.25A_f b_w + 0.25A_f \zeta_f + 0.125A_f t_f + 0.5b_f b_w \zeta_f + 0.25A_f + 0.5\zeta_f^2 b_f) \right] \tau \\
 & + \left[(0.25A_f b_w + 0.375A_f t_f + 0.25A_f \zeta_f - 0.5b_f b_w \zeta_f - 0.75A_f \zeta_f - 0.5\zeta_f^2 b_f) \right] \tau \\
 T_{botflange} &= (0.25A_f t_f - b_f b_w \zeta_f - A_f \zeta_f - \zeta_f^2 b_f) \tau \quad \text{B-3(b)}
 \end{aligned}$$

Similarly for the web

$$\begin{aligned}
 T_{web} &= \left[(0.5A_w + b_w \zeta_w) (0.25t_w - 0.5\zeta_w) \right] \tau + \left[(0.5A_w - b_w \zeta_w) (0.25t_w + 0.5\zeta_w) \right] \tau \\
 &= \left[(0.125A_w t_w - 0.25A_w \zeta_w + 0.25b_w t_w - 0.5\zeta_w^2 b_w) + (0.125A_w t_w + 0.25A_w \zeta_w - \right. \\
 & \left. 0.25b_w t_w - 0.5\zeta_w^2 b_w) \right] \tau \\
 T_{web} &= (0.25A_w t_w - \zeta_w^2 b_w) \tau \quad \text{B-3(c)}
 \end{aligned}$$

Adding the terms result in the torsion for the entire section as

$$T_u = T_{topflange} + T_{botflange} + T_{web}$$

$$T_u = (0.5A_f t_f - 2\zeta_f^2 b_f + 0.25A_w t_w - \zeta_w^2 b_w) \tau \quad \text{B-4}$$

Substituting the neutral-axis parameters ζ_f and ζ_w from Equation B-1 and B-2 into Equation B-4 gives

$$T_u - 0.5A_f t_f \tau - 0.25A_w t_w \tau = -\frac{S_x^2}{8\tau b_f} - \frac{S_y^2}{4\tau b_w}$$

$$T_u - 0.5A_f t_f \tau - 0.25A_w t_w \tau = \frac{-b_w S_x^2 - 2b_f S_y^2}{8\tau b_f b_w}$$

$$-8T_u b_f b_w \tau + 4A_f^2 b_w \tau^2 - 2A_w^2 b_f \tau^2 - b_w S_x^2 - 2b_f S_y^2 = 0$$

$$(4A_f^2 b_w + 2A_w^2 b_f) \tau^2 - 8T_u b_f b_w \tau - b_w S_x^2 - 2b_f S_y^2 = 0 \quad \text{B-5}$$

B.3 DEVELOPMENT OF DIFFERENT NEUTRAL-AXIS PATTERNS

B.3.1 Neutral-Axis Patterns intersecting the web

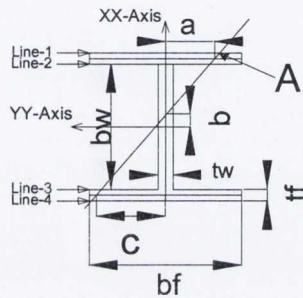
Warping strain applied in the negative direction

Neutral-axis passes through both flanges and web.

To determine the change in the pattern on addition of cases of Figure 4.11 to Figure 4.9(a), four lines are introduced as depicted in Figure B-1. Line-1 represents the outer edge of top flange, line-2 represents inner edge of the top flange, Line-3 represents the inner edge of bottom flange and Line-4 represents the outer edge of bottom flange. If values of the strain at the end of each line are known and there is a point in between each of them called A which represents the location of the neutral-axis, then the strain field, for example related to line-1, can be represented graphically as depicted in the left top figure (Figure B-2). Similarly strain fields due to line 2, 3 and 4 can be defined by similar figures.

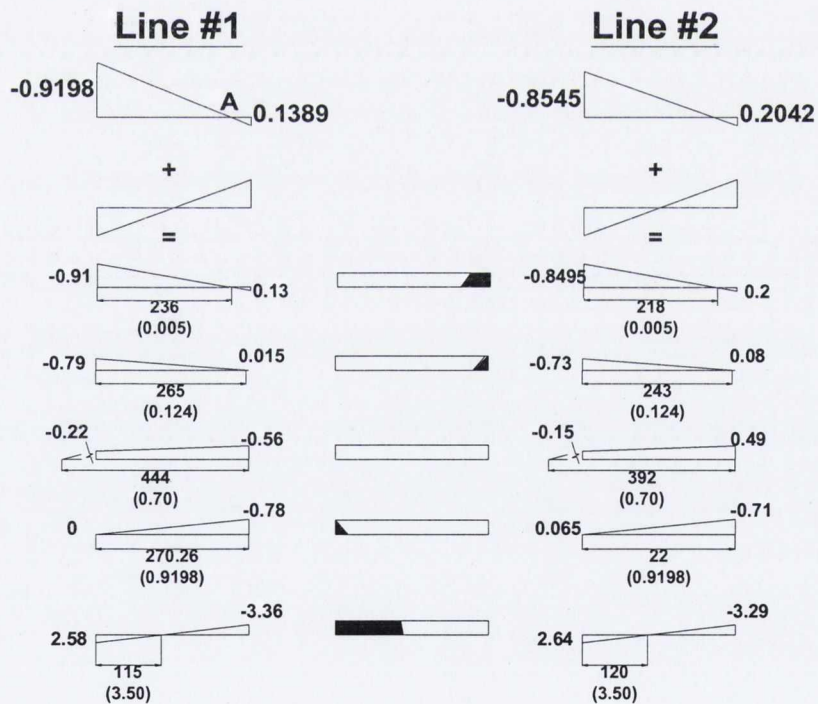
The resulting strains for line-1 is obtained by combining the strain field of line 1 to the warping strain field of the figure, shown in the left top two figures in Figure B-2. The resulting strain fields for different values of the warping strain are depicted in the figure. In the figure, values of the resulting strains at both the ends of each line are given. In addition new positions of the neutral-axis are also indicated in the figure.

Values of warping strain which are added to obtain the resulting strain fields are given in parenthesis. In a similar way the resulting strains for line-2 are given on the right hand side of the figure. In the middle figure, the resulting neutral-axis patterns are shown for the top flange with positive strain regions shown as black, in both the Appendix and the main text.



N.B $d = b_w + t_f$

Figure B-1 Lines representation of an I-section



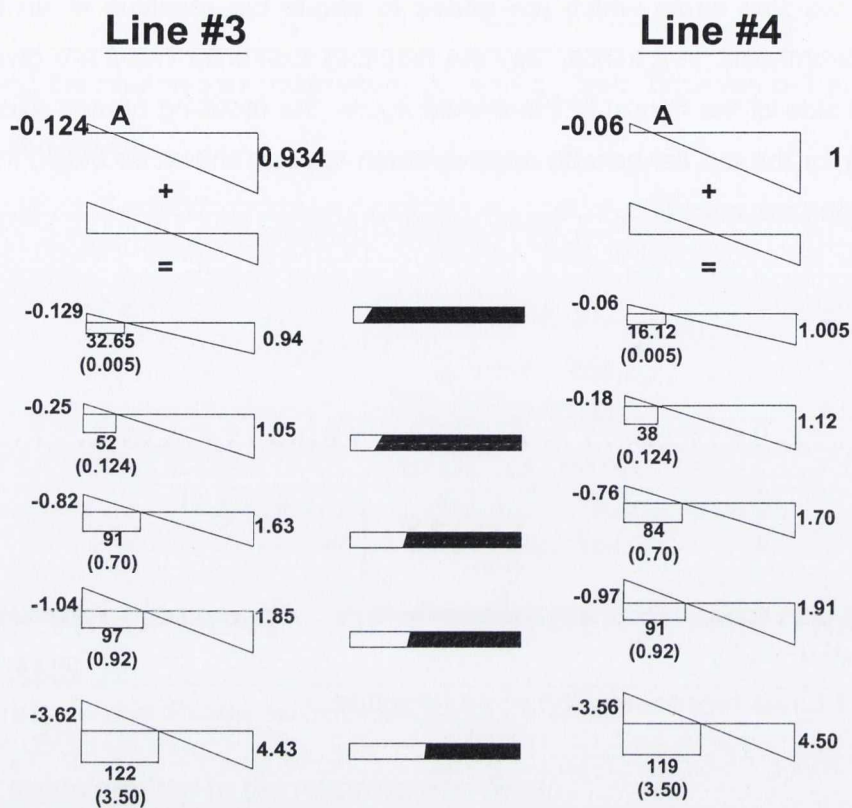


Figure B-2. Obtained strain patterns for Line No 1, 2, 3 and 4.

For the top flange, it can be deduced from the figure that for the first two diagrams, the axis move towards the right of the flange. Further addition of the value moves it out of the flange, as for the third case. Further increase of the warping strain will shift the neutral-axis to the left of the top flange which results in the last two cases. These are shown as numbers having number one for the first value and fifth for the last value in Figure 4.13.

Similarly such a figure for the bottom flange can be obtained, as depicted in Figure B-2. For the bottom flange the addition of the warping strains always causes the neutral-axis to move towards the right of the flange and never cross the centre line as can be inferred from the figure.

Hence it can be concluded that for the top flange, the neutral-axis will first shift towards the right of its initial position, and then it will move outside the flange and

then return to the left of its initial position, while movements of the axis for the bottom flange will always be on its left side. The two patterns, the transition phase and the parameters defining the position of the neutral-axis are shown in Figure 4.14. The relationships between those parameters are obtained as follows:

The neutral-axis patterns given by Figure 4.12 have one radius of curvature, therefore have one constant angle of curvature, hence the lines defined above in Figure B.1 must have the same slope for all of them. When the lines of the warping strain (Figure B-2), which has its own slope, is added to the bottom flange and subtracted from the top flange, it causes an increase of the slope for the neutral-axis in the bottom flange and a decrease of the slope for the neutral-axis in the top flange. Hence absolute values of the increase or decrease must be the same because the same amount of warping strains are added and subtracted from the bottom flange and top flange respectively. Therefore, the amount of the increase of α must be the same as the amount of decrease of γ , (which can be deduced from Figure B-2) as compare to their previous values. This relationship will be valid for all the obtained patterns and is written as

$$|\Delta\alpha| = |\Delta\gamma| \quad \text{B-6}$$

As the increase and decrease of α and γ are the same, therefore the following relationship can be written as

$$\alpha + \gamma = 2\beta \quad \text{B-7}$$

Although the change in the slope of the neutral-axis is the same for both top and bottom flanges for all the patterns obtained (Equation B-6), the obtained angles will be different for both the flanges. The reason is that the \tan^{-1} of the slopes will be different. For example the slope β before addition of the warping strain is -1. Following Equation B-6, assuming an increase of 0.5, resulted in $\alpha = -0.5$ and $\gamma = -1.5$, The \tan^{-1} for these values are respectively 153.5° and 123.70° when

measured relative to the positive YY-axis. Therefore a larger rotation for α exists as compared to γ .

Consider the extreme pattern of Figure 4.8(d) which is given in Figure 4.11, the maximum angle for which can be obtained as $\beta = 180^\circ - \tan^{-1}\left(\frac{b_w}{b_f}\right)$

From Figure B-2 it can be deduced that γ will always decrease and its angle will not decrease less than 90° . As γ is always decreasing therefore its maximum angle will always be less than the maximum angle of β . Therefore the following relationship for γ can be written

$$90^\circ \leq \gamma \leq 180^\circ - \tan^{-1}\left(\frac{b_w}{b_f}\right) \quad \text{B-8}$$

When the neutral-axis for the top flange is on the right of the flange, the angle α obtained will increase on addition of warping strain and the angle after the increase will be less than 180° , whereas, from the extreme pattern of Figure 4.8(d) given in Figure 4.11(case 2-2), the minimum angle which can be obtained for β is 90° . As α is obtained on addition of warping strain, therefore, it will always increase, and therefore 90° is also the minimum angle for α . Therefore the following relationship for α can be written:

$$90^\circ \leq \tan^{-1}(\alpha) \leq 180^\circ \quad \text{B-9}$$

From Figure B-2, it can be deduced that the neutral-axis has shifted to the left of the top flange (second pattern), but there are two differences as compared to its initial position; Firstly the strain at the left is positive, and secondly the angle at which the neutral-axis intersects the left side of the flange is less than 90° , but more than 0° . As the neutral-axis approaches towards the centre line there will always be an

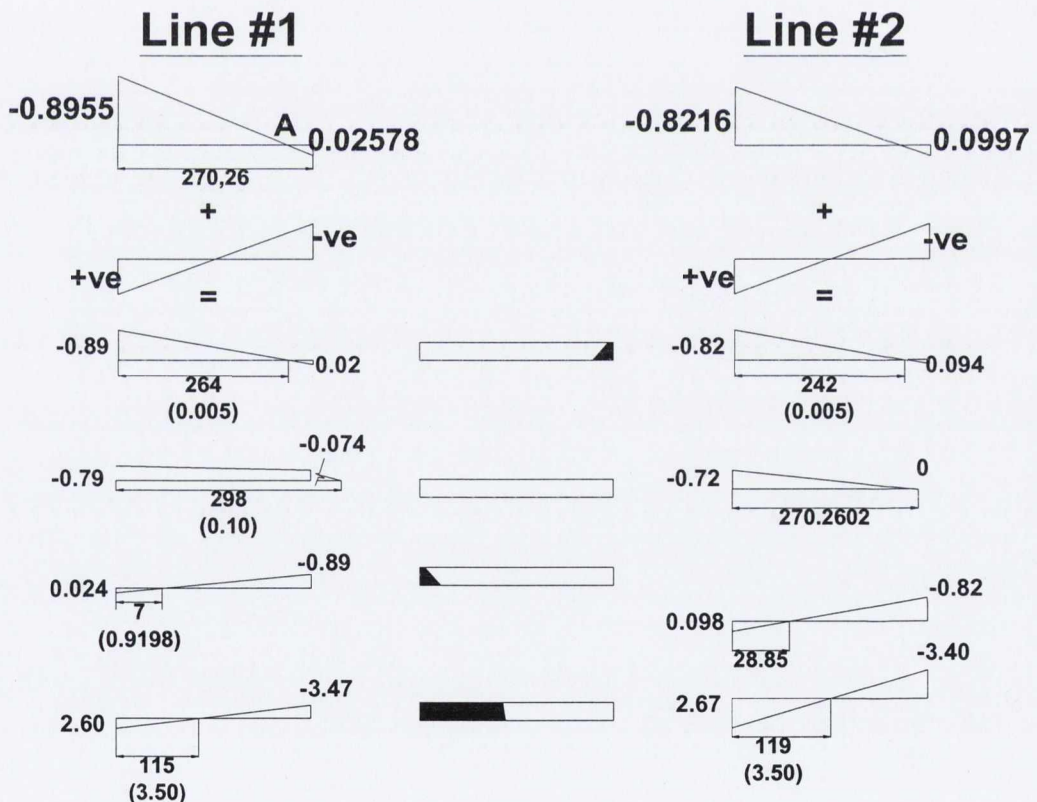
increase in the angle with a maximum angle always less than 90° . Therefore it can be written as

$$0^\circ \leq \tan^{-1}(\alpha) \leq 90^\circ$$

B-10

When Neutral-Axis passes through the top flange and web

Figure 4.10 shows two extreme cases (cases 7-7, and 8-8) of Figure 4.8(b). It is concluded in the previous section that the movement of the neutral-axis for both the top and bottom flanges are different, which is also valid for this case. For example the movement of the neutral-axis for case 7-7 is given in Figure B-3. From the figure, it can be deduced that the movement of the neutral-axis results in the second pattern and a transition phase as obtained in the previous case. The relationships obtained previously are also valid for these types of patterns.



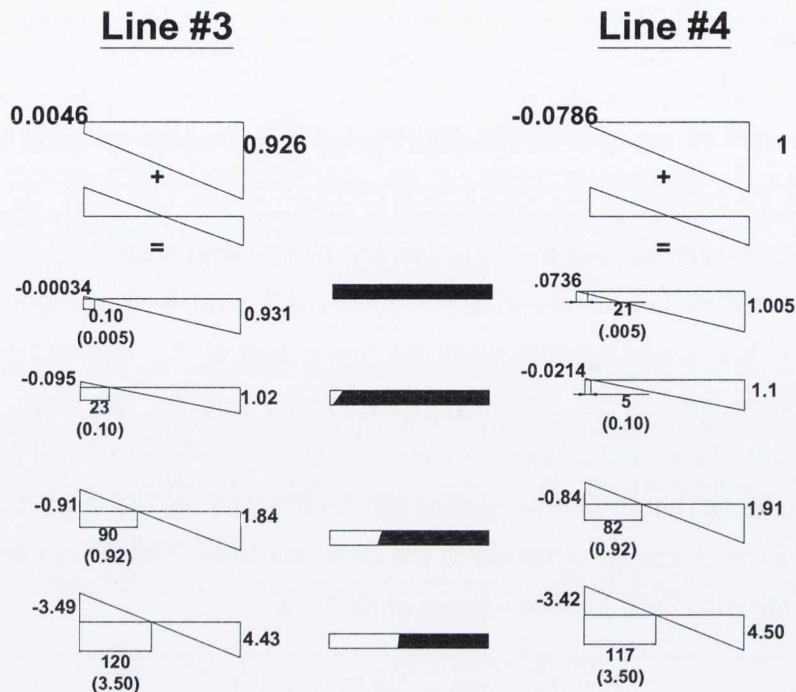


Figure B-3 One flange and one web strain pattern for Line No 1, 2, 3 and 4

From the values of the obtained strain and the obtained position of the neutral-axis, it can be deduced that Equation B-6, B-7, B-8, and B-9 are still valid, whereas Equation B-10 is also valid for the second pattern obtained in this case.

Warping strain applied in the positive direction

Neutral-Axis passes through both flanges and web

In this case, the neutral- axis movement will be opposite to the previous case. For the top flange the neutral-axis is always to the right of the XX-axis, while for the bottom flange the neutral-axis shifts from the left to the right of the XX-axis, having a transition phase between them. Two neutral-axis patterns are suggested based on the movement of the neutral-axis of the bottom flange.

For the top flange the angle of the neutral-axis always decreases on addition of warping strain. As the angle of α always decrease the maximum angle for this case

will be the maximum angle of Case 1-1 of Figure 4.11 which is $180^\circ - \tan^{-1}(b_w / b_f)$ whereas the decrease in the angle for the top flange can be a minimum to 90° . Therefore the following relationship can be written:

$$90^\circ \leq \tan^{-1}(\alpha) \leq 180^\circ - \tan^{-1}(b_w / b_f) \quad \text{B-11}$$

For the bottom flange, when the neutral-axis is on the left of XX-axis, there will be an increase of the angle of γ . Considering both the extreme cases, Case 1-1 and 2-2 of Figure 4.11, it is concluded that the maximum angle for the bottom flange is: $180^\circ - \tan^{-1}(b_w / b_f)$ while the minimum angle as given by case 2-2 is 90° . Therefore, the following relationship can be written:

$$90^\circ \leq \tan^{-1}(\gamma) \leq 180^\circ - \tan^{-1}(b_w / b_f) \quad \text{B-12}$$

For the bottom flange, when the neutral-axis is on the right of XX-axis, the minimum angle after considering both the cases of Figure 4.11, is $\tan^{-1}(b_w / b_f)$ while the maximum angle for the bottom flange is 90° . Therefore, the following relationship can be written:

$$\tan^{-1}(b_w / b_f) < \tan^{-1}(\gamma) < 90^\circ \quad \text{B-13}$$

The other relationships given by Equations B-6 and B-7 are still valid for this case.

Neutral-Axis passes through one flange and web

The extreme Case 8-8 of the pattern given by Figure 4.10 is used to determine the patterns and the relationship. It is found that movement of the neutral-axis for this case will not yield the first pattern, but the second pattern is obtained as depicted in Figure B.4. Equation B.13 will also be valid for this case.

For the top flange there is a decrease in the angle while the maximum angle is given by case 8-8, which is 180° . As there is a decrease of angle up to 90° , therefore Equation B-11 is modified for this case and is given as:

$$90^\circ \leq \tan^{-1}(\alpha) \leq 180^\circ$$

B-14

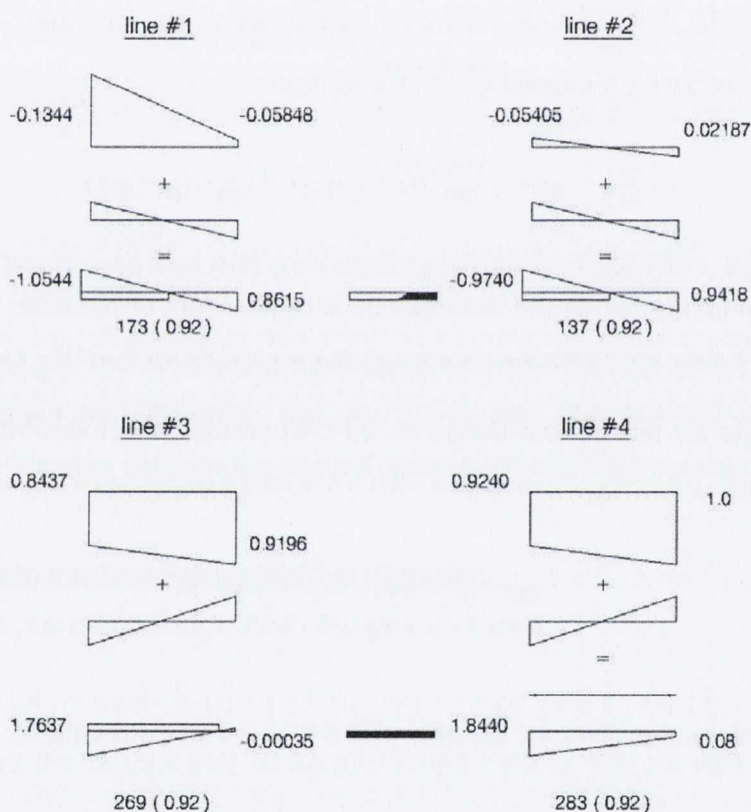


Figure B-4 Positive warping strain, one flange and web strain pattern

Neutral-axis passes through the web only (both negative and positive warping strains)

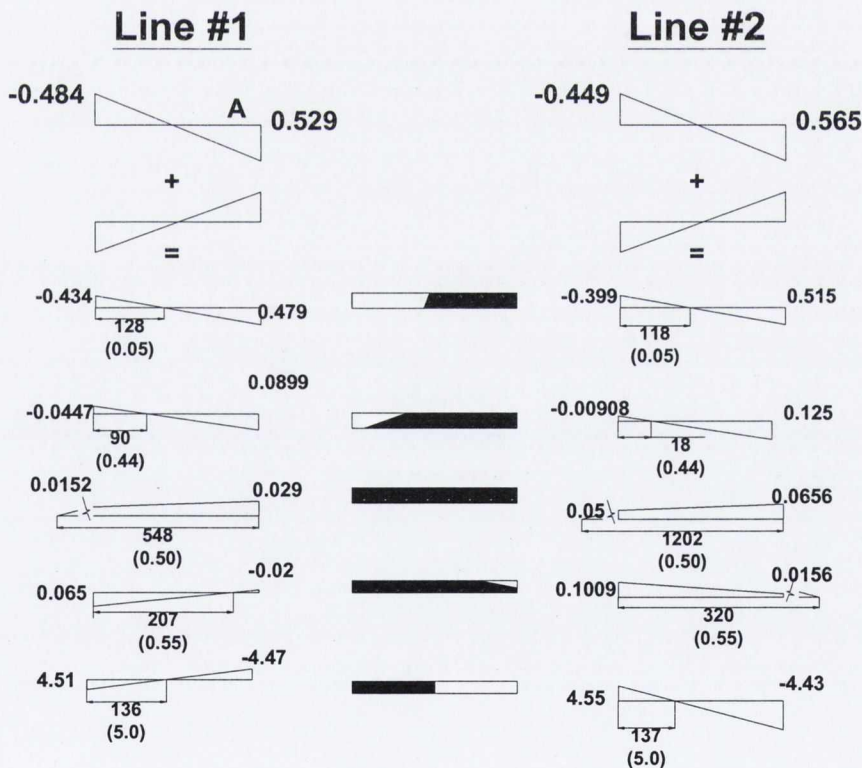
When the neutral-axis pass through the web, the second pattern and transition phase are possible for both the positive and negative warping strains, while the first patterns are not possible. The relationships obtained for this case always fulfills the relationships obtained in the previous cases for both the warping strains and are not discussed here.

B.3.2 Neutral-axis patterns not intersecting the web

Warping applied in the negative direction

Neutral-axis passes through both flanges

Following the procedure discussed previously, the resulting patterns for the case when the neutral-axis does not intersect the web is determined by considering one of the extreme Cases (11-11) depicted in Figure 4.10. The movements of the neutral-axis for the top and bottom flanges are depicted in Figure B-5.



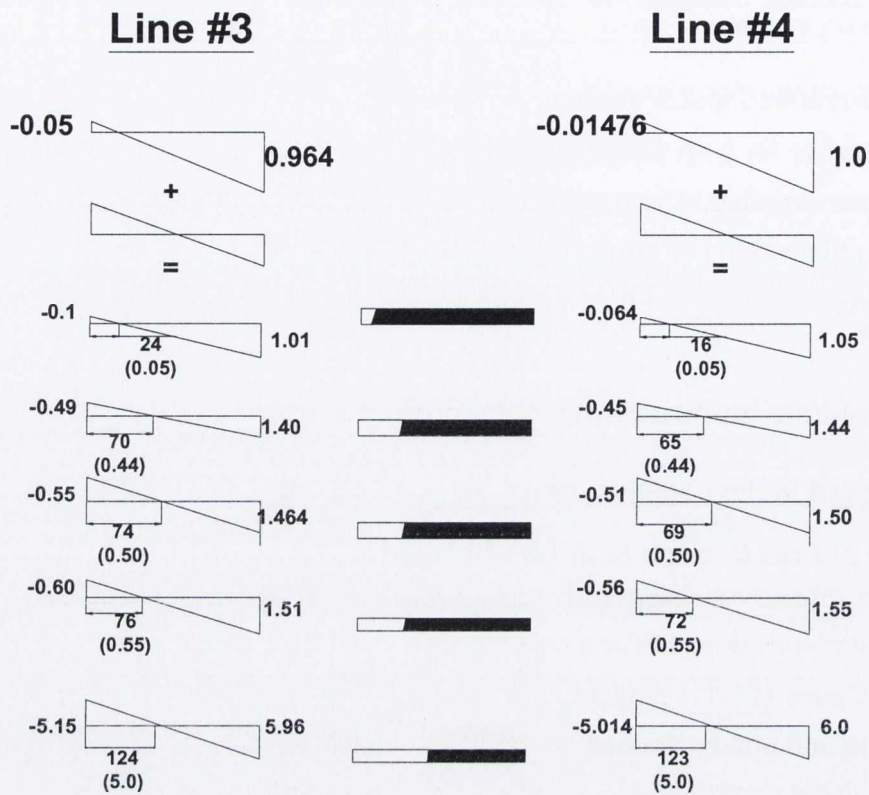


Figure B-5 Neutral-axis intersecting both flanges for Line No 1, 2, 3 and 4

For the top flange, it can be inferred from the figure that the neutral-axis moves towards the left of its initial position on addition of the warping strain and the X-component of the curvature of the top flange will be towards the negative XX-axis and is called the third pattern. During the movement there is an increase of angle which approaches up to an angle of 180° , while minimum angle for this case is 90° as can be deduced from Case 12-12 in Figure 4.10. For this case Equation B-14 will still be valid.

Further increase of the warping strain will shift the neutral-axis for the top flange out of the flange and into the transition phase. Further addition of warping strain will shift the neutral-axis to the right of the XX-axis and the X-component of the curvature of the flange will be towards the positive XX-axis and is called the fourth pattern. During the movement the neutral-axis intersects the flange at an angle nearly equal to 0°

and the angle will increase on further addition of warping strain but will always be less than 90° , and Equation B-10 will still be valid.

In the case of the bottom flange, the neutral-axis movement will remain to the left of the XX-axis. On addition of warping strain it will move towards the right, but always on the left of the axis, as can be deduced from the figure.

For the bottom flange, it can be deduced from the figure that the angle will always decrease. Considering the pattern given by Figure 4.8(c), the maximum angle which this pattern can achieve considering any one of its extreme patterns, as depicted in

Figure 4.10 and the details of the section in Figure B-1, is $180^\circ - \tan^{-1}\left(\frac{b_w}{0.5b_f}\right)$.

The angle for the bottom flange always decreases on addition of warping strain, and is always more than 90° . Therefore, based on the maximum angle, a relationship can be written :

$$90^\circ < \tan^{-1}(\gamma) < 180^\circ - \tan^{-1}\left(\frac{b_w}{0.5b_f}\right) \quad \text{B-15}$$

Neutral-axis passes through one flange

Considering the extreme Case 4-4 given by Figure 4.10, different patterns are obtained as depicted in Figure B-6. The movement of the neutral-axis for the top flange is the same as for the previous case when the neutral-axis passes through both flanges and results in the same patterns as can be deduced from the figure. In the case of the bottom flange, the nature of movement is the same as was observed in the previous case, as can be deduced from the figure.

Equations B-10 and B-14 are still valid for the top flange, whereas Equation B-15 is also valid for the pattern.

Warping applied in the positive direction

Neutral-axis passes through both flanges

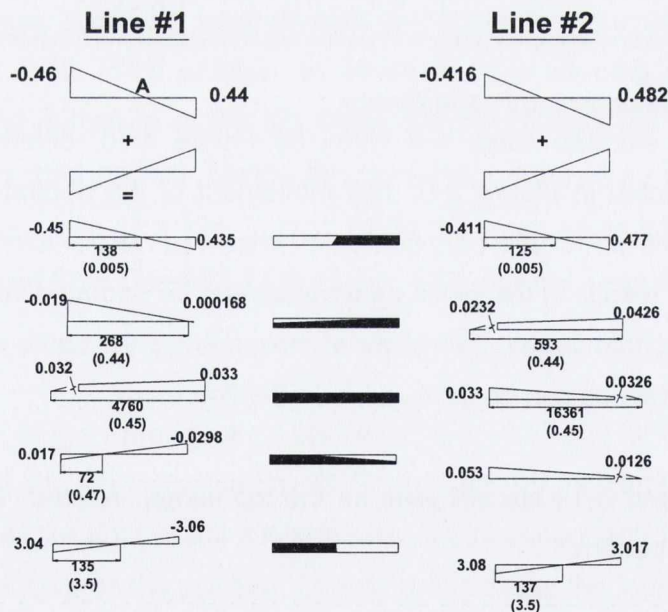
Considering the extreme Case 11-11 given by Figure 4.10, different patterns are obtained as depicted in Figure B-7.

For the case of the top flange, the neutral-axis will move towards the right of its initial position on addition of warping strain but remain on the left of XX axis as can be deduced from the figure. The maximum angle for the top flange is the angle which

Case 11-11 will make which is $180^\circ - \tan^{-1}\left(\frac{b_w}{0.5 * b_f}\right)$. On addition of warping strain

there is a decrease in the angle as can be deduced from the figure but the minimum angle will always less than 90° . Therefore the following relationship can be written as

$$90^\circ \leq \tan^{-1}(\alpha) \leq 180^\circ - \tan^{-1}\left(\frac{b_w}{0.5 * b_f}\right) \quad \text{B-16}$$



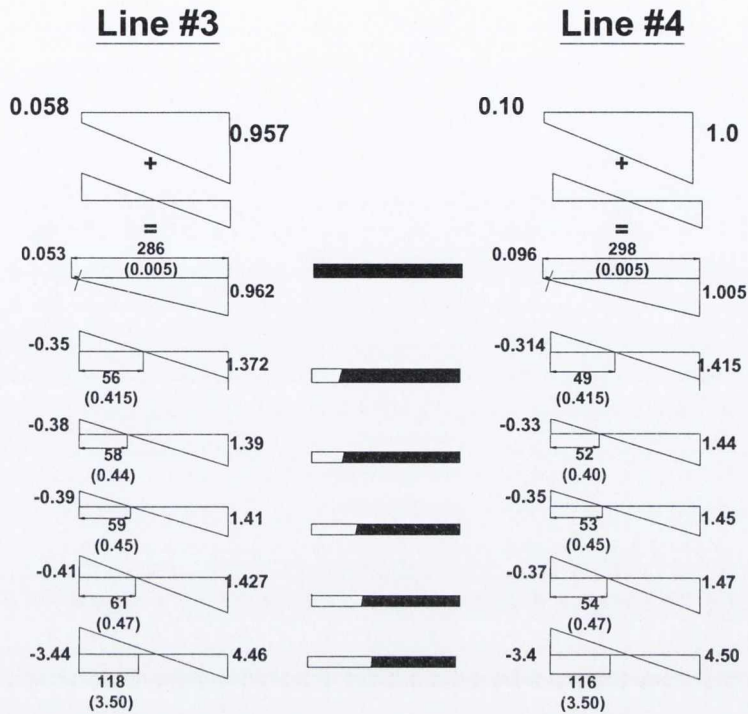


Figure B-6 Neutral-axis intersecting one flange for Line No 1, 2, 3 and 4.

The movement of neutral-axis for the bottom flange is such that first it moves towards the left of the positive XX-axis on addition of the strain and results in the third pattern. When the neutral-axis is on the left of the bottom flange, the angle will always increases on addition of the warping strain whereas the angle will always be less than the maximum angle given by Equation B-15. Equation B-15 is also valid for this case.

Further addition of the warping strain shifts the neutral-axis out of the bottom flange and result in the transition phase, and ultimately it is shifted towards the right of the flange on addition of the warping strain and result in the fourth pattern. When the neutral-axis shifts to the right of the bottom flange, it intersects the flange at an angle less than 90 degrees, as can be deduced from the figure. The minimum angle in this

case is $\tan^{-1}\left(\frac{b_w}{0.5 * b_f}\right)$ whereas as the angle increases and it never reaches more

than 90° Therefore the following relationship can be written:

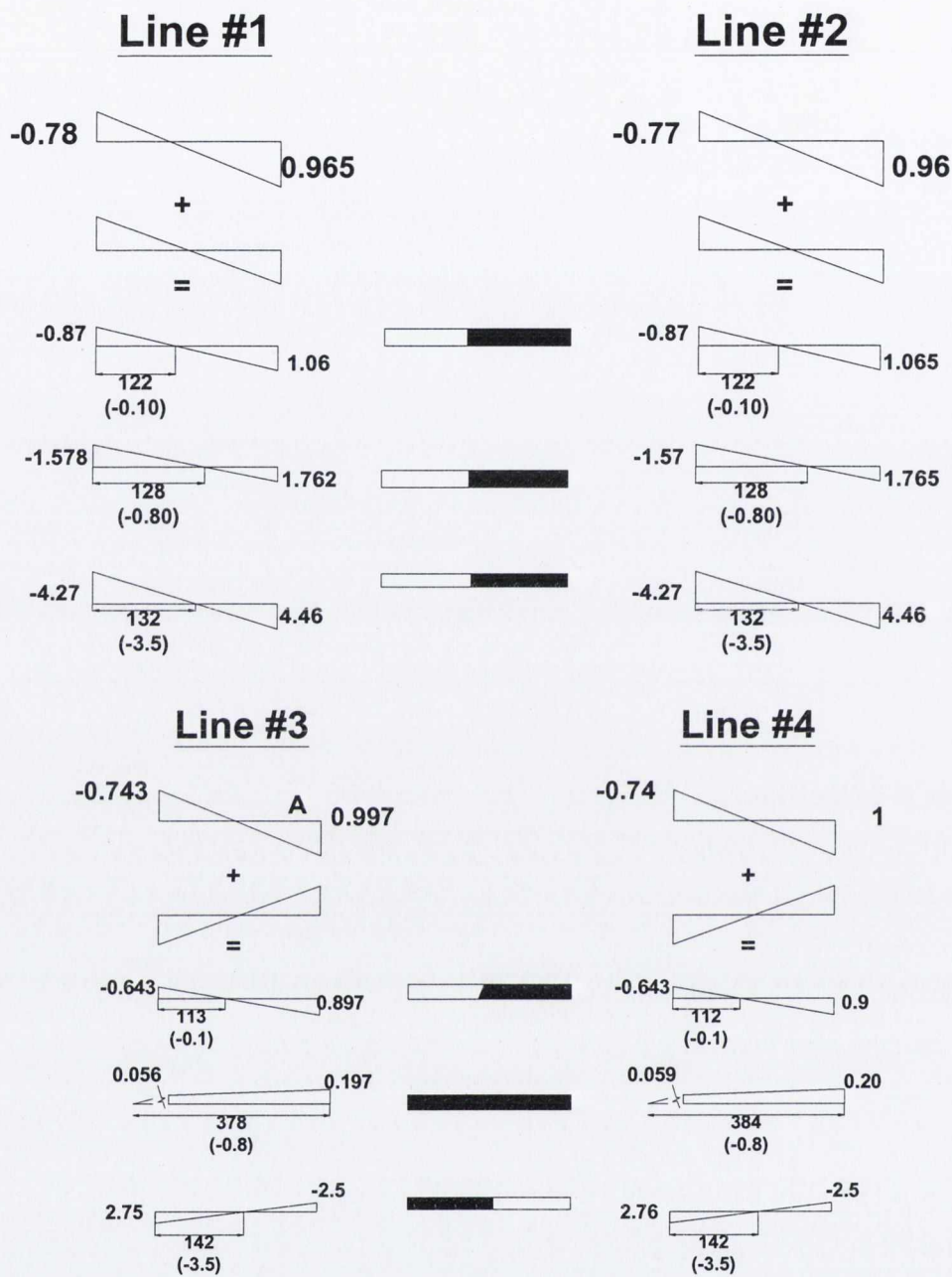


Figure B-7 Neutral-axis intersecting both flanges for Line No 1, 2, 3 and 4.

$$\tan^{-1}\left(\frac{b_w}{0.5*b_f}\right) \leq \tan^{-1}(\gamma) \leq 90^\circ$$

B-17

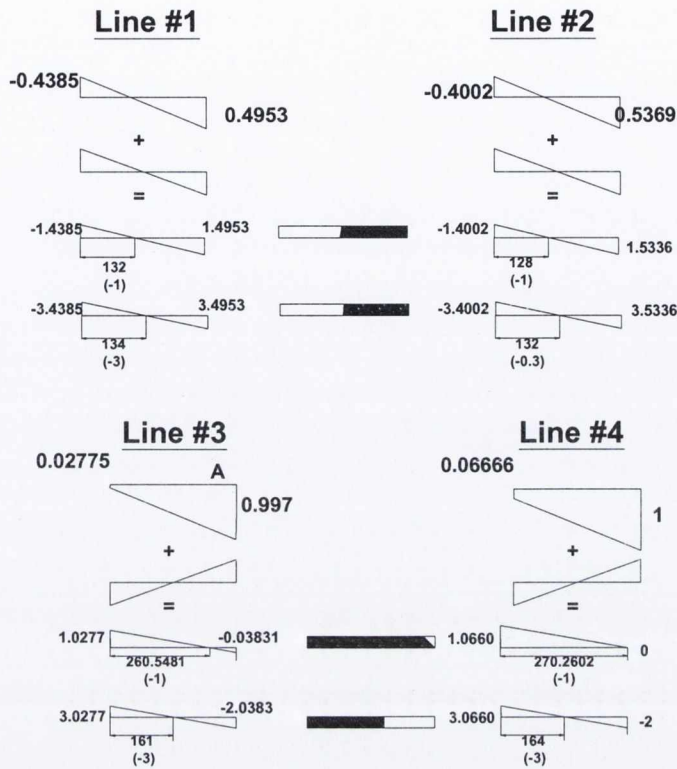


Figure B-8 Neutral-axis intersecting one flange for Line No 1, 2, 3 and 4

Neutral-axis passes through one flange

Considering the extreme Case 4-4 given by Figure 4.10, different patterns are obtained as depicted in Figure B-8.

In this case, the third pattern obtained in the previous case is not obtained as can be observed in the figure. Therefore, one neutral-axis pattern is suggested, i.e. the fourth pattern of the previous case and a transition phase before it.

The change of angle for the bottom flange will be the same as in the previous case as given by Equation B-16. For this type of pattern there are cases such as Cases 13-13 and 14-14 when the angle for the top flange reaches a maximum of 180° as depicted in Figure 4.10, whereas on increase of warping strain angle for the top

flange it can decrease down a minimum of 90° as can be deduced from Figure B-8. Therefore the following relationship can be written:

$$90^\circ \leq \tan^{-1}(\alpha) \leq 180^\circ \quad \text{B-18}$$

B.4 ELEMENT YIELD SURFACE

B.4.1 2D- Element Yield Surface

Axial force acting on the bottom flange can be obtained as

$$P_3 = 2\sigma_f t_f c \quad \text{B-19(a)}$$

Plastic axial yield load for the entire section is

$$P_p = (2A_f + A_w)\sigma_y \quad \text{B-19(b)}$$

Dividing Equation B.19(a) by B.19(b) to obtain the yield axial force p_3 in the bottom flange in normalized form as:

$$p_3 = \frac{P_3}{P_p} = \frac{2\sigma_f t_f c}{(2A_f + A_w)\sigma_y}$$

$$p_3 = \sigma_3 \frac{2t_f c}{A_s} \quad \text{B-19(c)}$$

where $A_s = (2A_f + A_w)$ and $\sigma_3 = \frac{\sigma_f}{\sigma_y}$

Moment M_{x3} acting in the X-direction of the bottom flange can be calculated based on Figure 4.24 as

$$M_{x3} = (0.25t_f b_f^2 - c^2 t_f)\sigma_f \quad \text{B-20(a)}$$

Plastic moment capacity M_{xp} for the entire section about the XX-axis (see Section 4.2) is

$$M_{xp} = 0.5A_f(b_f + 0.5c't_w)\sigma_y \quad \text{B-20(b)}$$

where $c' = A_w/A_f$

Dividing Equation B.20(a) by B.20(b) to obtain the moment in the bottom flange m_{x3} in normalized form as

$$m_{x3} = \frac{M_{x3}}{M_{xp}} = \frac{\sigma_3(0.5b_f^2 - 2c^2)}{(b_f^2 + 0.5c'b_ft_w)}$$

$$m_{x3}(b_f^2 + 0.5c'b_ft_w) = \sigma_3(0.5b_f^2 - 2c^2) \quad \text{B-20(c)}$$

Substituting the value of c from Equation B.19(c) in the above equation yields

$$2\sigma_3 t_f^2 m_{x3} (b_f^2 + 0.5c'b_ft_w) = \sigma_3^2 b_f^2 t_f^2 - p_3^2 A_s^2$$

Dividing the above equation by $\sigma_3^2 b_f^2 t_f^2$ and after rearrangement yields:

$$\frac{p_3^2 A_s^2}{\sigma_3^2 A_f^2} + \frac{2m_{x3}(b_f^2 + 0.5c't_w b_f)}{b_f^2 \sigma_3} = 1 \quad \text{B-21}$$

B.4.2 3D- Element Yield Surface

First Pattern

Axial force P_1 acting on the top flange can be obtained as (Santhadaporn and Chen, 1970)

$$P_1 = 2\sigma_f t_f a \quad \text{B-22(a)}$$

Dividing Equation B.22(a) by B.19(b) to obtain the yield force in the top flange in normalized form as

$$p_1 = \frac{P_1}{P_y} = \frac{2\sigma_f t_f a}{\sigma_y A_s} \quad \text{B-22(b)}$$

Obtaining the value of a from the above equation gives

$$a = \frac{p_1 A_s}{2\sigma_1 t_f} \quad \text{where } \sigma_1 = \frac{\sigma_f}{\sigma_y}$$

Moment M_{x1} acting in the local X-direction of the top flange can be calculated as (Santhadaporn and Chen, 1970)

$$M_{x1} = (0.25A_f b_f - 0.0833\alpha'^2 t_f^3 - a^2 t_f) \sigma_f \quad \text{B-23(a)}$$

where $\alpha' = 1/\alpha$

Dividing Equation B.23(a) by B.20(b) to obtain the moment m_{x1} in the top flange in normalized form as

$$m_{x1} = \frac{2\sigma_1 (0.25A_f b_f - 0.0833\alpha'^2 t_f^3 - a^2 t_f)}{c_1} \quad \text{B-23(b)}$$

where $c_1 = A_f (b_f + 0.5c' t_w)$

Moment M'_{y1} acting in the local Y-direction of the top flange can be calculated as (Santhadaporn and Chen, 1970)

$$M'_{y1} = \frac{1}{6} \sigma_f t_f^3 \alpha' \quad \text{B-24(a)}$$

Plastic moment capacity M_{yp} for the entire section about the YY-axis (see Section 4.2) is,

$$M_{yp} = \sigma_y A_f (d + 0.25b_w c') \quad \text{B-24(b)}$$

Dividing Equation B.24(a) by B.24(b) to obtain the moment m'_{y1} about the local Y axis in normalized form yields

$$m'_{y1} = \frac{\sigma_f t_f^3 \alpha'}{6\sigma_y c_2} \quad \text{B-24(c)}$$

where $c_2 = A_f (d + 0.25b_w c')$

Obtaining the value of α' from the above equation gives

$$\alpha' = \frac{6m'_{y1} c_2}{\sigma_1 t_f^3}$$

Putting the value of α' and a in equation B.23(b) yields

$$m_{x1} c_1 = 2\sigma_1 \left(0.25A_f b_f - 0.0833 \left(\frac{6m'_{y1} c_2}{\sigma_1 t_f^3} \right)^2 t_f^3 - \left(\frac{p_1^2 A_s^2}{4\sigma_1^2 t_f^2} \right)^2 t_f \right)$$

or

$$2m_{x1} c_1 \sigma_1 t_f^3 = A_f^2 t_f^2 \sigma_1^2 - 12m_{y1}^2 c_2^2 - p_1^2 A_s^2 t_f^2$$

Divide the above equation by $A_f^2 t_f^2 \sigma_1^2$ and after some rearrangement gives

$$p_1^2 \left(\frac{A_s^2}{A_f^2 \sigma_1^2} \right) + m_{x1} \left(\frac{2c_1 t_f}{A_f^2 \sigma_1} \right) + m_{y1}^2 \left(\frac{12c_2^2}{A_f^2 \sigma_1^2 t_f^2} \right) = 1 \quad \text{B-25}$$

Third Pattern

Axial force P_1 acting on the top flange can be obtained based on Figure 4.26 as

$$P_1 = (A_f - x_1 x_2) \sigma_f \quad \text{B-26(a)}$$

Dividing Equation B.26(a) by B.19(b) to obtain the yield force in the top flange in normalized form as

$$p_1 = \frac{P_1}{P_y} = \frac{\sigma_f (A_f - x_1 x_2)}{\sigma_y A_s} \quad \text{B-26(b)}$$

$$p_1 = \frac{\sigma_1 (A_f - x_1 x_2)}{A_s}$$

Obtaining the value of x_2 from the above equation gives

$$x_2 = \frac{(\sigma_1 A_f - p_1 A_s)}{\sigma_1 x_1}$$
$$x_2 = \frac{C_a}{\sigma_1 x_1}$$

where $C_a = (\sigma_1 A_f - p_1 A_s)$

Moment M_{x1} acting in the local X-direction of the top flange can be calculated as:

$$M_{x1} = x_1 x_2 (0.5b_f - 0.333x_1) \sigma_f \quad \text{B-27(a)}$$

Dividing Equation B.27(a) by B.20(b) to obtain the moment in the top flange in normalized form as

$$m_{x1} = \frac{2\sigma_1 x_1 x_2 (0.5b_f - 0.333x_1)}{c_1}$$

Putting the value of x_2 in the above equation yields

$$m_{x1}c_1 = 2\sigma_1x_1 \frac{C_a}{\sigma_1x_1} (0.5b_f - 0.333x_1)$$

$$x_1 = \frac{1.5C_a b_f - 1.5m_{x1}c_1}{C_a}$$

Moment M'_{y1} acting in the local Y-direction of the top flange can be calculated as:

$$M'_{y1} = \sigma_f \left[\left(\frac{x_1x_2}{2} \right) \left(\frac{t_f}{2} - \frac{x_2}{3} \right) + (t_f - x_2)x_1 \left(\frac{t_f}{2} - \frac{t_f - x_2}{2} \right) + \left(\frac{x_1x_2}{2} \right) \left(\frac{2x_2}{3} - \frac{t_f}{2} \right) \right]$$

which implies to

$$M'_{y1} = \sigma_f [0.5x_1x_2t_f - 0.333x_1x_2^2] \quad \text{B-28(a)}$$

Dividing Equation B.28(a) by B.24(b) to obtain the moment about the local Y axis in normalized form as

$$m'_{y1} = \frac{M'_{y1}}{M_{yp}} = \frac{\sigma_f [0.5x_1x_2t_f - 0.333x_1x_2^2]}{\sigma_y c_2}$$

Putting the value of x_2 in the above equation yields

$$m'_{y1}c_2\sigma_1x_1 = [0.5C_a t_f \sigma_1x_1 - 0.333C_a^2]$$

Putting the value of x_1 in the above equation gives

$$(m'_{y1}c_2\sigma_1 - 0.5C_a t_f \sigma_1) (1.5C_a b_f - 1.5m_{x1}c_1) + 0.333C_a^3 = 0 \quad \text{B-29}$$

B.5 Obtaining $\tan \beta$

B.5.1 Relationship between a, b', c and β

A straight line neutral-axis is taken when strain due to M_x , M_y and P are only considered and different possible patterns for the case is depicted in Figure 4.8. The initial positions for a_{orig} , b' and c_{orig} of the neutral-axis, for a straight line neutral-axis, are as defined in Figure A-1. If warping strain is added to the figure, the position of the neutral-axis will change only for flanges while it remains the same for the web. In the following a relationship is developed between new positions of a_{orig} and c_{orig} denoted as a and c respectively and between b' and β . Using this relationship β can be obtained if a , c and b' are known.

Warping strain (like the pattern shown in Figure 4.9) is added to the strain field with m_1 as the slope of the line of warping strain.

Top flange

Now consider the centre line of the top flange, as depicted in Figure A-1. The strain field in the YZ plane without the addition of warping strain is shown in Figure B-9

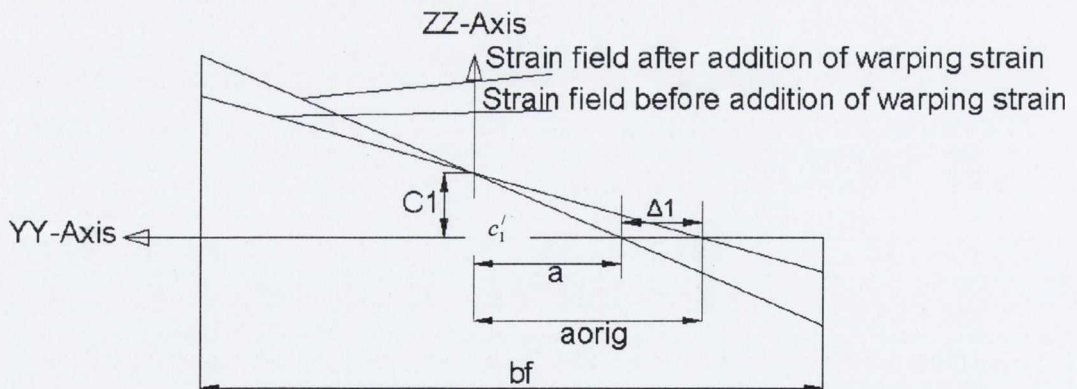


Figure B-9 Strain field of the centre line of top flange before and after addition of warping strain

The equation of the line in Figure B-9 can be written as

$$Z = -m_2 y - c_1' \quad \text{B-30(a)}$$

When $Z = 0$, $y = -a_{orig}$

Therefore,

$$m_2 = \frac{c_1'}{a_{orig}}$$

Where m_2 is the slope of line (in Figure B-9) of the strain field for the case when warping is not added to the figure, and from the figure it can be written as

$$m_2 = \frac{c_1'}{a + \Delta_1}$$

On addition of the warping strain for the top flange a new line is obtained as depicted in the figure having slope m_3 , The equation of the new line can be written as

$$Z = -m_3 y - c_1' \quad \text{B-30(b)}$$

When $Z = 0$, $y = -a$

Therefore,

$$m_3 = \frac{c_1'}{a}$$

The slope of the new line, m_3 (shown in Figure B-9) is the summation of the slopes of the line of warping strain m_1 and slope of the original line m_2 . Mathematically it can be written as

$$m_3 = m_1 + m_2$$

$$\text{B-30(c)}$$

Putting the value of m_2 and m_3 in the above equation yields

$$m_1 = \frac{c'_1 \Delta_1}{a(a + \Delta_1)} \quad \text{B-30(d)}$$

Bottom flange

Now consider the centre line of bottom flange, as depicted in Figure A-1. The strain field in the YZ plane without addition of warping strain is shown in Figure B-10.

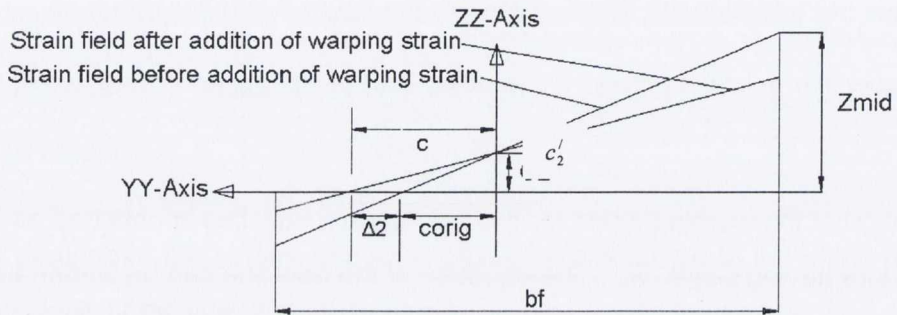


Figure B-10 Strain field of the centre line of bottom flange before and after addition of warping strain

The equation of the line in Figure B-10 before addition of warping strain can be written as:

$$Z = -m_4 y + c'_2 \quad \text{B-31(a)}$$

When $Z = 0$, $y = c_{orig}$

Therefore,

$$m_4 = \frac{c'_2}{c_{orig}}$$

Where m_4 is the slope of line (in Figure B-10) of the strain field for the case when warping is not added to the figure, and from the figure it can be written as:

$$m_4 = \frac{c'_2}{c - \Delta_2}$$

On addition of warping strain for the top flange a new line is obtained as depicted in the figure having slope m_3 . The equation of the new line can be written as:

$$Z = -m_5 y + c'_2 \quad \text{B-31(b)}$$

When $Z = 0$, $y = c$

Therefore

$$m_5 = \frac{c'_2}{c}$$

The slope of the new line, m_5 (shown in Figure B-10) is the summation of the slopes of the line of warping strain m_1 and slope of the original line m_4 . Mathematically it can be written as:

$$-m_5 = m_1 - m_4 \quad \text{B-31(c)}$$

Putting the value of m_4 and m_5 in the above equation yield

$$m_1 = \frac{c'_2 \Delta_2}{c(c - \Delta_2)} \quad \text{B-31(d)}$$

Equating both the values of m_1 given by Eqs. B-30(d) and B-31(d) gives

$$\frac{c'_1 \Delta_1}{a(a + \Delta_1)} = \frac{c'_2 \Delta_2}{c(c - \Delta_2)} \quad \text{B-32}$$

It is known that Figure B-1 has a radius of curvature denoted as κ then comparing Figure B-1, B-9 and B-10 c'_1 and c'_2 can be related to κ as

$$c'_1 = \kappa * a_{orig} * \cos(\tan^{-1}(\beta) - 90^\circ)$$

$$c'_2 = \kappa * c_{orig} * \cos(\tan^{-1}(\beta) - 90^\circ)$$

Replacing the above values in Equation B-32 results in

$$\frac{\kappa * a_{orig} * \cos(\tan^{-1}(\beta) - 90^\circ) \Delta_1}{a(a + \Delta_1)} = \frac{\kappa * c_{orig} * \cos(\tan^{-1}(\beta) - 90^\circ) \Delta_2}{c(c - \Delta_2)}$$

From Figure B-9 and B-10 it is known that $a_{orig} = a + \Delta_1$ $c_{orig} = c - \Delta_2$, which reduces the above equation to

$$\frac{\Delta_1}{a} = \frac{\Delta_2}{c} \quad \text{B-33}$$

Comparing Figures B-9 and B-10 and if L_1 and L_2 are as defined in Figure B-1 a relationship can be written as

$$\tan(180^\circ - \tan^{-1}(\beta)) = \frac{L_1}{a + \Delta_1}$$

or

$$\Delta_1 = \frac{L_1 - \tan(180^\circ - \tan^{-1}(\beta)) * a}{\tan(180^\circ - \tan^{-1}(\beta))}$$

Similarly, from the figures, a relationship can be written as

$$\tan(180^\circ - \tan^{-1}(\beta)) = \frac{L_2}{c - \Delta_2}$$

or

$$\Delta_2 = \frac{\tan(180^\circ - \tan^{-1}(\beta)) * c - L_2}{\tan(180^\circ - \tan^{-1}(\beta))}$$

Putting the values of Δ_1 and Δ_2 in equation B-33 gives

$$\frac{L_1 - \tan(180^\circ - \tan^{-1}(\beta)) * a}{a} = \frac{\tan(180^\circ - \tan^{-1}(\beta)) * c - L_2}{c}$$

$$\tan(180^\circ - \tan^{-1}(\beta)) = \frac{c * L_1 + a * L_2}{2ac}$$

B-34

where $L_1 = 0.5d - b'$ and $L_2 = 0.5d + b'$

B.5.2 Relationship between a, b, c and β . and third neutral-axis pattern

Equation B-34 is valid for the first pattern (Figure 4.25) for the web but it is not applicable to the third pattern of the figure. Therefore certain changes are made to the above equation to obtain angle β .

Consider Figure B.11, axial forces are related to the triangular shaded area $A1$ as

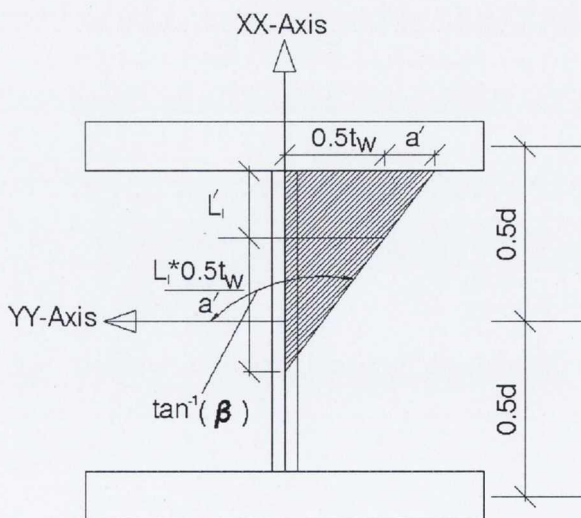


Figure B-11 Neutral-Axis passes through the web based on third pattern

From the figure it can be said that

$$P_{web} = A_w - 2A1 \quad \text{B-35(a)}$$

Obtaining L'_1

From the figure it can be said that

$$\begin{aligned} (a' + 0.5 * t_w) \left(L'_1 + \frac{0.5 * L'_1 * t_w}{a'} \right) &= 2A1 \\ (a' + 0.5 * t_w) \left(\frac{a' L'_1 + 0.5 * L'_1 * t_w}{a'} \right) &= 2A1 \\ (a' + 0.5 * t_w) (a' L'_1 + 0.5 * L'_1 * t_w) &= 2a' A1 \\ a'^2 L'_1 + a' L'_1 t_w + 0.25 * L'_1 * t_w^2 - 2a' A1 &= 0 \\ L'_1 &= \frac{2a' A1}{(a' + a' t_w + 0.25 * t_w^2)} \end{aligned} \quad \text{B-35(b)}$$

Assuming

$$\tan \theta = \tan(180^\circ - \tan^{-1}(\beta))$$

Therefore Equation B-34 can be written as

$$\frac{cL_1 + aL_2}{2ac} = \tan \theta \quad \text{B-35(c)}$$

Comparing Figure B-1 and B-11 it can be said that

$$L_1 = L'_1 + 0.5t_f \quad \text{and} \quad L_2 = d - L'_1 - 0.5t_f$$

Therefore putting the values of L_1 and L_2 in Equation B-35(c) gives

$$\frac{(L'_1 + 0.5t_f)c + (d - L'_1 - 0.5t_f)a}{2ac} = \tan \theta$$

From the Figure it can be said that $\tan \theta = \frac{L_1'}{a'}$, Therefore putting the value in the above equation gives

$$\frac{L_1'c + 0.5t_f c + ad - aL_1' - a0.5t_f}{2ac} = \frac{L_1'}{a'}$$

Putting the value of L_1' from Equation B-35(b) into the above equation gives

$$\frac{\frac{2a'Alc}{(a' + a't_w + 0.25*t_w^2)} + 0.5t_f c + ad - a0.5t_f - \frac{2a'Ala}{(a' + a't_w + 0.25*t_w^2)}}{2ac} = \frac{2a'Al}{(a' + a't_w + 0.25*t_w^2)} * \frac{1}{a'}$$

$$\frac{2a'Alc + 0.5t_f c(a' + a't_w + 0.25*t_w^2) + ad(a' + a't_w + 0.25*t_w^2) - a0.5t_f(a' + a't_w + 0.25*t_w^2) - 2a'Ala}{2ac(a' + a't_w + 0.25*t_w^2)} =$$

$$\frac{2a'Al}{(a' + a't_w + 0.25*t_w^2)} * \frac{1}{a'}$$

$$\frac{2a'Alc + 0.5t_f c(a' + a't_w + 0.25*t_w^2) + ad(a' + a't_w + 0.25*t_w^2) - a0.5t_f(a' + a't_w + 0.25*t_w^2) - 2a'Ala}{2ac} = 2Al$$

$$0.5*t_f c a'^2 - 0.5*t_f a d^2 + d^2 da + 2Aldc + 0.5d t_f t_w c - 2Alda - 0.5d t_f t_w a + d t_w da + .125 t_w^2 c$$

$$-.125 t_f t_w^2 a + .25 t_w^2 da = 4acAl \quad \text{B-36}$$

In the above equation a' is the only unknown while other parameters are known parameters.

B.5.3 Relationship between a, b, c and β . and second Neutral-Axis pattern

From Figure B-12 it can be said that

$$\tan \theta = \frac{L_2'}{b_o} \quad \text{B-37(a)}$$

where $\tan \theta = \tan(180^\circ - \tan^{-1}(\beta))$ and $L_2' = L_2 - 0.5 * d$

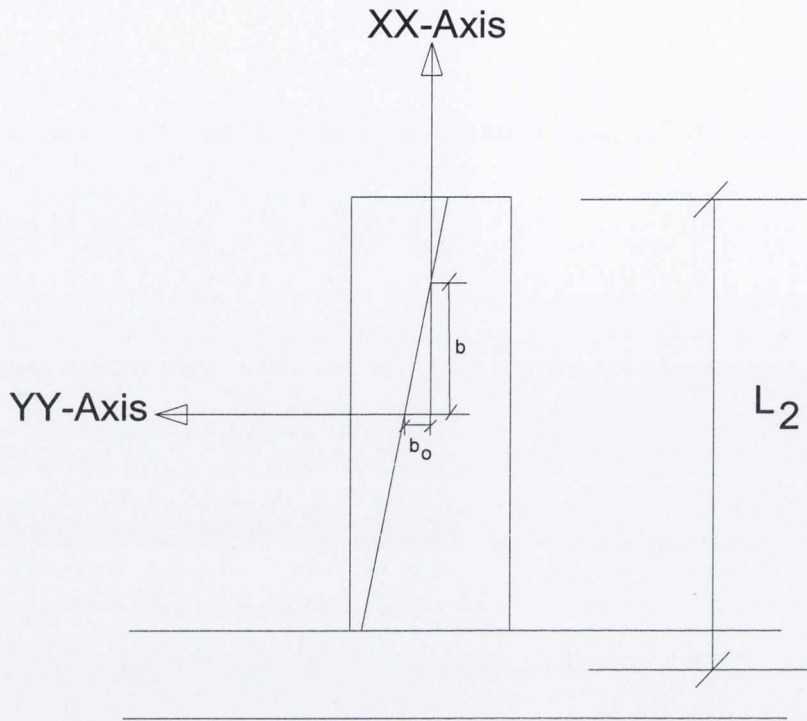


Figure B-12 Neutral-Axis passes through the web based on second pattern

Therefore, equating Equations B-35(c) and B-37(c) and putting the value of L_1 (based on Figure B-1) and L_2' it can be written as

$$\frac{c(d - L_2) + aL_2}{2ac} = \frac{L_2 - 0.5 * d}{b_o}$$

Solving the above equation for L_2 gives

$$L_2 = \frac{cdb_o + acd}{(cb_o - ab_o + 2ac)} \quad \text{B-37(b)}$$

This Neutral-axis pattern is reciprocal of first pattern, and same formula will be valid for this case with length replaced by thickness. Therefore formula of p given in

Equation 4.38(a) is also valid. In this case for the axial force for the web is P_{web} , and a is replaced by b_o and therefore b_o can be obtained as

$$b_o = P_{web} / 2b_w$$

when L_2 is known, b' can be determined as $L_2 = b' + 0.5d$, when b' is known β can be determined by obtaining an equation based on Figure B-12 as

$$\tan(180^\circ - \tan^{-1}(\beta)) = \frac{b}{b_o} \quad \text{B-38}$$

B.5.4 Obtaining α_{new} , $lb1_{new}$ and lb_{new}

From Figure B-13, following relationship can be concluded

$$c_{orig} = \frac{0.5b_w + 0.5t_f + b'}{\tan(180^\circ - \tan^{-1}(\beta))}$$

$$a_2 = a_1 + 0.5b_f * \sin(180^\circ - \tan^{-1}(\beta))$$

$$a_{mid} = a_2 - 0.5t_f * \cos(180^\circ - \tan^{-1}(\beta))$$

In the absence of warping strain the section has one curvature, κ . If it is assumed that curvature cause a unit strain in Z-direction related to its distance a_2 , then, $a_2 * \kappa = 1$ can be written.

If strain for a_{mid} is considered as Z_{mid} then $a_{mid} * \kappa = Z_{mid}$ can be written. Therefore based on above two relationships following relationship can be written

$$Z_{mid} = \frac{a_{mid}}{a_2}$$

Following right hand rule and considering YY-ZZ plane centre line of bottom flange as drawn in Figure B-10 shows the strain of the mid bottom flange, Considering the above figure a relationship can be written as

$$c_2' = \frac{Z_{mid} * c_{orig}}{c_{orig} + 0.5b_f}$$

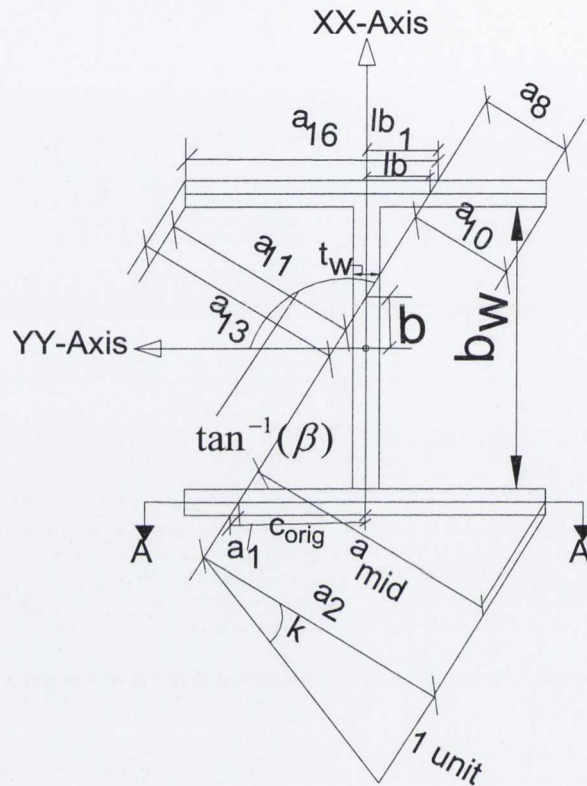


Figure B.13 Different dimensions of the beam to calculate $lb_{1_{new}}$ and lb_{new}

This line will make a slope m_4 which can be related to other parameters of the figure and is written again as

$$m_4 = \frac{c_2'}{c_{orig}}$$

When warping strain is added to the line of Figure B-10 another line is obtained having a slope m_5 which is also shown in the figure, and following relationship is written again as

$$m_5 = \frac{c_2'}{c}$$

Now considering Figure B-13 following distances indicated in the figure can be related to β as

$$lb1 = \frac{0.5b_w + t_f - b'}{\tan(180^\circ - \tan^{-1}(\beta))}$$

$$a_{16} = 0.5b_f + lb1$$

$$a_{13} = a_{16} * \sin(180^\circ - \tan^{-1}(\beta)) - (t_f * \cos(180^\circ - \tan^{-1}(\beta)))$$

$$a_{11} = a_{16} * \sin(180^\circ - \tan^{-1}(\beta))$$

$$a_8 = (b_f - a_{16}) * \sin(180^\circ - \tan^{-1}(\beta))$$

$$a_{10} = a_8 + (t_f * \cos(180^\circ - \tan^{-1}(\beta)))$$

If strain related to $a_8, a_{10}, a_{11}, a_{13}$ and a_{16} are $Z_8, Z_{10}, Z_{11}, Z_{13}$ and Z_{16} , then they can be related to a_2 as

$$Z_8 = \frac{a_8}{a_2}, Z_{11} = \frac{a_{11}}{a_2}, Z_{16} = \frac{a_{16}}{a_2}, Z_{10} = \frac{a_{10}}{a_2} \text{ and } Z_{13} = \frac{a_{13}}{a_2}$$

The difference of slope between m_4 and m_5 is the slope of warping strain m_1 , and are related to each other by Equation B-31(c). The maximum value of warping strain can be obtained by its slope using the following relationship

$$\varepsilon_{warp} = m_1 * 0.5b_f$$

The maximum value of warping strain will be the same for both the flanges.

Therefore considering top flange on addition of warping strain, strains $Z_8, Z_{10}, Z_{11}, Z_{13}$ are change to new values of strains which are $Z_{8new}, Z_{10new}, Z_{11new}, Z_{13new}$ respectively and can be defined as

$$Z_{8new} = -\varepsilon_{warp} + Z_8$$

$$Z_{10new} = -\varepsilon_{warp} + Z_{10}$$

$$Z_{11new} = -\varepsilon_{warp} + Z_{11}$$

$$Z_{13new} = -\varepsilon_{warp} + Z_{13}$$

Therefore Neutral-Axis position before and after the addition of warping strain are shown in Figure B-14 below

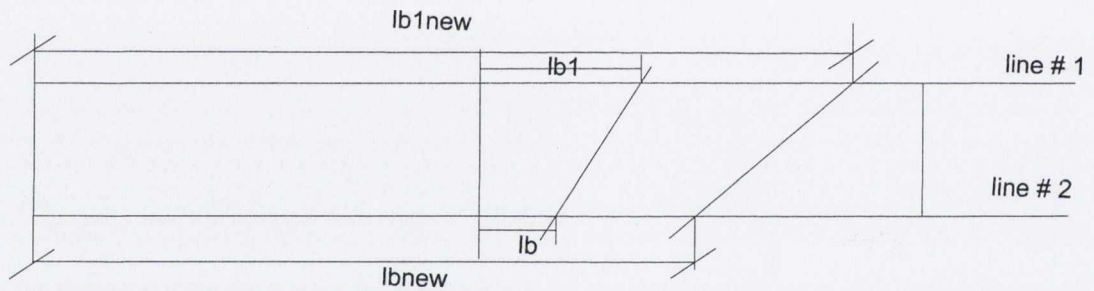


Figure B-14 Position of Neutral-Axis in the top flange before and after addition of warping strain

Line#1 as indicated in the figure can be drawn in YY-ZZ plane as

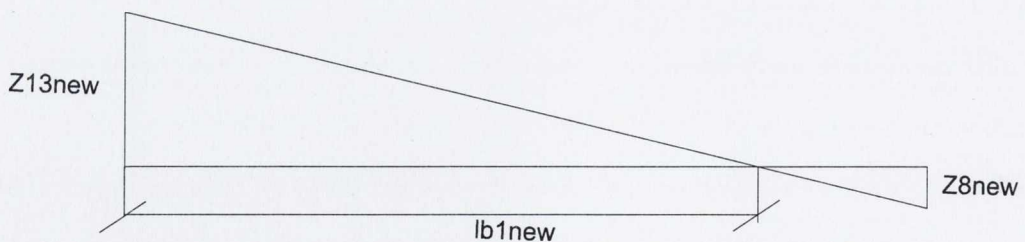


Figure B-15 Strain for line#1 after addition of warping strain

Therefore a relationship can be written based on line #1

$$\frac{lb1_{new}}{Z_{13new}} = \frac{b_f}{Z_{13new} - Z_{8new}}$$

Similarly Line#2 as indicated in the figure can be drawn in YY-ZZ plane as

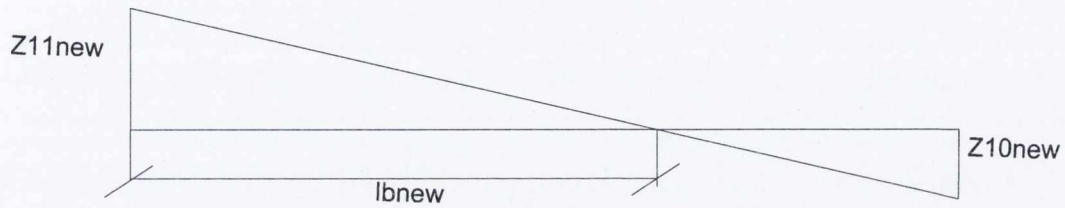


Figure B-16 Strain for line#2 after addition of warping strain

Therefore a relationship can be written based on line #2 as

$$\frac{lb_{new}}{Z_{11new}} = \frac{b_f}{Z_{11new} - Z_{10new}}$$

lb_{new} and $lb1_{new}$ can be found based on the above relationship, Hence α_{new} can be obtained as

$$\alpha_{new} = (lb1_{new} - lb_{new})/t_f$$

APPENDIX-D

D.1 CALCULATING ROTATION FOR ELASTIC LIMIT LOAD

Experiment 1

Using Equation 2.37, rotation at the end β can be calculated and written again as

$$\beta = \frac{T}{JG} \left(L - 2\alpha \tanh \frac{L}{2\alpha} \right) \quad \text{D.1}$$

J can be calculated using Equation 2.32 for experimental section (details of which are given in Figure 3.5), therefore based on the dimension of the experimental section J worked out to be

$$J = 9537.125 \text{mm}^4 \quad E = 201.7 \text{GPa} \quad (\text{From Section 5.2.1})$$

Therefore G , shear modulus can be obtained as

$$G = \frac{E}{2(1+\nu)} \quad \text{having poisson's ratio} = 0.25, \quad G = 80.68 \text{GPa}$$

L is the length of the sample which is 1.03m

$$\text{And as given from Equation 2.35(a)} \quad \alpha = \frac{h}{2} \sqrt{\frac{EI_z}{JG}}$$

h is the depth of beam centre to centre of flanges whose value is 96.76mm

Putting the given values will give $\alpha = 0.33$

Putting the above values β obtained for an elastic limit torsion of 0.155kN.m is

$$\beta = 0.07 \text{rad} = 4.6^\circ$$

Experiment 2

All the parameters will be the same as was in Experiment 1, Based on these parameters β obtained for an elastic limit torsion of $0.37kN.m$ is

$$\beta = 0.188rad = 10.8^\circ$$

Experiment 3

All the parameters will be the same as was in Experiment 1, Based on these parameters β obtained for an elastic limit torsion of $0.40kN.m$ is

$$\beta = 0.206rad = 11.8^\circ$$

D.2 CALCULATING BIMOMENT FOR ELASTIC LIMIT LOAD

Experiment 1

For an elastic limit torsion of $0.155kN.m$ using Equation 2.37 rewritten here as

$$M_{z_{\max}} = \frac{T}{h} \alpha \tanh \frac{L}{2\alpha}$$

D.2

All the values in the Equation are known, therefore will give

$$M_{z_{\max}} = 466.22N.m$$

which will give bimoment B as

$$B = .045kN-m^2$$

Experiment 2

Similarly using Equation D.2 and the elastic limit load of $0.37kN.m$ bimoment obtained is

$$B=.10kN-m^2$$

Experiment 3

Similarly using Equation D.2 and the elastic limit load of $0.40 kN.m$ bimoment obtained is

$$B=.11kN-m^2$$

D.3 YIELD SURFACE VERIFICATION

D.3.1 Comparison theory (Chapter 4) with elastic limit load

Experiment 1

From Table 6.2 forces in normalized form can be written as

$$b=0.32, m_y=0.62, m_x=.018$$

To determine the point of formation of hinge, it is first required to determine m_{xA} , (as the Y-axis of Chapter 4 is X axis here)

Based on given $b=0.32$ take $m_y=0.68$ so that their summation equal to 1

Using Equation 4.40(b) and (d) and not considering minor moment in the web gives

$$m_{y3}=0.50$$

$$m_{y1}=0.18$$

From Equation 4.37(b) using the top flange

$$P_3=0.0$$

$$P_1=0.243$$

Using Equation 4.40(a) P_2 can be calculated as

$$P_2=-0.243$$

Therefore using Equation 4.37(b) for the web

$$m_{x2}=0.15$$

using Equation 4.40(c) ignoring $m_{x'1}$

$$m_{xA}=0.45$$

Since $m_x < m_{xA}$ it means it is the case when loading if lie will be at the flat plateau.

Therefore at this summation of m_y and b are considered. In this case it is less than one it means section is elastic.

Experiment 2

From Table 6.2 forces in normalized form can be written as

$$b=0.69, m_y=0.22, m_x=.29$$

To determine the point of formation of hinge, it is first required to determine m_{xA} , (as the Y-axis of Chapter 4 is X axis here). Using the procedure discussed above and using the equations described m_{xA}

Is calculated which is 0.43

Since $m_x < m_{xA}$ it means it is the case when yield surface if lie will be at the flat plateau.

Therefore at this summation of m_y and b are considered. In this case it is less than one it means section is elastic.

Experiment 3

From Table 6.2 forces in normalized form can be written as

$$b=0.76, m_y=0.22, m_x=.31 \text{ and } p=0.1$$

To determine the point of formation of hinge, it is first required to determine m_{xA} , (as the Y-axis of Chapter 4 is X axis here). Using the procedure discussed above and using the equations described m_{xA} is calculated which is 0.49

Since $m_x < m_{xA}$ it means it is the case when yield surface if lie will be at the flat plateau. Therefore at this summation of m_y and b are considered. In this case it is less than one it means section is elastic.

D.3.1 Comparison theory (Chapter 4) with non-linear load

Experiment 1

As the load in the previous case were not reached the yield surface, therefore to determine the load which will lie in the flat plateau it is required that such a value of m_y and b is required for which it reach the yield surface i.e. their summation equal to one. Therefore, the load calculated is 1.9 kN , for this load values are

$$b=0.34, m_y=0.66, m_x=.018$$

For these values using the same procedure m_{xA} calculated which is 0.46

Since $m_x < m_{xA}$ and the summation of m_y and b are 1 it means load has reached the yield surface.

Experiment 2

Using the same procedure used in the previous section such load is calculated which will give summation of m_y and b equal to one. Therefore, the load calculated is 4.73 kN , for this load values are

$$b=0.76, m_y=0.24, m_x=0.32$$

Using the same procedure described above m_{xA} calculated which is 0.41, Since $m_x < m_{xA}$ and the summation of m_y and b are 1 it means load has reached the yield surface.

Experiment 3

Using the same procedure used in the previous section such load is calculated which will give summation of m_y and b equal to one. Therefore, the load calculated is 4.64 kN , for this load values are

$$b=0.78, m_y=0.22, m_x=.32 \text{ and } p=0.1$$

Using the same procedure described above m_{xA} calculated which is 0.49,

Since $m_x < m_{xA}$ and the summation of m_y and b are 1 it means load has reached the yield surface.

APPENDIX-E

E.3.1 Comparison theory (Chapter 4) with limit load

Experiment 2

It is known that

$$b=0.51, m_y=0.44, m_z=0.60$$

To determine the point of formation of a hinge, it is first required to determine m_{zA} .

Using the procedure described in Appendix-D m_{zA} calculated to be 0.45. As m_{zA} is less than m_z therefore yielding is to be checked

Based on the given value of $b=0.51$ take $m_y=0.44$ using Equations 4.40(b) and 4.40(d) and assuming minor moment in the web as zero. givesso that their summation equal to 1.

Using Equation 4.40(b) and (d) and not considering minor moment in the web gives

$$m_{y3}=0.475$$

$$m_{y1}=0.035$$

From Equation 4.37(b) now calculate

$$P_3=0.068$$

$$P_1=0.295$$

Using Equation 4.40(a) P_2 can be calculated as

$$P_2=-0.227$$

Therefore using Equation 4.37(b) for the web

$$m_{z2}=0.15$$

Using Equation 4.40(c) ignoring m_z' , yield

$$m_z = .61$$

Since $m_z = m_z$ calculated it means the point has reached the yield surface.

Experiment 3

$$b = 0.47, m_y = 0.33, m_z = .47, p = .1$$

Using the same procedure calculated to be .76, which shows that the finite element has not reached the yield surface at that loading.